

dc_301_11

MTA Doktora Pályázat

Tézises összefoglaló

**A májregeneráció és a daganatos áttétképzés tanulmányozása morfológiai
vizsgáló módszerekkel**

Paku Sándor

2011

TARTALOMJEGYZÉK

1. Bevezetés	3
2. Célkitűzések	6
3. Anyag és módszer	7
3.1. Állatkísérletek.....	7
3.2. Morfológiai módszerek.....	7
4. Eredmények és megbeszélés	9
4.1. Májregeneráció	9
4.1.1. A máj epeútszervejének szerkezete és immunfenotípusa (I,II).....	9
4.1.2 Májregeneráció hepatektómiát követően (III).	10
4.1.3. Májregeneráció a máj őssejtjeinek részvételével (I, IV-VII).	12
4.2. Tumor indukált angiogenezis (VIII, IX).....	18
4.2.1. Angiogenezis primer tumorokban	20
4.2.1.1. Melanómák vaszkularizációja (X).....	20
4.2.1.2 Az intusszusceptív angiogenezis egy új mechanizmusa (XI).....	22
4.2.2. Angiogenezis metasztázisokban	23
4.2.2.1. Glomeruloid testek kialakulása kísérletes agymetasztázisokban (XII).....	23
4.2.2.2. Angiogenezis vizsgálata kísérletes agymetasztázisokban (XIII).....	24
4.2.2.3. Májmetasztázisok vaszkularizációja (XIV).....	26
4.2.2.4. Májmetasztázisok vérellátásának vizsgálata (XV, XVI).....	29
4.3. Metasztázisképzés	32
4.3.1. Sejtmigráció (XVII).....	32
4.3.2. Extravazáció és szervpreferencia (XVIII, XIX).....	35
5. Új eredmények	42
6. Az értekezéshez felhasznált saját közlemények	45
6.1. Májregeneráció	45
6.2. Angiogenezis	46
6.3. Sejtmozgás, szervpreferencia	47
7. Irodalom	49
8. Köszönetnyilvánítás	54

1. Bevezetés

A biológiai rendszerekben a struktúra és a funkció szerves egységet alkot. A szövetek, szervek struktúrájának meghatározásában döntő szerepe van az extracelluláris mátrixnak, ezen belül is a bazális membránnak, mely kompartmentekre osztja fel a szöveteket, szerveket és a parenchimális sejtek differenciált állapotának fenntartásáért is felelős (1). Ugyan a morfológiai vizsgáló eszközök használata önmagában is hozzájárulhat a biológiai folyamatok jobb megértéséhez, a morfológiai vizsgálatok lényege, hogy az egyes molekuláris elemeket képes hozzárendelni a strukturális elemekhez. A fiziológiás és patológiás folyamatok megismeréséhez elengedhetetlen a strukturális elemek és a hozzájuk rendelt molekulák változásának nyomon követése. A molekuláris biológiai módszerek előretörésével azonban a morfológiai vizsgálatok érdemtelenül a háttérbe szorultak. Kiterjedt morfológiai vizsgálatok hiányában azonban a túlzott általánosítások csapdájába eshetünk, mely a nagy ráfordítással kidolgozott molekuláris terápiák hatékonyságát jelentősen csökkentheti. Ennek a szemléletnek a példái az angiogenezis kutatás témaköréből azok a nézetek, melyek szerint az érképződés domináló formája minden szövetben, szervben a bimbózó („sprouting”) angiogenezis, illetve hogy a daganat ereinek struktúrája alapvetően különbözik a normál erek struktúrájától (2,3). Ezek az egyszerűsítések összefüggésben lehetnek az anti-angiogenezis terápiák nem megfelelő hatékonyságával (4-6). Mint az alábbiakban majd láthatjuk, a kép sokkal árnyaltabb, igazán hatékony terápiák kidolgozásához elkerülhetetlen lesz az egyes célszervek és az azokban növekvő különböző daganatokban lezajló folyamatok részletes morfológiai vizsgálata.

Az alábbiakban két eltérő területen (májregeneráció és daganatos áttétképzés) tett megfigyeléseink alapján szeretnénk rámutatni a morfológiai vizsgálatok fontosságára.

A máj kitűnő regenerációs képessége régóta jól ismert (7). A klasszikus és alaposan tanulmányozott, patkányokon kialakított modellben a máj 2/3-ának eltávolítása után a májtömeg 7-10 nap alatt teljesen regenerálódik. Ez az egyik legtöbbet tanulmányozott in vivo, intenzív sejtproliferációval járó nem daganatos növekedési reakció. A regeneráció a megmaradt lebenyek sejtjeinek, döntően a hepatocitáknak a kompenzatórikus hiperpláziája révén valósul meg, tehát az eltávolított lebenyek nem nőnek vissza.

Az elmúlt két évtizedben a májregeneráció alternatív, „tartalék” mechanizmusaira derült fény. Ha a májsejtek proliferációja gátolt, akkor új májsejtek az őssejtek aktiválásával és az úgynevezett ovális sejtek közbeiktatásával keletkeznek. Az utóbbi években a kutatás homlokterébe került a hemopoetikus őssejtek segítségével lezajló szövetregeneráció. Bár számos közlemény igazolni látszik, hogy a hemopoetikus őssejtek transzdifferentiálódhatnak közvetlenül, vagy ovális sejtek közbeiktatásával májsejtekké, a folyamat hatásfoka nagyon alacsonynak bizonyult. Magát a transzdifferentiáció folyamatát is több szerző kétségbe vonja, hiszen kimutatták, hogy a legtöbb esetben csak sejtfúzióról van szó (8,9). A hemopoetikus őssejtek segítségével lezajló regeneráció jelentősége azért is megkérdőjelezhető, mivel mint fentebb láthattuk, maga a máj is több regenerációs mechanizmussal rendelkezik, melyek a körülményektől függően aktiválódnak (8).

A fentiek alapján látható, hogy a máj őssejtjeinek lokalizációja és fenotípusa nem ismert, tehát ezeknek a meghatározása nagyon fontos lenne ezen sejtpopuláció későbbi terápiás hasznosíthatóság szempontjából.

A malignus tumorok legjellemzőbb tulajdonsága, hogy növekedésük során távoli áttéteket képeznek. (10,11). Legtöbb esetben ez vezet a különböző malignus betegségekben szenvedő beteg halálához. A metasztázisképzés folyamatát több, egymástól többé-kevésbé elkülöníthető, de egyenként igen bonyolult lépésre oszthatjuk.

- 1/ Tumor növekedés, tumorsejt leszakadás, szövetinvázió
- 2/ Angiogenezis
- 3/ Intravazáció
- 4/ Kölcsönhatás a vér alakos elemeivel és oldott alkotórészeivel
- 5/ Mechanikus vagy specifikus elakadás/kitapadás a célszerv érrendszerében.
- 6/ Extravazáció

A metasztázisképzés folyamata többször is ismétlődhet, így másodlagos illetve harmadlagos metasztázisok is kialakulhatnak. Ezért, bár a tumorok klinikai felismerésekor már legtöbbször mikrometasztázisok vannak jelen, ezen lépések nagyobb részének gátlása megakadályozhatja újabb metasztázisok kialakulását.

A másodlagos és harmadlagos metasztázisok kialakulása nagyrészt úgynevezett generalizációs helyeken keresztül történik, melyek főleg nyirokcsomók, máj és tüdő

lehetnek. A generalizációs helyeket általában az anatómiai viszonyok határozzák meg, mely legtöbbször a vénás illetve nyirokelfolyásnak felel meg. Tumorsejtek azonban átjuthatnak a szervek kapillárisálózatán anélkül, hogy ott elakadnának és áttéteket hoznának létre. A két folyamat eredményeképpen jöhet létre a metasztázisok bizonyos tumorokra jellemző szerveszlása, melynek kialakulását két egymásnak ellentmondó, bár egymást nem kizáró elmélet próbálja magyarázni. Az egyik a "mechanikus" elmélet, mely szerint a primer tumorból elszabadult tumorsejtek az első elért szerv kapillárisálózatában hoznak létre áttéteket, míg a "mag-talaj" teória szerint a tumorsejtek és a célszerv specifikus tulajdonságai határozzák meg a metasztázisok kialakulását és ez független az anatómiai viszonyoktól. Mindkét hipotézist számos humán és állati tumor vizsgálatából származó adat támasztja alá (12,13)

A tumor indukált angiogenezis kettős szerepet játszik a tumorok progressziójában. Az újonnan képződött erek egyrészt tápanyaggal látják el a tumort, másrészt növelik a hematogén úton képződött metasztázisok kialakulásának valószínűségét. Az utóbbi évek kutatási eredményei bizonyították a nyirokér angiogenezis létét is, valamint az újabban elérhető specifikus nyirokér markerek segítségével összefüggést találtak a nyirokérdenzitás és a tumorok metasztatizáló képessége között (14). Az újonnan képződött erek nagyon vonzó terápiás célpontot kínálnak, hiszen az erek genetikailag stabil sejtekből épülnek fel, szemben a tumorokkal (bár újabb eredmények a proliferáló endotélsejtek genetikai instabilitására utalnak), azonban a számos próbálkozás ellenére az anti-angiogén terápia nem váltották be a hozzájuk fűzött reményeket (4-6).

A metasztázisképzés során, elsősorban az epiteliális tumorok esetében ahhoz, hogy a tumorsejtek megtelepedhessenek a célszervben, három bazális membránon kell áthatolniuk (epiteliális bazális membrán, vaszkuláris bazális membrán az intravazáció és extravazáció során), melyet a tumorterjedés legfőbb gátjának tekintenek. A tumorsejtek bazális membránon történő áthatolásának mechanizmusára még mindig a Liotta és mtsai. által korábban felállított háromlépéses hipotézis a legelfogadottabb (15). Eszerint a tumorsejtek specifikus a bazális membrán komponenseit felismerő, főleg integrin típusú receptorokkal tapadnak a bazális membránhoz. Ezután történik meg a bazális membrán emésztése proteolitikus enzimek kaszkádszerűen segítségével, melyet a tumorsejtek migrációja követ.

2. Célkitűzések

Vizsgálataink két nagy kérdéskört ölelnek fel, a májregenerációt illetve a metasztázisképzést. A legfontosabb megválaszolendő kérdéseket az alábbiakban foglalhatjuk össze.

1. Májregeneráció

Milyen a patkány illetve humán máj interlobuláris epeúthálózatának szerkezete és immunfenotípusa?

Hogyan zajlik le a máj szerkezetének helyreállítása májregeneráció során?

Hol helyezkedhetnek el a májregenerációban résztvevő őssejtek?

2. Metasztázisképzés

2a. Tumor indukált angiogenezis

Milyen alapvető angiogenezis formák figyelhetők meg primer tumorok környezetében?

Van-e eltérés az angiogenezis folyamatában különböző szervekben, szövetekben? Befolyásolja-e az angiogenezis folyamatát a tumorok differenciációs foka, a célszerv (bazális membrán) szerkezete?

Hogyan játszódik le a kísérletes májmetasztázisok arterializálódása?

2b. Tumorsejt motilitás és szervpreferencia

Hogyan változnak a tumorsejtek mozgása során a sejtadhéziós helyek és azok komponenseinek eloszlása?

Befolyással van-e a célszerv kapillárisainak szerkezete és extracelluláris mátrix összetétele az extravazáció folyamatára illetve a szervpreferenciára?

3. Anyag és módszer

3.1. Állatkísérletek

A máj epeútrendszerét normál különböző korú patkány illetve humán májajakon vizsgáltuk. A normál máj regenerációját a klasszikus parciális hepatektómia (2/3) modellben vizsgáltuk. Az ovális sejtek szerepét a májregenerációban egy, a Solt-Farber- féle karcinogenezis modell (patkány) módosított változatában vizsgáltuk, mely 2 hetes acetilaminofluorén (AAF) kezeléssel és a kezelés közepén elvégzett parciális hepatektómiából áll.

Az angiogenezis és metasztázis vizsgálatokhoz különböző humán in vitro, valamint egér in vivo fenntartott tumorvonalakat használtunk. Primer tumorokban lezajló angiogenezist a tumorsejtek (B16 melanóma, C38 kolon karcinóma illetve HT25 humán kolon karcinóma) intrakután vagy szubkután oltását követően vizsgáltuk.

Agy metasztázisokban lezajló angiogenezist a tumorsejtek karotiszba (3LL-HH karcinóma, B16, A2058, WM983 melanómák, 293 veserák), vagy direkt az agyszövetbe történő oltását követően vizsgáltuk (ZR-75-1 emlőrák, HT25 kolon karcinóma, H1650 tüdő adenokarcinóma, HT1080 fibroszarkóma).

Májmetasztázisok vaszkularizációját a tumorsejtek lépbe (C38 kolon karcinóma,) történő oltását követően vizsgáltuk. Az arterializáció folyamatát korróziós készítmények segítségével vizsgáltuk (A2058 melanóma, Lewis Lung karcinóma, C38 kolon karcinóma).

A tumorsejtek extravazációjának a vizsgálatához Lewis lung karcinóma sejteket oltottunk farokvénába, szív bal kamrába, és lépbe.

3.2. Morfológiai módszerek

Megfigyeléseink döntő többsége fagyasztott metszeteken illetve sejtkultúrákon elvégzett, immunfluoreszcens vizsgálatokon alapul. A minták analizisét legtöbbször konfokális mikroszkóppal végeztük el, mely lehetőséget adott a detektált jelek háromdimenziós rekonstrukciójára is. A kapott eredményeket normál illetve immun-elektronmikroszkópos vizsgálatokkal egészítettük ki. 3D rekonstrukciót félvékony sorozatmetszetek felhasználásával is végeztünk. A korróziós készítményeket sztereó- illetve szkenningszkennelési elektron mikroszkóp segítségével vizsgáltuk.

dc_301_11

Vinkulin eloszlását a sejtmigráció során élő sejtekben GFP-vinkulin konstrukció transzfekcióját követően vizsgáltuk.

Az ovális sejtek sorsának követését retrovírus jelöléssel végeztük el.

4. Eredmények és megbeszélés

4.1. Májregeneráció

4.1.1. A máj epeúrendszerének szerkezete és immunfenotípusa (I,II).

Mielőtt rátérnénk a májregeneráció tárgyalására vessünk egy pillantást a patkány és humán máj interlobuláris epeúrendszerének szerkezetére és fenotípusára, mert mint látni fogjuk ez a rendszer jelentős szerepet játszik majd a máj összejeteket is mobilizáló regenerációja során.

A Hering csatornák, az epeúrendszer legtávolabbi szakaszai, melyek összeköttetést biztosítanak az epeutak és a hepatociták alkotta epekanalikuskok között. Elnevezésüket leírójukról kapták, aki először figyelt meg olyan rövid, 2-3 sejtsor hosszúságú duktulusokat a májban, melyek alkotásában epeúthámsejtek és hepatociták egyaránt részt vesznek. Egyértelmű azonosításuk csak elektronmikroszkópos vizsgálattal lehetséges.

Patkánymájban ezek a struktúrák a „limiting plate”-en kívül periportálisan helyezkednek el, tehát sosem hatolnak be a parenchimába. Vizsgálataink kimutatták, hogy ezek a struktúrák a CK19+/CK7- immunfenotípust hordozzák. Ugyanakkor a nagyobb interlobuláris epeutak CK19+/CK7+ fenotípusúak. CK19+/CK7- immunfenotípusú epeutak azonban nem találhatóak humán májokban, ebben az esetben minden epeút CK19 illetve CK7 pozitív. A CK7 negatív epeutak sajátos entitását igazolja, hogy míg a CK7 pozitív epeutak mérete a máj hilusa felé fokozatosan növekszik, addig a CK7 negatívaké állandónak adódott, májbeli helyzetüktől függetlenül. A CK7 negatív epeutak több száz mikrométer hosszú kanyarult struktúrák, melyek több helyen kapcsolódhatnak a májsejtekhez. Bár a Hering kanálisok szorosabb definíciójának ezen epeutak nem minden szakasza felel meg, fenotípusuk alapján ez a struktúra az epeúrendszernek egy morfológiai és funkcionális egységét alkotja (I).

Ép, humán májokban is jellemeztük az epeúrendszer legdisztálisabb szakaszát (II). A CK7 immunreakció alkalmas volt az epeutak és a hepatociták egyértelmű elkülönítésére. A CK7-tel jelölt metszetek konfokális mikroszkóppal történő vizsgálata, illetve sorozatmetszetekből számítógép segítségével végzett 3D rekonstrukciós vizsgálatok segítségével megállapítottuk, hogy az ép emberi májokban az epeutak a periportális kötőszövetből kilépve látszólag betérjednek a májparenchimába. Az

infiltráció azonban csak látszólagos, mert az emberi májban is kezdetleges formában jelen vannak a néhány más állatfajban fellelhető jól fejlett interlobuláris vaszkuláris (kötőszövetes) szeptumok, amelynek mentén az epeutak terjednek, azaz intraparenchimálisak, de mégsem lépnek be a lebenykék állományába. Az epeutak közelében NG2 pozitív struktúrák is megfigyelhetők voltak, amely arteriolák jelenlétére utal. A tradicionális, eredetileg leírt Hering csatornák csak ezen epeutak terminális szegmentumának felelnek meg. Ezeknek a hosszú duktulusoknak az egységes, és nagyobb epeutaktól eltérő (EMA-/CD56+/CD133+) immunfenotípusa arra utal, hogy sajátos funkcionális egységet alkotnak.

Különböző életkorú humán és patkány májából származó minták vizsgálatával megállapítottuk, hogy ez az elrendeződés és immunfenotípus az újszülöttek májában még nem alakul ki, hanem posztnatálisan jön létre.

Összefoglalva tehát alapvető különbség van a patkány és a humán máj szerkezetében. Míg patkány májban az epeutak a „limiting plate”-en végződnek, humán májban az epeutak a lebenyke palástja mentén futnak. Ez a különbség hatással van az arteriális rendszer szerkezetére is. Miután az artériális rendszer a májban főleg az epeutak vérellátásáért felelős, a humán májban a szerteágazó és a parenchimába is beterjedő epútrendszert egy ugyanolyan felépítésű artériális rendszer is követi, mely végül a szinuszoidokba ömlik. Ezzel szemben patkány májban az epeutak nem hagyják el a portális teret, ezért az artériális rendszer elvezetése főleg a portális rendszerrel alkotott anasztomózisokon keresztül valósul meg. Az artériális rendszer hasonló szerkezetű egér májban is, melynek részletesebb ismertetésére alább kerül sor. Mind patkány, mind humán májban a kis epeutak morfológiai és funkcionális egységet alkotnak

4.1.2 Májregeneráció hepatektómiát követően (III).

A májszövet legáltalánosabban elfogadott morfológiai alapegysége a lebenyke (lobulus). Az egyes májlebenyek regeneratív növekedése elvileg háromféleképpen történhet meg: a/ a májlebenykék méretének növekedése, b/ új májlebenykék képződése, c/ a két folyamat kombinálódása révén. Meglepő módon napjainkig sem volt tisztázva, hogy a fenti három lehetőség közül melyik történik meg a májregeneráció során. Ennek magyarázata, hogy a máj lebenykéinek mérete meglehetősen nehezen vizsgálható. A májlebenykék egy bonyolult hierarchikus rendszert alkotva építik fel a

májszövetet. Ezen a hierarchián belül a lebenykék mérete változik a hilstól való távolság alapján, továbbá a különböző lebenykék tengelye sem párhuzamos. Ebből adódik, hogy hagyományos szövettani metszeteken a lebenykék méretéről szinte semmi felvilágosítás nem nyerhető. Munkacsoportunk kidolgozott egy új módszert mely lehetővé teszi a májlebenykék méretének objektív vizsgálatát. Azokat a korábbi megfigyeléseket használtuk ki, hogy a/ a májtok alatti lebenykék az említett hierarchiában azonos helyet foglalnak el b/ tengelyük, mely lényegében azonos a centrális vénák legperifériásabb ágával, merőleges a máj felszínére. Ezért ha a hepatikus vénákon keresztül fluoreszcens műgyantával retrográd módon feltöltjük a centrális vénák ágrendszerét és rajtuk keresztül a szinuszoidokat, a máj felszínén megbízhatóan kirajzolódnak a lebenykék határai. A máj felszínéről készített felvételeken a lebenykék tetszőleges paraméterei objektíven meghatározhatók. Módszerünk természetesen csak a felszíni lebenykék méretéről nyújt egyértelmű felvilágosítást, de az említett hierarchikus elrendeződés miatt ez legalábbis tendenciájában tükrözi a mélyben zajló folyamatokat is.

A fenti módszert alkalmazva összehasonlítottuk a máj posztnatális, fiziológiás növekedését a sebészi parciális hepatektómiát követő regenerációval. Megállapítottuk, hogy az egyedfejlődés születést követő fázisában a máj tömegének gyarapodásához új lebenykék képződése és a lebenykék fokozatos növekedése is hozzájárul, ez utóbbi folyamatban pedig szerepe van a hepatociták megnagyobbodásának is. A regeneratív növekedés során viszont kizárólag a már meglévő lebenykék mérete növekszik, új lebenykék nem képződnek és a hepatociták sem képesek további megnagyobbodásra. A regeneráció eredményeként megnagyobbodott lebenykék viszont bonyolultabb szerkezetűek. Ez tükröződik az egy centrális vénát körülvevő portális vénaágak számának megnövekedésében, továbbá abban, hogy különböző zonális megoszlást mutató enzimek (pl. CYP450IIE1, glutamin szintetáz) a szokásos koncentrikus elrendeződés helyett karéjzotot mutatnak. Feltételezésünk szerint ezen utóbbi szerkezeti változások oka, hogy az ideális porto-centrális távolság ne növekedjen jelentős mértékben a lebenykék megnagyobbodása következtében.

4.1.3. Májregeneráció a máj őssejtjeinek részvételével (I, IV-VII).

Az őssejtek részvételével lezajló májregenerációt az úgynevezett AAF/Ph modellben vizsgáltuk, melynek lényege, hogy AAF kezelés hatására a hepatociták osztódása gátolt, aminek következtében a parciális hepatektómiával kiváltott proliferációs stimulus hatására őssejtek aktiválódásával zajlik le a regeneráció. Proliferáló ovális/progenitor sejtek - az őssejtek leszármazottjai - szaporodnak fel a májban és később májsejteké differenciálódnak. Az őssejtek lokalizációja a májban, fenotípus markerük nem lévén, pontosan nem ismert. A legtöbb adat arra utal, hogy az őssejtek az epeutak és a hepatociták között elhelyezkedő speciális képletek a fentebb jellemzett Hering csatornák sejtjei között található. Más elképzelések szerint az epeúrendszer összes sejtje rendelkezik őssejt tulajdonsággal. Novikoff és mtsai. (16) szerint szintén a terminális epeutakban található, de a bazális membránhoz nem kitapadt primitív sejtek lennének a máj őssejtjei. Ezekkel szemben olyan elképzelések is napvilágot láttak, hogy az ovális sejtek a periportális térben elhelyezkedő nem jellemezett sejtek, illetve csontvelőből származó őssejtek leszármazottjai lennének (17).

A következőkben az őssejtek lokalizációjának meghatározására vonatkozó vizsgálatainkat ismertetjük. Azt már korábban tapasztalták, hogy bár az ovális sejtek portális térből történő kivándorlása csak a hepatektómiát követően kezdődik meg, a sejtproliferáció a portális térben már két AAF kezelést követően megindul. A proliferáló sejtek pontos lokalizációja azonban nem volt ismert. Vizsgálatainkban immun-elektronmikroszkópia segítségével állapítottuk meg a brómdeoxiuridint (BrdU) inkorporáló sejtek pontos elhelyezkedését. Összehasonlításképpen epeútlekötésen átesett állatok máját is vizsgáltuk, mivel ebben az esetben a lezajló epeút proliferáció nem jár ovális sejtek megjelenésével, tehát őssejt aktivációval sem. Megállapítottuk, hogy két AAF kezelést követően a legnagyobb arányban a Hering kanálisok sejtjei proliferáltak szemben az epeút lekötéssel, ahol a nagyobb epeutak sejtjei voltak többségben a proliferáló sejtek között **(IV)**. Ez a megfigyelés azt támasztotta alá, hogy az őssejtek a Hering kanálisok sejtjei között helyezkednek el. A Hering kanálisok azonban a definíció szerint, mindössze a májsejtekhez kapcsolódó és bazális membrán által félkör alakban körülvett néhány sejtből álló struktúrák, melyek valószínűleg nem tartalmazznak annyi őssejtet amennyi a máj teljes regenerációjához

szükséges. A fentebb ismertetett (CK19+/CK7-) epeút kompartment azonban, mely megfelel a legkisebb terminális epeutaknak és magában foglalja a Hering kanálisokat is, elegendő őssejtet tartalmazhat a máj regenerálásához. Ezen epeutak sejtjei is nagyobb proliferációs aktivitást mutattak két AAF dózist követően, mint a nagyobb CK7+ epeutak **(I)**. Véleményünk szerint ezek tartalmazzák a legnagyobb valószínűséggel a máj őssejtjeit. Sajnos ez a fenotípus nem volt stabil, tehát nem használható az őssejtek leszármazottjainak követésére, hiszen a proliferáló ovális sejtek expresszálják a CK 7-et. Figyelemreméltó az is, hogy a regeneráció teljes lezajlását követően az ovális sejt-csövek maradványait reprezentáló bazális membránnal körülvett kis epeutakat lehet megfigyelni a patkányok májában, melyek újra az eredeti fenotípust mutatják. Ez arra utal, hogy a CK7+/CK19+ fenotípus (nagyobb mechanikai stabilitás?) megjelenése a növekvő, illetve regenerálódó máj kis epeútjaiban az epeutak intenzív növekedésével illetve a sejtproliferációval jár együtt.

Mint fentebb említettük, ovális sejtek megjelenésére a parenchimában, melyek bizonyítottan a periportálisan proliferáló sejtek leszármazottjai csak az AAF kezelés közepén elvégzett hepatektómiát követően kerül sor. Bár azt már korábban kimutatták, hogy az ovális sejtek a máj epeútrendszerével folytonosságot mutató, elektronmikroszkópos vizsgálatok alapján nem folytonos bazális membránnal körülvett csőrendszert alkotnak, ezen struktúrák pontos viszonya a portális térhez illetve máj parenchimájához ismeretlen volt. Olyan elképzelések is napvilágot láttak, hogy az ovális sejtek egyesével vagy kisebb csoportokban a Disse térben migrálnak, majd beépülnek a hepatociták közé. Mi konfokális mikroszkóp segítségével vizsgáltuk az ovális sejtek és a bazális membrán viszonyát a parciális hepatektómiát követően azon időponttól kezdve, amikor az ovális sejtek már áttörték a „limiting plate”-et. Megfigyeltük, hogy a néhány sejt hosszúságú csövek körül a bazális membrán ugyanolyan „U” formában helyezkedik el, mint a Hering kanálisok körül, amely azt mutatja, hogy az ovális sejt-csövek a Hering kanálisok meghosszabbításai. A csövek az idő előrehaladtával egyre hosszabbak és kanyargósabbak lettek, de végük mindig hepatocitákhoz kapcsolódott, így összeköttetésben maradt májsejtek közötti elemi epeút rendszerrel **(IV)**. Ez a tény nagy jelentőséggel bír, hiszen azt mutatja, hogy az epevezetés és így a szerv funkciója a regeneráció során végig biztosított. Ez kiegészül azzal a megfigyeléssel is, hogy az ovális sejt-csövek a szinuszoidok között helyezkedtek

el arra utalva, hogy növekedésük során a károsodott hepatocita lemez helyét foglalják el, ezzel a szerv vérkeringésének zavartalansága is biztosított. Soha nem figyeltünk meg bazális membrán nélküli CK19-et expresszáló, a kötőszövetben vagy a Disse térben elhelyezkedő sejteket, mely azt jelzi, hogy az ovális sejtek által alkotott csövek növekedése szabályozottan, a sejtek polarizált állapotát megtartva történik. Ezt a tényt szem előtt tartva hasonlóképpen nem tartjuk elképzelhetőnek, hogy a máj őssejtjei az epeútszáron kívül helyezkedjenek el a portális térben, melyet alátámaszt az a megfigyelésünk, hogy nem találtunk citokeratin illetve AFP pozitív sejteket a bazális membránon kívül, sem pusztán az AAF kezelést követően sem az ovális sejt-csövek növekedése során. Ezzel összhangban nem figyeltünk meg bazális membránon átmigráló sejteket sem. Találtunk ugyan a Novikoff által leírt bazális sejtekhez hasonló primitív hemopoetikus sejtekre emlékeztető sejteket a növekvő ovális sejt csövekben, de osztódó alakokat nem találtunk közöttük. Ilyen sejtek nem voltak jelen a Hering kanálisokban illetve a kis epeutakban a két AAF kezelést követően sem **(IV)**. Hemopoetikus sejtekhez hasonló sejtek jelenléte az ovális sejt csövekben felveti annak lehetőségét, hogy ezek a sejtek csontvelői eredetűek és ovális sejtekké transzifferenciálódnak, mint ahogy azt Petersen és munkatársai leírták (17). Ezt a nagyon vonzó lehetőséget alátámasztja az is, hogy az ovális sejtek hemopoetikus őssejt fenotípus jegyeit viselik (c-kit, CD34). Hemopoetikus sejtek ovális sejtekké történő transzifferenciálódását azonban többen kétségbe vonják (6). Az ovális sejtek csontvelői eredetét saját eredményeink is cáfolják **(V)**, hiszen kimutattuk, hogy a csontvelői őssejt markereként ismert Thy-1 molekulát nem az ovális sejtek - mint ahogy azt Petersen és munkatársai leírták-, hanem a bazális membránon kívül elhelyezkedő SMA pozitív miofibroblaszt populáció expresszálja, míg a dezmin pozitív aktivált „stellate” sejtek elenyésző mértékben mutattak Thy-1 pozitivitást. Kollagenáz perfúziót követően izolált ovális sejtekből illetve szövettani metszetekből mikrodisszekált ovális sejtekből izolált RNS-ben valós idejű RT-PCR módszerrel nem volt kimutatható a Thy-1 mRNS, ami viszont jelen volt a miofibroblasztokat is tartalmazó frakcióból izolált RNS-ben, igazolva, hogy a Thy-1 molekula RNS szinten sem termelődik az ovális sejtekben. A Thy-1-et expresszáló sejtek szorosan követik a növekvő ovális sejt csöveket, és a feltételezések szerint növekedési faktorok termelésével segítik az ovális sejtek proliferációját. Szerepük lehet azonban az ovális

sejt- csövek növekedéséhez szükséges extracelluláris mátrix illetve bazális membrán termelésében is, hiszen kimutatták például, hogy a tüdőfibrózis kialakulása során a fibroblasztok által expresszált Thy-1 „shedding”-je következik be (18).

Összefoglalva tehát vizsgálataink eredményeit azt mondhatjuk, hogy a máj őssejtek a Hering kanálisokat is magukba foglaló terminális epeutakban helyezkednek el és hasonlóan más szervek őssejtjeihez (bél, bőr, agy), a bazális membránon nyugszanak (19). Utódsejtjeik (ovális sejtek) polarizált sejtek melyek duktusokat alkotnak és migrációjuk illetve szaporodásuk során folytonos bazális membránt építenek fel.

Az őssejtek részvételével megvalósuló májregeneráció utolsó lépése az ovális sejtek májsejteké történő differenciációja, mely folyamatra vonatkozó vizsgálatainkat ismertetjük az alábbiakban.

Korábbi vizsgálatokból kiderült, hogy az általunk használt modellben az ovális sejtek differenciációja májsejteké függ az AAF alkalmazott dózistól. Eszerint a nagy dózisú AAF gátolta az ovális sejtek differenciációját, míg az AAF alacsonyabb koncentrációja gyors májsejt irányú differenciációt eredményezett. Alaposabban megvizsgálva ezt a jelenséget két különböző típusú differenciációt figyeltünk meg az AAF dózistól függően **(VI)**. Kis dózisú AAF kezelés az ovális sejtek szinte egyidejű differenciációját eredményezte 5-6 nappal a hepatektómiát követően. Ezzel szemben differenciálódó sejtek csak később (11-13. nap a hepatektómiát követően) jelentek meg a májban fókuszokat alkotva és az ovális sejtek nagy többsége nem alakult át májsejteké nagy dózisú kezelést követően. Itt fontos megjegyezni, hogy a portális térből kiinduló ovális sejtes reakció nagysága is függött az AAF dózistól, jelezve, hogy a hepatocita károsodás méretének megfelelően változik az ovális sejtek által létrehozott csövek hossza, vagyis a regenerációhoz szükséges sejtek száma. Nem tudunk magyarázatot adni arra, hogy a nagy dózisú AAF kezelés esetében miért nem differenciálódott az összes ovális sejt májsejtté. Egy lehetséges magyarázat, hogy nagy dózisú AAF valóban gátolja a differenciációt, és az AAF koncentráció csökkenésével bizonyos ovális sejtek gyorsan differenciálódnak és tovább szaporodnak, mely a többi ovális sejt átalakulását már feleslegessé teszi. Felmerülhet az AAF mutagén hatása is, mely a feltehetően klonális proliferációhoz vezet, de ennek ellentmond, hogy az AAF ezen dózisa nem bizonyult karcinogénnek, valamint, hogy ez a folyamat is funkcionális

regenerált májat eredményezett. Ezek után nem meglepő, hogy az ovális sejtek májsejteké történő differenciációja teljesen hasonló módon zajlott le, az eredmény mindkét esetben kis hepatociták megjelenése volt. A kis dózis esetében a kis hepatociták elrendeződése megegyezett az ovális sejtek elrendeződésével, vagyis duktusokat alkottak, melyek a portális terek körül sugár irányban helyezkedtek el. Nagy dózis esetében a kis hepatociták fókuszokba rendeződtek, de ezen belül ebben az esetben is duktusokat formáltak. Mindkét esetben a kis hepatociták által formált duktusok összeköttetésben maradtak a máj epeútrendszerével. A differenciálódás legmarkánsabb jele a bazális membrán eltűnése volt az ovális sejt-csövek körül, amellyel teljesen párhuzamosan történt a HNF-4 α -nak, a májsejtek terminális differenciációját meghatározó transzkripciós faktornak a megjelenése **(VI)**. Közvetlen összefüggés azonban valószínűleg nincs a bazális membrán lebomlása és a HNF-4 α megjelenése között, hiszen a bazális membrán lebomlásának elmaradása és a HNF-4 α megjelenése a nagy dózisú kezelés során gyakran megfigyelt intesztinális metapláziához vezet. HNF-4 α kondicionális mutáns egerek vizsgálata azt mutatta, hogy a HNF-4 α rendkívül sok fehérje expressziójának regulációja mellett közvetlenül felelős a hepatocita funkció ellátását alapvetően meghatározó sejtkapcsoló struktúrák, köztük a connexinek kifejeződéséért (20). Saját vizsgálataink is azt mutatták, hogy a kis májsejtek megjelenése együtt jár az epeút specifikus connexin 43 eltűnésével, illetve a májsejtspecifikus connexin 32 megjelenésével. A kis dózisú differenciálódás esetében lehetett a legjobban megfigyelni a duktusok disztális részén ultrastukturálisan a bazális membrán fragmentálódását, illetve teljes lebomlását, valamint a májsejtekre jellemző sejtoranellumok megjelenését. A bazális membrán eltűnésével párhuzamosan az $\alpha 6$ integrin alegység expressziója is csökkent, amely fehérje a kizárólagosan laminint kötő integrinek alegysége és jelen van a máj epeútrendszerének minden szegmensében. Ezzel szemben a duktuláris struktúrákat alkotó kis hepatociták bazális és laterális részén megjelenik a $\alpha 1$ integrin amely elsősorban kollagént köt és a normál hepatociták jellemző adhézions molekulája **(VI)**. Megfigyeléseinket alátámasztják Sell munkacsoportjának eredményei (21) is miszerint izolált progenitor sejteket bazális membrán mátrixon tenyésztve azok epeút irányú differenciációt mutattak. A bazális membrán lebomlása nem jár együtt a duktuláris szerkezet azonnali felbomlásával és egyelőre nem tudjuk, hogy a normál májsejt gerendák hogyan alakulnak ki. Annyi

azonban bizonyos, hogy a bazális membrán lebomlását követően rögtön megkezdődik az elemi epeutak kialakulása a kis májsejtek között, amit az igen sajátos csillagszerű elrendeződést mutató CD26 expresszió jelez. A differenciálódás során képződő elemi epeutak közvetlen kapcsolatban maradnak az elvezető nagyobb epeutak lumenével, melyet az epeúrendszer fluoreszcens lektinnel való retrográd feltöltésével sikerült igazolnunk.

Összefoglalva a normál és az őssejtek segítségével történő májregenerációra vonatkozó vizsgálatainkat azt mondhatjuk, hogy a regeneráció a máj eredeti szerkezetének felhasználásával zajlik le, új szöveti struktúrák nem keletkeznek.

Az úgynevezett primer hepatocita mitogének előzetes májkárosodás nélkül is jelentős hepatocita hiperpláziát képesek előidézni. Ha a nagy dózisú AAF/Ph protokollal kezelt állatokat primer mitogénekkal kezelünk, (trijódtironin (T3) vagy ólomnitrát) a májsejtek proliferációja elmarad. Ehelyett az ovális sejtek mitotikus aktivitásának fokozódását lehetett megfigyelni, melyet nagyon gyorsan, a kezelést követő 48 órán belül az ovális sejtek jelentős részének hepatocita irányú differenciálódása követett **(VII)**. A differenciálódás folyamata teljesen megegyezett a fentebb leírt alacsony dózisú differenciálódás folyamatával. A hormonkezelt állatok szérumban a bilirubin szint szignifikáns csökkenését, illetve a máj szintetikus funkcióját tükröző protrombin szint emelkedését is meg lehetett figyelni, jelezve, hogy a differenciálódásnak szervezet szintjén is észlelhető májfunkció javulás volt a következménye. Annak igazolására, hogy a májban hirtelen megjelenő „kis” hepatociták valóban az ovális sejtekből származnak, az ovális sejteket a hormonkezelés előtt retrovírussal „jelöltük meg”, mely jelzés később a kis hepatocitákban volt fellelhető.

Eredményeink azt bizonyítják, hogy a máj őssejtek részvételével zajló regenerációja felgyorsítható. Ez a megfigyelés elvi háttérül szolgálhat a klinikai gyakorlatban például fulmináns májelégtelenségben a regeneráció felgyorsítására irányuló próbálkozásokhoz.

4.2. Tumor indukált angiogenesis (VIII, IX)

Mint a bevezetőben említettük az anti-angiogenesis terápiák csak részben váltották be a hozzájuk fűzött reményeket. Ennek egyik oka lehet, hogy a terápiák tervezésekor figyelmen kívül hagyták azt a lehetőséget, hogy a tumorok vaszkularizációja eltérő mechanizmussal játszódhat le különböző szervekben, szövetekben. (VIII, IX).

Az első angiogenesis modellt Folkman és mtsai. dolgozták ki a 70-es évek végén. Megállapították, hogy a tumorok angiogenesis függők, azaz nem képesek növekedni egy bizonyos (1-2 mm) méretnél túl, a tápanyagellátást biztosító új erek képződése nélkül (22). Vizsgálataikban főleg az újonnan, bimbózással („sprouting”) képződött erekre koncentráltak, melyekről feltételezték, hogy azok a tumorsejtek inváziójához hasonlóan növekednek, majd a tumorokba belenőve hozzájárulnak a növekedéshez szükséges tápanyagellátást biztosító érhálózatot. A tumorsejt invázió és az angiogenesis közötti hasonlóság abban áll, hogy az angiogenesis első lépésében is a bazális membrán degradációja következik be, melyet a polarizációjukat veszített endotélsejteknek a kötőszövetbe történő migrációja követ. Az új erek lumenének kialakulására ez a modell semmilyen magyarázatot nem tudott adni. Ezzel szemben mi korábban egy ettől eltérő angiogenesis modellt írtunk le, mely szerint az endotélsejtek megtartják polarizált állapotukat (a sejtkapcsoló struktúrák nem bomlanak fel az endotélsejtek proliferációjának migrációjának megindulásakor) és a bazális membrán lokális degradációja után az endotélsejtek egymással párhuzamosan migrálnak, így az endotélsejtek között azonnal egy résszerű lumen keletkezik, amely folytonos az eredeti ér lumenével. Az éretlen kapilláris növekedése során folyamatosan történik a bazális membrán szintézise és depozíciója. (VIII, IX).

Itt érdemes egy kis kitérőt tennünk, hogy összehasonlítsuk az általunk leírt sprouting típusú angiogenesis valamint májregeneráció során megfigyelt eseményeket. A legfontosabb hasonlóság a két folyamat között hogy a kapillárisok és az ovális sejtek által felépített csatornák növekedésekor résztvevő sejtek dedifferenciációja nem következik be (véleményünk szerint ez a jelenség szövetregeneráció során lezajló biológiai folyamatok egy alapvető törvénye lehet), amiben kulcsszerepet játszik a bazális membránnak a migráló sejtek által történő folyamatos felépítése. A bazális membrán azonban, mint arra több adat is utal nem a polarizáltság kialakulásában,

hanem főleg a differenciált állapot fenntartásában játszik szerepet (1). Ezt alátámasztja, hogy az angiogenezis során a növekvő kapilláris csúcsán migráló endotélsejtek is polarizáltak maradnak, feltehetően az intakt sejtkapcsoló struktúráknak köszönhetően, miközben közvetlen kapcsolatban vannak a kötőszöveti kollagénnel. Eltérés van azonban a két folyamat között abban, hogy a májregeneráció során a növekvő ovális sejt-csővek csúcsán elhelyezkedő sejtek sejtkapcsolókkal kötődnek májsejtekhez (ami ebben az esetben is meghatározza a polaritást), tehát a duktusok növekedési iránya a májgerendák által többé-kevésbé meghatározott. (Ebben az esetben nem is volt megfigyelhető bazális membrán mentes rész a duktusok májsejtekhez kapcsolódó részén, bár meg kell jegyezni, hogy ez a terület kapillárisok esetében is csak maximálisan egy sejt hosszúságú volt). Ezzel szemben a kapillárisnövekedés során, a csúcson elhelyezkedő sejtek a kemotaktikus szignálok érzékelésében játszhatnak kulcsszerepet. Fontos eltérés a két folyamat között az is, hogy míg a májregeneráció esetében a duktusok lumene növekedés során is funkcionális marad, addig az angiogenezis folyamata során a lumen kitágulása és a vérkeringés megindulása csak egy későbbi stádiumban, a periciták megjelenése után következik be. Ennek fő oka lehet, hogy ezen angiogenezis típusban az erek növekedése intersticiális kollagént tartalmazó kötőszövetben folyik, így a réslumen kialakulása a szövet mechanikai ellenállásának minimálisra csökkentését szolgálja.

A malignus tumorok vérellátásáért több, egymástól eltérő mechanizmus is felelős lehet. Ezek közül a talán legjelentősebbnek tartható érbimbózás (sprouting) fentebb ismertetett két angiogenezis modellje azonban csak azon, főként primer tumorok (melanóma, emlő, vastagbélrák) kiindulási helyeként szereplő szövetek esetében érvényes, melyek nagy arányú kötőszöveti kollagént tartalmaznak, ami teret biztosít új kapillárisok növekedéséhez. Az érdenzitás növekedését a fenti tumorok esetében egy másik mechanizmus, az úgynevezett „intussuszeptív” angiogenezis is biztosíthatja, mely valójában a venulák osztódását jelenti, lefolyásának mechanizmusa azonban vitatott.

4.2.1. Angiogenezis primer tumorokban

4.2.1.1. Melanómák vaszkularizációja (X).

Mint fentebb említettük a melanómák vaszkularizációja esetében a bimbózó angiogenezis játszhatja a fő szerepet. Humán melanómák esetében a vaszkularizáltság és a prognózis között összefüggést kereső tanulmányokban már korábban leírták, hogy a tumor szélén az érdenzitás mindig sokkal magasabb, mint a tumorok belsejében. Saját vizsgálataink hasonló eredményt hoztak kiegészítve azzal a fontos megfigyeléssel, hogy a vastagabb tumorok belsejében az erek kerülete szignifikáns emelkedést mutatott a peritumorális szövethez képest. Érdekes módon a metasztázisok kialakulása és a túlélés az intratumorális érdenzitással mutatott szoros összefüggést. Ez a megfigyelés megkérdőjelezi az úgynevezett „hot spot”-ok (23) (különböző tumorok érdenzitásának meghatározására alkalmazott módszer, melyek során kiválasztják a legvaszkularizáltabb régiót a tumorban és azon belül határozzák meg a látótérre eső erek számát) használhatóságát, legalábbis melanómák esetében, a prognózis és az érdenzitás közötti összefüggés vizsgálatára. A humán melanómákban megfigyelt érelaszítás létrejöttének részletesebb vizsgálatára, egy a humán viszonyokat hűen visszaadó egér modellt alakítottunk ki, mely során a tumorsejteket intrakután (ortotopikusan) oltottuk. Az egér melanóma növekedése során is kialakult a tumor alapján a humán tumorokban megfigyelt denz érálózat, melynek sűrűsége a tumor belseje felé csökkent. Az egyes régiók érdenzitásának időbeni változását vizsgálva azt tapasztaltuk, hogy a tumor perifériáján az érdenzitás sokkal gyorsabban növekszik, mint a peritumorális régióban, azt jelezve, hogy a növekvő tumor a bőr eredetileg is meglévő ereit az újonnan képződött kapillárisokkal együtt inkorporálja. Ezt a következtetést alátámasztotta a tumor-stróma határon levő érálózat szerkezetének háromdimenziós analízise is, ami kimutatta, hogy mind a humán mind az egér melanómák esetében a kapillárisálózat a daganat felszínével párhuzamos lefutású, sűrűn egymás mellett elhelyezkedő kapillárisok kötegeiből épül fel. A tény, hogy a daganatok érstruktúrájának vizsgálatokor radiális lefutású, a tumor centruma felé mutató kapillárisokat nem észleltünk, már önmagában bizonyítja, hogy a melanómák elsősorban a peritumorális kapillárisfonat bekebelezésével tesznek szert a vérellátásukat biztosító érálózatra.

Az érdenzítésnek a tumor belseje felé megfigyelt csökkenése elsősorban annak a következménye, hogy a tumor a növekedése során „felhígítja” az inkorporált érhalózatot. Az endotélsejtek proliferációjára vonatkozó vizsgálataink kimutatták, hogy a tumor belsejében az endotél proliferáció kisebb, mint peritumorálisan, ami szintén alátámasztja az érdenzítés ebben a régióban megfigyelt csökkenését. Az érdenzítés csökkenésének egy másik nagyon fontos oka lehet, hogy a tumorban megszűnik az erek bimbózása, ennek következtében az alacsony szintű endotél proliferáció az erek méretének növekedését eredményezi. Az érbimbózás megszűnésének egyik oka, hogy a tumorban (melanómák) nem áll rendelkezésre megfelelő extracelluláris mátrix (kollagén I) a kapillárisok növekedéséhez, illetve a tumorba került erek bazális membrán szerkezetének megváltozása sem teszi lehetővé a bimbózást. Ez utóbbi lehetőségre utalnak azok a megfigyeléseink, melyek szerint a tumor belsejében levő erek tumorsejtek általi folyamatos inváziója zajlik, ami az erek körüli koncentrikusan elhelyezkedő bazális membrán rétegek kialakulásához vezet, feltehetően meggátolva ezzel a bimbózást. A bazális membrán inváziója azonban szerepet játszhat az erek területének megfigyelt növekedésében.

Általánosan elfogadott nézet, hogy az újonnan képződött kapillárisok érési folyamatának fontos eleme a periciták megjelenése az erek körül (24). Pericita borítás nélkül az újonnan képződött kapillárisok regressziója figyelhető meg VEGF illetve PDGF megvonását követően (25). Megfigyeléseink szerint intrakután növekvő melanómák esetében mind a peritumorális mind az intratumorális erek pericita borítása komplett volt. Ez azt jelenti, hogy a bőrben lezajló angiogenezis során, szemben a szubkután tumorok esetében megfigyelt angiogenezissel, a periciták rögtön megjelennek a bimbózó kapilláriskezdemények körül, így érett kapillárisok kerülnek inkorporációra. Bár az általánosan elfogadott, hogy a tumorokban található erek szerkezete nagymértékben eltér a normál erekétől, amit a tumorinváziót elősegítő tényezőnek tartanak (26), eredményeink alapján azonban melanómák esetében ez a jelenség nem lehet az intratumorális érdenzítés és metasztázisképzés közötti összefüggés oka.

4.2.1.2 *Az intusszuszeptív angiogenezis egy új mechanizmusa (XI)*

Megfigyeléseink szerint egerekben növe szubkután oltott kolonrákok esetében az angiogenezis fő formája az intusszuszeptív angiogenezis (érostódás), míg a sprouting (bimbózó) típus alig fordul elő. Ezen daganatok vaszkularizációjának vizsgálata során érdekes jelenséget figyeltünk meg. Venulák lumenében úgynevezett oszlopok („pillar”) voltak jelen, amelyek erre az angiogenezis típusra jellemző struktúrák (27). Eltérően azonban az elfogadott pillar szerkezettől, kezdeti stádiumban ezek az oszlopok nem tartalmaztak kötőszöveti sejteket illetve pericitákat, hanem kizárólag egy kollagén kötegből álltak, melyet endotélsejtek borítottak. Az intusszuszeptív angiogenezis elfogadott mechanizmusa szerint a pillar képződés első lépése az érlumen szemközti falainak benyomódása, mely az endotélsejtek érintkezéséhez, illetve később a sejtkepcsoló struktúrák reorganizációjához vezet. Arra azonban nincs kielégítő magyarázat, hogy mi szolgáltatja az erőt ehhez a folyamathoz. Az elfogadott magyarázat erre a jelenségre, hogy perivaszkuláris sejtek nyomják be az erek falát, ami erősen megkérdőjelezhető, hiszen sejtek csak elenyésző mértékben képesek nyomóerő kifejtésére. Ezzel szemben több százszor akkora húzóerőt képesek kifejteni. Megfigyeléseink szerint azokon a területeken ahol intenzív intusszuszeptív angiogenezis zajlott, mindig megfigyelhető volt az úgynevezett „bridging” is, vagyis endotél hidak voltak jelen az érlumenben. Elképzelésünk szerint ezek az endotél hidak képesek a kötőszöveti kollagén kötegeket az érlumenen áthúzni. Ezt alátámasztja, hogy az oszlopokban található kollagén kötegek mérete szinte teljesen megegyezik a kötőszövetben található kötegek méretével. Ezenkívül számos vinkulint tartalmazó adhéziós pont található a kollagén kötegek mentén, valamint az oszlopot felépítő endotélsejtek nagy mennyiségben tartalmaznak mikrofilamentumokat, mely struktúrák összehúzó erő kifejtésére utalnak. Megfigyelhetők voltak olyan kollagén kötegek is, melyek nem teljesen értek végig az oszlopon, egy részük viszont a kötőszövetben helyezkedett el, ami szintén arra utal, hogy a kötegek a kötőszövetből kerülnek az oszlop belsejébe, nem ott szintetizálódnak. Ultrastrukturális vizsgálatok nem mutattak ki bazális membránt az endotélsejtek és a kollagén köteg között, az endotélsejtek közvetlenül tapadtak a kollagén rostokhoz. Az adhéziós helyek szerkezete különlegesen érdekes volt, mivel az egyes kollagén rostok mentén szabályosan számos elektrondenz adhéziós pont (~50nm) helyezkedett el, melyeket mikrofilamentumok kötöttek össze.

Az oszlopok érése során kötőszöveti sejtek és periciták migrálnak be az oszlopokba, amit új kollagén tartalmú mátrix deposíciója, ezáltal az oszlop méretének növekedése követ, mely folyamat végül az ér osztódásához vezet.

4.2.2. Angiogenezis metasztázisokban

4.2.2.1. Glomeruloid testek kialakulása kísérletes agymetasztázisokban (XII)

A glomeruloid testek kapillárisokból felépülő, jellegzetes érstruktúrák, amelyek nevüket a vese glomerulusaihoz való látszólagos hasonlóságuk alapján kapták. Leggyakrabban a központi idegrendszer primer daganataiban és metasztázisaiban figyelhetők meg. Előfordulnak azonban más szövetek tumoraiban is (tüdő-, prosztata-, emlőrák, melanóma), jelenlétüket pedig összefüggésbe hozták a rossz prognózissal (28). Kialakulásuk pontos mechanizmusa nem ismert, de az erek dilatációja, majd az ezt követő endotél proliferáció, valamint hídképződés, az intusszusceptív angiogenezishez hasonló folyamatra enged következtetni. Legrészletesebben Dvorak és mtsai. foglalkoztak a VEGF-A hatására kialakuló glomeruloid testek vizsgálatával szubkután- és agyszövetben tumormentes környezetben (29). Ők az értágulatot és hídképződést követően az endotélsejtek erőteljes proliferációját figyelték meg az érfalban mely később a sejtszaporulat érlumenbe való expansziójához vezetett. Ebben a fejlődési stádiumban ugyan megfigyeltek néhány kapilláris lument az eredeti ér lumenén belül, de modelljük végül is arra alapozódik, hogy az endotélsejtek elvesztik eredeti polaritásukat és a felszaporodott bazális membrán mátrixban tovább osztódva, a későbbiekben nagyszámú új lument képeznek, melyeket periciták vesznek körül.

Mi a glomeruloid testek kialakulásának egy további, nagyon egyszerű formáját írtuk le agymetasztázisokban (XII). Érdekes, hogy a számos felhasznált különböző eredetű humán és rágcsáló tumor (tüdőrák, melanóma, veserák) megegyező struktúrájú glomeruloid testeket hozott létre. Vizsgálataink kimutatták, hogy a tumorsejtek az extravazációt követően az agykapillárisok bazális membránjához tapadtak és azon kiterültek. Már egyes sejtek estében is megfigyelhető volt az a jelenség, hogy a tumorsejtek által befedett kapilláris szegmenseken először egy, majd több egyszerű csavarulat keletkezett. A tumorsejtek szaporodásuk közben nem távolodtak el a kapillárisoktól, hanem annak mentén terjedtek, illetve több rétegben helyezkedtek el a kapillárisok körül. A mikrometasztázisok növekedése során, a kapillárisokon képződött

hurkok egyre bonyolultabbak lettek és végül kaotikus, a tumorsejt fészkek belsejében elhelyezkedő érgombolyagok alakultak ki. A folyamat magyarázata lehet, hogy a kapillárisok bazális membránjához $\alpha 6$ integrin segítségével tapadó és azon kiterült tumorsejtek aktin citoskeletonja a kapillárisurkok kialakulásához vezető húzóerőt fejt ki. Ezt alátámasztja az a megfigyelésünk, hogy a szomszédos tumorsejt fészkek között levő kapilláris szakaszok sokszor elvékonyodtak, sőt néhány esetben el is szakadtak. A folyamatban nagy szerepet játszhat, hogy az agyszövetben nincs kötőszöveti típusú extracelluláris mátrix, így az agyszövet mechanikai stabilitása kicsi, lehetővé téve a kapillárisok elmozdulását. További érdekessége a folyamatnak, hogy az endotélsejtek proliferációs indexe nem emelkedik, jelezve, hogy sem bimbózó sem egyéb más endotél proliferációt igénylő angiogén folyamat nem zajlik (erre az erek morfológiája sem utalt), az érdenzitás növekedése a tumorban kizárólag az agyszövet meglévő érhálózatának átrendeződésével jött létre.

4.2.2.2. *Angiogenezis vizsgálata kísérletes agymetasztázisokban (XIII)*

A fentiekben ismertettük a glomeruloid testek egy lehetséges keletkezési mechanizmusát, amihez a tumorsejteket az állatok karotiszába oltottuk. A módszer hátránya, hogy nagyszámú mikrometasztázist eredményez, ami gyorsan az állatok pusztulásához vezet. Ezért egy másik kísérletsorozatban a tumorsejteket közvetlenül az agyszövetbe oltottuk, hogy a tumorok elérjék az angiogenezis megindulásához szükséges méretet („angiogenic switch”, 1-2 mm átmérő) (22). Morfometriai vizsgálatok azt mutatták, hogy angiogenezis nem zajlik a peritumorális területeken. Ezzel összhangban angiogenezis egyszerű sebzést követően sem volt megfigyelhető az agyszövetben. A tumorok csupán a meglévő erek bekebelezése által tettek szert saját érrendszerre. Ezek a megfigyelések szöges ellentétben állnak az elfogadott nézettel, miszerint agytumorokban és metasztázisokban valamint érelzáródást követően intenzív angiogenezis tapasztalható a sérülés határterületén. Mindegyik tumor esetében az érdenzitás alacsonyabb, emellett az érátmérő, illetve az ereket alkotó sejtek proliferációja magasabb volt intratumorálisan, mint peritumorálisan. Ez a már fentebb említett jelenségre utal miszerint a tumorok növekedésük következtében az inkorporált érhálózatot folyamatosan „kihígtják”. Negatív összefüggést találtunk a bekebelezett erek száma, valamint az ereket alkotó sejtek proliferációja között, aminek hátterében az

állhat, hogy az alacsony érdenzítésű tumorokban az egyes erek felületének nagyfokú növelésével jön létre a tumor növekedéséhez szükséges érfelület. A differenciáltabb tumorokban, melyek ún. „pushing” típusú növekedési mintázatot mutattak, alacsonyabb volt az érdenzítés, magasabb az erek sejtjeinek proliferációja, szemben az invazív növekedési mintázatú tumorokkal. A tumor differenciációs foka tehát hatással van a vaszkularizáció mintázatára, azaz nyilvánvaló hogy a kompakt szerkezetű (differenciált) tumorok inkorporációs képessége alacsonyabb, mint a lazább szerkezetű differenciálatlanabb tumoroké. A bekebelezett erek amellet, hogy a tumorsejtek eltávolították róluk az asztrocitákat, megtartották normál struktúrájukat. Az ér bazális membránjával létrejött kapcsolat az emlőkarcinóma sejtek differenciációjához vezetett. A tumor szélén a parenchimában mintegy „úszó” izolált sejtek az erek bazális membránjával való kölcsönhatást követően mirigyszerű struktúrákba szerveződtek apikális felszínükön klaudin 3-t és EMA-t expresszáltak, míg bazális felszínükön laminin5-öt tartalmazó extracelluláris mátrixot szekretáltak, ami az agykapillárisok bazális membránjának felszínéhez kötődött.

Az intussuszceptív angiogenezishez rendkívül hasonló folyamat volt megfigyelhető a fibroszarkóma sejtvonala agymetasztázisaiban. A tumorsejtek érfalhoz tapadása ismeretlen módon az érlumen kettéosztását eredményezte, és az így kialakult üreket tumorsejtek töltötték meg. Az érhálózat ilyen formában történő átrendeződése azonban nem tekinthető igazi angiogenezisnek, mivel a folyamat a tumorsejtek aktivitásától függ. Érdekes módon sem a sejtvonalak fehérje szintű VEGF expressziója, sem az intratumorális VEGF mRNS szintje nem mutatott korrelációt az intratumorális erek sejtjeinek proliferációjával. Mindemellett az emelkedett növekedési faktor receptor szintek (VEGFR1, PDGFR β , Tie-2) kapcsolatban állhatnak az erek sejtjeinek megnövekedett proliferációjával, illetve a bekebelezett erek struktúrájának stabilizációjával.

Ezek az adatok arra utalnak, hogy kísérletes körülmények között az agymetasztázisok növekedéséhez nem szükséges bimbózó (sprouting) angiogenezis.

4.2.2.3. Májmetasztázisok vaszkularizációja (XIV)

A máj a metasztázisképzés egyik leggyakoribb célszerve. Vermeulen és mtsai. három különböző kolorektális karcinóma metasztázis típust írtak le: „replacement”, „pushing” és „desmoplastic” (30). Az első metasztázis típusnál a tumor növekedése során a máj szinuszoidális szerkezete többé-kevésbé megtartott, de a májsejtek helyét tumorsejtek foglalják el. A második és harmadik típusú metasztázis növekedése során a máj szerkezete torzul, a tumorsejtek komprimálják a májszövetet, illetve nagy mennyiségű kötőszövet halmozódik fel a metasztázisok perifériáján.

A „pushing” típusú metasztázisok vaszkularizációjára egy új mechanizmust írtunk le a C38 egér kolonrák tumorvonal esetében (XIV). A májszinuszoidokba bejuttatott tumorsejtek szolid fészkeket képeztek, mely struktúrák avaszkulárisak maradtak, amíg méretük el nem érte az 500-600 μm -t. A tumorok felszínén azonban már ekkor megjelentek simaizom aktint kifejező sejtek, és megkezdődött a szinuszoidok kapillarizációja (fenesztrációk számának csökkenése, $\alpha 6$ integrin megjelenése, emelkedett laminin depozíció). A simaizom aktint kifejező sejtek megjelenésével párhuzamosan a májsejtek eltűntek a tumor felszínével szomszédos szinuszoidok közül („hátraléptek”), amelynek következtében szinuszoidok fúzióját lehetett megfigyelni. Ez a folyamat egy fordított intusszuszeptív angiogenezisnek is tekinthető. Később a simaizom aktint expresszáló sejtek teljesen körbevették a fuzionált szinuszoidokat. Ezek a sejtek azonban nem tekinthetők pericitáknak mivel nem voltak közvetlen kapcsolatban az endotélsejtekkel és bazális membrán sem volt megfigyelhető körülöttük.

Felmerül annak a lehetősége is, hogy a kontraktilis sejtek megjelenésének oka a növekvő metasztázisok által okozott nyomásnövekedés lenne. Ezt alátámasztja azon megfigyelésünk is, hogy epeútlekötést követően két nappal is hasonló sejtek jelennek meg a proliferáló epeutak körül. A simaizom aktin pozitív sejtek egyrészt elhatárolják a metasztázist a környező májszövettől, másrészt biztosítják, hogy a keletkezett „sérülés” mérete a lehető legkisebb maradjon. Érdekes, hogy a tumor felszínének közelében sem apoptotizált sem nekrotizált májsejteket nem tudtunk megfigyelni, ami arra utal, hogy a májsejtek feltehetően a tumor nyomása valamint a simaizom aktint kifejező és intersticiális kollagént szintetizáló sejtek felszaporodása következtében szorultak ki erről a területről.

A tumor szferoidoknak csak a felszíni 100 µm-es rétegében voltak élő tumorsejtek. Az egyre növekvő méretű centrális nekrosis feltehetően megakadályozta, hogy a tumor továbbra is gömb formában növekedjék, amely végül azt eredményezte, hogy a tumorban jellegzetes szerkezetű invaginációk keletkeztek. Az invaginációkat kívülről a tumor bazális membránja határolta, ennek közvetlen közelében a simaizom aktint expresszáló sejtekbe ágyazott fuzionált szinuszoidok helyezkedtek el, legbelül pedig májsejtek voltak találhatóak. Érdekes, hogy ezen májsejtek között szinuszoidok nem voltak megfigyelhetők, ami tovább erősíti annak lehetőségét, hogy a májsejtek kimigráltak a szinuszoidok közül és az invaginációk közepén torlódtak fel. Kezdetben annak a lehetőségét is felvetettük, hogy a májsejtek epiteliális-mezenchimális átalakulása következik be, és ez vezet a májsejtek eltűnéséhez, valamint a simaizom aktint expresszáló sejtek megjelenéséhez a tumor perifériáján. Számos közlemény bizonyítja ugyanis, hogy például vese- illetve tüdőfibrosis esetében ez az átalakulási folyamat lezajlik. Tüdő esetében in vitro és in vivo is kimutatták, hogy II. típusú pneumocitákban egyszerre lehet jelen az epiteliális eredetre utaló TTF-1 magi transzkripciós faktor és a mezenchimális átalakulásra utaló simaizom aktin (31). Mi nem tudtunk azonosítani olyan sejteket, amelyek egyszerre expresszálták volna egy májsejtspecifikus transzkripciós faktort (HNF-4) illetve a mezenchimális eredetre utaló simaizom aktint, ezért inkább azon egyszerűbb magyarázatot fogadtuk el, hogy a simaizom aktint expresszáló sejtek vagy a máj miofibroblasztjainak vagy aktivált Ito sejteknek felelnek meg, míg a májsejtek eltűnését más okok („hátralépés”) magyarázhatják.

Az invaginációknak a tumor centruma felé eső részén azonban már csak ritkán voltak májsejtek megfigyelhetők, itt a kapillárisok centrális pozíciót foglaltak el. Az invaginációk mélyülésével párhuzamosan feltehetően a tumor által kifejtett nyomás is nőtt, főleg az invaginációk alapjára, ami végül ahhoz vezetett, hogy az invaginációk belső része részlegesen elvált a környező májszövetből. A folyamat végül kötőszövetes oszlopok kialakulásához vezetett a tumorszövetben. Ezen oszlopokban, melyeket a tumor bazális membránja határol, simaizom aktint kifejező sejtek, nagy mennyiségű újonnan szintetizált kötőszöveti kollagén, valamint egy centrálisan elhelyezkedő kapilláris található. Kialakulásukhoz azonban szükség volt a tumor bazális membránjának úgynevezett „back-to-back” fúziójára, melyet humán kolorektális

karcinómák esetében írtak le először (32). A képződött oszlopok azonban tengelyirányban összeköttetésben maradtak a máj szinuszoidális rendszerével, ami a vérkeringés fennmaradására utal. Ez a jelenség azt is sejteti, hogy a metasztázisok vérellátása szinuszoidális, tehát főleg vénás eredetű.

Hasonlóan a korábban Lewis lung karcinóma esetében leírtakhoz **(IX)**, a C38 kolonrák esetében sem figyeltünk meg a tumorok közvetlen közelében elhelyezkedő szinuszoidokban emelkedett endotél proliferációt, ami kizárja, hogy érbimbózás folyna ebben a régióban. Tekintve azonban a máj szinte maximális vaszkularizáltságát, megfelelő tér sem áll rendelkezésre az ilyen típusú angiogenezishez. Érdekes azonban, hogy mindkét tumor esetében megindult az endotélsejtek proliferációja az inkorporációt követően, bár a kialakult érszerkezet teljesen eltérő volt. A kolon karcinómában található oszlopokban felhalmozódott kötőszövet már elég teret biztosított a „sprouting” típusú angiogenezis beindulásához is.

Vizsgálataink arra utalnak, hogy a tumor differenciációs foka hatással lehet a májmetasztázisok vaszkularizációjára. Alacsonyan differenciált tumorok „replacement” típusú növekedést mutatnak. Erre jó példa a Lewis lung karcinóma általunk korábban leírt szinuszoidális típusú metasztázisainak vaszkularizációja, melynek során a tumorsejtek a szinuszoidális bazális membránok mentén, a Disse térben migrálnak és leválasztják az endotélsejteket saját bazális membránjukról, aminek következtében kanyarulatós érrendszer alakul ki a metasztázisokban **(IX)**. Differenciáltabb tumorok „pushing” típusú növekedést mutatnak. Az érhálózat kialakulásában mindkét típusú növekedés során nagy szerepet játszik a módosult (füzionált) májszinuszoidok inkorporációja, mely a primer melanómák és az agymetasztázisok esetében megfigyelt jelenségekkel együtt arra utal, hogy a gazdaszövet meglévő ereinek inkorporációja, függetlenül a gazdaszövettől, alapvető szerepet játszik a tumorok vaszkularizációjában.

Véleményünk szerint a kolon karcinóma esetében lezajló vaszkularizáció egy általános érvényű, minden a májban növekvő differenciált tumorra alkalmazható modell lehet, az oszlopokat felépítő és a kötőszöveti kollagént szintetizáló simaizom aktint és fibronektin receptort expresszáló sejtek jelenthetnek egy új terápiás célpontot. A kolon karcinómában található oszlopokat felépítő simaizom aktint expresszáló sejtek nem tekinthetők pericitáknak, valamint a Lewis lung karcinóma metasztázisainak

érhálózata is pericita sőt bazális membrán mentes volt, aminek terápiás vonzata is lehet, hiszen kimutatták, hogy a pericita borítás nélküli éretlen erek érzékenyebbek a különböző angiogenezis ellenes terápiákra (25).

4.2.2.4. *Májmetasztázisok vérellátásának vizsgálata (XV, XVI)*

A májmetasztázisok kezelésének napjainkban is elfogadott módszerei (intra-arteriális kemoterápia, embolizáció) azon az elven alapulnak, hogy vérellátásuk artériás eredetű (33). Olyan közlemények is napvilágot láttak azonban, melyek a portális véna szerepét hangsúlyozzák a májmetasztázisok vérellátásában (34). Korábban leírtuk a vaszkularizáció egy lehetséges folyamatát Lewis lung karcinóma esetében **(IX)** ami a fentebb ismertetett „pushing” típusú metastázisok vaszkularizációja során tett megfigyeléseinkkel együtt azt mutatta, hogy a metastázisokban található erek közvetlen kapcsolatban vannak a szinuszoidokkal. Ez a jelenség azt sugallja, hogy a metastázisok vérellátása szinuszoidális eredetű tehát a tumorok döntő többségükben kevert vért kapnak. Ezen megfigyelések lehetséges hatását a májmetasztázisok kezelésére egy levélben összegeztük, hangsúlyozva a portális rendszer szerepét a kemoterapiás szerek májmetasztázisokba történő eljuttatásában, mely közlésére sor is került, de a leírtak nagyobb visszhangot nem kaptak **(XV)**.

Három tumorvonal esetében végeztük el a májmetasztázisok vérellátásának vizsgálatát **(XVI)**. (Lewis lung karcinóma, C38 kolon karcinóma, A2058 humán melanóma). Miután a három tumor különböző növekedési mintázatot mutatott kísérleteink során arra is választ kaptunk, hogy a tumor invazivitása milyen módon befolyásolja a metastázisok vérellátását.

Normál egér mikrovaszkulaturájának vizsgálata megmutatta, hogy nagyszámú anasztomózis található az artériás és a vénás rendszer között, valamint hogy az artériás rendszernek minden lebenykehez általában egy csatlakozópontja van, mely a lebenyke alján helyezkedik el. Ezek a csatlakozópontok megtalálhatók mind a nagy portális ágak mentén, mind a periférián elhelyezkedő lebenyek esetében. A korróziós készítményeken az artériákból a szinuszoidokba ömlő vér piramis formájú struktúrák alakjában jelenik meg, melyeknek csúcsa a centrális véna felé mutat. Hasonló struktúrákat írtak le korábban a portális rendszer feltöltése során, amelyeket mikrocirkulációs alegységeknek neveztek el (HMS, Hepatic Microcirculatory Subunit)

(35). Ennek alapján, a megfigyelt struktúrákat arteriális mikrocirkulációs alegységnek neveztük el (aHMS). Az arteriális HMS azonban egy virtuális alegység, nem szabad tehát figyelmen kívül hagyni azt, hogy bár ezek a struktúrák az arteriális rendszernek szinuszoidokkal való közvetlen kapcsolata révén jönnek létre, ezek is kevert vért tartalmaznak. Elhelyezkedésük azt mutatja, hogy lebenykének csak egy "szelete" kap emelkedett oxigén koncentrációjú artériás vért, ami egyrészt megkérdőjelezi az artériás vér szerepének jelentőségét májsejtek ellátásában, másrészt arra is utal, hogy ezek a struktúrák csak az epeutak által elhasznált vér vénás rendszerbe történő eljuttatására szolgálnak.

A májmetasztázisokat vizsgálva azt tapasztaltuk, hogy a metasztázisok növekedésük során új erek képződése helyett a szinuszoidok fúzióját váltják ki (mely folyamatot az előző fejezetben ismertettünk), és ezek inkorporációja során alakul ki a tumorok érhálózata, függetlenül attól, hogy a tumor milyen növekedési mintázatot mutat. A folyamat során az arteriális HMS-ek szinuszoidjainak fúziója is bekövetkezik, ami végül az artériás rendszert határoló struktúrák destrukciójához és a metasztázisok arterializálódásához vezet. A metasztázisok elméletileg tehát egy lebenykének megfelelő méret elérése után már arterializálódnak. Adataink szerint azonban a metasztázisok 95%-a csak a 2mm-es méret elérése után arterializálódik, de ebben eltérések mutatkoznak a tumorok növekedési mintázatának és a növekedési sebességének megfelelően. Differenciált és/vagy lassan növekvő tumorok később arterializálódnak, de 2,5mm-es méret felett minden metasztázis elsődlegesen artériás ellátású. Az artériás ellátás kialakulása együtt jár a tumorba vezető artériák kitágulásával. Érdekes, hogy az 1,8 mm átmérőnél kisebb metasztázisok 85-95%-át egyetlen artéria látja el és ezek az artériák nagyrészt a metasztázis centrumában helyezkednek el. Ennek a jelenségnek a hátterében feltehetően az áll, hogy a növekvő tumorok nem képesek, szemben a portális és centrális rendszer ágaiival, a nagynyomású arteriális ágakat komprimálni illetve a tumor perifériájára szorítani. A metasztázis tágult véredényrendszere, amelyben feltehetően az arteriális nyomáshoz közeli nyomás uralkodik (prekapilláris záróizom szinuszoid fúzió során történő destrukciója) tulajdonképpen egy söntöt képez az artériás és vénás (centrális) rendszer között. A fenti eredmények azt mutatják, hogy korábbi nézetünket felülvizsgálni szükséges, mert annak ellenére, hogy a máj szinuszoidális rendszere és a tumor vaszkulaturája

között közvetlen kapcsolat van, a metasztázisok nem portális (szinuszoidális) ellátásúak. A szinuszoidok fúziójuk következtében csak a metasztázis véredényrendszerének kialakításában játszanak szerepet az arteriális HMS-ek inváziója elengedhetetlenül már nagyon korán a metasztázisok arterializációjához vezet. A metasztázis centrumában elhelyezkedő artéria következtében a vér feltehetően a metasztázisból kifelé a centrális vénák felé áramlik. Az intra-arteriális kemoterápiák létjogosultsága tehát megkérdőjelezhetetlen.

Összefoglalva, tumor indukált angiogenesis tanulmányozása során tett megfigyeléseinket, azt mondhatjuk, hogy hatásos anti-angiogenesis vagy anti-vaszkuláris terápiák csak akkor lesznek kialakíthatók, ha minden fontos célszerv esetében sikerül feltérképezni az alapvető ereződési típusokat.

4.3. Metasztázisképzés

4.3.1. Sejtmigráció (XVII)

A tumorsejtek motilitási képessége alapvető szerepet játszik a metastázisok kialakulásában (36). A tumorsejteknek jelentős távolságot kell leküzdeniük, míg a primer tumorból eljutnak az első vér- vagy nyirokérig, ahol aztán át kell hatolniuk az érfalon (intravazáció). A célszervbe eljutva a kitapadás után újabb migráció, a kapilláris falon való áthatolás történik meg (extravazáció), végül a tumorsejt megtelepszik a célszerv kötőszövetében. Mint a bevezetőben említettük a bazális membránok nagyon fontos szerepet játszanak ezekben a folyamatokban. Számos in vitro kísérleti rendszert dolgoztak ki a bazális membránok inváziójának vizsgálatára. Ezekben a modellekben azonban legtöbbször nagyon vastag bazális membrán komponensekből felépített mátrixot használnak, mely jelentősen eltér a bazális membrán fiziológiás, gyakorlatilag kétdimenziós szerkezetétől. Tekintve a bazális membrán vastagsága és a tumorsejtek mérete közötti jelentős eltérést, in vivo a bazális membrán inváziójának már kezdeti stádiumában más kötőszöveti mátrix elemek is befolyásolni fogják a tumorsejtek viselkedését. A bazális membránok felszíne mentén történő migráció kevesebb figyelmet kapott, pedig a jelenség fontos szerepet játszik a szövetinvázióban és vaszkularizációban.

A sejtek kitapadása az extracelluláris mátrixhoz főképpen integrinek segítségével történik. In vitro ezeket a kitapadási helyeket fokális adhézióknak nevezik, melyek az integrinek erőteljes aggregációja következtében jönnek létre. A membrán citoplazma felőli oldalán található a fokális adhéziók azon komponensei (valamint számos más szignáltranszdukciós elem), melyek az integrinek és az aktin citoskeleton közötti összeköttetést biztosítják (37). A ma elfogadott és a tumorsejtek kétdimenziós migrációjára is érvényes modell szerint a sejtekben keletkező erő párhuzamos a mozgás irányával. Ez a modell azonban számos jelenséget nem tud magyarázni. 1. Tekintve a mozgó sejtek in vitro általánosan megfigyelt legyező formáját, nem világos, hogy mi lesz a sorsa azon nagyszámú adhézióknak, melyek a vezető lamella élén keletkeznek, és mint ismeretes stacionáriusak maradnak a szubsztráthoz képest, miközben a sejt elhalad felettük, hiszen a mozgó sejtek hátsó részén általában csak néhány adhézió található. 2. A sejtek kontraktilitását aktin kötegek biztosítják, melyek polarizáltan a fokális adhéziókban végződnek. A migráció során tehát a sejtek teljesen át kellene rendezni

a citoszkeletonját ahhoz, hogy a sejt elején keletkezett adhéziókhöz tapadó aktin kötegek ellentétes irányultsággal tapadjanak ugyanezekhez az adhéziókhöz, amikor a sejt már elhaladt felettük. 3. A mozgó sejtekben gyakran figyelhetők meg aktin kötegek, melyek a sejt teljes hosszát áthidalják. Az adhézióknak a sejt hátulján történő megszűnésekor a vezető élen található adhézió is szükségszerűen megszűnik, hiszen az adhéziók létének feltétele, hogy a hozzájuk tapadó aktin kötegek feszültség alatt legyenek. Ez a jelenség jelentősen csökkentené a vezető lamella stabilitását.

Létezik azonban egy másik sejtmigrációs modell, melyet hal keratociták migrációjára dolgoztak ki. Ebben az esetben érdekes módon a legnagyobb erők a migráció irányára merőlegesek, de a mérések szerint a sejt mozgásáért kisebb közel sugárirányú erők felelősek. Ezek a sejtek a mozgásuk során félkör alakot vesznek fel melyet hosszabb idejű migráció során is fenn tudnak tartani. A mozgásukra kidolgozott kinematikai modell szerint (Graded Radial Extension, GRE modell) ahhoz, hogy a sejtek a mozgás során félkör alakjukat megtarthassák, minden, a félkörön található pontnak az érintőre merőleges irányban kell elmozdulnia (38). Mivel ez az elmozdulás a sejt csúcsától az átmérő felé haladva a szubsztráthoz képest egyre kisebb, a vezető él minden pontja egy görbe vonalat ír le, míg a sejthez viszonyítva a pontok a sejt csúcsától a sejt egyenlítője felé mozognak.

Humán fibroszarkóma sejtek mozgását vizsgálva bazális membrán mátrix (Matrigél) felszínén egy érdekes jelenségre figyeltünk fel **(XVII)**. Meglepő módon a kiterülést követően a tumorsejtek a hal epidermisz sejtekhez hasonlóan mozogtak. Mozgó sejtek fokális adhézióit tanulmányozva azt figyeltük meg, hogy adhéziók csak a vezető élen, egy-két sorban, félkör alakban, az sejt peremére merőlegesen helyezkedtek el. Ezek az adhéziók tartalmaztak minden, a fokális adhéziókra jellemző komponenst, (vinkulin, talin, FAK, $\alpha 6$ integrin), ami nem támasztja alá az adhéziók korábban feltételezett érési folyamatát a sejtmigráció során.

GFP-vinkulint kifejező humán fibroszarkóma sejtek fluoreszcens video mikroszkópiával történő vizsgálata azt mutatta, hogy az adhéziók a sejtmigráció során a GRE modellnek megfelelően előre és oldalra haladnak, majd elérve a sejt egyenlítői régióját a sejt belseje felé kezdenek csúszni a szubsztrát felszínén, végül eltűnnek a sejtben. Ezzel szemben az adhéziók a vezető élen diszkrét pontok formájában keletkeztek néhány mikrométerre a már meglévő adhéziósor előtt. A mozgó sejtek

aktin citoszkeletonját vizsgálva azt figyeltük meg, hogy a nagyobb aktin kötegek a mozgásirányra merőlegesen, de enyhén ívelt formájúak voltak. (homorú oldaluk mutatott a mozgás irányába). Miután az aktin kötegek a sejt szélén elhelyezkedő fokális adhéziókhoz tapadnak, és azokon keresztül fejtenek ki erőt a szubsztrátra, a megfigyelt ívek összehúzódása nagyon hatékonyan képes előre mozgatni a sejttestet, amihez hozzájárul az is, hogy adhéziók nem voltak megfigyelhetők a sejttest alatt. A mozgás során az aktin kötegek ívelt formája a sejtmag tehetetlenségéből eredő ellenérő következtében alakulhat ki. A modellünk szerint a sejt csúcsán mindig újabb adhéziók és aktin kötegek képződnek, mely utóbbiak folyamatosan nőnek, ahogy a sejt előre halad. Az aktin kötegek elrendeződése arra utal, hogy a szubsztrátra kifejtett erő közelítőleg sugár irányú a vezető élen és ezen erők eredője felelős a sejt mozgásáért. Modellünk egyszerűen képes magyarázni a fibroblasztok mozgására kidolgozott modell által felvetett problémákat. 1. Az adhéziók a vezető élen állandóan újraképződve, GRE modell által megadott utat követve jutnak el a sejt két széléig. 2. Az aktin kötegek irányultságának hirtelen nagymértékű megváltozására nincs szükség, hiszen az adhéziók folyamatosan újraképződnek a vezető élen miközben orientációjuk feltehetően az aktin ívek által kifejtett egyre növekvő erő hatására folyamatosan változik (0-90 fok). 3. Az adhéziók egyszerre bomlanak le egy-egy aktin köteg végén (melyek már elérték a sejt egyenlítői vonalát), melynek következtében az egész aktin köteg is lebomlik. Ez a folyamat nincs hatással a lamella többi adhéziójának és aktin kötegének stabilitására.

A GRE modell, valamint az általunk kidolgozott sejtmozgás modell segítségével összefüggést találhatunk a sejtmozgás és a sejtek kiterülésének („spreading”) folyamata között. A kiterülés során a sejtek kör alakúak (adhéziók csak a sejt szélén figyelhetők meg), az általuk elfoglalt terület nő, tehát a sejt kerületének minden pontja az érintőre merőlegesen mozdul el, ugyanakkor ez az elmozdulás a sejtmozgással szemben minden irányban egyforma. A kiterült sejtekben is hasonló ívelt aktin kötegeket figyelhetünk meg mint a mozgó sejtekben, azonban ebben az esetben az ívek több irányba mutatnak. Az aktin kötegek ívelt formája a többi aktin köteg erejének hatására alakul ki, hasonlóan egy kifeszített tűzoltóponyvához. Az összes ív által kifejtett erő egyensúlyban van, ami rögzíti a sejtmagot és a többi sejtalkotót. A migráció megindulásakor a sejtadhéziók megszűnnek a mozgás irányával ellentétes

oldalon, ami az erőegyensúly megbomlásához és a migráció azonnali megindulásához vezet.

Természetesen ez a modell csak a sejtek kétdimenziós mozgását írja le, ami ebben a formában nem alkalmazható közvetlenül a sejtek háromdimenziós szövetben történő mozgására, egyrészt a sejtek geometriájának másrészt a szubsztrát fizikai tulajdonságának megváltozása miatt. Ezzel összefüggésben Yamada munkacsoportja kimutatta, hogy az adhéziók összetétele különbözik a szubsztrát képlékenységtől függően (39). Merev szubsztrátokon stacionárius sejtekben a sejtek periferiáján elhelyezkedő fokális adhéziókban nincs jelen $\alpha 5$ integrin, mely ezen a szubsztráton a sejtestest alatt található fibrilláris adhéziók komponense, ahol a sejt a fibronectin filamentumokhoz kapcsolódik. Ezzel szemben háromdimenziós gélekben megfigyelt adhéziókban az előbb leírt adhéziók összes komponense jelen van. Miután mindkét adhézióhoz tapadnak a sejtek mozgásáért felelős aktin filamentumok modellünk érvényességét csak az adhéziók, illetve az aktin filamentumok eloszlásának illetve szerkezetének háromdimenziós gélekben történő meghatározása tudná eldönteni. A fibroszarkóma sejtek háromdimenziós, merev szubsztráton történő mozgására vonatkozó előzetes vizsgálataink során azt tapasztaltuk, hogy ebben az esetben is csak egy adhézió sor található a sejtek elején, ami azt sejteti, hogy a modell érvényes lehet háromdimenziós mozgásra is.

4.3.2. Extravazáció és szervpreferencia (XVIII, XIX)

A szervpreferencia problémájának vizsgálatára már a 80-as évek elejétől kezdve próbáltak olyan sejt- és tumorvonalakat kialakítani melyek szervpreferenciát, illetve magas metasztatizáló képességet mutattak. Ezek segítségével számos tényezőt (sejtadhéziót, migrációt illetve proliferációt befolyásoló faktorok) sikerült ugyan azonosítani, de csak néhány olyan fehérjét illetve gént sikerült izolálni, melyek szerepet játszanak a szervpreferencia kialakulásában. A területen végzett kutatásoknak újabb lendületet adhat Ruoslahti és munkacsoportjának kutatási stratégiája, melyben fág könyvtárakban expresszált peptidek különböző szervek endotélsejtjeihez való kitapadását vizsgálják in vivo. Ennek a módszernek a segítségével sikerült izolálni egy emlőráksejtek felszínén található proteint, a metadherint, mely felelős a tüdőmetasztázisok kialakulásáért (40). Sajnos az endotélsejtek felszínén található

ligandját még nem sikerült izolálni. Egyéb, a tüdő- és csontmetasztázisok kialakulását meghatározó receptor-ligand párokat is azonosítottak már, melyek közül a tüdő endotélsejtjeinek felszínén található CD26-nak (a molekula enzimatis aktivitásától függetlenül köti a tumorsejtek felszínén található fibronektint), CLCA-1-nek (klór csatorna fehérje, mely a tumor sejtek felszínén található $\alpha 4$ integrint köti) illetve a CXCR4 kemokin receptor ligandjának a SDF-1-nek a szerepét sikerült bizonyítani a metasztázisképzés folyamatában (41-43). Utóbbi ugyan egy a fehérvérsejtek kemotaxisát befolyásoló faktor, de már korábban kimutatták, hogy a kemokinek által kiváltott endotélsejtekhez történő specifikus kitapadást nem a kemokin grádiense, hanem az endotélsejtek által prezentált szolid fázisú kemokin határozza meg (45).

A tumorsejtek extravazációját tekintve az általánosan elfogadott nézet, hogy azok a limfocitákhoz hasonlóan, tekintet nélkül a célszerv endotélsejtjeinek szerkezetére egy lépésben hatolnak át az endotélsejteken és a bazális membránon. A helyzet azonban ennél sokkal összetettebb, hiszen már a neutrofil leukociták is, mint később látni fogjuk, ettől eltérő módon extravazálnak. A tumorsejtek esetében a helyzet pedig még árnyaltabb, hiszen az irodalomban található adatok szerint különböző tumorvonalak tüdőben történő extravazációját vizsgálva a fentebb említetten kívül a tumorsejtek a kötőszövetbe való kijutásának még legalább háromféle módja ismeretes. Ezek a következők: 1/ a tumorsejtek intravaszkuláris szaporodása, amely folyamat végül az ér destrukciójához vezet, 2/ az endotélsejtek retrakcióját követően a tumorsejttel érintkező bazális membrán számos tumorsejt nyúlvány által történő fragmentációja, amely szintén a kapilláris destrukciójához vezet, 3/ a tumorsejtek endotelizációja (endotélsejtekkel történő befedése) és az azt követő áthatolás a bazális membránon.

Mi a Lewis lung tumorvonal extravazációját vizsgáltuk ultrastrukturálisan, amelynek során kimutattuk, hogy különböző szervekben (máj, tüdő, mellékvese, vese, agy) a tumorsejtek extravazációja eltérő módon (szervspecifikusan) zajlik le **(XVIII)**. A tumorsejtek endotelizációja történik meg tüdőben, májban és részben vesében, míg a tumorsejtek egyszerre hatolnak át az endotéliumon és a bazális membránon a mellékvesében és az agyban. Az endotelizáció folyamatának kezdeti lépésében az endotélsejtek az apikális felszínükről nyúlványokat bocsátanak ki, melyek a tumorsejtek felszínéhez tapadnak. Ezt követően a nyúlványok növekedése valamint az endotélsejtek retrakciója következik be, mely folyamat a tumorsejtek endotélsejtekkel történő teljes

befedéséhez vezet. Ekkor azonban már az endotélsejtek bazális felszíne érintkezik a tumorsejtekkel, jelezve, hogy a nyúlvány növekedése során a tumorsejtekkel kapcsolatban levő plazmamembrán polaritás váltása történik meg (apikális-bazális). Az endotelizáció fentebb ismertetett folyamata arra utal, hogy az endotélsejtek sokkal aktívabb szerepet játszanak az extravazáció folyamatában, mint korábban gondoltuk.

A nyolcvanas évek elején Liotta és munkatársai foglalkoztak a tumorsejtek felszínén található extracelluláris mátrix molekulák metasztázisképzésben játszott szerepével (46). Azt tapasztalták, hogy intravénás oltás előtt a tumorsejteket lamininnal inkubálva a tüdőmetasztázisok száma megemelkedett. Ultrastrukturális vizsgálatokat nem végeztek, így nem ismert, hogy az exogén laminin milyen mechanizmus szerint hatott a tumorsejtek extravazációjára. Ezt annál inkább is fontos lenne tudni, mivel később kimutattuk, hogy a vizsgálatokhoz használt B16 melanóma egy másik variánsának sejtjei endotelizálódnak az extravazáció során (47). Érdekes, hogy az idézett munkacsoport vizsgálatait ez irányban nem folytatta, így eredményeik később feledésbe merültek. Azonban mint fentebb láthattuk a tumorsejtek által termelt extracelluláris mátrix molekulák újabb vizsgálatok szerint is fontos szerepet játszhatnak a metasztázisképzésben hiszen fibronectin és kollagén-I mediálhatja a tüdőmetasztázisok kialakulását az endotélsejtek felszínén található CD26-hoz kapcsolódva. Hogy e folyamat során a tumorsejtek endotelizációja lezajlik-e nem ismert, de újabban kimutatták, hogy neutrofil leukociták is képesek laminin termelésre (48), amely jelentős szerepet játszhat a leukociták extravazációjában, hiszen ismert, hogy ezen sejtek is endotelizálódhatnak a bazális membrán áttörése előtt (49). Saját, még nem publikált adataink szerint az LLT-HH valamint a B16 tumorsejtek jelentős mennyiségű laminint expresszálnak a sejtfelszínen, amely mind az LLT-HH mind a B16 tumorsejtek tüdőben korábban megfigyelt endotelizációjáért felelős lehet. Lamininnal bevont mikrogömbök intravénás beoltását követően azt tapasztaltuk, hogy a mikrogömbök endotélsejtekkel történő befedése a tumorsejtekhez hasonló időbeni lefutást mutat tüdőben, bár a mikrogömbök nem kerülnek kapcsolatba a bazális membránnal. Ez a jelenség arra utalhat, hogy bizonyos szervekben a tumorsejtek extraluminális helyzetbe történő kerüléséhez elegendő az extracelluláris mátrix molekulák jelenléte a sejtfelszínen. E feltétel teljesülése annál is valószínűbb, hiszen jól ismert, hogy epiteliális eredetű tumorok esetében a bazális membrán folytonosságának

hiánya nemcsak az emelkedett degradáció illetve csökkent szintézis eredménye, hanem a helytelen depozíció is, amely magában foglalja annak lehetőségét, hogy a tumorsejtek felszínükön bazális membrán komponenseket hordozzanak inváziójuk során és az intravazációt követően. Ezzel szemben laminin szerepét a tumorsejtek kitapadásában Mushel és munkacsoportja abban látja, hogy a tumorsejtek a tüdő endotéliumában normális körülmények között is előforduló résekhez tapadnak a laminin 5 kötő $\alpha 3\beta 1$ integrin segítségével (50). Mi nagyszámú tumorsejtet vizsgáltunk ultrastrukturálisan több sejtvonal esetében, de a tumorsejtek kezdeti kitapadása mindig intakt endotél réteghez történt.

Az LLT-HH tumorsejtek endotelizációját követően a tüdőben a bazális membrán lokális degradációja következett be. A tumorsejtek a keletkezett 1-2 μm méretű résen keresztül a kötőszövetbe migráltak. A máj szinuszoidjaiban nem található jól strukturált bazális membrán, egyes komponensek amorf formában vannak jelen a májsejtek mikrovillusai között (Disse tér). Itt nem is figyeltük meg a tüdő, a mellékvese és az agy esetében előforduló jellemző morfológiájú a bazális membrán kis résén átmigráló tumorsejteket. Ehelyett itt a tumorsejtek az endotelizáció után alakváltoztatás nélkül mintegy belesüllyedtek a májsejtekbe (XVIII).

Az extravazáció intravitális és ultrastrukturális vizsgálatából származó megfigyelések legnagyobb része arra utal, hogy a tumorsejtek többsége a célszervbe való bejutást követően a kapillárisokban mechanikusan, a kapillaris és a tumorsejt méretéből adódó különbség miatt akad el. Ez a mechanikai stressz a tumorsejtek nagymértékű pusztulásához vezet, ami egyik fő oka a metasztázisképzés megfigyelt alacsony hatékonyságának. Érdekes, hogy ezt a széles körben elfogadott elméletet korábban megkérdőjelezte Chambers és munkacsoportja, akik szerint minden a célszervbe bejutott sejt extravazál, és életképes marad (alvó tumorsejtek) (51). Mi nem osztjuk ezt a nézetet, és bár részletes kvantitatív analízist nem végeztünk, több tumorvonal extravazációjának ultrastrukturális vizsgálata azt mutatta, hogy a tüdőben fellelhető tumorsejtek száma az idő előrehaladtával egyértelműen csökken. A tumorsejtek a célszerv kapillárisaiban történő mechanikus elakadását több munkacsoport is megkérdőjelezte, sőt eredményeik szerint a tumorsejtek a tüdőben a már nagyobb arteriolákban kitapadnak az érfalhoz és nem extravazálnak, ehelyett a metasztázisok a tumorsejtek intravaszkuláris növekedése útján alakulnak ki (52). Ez az

elképzelés ellentétben áll a mi megfigyeléseinkkel, hiszen az LLT-HH és négy további tumorvonal sorsának a tüdőben történt ultrastrukturális vizsgálata azt mutatta, hogy a tüdőkapillárisokban túlélő tumorsejtek az oltást követő egy napon belül extravazálnak. Az LLT-HH tumorvonal esetében azt tapasztaltuk, hogy a tumorsejtek szinte kizárólag kapillárisokban akadtak el jelezve, hogy ezen tumorvonal esetében, a leukociták végleges adhézióját megelőző és a tumorsejtek esetében is vizsgált úgynevezett „rolling”, nem játszik jelentős szerepet az endotélsejtekhez történő kitapadásban. Korábbi B16 melanóma sejtekkel végzett vizsgálataink azt mutatták, hogy ezek a sejtek képesek voltak kitapadni arteriolákban, de ennek során a tumorsejtek kezdetben nem kerültek kapcsolatba az endotélsejtekkel, mivel a tumorsejtek trombusok belsejében helyezkedtek el, tehát a kitapadást nem a tumorsejtek, hanem a trombus alkotóelemei mediálták (47). A nagyobb erekben való kitapadási hajlam mögött feltehetően, a B16 tumorvonal erősebb véralvadást indukáló képessége rejlik. Meg kell azonban jegyezni, hogy több tumorvonal esetében is megfigyeltük, hogy az oltást követően nagy számban keletkeznek olyan trombusok melyek nem tartalmaznak tumorsejteket. Ezek és a tumorsejteket is tartalmazó trombusok endotelizációja (mely folyamat a trombus szervülésének első lépése) hasonlóképpen zajlott le, a trombusok sokszor több endotélsejt részvételével feltehetően a trombus alkotóelemeinek (fibrin, fibronectin) hatására, mintegy fagocitálódtak. Feltehető, hogy az endotelizáció jelensége a tüdő és a máj esetében egy olyan védekezési mechanizmus része, amely minden szilárd fázisú anyagnak a keringésből történő eltávolítására szolgál, és amelyet a tumorsejtek felhasználnak a keringésből történő minél gyorsabb kikerülésre.

Korábban kimutattuk az intézetünkben izolált magas metasztatizáló képességű Lewis lung tumorvonal úgynevezett „látens” májpreferenciáját (53). A kifejezés arra utal, hogy a szervpreferencia csak az arteriális rendszerbe történő oltást követően nyilvánult meg. A metasztázisok látszólag ebben az esetben is a mechanikus elméletnek megfelelően az első elért szerv(ek)ben képződnek, azonban különösen a májban, de a mellékvesékben is, a lökettérfogati arányokat messze meghaladó gyakorisággal alakultak ki metasztázisok. Ezzel szemben, a tumorvonal agy, de izom, bél, bőr esetében is negatív preferenciát mutatott. Mint fentebb említettük a metasztázisképzés hatékonysága nagyon alacsony, amelynek fő oka a tumorsejtek mechanikus és immunológiai hatásokra bekövetkező pusztulása lehet, így döntő jelentőséggel bírhat,

hogy a tumorsejtek mennyi időt töltenek el ellenséges környezetben az extravazációt megelőzően. Vizsgálataink azt mutatták, hogy az extravazáció a leghamarabb a májban és a mellékvesékben zajlik le (6 óra) mely szervekre pozitív preferencia mutatkozik, míg a leghosszabb időt a kapillárisokban a tumorsejtek az agyban töltik, mely szervre a tumorvonal negatív preferenciát mutat. Miután az extravazáció módja (endotelizáció vs. direkt áthatolás az endotélsejteken és a bazális membránon) és a szervpreferencia között nem volt összefüggés azt mondhatjuk, hogy a szervpreferencia kialakulásában az extravazáció sebessége lehet az egyik meghatározó tényező **(XVIII)**.

A szervpreferencia lehetséges okait vizsgálva, ellentétben számos más korábbi vizsgálattal, nem találtunk összefüggést a tumorvonal szervkolonizációs képessége és a különböző szervekből származó kemotaktikus faktorok által kiváltott migráció között. Hasonlóképpen nem volt összefüggés a tumorvonal fagyasztott metszetekhez való adhéziós képessége és a májpreferencia között. Megfigyeltük azonban, hogy a tumorsejtek a különösen májból származó fagyasztott metszetek esetében előszeretettel tapadtak az erekhez. A metszetek részletes elektronmikroszkópos vizsgálata kimutatta, hogy a tumorsejtek a portális venulák és szinuszoidok bazális membránjához tapadtak **(XIX)**. Ez a jelenség felvetette annak lehetőségét, hogy az erek bazális membránja szerepet játszhat a szervpreferencia kialakulásában. Ennek részletesebb vizsgálatára különböző bazális membrán komponensek elleni antitestekkel (perlekán, laminin, fibronektin) kezeltünk egereket intravénásan, majd a szív bal kamrájába oltottuk a májpreferenciát mutató LLT-HH tumorsejt vonalat. Azt tapasztaltuk, hogy bár mindhárom antitest csökkentette a vese, illetve a laminin és fibronektin elleni antitestek a tüdő kolonizációját is, a májmetasztázisok kialakulását csak a perlekán elleni antitest volt képes jelentősen gátolni. Tovább vizsgálva a kérdést megállapítottuk, hogy az egerek májából izolált nagy molekulású proteoglikán frakció nem fejt ki kemotaktikus hatást a tumorsejtekre. Ezzel szemben perlekán elleni antitest gátolta a tumorsejtek adhézióját a májból izolált proteoglikánhoz. Ultrastrukturális vizsgálataink azt mutatták, hogy a szinuszoidokban elakadt tumorsejtek az endotélsejtek fenestrációján keresztül nyúlványokat bocsátanak a Disse térbe, ahol nagy mennyiségű perlekán található **(XVIII)**. Ezt nem követi ugyan a tumorsejtek migrációja, de a jelenség szerepet játszhat a tumorsejtek specifikus kitapadásában vagy specifikus növekedési szignálok közvetítésében. Utóbbi megvalósulhat különböző növekedési

faktorok prezentálásában a tumorsejtek számára, illetve a máj bazális membránjában jelenlévő perlekán laminin kötő képességén keresztül. Meg kell azonban jegyezni, hogy a perlekán mellett más molekulák is szerepet játszhatnak a májpreferencia kialakulásában, hiszen csak a máj esetében figyeltünk meg specifikus elektrondenz sejtkepcsoló struktúrákat a tumor és endotélsejtek között (**XVIII**), melyek molekuláris összetétele egyelőre ismeretlen.

5. Új eredmények.

1. A patkánymáj epeút rendszerének egy új, CK7-/CK19+ kompartmentjét írtuk le, mely magába foglalja a Hering kanálisokat is, és a legnagyobb valószínűséggel tartalmazza a máj őssejtjeit. Humán májban ezek a struktúrák CK7 pozitívak, benyúlnak a vaszkuláris szeptumba, ahol arteriolák kísérik őket. Fenotípusuk: EMA-, CD56+, CD133+.

2. Az ovális sejtek által képzett struktúrák a Hering kanálisok meghosszabbításának tekinthetők. Az ovális sejtek proliferációjuk és migrációjuk során folyamatosan bazális membránt szintetizálnak és megtartják polarizált állapotukat. Az általuk alkotott csőrendszert funkcionális kapcsolatot biztosít a hepatociták és az epeút rendszer portális térben elhelyezkedő elemei között.

3. Az ovális sejtek nem fejezik ki a Thy-1 (CD90) hemopoetikus őssejt markert, tehát megjelenésükben transzdifferentiáció nem játszik szerepet. Thy-1-t a máj miofibroblasztjai expresszálják.

4. Az ovális sejtek májsejteké történő differenciálódása két, hisztológiailag jelentősen eltérő módon mehet végbe, a sejtszintű események - melyek legfontosabb jellemzője a bazális membrán eltűnése illetve a HNF4, májsejtspecifikus transzkripciós faktor megjelenése- azonban megegyeznek a két folyamat során. Az ovális sejtek differenciálódása primer hepatocita mitogén kezeléssel elősegíthető.

5. Kimutattuk, hogy a humán és kísérletes melanómák beereződése a tumor felszínén képződött kapilláris hálózat bekebelezésével megy végbe, ami a kapilláris denzitás csökkenéséhez és az erek méretének növekedéséhez vezet a tumor centrum irányában. Humán melanómák esetében az intratumorális érdenzitás bír prognosztikus jelentőséggel.

6. Az intussuszeptív angiogenezis egy új formáját írtuk le, melynek során a „pillar” képződés első lépése endotélsejt hidak kialakulása az ér lumenében majd kötőszöveti kollagén kötegek transzportja az érlumenen keresztül az endotélsejtek segítségével.

7. A glomeruloid test képződés egy új formáját írtuk le agyi mikrometasztázisok esetében. A folyamat során érdenzitás növekedés a tumorban jelentősebb endotélsejt proliferáció nélkül, az agy meglévő kapillárisrendszerének a tumorsejtek által előidézett átrendeződésével megy végbe.

8. Kimutattuk, hogy kísérletes agymetasztázisok környezetében nem zajlik angiogenezis, a tumorok érhálózatukat kizárólag a már meglévő erek inkorporációjával hozzák létre.

9. A vaszkularizáció egy új formáját írtuk le jól differenciált kísérletes kolonrák májmetasztázisainak esetében. A folyamat lényege a tumor felszínén keletkező fuzionált szinuszoidok inkorporációja.

10. Kimutattuk, hogy a kísérletes májmetasztázisok artériás vérellátásra tesznek szert 2mm-es tumor méret felett. Az arterializálódás folyamata a májlebenyekék arteriális mikrocirkulációs alegységét felépítő szinuszoidok fúziójának és az ezt követő inkorporációjának következtében alakul ki.

11. A sejtmozgás egy új mechanizmusát írtuk le in vitro. A sejt folyamatos mozgását a vezető élen folytonosan megújuló, de a mozgás során ív formában haladó adhéziós pontokhoz kapcsolódó konkáv aktin kötegek biztosítják.

12. Kimutattuk, hogy az extravazáció folyamata szervfüggő lehet. Az extravazáció sebessége, nem módja függ össze a szervpreferenciával.

13. Kimutattuk, hogy a Lewis lung karcinóma májpreferenciája mögött legnagyobb valószínűséggel a tumorsejtek szinuszoidok heparánszulfát proteoglikánjához történő specifikus adhéziója áll.

6. Az értekezéshez felhasznált saját közlemények

6.1. Májregeneráció

I. Paku S, Dezső K, Kopper L, Nagy P. Immunohistochemical analysis of cytokeratin 7 expression in resting and proliferating biliary structures of rat liver.

Hepatology 42: 863-870. 2005.

IF: 9,792

II. Dezső K, **Paku S**, Papp V, Turányi E, Nagy P.

Architectural and immunohistochemical characterization of biliary ductules in normal human liver.

Stem Cells Dev. 18: 1417-22. 2009

IF: 4,146

III. Papp V, Dezső K, László V, Nagy P, **Paku S**.

Architectural changes during regenerative and ontogenic liver growth in the rat.

Liver Transplantation 15: 177-183. 2009.

IF: 3,751

IV. Paku S, Schnur J, Nagy P, Thorgeirsson SS. Origin and structural evolution of the early proliferating oval cells in rat liver.

Am J Pathol. 158:1313-1323. 2001.

IF: 7,103

V. Dezső K, Jelnes P, László V, Baghy K, Bödör C, **Paku S**, Tygstrup N, Bisgaard H.C, Nagy P. Thy-1 is expressed in hepatic myofibroblasts and not oval cells in stem cell-mediated liver regeneration.

Am J Pathol 171:1529-1537. 2007.

IF: 5,796

VI. Paku S, Nagy P, Kopper L, Thorgeirsson SS. AAF-dose dependent differentiation of oval cells into hepatocytes: confocal and electron microscopic studies.

Hepatology 35: 1353-1361. 2004.

IF: 10,416

VII. László V, Dezső K, Baghy K, Papp V, Kovalszky I, Sáfrány G, Thorgeirsson SS, Nagy P, **Paku S**.

Triiodothyronine accelerates differentiation of rat liver progenitor cells into hepatocytes. Histochem Cell Biol. 130:1005-14. 2008.

IF: 2,320

6.2. Angiogenesis

VIII. Döme B, Hendrix MJC, **Paku S**, Tóvári J, Tímár J.

Alternative vascularization mechanisms in cancer.

Am J Pathol 170: 1-15. 2007.

IF: 5,796

IX. Paku, S.: Current concepts of tumor-induced angiogenesis.

Pathol Oncol Res 4: 62-75. 1998.

X. Döme B, **Paku S**, Somlai B, Tímár J. Vascularization of cutaneous melanoma involves vessel co-option and has clinical significance.

J Pathol. 197: 355-62. 2002.

IF: 4,563

XI. Paku S, Dezső K, Bugyik E, Tóvári J, Tímár J, Nagy P, László V, Klepetko W, Döme B. A new mechanism for pillar formation during tumor-induced intussusceptive angiogenesis.

Am J Pathol 179: 1573-1585. 2011.

IF: 5,224

XII. Döme B, Tímár J, **Paku S.** A novel concept of glomeruloid body formation in experimental cerebral metastases.

J Neuropathol Exp Neurol 62: 655-661. 2003.

IF: 5,005

XIII. Bugyik E, Dezső K, Reiniger L, László V, Tóvári J, Tímár J, Nagy P, Klepetko W, Döme B, **Paku S.** Lack of angiogenesis in experimental brain metastases.

J Neuropathol Exp Neurol 70: 979-991. 2011.

IF: 4,190

XIV. **Paku S,** Kopper L, Nagy P. Development of the vasculature in “pushing-type” liver metastases of an experimental colorectal cancer.

Int J Cancer 115: 893-902. 2005.

IF: 4,700

XV. **Paku, S.,** Bodoky, G., Kupcsulik, P., Tímár, J.: Blood supply of tumor metastatic hepatic tumors: suggestions for improved delivery of chemotherapeutic agents.

J Natl Cancer Inst **90**: 936-937. 1998. (letter)

XVI. Dezső K, Bugyik E, Papp V, László V, Döme B, Tóvári J, Tímár J, Nagy P, **Paku S.** Development of Arterial Blood Supply in Experimental Liver Metastases.

Am J Pathol. 175: 835-843. 2009.

IF: 5,673

6.3. Sejtmozgás, szervpreferencia

XVII. **Paku S,** Tóvári J, Lőrincz Zs, Tímár F, Döme B, Kopper L, Raz A, Tímár J. Adhesion dynamics and cytoskeletal structure of gliding human fibrosarcoma cells: a hypothetical model of cell migration.

Exp Cell Res 290: 246-253. 2003.

IF: 3,949

XVIII. Paku S, Döme B, Tóth R, Tímár J. Organ-specificity of the extravasation process: an ultrastructural study.

Clin Exp Metastasis.18:481-92. 2001.

IF: 1,966

XIX. Tóvári, J., Paku, S., Rásó, E., Pogány, G., Kovalszky, I., Ladányi, A., Lapis, K., Tímár, J. Role of sinusoidal heparan sulphate proteoglycan in liver metastasis formation.

Int. J. Cancer **71**: 825-831. 1997.

IF: 3.362

7. Irodalom

1. Bissel M, Hines WC. Why we don't get more cancer? A proposed role of the microenvironment in restraining cancer progression. *NATURE MEDICINE* 17: 320-329. 2011.
2. Senger DE, Davis DE. Angiogenesis. *Cold Spring Harb Perspect Biol* 3:a005090. 2011.
3. Carmeliet P, Jain RK. Molecular mechanisms and clinical applications of angiogenesis. *NATURE* 473: 298-307. 2011.
4. Hida K, Hida Y, Amin DN, Flint AF, Panigrahy D, Morton CC, Klagsbrun M. Tumor-associated endothelial cells with cytogenetic abnormalities. *CANCER RESEARCH* 64: 8249-8255. 2004.
5. Jain RK, Duda DG, Clark JW, Loeffler JS. Lessons from phase III clinical trials on anti-VEGF therapy for cancer. *NATURE CLINICAL PRACTICE ONCOLOGY* 3: 24-40. 2006.
6. Azam F, Mehta S, Harris AL. Mechanisms of resistance to angiogenesis therapy. *EUR J CANCER* 46: 1323-1332. 2010.
7. Riehle KJ, Dan YY, Campbell JS, Fausto N. New concepts in liver regeneration *J GASTROENTEROL HEPATOL* 26: 203-212. 2011.
8. Fausto N. Liver regeneration and repair: Hepatocytes, progenitor cells, and stem cells. *HEPATOLOGY* 39: 1477-1487. 2004.
9. Thorgeirsson SS, Grisham JW. Hematopoietic cells as hepatocyte stem cells: A critical review of the evidence. *HEPATOLOGY* 43: 2-8. 2006.
10. Gupta GP, Massague J. Cancer metastasis: Building a framework. *CELL* 127 (4): 679-695. 2006.
11. Tarin D. Cell and tissue interactions in carcinogenesis and metastasis and their clinical significance. *SEMINARS IN CANCER BIOLOGY* 21: 72-82. 2011.
12. Weiss L. Patterns of metastasis. *CANCER METASTASIS REVIEWS* 19: 281-301. 2000.
13. Fidler IJ. Timeline - The pathogenesis of cancer metastasis: the 'seed and soil' hypothesis revisited. *NATURE REVIEWS CANCER* 3: 453-458. 2003.

14. Das S, Skobe M. Lymphatic vessel activation in cancer. ANN NY ACAD SCI 1131: 235-241. 2008.
15. Liotta LA. Tumor invasion and metastases- role of the basement membrane. AMERICAN JOURNAL OF PATHOLOGY 117: 339-348. 1984.
16. Novikoff PM, Yam A, Oikawa I. Blast-like cell compartment in carcinogen induced proliferating bile ductules. AM J PATHOL 148: 409-422. 1996.
17. Petersen BE, Goff JP, Greenberger JS, Michalopoulos GK. Hepatic oval cells express the hematopoietic stem cell marker Thy-1 in the rat. HEPATOLOGY 27: 433-445. 1998.
18. Hagood JS, Prabhakaran P, Kumbala P, Salazar L, MacEwen MW, Barker TH, Ortiz LA, Schoeb T, Siegal GP, Alexander CB, Pardo A, Selman M. Loss of fibroblast Thy-1 expression correlates with lung fibrogenesis. AMERICAN JOURNAL OF PATHOLOGY 167: 365-379. 2005.
19. Fuchs E, Tumber T, Guasch G. Socializing with the neighbors: Stem cells and their niche. CELL 116: 769-778. 2004.
20. Battle MA, Konopka G, Parviz F, Gaggli AL, Yang CH, Sladek FM, Duncan SA. Hepatocyte nuclear factor 4 alpha orchestrates expression of cell adhesion proteins during the epithelial transformation of the developing liver. PROCEEDINGS OF THE NATIONAL ACADEMY OF SCIENCES OF THE UNITED STATES OF AMERICA 103: 8419-8424. 2006.
21. Yin L, Sun M, Ilic Z, Leffert HL, Sell S. Derivation, characterization and phenotypic variation of hepatic progenitor cell lines isolated from rats. HEPATOLOGY 35: 315-324. 2002.
22. Folkman J. How is blood vessel growth regulated in normal and neoplastic tissue? CANCER RES 46:467-473. 1986.
23. Hlatky L, Hahnfeldt P, Folkman J. Clinical application of antiangiogenic therapy: Microvessel density, what it does and doesn't tell us. JOURNAL OF THE NATIONAL CANCER INSTITUTE 94: 883-893. 2002.
24. Hellberg C, Ostman A, Heldin CH. PDGF and vessel maturation. RECENT RESULTS CANCER RES 180: 103-114. 2010.
25. Erber R, Thurnher A, Katsen AD, Groth G, Kerger H, Hammes HP, Menger MD, Ullrich A, Vajkoczy P. Combined inhibition of VEGF- and PDGF-signaling enforces

- tumor vessel regression by interfering with pericyte-mediated endothelial cell survival mechanisms. *FASEB JOURNAL* 17: 338-340. 2003.
26. Nagy JA, Chang SH, Shih SC, Dvorak AM, Dvorak HF. Heterogeneity of the tumor vasculature. *Semin Thromb Hemost* 36: 321–331. 2010.
27. Styp-Rekowska B, Hluschuk R, Pries AR, Djonov V. Intussusceptive angiogenesis: pillars against the blood flow. *Acta Physiol* 202: 213-223. 2011.
28. Straume O, Chappuis PO, Salvesen HB, Halvorsen OJ, Haukaas SA, Goffin JR, Begin LR, Foulkes WD, Akslen LA. Prognostic importance of glomeruloid microvascular proliferation indicates an aggressive angiogenic phenotype in human cancers. *CANCER RESEARCH* 62: 6808-6811. 2002.
29. Stiver SI, Tan X, Brown LF, Hedley-Whyte ET, Dvorak HF. VEGF-A angiogenesis induces a stable neovasculature in adult murine brain. *JOURNAL OF NEUROPATHOL AND EXP NEUROLOGY* 63: 841-855 2004.
30. Vermeulen PB, Colpaert C, Salgado R, Royers R, Hellemans H, Van den Heuvel E, Goovaerts G, Dirix LY, Van Marck E. Liver metastases from colorectal adenocarcinomas grow in three patterns with different angiogenesis and desmoplasia. *J PATHOL* 195: 336-342. 2001.
31. Willis BC, Liebler JM, Luby-Phelps K, Nicholson AG, Crandall ED, du Bois RM, Borok Z. Induction of epithelial-mesenchymal transition in alveolar epithelial cells by transforming growth factor-ss 1 - Potential role in idiopathic pulmonary fibrosis. *AMERICAN JOURNAL OF PATHOLOGY* 166: 1321-1332. 2005.
32. Hewitt RE, Powe DG, Holland CM, Gray T, Turner DR. Apparent fusion of basement membranes in colorectal carcinoma. *INT J CANCER* 50: 20-25. 1992.
33. Ong ES, Poirier M, Espat NJ. Hepatic intra-arterial chemotherapy. *ANNALS OF SURGICAL ONCOLOGY* 13: 142-149. 2006. .
34. Terayama N, Terada T, Nakanuma Y. A morphometric and immunohistochemical study on angiogenesis of human metastatic carcinomas of the liver. *HEPATOLOGY* 24:816-9. 1996.
35. McCuskey RS: Morphological mechanisms for regulating blood flow through hepatic sinusoids. *Liver* 2000, 20:3-7.
36. Yamaguchi H, Wyckoff J, Condeelis J. Cell migration in tumors. *CURRENT OPINION IN CELL BIOLOGY* 17: 559-564. 2005.

37. Mitra SK, Hanson DA, Schlaepfer DD. Focal adhesion kinase: In command and control of cell motility. *NATURE REVIEWS MOLECULAR CELL BIOLOGY* 6: 56-68. 2005.
38. Lee J, Ishihara A, Theriot JA, Jacobson K. Principles of locomotion for simple-shaped cells. *Nature* 362, 167-171. 1993.
39. Harunaga JS, Yamada KM. Cell matrix interactions in 3D. *MATRIX BIOL* 30: 363-368. 2011.
40. Brown DM, Ruoslahti E. Metadherin, a cell surface protein in breast tumors that mediates lung metastasis. *CANCER CELL* 5: 365-374. 2004.
41. Cheng HC, Abdel-Ghany M, Pauli BU. A novel consensus motif in fibronectin mediates dipeptidyl peptidase IV adhesion and metastasis. *JOURNAL OF BIOLOGICAL CHEMISTRY* 278: 24600-24607. 2003.
42. Abdel-Ghany M, Cheng HC, Elble RC, Pauli BU. Focal adhesion kinase activated by beta(4) integrin ligation to mCLCA1 mediates early metastatic growth. *JOURNAL OF BIOLOGICAL CHEMISTRY* 277 (37): 34391-34400. 2002.
43. Kaplan RN, Riba RD, Zacharoulis S, Bramley AH, Vincent L, Costa C, MacDonald DD, Jin DK, Shido K, Kerns SA, Zhu ZP, Hicklin D, Wu Y, Port JL, Altorki N, Port ER, Ruggero D, Shmelkov SV, Jensen KK, Rafii S, Lyden D. VEGFR1-positive haematopoietic bone marrow progenitors initiate the pre-metastatic niche *NATURE* 438: 820-827. 2005.
44. Cabioglu N, Sahin A, Doucet M, Yavuz E, Igci A, Yildirim EO, Aktas E, Bilgic S, Kiran B, Deniz G, Price JE. Chemokine receptor CXCR4 expression in breast cancer as a potential predictive marker of isolated tumor cells in bone marrow. *CLINICAL & EXPERIMENTAL METASTASIS* 22: 39-46. 2005.
45. Rot A, von Andrian UH. Chemokines in innate and adaptive host defense: Basic chemokine grammar for immune cells. *ANNUAL REVIEW OF IMMUNOLOGY* 22: 891-928. 2004.
46. Barsky SH, Rao CN, Williams JE, Liotta LA. Laminin molecular domains which alter metastasis in a murine model. *J CLIN INVEST* 74: 843-848. 1984.
47. Lapis K, Paku S, Liotta L.A. Endothelialization of embolised tumor cells during metastasis formation. *CLIN EXP METAST* 6: 73-89. 1988.

48. Wondimu Z, Geberhiwot T, Ingerpuu S, Juronen E, Xie X, Lindbom L, Doi M, Kortessmaa J, Thyboll J, Tryggvason K, Fadeel B, Patarroyo M .An endothelial laminin isoform, laminin 8 (alpha 4 beta 1 gamma 1), is secreted by blood neutrophils, promotes neutrophil migration and extravasation, and protects neutrophils from apoptosis. BLOOD 104: 1859-1866. 2004.
49. Feng D, Nagy JA, Pyne K, Dvorak HF, Dvorak AM. Neutrophils emigrate from venules by a transendothelial cell pathway in response to FMLP. J EXP MED 16;187: 903-915. 1998.
50. Wang H, Fu WL, Im JH, Zhou ZY, Santoro SA, Iyer V, DiPersio CM, Yu QC, Quaranta V, Al-Medhi A, Muschel RJ. Tumor cell alpha(3)beta(1) integrin and vascular laminin-5 mediate pulmonary arrest and metastasis. JOURNAL OF CELL BIOLOGY 164: 35-941. 2004.
51. Luzzi KJ, MacDonald IC, Schmidt EE, Kerkvliet N, Morris VL, Chambers AF, Groom AC. Multistep nature of metastatic inefficiency - Dormancy of solitary cells after successful extravasation and limited survival of early micrometastases. AMERICAN JOURNAL OF PATHOLOGY 153: 865-873.1998
52. Wong CW, Song C, Grimes MM, Fu WL, Dewhirst MW, Muschel RJ, Al-Mehdi AB.Intravascular location of breast cancer cells after spontaneous metastasis to the lung.AMERICAN JOURNAL OF PATHOLOGY 161: 749-753. 2002.
53. Paku S, Rot A, Ladányi A, Lapis K.
Demonstration of the organ preference of liver selected high metastatic Lewis lung tumor cell line. Clin. Expl. Metastasis 7: 599-607. 1989.

8. Köszönetnyilvánítás

Köszönettel tartozom az Isz. Patológiai és Kísérleti Rákkutató Intézet igazgatóinak, Lapis Károlynak, Szende Bélának, Kopper Lászlónak, valamint Matolcsy Andrásnak, hogy biztosították számomra a szabad és önálló tudományos munkavégzés feltételeit. Közülük is kiemelném Lapis Károlyt, aki közel 30 éve a morfológiai vizsgálatok és metasztázis kutatás felé terelte figyelmemet és Kopper Lászlót, aki az akadémiai munkacsoport megszűnte után lehetővé tette, hogy továbbra is az intézetben folytathassam tudományos munkámat. Köszönettel tartozom Schaff Zsuzsának, akinek a laborjában az elektronmikroszkópos technikákat elsajátítottam.

Közvetlen munkatársaim közül kiemelném Nagy Pétert és Dezső Katalint, akikkel a májregeneráció, illetve Döme Balázst, Tímár Józsefet és Tóvári Józsefet, akikkel az metasztázisképzés és az angiogenezis témakörben dolgoztam együtt és még remélhetőleg a jövőben is együtt fogok dolgozni.

Köszönettel tartozom Neidhard Paweletz-nek, Avraham Raz-nak és Alex Eberle-nek akiknek a laborjában sok hasznos tudományos tapasztalattal gazdagodtam.

Immunohistochemical Analysis of Cytokeratin 7 Expression in Resting and Proliferating Biliary Structures of Rat Liver

Sándor Paku,¹ Katalin Dezső,² László Kopper,² and Peter Nagy²

Cytokeratins are the largest subfamily of intermediate filament proteins and include more than 20 different gene products, which are expressed in an epithelial tissue-specific manner. We studied by immunohistochemistry and confocal microscopy the distribution of cytokeratin subtypes in the biliary system of adult rat liver. A cytokeratin (CK)19+/7- cholangiocyte population was observed in the smaller branches of the biliary tree including the canals of Hering. They proliferated after 2-acetaminofluorene (AAF) administration, although later the typical oval cells expressed CK7. This observation suggests that cholangiocytes with this cytokeratin phenotype may harbor adult hepatic stem cells. The CK19+/7- cholangiocytes were not present in the rat liver at birth, but developed postnatally. Similar cell populations were not observed in human livers. **In conclusion**, we propose that the CK19+/7- phenotype may be characteristic for adult hepatic stem cells in rat liver and that these cells are generated *de novo* after birth. *Supplementary material for this article can be found on the HEPATOLOGY website (<http://www.interscience.wiley.com/jpages/0270-9139/suppmat/index.html>). (HEPATOLOGY 2005;42:863-870.)*

The canals of Hering or terminal ductules are transitional structures between the hepatocytes and bile ducts. The cells of these structures are the primary candidates for the liver-residing adult hepatic stem cell. This explains the tremendously increased interest for these ductules. Unfortunately, identifying them unequivocally is not always easy. Several markers exist for the cholangiocytes, such as OV-1, OV-6 antibodies, and the histochemical reaction for gamma glutamyltransferase,¹⁻³ but these reactions decorate all segments of the biliary tree equally. Therefore, the canals of Hering can be reliably recognized from their position only by electron- or confocal microscopy.⁴ Because the compositions of cy-

tokerin subtypes are characteristic for cell types, we decided to analyze the distribution of different cytokeratin filaments in the liver. Hepatocytes have long been known to contain CK8 and 18, whereas CK7 and 19 occurs in the biliary epithelium in addition to 8/18.^{5,6} A detailed examination showed a slightly different situation. All the biliary structures in the adult rat liver contained CK19. However, CK7 was present only in the larger biliary ducts, whereas the smaller branches, including the canals of Hering, were consistently negative. Thus, the stem cell population of the adult rat liver may be recognized from the CK19+/7- cytokeratin expression. This suggestion is supported by the preferential proliferation of CK19+/7- cholangiocytes after 2-acetaminofluorene (AAF) administration.

Abbreviations: AAF, 2-acetaminofluorene; PH, partial hepatectomy; CK, cytokeratin.

From the ¹Department of Molecular Pathology, Joint Research Organization of the Hungarian Academy of Sciences and Semmelweis University, Budapest, Hungary; and the ²First Department of Pathology and Experimental Cancer Research, Semmelweis University, Budapest, Hungary.

Received January 26, 2005; accepted July 3, 2005.

Supported by The Hungarian Scientific Research Fund (OTKA) T 42674 and TS 04887.

Address reprint requests to: Peter Nagy, First Department of Pathology and Experimental Cancer Research, Semmelweis University, Üllői út 26, Budapest H-1086, Hungary. E-mail: nagy@korp1.sote.hu; fax: (36) 1-317-1074.

Copyright © 2005 by the American Association for the Study of Liver Diseases.

Published online in Wiley InterScience (www.interscience.wiley.com).

DOI 10.1002/hep.20858

Potential conflict of interest: Nothing to report.

Materials and Methods

Animal Experiments. Male F-344 rats (160-180 g) were used for all experiments and were kept under standard conditions. At least 4 animals were used for each experimental time point (unless otherwise marked). The animal study protocols were conducted according to National Institutes of Health guidelines for animal care.

AAF/Partial Hepatectomy Experiment. AAF (2 mg/mL suspended in 1% dimethylcellulose) 5 mg/kg was administered to rats daily for 4 consecutive days by ga-

Table 1. Primary Antibodies Used for the Immunohistochemical Studies

Antibody	Species	Manufacturer	Catalog Number	Dilution
Pan cytokeratin FITC labeled		Dako	F0859	1:20
Laminin	Rabbit polyclonal	Dako	Z0097	1:300
BrdU	Mouse monoclonal	Becton Dickinson	347580	1:50
CK7	Mouse monoclonal	Biogenex	MU 255-UC	1:50
CK7	Mouse monoclonal	Dako	N7018	1:50
CK19	Mouse monoclonal	Novocastra	NCL-CK19	1:50

vage. Traditional two-thirds partial hepatectomy (PH) was performed⁷ on the 5th day, which was followed by 5 additional AAF treatments. Animals were killed at various times as indicated in the text.

Bile Duct Ligation. The common bile duct was ligated, and the animals were killed 2 days after the operation.

Young Rats. The rats were killed at birth and at 14 and 28 days of age.

Human Samples. Three morphologically normal human liver specimens were taken from the non-tumorous part of the liver removed for colorectal tumor metastases. The experimental procedure was approved by the ethical committee of our University under the code TUKEB 156/2003.

Morphological Analysis. Frozen sections (10–20 μm) were fixed in methanol and were incubated overnight with a mixture of the primary antibodies (Table 1) and with appropriate secondary antibodies afterward (Jackson Immunoresearch, West Grove, PA). All samples were analyzed by confocal laser-scanning microscopy using Bio-Rad MRC-1024 system (Bio-Rad, Richmond, CA).

BrdU Incorporation. BrdU incorporation was analyzed on serial sections. Portal tracts were selected on the CK7 and pancytokeratin stained sections. The same portal tracts were identified on pancytokeratin-, BrdU-, and 4',6-diamidino-2-phenylindole (DAPI)-stained sections. BrdU pulse (100 mg/kg) was given 24 hours after the last AAF dose and 1 hour before killing. The labeling index of the CK7 negative and positive biliary cells were determined after 2 days of AAF treatment, using 4 animals and counting 217 to 555 cells in the CK7-negative and 170 to 396 cells in the CK7-positive compartment. BrdU reaction was performed as described.⁴

Morphometry. Frozen sections from 3 control rats (15 μm) were stained for CK7, laminin, and pancytokeratin. The combination of pancytokeratin and CK7

staining was chosen for these experiments because the pancytokeratin antibody decorated all the biliary duct(ule)s and hepatocytes to let us study the connection between these 2 cell compartments. The portal tracts were divided into 3 categories according to their CK7 staining:

1. Portal tracts containing no CK7-positive bile ducts

2. Portal tracts containing ducts stained partially by CK7 (majority of cells stained positively for CK7 but negative cells were also present in the duct) beside the CK7-negative ductules

3. Portal tracts containing large bile ducts stained completely by CK7 in addition to the structures of the previous categories. Cells of the large ducts of category 3 stained more brightly for CK7 than the cells of the CK7-positive ducts in category 2

The smallest diameter of all bile duct(ule)s and portal veins, present on a given cryosection, was determined, using the Bio-Rad Lasersharp software.

The total area of the cryosections were determined using the Olympus Vanox Cue 2 software.

To determine the length of the CK7-negative bile ductules, series of 15- μm thick (15–40 sections) were cut. A canal of Hering was selected based on its characteristic U-shaped laminin staining. This structure was followed through the serial sections until it reached its end, then in the opposite Z direction the bile ductule was tracked down until it opened into a CK7-positive bile duct. The length of the ductule was calculated by multiplying the number of sections in Z direction by the thickness of the sections and by adding the extension of the duct in the XY dimensions. Only those ductules were counted in which both ends could be identified with certainty.

Results

Cytokeratin Expression in the Adult Rat Liver.

Because all commercially available cytokeratin subtype specific antibodies are monoclonal, their colocalization can be analyzed only on serial sections. The cytokeratin antibodies were usually co-stained with a polyclonal laminin antibody, which outlined the blood vessels, bile ducts, and made orientation on the section easier. The canals of Hering can be identified as biliary structures circumscribed only partially by laminin-positive basement membrane.

A pancytokeratin antibody reacted with all the cholangiocytes as well as hepatocytes, but the staining pattern was completely different between the 2 cell types (Fig. 1A). The hepatocytes showed faint reticular staining, whereas there was a strong cytoplasmic reaction in the

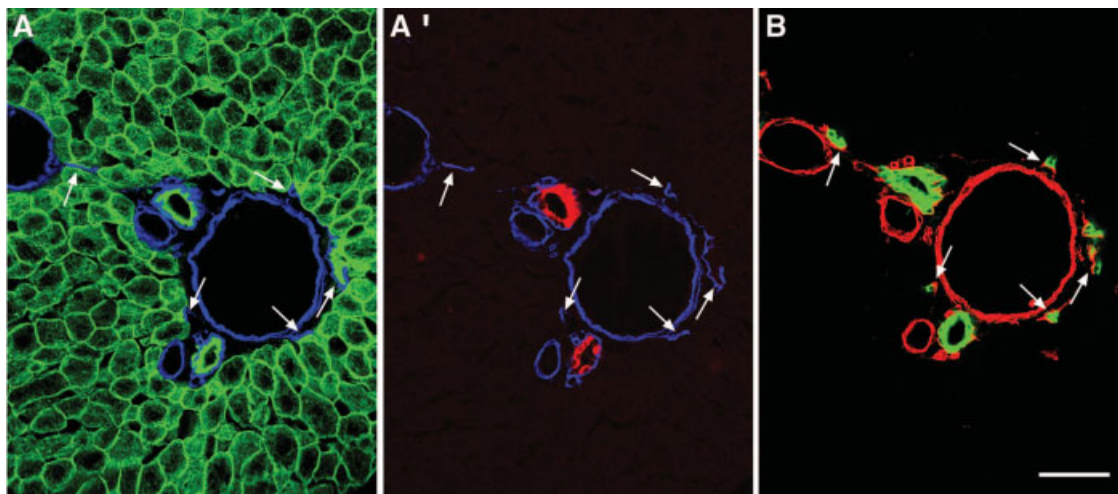


Fig. 1. Portal area of a normal adult rat liver; panels A and B are serial sections (10- μ m distance). Section A was triple labeled for pancytokeratin (green), CK7 (red), and laminin (blue). For clarity, the localization of pancytokeratin, laminin and CK7, laminin are shown in panels A and A', respectively. Section B was double labeled for CK19 (green) and laminin (red). Pancytokeratin (A) and CK19 (B) stains equally the small, including canals of Hering (arrows), and large bile duct(ule)s, whereas CK7 (A') stains only the larger ones. Note that the lower large duct is stained only partially by CK7 and the upper large bile duct is stained more brightly than the lower one. (Type 3 portal area). Scale bar: 50 μ m.

cholangiocytes and they were surrounded by continuous basement membrane. All the biliary structures labeled by the pancytokeratin antibody were CK19 positive on a parallel section (Fig. 1B). However, small biliary structures remained unstained with 2 different CK7 antibodies, whereas the large bile ducts showed a bright positive reaction with these antibodies (Fig. 1A'). The canals of Hering, recognized from the U-shaped laminin staining,⁴ were consistently negative for CK7 albeit they were stained by CK19 (Fig. 1 A',B). We were curious whether there are CK7-negative biliary structures in addition to the canals of Hering and followed 45 CK7-negative ductules through serial sections derived from 3 different animals (Table 2). Three main types of these ductules could be observed (Fig. 2A-F and online Supplementary Materials for Fig. 2A,C-D):

1. Simple ductules, showing no ramifications with a single attachment to hepatocytes (Fig. 2A-B),
2. Ductules divided into generally 2 to 4 branches (each branch had contact with hepatocyte(s) (Fig. 2C-D),
3. Ductules with attachments to 2 to 4 hepatocytes of the limiting plate (Fig. 2C-E). Occasionally there were branching ductules with attachments to more than 1 hepatocyte.(Fig. 2C-D).

The 3 types were represented roughly equally. These structures never entered into the liver lobule through the limiting plate. Where there was no contact with the liver plate, the ductules were covered completely with continuous basement membrane. When these small ductules joined to larger bile ducts, a clearly recognizable border was usually present between the CK7-negative ductular and CK7-positive ductal cells. (Figs. 2B, 3).

Table 2. Morphometric Characteristics of CK7-Negative Bile Ductules

	Type of Portal Area		
	CK7 Negative Bile Ductules Only	CK7 Negative and Partially CK7 Positive Bile Duct(ule)s	CK7 Negative. Completely (and Partially) CK7 Positive Bile Duct(ule)s
Total area		293.4 mm ²	
Number of portal areas	111	306	53
Diameter of CK7-ductules, mean \pm SE	7.9 \pm 0.8 μ m	7.4 \pm 0.7 μ m	8.2 \pm 0.4 μ m
Range (n: SD)	4-18 μ m (193:6.7)	4-17 μ m (537:6.4)	4-17 μ m (171:7.9)
Diameter of CK7+ ducts	NA	13.2 \pm 2.2 μ m	23.5 \pm 3.4 μ m
Range (n: SD)	NA	5-33 μ m (368:11.9)	7-70 μ m (90: 34.8)
Number of duct(ule)s/portal area	1.74	2.96	4.92
Diameter of portal vein	17.9 \pm 1.4 μ m	25.9 \pm 2.9 μ m	62.6 \pm 9.3 μ m
Length of CK7-ductules, mean \pm SD		104 \pm 66 μ m	
Range (n)		18-315 μ m (45)	

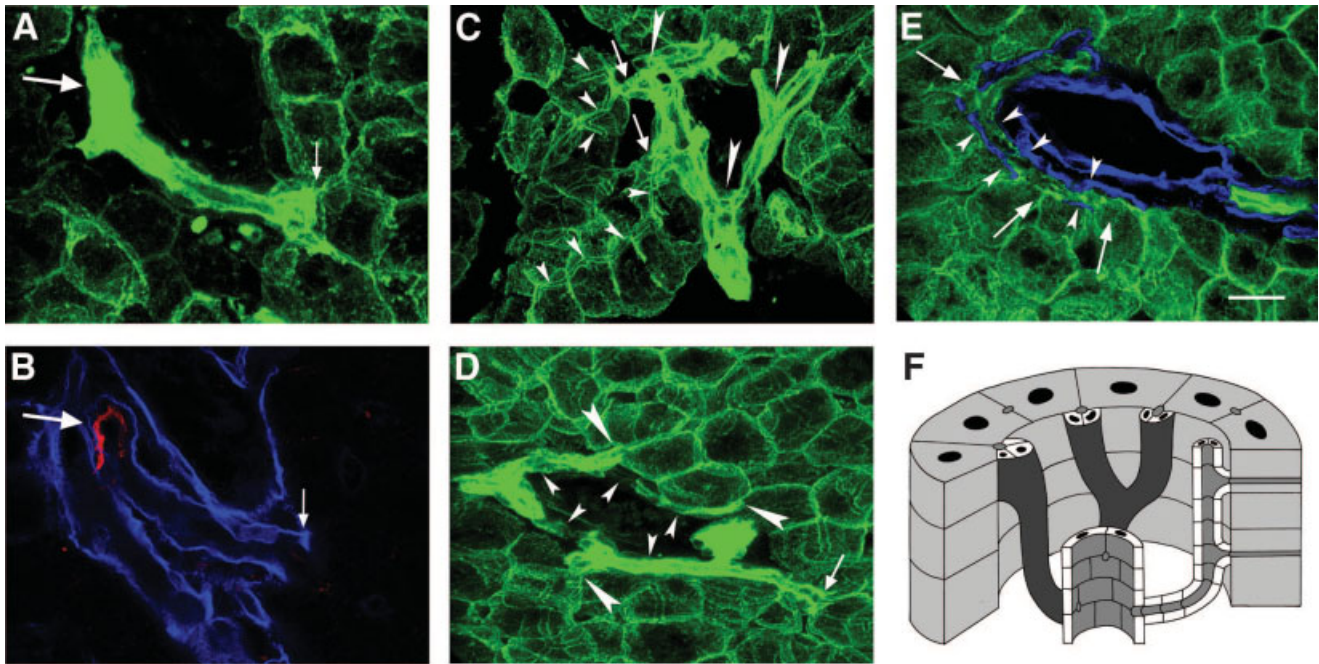


Fig. 2. (A-B) Short bile ductule (type A) having single contact site with the limiting plate (small arrow). The section was triple labeled for pancytokeratin (green), CK7 (red), and laminin (blue). (A) Single horizontal view of the pancytokeratin staining (37 optical sections taken at 0.4- μ m distance). (B) Single optical sections of the CK7 and laminin staining, demonstrating that the ductule is covered by basement membrane as it leaves the limiting plate, and enters into a CK7 positive duct (large arrow). (C-D) Single horizontal view of pancytokeratin-stained sections. Both views contain 40 optical sections taken 0.4 μ m apart. (C) Branching (type B) bile ductule. Large arrowheads indicate the branching points. Note the bile canaliculi (small arrowheads) running toward and entering into the canals of Hering (arrows). (D) Bile ductule (type C) running along the limiting plate (small arrowheads). The ductule is connected to hepatocytes at 3 different points (large arrowheads). Before it enters the large duct, it meets another short ductule, which has only 1 attachment site (arrow). (E) Type C bile ductule connected to the limiting plate at 3 different locations (arrows). The section is stained for pancytokeratin (green) and laminin (blue). Note that laminin is present only at the connective tissue side of the ductule, where it is connected to the hepatocytes. It is delineated on both sides by basement membrane (arrowheads) between the attachments. (F) Schematic representation of the 3 main types of the CK7-negative ductules. On the left, type A ductule with a single attachment to the limiting plate. At the center, type B ductule with 2 branches each connected to a hepatocyte. On the right, type C ductule has segmental contact with hepatocytes. Types B and C ductules are interrelated, depending on the length of the branches. Scale bar: 20 μ m.

We also analyzed the size (diameter, length) of the bile duct(ule)s. The examined portal areas were divided into 3 groups based on the CK7 staining pattern of biliary structures (Table 2). The portal areas containing only CK7-negative ductules had the narrowest portal veins. The diameter of the portal veins was larger alongside the partially CK7-positive ductules and increased further in the portal tracts with completely CK7-positive bile ducts. The diameter of the partially and completely positive ducts correlated with that of the actual portal veins. Interestingly, the size of the small CK19+/7- biliary ductules was almost independent of the above parameters of the portal tract. The standard diameter throughout the liver and the unique cytokeratin composition may indicate that these structures constitute a well-defined entity in the biliary system.

Cytokeratin Staining in the Postnatal Developing Liver. Many bile duct(ule)s were arranged at the periphery of the portal spaces in the newborn rat liver at birth. All these ducts were surrounded by laminin-positive base-

ment membrane, and the cells were stained by CK19 as well as by CK7 antibodies (Fig. 4A-B). We could not identify any CK7-negative biliary structure. The number of the bile ducts decreased by 14 days of age, but their cytokeratin composition did not change (Fig. 4C-D). However, CK19+/7- biliary ductules were observed in the liver of 28-day-old rats (Fig. 4E-F).

Cytokeratin Staining of Proliferating Biliary Cells.

The AAF/PH experiment is an established protocol to induce oval cell proliferation.⁸ AAF treatment itself is able to induce the proliferation of the biliary cells, although they remain in the periportal space.⁹ Later, after PH, these ductularly arranged cells invade the liver lobule and form the typical oval cell ducts.

Two AAF treatments did not change the cytokeratin expression compared with the normal liver (Fig. 5A-B), but the CK7-negative biliary ductules showed more than 3-fold higher proliferative activity than the positive ones (Table 3). When the oval cells invaded the liver lobule, after PH, they gained weak CK7 positivity (Fig. 5C-F),

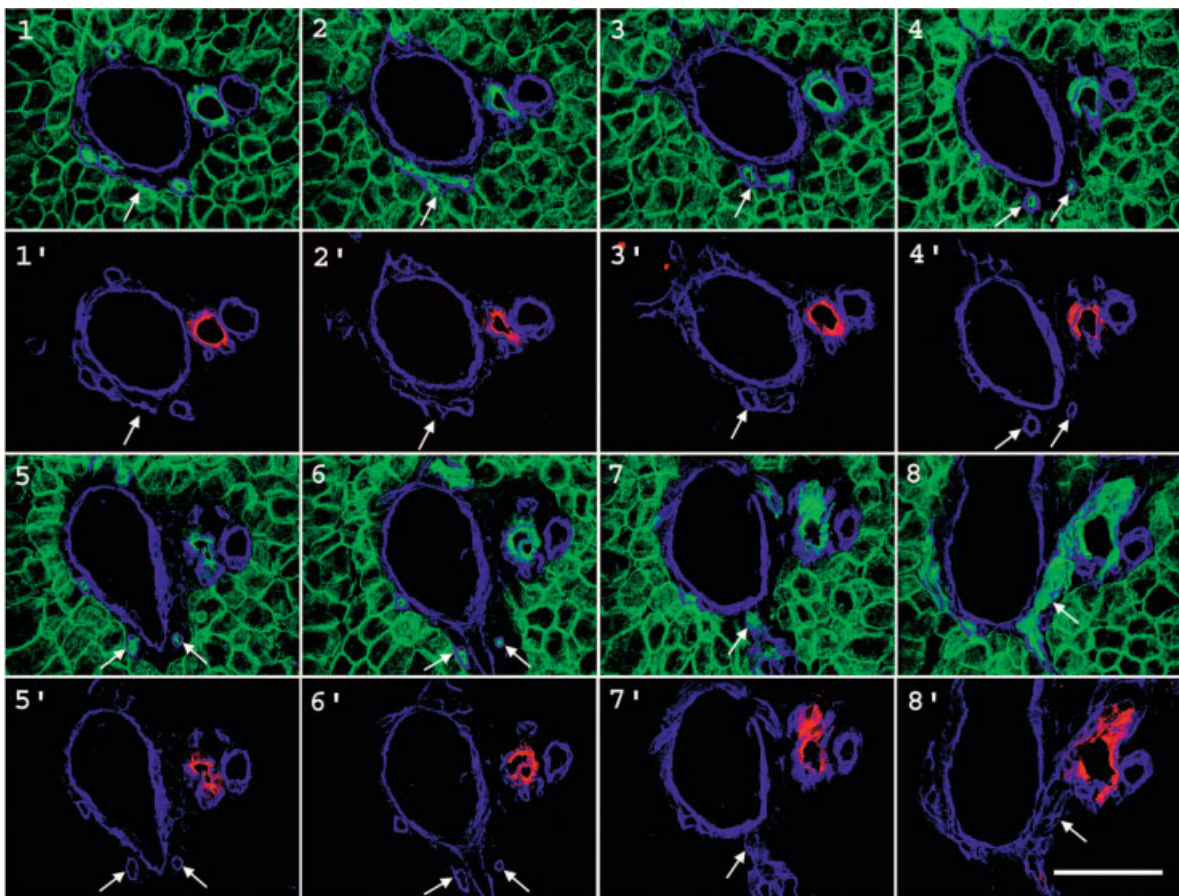


Fig. 3. Serial sections follow a CK7-negative ductule (arrows) as it enters into a CK7-positive interlobular bile duct. The sections were cut at 15- μ m distances and triple-labeled for pancytokeratin (green), CK7 (red), and laminin (blue). For clarity, the localization of pancytokeratin and laminin is shown on pictures 1-8, and CK7 and laminin is shown on pictures 1'-8'. The ductule is confined throughout its pass to the periportal space. At its origin, it is partially surrounded by laminin (traditional canals of Hering) (pictures 1-2). It enters into another CK7-negative ductule (picture 2), which separates into 2 branches as it passes around a vessel leaving the portal vein (pictures 4-6). Under the vessel (picture 7), the branches are joined and the ductule takes a sharp turn (picture 8), thereby running in the plane of the section, and enters the CK7-positive duct. During its path, the ductule remains CK7 negative until it reaches an interlobular bile duct (picture 8). Scale bar: 100 μ m.

but the staining intensity was obviously weaker than in the large bile ducts.

Three months after PH, the oval cells disappeared, but numerous bile duct-like tubules crossing the lobules remained in the liver. These ducts inside the liver lobule were CK7 negative but reacted with CK19 antibody and were surrounded by laminin (Fig. 5G-H).

Biliary cell proliferation also can be induced by the ligation of the common bile duct, which results in the development of tortuous interlobular bile ducts. This reaction is frequently referred to as "bile duct proliferation." All of these well-differentiated bile ducts were CK19/CK7 positive (Fig. 6). Essentially all of the CK7-negative ductules disappeared from the livers 48 hours after the ligation of the common bile duct.

Cytokeratin Staining in the Normal Human Liver.

Three histologically normal adult human liver specimens were stained for the cytokeratin subtypes. All the biliary

structures were positive for pancytokeratin as well as for CK7 (Fig. 7) and CK19 (not shown). As opposed to the rat liver, no CK7-negative biliary cells were observed.

Discussion

Here we report the existence of a CK19+/7- biliary cell population in the adult rat liver. The small biliary branches including the canals of Hering are composed of CK7-negative cholangiocytes. These CK7-negative cells are the precursors of the oval cells, but they are able to differentiate into CK19+/7+ biliary cells as well. They are not present in the liver at birth but are generated *de novo* in the postnatal period.

The cholangiocytes are morphologically and functionally heterogeneous along the intrahepatic biliary tree.^{10,11} The canals of Hering are the most distal part of this system. Unfortunately, they have no specific immunophe-

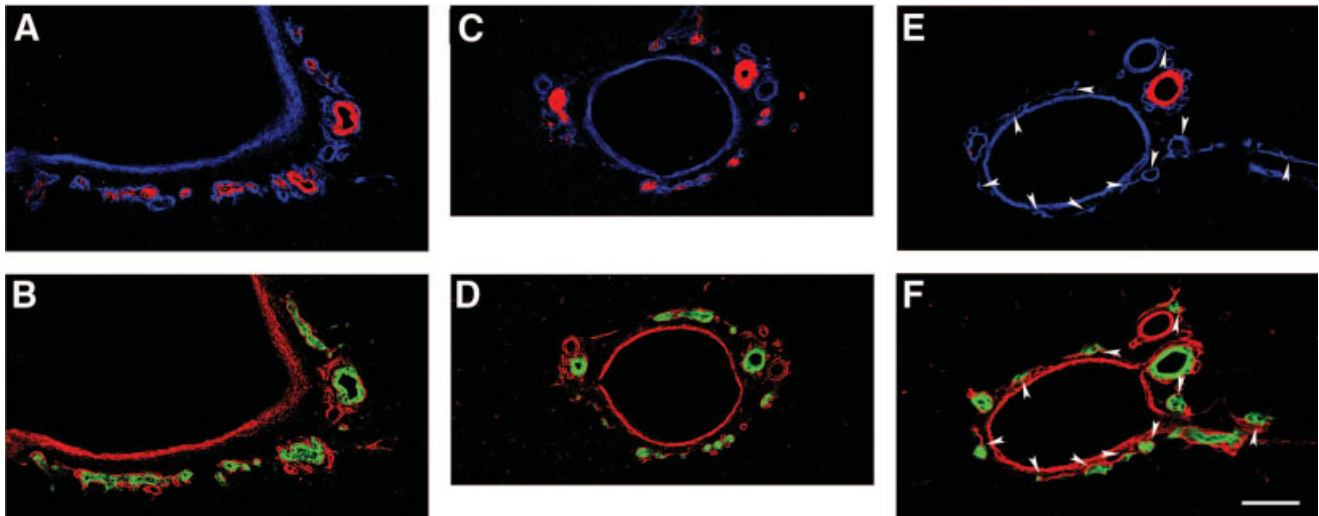


Fig. 4. Portal field of a newborn (A-B), 14- (C-D), and 28-day (E-F)-old rat liver. Serial sections were double labeled for CK7 (red), laminin (blue) (A,C,E), and for CK19 (green) and laminin (red) (B,D,F). All the bile ducts and ductules are CK7 and CK19 positive in newborn (A-B) and 14-day-old (C-D) rat livers regardless of their size. The bile ductules (arrows) of the 28-day-old rat liver (E-F) express CK19 but not CK7. Scale bar: 50 μ m.

notypic or other morphological marker. They can be identified only from their position as an interface between the hepatocytes and bile ducts.^{4,12} In all cases, in our hands these positively identified structures are negative for CK7. When the CK7-negative ductules are followed through serial sections, they do not have continuous contact with the hepatocytes. That is, if we apply strictly the definition of the canal of Hering, not all segments fulfill the criteria. These CK7-negative ductules form a functional and anatomical unit, however. Contrary to the traditional view of the canals of Hering, the CK7-negative ductules can be long, winding, dividing but uniform-sized tubules, which have contact segmentally with hepatocytes of the limiting plate collecting the bile from the canalicular system. Based on this arrangement, we propose that the CK7-negative biliary ductules, including the traditional canals of Hering, constitute a special morphological and functional segment of the biliary system in the rat liver.

Cytokeratin molecules are extremely labile unless they can find a partner for the assembly of the filaments. Usually CK7 and 19 are partners in the cholangiocytes. CK7 protein disappears spontaneously in CK18 null mice,¹⁴ and CK19 in this case can be a partner of CK8. That is, the lack of CK7 does not result in the instability of CK19 in the ductules.

We have previously shown that AAF treatment induces biliary proliferation in rat and these proliferating cells are the precursors of later oval cells.⁹ Because oval cells are considered the progenies and amplifying compartment of the hepatic stem cells, the AAF administration can be regarded as a functional assay for hepatic stem cell activa-

tion. In our experiment, AAF induces the preferential proliferation of CK7-negative biliary cells. Therefore, we suggest that the CK19+/7- cholangiocytes may harbor the adult hepatic stem cells in rat. Several "oval" or hepatic "stem cell" markers exist, such as OV1, OV6, A-6,¹³ c-kit,¹⁵ but they react with all the cholangiocytes. The CK19+/7- phenotype distinguishes a special segment of the biliary tree. As far as we know, this cytokeratin composition is the most stringent immunophenotypic confinement of the liver-residing adult stem cell compartment. Stem cells in other organs also have unique cytokeratin composition.^{16,17} Marceau¹⁸ postulated that the hepatic stem cells should be CK7 negative and CK14 positive, but we could not reveal any CK14 positivity in our experimental models (data not shown).

The ligation of the common bile duct induces the proliferation of biliary cells.¹⁹ All these bile ducts stain positively with the CK7 antibody, as well as CK19. Interestingly, the CK7-negative biliary ductules almost completely disappear from these livers. Thus, we can conclude that BDL induces CK7 upregulation associated with biliary differentiation of the stem cell population.

The early proliferative ductules were completely negative in the AAF/PH experimental system. However, the classical oval cells, after PH, stained weakly. Why the CK7 protein becomes visible at this step, before it disappears again, is not clear. The CK7 positivity appears when the bile ducts are rapidly elongating (ontogenic liver development, expansion of oval cells, bile duct ligation) and disappears when their growth is arrested (adult liver, remnants of oval cells). The CK7 negativity is not stable on

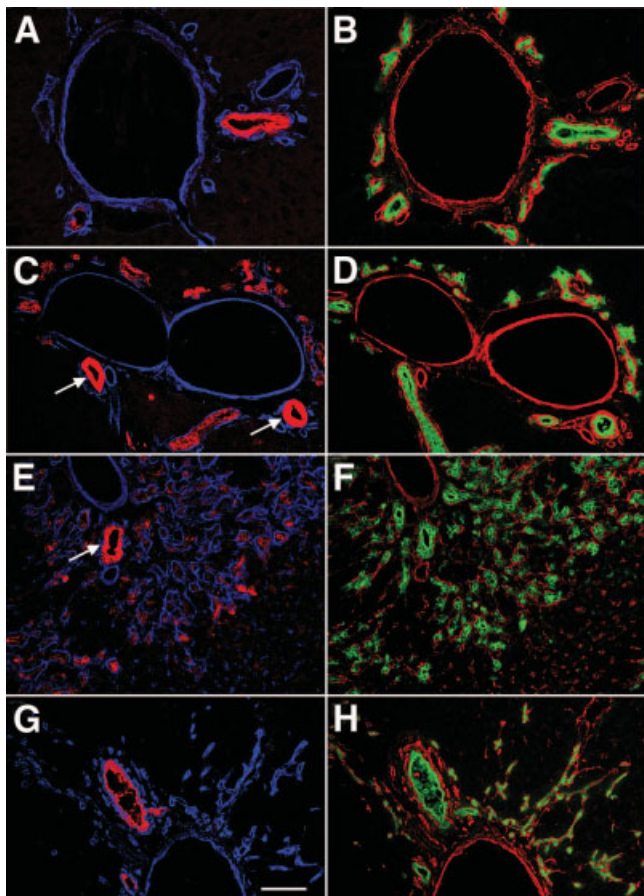


Fig. 5. Distribution of cytokeratins (CK7, CK19) in the AAF/PH experiment. (A-B) Sections of a rat liver treated by 2 doses of AAF (no partial hepatectomy). (C-H) Sections of rat livers that underwent the AAF treatment and partial hepatectomy. (C-D) 2 days, (E-F) 6 days, and (G-H) 3 months after partial hepatectomy. Serial sections were double-labeled for CK7 (red), laminin (blue) (A,C,E,G), and for CK19 (green) and laminin (red) (B,D,F,H). Most of the CK19-positive ductules remain CK7 negative after 2 AAF treatments (A-B). Two and 6 days after PH, the oval cells penetrate the limiting plate and become CK7 positive, although the expression is weaker than in the interlobular bile duct (arrows) (C-F). CK19-positive ducts surrounded by laminin staining are inside the lobule 3 months after the beginning of the experiment, but the CK7 staining disappears (G-H). Scale bar: 50 μ m.

manipulation; thus, it is not suitable for tracing progenies of stem cells.

The generation of the adult stem cells is a relatively neglected field of stem cell biology. Two options exist:

Table 3. Proliferation of CK7 Negative and Positive Compartments of the Biliary Tree After 2 Days of AAF Administration

	CK7 Negative Cells	CK7 Positive Cells
Total number of cell nuclei examined	1,384	1,050
Labeling index (%)	6.9 \pm 1.8	2.1 \pm 0.7*

* $P < .05$.

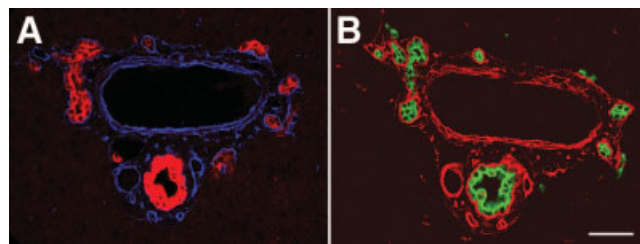


Fig. 6. Rat liver 2 days after the ligation of the common bile duct (A). Serial sections were double labeled for CK7 (red), laminin (blue) (A), and for CK19 (green) and laminin (red) (B). All "proliferating" bile ducts are positive for CK7 and CK19. Scale bar: 50 μ m.

either the stem cells are leftover undifferentiated cells from embryogenesis or they develop *de novo*. Initial data favor the second hypothesis.^{20,21} CK7 is the last cytokeratin subtype upregulated during the development of the biliary system.^{22,23} Therefore, the CK7-negative cholangiocytes might have been left-over, not terminally differentiated cholangiocytes. However, our data, that the CK19+/7- cells are not present at birth but appear in the liver 4 weeks later, indicate that the adult hepatic stem cell compartment is generated postnatally. We do not know whether the presence of CK7 molecules has any influence on the "stemness" of this cell population, but experimental data demonstrate the different behavior of the cholangiocytes at 3 weeks of age.²⁴ By all means the disappearance of CK7 might be an indicator for the development of stem cell population.

In conclusion, Thiese et al.¹⁵ described elongated CK19+ canals of Hering in the human liver (CK7 expression was not studied). We could not find CK19+/CK7- biliary structures in human liver. There is an additional basic difference between the rat and human liver. In the normal rat liver, we could never observe the spreading of the canals of Hering into the hepatic lobule through the limiting plate. Nonetheless, this was common in the human specimens studied by Thiese et al.¹⁵ We saw similar structures in the rat liver 3 months after

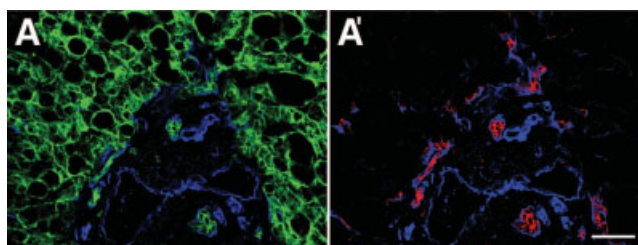


Fig. 7. Human liver (A,A'). The section was triple labeled for pancytokeratin (green), CK7 (red), and laminin (blue). For clarity, the localization of pancytokeratin, laminin and CK7, laminin are shown on A and A', respectively. No CK7 negative ductules are present in the normal human liver tissue. Scale bar: 50 μ m

the AAF/PH experiment in otherwise normal liver tissue and thought them the remnants of oval cells, which lost CK7 expression again. Because Thiese et al. used livers containing metastatic cancer, the entrance of the small ductules into the liver lobule may not represent the normal situation.

Acknowledgment: The authors thank Dr. Elizabeth A. Conner for correcting the English language.

References

- Grisham JW, Thorgeirsson SS. Liver stem cells. In: Potten CS, ed. *Stem Cells*. London: Academic Press, 1997:233-282.
- Fausto N. Liver regeneration and repair: hepatocytes, progenitor cells, and stem cells. *HEPATOLOGY* 2004;39:1477-1487.
- Alison MR, Vig P, Russo F, Bigger BW, Amofah E, Themis M, et al. Hepatic stem cells: from inside and outside the liver? *Cell Prolif* 2004;37:1-21.
- Paku S, Schnur J, Nagy P, Thorgeirsson SS. Origin and structural evolution of the early proliferating oval cells in rat liver. *Am J Pathol* 2001;158:1313-1323.
- Van Eyken P, Desmet VJ. Cytokeratins and the liver. *Liver* 1993;13:113-122.
- Zatloukal K, Stumptner C, Fuchsbichler A, Fickert P, Lackner C, Trauner M, et al. The cytokeratin cytoskeleton in liver diseases. *J Pathol* 200;204:367-376.
- Higgins GM, Anderson RM. Experimental pathology of the liver: restoration of the liver on the white rat following partial surgical removal. *Exp Pathol* 1931;12:186-202.
- Evarts RP, Nagy P, Marsden E, Thorgeirsson SS. A precursor-product relationship exists between oval cells and hepatocytes in rat liver. *Carcinogenesis* 1987;8:1737-1740.
- Bisgaard HC, Nagy P, Santoni-Rugiu E, Thorgeirsson SS. Proliferation, apoptosis and induction of hepatic transcription factors are characteristics of the early response of biliary epithelial (oval) cells to chemical carcinogens. *HEPATOLOGY* 1996;23:62-70.
- Alpini G, Roberts S, Kuntz SM, Ueno Y, Gubba S, Podila PV, et al. Morphological, molecular, and functional heterogeneity of cholangiocytes from normal rat liver. *Gastroenterology* 1996;110:1636-1643.
- Alpini G, Glaser SS, Ueno Y, Pham L, Podila PV, Caliuri A, et al. Heterogeneity of the proliferative capacity of rat cholangiocytes after bile duct ligation. *Am J Physiol* 1998;274:G767-G775.
- Grisham JW, Porta EA. Origin and fate of proliferated hepatic ductal cells in the rat: electronmicroscopic and autoradiographic studies. *Exp Mol Pathol* 1964;3:242-261.
- Engelhardt NV, Factor VM, Yasova AK, Poltorarina VS, Baranov VN, Lazareva MN. Common antigen of mouse oval and biliary epithelial cells: expression on newly formed hepatocytes. *Differentiation* 1990;6:821-834.
- Magin TM, Schröder R, Leitgeb S, Wanninger F, Zatloukal K, Grund C, et al. Lessons from cytokeratin 18 knockout mice: formation of novel cytokeratin filaments, secondary loss of cytokeratin 7 and accumulation of liver-specific cytokeratin 8-positive aggregates. *J Cell Biol* 1998;140:1441-1451.
- Thiese ND, Saxena R, Portmann BC, Thung SN, Yee H, Chiriboga L, et al. The canals of Hering and hepatic stem cells in humans. *HEPATOLOGY* 1999;30:1425-1433.
- Böcker W, Moll R, Poremba C, Holland R, Van Diest PJ, Dervan P, et al. Common adult stem cells in the human breast give rise to glandular and myoepithelial cell lineages: a new cell biological concept. *Lab Invest* 2002;82:737-746.
- Michel M, Török N, Godbout MJ, Lussier M, Gaudreau P, Royal A, et al. Cytokeratin 19 as a biochemical marker of skin stem cells in vivo and in vitro: cytokeratin 19 expressing cells are differentially localized in function of anatomic sites, and their number varies with donor age and culture stage. *J Cell Sci* 1996;109:1017-1028.
- Marceau N. Cell lineages and differentiation programs in epidermal, urothelial and hepatic tissues and their neoplasms. *Lab Invest* 1990;63:4-16.
- Slott PA, Liu MH, Tavoloni N. Origin, pattern, and mechanism of bile duct proliferation following biliary obstruction in the rat. *Gastroenterology* 1990;99:466-477.
- Fu X, Sun X, Li X, Sheng Z. Dedifferentiation of epidermal cells to stem cells in vivo. *Lancet* 2001;358:1067-1068.
- Nakano T. Hematopoietic stem cells: generation and manipulation. *Trends Immunol* 2003; 24:589-594.
- Van Eyken P, Sciot R, Desmet V. Intrahepatic bile duct development in the rat. *Lab Invest* 1988;59:52-59.
- Cocjin J, Rosenthal P, Buslon V, Barajas L, Geller SA, Ruebner B, et al. Bile duct formation in fetal, neonatal and infant livers compared with extrahepatic biliary atresia. *HEPATOLOGY* 1996;24:568-574.
- Omori M, Evarts RP, Omori N, Hu Z, Marsden ER, Thorgeirsson SS. Expression of alpha-fetoprotein and stem cell factor/c-kit system in bile duct ligated young rats. *HEPATOLOGY* 1997;25:1115-1122.

Architectural and Immunohistochemical Characterization of Biliary Ductules in Normal Human Liver

Katalin Dezső, Sándor Paku, Veronika Papp, Eszter Turányi, and Peter Nagy

The canals of Hering or biliary ductules have been described to connect the bile canaliculi with the interlobular bile ducts, and thus forming the distal part of the biliary tree. Studies in the last two decades suggested that the cells constructing these ductules could behave as hepatic progenitor cells. The canals of Hering are confined to the periportal space in the rat, while they have been reported to spread beyond the limiting plate in human liver. The distribution of the distal biliary ductules in normal human hepatic tissue has been investigated in our recent experiments. We could demonstrate the presence of interlobular connective tissue septa in a rudimentary form in healthy livers. The canals of Hering run in these septa in line with the terminal branches of the portal vein and hepatic arteries. This arrangement develops in the postnatal period but regresses after early childhood. The canals of Hering can be identified by the unique epithelial membrane antigen (EMA)⁻/CD56⁺/CD133⁺ immunophenotype. The canals of Hering leave the periportal space and spread into the liver parenchyma along rudimentary interlobular septa outlining the hepatic lobules. Our observations refine the original architectural description of the intraparenchymal portion of the canals of Hering in the human liver. The distinct immunophenotype supports their unique biological function.

Introduction

THE EXISTENCE OF A progenitor cell population in the liver has become generally accepted [1,2], and the clinical application of these cells have been of tremendous interest [3,4]. Today, liver transplantation is the only available curative treatment for liver failure, either in cirrhosis or in fulminant liver necrosis. However, the number of available donor livers sets the limit for the application of this procedure and alternative treatments are being sought. Transdifferentiation of bone marrow cells into hepatocytes does not seem to be efficient enough for clinical application [5–7]. Conversely, efficient hepatic regeneration has been recorded from the endogenous liver progenitor cells in human [8,9].

Most data refer to the canals of Hering as the site of the hepatic progenitor cell compartment [1,2,10]. This structure was described by Hering as “hepatic capillaries” [11], which maintained the link between bile ducts and the hepatocyte canalicular system. Later, it had been proposed to be the niche for hepatic progenitor cells [12,13]. The niche is a special microenvironment, which has a major impact on the maintenance and activation of the stem/progenitor cell compartment [14]. Therefore, the exact identification and

characterization of this structure is necessary to understand its behavior under normal and pathological conditions.

The canals of Hering are usually shown as short, straight ductules at the border of the periportal connective tissue and liver parenchyma, but probably this conformation is oversimplified. We have recently characterized the hepatic progenitor cell niche in rat liver by laser scanning confocal microscopy [15]. Long, branching ductules have been observed, strictly inside the periportal connective tissue. They had contact with the bile canalicular system at the limiting plate. Their unique CK19⁺/CK7⁻ immunophenotype has made their identification within the biliary tree easier. However, no CK7⁻ biliary structures could be observed in human liver specimens. Furthermore, the canals of Hering have been described to spread into the hepatic lobule in the normal human liver [16]. These observations suggest that the organization of the canals of Hering in human liver is different from the traditional simple view as well as from the architecture we saw in rat liver.

In our present study, we set out to collect normal human liver tissue from individuals of various ages and analyzed the architecture and immunophenotype of the biliary ductules by confocal microscopy.

Materials and Methods

Normal human liver specimens were collected from cadavers of spontaneous premature birth neonates without developmental abnormalities and individuals who died suddenly in accidents without morphological signs and anamnestic data of any liver disease. (Age and gender of the patients: 3 males, 23rd week of pregnancy; 4 females, 23rd week of pregnancy; 1 male, 39th week of pregnancy; 2 males, 3 years; 1 female, 3 years; 1 female, 13 years; 1 male, 20 years; 1 male, 26 years old.) All autopsies were performed within 24 h following death. The liver samples were thoroughly examined on formalin-fixed, paraffin-embedded liver sections with H&E, diastase PAS, Prussian blue, orcein and Masson's trichrome stainings; no fibrosis, ductular reaction, or other pathological alterations were observed. Snap frozen liver samples were stored at -80°C .

Frozen sections (10–20 μm) were fixed in methanol and were incubated at room temperature (1 h) with a mixture of primary antibodies (Supplementary Table 1; Supplementary materials are available online at <http://www.liebertpub.com/>) followed by the appropriate fluorescent secondary antibodies (Jackson ImmunoResearch, West Grove, PA). All samples were analyzed by confocal laser scanning microscopy using Bio-Rad MRC-1024 system (Bio-Rad, Richmond CA).

The procedure has been approved by the ethical committee of Semmelweis University.

Quantitative analysis of immunohistochemical staining

The livers of two 3-year-old children and the 20-, 26-year-old adults were used for quantitation. Consecutive frozen sections were co-stained for CK7/EMA, CK7/CD56, and CK7/CD133. The number of CK7-stained structures was determined. The double-stained structures were counted and the results were given as percent of the CK7+ structures.

Results

Distribution of hepatic ductules in the liver parenchyma

When sections from the livers of 3-year-old healthy children were stained for panCK, CK7, and laminin, hepatic ductules surrounded by basement membrane could be observed in the parenchyma far from the portal spaces (Fig. 1A and 1B). Low power examination revealed that these ductules were not randomly arranged. They outlined dimly polygonal structures with terminal veins in the centers and portal triads at the corners, that is, the classical hepatic lobules. When micrographs of 40 serial sections stained for cytokeratin-7 were digitally aligned and merged (Fig. 1C), this kind of perilobular arrangement of the ductules was even more obvious. Two other characteristics could be observed on this composite image: (i) no CK7+ biliary ductules were present inside the hepatic lobules; (ii) the ductules at the interlobular border spread until the half of the porto-portal distances, which resulted in watershed-like empty gaps in the middle of these stretches.

High power examination of individual biliary ductules showed that these narrow tubules did really extend beyond the limiting plate. The ductules spread in virtual "empty" spaces among hepatocytes on cytokeratin antibody stained sections (Fig. 1D), where only the epithelial elements of the hepatic tissue were decorated. When the ductules terminated

on hepatocytes, they were surrounded by typical U-shaped basement membrane (Fig. 2B inset), and the hepatocytes did not participate in the composition of the ductules beyond these connections. The "empty" space around the ductules was filled by collagenous matrix (Fig. 2A) and contained CD31+ small blood vessels (Fig. 2B), some of which were also labeled by the arterial marker NG-2 [17] (Fig. 2C). Taken together, confocal analysis of normal human liver revealed the deposition of small amounts of extracellular matrix between hepatic lobules, with expanding biliary ductules and blood vessels. This kind of arrangement of the blood vessels was described earlier as the vascular septum [18,19]. The small amount of matrix could not be visualized on traditional histological sections by special stainings on any of our liver samples.

Alterations of the hepatic ductules with age

The maturation of the biliary system continues in post-natal life in humans [20,21], and major changes are also observed in rats [15,22]. Therefore, we decided to examine the distribution of the canals of Hering in healthy livers of individuals of various ages.

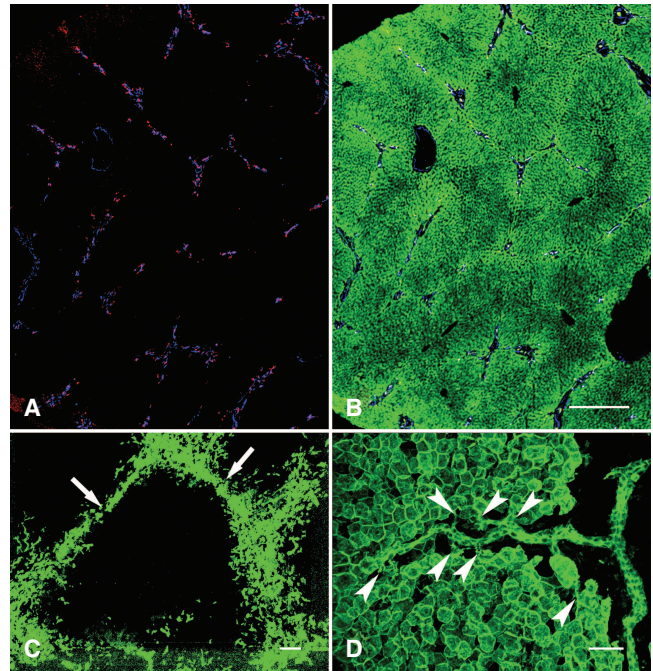


FIG. 1. Confocal images of normal human liver from a 3-year-old child. (A and B) Triple labeling for CK7 (red), laminin (blue), and panCK (green). (A) CK7 (red) and laminin (blue) staining. (B) Merged image. Comparing the two images, the perilobular arrangement of the laminin-framed ductules is clearly discernible. (C) CK7 (green)-stained biliary ductules sharply outline the hepatic lobule when 40 thick serial sections are merged. Note the "gaps" (arrows) halfway of the porto-portal distances. (D) Horizontal view of 42 optical sections stained for panCK. Note the numerous connections of the bile ductules with the liver parenchyma (arrowheads). The collecting bile ductule is running in an "empty" space toward the portal area. Scale bars for A and B = 500 μm ; C = 100 μm ; and D = 50 μm .

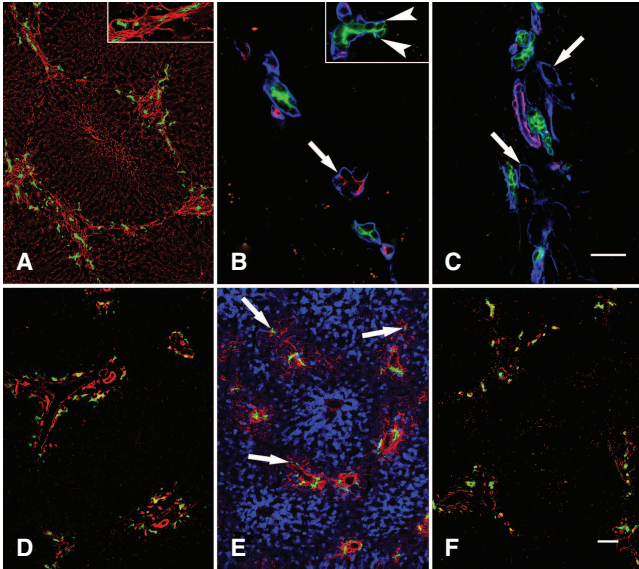


FIG. 2. Confocal images of normal human livers from a (A and B) 3- and a (C) 13-year-old child. (D–F) hepatic lobules in (D) 23- and (E) 39-week-old fetuses and (F) in a 26-year-old adult liver. (A) Double staining for CK7 and collagen I. CK7 (green)-stained perilobular ductules are embedded in rudimentary collagenous matrix (red) in the portal spaces and in the interlobular septa. The inset shows the vascular septum at a higher magnification on a different section. (B and C) High power view of the “vascular septum.” (B) Laminin (blue) surrounded CK7+ (green) ductules are accompanied by CD31 (red)-decorated blood vessels (arterioles). The larger vessel (arrow) probably represents a terminal branch of the portal vein. The inset shows the connection of a ductule on the hepatic plate (cannot be seen with this staining); note the sharp ending of the U-shaped basement membrane at the ducto-parenchymal border (arrowheads). (C) Note the proximity of NG-2+ (red) arterioles to the CK7 (green)-stained ductules. The empty laminin (blue) circles (arrows) probably represent portal vein branches. (D) The portal tracts are “closed”; laminin (red) surrounded CK7+ (green) ductules are confined to the border of the portal space. Note the high number of ductules marking the ductogenesis from the ductal plate. (E) Thy-1 (red)-stained myofibroblasts initiate the formation of the interlobular septa with a few CK7+ (green) ductules (arrows). The CYP450 (blue) staining shows the zonality of the hepatic lobule with a Thy-1-positive terminal vein in the center. (F) Laminin (red) and CK7 (green) marked ductules outline the hepatic lobule in the adult liver, but they are rarer in the septa than in children (compare with Fig. 1C, 1D). Scale bar for A, D, E, and F = 100 μm ; and B and C = 50 μm .

The portal areas in the liver of immature neonates born on the 23rd week of pregnancy were “closed.” There were numerous bile ducts in the periportal connective tissue, especially at the periphery, as the remnants of the ductal plate. However, no signs of vascular septa were seen; no matrix deposition, blood vessels, or biliary ductules could be observed outside the limiting plate in any of the examined specimens (Fig. 2D).

Early signs of vascular septum formation could already be recognized in a liver sample derived from a fetus of the

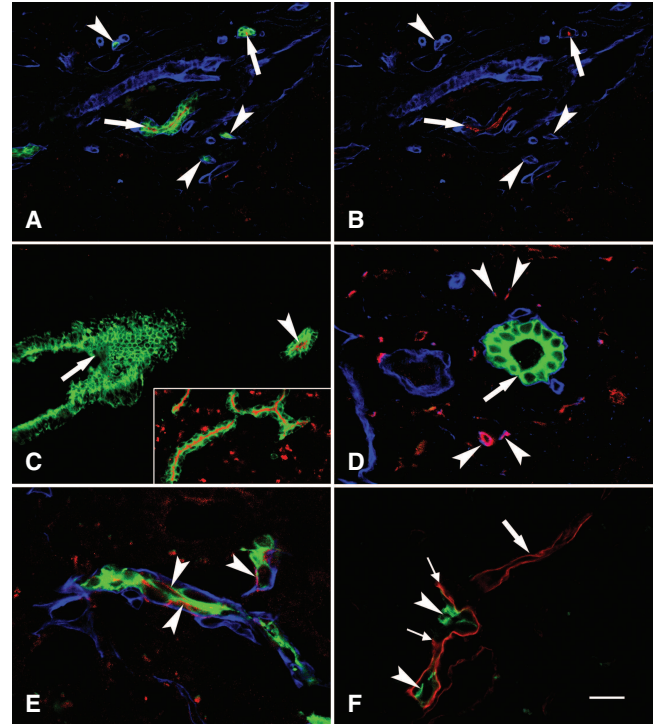


FIG. 3. Immunophenotypical characterization of the hepatic ductules in (A–C) adult and (D–F) 3-year-old livers. (A and B) There is a sharp apical epithelial membrane antigen (EMA) (red) staining in CK7 (green) and laminin (blue) marked bile ducts (arrows) inside the portal space, while EMA staining is absent in the small ductules (arrowheads) at the periphery. For better visibility of the EMA staining, B shows only the red and blue channels. (C) There is an apical CD133 (red) staining in a CK7 (green) marked ductule (arrowhead), while this marker is not present in an interlobular bile duct (arrow). The inset shows the apical CD133 positivity of ductules. (D) CD56 (red) stains only the small nerves (arrowheads) in the portal space, the CK7 (green) and laminin (blue) labeled bile duct is negative (arrow). (E) High magnification of a CK7 (green) and laminin (blue) stained ductule within the septum reveals membranous CD56 (red) positivity (arrowheads). (F) CD56+ (green) bile ductules (arrowheads) are attached to hepatocytes (not highlighted by this staining), are surrounded by laminin-positive (red) U-shaped basement membrane (small arrows). The laminin (red)-positive “empty” structure surrounded by basement membrane (large arrow) represents a blood vessel. Scale bar = 50 μm .

39th week of pregnancy. It was mostly outlined by Thy-1-positive myofibroblasts, but a few CK7+ ductules were also present in these septum fundamentals outside the portal fields (Fig. 2E).

The vascular septa and all of its components were mostly developed in the livers of young children of the age of 3 years (Fig. 1A and 1B). The only available liver specimen from a 13-year-old girl contained relatively regressed vascular septa, and although all the elements described earlier were present in the livers of young adults (20 and 26 years), they were more scarce (Fig. 2F).

Immunophenotypic characterization of bile ductules

There are several proposed markers for hepatic progenitor cells in human liver (1,2), but most of them did not distinguish hepatic ductules of the vascular septa from larger interlobular bile ducts in our hands. Some of the markers (AFP, chromogranin, synaptophysin, DMBT, DLK, CEA, CK20, CK14) did not label any biliary structures, while others (EpCAM, E-cadherin, CK7, CK19) stained the complete biliary tree (data not shown). Only three markers reacted differentially with bile ducts and ductules. Epithelial membrane antigen (EMA) resulted in a very sharp characteristic linear apical staining in the interlobular bile ducts. Conversely, it was absent in the ductules even on cross sections (Fig. 3A and 3B). The staining pattern of CD133 (Fig. 3C) and CD56 (Fig. 3D, 3E, and 3F) was opposite. In specimens up to the age of 3 years, there was a consistent apical CD133 staining in all segments of the biliary tree. However, in samples from older individuals the staining was strictly confined to the small ductules of the vascular septa. The distribution of CD56 in all specimens was similar to this latter case: it labeled exclusively the small ductules.

Quantitative evaluation of the immunohistochemical reactions (Table 1) showed that only a small portion of the biliary structures were stained for EMA, and this staining was restricted to the periportal area. No such preferential distribution was noticed with the two other markers. Almost all ducts/ductules were decorated by CD133 in the livers of the children, while in adulthood the ratio of CD56+ and CD133+ ductules were similar. The CK7 antibody reacted sometimes with very small bile ductules occasionally appearing as single cells especially along the vascular septa. Since the CD56 and CD133 reaction was not as strong and diffuse as the CK7, the number of the CD56 and CD133 ductules was probably underestimated.

Discussion

We have analyzed the architecture of biliary ductules in normal human livers and observed them to circumscribe the classical hepatic lobules by participating in the formation of the so-called vascular septa (Fig. 4). This arrangement develops in postnatal life and can be most obviously seen in early childhood. The hepatic ductules are characterized by a unique EMA−/CD56+/CD133+ immunophenotype.

There are several candidates for the liver stem/progenitor cell niche. Kuwahara et al. [10] proposed four structures to harbor such cells: the canals of Hering, intralobular bile ducts, periductal “null” mononuclear cells, and peribiliary hepatocytes. After all, stemness has been proposed to be not an entity but function [23] and—depending on the situation—different cell populations can behave as hepatic progenitor

cells. Insofar, most evidence shows that the canals of Hering have the highest potential to behave as hepatic progenitor cells [1,2,6,13]. Therefore, the accurate architecture of these structures is a key issue to understand their behavior under normal and pathological conditions.

The canals of Hering were originally described [11] as short straight ducts at the limiting plate, which connect the bile canaliculi to the interlobular bile ducts. However, Theise et al. [16] demonstrated the extension of hepatic ductules through the limiting plate into the hepatic lobule. Our results confirm the presence of these structures deep in the hepatic parenchyma; moreover, a clear orientation of the ductules could be observed on our confocal images. The ductules spread into the parenchyma along the porto-portal axis. The hexagonal structures outlined by hepatic ductules correspond to the classical hepatic lobules. High power examination of individual ductules revealed their close correlation with bile canaliculi enabling their drainage.

In addition to former observations [19,24] that venular branches are present in vascular septa, we noticed NG-2-stained arterioles running in line with the ductules. There have been speculations about bile ductule escorting hepatic arterioles [18,19,25,26,27] but no convincing evidence has been published so far. Gouw et al. [19] and van der Heuvel et al. [28] emphasize the importance of the microvascular compartment for the efficient regeneration of ductules. Since—contrary to several other species—no arterio-portal anastomoses exist in the human liver, the presence of arterial

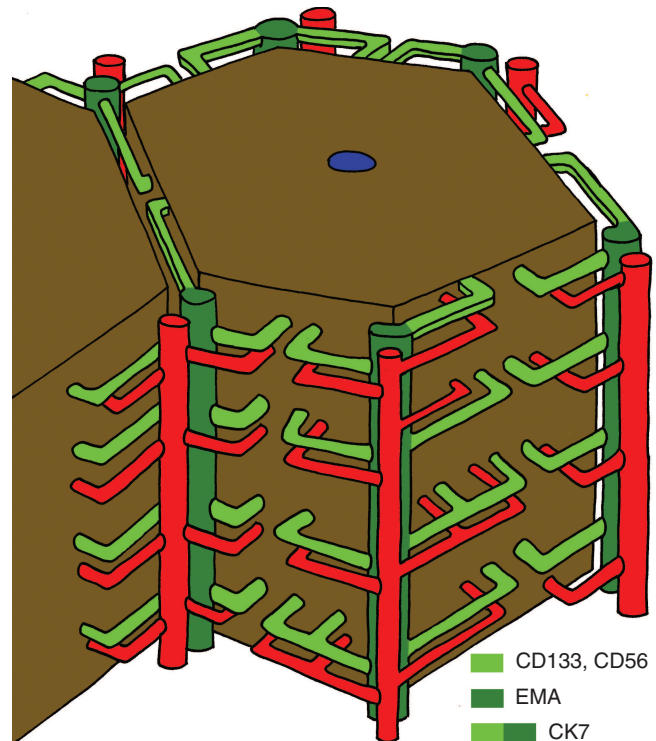


FIG. 4. Schematic representation of hepatic lobule (brown), with bile ducts/ductules (green) and accompanying arterioles (red). Note that these structures extend only halfway into the porto-portal distances; however, they cover the whole “lateral” surface of the lobule. For simplicity, the portal vein branches are not shown.

TABLE 1. IMMUNOPHENOTYPE OF BILIARY STRUCTURES IN NORMAL LIVER

Sample	CK7+	EMA+	CD56+	CD133+
3 years	100% (1,112)	4.8%	62.9%	96.3%
Adult	100% (1,125)	6.7%	54.4%	59%

Abbreviation: EMA, epithelial membrane antigen.

() Total number of counted bile ducts.

blood would be advantageous for the regenerative function of the ductules. The proximity of the blood vessels to the bile ductules corresponds very well to the close correlation between the development of biliary and vascular structures [29]. This architecture of the intraparenchymal ductules and the escorting vessels is in full agreement with the proposed model of Matsumoto [18] based on 3D reconstruction of the human liver from thousands of serial sections.

According to the original description [18], the “vascular septum” is not a fibrous septum but a vascular surface from which sinusoids originate. However, we observed a collagenous matrix in this location. Since all the studied liver samples were normal and no fibrosis could be seen by traditional connective tissue staining, we suggest that a minimal amount of matrix material in the vascular septum, which can be visualized only by careful immunohistochemical analysis, is a component of the normal human hepatic tissue. Hepatic lobules are separated by well-defined connective tissue septa in several species [30], and the vascular septum of the human liver with its matrix components can be regarded as a rudimentary interlobular septum.

We have observed a peculiar age dependence of the vascular septa. Obviously, a more detailed age-related analysis of these structures is required. The interlobular bile ducts develop from the ductal plate [21], but ductal plates disappear shortly after birth and new bile ducts/ductules arise from pre-existent ducts by branching and elongation [31]. This “cholangiogenesis” could follow the primitive septa we observed in the liver of the 39-week-old fetus. The postnatal maturation of the biliary tree is well documented in humans [21] and rats [22] as well. Furthermore, the interlobular septum also develops postnatally in pigs [30].

The progressing scarcity of the ductular system with age should also be analyzed in more detail. We do not know if this process is absolute due to the apoptosis of biliary cells or just relative. The size of the hepatic lobules increases during ontogeny [32], and if the growth of the ductules is arrested earlier, it may be responsible for their relative regression.

We were curious if the biliary ductules could be characterized by a special immunophenotype. Three different antibodies were able to distinguish reliably the canals of Hering from larger bile ducts: the canals of Hering were EMA-/CD56+/CD133+; whereas, interlobular bile ducts were EMA+/CD56-/CD133-. All of these markers have already been mentioned in connection with the hepatic progenitor cell compartment. Atypical ductular reactions have been reported EMA-/CD56+, while the typical ones, which are similar to the interlobular bile ducts, are EMA+/CD56- [33]. CD56 has been demonstrated in proliferating ductules, while it could not be observed in normal canals of Hering [34,35], but recent studies found CD56 mRNA and protein in ductules of normal human livers [36,37]. CD133 has originally been described as a hematopoietic stem cell marker, and its mRNA has been detected in the liver by Northern hybridization, but no immunostaining was identified in paraffin sections by Miraglia et al. [38]. However, the protein could be detected by immunohistochemistry in the canals of Hering of normal human liver [39] and in regenerating ductules related to fulminant liver failure [40]. In our present experiments, the distribution of this marker showed an age-dependent change. This is similar to our results on rat liver, where the immunophenotype of the canals of Hering developed postnatally [15]. Interestingly, CD133+ cells isolated

from HCC proved to be highly tumorigenic and have been reported as tumor stem cells [41]. Increased expression of CD133 has also been reported in a subset of cholangiocellular carcinomas, which were claimed to have a progenitor cell origin [42].

The combined application of these three antibodies provides an efficient tool for the identification of the canals of Hering in the normal human liver. Furthermore, the distinct immunophenotype of the hepatic ductules supports their different biological potential.

In conclusion, we present a refinement for the widely cited architectural description [16,27,43] of the intraparenchymal biliary ductules in normal human liver. The canals of Hering with escorting vessels are situated in the vascular septum and are components of a rudimentary interlobular septum. They can be distinguished from larger bile ducts by a unique immunophenotype. Better comprehension of canals of Hering’s architecture in normal human liver may promote our understanding of their behavior in various pathological/biological reactions.

Acknowledgments

The authors appreciate the help of Dr. Nóra Szilávik, Dr. Éva Görbe, and Dr. Júlia Hajdú in collecting the samples. The article is supported by OTKA K 67697.

Author Disclosure Statement

We declare that we have no duality of interest.

References

1. Alison MR, P Vig, F Russo, BW Bigger, E Amofah, M Themis and S Forbes. (2004). Hepatic stem cells: from inside and outside the liver? *Cell Prolif* 37:1–21.
2. Santoni-Rugiu E, P Jelnes, SS Thorgeirsson and HC Bisgaard. (2005). Progenitor cells in liver regeneration: molecular responses controlling their activation and expansion. *APMIS* 113:876–902.
3. Dahlke MH, FC Popp, S Larsen, HJ Schlitt and JEJ Rasko. (2004). Stem cell therapy of the liver—fusion or fiction? *Liver Transpl* 10:471–479.
4. Tosh D and A Strain. (2005). Liver stem cells—prospects for clinical use. *J Hepatol* 42:S75–S84.
5. Thorgeirsson SS and JW Grisham. (2006). Hematopoietic cells as hepatocyte stem cells: a critical review of the evidence. *Hepatology* 43:2–8.
6. Fausto N. (2004). Liver regeneration and repair: hepatocytes, progenitor cells, and stem cells. *Hepatology* 39:1477–1487.
7. Grompe M. (2003). The role of bone marrow stem cells in liver regeneration. *Semin Liver Dis* 23:363–371.
8. Fujita M, H Furukawa, M Hattori, S Todo, Y Ishida and K Nagashima. (2000). Sequential observation of liver cell regeneration after massive hepatic necrosis in auxiliary partial orthotopic liver transplantation. *Mod Pathol* 13:152–157.
9. Eleazar JA, L Memeo, JS Jhang, MM Mansukhani, S Chin, SM Park, JH Lefkowitz and G Bhagat. (2004). Progenitor cell expansion: an important source of hepatocyte regeneration in chronic hepatitis. *J Hepatol* 41:983–991.
10. Kuwahara R, AV Kofman, CS Landis, ES Swenson, E Barendsward and ND Theise. (2008). The hepatic stem cell niche: identification by label-retaining cell assay. *Hepatology* 47:1994–2002.
11. Hering E. (1867). Über den Bau der Wirbelthierleber. *Arch Mikrosk Anat* 3:88–114.

12. Grisham JW and EA Porta. (1964). Origin and fate of proliferated hepatic ductal cells in rat: electron microscopic and autoradiographic studies. *Exp Mol Pathol* 3:242–261.
13. Paku S, J Schnur, P Nagy and SS Thorgeirsson. (2001). Origin and structural evolution of the early proliferating oval cells in rat liver. *Am J Pathol* 158:1313–1323.
14. Scheres B. (2007). Stem-cell niches: nursery rhymes across kingdoms. *Nature Rev Mol Cell Biol* 8:345–354.
15. Paku S, K Dezső, L Kopper and P Nagy. (2005). Immunohistochemical analysis of cytokeratin 7 expression in resting and proliferating biliary structures of rat liver. *Hepatology* 42:863–870.
16. Theise ND, R Saxena, BC Portmann, SN Thung, H Yee, L Chiriboga, A Kumar and JM Crawford. (1999). The canals of Hering and hepatic stem cells in humans. *Hepatology* 30:1425–1433.
17. Fukushi J, IT Makagiansar and WB Stallcup. (2004). NG2 proteoglycan promotes endothelial cell motility and angiogenesis via engagement of Galectin-3 and $\alpha 3\beta 1$ integrin. *Mol Biol Cell* 15:3580–3590.
18. Matsumoto T, R Komori, T Magara, T Ui, M Kawakami, T Tokuda, S Takasaki, H Hayashi, K Jo, H Hano and H Tanaka. (1979). A study on the normal structure of the human liver, with special reference to its angioarchitecture. *Jikeikai Med J* 26:1–40.
19. Gouw AS, MC van der Heuvel, M Boot, MJ Slooff, S Poppema and KP de Jong. (2006). Dynamics of the vascular profile of the finer ranches of the biliary tree in normal ad diseased human livers. *J Hepatol* 45:393–400.
20. Crawford JM. (2002). Development of the intrahepatic biliary tree. *Semin Liver Dis* 22:213–226.
21. Lemaigre FP. (2003). Development of the biliary tract. *Mech Dev* 120:81–87.
22. Van Eyken P, R Sciot and V Desmet. (1988). Intrahepatic bile duct development in the rat. *Lab Invest* 59:52–59.
23. Blau HM, TR Brazelton and JM Weimann. (2001). The evolving concept of a stem cell: entity or function? *Cell* 105:829–841.
24. Teutsch HF. (2005). The modular microarchitecture of human liver. *Hepatology* 42:317–325.
25. Yamamoto K, I Sherman, MJ Phillips and MM Fisher. (1985). Three-dimensional observations of the hepatic arterial terminations in rat, hamster and human liver by scanning electron microscopy of microvascular casts. *Hepatology* 5:452–456.
26. RNM MacSween, VJ Desmet, T Roskams and RJ Scotthorne. (2002). Developmental anatomy and normal structure. In: *Pathology of the Liver*. MacSween RNM, AD Burt, BC Portmann, KG Ishak, PJ Scheuer, PP Anthony, eds. Churchill Livingstone, London, pp 1–66.
27. Saxena R, ND Theise and JM Crawford. (1999). Microanatomy of the human liver-exploring the hidden interfaces. *Hepatology* 30:1339–1346.
28. Van der Heuvel MC, KP de Jong, M Boot, MJ Sloff, S Poppema and AS Gouw. (2006). Preservation of bile ductules mitigates bile duct loss. *Am J Transplant* 6:2660–2671.
29. Libbrecht L, D Cassiman and V Desmet. (2002). The correlation between portal myofibroblasts and development of intrahepatic bile ducts and arterial branches in human liver. *Liver* 22:252–258.
30. Ekataksin W and K Wake. (1997). New concepts in biliary and vascular anatomy of the liver. *Prog Liver Dis* 15:1–30.
31. Roskams T and V Desmet. (2008). Embryology of extra- and intrahepatic bile ducts, the ductal plate. *Anat Rec* 291:628–635.
32. PappV, K Dezső, V László, P Nagy and S Paku. (2009). Architectural changes during regenerative and ontogenic liver growth in the rat. *Liver Transplant* 15:177–183.
33. Sonzogni A, G Colloredo, L Fabris, M Cadamuro, B Paris, L Roffi, M Pozzi, G Bovo, P Del Poggio, BC Portmann and M Strazzabosco. (2004). Isolated idiopathic bile ductular hyperplasia in patients with persistently abnormal liver function tests. *J Hepatol* 40:592–598.
34. Van der Heuvel MC, MJH Slooff, L Visser, M Muller, KP DeJong, S Poppema and AS Gouw. (2001). Expression of anti-OV6 antibody and anti-N-CAM antibody along the biliary line of normal and diseased human livers. *Hepatology* 33:1387–1393.
35. Zhou H, LE Rogler, L Teperman, G Morgan and CE Rogler. (2007). Identification of hepatocytic and bile ductular cell lineages and candidate stem cells in bipolar ductular reactions in cirrhotic human liver. *Hepatology* 45:716–724.
36. Schmelzer E, E Wauthier and LM Reid. (2006). The phenotypes of pluripotent human hepatic progenitors. *Stem Cells* 24:1852–1858.
37. Zhang L, N Theise, M Chua and LM Reid. (2008). The stem cell niche of human livers. *Hepatology* 48:1598–1607.
38. Miraglia S, W Godfrey and AH Yin. (1997). A novel five-transmembrane hematopoietic stem cell antigen: isolation, characterization, and molecular cloning. *Blood* 90:5013–5021.
39. Karbanová J, E Missol-Kolka, A Fonseca, C Lorra, P Janich, H Hollerová, J Jászai, J Ehrmann, Z Kolar, C Liebers, S Arl, D Subrtová, D Freund, J Mokry, WB Huttner and D Corbelli. (2008). The stem cell marker CD 133 (Prominin-1) is expressed in various human glandular epithelia. *J Histochem Cytochem* 56:977–993.
40. Craig CEH, A Quaglia, C Selden, M Lowdell, H Hodgson and AP Dhillon. (2004). The histopathology of regeneration in massive hepatic necrosis. *Semin Liver Dis* 24:49–64.
41. Ma S, K Chan, L Hu, TK Lee, JY Wo, IO Ng, BJ Zheng and XY Guan. (2007). Identification and characterization of tumorigenic liver cancer stem/progenitor cells. *Gastroenterology* 132:2542–2556.
42. Komuta M, B Spee, SV Borghot, R De Vos, C Verslype, R Aerts, H Yano, T Suzuki, M Matsuda, H Fujii, V Desmet, M Kojiro and T Roskams. (2008). Clinicopathological study on cholangiolocellular carcinoma suggesting hepatic progenitor cell origin. *Hepatology* 47:1544–1556.
43. Roskams TA, ND Theise, C Balabaud, G Bhagat, PS Bhathal, P Bioulac-Sage, EM Brunt, JM Crawford, HA Crosby, V Desmet, MJ Finegold, SA Geller, AS Gouw, P Hytiroglou, AS Knisely, M Kojiro, JH Lefkowitz, Y Nakanuma, JK Olynyk, YN Park, B Portmann, R Saxena, PJ Scheuer, AJ Strain, SN Thung, IR Wanless and AB West. (2004). Nomenclature of the finer branches of the biliary tree: canals, ductules, and ductular reactions in human livers. *Hepatology* 39:1739–1745.

Address correspondence to:

Dr. Peter Nagy
 First Department of Pathology and
 Experimental Cancer Research
 Semmelweis University
 Üllői út 26
 Budapest 1085
 Hungary

E-mail: nagy@korkb1.sote.hu

Received for publication April 1, 2009

Accepted after revision June 24, 2009

Prepublished on Liebert Instant Online June 24, 2009

Architectural Changes During Regenerative and Ontogenic Liver Growth in the Rat

Veronika Papp, Katalin Dezső, Viktória László, Peter Nagy, and Sándor Paku

First Department of Pathology and Experimental Cancer Research, Semmelweis University, Budapest, Hungary

Although liver architecture has a major impact on function, morphological aspects of liver growth are relatively neglected. In our recent experiments, the architectural changes of the rat liver were compared during 2 basic processes: ontogeny and regenerative liver growth. The hepatic tissue is constructed as structural/functional units, and probably the most established and well-defined such unit is the classic lobule. The extent and orientation of the lobules are variable in the liver, and this renders their accurate size determination more difficult. The filling of the liver vasculature by a colored resin nicely outlined the surface lobules, enabling an analysis of the alterations of these structures during liver growth. There are 3 structural components of postnatal physiological liver development: enlargement of the hepatocytes and expansion and multiplication of the liver lobules. However, the enlargement of the lobules is exclusively responsible for the regenerative liver growth following partial hepatectomy. The number of hepatic lobules does not change during this latter reaction, but they gain a more complex, irregular structure. *Liver Transpl* 15:177-183, 2009. © 2009 AASLD.

Received April 15, 2008; accepted August 18, 2008.

Partial hepatectomy (Phx) along with the subsequent regenerative response is one of the most studied non-tumorous growth processes in mammals. There are several excellent reviews summarizing the available information about the regulation of this well-synchronized hyperplastic process.¹⁻³ The dynamics of cell proliferation/apoptosis are also well documented; therefore, that was not the object of this study. Unfortunately, our knowledge is much more limited regarding the structural changes,⁴ so this aspect of the growth was analyzed in this work. Although this process is mostly called liver regeneration, in a biological sense it should be referred to as compensatory hyperplasia because the resected lobes do not grow back. Instead, the remaining lobes enlarge as a result of hepatocyte proliferation. The liver size also increases several-fold during postnatal life. This growth process has been studied in several species,⁵⁻⁸ but it has not been compared with compensatory hyperplasia. The liver has a modular architecture.^{9,10} Although the liver lobules may not be the true functional units, they are well-defined compartments that build up the liver. Therefore, hepatic growth

can be achieved by an increase in the size and/or number of lobules. This question was addressed in our recent experiment in rats. The filling of the hepatic and portal venous system outlined the lobules on the liver surface very nicely. Morphometric analysis of the right lateral liver lobe revealed that the number of liver lobules did not change, but their size increased during compensatory growth. Conversely, during the studied postnatal period, the liver grew by enlargement and multiplication of the lobules. In summary, the adult liver lobes seem to be constructed with a standard number of lobules, and the fully developed liver is not able to form new lobules upon a further proliferative trigger.

MATERIALS AND METHODS

Experimental Design

Several parameters of the hepatic lobules were measured in 4-week-old (50 g), 8-week-old (160 g), and 12-week-old (250 g) male F344 rats; in rats 4 weeks

Abbreviations: CTR, control; nd, not determined; Phx, partial hepatectomy; RLL, right lateral lobe. This study was supported by the Hungarian National Science Foundation (K67697) and the Hungarian Ministry of Health (32/2006). Address reprint requests to Peter Nagy, First Department of Pathology and Experimental Cancer Research, Semmelweis University, Üllői út 26, Budapest H-1085, Hungary. Telephone: 36-1-266 1638; FAX: 36-1-317 1074; E-mail: nagy@korb1.sote.hu

DOI 10.1002/lt.21665

Published online in Wiley InterScience (www.interscience.wiley.com).

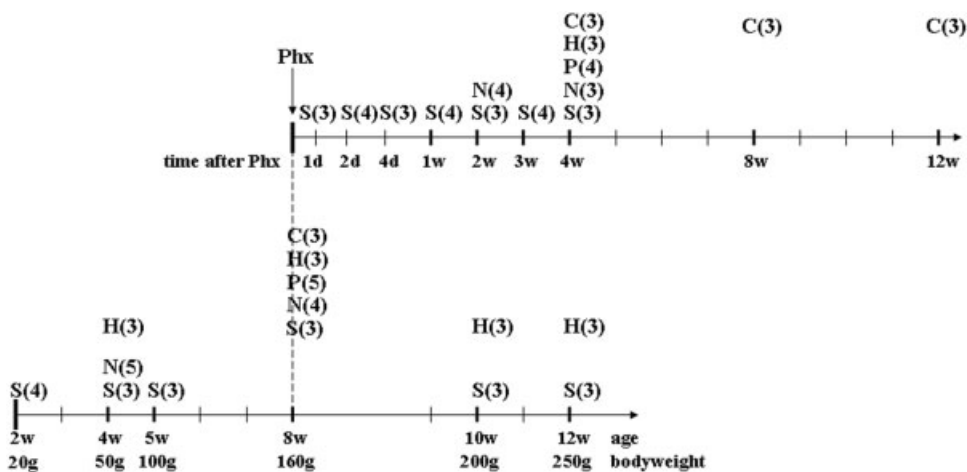


Figure 1. Schematic representation of the experimental design. The upper line illustrates the time points of experiments after partial hepatectomy; the lower illustrates those during ontogeny. Numbers in parentheses represent the number of investigated rats. Abbreviations: C, CYP450 II E1 expression; H, hepatocyte size determination; N, total number of hepatic lobules on the convex surface of the right lateral lobe; P, portal vein number around the central vein; S, size determination (surface area and circumference) of hepatic lobules.

(250 g) after Phx at 8 weeks of age (160 g); and at certain interim experimental points. The schema of the measurements and the number of the investigated rats are shown on Fig. 1. The animal study protocols were conducted according to the National Institutes of Health guidelines for animal care.

Liver Regeneration

Traditional, two-thirds Phx¹¹ was performed on rats weighing 160 g under ether anesthesia. The size of the liver lobules was measured 1, 2, and 4 days and 1, 2, 3, and 4 weeks after the operation. The surface lobules of the right lateral lobe were counted on control rats (160-g bodyweight) and 2 and 4 weeks after Phx. The size of the hepatocytes was determined 4 weeks after the operation.

Physiological Liver Growth

The size of the surface lobules was measured in normal rats with the following bodyweights: 20, 50, 100, 160, 200, and 250 g. The number of surface lobules was counted on the right lateral lobe of rats with a bodyweight of 50 or 160 g. The average size of the hepatocytes was also measured for rats with a total bodyweight of 50, 160, 200, or 250 g.

Determination of the Size of the Lobules

For outlining the surface liver lobules, a cannula, washed with heparin, was inserted into the inferior vena cava. The blood was washed out from the liver with phosphate-buffered saline through the left ventricle of the heart. When the flush fluid became colorless, the vena cava was ligated above the level of the hepatic veins, and the portal vein was opened. The hepatic veins and the sinusoids were filled up through the vena cava cannula by a fluorescent dye containing polystyrol resin and were monitored by eye with a stereomicroscope. The filling was stopped when the resin filled up the central veins and partially filled the hepatic sinusoids on the surface of the liver. At this stage, the negatives of the interlobular borders were outlined by

the resin. The right lateral liver lobe was removed from the rats, its weight was recorded, and all further measurements were performed on this lobe.

The lobe was placed onto a wet slide and examined with a Nikon TE200 inverted microscope. The surface image of the lobe was captured with a Bio-Rad (Richmond, CA) MRC1024 confocal system (Ex488/Em520 ± 16 nm). The periportal zone appeared on the pictures as black areas. Interlobular borders were highlighted by a line drawn halfway between the central veins (along the vascular septa). The approximate center of the black areas determined the corners of the polygon representing the lobules. In cases of neighboring overfilled central veins, the border was determined by an analysis of the direction of the sinusoids. At the border zone, the sinusoids changed their direction from running toward one another to running along the border. The circumference and surface area of the lobules were determined with the Image J program.

Counting of the Surface Liver Lobules

In another set of rats, the portal venous system was filled with a blue-stained resin in addition to the red resin-outlined hepatic veins. The blood was removed from the liver as described previously. The portal vein was filled with blue resin until it just entered the sinusoids, and this was followed by filling of the central veins. This method could not be applied to the determination of the size of lobules because of the slight enlargement of the liver. These animals were used to count the absolute number of liver lobules on the convex surface of the right lateral lobe. Counting of the lobules was performed by the placement of a mark on each lobule with an Indian ink pen with a 0.2-mm line width. The number of portal vein branches around a central vein was also counted on these specimens.

Hepatocyte Size Determination

Frozen sections from the liver were stained with fluorescein isothiocyanate-labeled pancytokeratin antibody (catalog number F0859, Dako, Glostrup, Den-

mark; dilution, 1:10), which outlined the cell membranes of the hepatocytes. The nuclei were stained with propidium iodide. The circumference and surface of 50 pericentral hepatocytes were measured in each liver lobule on 3 randomly selected fields. The size of hepatocytes is dependent on their zonal position,¹² so data from different animals are more comparable if they are referring to a confined compartment, such as the pericentral zone. Furthermore, the radial orientation of the pericentral sinusoids makes possible a more exact determination of the outline of the hepatocyte borders versus the more irregular arrangement of the periportal hepatocytes.

Zonality of the Liver Lobules

The right lateral liver lobe was frozen under slight pressure to produce a flat surface for cutting. Frozen sections were made from the livers of control rats and the livers of rats 4, 8, and 12 weeks after Phx in a plane parallel with the surface. The section was fixed in methanol (-20°C) and stained for CYP450 II E1 (catalog number BV-3084-3, MBL, Woburn, MA; dilution, 1:100) for an hour at room temperature, and the reaction was visualized by a fluorescein isothiocyanate-labeled secondary antibody (30 minutes at room temperature). The sections were counterstained with propidium iodide.

Statistical Analysis

Statistical analysis was performed with the Student *t* test.

RESULTS

Morphometric Analysis of the Surface Liver Lobules During Liver Regeneration

The partial filling of the central veins and liver sinusoids through the hepatic veins outlined the lobules on the liver surface. This image was captured with a microscope, and the lobule borders were drawn on the digitalized image (Fig. 2A-C). Phx was performed on young, adult rats (8 weeks old, 160-g bodyweight), which are optimal for this procedure. All the investigated parameters of the livers were compared to the values measured on the right lateral lobe of unoperated rats (controls, 160 g). Both the circumference and surface area of the lobules grew gradually during the regenerative growth of the right lateral liver lobe. Both parameters increased rapidly in the first 7 days, and this was followed by a slight but not significant increase in the upcoming 3 weeks. Finally, the average lobular circumference increased 1.51-fold and the surface area increased 2.3-fold during our observation period. The weight of the studied lobe was also recorded, and it grew 3.29-fold (Fig. 3A). The number of liver lobules on the convex surface of the right lateral lobe was also counted in 160-g unoperated control rats and at 2 selected time points during regeneration. It did not show any significant alterations (Table 1). In brief, the liver

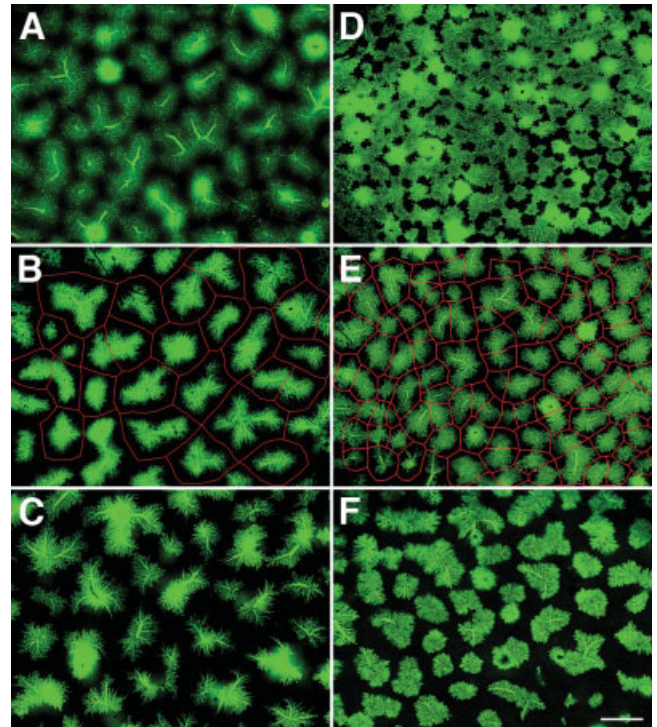


Figure 2. Retrograde filling of the hepatic sinusoids through the terminal (central) veins with green fluorescent resin: (A-C) 2, 4, and 28 days after partial hepatectomy and (D-F) livers of rats with bodyweights of 50, 160, and 250 g. The lobular borders (red lines) are shown in parts B and E. Note the enlargement of the lobules with increasing time (after partial hepatectomy) and age. Scale bar: 1 mm.

grew by the enlargement of the liver lobules, whereas their number did not change.

However, the architecture of the enlarged lobules showed some characteristic changes. The images of the central veins on the liver surface became elongated and more branched. The shape of the lobules became more variable and polygonal. This observation was supported by the increased number of portal vein branches around the central veins (Fig. 4A-D and Table 1). The CYP II E1 enzyme showed a typical zonal distribution in the liver lobule.¹³ It was preferentially expressed by the pericentral and midzonal hepatocytes. The positive cells were surrounded by an evenly broad band of the negative cells in the control liver. The immunostaining of this enzyme showed a peculiar, arborescent distribution in the regenerated liver throughout our 3-month observation period, demonstrating the permanent functional modification of the lobular structure (Fig. 4E,F).

Structural Characterization of Postnatal Liver Growth

In order to compare the regenerative/hyperplastic growth response of the liver lobules with the physiological, ontogenic liver growth, similar measurements were performed on the livers of rats of various ages. All these studies were also confined to the right lateral liver lobe.

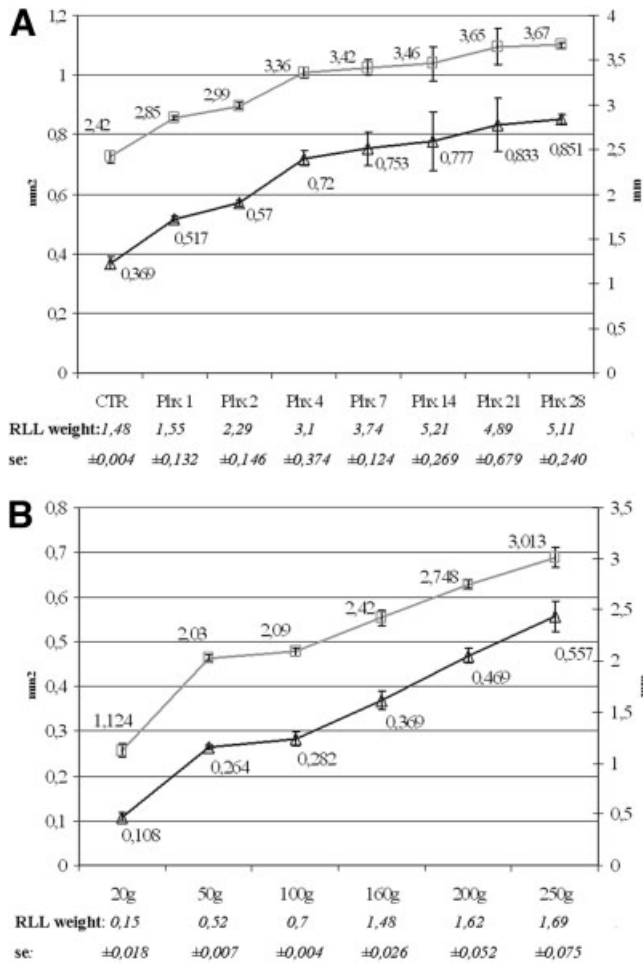


Figure 3. The numerical dimensions of the growing liver during regeneration following (A) Phx and (B) ontogeny: (□) the circumference and (△) the surface of the hepatic lobules. The bars represent the standard error. Abbreviations: CTR, control; Phx, partial hepatectomy; RLL, right lateral lobe.

Similarly to the regenerative growth, the enlargement of the hepatic lobules was recorded with age (Fig. 2D-F). Although the bodyweight of the rats increased from 20 to 250 g (12.5-fold), the weight of the studied lobe increased 11.27-fold. The average surface area of the lobules increased 5.16-fold, and the circumference increased 2.68-fold. Additionally, the number of surface lobules also increased by approximately 30% (Table 1) while the bodyweight changed from 50 to 160 g (Fig. 3B). It is important to emphasize that the absolute values of these parameters are not comparable to those of the hepatectomized rats because the studied lobe represents a much smaller portion of the whole liver than that in the other experimental model.

Alteration of Hepatocyte Size During Liver Growth

Expansion of the lobules can be a result of hepatocyte enlargement. Therefore, the size of these cells was also measured. Indeed, obvious hepatocyte enlargement could be observed in the rats while the bodyweight

increased from 50 to 160 g (Fig. 5). The average hepatocyte surface area grew 1.66-fold, and the circumference grew 1.29-fold. The weight of the investigated lobe increased 2.9-fold during this period. The size of the hepatocytes slightly but statistically not significantly increased further during ontogeny. Although the investigated lobe grew more than 3-fold during the regeneration, the size increase of the hepatocytes did not reach a significant level (Figs. 5 and 6) in that model either.

DISCUSSION

We have investigated the size of the surface liver lobules in 2 different liver growth models: during the regenerative response following Phx and during physiological postnatal liver growth. The liver grew exclusively by enlargement of the hepatic lobules during regeneration. Conversely, an increase in the number and size of the lobules contributed to the postnatal liver growth of ontogeny.

The liver tissue has a modular architecture.^{9,10} There is relatively little information available about the behavior of these modules during hepatic growth. There are still ongoing debates about the real functional unit of the liver.¹⁴ This issue was not addressed by these experiments. We chose to study the classic liver lobule^{15,16} because it is widely used and can be defined even in species (eg, in rat) in which it is not surrounded by interlobular connective tissue septa. However, the examination of these lobules is not an easy task, and this may be the explanation for the fact that the model of liver regeneration was described almost a century ago, but what happens with the lobules during this process is still not known.¹ There are observations indicating the enlargement of the hepatic lobules during regeneration,^{17,18} but this process has not been analyzed in detail. The 3-dimensional construction of the rat liver was carefully analyzed by Teutsch et al.⁹ According to this study, the size and shape of Teutsch et al.'s primary hepatic units (which correspond to the classic liver lobule) are variable. They are arranged in cone-shaped secondary units. The size of the primary units decreases toward the top of the secondary unit (the liver surface). Such morphogenetic plasticity explains why a traditional histological section does not provide reliable and comparable information regarding the size of the lobules: it will cut lobules at different positions in the hierarchy at different angles. In our present work, we took advantage of the fact that superficial lobules (in contact with the Glisson capsule) have a uniform apicobasal arrangement (perpendicular to the liver surface) and occupy an identical position in the liver hierarchy,⁵ contrary to the variable orientation, size, and situation of the lobules that are located deep in the parenchyma and are visible on a traditional histological section. The terminal branch of the hepatic vein is in the center of these lobules, generally oriented perpendicularly to and opening at the surface. Because the terminal portal venules terminate about 0.2 mm below the liver surface,⁹ only filling the liver retrogradely through the hepatic vein allowed us to deter-

TABLE 1. Number and Complexity of Surface Lobules in the Right Lateral Lobe of Growing Livers

	Control (Body Weight)		Days After Phx	
	50 g	160 g	14	28
Number	586 ± 10.29	794.5 ± 37.1*	730.75 ± 54.15	719.33 ± 31.18
Number of portal vein branches around the central vein	nd	6.04 ± 0.2	nd	8.13 ± 0.38#

Abbreviations: nd, not determined; Phx, partial hepatectomy.

* $P < 0.05$ between the 160-g control and the 50-g control.

$P < 0.05$ between 28 days after Phx and the 160-g control.

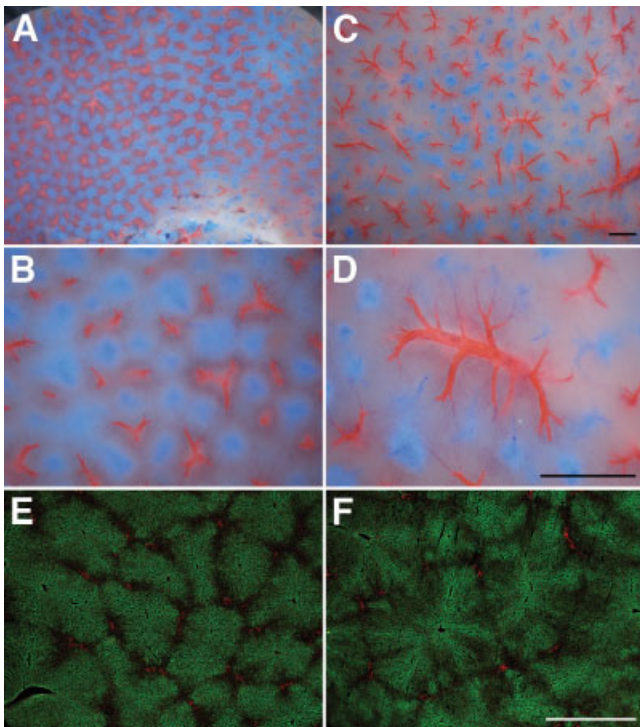


Figure 4. Architectural changes of the liver lobules during regeneration. (A-D) Double filling of the liver vasculature by blue (portal veins) and red (central veins) resins: (A,B) control liver and (C,D) 28 days after partial hepatectomy. Note the enlargement of the hepatic lobules and the more complex branching pattern of the central veins in the regenerated livers. (E,F) Immunohistochemical staining for CYP450 II E1 (green) on (E) a control liver and (F) a regenerated liver 28 days after partial hepatectomy. Note the arborescent distribution of CYP450 II E1 on the regenerated liver. Nuclei were stained with propidium iodide. Scale bar: 1 mm.

mine the size of the surface lobules precisely. Thus, when sinuses of the surface lobules were filled up retrogradely through the hepatic veins, the outlines of the lobules provided reliable information about the 2-dimensional extension of these structural units. Enlargement of the liver lobules during the regenerative growth could be clearly demonstrated in this way. Because the number of subcapsular liver lobules did not change, the enlargement of the lobules was alone responsible for restoration of the liver mass. The measurements were confined to the 2-dimensional extension of the subcap-

sular hepatic lobules, and so they do not provide direct information about the changes deep in the liver tissue. However, considering the strictly defined cone shape of the primary and secondary units in Teutsch et al.'s model, we must assume an increase in the axial dimension of the subcapsular lobules as well as similar alterations of the deep hepatic lobules. Furthermore, Wagenaar et al.¹⁸ measured increased portocentral distances on traditional histological sections in regenerating livers and concluded that the lobules were enlarged; this experiment provided rough data about the deep lobules.

Teutsch et al.'s model^{9,10} also maintains that rat and human livers are constructed of several layers of lobules. The weight/volume of the right lateral liver lobe expanded more than 3-fold during regeneration. This could have been accomplished, according to Teutsch et al.'s model, either by enlargement of the lobules or by the formation of an additional layer of lobules on the liver surface. Our results clearly support the first option. Highly developed mammalian organisms have a quite limited capacity for regeneration of complex structures.¹⁹ Therefore, it is reasonable that the lost liver parenchyma is regenerated exclusively by the enlargement of the preexisting lobules.

The enlarged liver lobules had a more complex structure throughout our observation period. The projection of the central vein on the liver surface was elongated and frequently divided. The number of portal vein branches at the periphery of the lobules also increased. This more complex structure of the lobules was reflected very well in the arborescent shape of the zonally distributed CYP II E1 expression, which was the result of the adaptive changes of hepatocytes.²⁰ The distribution of 2 other zonally expressed enzymes (glutamine synthase and carbamoyl phosphate synthase) showed similar alterations (data not shown). This modified expression pattern was present throughout our observation period (3 months), indicating a permanent or at least long-lasting architectural change. The cause of the altered lobular structure is not clear, but it probably helps to maintain or approach the normal portocentral distance.

Although the size of the lobules grew during the investigated postnatal period of ontogeny, their number also increased. This is in agreement with previous observations. It is well known that the maturation of the

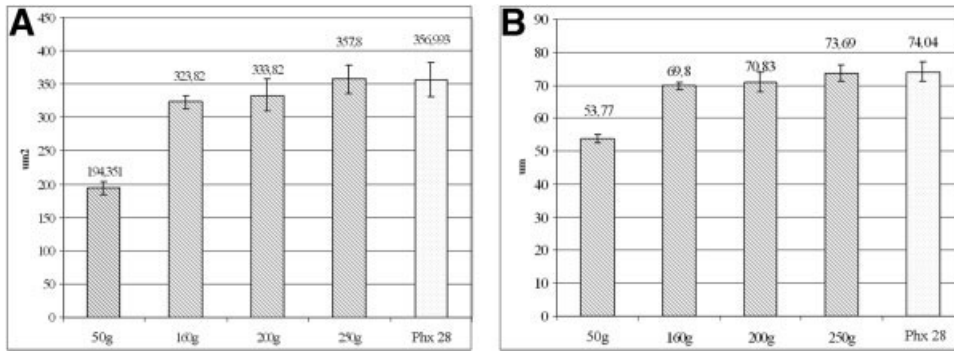


Figure 5. (A) Surface and (B) circumference of the pericentral hepatocytes in rats with different liver weights and 28 days after partial hepatectomy. The bars represent the standard error.

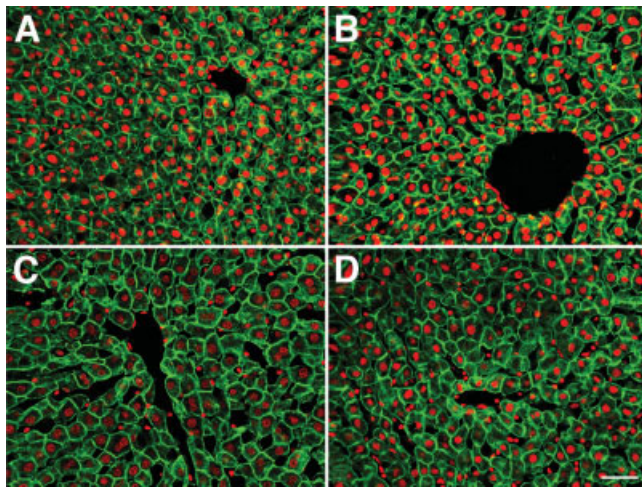


Figure 6. Immunohistochemical staining for cytokeratin (green) outlines the cell membranes of the hepatocytes; the nuclei are decorated by propidium iodide (red). Representative images of pericentral hepatocytes in the livers of rats with different bodyweights are shown: (A) 50 g, (B) 160 g, (C) 250 g, and (D) 28 days after Phx. Note the increasing cell size from part A to part C. (D) The examined liver lobe grew further during regeneration without a change in the size of the hepatocytes. Scale bar: 50 μ m.

biliary system and thus that of the lobular arrangement are completed only postnatally.²¹ The hilar-peripheral orientation of this process has been clearly demonstrated by the characterization of the liver of Alagille's patients.²² That is, a new layer of lobules might be formed postnatally. Ekataksin also reported the elongation of the porto-central distance^{13,15} and multiplication of the liver lobules in the developing human liver. The size of lobular units increasing with age has been described in the rat liver.⁷ Studies of pigs have also shown that the average diameter, as well as the numbers of lobules, increases during normal growth of the liver.⁸ This growth involves an increase in the number and size of the hepatocytes. In fact, we have also observed the enlargement of the hepatocytes during the earlier period of the postnatal liver growth, as reported before.²³ The periphery of the hepatocytes increased 1.29-fold during this period, and this predicted growth in the liver volume of 1.29³ (2.15-fold). However, the liver weight (which is related to the liver volume) increased 2.9-fold, and this indicated that an increase in

the cell number also contributed to liver growth. Later, during ontogeny and liver regeneration, the size of the hepatocytes did not grow significantly, probably because they approached the limit beyond which they could not function properly.

In conclusion, we observed 3 different structural mechanisms—enlargement of hepatocytes and multiplication and expansion of the hepatic lobules—contributing to postnatal liver growth during ontogeny. It seems that 2 of these parameters, the size of the hepatocytes and the number of lobules in a given liver lobe, are fixed by adulthood, and the liver is able to adapt by changing the size of the lobules. Under extreme conditions, the hepatocytes are able to further enlarge,²⁴ but this state of the liver is not stable. The potential functional consequences and limitations of lobular enlargement remain to be studied.

ACKNOWLEDGMENT

The authors thank Noemi Baffy for correcting their use of the English language in this article.

REFERENCES

1. Michalopoulos GK, DeFrances M. Liver regeneration. *Science* 1997;276:60-66.
2. Taub R. Liver regeneration: from myth to mechanism. *Nat Rev Mol Cell Biol* 2004;5:836-847.
3. Fausto N, Campbell JS, Riehle KJ. Liver regeneration. *Hepatology* 2006;43:S45-S53.
4. Fausto N, Webber EM. Liver regeneration. In: Arias IM, Boyer JL, Fausto N, Jakoby WB, Schachter DA, Schafritz DA, eds. *Liver Biology and Pathobiology*. New York, NY: Raven Press; 1994:1059-1084.
5. Ekataksin W, Wake K. Liver units in three dimensions. I. Organization of argyrophylic connective tissue skeleton in porcine liver with particular reference to the compound hepatic lobule. *Am J Anat* 1991;191:113-153.
6. Ekataksin W, Nishida J, McDonnel D, Krasovich M, McCuskey RS. Postnatal development of the hepatic microvasculature and microcirculation in rats [abstract]. *Hepatology* 1993;18:157A.
7. Vollmar B, Pradarutti S, Richter S, Menger MD. In vivo quantification of ageing changes in the rat liver from early juvenile to senescent life. *Liver* 2002;22:330-341.
8. Ekataksin W, Kaneda K. Liver microvascular architecture: an insight into the pathophysiology of portal hypertension. *Semin Liver Dis* 1999;19:359-382.
9. Teutsch HF, Scheuerfeld D, Groezinger E. Three-dimen-

- sional reconstruction of parenchymal units on the liver of the rat. *Hepatology* 1999;29:494-505.
10. Teutsch HF. The modular microarchitecture of human liver. *Hepatology* 2005;42:317-325.
 11. Higgins GM, Anderson RM. Experimental pathology of the liver. *Arch Pathol* 1931;12:186-202.
 12. Schmucker DL, Mooney JS, Jones AL. Stereological analysis of hepatic fine structure in the Fischer 344 rat. *J Cell Biol* 1978;78:319-337.
 13. Ingelman-Sundberg M, Johansson I, Penttila KE, Glaumann H, Lindros KO. Centrilobular expression of ethanol inducible cytochrome P-450 (II E1) in rat liver. *Biochem Biophys Res Commun* 1988;157:55-60.
 14. MacSween NM, Desmet VJ, Roskams T, Scothorne RJ. Developmental anatomy and normal structure. In: MacSween NM, Burt AC, Portmann BC, Ishak KG, Scheuer PJ, Anthony PP, eds. *Pathology of the Liver*. London, England: Churchill Livingstone; 2002:2-66.
 15. Kiernan F. The anatomy and physiology of the liver. *Philos Trans R Soc London (Biol)* 1833;123:711-770.
 16. Ekataksin W, Wake K. New concepts in biliary and vascular anatomy of the liver. *Prog Liver Dis* 1997;15:1-30.
 17. Huang RQ, Schiano TD, Amolat MJ, Miller CM, Thung SN, Saxena R. Hepatocellular proliferation and changes in microarchitecture of right lobe allografts in adult transplant recipients. *Liver Transpl* 2004;10:1461-1467.
 18. Wagenaar GTM, Chamuleau AFM, Pool CW, deHan JG, Maas MAW, Korfage HAM, Lamers WH. Distribution and activity of glutamine synthase and carbamoylphosphate synthase upon enlargement of the liver lobule by repeated partial hepatectomies. *J Hepatol* 1993;17:397-407.
 19. Elder D. Why is regenerative capacity restricted in higher organisms? *J Theor Biol* 1979;81:563-568.
 20. Christoffels VM, Sassi H, Ruijter JM, Moorman AFM, Grange T, Lamers WH. A mechanistic model for the development and maintenance of portocentral gradients in gene expression in the liver. *Hepatology* 1999;29:1180-1192.
 21. Lemaigre FP. Development of the biliary tract. *Mech Dev* 2003;120:81-87.
 22. Libbrecht L, Spinner NB, Moore EC, Cassiman D, Van Damme-Lombaerts R, Roskams T. Peripheral bile duct paucity and cholestasis in the liver of a patient with Alagille syndrome. *Am J Surg Pathol* 2005;29:820-826.
 23. Gupta S. Hepatic polyploidy and liver growth control. *Semin Cancer Biol* 2000;10:161-171.
 24. Nagy P, Teramoto T, Factor VM, Sanchez A, Schnur J, Paku S, et al. Reconstitution of liver mass via cellular hypertrophy in the rat. *Hepatology* 2001;33:339-345.

Origin and Structural Evolution of the Early Proliferating Oval Cells in Rat Liver

Sandor Paku,* Janos Schnur,[†] Peter Nagy,^{††} and Snorri S. Thorgeirsson[‡]

From the Joint Research Organization of the Hungarian Academy of Sciences and Semmelweis University of Medicine, Budapest, Hungary; the First Institute of Pathology and Experimental Cancer Research,[†] Semmelweis University of Medicine, Budapest, Hungary; and the Laboratory of Experimental Carcinogenesis,[‡] National Cancer Institute, National Institutes of Health, Bethesda, Maryland*

We have analyzed the histological changes in rat liver after 2-acetylaminofluorene (AAF) administration. The data demonstrate that AAF-induced oval cells were preferentially generated by proliferation of the terminal biliary ductules that we suggest constitute the primary hepatic stem cell niche. The oval cells formed ductular structures, representing an extension of the canals of Hering. This histological organization provides continuous bile drainage of the hepatocytes and uninterrupted blood flow in the sinusoids. The oval cell ductules are surrounded by a continuous basement membrane that is intermittently disrupted by processes of stellate cells that form direct cell-cell contact with the oval cells. Although both AAF treatment and bile duct ligation results in proliferation of biliary epithelial cells, the mechanism(s) responsible for the proliferation of the biliary epithelium seems to differ in the two models. In contrast to the biliary proliferation stimulated by bile ligation, AAF-induced oval cell proliferation as well as the capacity of these cells to differentiate into hepatocytes, bile epithelial cells and possibly other cell lineages can be blocked by administration of dexamethasone. (*Am J Pathol* 2001, 158:1313–1323)

Although a substantial amount of knowledge has been accumulated throughout the last 2 decades about liver stem cells,^{1,2} numerous aspects of this intriguing cell compartment remain undefined. Indeed, there are conflicting data on the exact location of liver stem cells and even the growth pattern of these cells is not completely understood. The proliferating oval cells—the progeny of the stem cells—always expand into liver parenchyme from the portal area. Furthermore, selective damage of the periportal zone reduces oval cell proliferation.³ These observations support the notion that the stem cells must

reside somewhere in the periportal region. The phenotypic resemblance between the oval cells and biliary epithelium suggests that they derive from the biliary tree, and terminal hepatic ductules (canals of Hering) that connect the most distal hepatocyte of the hepatic plate to the interlobular bile ducts are thought to harbor the hepatic stem cells.^{4–7} However, there is no general agreement on this issue. In fact, potential candidates for the stem cells outside the biliary system have been proposed.⁸

In the absence of a specific marker for the hepatic stem cells, several investigators using different models have attempted to identify the stem cells by labeling the dividing cells in the early phase of oval cell expansion.^{4,8–10} However, most of the experimental protocols for the activation of the hepatic stem cell compartment require a relatively long time and this may explain the divergent results. The 2-acetylaminofluorene (AAF)/partial hepatectomy (PH) model of oval cell proliferation/differentiation has been extensively used to analyze the hepatic stem cell compartment during the last few years.^{11–13} We have recently modified the classical AAF/PH model¹⁴ and demonstrated that after a single dose of AAF administration a notable cell proliferation takes place in the periportal zone and at least some of these proliferating cells are the precursors of oval cells. Therefore AAF administration provides a uniquely fast and synchronized activation of the oval cell precursors without any major disruption of the hepatic structure. We could identify dividing cells in the interlobular bile ducts after AAF treatment, whereas the exact nature of the rest of the thymidine-labeled cells could not be unambiguously defined by traditional light microscopy.¹⁴

Biliary cell proliferation can also be induced in rats by the ligation of the common bile duct (BDL).^{15,16} This reaction is, however, morphologically and phenotypically very different from the oval cell proliferation. After BDL, proliferating biliary cells do not show any signs of differentiation into other cell types. Another difference between BDL- and AAF-induced biliary cell proliferation is illustrated by selective inhibition of oval cell proliferation by dexamethasone.¹⁷

Supported by OTKAT 22737, T29006, and North American Treaty Organization Collaborative Research grant HTECH-EV 973276.

Accepted for publication December 27, 2000.

Address reprint requests to Dr. Peter Nagy, National Cancer Institute, NIH, 37 Convent Dr. MSC 4255, Building 37, Room 3C28, Bethesda, MD 20892-4255.

In the present work we have characterized the early cellular events in the liver during the proliferative response induced by AAF or BDL. To obtain a more detailed morphological assessment, the samples were analyzed by, in addition to traditional light microscopy, both confocal and electron microscopy. Both AAF and BDL induced an intense biliary cell proliferation. The frequency of dividing cells after AAF treatment was significantly higher in the terminal hepatic ductules. Morphological analysis revealed that the early oval cells are strictly confined to ductular structures surrounded by basement membrane, representing an extension of the canals of Hering.

Materials and Methods

Animal Experiments

Male F-344 rats (180 to 200 g) were used for all experiments and kept under standard conditions. The animal study protocols were conducted according to NIH guidelines for animal care.

AAF/PH Experiment

AAF (1.5 mg) suspended in dimethyl-cellulose was given to the rats on 4 consecutive days by gavage. Traditional 70% PH¹⁸ was performed on the fifth day, which was followed by five additional AAF treatments. Animals were sacrificed at the described time points (at least three at each time point).

BDL

BDL was done according to Cameron and Oakley.¹⁹ The rats were sacrificed 48 hours after the operation.

Electron Microscopy

Preparation of liver tissue for electron microscopy was done by perfusing the livers under anesthesia (35 mg/kg, Nembutal; Serva, Heidelberg, Germany) via the portal vein with phosphate-buffered saline (PBS) for 10 minutes and with 2.5% glutaraldehyde in 0.05 mol/L Na-cacodylate (pH 7.2) for 15 minutes at room temperature. Livers were cut into 1 × 3 mm pieces and immersed in 2.5% glutaraldehyde for 2 hours. The pieces were postfixed in 1% OsO₄, 0.05% K-ferrocyanide in 0.05 mol/L Na-cacodylate for 1 hour, dehydrated in a graded series of alcohol, contrasted *en bloc* with 2% uranylacetate, and embedded in Spurr's mixture. Ultrathin sections were stained with lead citrate and examined on a Philips CM10 electron microscope.

Ultrastructural Analysis of 5-Bromo-2'-Deoxy-Uridine (BrdU)-Labeled Periportal Cell

BrdU (100 mg/kg) was injected intraperitoneally after two doses of AAF, 24 hours after the second treatment or 2

days after BDL. One hour after the injection, the animals were anesthetized and perfused via the portal vein with PBS for 10 minutes, followed by 4% paraformaldehyde for 20 minutes. Livers were removed, cut into 5-mm thick slices and postfixed for 24 hours. The fixed tissues were washed in PBS and immersed in 15% sucrose for 24 hours followed by 30% sucrose for another 24 hours. Specimens were frozen in isopentane cooled by liquid nitrogen.

Cryosections (15 μm thick) were mounted on microscope slides coated with parlodion. The cryosections were rinsed in PBS and incubated for 20 minutes in 3 N HCl at room temperature. After washing in PBS, the sections were incubated with monoclonal anti-BrdU antibody (diluted 1:100; Becton-Dickinson, Mountain View, CA) for 3 hours and later with biotinylated anti-mouse antibody (Vector Laboratories, Burlingame, CA) for 2 hours. The reaction was developed by an ABC reaction (Elite ABC Kit, Vector Laboratories) using diaminobenzidine as chromogen. The sections were osmificated (1% OsO₄ in PBS), dehydrated in graded series of ethanol, and embedded in Epon 812. Blocks were removed by immersing the slides in liquid nitrogen. Semithin sections were slightly stained by 0.5% toluidine blue (pH 8.5), portal areas containing BrdU-labeled cells were trimmed out and unstained ultrathin sections were analyzed on a Philips CM 10 electron microscope. Labeled cells were divided into three categories based on their localization: 1) cells residing outside the basement membranes in the periportal connective tissue; 2) cells confined within the basement membrane, as part of bile ducts; and 3) cells of the canals of Hering. The cells comprising the canals of Hering were in direct contact with a hepatocyte or were separated from a hepatocyte by only one biliary cell.

Immunofluorescent Analysis

Double Labeling for Laminin-Cytokeratin and Laminin-Desmin

Cryostat sections (6 μm) were fixed in acetone (−20°C for 20 minutes) and incubated overnight with a mixture of rabbit polyclonal anti-laminin antibody (diluted 1:50, Z0097; DAKO, Glostrup, Denmark) and fluorescein isothiocyanate-conjugated mouse monoclonal antibody directed against human cytokeratin 5, -6, -8, -17, and -19 (diluted 1:10, M0859; DAKO) or anti-laminin and mouse monoclonal anti-desmin (diluted 1:50, M0724; DAKO), respectively. After washing with PBS the sections were incubated for 60 minutes with tetramethylrhodamine B isothiocyanate-conjugated anti-rabbit IgG (diluted 1:20, R0156; DAKO) for the laminin-cytokeratin double labeling or with the combination of the same tetramethylrhodamine B isothiocyanate-conjugated anti-rabbit IgG and fluorescein isothiocyanate-conjugated anti-mouse IgG (diluted 1:50, F5262; Sigma) for the simultaneous detection of laminin and desmin.

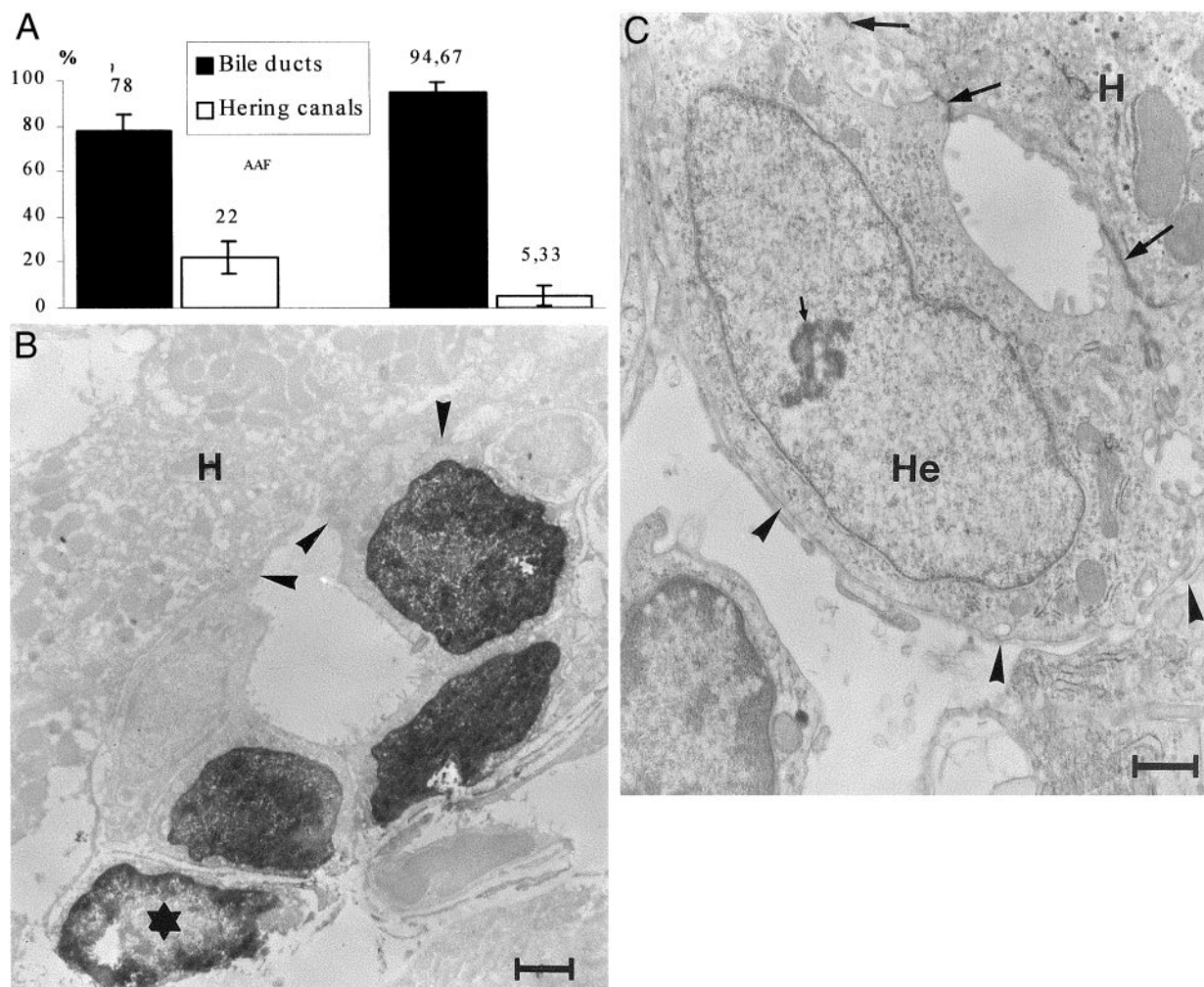


Figure 1. A: Distribution of BrdU-labeled cells, between bile ducts and canals of Hering, analyzed by immunoelectronmicroscopy. The first two columns represent the distribution after two treatments with AAF, and the second two 48 hours after BDL. Total number of labeled cells analyzed was 141 in the AAF-treated group and 143 in the BDL group. **B:** Immunoelectron micrograph 2 days after AAF treatment showing a canal of Hering consisting of four cells. Three of them are labeled by BrdU. Two cells of the canals are attached to the hepatocytes (H) (arrowheads). The fourth labeled cell (asterisk) is located in the periportal connective tissue outside the basement membrane of the terminal hepatic ductule. Scale bar, 2 μ m. **C:** Activated cell in the canal of Hering (He) 2 days after AAF treatment. The nucleus is enlarged and contains euchromatin and a prominent nucleolus (small arrow). Continuous basement membrane is visible on the connective tissue side of the cell (arrowheads). The bile ductule lumen is sealed by intercellular junctions (large arrows) (H, hepatocyte). Scale bar, 1 μ m.

Double Labeling for Laminin and α -Fetoprotein (AFP)

Liver samples were fixed in 10% formaldehyde, embedded, and cut. After deparaffinization and hydration, the sections were microwaved for 15 minutes in ethylenediaminetetraacetic acid buffer (pH 8.0), followed by incubation in 0.1% Triton X-100 in PBS for 20 minutes, and digested with Proteinase K (2 μ g/ml, 15 minutes, 37°C). The sections were washed with PBS and incubated overnight with a mixture of rabbit polyclonal anti-laminin (diluted 1:20, Z0097; DAKO) and goat anti-rat AFP no. 89 antibody (diluted 1:100; generous gift from Dr. Stewart Sell, Department of Pathology and Laboratory Medicine, Albany Medical College, Albany, NY). Tetramethylrhodamine B isothiocyanate-conjugated anti-rabbit IgG (as described above), and in a second step, fluorescein isothiocyanate-conjugated anti-goat IgG (diluted 1:400, F7367; Sigma), were used as secondary antibodies. All samples were analyzed by confocal laser-scanning

microscopy using the Bio-Rad MRC-1024 system (Bio-Rad, Richmond, CA).

Results

BrdU Labeling of Dividing Cells after BDL and AAF Administration

The ligation of the common bile duct resulted in a very intensive biliary cell proliferation. The cells were labeled with BrdU 48 hours after the ligation. In agreement with previous results,²⁰ most of the labeled cells were in the interlobular bile ducts. Immunoelectron-microscopic analysis of the localization of labeled cells revealed <6% of the BrdU-positive biliary epithelial cells in the canals of Hering (Figure 1A). Additionally, dividing inflammatory and fibroblastic cells could be found in the periportal connective tissue and a few labeled hepatocytes were also present.

Similarly to our earlier observations,¹⁴ a single dose of AAF resulted in cell proliferation in the periportal region. However, because the number of the BrdU-labeled cells was higher after two doses of AAF, without any apparent adverse effects, we selected the 48-hour time point for the quantitative electron-microscopic analysis. Approximately 80% of the labeled biliary cells were inside the well-defined interlobular bile ducts. However, 22% of the BrdU-positive epithelial cells were located in the canals of Hering (Figure 1A). Only those biliary cells having direct connection with a hepatocyte or separated by only one interposed biliary cell from the hepatocyte were counted as lining cells of the canals of Hering (Figure 1B). It is possible that by using these strict criteria we underestimated the number of labeled cells in the canals of Hering. However, the observation that 22% of the labeled biliary cells were in these structures can be taken as preferential labeling, considering that the overwhelming majority of the biliary epithelial cells belong to the interlobular and larger bile ducts.

After AAF treatment the terminal hepatic ductules were surrounded, by an almost continuous basement membrane that terminated on a hepatocyte of the limiting plate (Figure 1C). In addition, administration of AAF also induced proliferation outside the biliary system. Mostly single cells residing in the periportal extracellular matrix were labeled. Although the exact nature of these cells could not be established by electron microscopy they most likely represent mesenchymal cells.

Immunohistochemical Analysis of the Liver 2 Days after AAF Administration

The cell density increased in the periportal space after one or two doses of AAF, but the proliferating ductules did not infiltrate the liver lobules. To determine the characteristics of the proliferating cells in the periportal space, double labeling for laminin/cytokeratin, laminin/desmin, and laminin/AFP was performed. Immunofluorescent-stained liver sections were analyzed by confocal microscopy. The cytokeratin antibody gave a weak membrane and reticular cytoplasmic staining in the hepatocytes, whereas producing a strong cytoplasmic reaction in the biliary epithelial cells. Therefore, the two cell populations could be easily distinguished. The laminin antibody, a well-established marker of the basement membrane, sharply circumscribed the bile ducts and the blood vessels, whereas the liver acini were completely negative. The terminal hepatic ductules were intensely decorated by the laminin/cytokeratin double labeling. In the appropriate plane of the section, the basement membrane stained with laminin surrounded the bile ductules and terminated on hepatocytes at the limiting plate (Figure 2A). The basement membrane extended without interruption along the biliary ducts and ductules. If the nuclei were stained by propidium iodide in combination with the double-immunofluorescent reaction, increased cell density was revealed periportally after AAF treatment (Figure 2, A and B). However, we did not observe cytokeratin-labeled cells outside the basement membrane in

the periportal space. Combined laminin/AFP immunohistochemistry showed that basement membrane surrounded a few AFP-positive biliary cells after two doses of AAF (Figure 2C). Similar to the cytokeratin reaction, no AFP-stained cells were observed outside the basement membrane. Immunostaining with a desmin antibody revealed an increased number of activated stellate cells outside the basement membrane. These cells and their processes showed a very intimate connection with the proliferating ductules (Figure 2D).

Morphological Alterations after PH in AAF-treated Rats

To study later events during stem cell activation, we used the AAF/PH model and the structural alterations were analyzed 3 days after the partial hepatectomy. By this time the oval cells had extensively infiltrated the liver lobules. Electron microscopic examination revealed that the oval cells always formed ductules (Figure 3A). These growing ductules reached the sinusoids and passed along or between them. During this process the sinusoids were left intact, preserving their normal function. The basic structure of these oval cell ductules was not different from the normal canals of Hering except for the elongation. The ductules grew by the continuous proliferation of the ductular epithelial cells (Figure 3B), whereas the sides of these tubules were continuously sealed by desmosomes. Also, the ductules always terminated at a hepatocyte (Figure 3C). This hepatocyte was probably the one connected with the original canal of Hering. In this way the original connection between the bile canaliculi and the bile duct system was preserved throughout the regenerative process. The growing tubules were surrounded mostly by basement membrane that terminated on the hepatocyte. However, there were segments along these growing ductules where no structured basement membrane could be seen by electron microscope. Again no cells penetrating through the basement membrane could be observed. There were, however, plenty of proliferating cells outside the basement membrane without characteristic ultrastructural features. These cells did not show epithelial phenotype or form desmosomes, yet had a very close contact with the expanding ductular epithelial cells. Higher magnification showed that small processes of these nonepithelial cells appeared to have direct cell-cell contact with the epithelial cells (Figure 3D).

Immunohistochemical observations confirmed the electron-microscopic data. The cytokeratin-stained oval cells formed ductules that were elongations of the portally located canals of Hering. The tubular structure of these ductules with a central lumen was much more obvious in the pictures generated by confocal microscopy. The major difference between the two methods was that, although the basement membrane could not be continuously followed along these ductules ultrastructurally, the immunohistochemistry showed consistent laminin positivity around them (Figure 4A). The cylinder formed by the basement membrane had an open end plugged by a

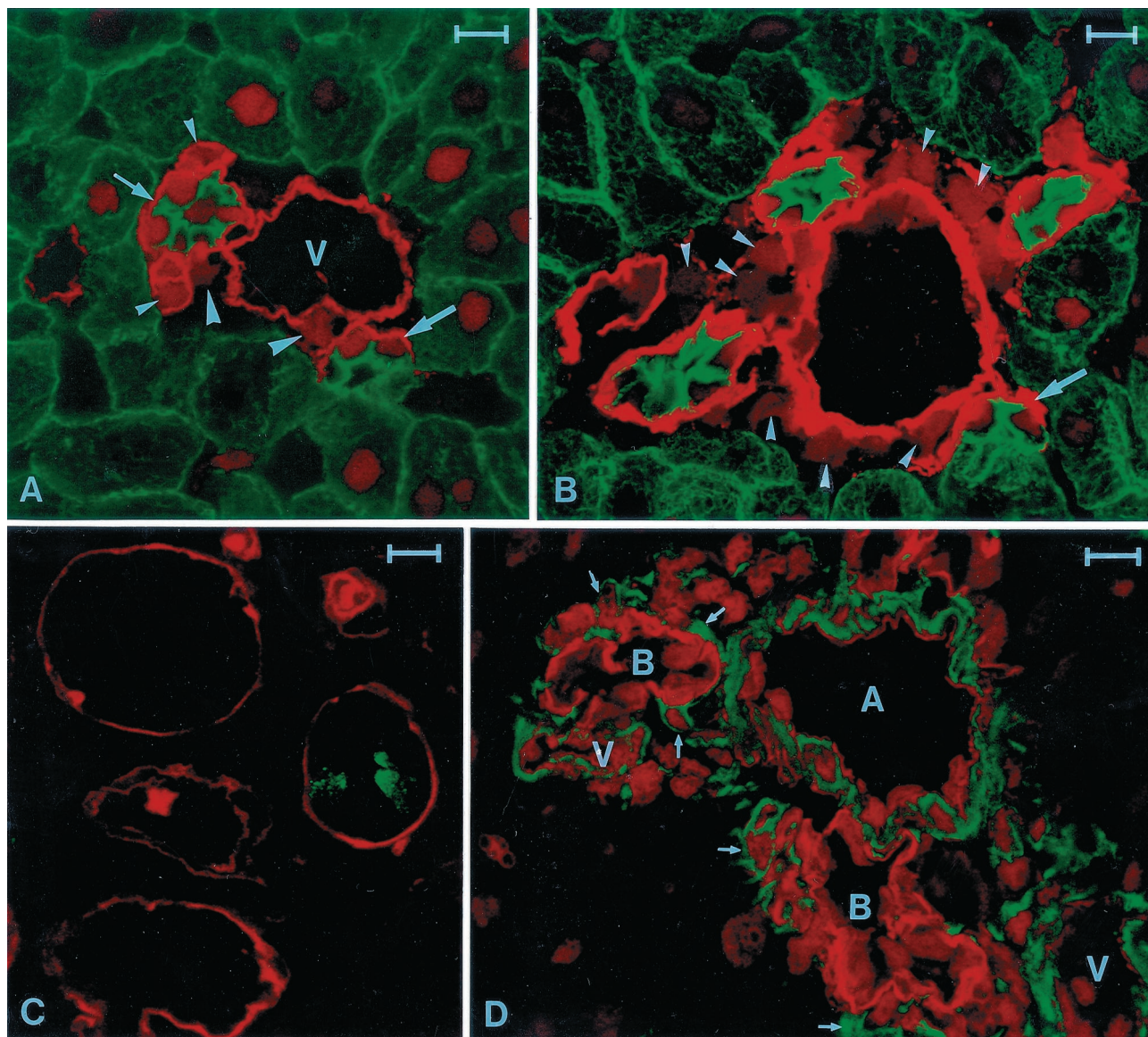


Figure 2. A: Portal area of a control liver stained for cyokeratin (green) and laminin (red). The section was additionally stained with propidium iodide to localize nuclei. Basement membrane of portal vein (V), capillaries (**small arrowheads**), bile duct (**small arrow**), and a canal of Hering (**large arrow**) are stained by the anti-laminin antibody. Nuclei of two connective tissue cells can be detected (**large arrowheads**) in the periportal area. The bile duct and canal of Hering lining cells show a stronger cytoplasmic staining for cyokeratin than the hepatocytes. Scale bar, 10 μ m. **B:** Portal area stained for cyokeratin and laminin 2 days after AAF treatment. Localization of basement membranes are similar to that of control liver. Note the presence of numerous cyokeratin-negative cells in the periportal connective tissue (**arrowheads**), but there are no cyokeratin-positive cells in the periportal space outside the basement membrane. The canal of Hering (**arrow**) shows normal structure. Scale bar, 10 μ m. **C:** Two days after AAF treatment AFP-positive (green) bile ductule cells are present strictly within basement membrane (red). Scale bar, 10 μ m. **D:** Portal area 2 days after AAF treatment, stained for laminin (red) and desmin (green). The section was additionally stained with propidium iodide to localize nuclei, as shown in **A** and **B**. Numerous cells in the connective tissue, which proved to be negative for cyokeratin (**B**), stain positively for desmin. Some of the desmin-positive cells positioned closely to the basement membrane of the bile ducts (**B**) (**arrows**). A, arteriole; V, venule. Scale bar, 10 μ m.

hepatocyte, and desmin-positive stellate cells accompanied the ductular structures outside the basement membrane (Figure 4B).

Ten days after the partial hepatectomy the cyokeratin-laminin immunohistochemistry did not reveal any basic change in the structure of advancing ductules, demonstrating that the oval cells still formed ductular structures extensively infiltrating into the liver parenchyma and maintained contact with hepatocytes at their origin (Figure 5, A and B). The oval cells still could be easily distinguished from the hepatocytes by the strong

cytoplasmic cyokeratin staining. The proliferating oval cells were heterogeneously decorated by the AFP antibody. Similar to earlier time points, these cells were always surrounded by basement membrane and no AFP-positive cells were seen outside the laminin staining (Figure 5C). At this stage, oval cells were neither identified outside the ductular structures nor interposed between hepatocytes. The desmin reaction verified that activated stellate cells surrounded the advancing ductules and formed processes that penetrated and caused focal discontinuity of the basement membrane (Figure 5D).

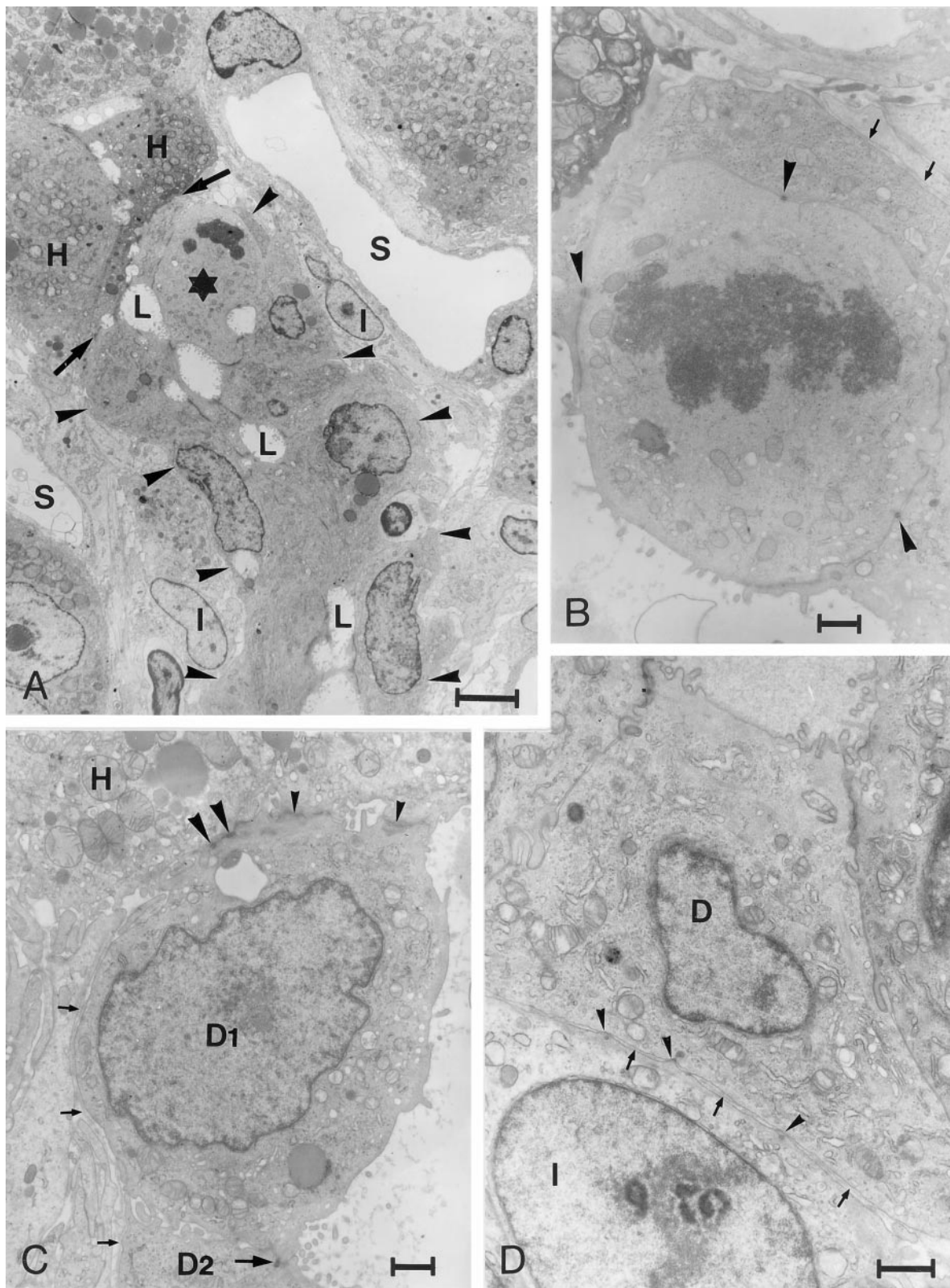


Figure 3. Ultrastructure of a portal area 3 days after PH in an AAF-treated rat. **A:** Oval cells forming a ductule (arrowheads; L, ductule lumen), squeeze between sinusoids (S). The ductule terminates on hepatocytes (H, arrows). One cell of the ductule is in mitosis (asterisk). Several stellate-like cells (I) are located closely to the advancing ductule. Scale bar, 5 μ m. **B:** Higher magnification of the mitotic oval cell shown in **A** in a different sectioning plane. The cell is connected to the other cells forming the ductule by desmosomes (arrowheads). A small amount of basement membrane-like material (arrows) is visible under the process of a ductule cell. Scale bar, 1 μ m. **C:** Detail of the ductule shown in **A**. Terminal cell of the growing ductule D1 is connected to the hepatocyte (H) by desmosomes (arrowhead) and tight junctions (small arrowheads). Desmosome (large arrow) is also discernible between the two ductule cells (D1, D2). Well-defined basement membrane (small arrows) with small gaps can be observed under the ductule cells. Scale bar, 1 μ m. **D:** Ito-like cell (I) is in direct contact with the ductule cell (D), through the small gaps (arrowheads) of the basement membrane (arrows). Scale bar, 1 μ m.

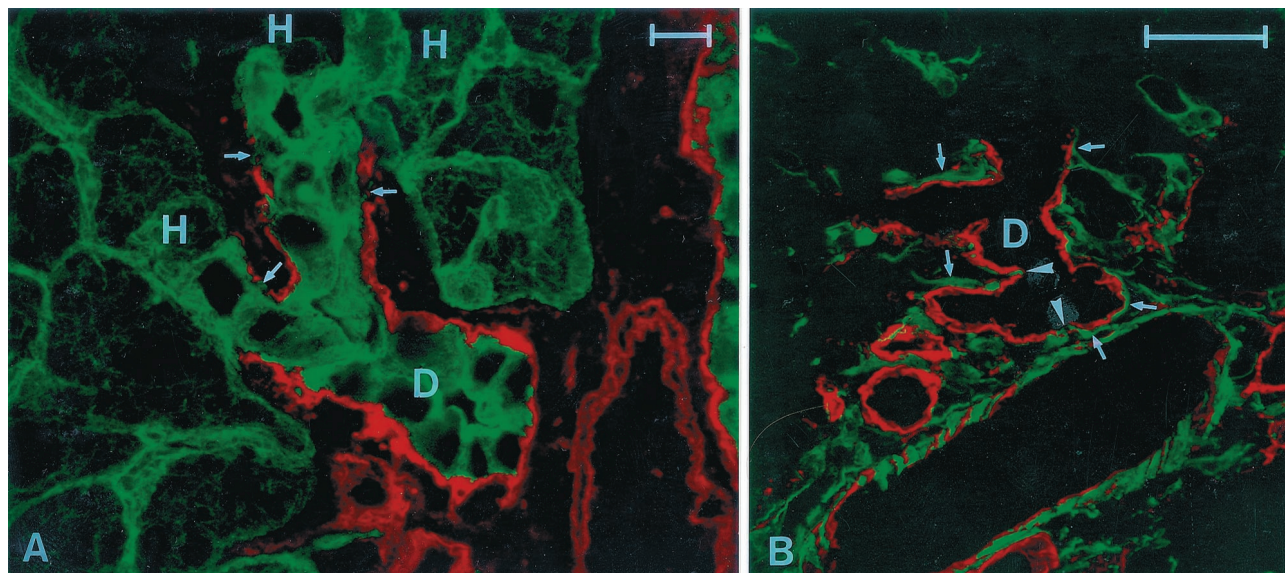


Figure 4. A: Portal area stained for cyokeratin (green) and laminin (red) 3 days after PH in an AAF-treated rat. The bifurcating ductule (D) strongly positive for cyokeratin, is surrounded by continuous basement membrane. Minute discontinuities (**arrows**) can be observed only at the vicinity of hepatocytes (H). Scale bar, 10 μ m. **B:** Portal area containing a bifurcating ductule (D) stained for laminin (red) and desmin (green). The basement membrane is continuous, except minute gaps where it is penetrated by desmin-positive Ito cell processes (**arrowhead**). Numerous other desmin-positive cells are spread along the basement membrane (**arrows**). Scale bar, 50 μ m.

Discussion

We have compared the BDL- and AAF-induced ductular cell proliferation in the rat liver by electron microscopy and immunohistochemistry. Both treatments resulted in the proliferation of the biliary epithelial cells. However, the distribution of the dividing biliary cells was different. The percentage of BrdU-labeled cells in the canals of Hering was significantly higher after AAF administration. Analysis of morphological changes in the AAF/PH model revealed that proliferating oval cells always formed ductules that were elongated and tortuous extensions of the pre-existing canals of Hering. These oval cell ductules were always surrounded by laminin and terminated at hepatocytes located at the limiting plate. These ductular structures were always accompanied by activated and proliferating stellate cells.

Studies similar to our own have been done by several investigators^{8,13,21-24} using the AAF-induced oval cell reaction. The difference between these studies and ours is that we examined earlier time points of the model to observe the first proliferating cells under conditions in which the original histological structure of the liver is minimally affected. Our results support the notion of oval cells being derived from the biliary epithelium, strongly indicating that liver stem cells are located in the biliary system.

Among other candidates for liver stem cells are the so-called "nondescript" periductular cells. Sell and Salman⁹ observed that the first proliferating cells after AAF feeding in rats maintained on a choline-deficient diet are periductular and the ductular cells follow them 1 or 2 days later. These periductular cells are located outside the basement membrane and contained no ultrastructural features that identified them. Interestingly, the increase in the number of thymidine-labeled periductular cells was

equal to or greater than the labeled ductal cells. Studying a similar model to that of Sell and colleagues²¹ (but without the choline-deficient diet), we have also observed periductular proliferating cells. Cyokeratin, however, decorated strictly laminin-surrounded cells in the periportal area, ie, no epithelial cells were seen outside the basement membrane. AFP is an extensively used marker of the oval cells in the rat liver^{25,26} and the presence of AFP also indicates a hepatocytic directed commitment of the cells. AFP staining in some of the biliary epithelial cells after two doses of AAF supports the hypothesis that these cells are the precursors of the oval cells. In addition, the persistent lack of AFP staining outside the basement membrane throughout the experimental period strongly argues against the potential periductular origin of the oval cells. According to studies in other stem cell systems,²⁷ in which a high cell production rate is required, the stem cells fulfill this task via a dividing transit or amplification cell population. The cells of this compartment constitute an intermediary or transition population between the stem cells and the mature functional compartment, and they usually acquire one or more differentiation markers. Traditionally the oval cells are thought to represent this amplification compartment in this experimental model.¹ If the nondescript periductular cells studied by Sell and colleagues²¹ were the stem cells, we would not expect them to proliferate at the same rate as the dividing transit compartment represented by the oval cells. Another possibility might be that the periductular cells are (alone or together with the ductular cells) the amplification compartment. These cells are, however, cyokeratin- and AFP-negative, and do not show any phenotypic or morphological (even at the ultrastructural level) sign of differentiation. Furthermore, the nondescript periductular cells would be expected to penetrate the basement mem-

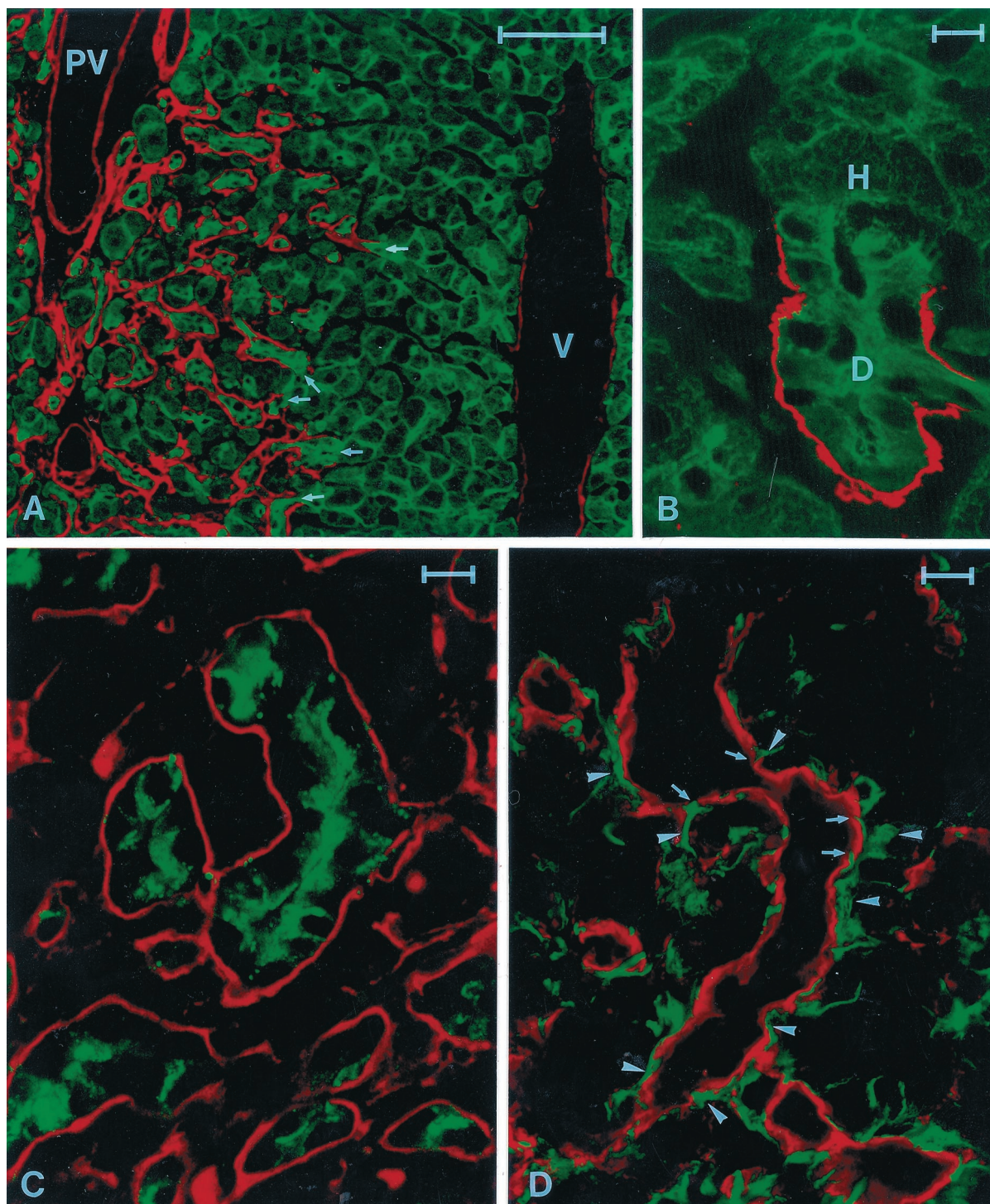


Figure 5. Immunohistochemistry of the liver 10 days after partial hepatectomy in the AAF/PH-treated rat. **A:** Low-power micrograph of a liver lobule stained for cytokeratin (green) and laminin (red). Numerous ductules surrounded by laminin are infiltrating the liver parenchyma toward the central vein (V). Several U-shaped laminin-stained structures, with open endpoints toward the central vein (arrows), can be seen at the border of the oval cell infiltration. (PV, portal vein). Scale bar, 100 μm . **B:** High magnification of a ductule (D) at the infiltration border. Oval cells are attached to a hepatocyte (H). Laminin staining encloses only the ductule, and it does not extend over the hepatocyte (H). Scale bar, 10 μm . **C:** Tortuous oval cell built ductules in the liver lobule stained for laminin (red) and AFP (green). The ductules are surrounded by laminin and AFP staining is observable only inside the basement membrane. Scale bar, 10 μm . **D:** Similar ductules as in C stained for laminin (red) and desmin (green). Numerous desmin-positive cells are spreading along the basement membrane (arrowheads). At several places processes of these cells puncture the basement membrane (arrows), but these processes never extend over the basement membrane. Scale bar, 10 μm .

brane in great numbers during the process of differentiation, but neither Sell and Salman⁸ nor we observed any sign of this. Therefore, our data do not support the stem cell nature of the periductal cells. There are, however,

plenty of desmin-positive stellate cells actively proliferating around the ductules in the AAF/PH model. Although we have not precisely quantitated the number of stellate cells, it seems to be approximately equal to that of oval

cells. It is therefore possible that at least some of the periductal proliferating cells described by Sell and Salman⁸ might be stellate cells.

Several studies have supported possibilities of the stem cells being located in the biliary system. These include terminal hepatic ductules;^{4,5,22,28} all biliary epithelial cells,^{29–32} and a very primitive looking cell, referred to as a “basal cell” inside the bile duct.^{23,24} The basal cells proliferated 2 to 3 days after the partial hepatectomy in the livers of rats treated according to Solt and colleagues³³ carcinogenesis schedule. We also saw these small, intraepithelial cells in our sections, but they never incorporated BrdU or showed morphological signs of proliferation. The reason for this difference is not altogether clear. Novikoff and colleagues²³ and Novikoff and Yam²⁴ used the DEN-initiated Solt-Farber model, whereas we avoided DEN administration. Although the oval cell reaction is similar, the histological changes are more complex in the Solt-Farber model according to our experience. Anilkumar and colleagues³⁴ also described divergent histological reactions in the two models. It is however evident that oval cell proliferation can be induced without the participation of the basal cells in our experimental model. Therefore, the biliary epithelial cells can function as facultative liver stem cells in the AAF/PH experimental model. We can, of course, not exclude the possibility that the basal cells represent an even more ancient stem cell population that is activated by a more drastic, carcinogenic protocol and may be responsible, eg, for the frequently observed metaplastic hemopoiesis in hepatocarcinogenesis experiments.^{35,36} Recently Petersen and colleagues³⁷ and Theise and colleagues³⁸ have provided evidence that hemopoietic stem cells can give rise to oval cells and hepatocytes. The basal cells may perhaps represent a common precursor for the two systems. Although these observations have a dramatic impact on our view of stem cell biology, there is a general agreement that under most circumstances the liver regenerates from cell populations confined to the liver. These cells are the focus of this study and the participation of hemopoietic cells in liver regeneration is not addressed here.

The notion of which segment(s) of the biliary tree harbors the stem cells is still controversial. Although a substantial amount of data indicate that the liver stem cells are confined to the terminal hepatic ductules, arguments have been made suggesting that any component of the biliary tree can give rise to oval cells.^{29–32} We have previously shown that chronic dexamethasone treatment is able to prevent the oval cell proliferation triggered by the AAF/PH protocol while not at all inhibiting the BDL-induced proliferation of the larger, mostly interlobular bile ducts.¹⁷ The preferential BrdU labeling of cells in the canals of Hering after AAF administration, suggested that selective inhibition of cell proliferation in these cells might be achieved by dexamethasone. Contrary to expectations dexamethasone completely inhibited the AAF-induced biliary cell proliferation regardless of their location.¹⁷ These results fail to provide a functional confirmation that the terminal ductules are the exclusive sources of the oval cells. Furthermore, the proliferations

of morphologically and topologically identical biliary cells were differently regulated by dexamethasone. These data suggest that there are at least two different mechanisms regulating proliferation of the biliary epithelium, each providing functionally different progeny. Although the dexamethasone-sensitive pathway provides cells with stem cell potential, the dexamethasone-resistant pathway produces only biliary epithelial cells. These results may, at least in part, be analogous to the regulation of hepatocyte cell cycle induced by the partial hepatectomy and primary mitogens.³⁹ It is well established that these proliferative models have different biological potentials; eg, hepatocyte proliferation induced by partial hepatectomy has carcinogenic promoting capacity whereas the other one induced by direct mitogens has none.⁴⁰ There are already observations indicating the differential regulation of these two biliary reactions. Mice harboring congenitally defective SCF/c-kit system retain an intact proliferative response after BDL,⁴¹ whereas the oval cell proliferation is remarkably suppressed in rats with deficient c-kit kinase activity.⁴²

The fact that hepatocytic differentiation occurs in the pancreas^{43,44} and extrahepatic bile ducts⁴⁵ also argues against the restricted occurrence of multipotential stem cells in the canals of Hering. Our observation that AAF targets preferentially the cholangioles while BDL targets the larger bile ducts can be explained by topological factors. The primary stimulus for biliary proliferation after BDL is the increased intraductal pressure.¹⁵ The pressure is probably higher in the interlobular bile ducts, than in the ductules. Differential expression of drug metabolizing enzymes by different segments of the biliary tree⁴⁶ may provide an alternative or additional explanation for the differential response to AAF. Potten⁴⁷ described a hierarchy of the stem cells in the small intestine glands. Depending on the severity of injury, more and more resistant cells participate in the repair. Additionally, this hierarchy is related to the topography of the cells. A similar arrangement cannot be excluded in the biliary system. This notion is supported by the well-known heterogeneity of cholangiocytes.^{48,49}

Experiments using injection of pigmented gelatin medium and related substances into the biliary tree have demonstrated that the majority of oval cells are part of a ductular reaction.^{10,13,50} However, together with these observations, occurrence of isolated oval cells, sometimes located between pre-existent fully mature hepatocytes, have been described.¹³ There is also conflicting assessments on the continuity of the basement membrane around the ductules.^{24,50} To address this problem we studied earlier time points and complemented the electron microscopy with confocal laser microscopy. The confocal microscopy provided a much better overview of the histological reaction in addition to allowing simultaneous use of more than one marker. The laminin/cytokeratin double staining decorated very clearly the biliary ductules that would otherwise be difficult to recognize. There was a distinct continuous laminin staining around the canals of Hering that terminated at hepatocytes located at the limiting plate.

The traditional light microscopic view of the oval cell reaction is very complicated. The confocal microscopy, however, clearly revealed that the oval cells always form ductules surrounded by basement membrane that originate from the canals of Hering and terminate on a hepatocyte. As these oval cell ductules grow, they become tortuous, but they appear not to lose contact with their terminating hepatocyte, as was described by Betto and colleagues⁵¹ in Long-Evans rats. To accomplish this task, it seems that the canal of Hering is ideally situated and therefore may provide the stem cell niche in the liver. Furthermore, this arrangement allows for continuous bile drainage throughout this complex reaction. The preservation of the original contact between the liver plate and the extending biliary ductule, which is composed of oval cells, may be extremely important for the maintenance of the liver architecture. We hypothesize that the disruption of the contact between the ductules and hepatocytes may occur in chronic interface hepatitis resulting in aimless ductular proliferation, followed by fibrosis, and finally reorganization of the liver structure resulting in cirrhosis.

The basement membranes frequently play an important role in the regenerative process. In certain tissues (eg, kidney tubules) the integrity of the basement membrane is required for the regeneration because it provides a track for the dividing epithelial cells.⁵² The situation is probably different in the liver. There is no structured basement membrane along the liver plates. The fact that the regular basement membrane is sometimes missing ultrastructurally around the ductules, while they are always surrounded by laminin according to our immunohistochemical data, may indicate that it is in *stadium nascendi*, providing a substrate for proliferation and migration. This process is similar to that observed during angiogenesis.⁵³ Activated stellate cells are always intimately associated with these ductules. Sometimes the processes of the stellate cells brake through the basement membrane and form direct cell-cell contact with the ductular epithelial cells. This connection that has not been described before may form the structural basis for the intensive cross talk between these two cell types.

In conclusion, although it has been known that most of the oval cells are organized into ductular structures sprouting from pre-existing bile ductules, this was not generalized to every oval cell and the development of these ductules was obscure. We suggest that the oval cell-formed ducts are simply extensions of the biliary ductules. The connection between the last ductular biliary cell and the corresponding hepatocyte is maintained for an extended period of time. The oval cells are preferentially generated by proliferation of the terminal biliary ductules that we suggest constitute the primary hepatic stem cell niche. However, the stem cell potential of the larger biliary ducts cannot be excluded. In fact, there seems to be two independently activated and regulated mechanisms for the proliferation of the biliary epithelium. One of these that can be blocked by dexamethasone results in progenies with the capacity for both differentiating into hepatocytes and possibly other cell lineages. The ductules are composed of oval cells and surrounded by continuous basement membrane that is intermittently

disrupted by processes of stellate cells that form direct cell-cell contact with the oval cells.

Acknowledgments

We thank Dr. Stewart Sell for providing the AFP antibody and Dr. Valentina Factor for valuable comments on the manuscript.

References

1. Grisham JW, Thorgeirsson SS: Liver stem cells. *Stem Cells*. Edited by CS Potten. London, Academic Press, 1997, pp 233–282
2. Alison M: Liver stem cells: a two compartment system. *Curr Opin Cell Biol* 1998, 10:710–715
3. Petersen BE, Zajac VF, Michalopoulos GK: Hepatic oval cell activation in response to injury following chemically induced periportal or pericentral damage in rats. *Hepatology* 1998, 27:1030–1038
4. Grisham JW, Porta EA: Origin and fate of proliferated hepatic ductal cells in the rat: electronmicroscopic and autoradiographic studies. *Exp Mol Pathol* 1964, 3:242–261
5. Sell S: Is there a liver stem cell? *Cancer Res* 1990, 50:3811–3815
6. Shiojiri N, Lemire JM, Fausto N: Cell lineages and oval cell progenitors in rat liver development *Cancer Res* 1991, 51:2611–2620
7. Fausto N, Lemire JM, Shiojiri N: Cell lineages in hepatic development and the identification of progenitor cells in normal and injured liver. *Proc Soc Exp Biol Med* 1993, 204:237–241
8. Sell S, Salman J: Light- and electron-microscopic autoradiographic analysis of proliferating cells during the early stages of chemical hepatocarcinogenesis in the rat induced by feeding N-2-fluorenylacetylamide in a choline-deficient diet. *Am J Pathol* 1984, 114:287–300
9. Evarts RP, Nakatsukasa H, Marsden ER, Hsia CC, Dunsford HA, Thorgeirsson SS: Cellular and molecular changes in the early stages of chemical hepatocarcinogenesis in the rat. *Cancer Res* 1990, 50:3439–3444
10. Lenzi R, Liu MH, Tarsetti F, Slott PA, Alpini G, Zhai W, Paronetto F, Lenzen R, Tavoloni R: Histogenesis of bile duct-like cells proliferating during ethionine hepatocarcinogenesis. *Lab Invest* 1992, 66:390–402
11. Evarts RP, Nagy P, Nakatsukasa H, Marsden E, Thorgeirsson SS: In vivo differentiation of rat liver oval cells into hepatocytes. *Cancer Res* 1989, 49:1541–1547
12. Thorgeirsson SS, Evarts RP, Bisgaard HC, Fujio K, Hu Z: Hepatic stem cell compartment: activation and lineage commitment. *Proc Soc Exp Biol Med* 1993, 204:253–260
13. Sarraf C, Lalani E, Golding M, Anilkumar TV, Poulosom R, Alison M: Cell behavior in the acetylaminofluorene-treated regenerating rat liver. Light and electron microscopic observations. *Am J Pathol* 1994, 145:1114–1126
14. Bisgaard HC, Nagy P, Santoni-Rugiu E, Thorgeirsson SS: Proliferation, apoptosis and induction of hepatic transcription factors are characteristics of the early response of biliary epithelial (oval) cells to chemical carcinogens. *Hepatology* 1996, 23:62–70
15. Slott PA, Liu MH, Tavoloni N: Origin, pattern, and mechanism of bile duct proliferation following biliary obstruction in the rat. *Gastroenterology* 1990, 99:466–477
16. Polimeno L, Azzarone A, Zeng QH, Panella C, Subbotin V, Carr B, Bouzahzah B, Francavilla A, Starzl TE: Cell proliferation and oncogene expression after bile duct ligation in the rat: evidence of a specific growth effect on bile duct cells. *Hepatology* 1995, 21:1070–1078
17. Nagy P, Kiss A, Schnur J, Thorgeirsson SS: Dexamethasone inhibits the proliferation of hepatocytes and oval cells but not bile duct cells in rat liver. *Hepatology* 1998, 28:423–429
18. Higgins GM, Anderson RM: Experimental pathology of the liver: restoration of the liver of the white rat following partial surgical removal. *Exp Pathol* 1931, 12:186–202
19. Cameron GR, Oakley CR: Ligation of the common bile duct. *J Pathol Bacteriol* 1932, 35:769–798
20. Alpini G, Glaser SS, Ueno Y, Pham L, Podila PV, Caligiuri A, LeSage

- G, LaRusso NF: Heterogeneity of the proliferative capacity of rat cholangiocytes following bile duct ligation. *Am J Physiol* 1998, 274: G767-G775
21. Sell S, Osborn K, Leffert HL: Autoradiography of "oval cells" appearing rapidly in the livers of rats fed N-2-fluorenylacetylamide in a choline devoid diet. *Carcinogenesis* 1981, 2:7-14
 22. Factor VM, Radaeva SA, Thorgeirsson SS: Origin and fate of oval cells in dipin-induced hepatocarcinogenesis in the mouse. *Am J Pathol* 1994, 145:409-422
 23. Novikoff PM, Yam A, Oikawa I: Blast-like cell compartment in carcinogen-induced proliferating bile ductules. *Am J Pathol* 1996, 148: 1473-1492
 24. Novikoff PM, Yam A: Stem cells and rat liver carcinogenesis: contributions of confocal and electron microscopy. *J Histochem Cytochem* 1998, 46:613-626
 25. Sell S, Leffert HL: An evaluation of cellular lineages in the pathogenesis of experimental hepatocellular carcinoma. *Hepatology* 1982, 2:77-86
 26. Petropoulos CJ, Yaswen P, Panzica M, Fausto N: Cell lineages in liver carcinogenesis: possible clues from studies of the distribution of a-fetoprotein RNA sequences in cell populations isolated from normal, regenerating, and preneoplastic rat livers. *Cancer Res* 1985, 45:5762-5768
 27. Potten CS, Loeffler M: Stem cells: attributes, cycles, spirals, pitfalls and uncertainties. Lessons for and from the crypt. *Development* 1990, 110:1001-1020
 28. Lemire JM, Shiojiri N, Fausto N: Oval cell proliferation and the origin of small hepatocytes in liver injury induced by D-galactosamine. *Am J Pathol* 1991, 139:535-552
 29. Sirica AE, Mathis GA, Sano N, Elmore LW: Isolation, culture and transplantation of intrahepatic biliary epithelial cells and oval cells. *Pathobiology* 1990, 58:44-64
 30. Nomoto M, Uchikosi Y, Kajikazawa W, Tanaka Y, Asakura H: Appearance of hepatocyte like cells in the interlobular bile ducts of human liver in various liver disease states. *Hepatology* 1992, 16:1199-1205
 31. Golding M, Sarraf CE, Lalani EN, Anilkumar TV, Edwards RJ, Nagy P, Thorgeirsson SS, Alison MR: Oval cell differentiation into hepatocytes in the acetylaminofluorene-treated regenerating rat liver. *Hepatology* 1995, 22:1243-1253
 32. Alison MR, Golding MH, Sarraf CE: Pluripotential liver stem cells: facultative stem cells located in the biliary tree. *Cell Prolif* 1996, 29:373-402
 33. Solt DB, Medline A, Farber E: Rapid emergence of carcinogen-induced hyperplastic lesions in a new model for the sequential analysis of liver carcinogenesis. *Am J Pathol* 1997, 88:595-610
 34. Anilkumar TV, Golding M, Edwards RJ, Lalani E, Sarraf CE, Alison MR: The resistant hepatocyte model of carcinogenesis in the rat: the apparent independent development of oval cell proliferation and early nodules. *Carcinogenesis* 1995, 16:845-853
 35. Enomoto K, Dempo K, Mori M, Onoe T: Histopathological and ultrastructural study on extramedullary hematopoietic foci in early stage of 3'-methyl-4-(dimethylamino)-azobenzene hepatocarcinogenesis. *Gann* 1978, 69:249-254
 36. Taniguchi H, Toyoshima T, Fukao K, Nakauchi H: Presence of hematopoietic stem cells in the adult liver. *Nat Med* 1996, 2:198-203
 37. Petersen BE, Bowen WC, Patrene KD, Mars WM, Sullivan AK, Murase N, Boggs SS: Bone marrow as a potential source of hepatic oval cells. *Science* 1999, 284:1168-1170
 38. Theise ND, Badve S, Saxena R, Henegariu O, Sell S, Crawford JM, Krause DS: Derivation of hepatocytes from bone marrow cells in mice after radiation-induced myeloablation. *Hepatology* 2000, 31:235-240
 39. Ledda-Columbano GM, Curto M, Piga R, Zedda AI, Menegazzi M, Sartori C, Shinozuka H, Bluethmann H, Poli V, Ciliberto G, Columbano A: In vivo hepatocyte proliferation is inducible through a TNF and IL-6-independent pathway. *Oncogene* 1998, 17:1039-1044
 40. Columbano A, Shinozuka H: Liver regeneration versus direct hyperplasia. *FASEB J* 1996, 10:1118-1128
 41. Omori M, Omori N, Evarts RP, Teramoto T, Thorgeirsson SS: Coexpression of flt-3 Ligand/flt-3 and SCF/c-kit signal transduction systems in bile-duct-ligated S1 and W mice. *Am J Pathol* 1997, 150: 1179-1187
 42. Matsusaka S, Tsujimura T, Toyosaka A, Nakasho K, Sugihara A, Okamoto E, Uematsu K, Terada N: Role of c-kit receptor tyrosine kinase in development of oval cells in the rat 2-acetylaminofluorene/partial hepatectomy model. *Hepatology* 1999, 29:670-676
 43. Rao MS, Subbarao V, Sato K, Reddy JK: Alterations of pancreatic hepatocytes in rats exposed to carcinogens. *Am J Pathol* 1991, 139:1111-1117
 44. Krakowski ML, Kritzik MR, Jones EM, Krahl T, Lee J, Arnush M, Gu D, Sarvetnick N: Pancreatic expression of keratinocyte growth factor leads to differentiation of islet hepatocytes and proliferation of duct cells. *Am J Pathol* 1999, 154:683-691
 45. Park CM, Cha IH, Chung KB, Suh WH, Lee CH, Choi SY, Chae YS: Hepatocellular carcinoma in extrahepatic bile ducts. *Acta Radiol* 1991, 32:34-36
 46. LeSage GD, Glaser SS, Marucci L, Benedetti A, Phinizo JL, Rodgers R, Caligiuri A, Papa E, Trejcek Z, Jezequel AM, Holcomb LA, Alpini G: Acute carbon tetrachloride feeding induces damage of large but not small cholangiocytes from BDL rat liver. *Am J Physiol* 1999, 276: G1289-G1301
 47. Potten CS: Stem cells in gastrointestinal epithelium: numbers, characteristics and death. *Philos Trans R Soc Lond B Biol Sci* 1998, 29:821-830
 48. Alpini G, Roberts S, Kuntz SM, Ueno Y, Gubba S, Podila PV, LeSage G, Larusso NF: Morphological, molecular, and functional heterogeneity of cholangiocytes from normal rat liver. *Gastroenterology* 1996, 110:1636-1643
 49. Kanno N, LeSage G, Glaser S, Alvaro D, Alpini G: Functional heterogeneity of the intrahepatic biliary epithelium. *Hepatology* 2000, 31: 555-561
 50. Dunsford HA, Maset R, Salman J, Sell S: Connection of ductlike structures induced by a chemical hepatocarcinogen to portal bile ducts in the rat liver detected by injection of bile ducts with a pigmented barium gelatin medium. *Am J Pathol* 1985, 118:218-224
 51. Betto H, Kaneda K, Yamamoto T, Kojima A, Sakurai M: Development of intralobular bile ductules after spontaneous hepatitis in Long-Evans mutant rats. *Lab Invest* 1996, 75:43-53
 52. Vracko R, Benditt EP: Basal lamina: the scaffold for orderly cell replacement. Observations on regeneration of injured skeletal muscle fibers and capillaries. *J Cell Biol* 1972, 55:406-419
 53. Paku S, Paweletz N: First steps of tumor related angiogenesis. *Lab Invest* 1991, 65:334-346

Gastrointestinal, Hepatobiliary and Pancreatic Pathology

Thy-1 Is Expressed in Hepatic Myofibroblasts and Not Oval Cells in Stem Cell-Mediated Liver Regeneration

Katalin Dezső,* Peter Jelnes,[†] Viktória László,* Kornélia Baghy,* Csaba Bődör,* Sándor Paku,* Niels Tygstrup,[‡] Hanne Cathrine Bisgaard,[†] and Peter Nagy*

From the First Department of Pathology and Experimental Cancer Research,* Semmelweis University, Budapest, Hungary; the Department of Cellular and Molecular Medicine,[†] The Danish Stem Cell Research Centre, The Panum Institute, University of Copenhagen, Copenhagen, Denmark; and the Department of Hepatology,[‡] Rigshospitalet, Copenhagen University Hospital, Copenhagen, Denmark

Thy-1, a marker of hematopoietic stem cells, has been reported to be expressed by oval cells proliferating during stem cell-mediated regeneration in rat liver, suggesting a relationship between the two cell populations. Consequently, Thy-1 has become an accepted cell surface marker to sort hepatic oval cells. In the present study we used the well-characterized 2-acetylaminofluorene/partial hepatectomy model to induce transit-amplification of hepatic oval cells in the regenerating liver and characterized Thy-1 expression using Northern hybridization, quantitative reverse transcriptase-polymerase chain reaction analysis, immunofluorescence confocal microscopy, and immunoelectronmicroscopy. We found that Thy-1 expression was induced during transit-amplification of the oval cell population, but Thy-1 mRNA was not present in the α -fetoprotein-expressing oval cells. Thy-1 protein was consistently present outside the basement membrane surrounding the oval cells. It overlapped frequently with smooth muscle actin staining. A similar cellular localization of the Thy-1 protein was found on human liver specimens with ductular reactions obtained from patients with fulminant liver failure. Furthermore, Thy-1 was expressed by myofibroblasts in experimental liver fibrosis models without oval cell proliferation. We conclude that Thy-1 is not a marker of oval cells but is present on a subpopula-

tion of myofibroblasts/stellate cells. (Am J Pathol 2007, 171:1529–1537; DOI: 10.2353/ajpath.2007.070273)

Thy-1 (CD-90) is a rather promiscuous molecule. It is expressed by several different cell types, and, among others, it is present on the surface of the bone marrow stem cells. It was also reported to be present in the rat liver on the oval/progenitor cells in stem cell-mediated liver regeneration.^{1–4} Later, a precursor-product relationship was described between bone marrow cells and oval cells/hepatocytes in several experimental models^{1,3,5,6} as well as in humans,⁷ raising the very exciting possibility of liver cells being derived from hematopoietic cells. Several groups confirmed the Thy-1 expression in oval cells,^{1–4} resulting in the extensive use of Thy-1 as a cell surface marker to sort out liver progenitor cells. However, the issue of stem cell transdifferentiation has subsequently been one of the most debated issues in hepatic pathobiology, and most of these observations can now be explained by cell fusion and not transdifferentiation. The most comprehensive review of this topic recently concluded that although “data are sufficient to indicate that mesodermal hematopoietic cells can generate hepatocytes at a very low frequency, this is not an effective pathway under most conditions.”⁸ At the same time, others described cells coexpressing Thy-1 and smooth muscle actin (SMA) in similar experimental settings,⁹ questioning the identity of the Thy-1-expressing cells in the liver. To resolve this contradic-

Supported by Országos Tudományos Kutatási Alap (Hungary) (grants T42674 and TS49887), Egészségügyi Tudományos Tanács (Egészségügyi Minisztérium, Hungary) (grant 032/2006), and the Danish Medical Research Council (grants 22-03-0277 to H.C.B. and 2052-01-0045 to The Danish Stem Cell Research Centre).

Accepted for publication August 14, 2007.

H.C.B. and P.N. contributed equally as senior investigators of this work.

Supplemental material for this article can be found on <http://ajp.amjpathol.org>.

Address reprint requests to Peter Nagy, First Department of Pathology and Experimental Cancer Research, Semmelweis University, Üllői út 26, Budapest, H-1085, Hungary. E-mail: nagy@korp1.sote.hu.

tion we performed detailed morphological expression analysis to identify the location of Thy-1 in the normal liver and in damaged liver with and without oval cell proliferation.

Materials and Methods

Animal Experiments

Male F-344 rats (160 to 180 g) were used for all experiments and were kept under standard conditions. Animal protocols were approved by the Danish Council for Supervision with Experimental Animals.

AAF/PHx Experiment

The animals received 2-acetylaminofluorene (AAF) (suspended in 1% dimethylcellulose) at 4.5, 9, 12, or 18 mg/kg/day administered daily for 4 consecutive days by gavage. Traditional two-thirds partial hepatectomy (PHx)¹⁰ was performed on the 5th day, followed by four additional AAF treatments. Groups of three animals were sacrificed 1, 5, 9, 14, and 21 days after PHx. Controls included untreated animals and rats subjected to a PHx or a sham laparotomy only. After resection of the liver, samples were taken for histological examinations and the rest snap-frozen in liquid nitrogen for RNA extraction.

Bile Duct Ligation

Ligation of the common bile duct was done according to Cameron and Oakley.¹¹ The rats were sacrificed 2 weeks after the operation.

CCl₄ Fibrosis

Twenty percent CCl₄ (0.5 ml/kg, dissolved in vegetable oil) was administered by gavage to rats twice a week while the animals were kept on 0.05% phenobarbital in the drinking water. The experiment was terminated after 8 weeks.¹²

Human Tissue

Snap-frozen human liver specimens for immunohistochemical examination were obtained from two patients who underwent orthotopic liver transplantation because of fulminant liver failure of unknown etiology. The procedure was approved by the ethical committee of the Semmelweis University.

Isolation of Oval Cells for Northern Blot Analysis

Isolation of oval cells was performed using control liver, and animals were treated according to the AAF/PHx protocol (18 mg/kg/day) and sacrificed at day 9 after PHx. The isolation and enrichment procedure has been described in detail.¹³ In brief, liver cells were released by a three-step perfusion procedure *in situ*. Viable nonparen-

chymal cell populations were purified by centrifugation through a two-step Percoll gradient. Kupffer cells were removed by selective adherence to plastic tissue culture dishes. Removal of macrophages, endothelial cells, and red blood cells was achieved by selective panning using the mouse monoclonal antibody OX43 (catalog no. MCA276; Serotec, Oxford, UK). Cell preparations were snap-frozen in liquid nitrogen and stored at -70°C until processed for total RNA isolation and Northern blot analysis.

Northern Blot Analysis

Northern blotting with cDNA probes was performed as previously described.¹⁴ The cDNA for rat Thy-1 encompassed nucleotides 46 to 531 (GenBank accession no. NM_012673), and for α -fetoprotein (AFP), nucleotides 101 to 329 (GenBank accession no. X02361). The filters were hybridized with rat S18 to assess the integrity and ensure equal loading of the RNA.

Quantitative Real-Time Reverse Transcriptase-Polymerase Chain Reaction Analysis

Frozen sections (8 μm) were fixed in acetone, dried at room temperature, and stained with RNase-free hematoxylin. Laser microdissection of oval cells was performed by using the PALM MicroBeam system, and 500 to 1000 cells were collected in RNA-Later. For whole liver quantitative real-time reverse transcriptase-polymerase chain reaction (qRT-PCR) analysis, frozen sections from normal and AAF/PHx-treated liver were collected in lysis buffer.

Total RNA was isolated by RNAqueous micro kit (catalog no. AM 1931; Ambion, Austin, TX). A high capacity cDNA reverse transcription kit (catalog no. 4368814; ABI) was used for cDNA synthesis as recommended by the supplier. PCR was performed by the ABI Prism 7300 sequence detection system (Applied Biosystems, Weiterstadt, Germany), using ABI TaqMan gene expression assays for AFP (assay ID: Rn00560661_m1), SMA (assay ID: Rn01759928_g1), and Thy-1 (assay ID: Rn00562048_m1) according to the manufacturer's instructions. Glyceraldehyde-3-phosphate dehydrogenase (GAPDH) was used as endogenous control. All samples were run in triplicate, in a 20- μl reaction volume. Results were obtained as threshold cycle (C_T) values. Expression levels were calculated using the ΔC_T method. The values were calculated as the mean values of three independent measurements, and the expression levels of mRNA in all samples were defined as a ratio to GAPDH expression.

Morphological Analysis

Frozen sections (10 to 20 μm) were fixed in methanol and were incubated at room temperature (1 hour) with a mixture of the primary antibodies (Table 1) and with appropriate secondary antibodies afterward (Jackson ImmunoResearch, West Grove, PA). All samples were analyzed by confocal

Table 1. Primary Antibodies Used for the Immunohistochemical Studies

Antibody	Species	Manufacturer*	Catalog number	Dilution
Laminin	Rabbit polyclonal	DAKO	Z0097	1:200
Anti-rat Thy-1	Mouse monoclonal	BD Pharmingen	554895	1:100
FITC-labeled anti-rat Thy-1	Mouse monoclonal	BD Pharmingen	554897	1:50
Anti-human Thy-1	Mouse monoclonal	BD Pharmingen	550402	1:100
FITC-labeled anti-human Thy-1	Mouse monoclonal	BD Pharmingen	555595	1:50
GFAP	Mouse monoclonal	BD Pharmingen	556330	1:100
Anti-human cytokeratin-19	Mouse monoclonal	BioGenex	MU246-UC	1:50
Anti-rat cytokeratin-19	Mouse monoclonal	Novocastra	NCL-CK19	1:50
OV-6	Mouse monoclonal	R&D Systems	MAB2020	1:100
FITC-labeled cytokeratin	Mouse monoclonal	DAKO	F0859	1:10
Desmin	Rabbit polyclonal	Neomarkers	RB-9014-P1	1:100
Smooth muscle actin	Mouse monoclonal	DAKO	M0851	1:100
OX-62	Mouse monoclonal	Serotec	MCA1029G	1:100
Mononuclear phagocyte (rMPh/ED-1)	Mouse monoclonal	BD Pharmingen	554954	1:100
Lyve-1	Rabbit polyclonal	Reliatech	102-PA505	1:100
CD45	Mouse monoclonal	BD Pharmingen	550566	1:100

DAKO, Glostrup, Denmark; BD Pharmingen, San Jose, CA; Biogenex, San Ramon, CA; Novocastra, Newcastle upon Tyne, UK; R & D System, Minneapolis, MN; Neomarkers, Fremont, CA; Serotec, Oxford, UK; Reliatech, Bvaunschweig, Germany.

laser-scanning microscopy using the Bio-Rad MRC-1024 system (Bio-Rad, Richmond, CA). Negative controls were performed by replacing the primary antibodies with preimmune sera (data not shown).

Co-localization analysis was performed using the Image J program (National Institutes of Health, Bethesda, MD). The red (channel 1) and green (channel 2) images were acquired separately and sequentially to avoid bleed-through. The area fraction (%) occupied by red and green fields was determined by manual thresholding. Analysis of co-localized points (%) was determined using the co-localization plug-in.

Preparation of liver tissue for immunoelectronmicroscopy was described by Paku and colleagues.¹⁵ Cryosections were rinsed in phosphate-buffered saline and incubated with the primary antibody Thy-1 (dilution 1:100, 3 hours), followed by peroxidase-conjugated anti-mouse antibody (dilution 1:500, catalog no. 715-035-1500; Jackson ImmunoResearch). Semithin sections were slightly stained by 0.5% toluidine blue (pH 8.5), and unstained ultrathin sections were analyzed on a Philips CM 10 electron microscope (Philips, Eindhoven, The Netherlands).

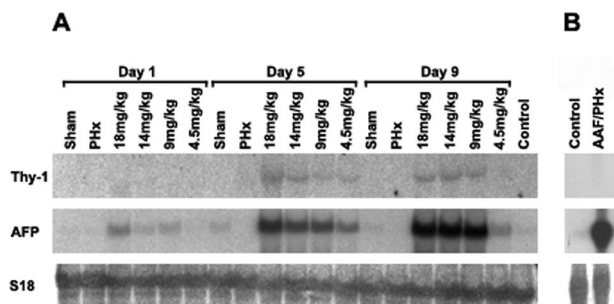


Figure 1. Northern blot analysis for the expression of Thy-1, AFP, and S18. **A:** RNA was isolated from whole liver of normal, sham-operated (sham), partially hepatectomized (PHx), and AAF/PHx-treated animals. The numbers refer to the daily dose of AAF. Animals were sacrificed at 1, 5, and 9 days after PHx. **B:** RNA was isolated from the oval cell fraction from control and AAF/PHx (AAF dose, 18 mg/kg/day)-treated rats. The strong AFP band in the second lane confirms the presence of oval cells in the enriched cell population. Notice the lack of Thy-1 expression in this cell population.

Results

Thy-1 Expression in the Normal Liver

Transcripts for Thy-1 were not detected by Northern blot analysis in mRNA preparations from whole normal liver (Figure 1A) and were undetectable in preparations of nonparenchymal cells isolated from normal liver and enriched with a protocol for oval cells (Figure 1B). Likewise, qRT-PCR analysis detected low AFP, Thy-1, and SMA expression in normal liver (Figure 2).

Thy-1 expression by immunohistochemistry was detectable and confined to the periportal region (Figure 3, A, B, C, and E; and Supplemental Figure 1A available at <http://ajp.amjpathol.org>). There was some faint cloudy staining around the major interlobular bile ducts (Figure 3A, and Supplemental Figure 1A available at <http://ajp.amjpathol.org>).

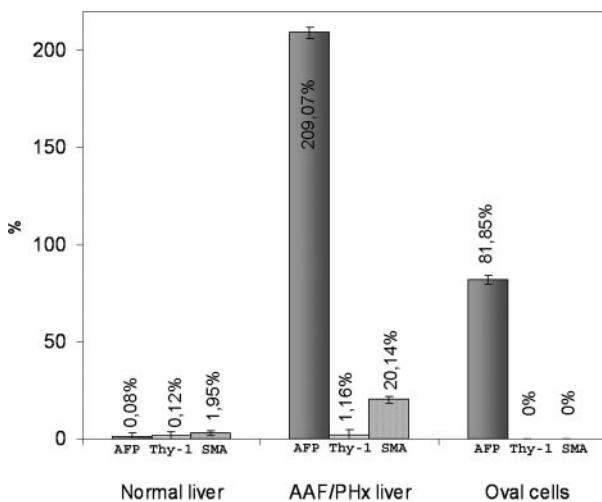
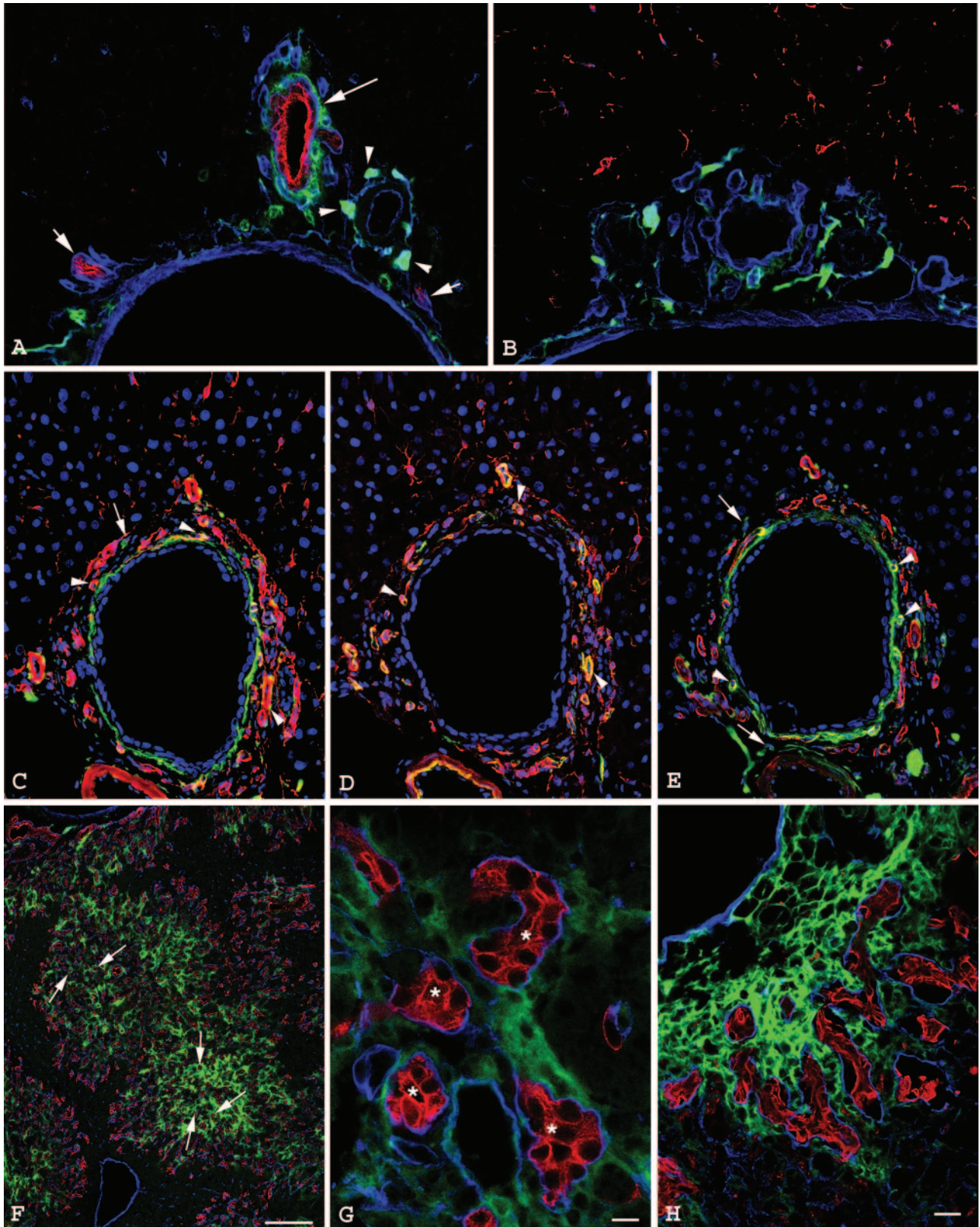


Figure 2. qRT-PCR analysis of AFP, Thy-1, and SMA mRNA in whole liver of normal and AAF/PHx (9 days after PHx)-treated animals and in microdissected oval cell populations. The relative expression levels of AFP, Thy-1, and SMA were determined by comparing with that of GAPDH expression level (100%).

Thy-1 antibody decorated more intensely and sharply the cross sections of peripheral nerves (Figure 3A, and Supplemental Figure 1A available at <http://ajp.amjpathol.org>). These nerves were also positive for synaptophysin

(data not shown). Scattered undefined cells inside the portal areas also expressed Thy-1 (Figure 3, C and E).

Desmin antibody reacted with nonparenchymal cells in the liver lobule in addition to the muscular wall of the



blood vessels and scattered single cells in the periportal connective tissue (Figure 3, C and D). Conversely, no SMA-positive cells were seen inside the liver lobule; only the vessel walls were stained (Figure 3, D and E). Glial fibrillary acidic protein (GFAP), an established marker of hepatic stellate cells, decorated scattered single cells in the liver lobules. There was no overlap between the GFAP and Thy-1 reaction (Figure 3B).

Thy-1 Expression in the Stem Cell-Mediated Liver Regeneration

In rat liver treated according to the AAF/PHx protocol, oval cells formed ductules invading the liver lobules during the first 7 to 10 days. These ductules are surrounded by continuous basement membrane, and there are numerous stellate cells/myofibroblasts around them.¹⁵ The number of transit-amplifying oval cells depends on the dose of AAF as demonstrated by the levels of AFP transcripts—the most widely used marker for rat oval cells (Figure 1A). A similar expression pattern was found in whole liver for Thy-1, confirming that Thy-1 expression is induced during oval cell-mediated liver regeneration (Figure 1A). However, when isolated oval cells from AAF/PHx-treated animals were examined, no expression of Thy-1 was detectable despite increased levels of AFP transcripts (Figure 1B). qRT-PCR also failed to detect Thy-1 (and SMA) expression in RNA isolated from microdissected oval cells, while AFP RNA was present. However, Thy-1 and SMA expression could be demonstrated by qRT-PCR from whole liver sections. Therefore, we performed a thorough immunohistochemical analysis of the Thy-1 expression.

The staining pattern with the different antibodies was identical in all studied time points. The laminin-containing basement membrane surrounded the CK-19-positive oval cell ductules. The Thy-1 reaction was observed consistently outside the basement membrane (Figure 3, F and G; and Supplemental Figure 1, B and C, available at <http://ajp.amjpathol.org>). The antibody sometimes labeled round, cellular body-like elements, but frequently only stripes or cell processes were positive. Thy-1 immunoreactions were easily abolished by detergent pretreatment. If sections were pretreated for 5 minutes in 0.05% Triton X-100, the staining was faint whereas pretreatment for 10

minutes resulted in complete disappearance of the reaction (data not shown). Thy-1 antibody also decorated cellular elements and long processes outside the basement membrane in human livers with extensive ductular reactions because of fulminant liver failure (Figure 3H).

The pattern of Thy-1 reaction was reminiscent of stellate cell/myofibroblast architecture, which also could be found outside the basement membrane. Therefore, in the rat liver we performed co-staining of Thy-1 and SMA or desmin, the two most widely used stellate cell/myofibroblast markers. SMA-positive cells appeared very early in the experiment at the limiting plate and spread along the ductules formed by oval cells into the parenchyma. The desmin antibody reacted with scattered nonparenchymal cells throughout the liver lobule from the beginning of the experiment, but they became more frequent in the zone of the oval cells. In the co-staining experiments, Thy-1 showed frequent co-localization with SMA (Figure 4, A–C). Of the Thy-1-positive areas $80.3 \pm 9.6\%$ stained with SMA, but only $58 \pm 9.3\%$ of the SMA-positive field was decorated by Thy-1.

Thy-1 positivity hardly overlapped with desmin; the value of co-localization index was $6.8 \pm 2.3\%$ (Figure 4D and Supplemental Movie 1 available at <http://ajp.amjpathol.org>). This was surprising because SMA and desmin have been used to identify stellate cells/myofibroblasts. The co-localization index of these two markers was also negligible ($7.16 \pm 1.2\%$) (Figure 4E).

To investigate Thy-1 co-localization with other marker antigens, we performed further double-staining experiments. Lyve-1, a new marker for the endothelial cells of lymphatic vessels and hepatic sinusoids,^{16,17} did not show any co-staining with Thy-1 in the neighborhood of the oval cells (Figure 4F), a result that was similar to OX 62 and rMph markers of hepatic dendritic¹⁸ and Kupffer cells (data not shown). In addition, CD45, a general leukocyte marker, did not stain the Thy-1-positive structures (Figure 4G).

Immunoelectron microscopic examination of Thy-1 expression also revealed long cell processes running clearly outside the basement membrane. Because of immunoelectronmicroscopic processing of the samples, the ultrastructure of labeled cells could not be examined in detail. However, our morphological evaluation suggested that the marked cells displayed features of stellate cells/myofibroblasts (Figure 5, A and B).

Figure 3. Thy-1 expression examined by confocal microscopy. **A–E:** Normal rat liver. **F and G:** Rat liver from an AAF/PHx experiment, 14 and 21 days after PHx. **H:** A human liver with ductular reaction. **C–E:** Serial sections of an interlobular bile duct and its neighborhood. **A:** The section is triple labeled for Thy-1 (green), cytokeratin-19 (red), and laminin (blue). The portal vein, the hepatic artery branch, and the major interlobular bile duct are surrounded by laminin-positive (blue) basement membrane. Thy-1-positive nerve fibers (**arrowheads**) are present around the vessels. There is a fine Thy-1 staining around the larger interlobular bile ducts (**large arrow**), but it cannot be observed around the small bile duct branches (**small arrows**). **B:** The section is triple labeled for Thy-1 (green), GFAP (red), and laminin (blue). GFAP-positive stellate cells are present only in the liver parenchyma. Thy-1 and GFAP staining show separate structures in normal liver. **C:** The sections are stained for Thy-1 (green) and desmin (red). Desmin positivity can be observed in the wall of hepatic artery branches and in the capillaries of peribiliary plexus. Note the co-localization of desmin and Thy-1 in the wall of peribiliary vascular plexus (**arrowheads**). Desmin-positive cells can also be discerned within the portal area and in the liver parenchyma. There are scattered Thy-1-positive cells in the portal area (**arrow**). The nuclei are stained with toto-3 (blue). **D:** The section is stained for SMA (green) and desmin (red). SMA and desmin co-localize in hepatic artery branches and in the wall of capillaries of the peribiliary plexus (**arrowheads**). SMA-positive cells cannot be found in the liver parenchyma. The nuclei are stained with toto-3 (blue). **E:** The section is stained for Thy-1 (green) and SMA (red). Note the co-localization of SMA and Thy-1 in the wall of peribiliary vascular plexus (**arrowheads**). Scattered Thy-1-positive cells are present in the portal area (**arrows**). **F:** AAF/PHx experiment, 14 days after PHx. Triple staining for Thy-1 (green), CK-19 (red), and laminin (blue). The CK-19-positive (red) oval cell-formed ductules (**arrows**) are surrounded by laminin-positive (blue) basement membrane. The oval cells are not labeled by the Thy-1 antibody. Thy-1-positive cells were situated exclusively among the ductules, strictly outside the basement membrane. **G:** AAF/PHx experiment, 22 days after PHx. Thy-1-positive (green) cells are clearly localized outside the basement membrane (laminin-positive, blue) of CK-19-positive (red) oval cell ductules (**asterisks**). **H:** Thy-1-positive (green) cells are outside the laminin-containing basement membrane (laminin, blue) surrounding the proliferating ductules (CK-19, red) in human liver. Scale bars: 20 μm (**A–E, H**); 200 μm (**F**); and 10 μm (**G**).

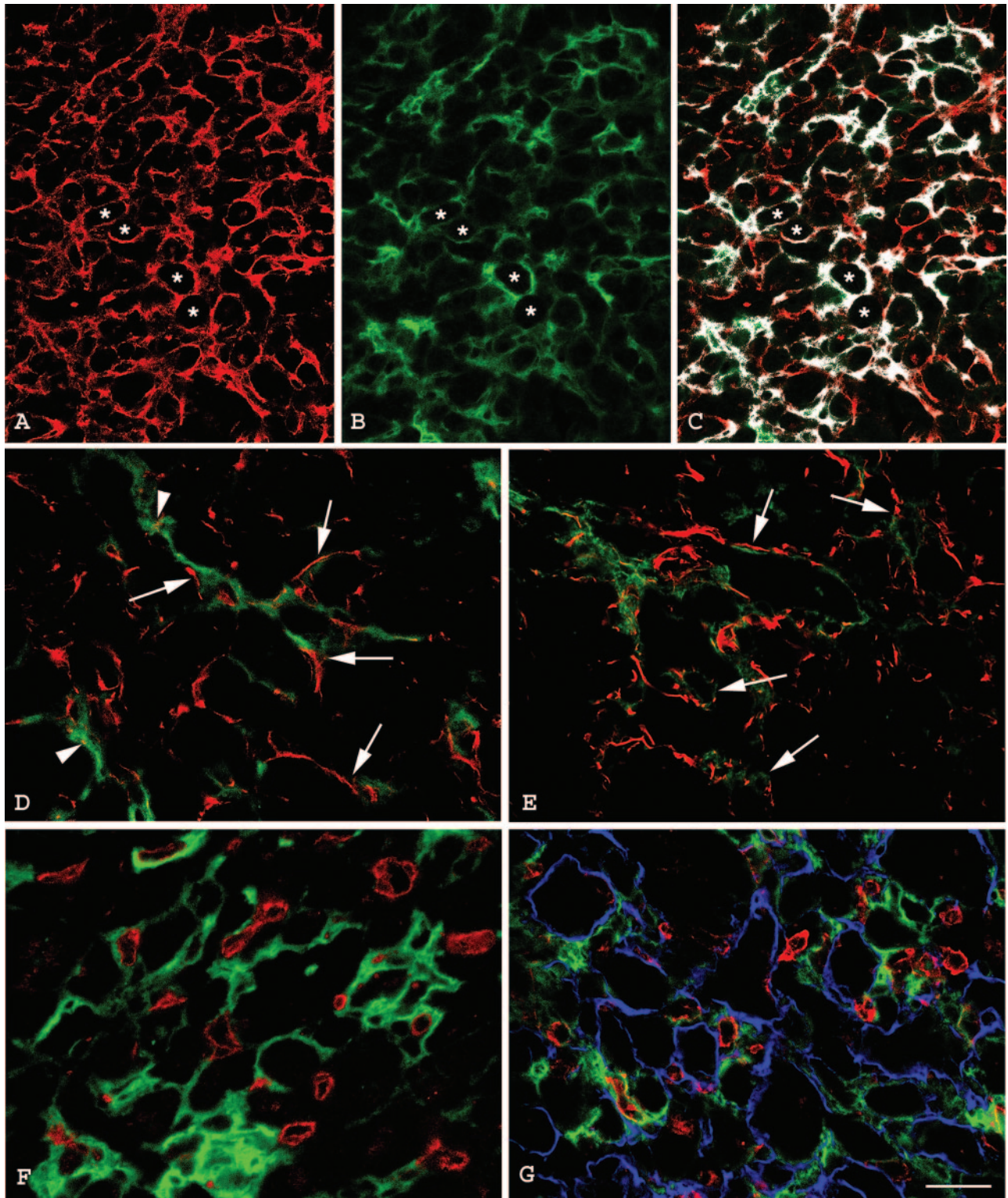


Figure 4. Confocal microscopy of Thy-1 expression combined with stellate cell/myofibroblast markers SMA and desmin. Sections are from a rat liver treated according to the AAF/PHx protocol, 9 days after PHx. **A** and **B**: Double labeling for SMA (red) and Thy-1 (green). SMA-positive myofibroblast (**A**) and Thy-1-positive cells (**B**) are present among the oval cell ductules (**asterisks**). **C**: The white areas on the merged image show co-localization of SMA and Thy-1. **D**: Double immunofluorescence for Thy-1 (green) and desmin (red). The overwhelming majority of the green and red staining marks separate structures (**arrows**). There are only a few spots showing yellow signal (**arrowheads**), suggesting occasional co-localization of the two antibodies. **E**: Double-immunofluorescent staining for SMA (green) and desmin (red) labels different structures (**arrows**). **F**: Double labeling for Thy-1 (green) and Lyve-1 (red) in the area of proliferating ductules. Lyve-1-positive endothelium does not express Thy-1; it is localized outside the vessels. **G**: The CD45 (red) staining does not overlap with Thy-1 (green). Scale bar = 50 μ m.

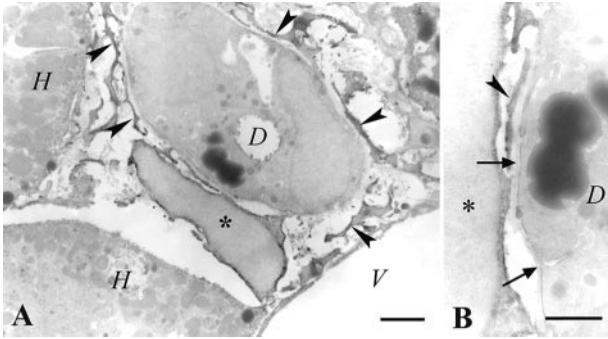


Figure 5. Ultrastructural localization of Thy-1 in a rat liver treated according to the AAF/PHx protocol, 9 days after PHx. **A:** Black reaction product labels the surface of a periductal cell (asterisk). Numerous long cytoplasmic processes showing positive reaction for Thy-1 (arrowheads) can be observed close to the basal surface of the oval cell ductule (D). H, Hepatocyte; V, vessel lumen. **B:** Detail of A. Thy-1-positive cytoplasmic process (arrowhead) is localized outside the basement membrane (arrows) of the ductule (D). Scale bars: 2 μm (A); 1 μm (B).

Thy-1 Expression in Rat Liver Fibrosis Model

Thy-1 also decorated the myofibroblasts in two liver fibrosis models (bile duct ligation-induced cholangiofibrosis and CCl_4 /phenobarbital-induced cirrhosis), which were not characterized by oval cell proliferation (Figure 6).

Discussion

We have investigated Thy-1 expression in rat livers regenerating by the recruitment of oval/progenitor cells. The oval cells were not labeled by the Thy-1 antibody, but we observed a strong periductal reaction outside the basement membrane. There was a partial overlap between the Thy-1 and SMA staining, but no co-staining of Thy-1 and desmin could be observed. Furthermore, Thy-1 also marked myofibroblasts in two liver fibrosis models without oval cell reactions.

Thy-1 is a highly conserved protein anchored by a phosphatidylinositol to the cell membrane. Its exact function is unknown, but it has been proposed to be involved

in cell recognition, adhesion, and lymphocyte activation.¹ It is expressed in a wide variety of different tissues.^{1,19–23} Its expression has been extensively studied in the liver. Petersen and colleagues¹ reported that hepatic oval cells expressed the hematopoietic stem cell marker Thy-1 in the rat. This observation led to further experiments suggesting that bone marrow cells can be the precursors of oval cells/hepatocytes. Hepatic progenitor cells in human fetal liver also have been reported to be Thy-1-positive.⁷ However, Hoppo and colleagues⁹ found in mouse that Thy-1-positive mesenchymal cells promoted the maturation of Thy-1-negative hepatic progenitor cells. A subpopulation of the Thy-1-positive cells also expressed SMA.

Our results in the rat are similar to this latter group's observation. In our case the CK-19-positive, laminin-surrounded oval/progenitor cells were not decorated by the Thy-1 antibody. CK-19 is an established marker of oval cells. It is also generally accepted that the oval cells are surrounded by continuous basement membrane, which can be visualized by laminin immunohistochemistry. The co-staining of these three antigens on the same section combined by confocal microscopic analysis is a very reliable morphological examination. Thy-1-positive cells were also outside the proliferating ductules in human liver, confirming the observation of Crosby and colleagues.²⁴ Furthermore, immunoelectronmicroscopy confirmed that the Thy-1-positive cells are outside the basement membrane. On traditional histological sections, it is very difficult to distinguish conclusively between the oval and the closely associated stellate cells/myofibroblasts. Serial sections stained by an oval cell marker, which was used by Petersen and colleagues,¹ do not provide much help. Individual cells cannot be analyzed on serial sections, and the histological arrangement of the two cell populations is similar (spreading outward from the periportal region). Our Northern hybridization and qRT-PCR analysis also strongly support the morphological observations.

The Thy-1 molecule is bound weakly to the cell membrane.^{25,26} Triton X-100 pretreatment in our study also deleted the Thy-1 signal from the sections. Soluble Thy-1

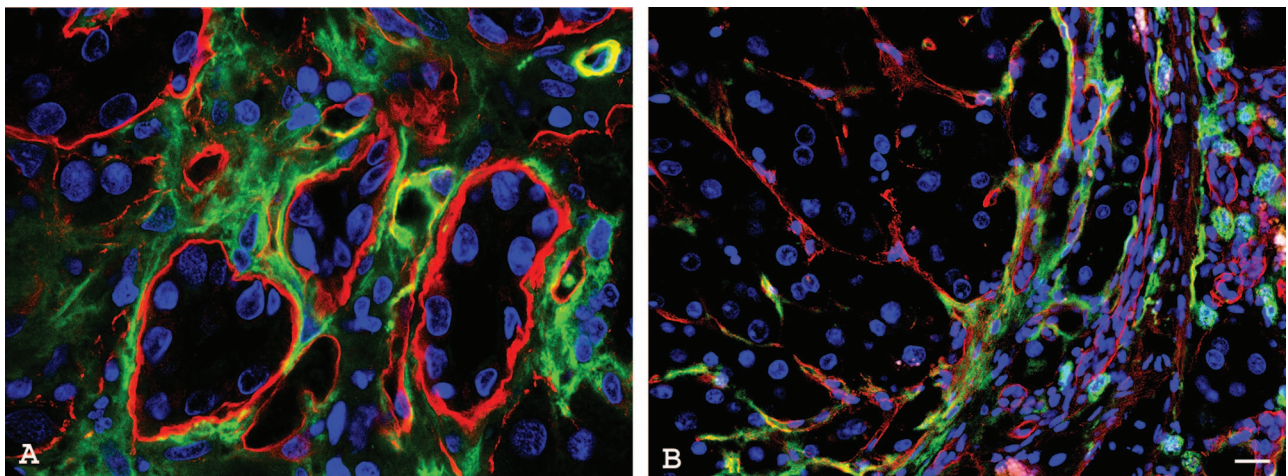


Figure 6. Thy-1 expression in other rat hepatic fibrosis models. **A:** Bile duct ligation-induced cholangiofibrosis. **B:** CCl_4 /phenobarbital cirrhosis model. **A:** Thy-1-positive (green) cells surrounding the large proliferating bile ducts. The nuclei are stained with toto-3 (blue); the basement membrane is marked by laminin (red). **B:** Thy-1-positive (green) cells are situated on the edge of the laminin-positive (red) cirrhotic septum. The nuclei are stained with toto-3 (blue). Scale bar = 20 μm .

has been also described in the serum.²⁷ Enzymatic digestion during the cell isolation procedures may cause detachment of the Thy-1 molecule, which might associate later to other cells causing misleading results in cell suspension.

To identify the Thy-1-expressing cells, we co-stained Thy-1 with several other marker antibodies. The negative results with OX-62, rMPH, and Lyve-1 excluded hepatic dendritic, Kupffer, and sinusoidal endothelial cells as the sources of Thy-1 expression. The position and shape of the Thy-1-positive cells refers strongly to the so-called stellate cells/myofibroblasts, which are well known to have close spatial relationship with the oval cells in all oval cell proliferation models. The partial co-staining with SMA supports this option, as well as the Thy-1 positivity of myofibroblasts in two hepatic fibrosis models. Thy-1-positive myofibroblasts were described in other tissues, and the ratio of the Thy-1^{+/-} populations was a function of their activation stage.²⁸⁻³¹

Surprisingly, co-staining of Thy-1 with desmin, another marker of stellate cells, could not be demonstrated. Desmin and SMA are alternatively used markers for stellate cells.³² These antibodies stain comparably located and shaped cell populations, but according to our result, the two reactions do not overlap. The origin and phenotype of hepatic stellate cells/myofibroblasts is one of the most controversial issues of liver pathobiology. It is not known if there are different differentiation/activation stages of the same cell population, or as Ramadori and Saile³² propose, there are two (or more) cell types with partially overlapping phenotype. Our observations on the normal liver and during the progression of oval cell proliferation in the rat are in support of the view of Ramadori and Saile.³² Scattered desmin/GFAP-positive cells were observed in the parenchyma of the normal liver, which might correspond to the (classical, perisinusoidal, vitamin A-storing) stellate cells. SMA-decorated cells were confined to the vessel walls in the normal liver, but they appeared in the periportal region very early after treatment with AAF alone (data not shown) and later spread along the oval cell ductules. This would imply that the SMA-positive cells would be myofibroblasts, derived from the periportal fibroblasts, as proposed by Ramadori and Saile³² and Beaussier and colleagues.³³ As far as we know, co-staining for SMA and desmin has not been published in oval cell proliferation experiments. Considering the above data, the Thy-1-positive cells in the zone of the oval cells show the closest association with the myofibroblasts. The increased expression of Thy-1 in two liver fibrosis models also supports the myofibroblastic origin of this marker molecule.

The appearance of Thy-1-positive cells in the liver parenchyma can be explained if some of the myofibroblasts acquire the Thy-1 expression during the invasion of the liver lobule. Alternatively, it has been found that the mesenchymal stem cells in the bone marrow are Thy-1-positive and that this cell compartment can contribute to wound-healing processes³⁴ including the fibrogenesis of the liver.³⁵ It cannot be excluded that the Thy-1 antibody recognizes bone marrow-derived mesenchymal cells, which may participate in oval cell-mediated liver regeneration. At present, we cannot distinguish between these

two possibilities, but transplantation experiments are under way to study the presence of bone marrow-originated cells among the stellate cells/myofibroblasts. Recently, Kisseleva and colleagues³⁶ have described a unique CD45⁺ fibrocyte population in the liver. However, in accordance with our results, Kamo and colleagues³⁷ could not demonstrate co-expression of Thy-1 and CD45.

In conclusion, we did not find Thy-1 expression in the hepatic oval/progenitor cell population in stem cell-mediated rat liver regeneration or in human ductular reactions. Instead, Thy-1 was localized to a subpopulation of stellate cells/myofibroblasts. Therefore, the use of Thy-1 as a cell surface marker for isolation of oval/progenitor cells from the liver is not recommended. The exact origin and function of Thy-1-expressing cells remains to be studied. Our results are in complete agreement with the recently published study of Dudas and colleagues.³⁸

Acknowledgment

We thank Sándor Spisák for helping in microdissection.

References

1. Petersen BE, Goff JP, Greenberger JS, Michalopoulos GK: Hepatic oval cells express the hematopoietic stem cell marker Thy-1 in the rat. *Hepatology* 1998, 27:433-445
2. Shu SN, Wei L, Wang JH, Zhan YT, Chen HS, Wang Y: Hepatic differentiation capability of rat bone marrow-derived mesenchymal stem cells and hematopoietic stem cells. *World J Gastroenterol* 2004, 10:2818-2822
3. Laurson J, Selden C, Hodgson HJ: Hepatocyte progenitors in man and in rodents—multiple pathways, multiple candidates. *Int J Exp Pathol* 2005, 86:1-18
4. Pi L, Oh SH, Shupe T, Petersen BE: Role of connective tissue growth factor in oval cell response during liver regeneration after 2-AAF/PHX in rats. *Gastroenterology* 2005, 128:2077-2088
5. Theise ND, Krause DS: Bone marrow to liver: the blood of Prometheus. *Semin Cell Dev Biol* 2002, 13:411-417
6. Petersen BE, Bowen WC, Patrene KD, Mars WM, Sullivan AK, Murase N, Boggs SS, Greenberger JS, Goff JP: Bone marrow as a potential source of hepatic oval cells. *Science* 1999, 284:1168-1170
7. Masson NM, Currie IS, Terrace JD, Garden OJ, Parks RW, Ross JA: Hepatic progenitor cells in human fetal liver express the oval cell marker Thy-1. *Am J Physiol Gastrointest Liver Physiol* 2006, 291:G45-G54
8. Thorgeirsson SS, Grisham JW: Hemopoietic cells as hepatocyte stem cells: a critical review of the evidence. *Hepatology* 2006, 43:2-8
9. Hoppo T, Fujii H, Hirose T, Yasuchika K, Azuma H, Baba S, Naito M, Machimoto T, Ikai I: Thy1-positive mesenchymal cells promote the maturation of CD49f-positive hepatic progenitor cells in the mouse fetal liver. *Hepatology* 2004, 39:1362-1370
10. Higgins GM, Anderson RM: Experimental pathology of the liver: restoration of liver of white rat following partial surgical removal. *Exp Pathol* 1931, 12:186-202
11. Cameron GR, Oakley CR: Ligation of the common bile duct. *J Pathol Bacteriol* 1932, 35:769-798
12. Proctor E, Chatamra K: High yield micronodular cirrhosis in the rat. *Gastroenterology* 1982, 83:1183-1190
13. Bisgaard HC, Santoni-Rugiu E, Nagy P, Thorgeirsson SS: Modulation of the plasminogen activator/plasmin system in rat liver regenerating by recruitment of oval cells. *Lab Invest* 1998, 78:237-246
14. Bisgaard HC, Müller S, Nagy P, Rasmussen LJ, Thorgeirsson SS: Modulation of the gene network connected to interferon- γ in liver regeneration from oval cells. *Am J Pathol* 1999, 155:1075-1085
15. Paku S, Schnur J, Nagy P, Thorgeirsson SS: Origin and structural evolution of the early proliferating oval cells in rat liver. *Am J Pathol* 2001, 158:1313-1323

16. Banerji S, Ni J, Wang SX, Clasper S, Su J, Tammi R, Jones M, Jackson DG: LYVE-1, a new homologue of the CD44 glycoprotein, is a lymph-specific receptor for hyaluronan. *J Cell Biol* 1999, 144:789–801
17. Mouta Carreira C, Nasser SM, di Tomaso E, Padera TP, Boucher Y, Tomarev SI, Jain RK: Lyve-1 is not restricted to the lymph vessels: expression in normal liver blood sinusoids and down-regulation in human liver cancer and cirrhosis. *Cancer Res* 2001, 61:8079–8084
18. Brenan M, Puklavec M: The MRC OX-62 antigen: a useful marker in the purification of rat veiled cells with the biochemical properties of an integrin. *J Exp Med* 1992, 175:1457–1465
19. D'Arena G, Musto P, Cascavilla N, Carotenuto M: Thy-1 (CDw90) and c-kit receptor (CD117) expression on CD34⁺ hematopoietic progenitor cells: a five dimensional flow cytometric study. *Haematologica* 1998, 83:587–592
20. Boiret N, Rapatel C, Boisgard S, Charrier S, Tchirkov A, Bresson C, Camilleri L, Berger J, Guillovard L, Guerin JJ, Pigeon P, Chassagne J, Berger MG: CD34⁺CDw90(Thy-1)⁺ subset colocalized with mesenchymal progenitors in human normal bone marrow hematopoietic units is enriched in colony-forming unit megakaryocytes and long-term culture-initiating cells. *Exp Hematol* 2003, 31:1275–1283
21. Timper K, Seboek D, Eberhardt M, Linscheid P, Christ-Crain M, Keller U, Muller B, Zulewski H: Human adipose tissue-derived mesenchymal stem cells differentiate into insulin, somatostatin, and glucagon expressing cells. *Biochem Biophys Res Commun* 2006, 341:1135–1140
22. Saalbach A, Hildebrandt G, Hausteiner UF, Anderegg U: The Thy-1/Thy-1 ligand interaction is involved in binding of melanoma cells to activated Thy-1-positive microvascular endothelial cells. *Microvasc Res* 2002, 64:86–93
23. Koumas L, Smith TJ, Feldon S, Blumberg N, Phipps RP: Thy-1 expression in human fibroblast subsets defines myofibroblastic or lipofibroblastic phenotypes. *Am J Pathol* 2003, 163:1291–1300
24. Crosby HA, Nijjar SS, de Goyet J de V, Kelly DA, Strain AJ: Progenitor cells of the biliary epithelial cell lineage. *Semin Cell Dev Biol* 2002, 13:397–403
25. Heffer-Lauc M, Lauc G, Nimrichter L, Fromholt SE, Schnaar RL: Membrane redistribution of gangliosides and glycosylphosphatidylinositol-anchored proteins in brain tissue sections under conditions of lipid raft isolation. *Biochim Biophys Acta* 2005, 1686 3:200–208
26. Heffer-Lauc M, Viljetic B, Vajn K, Schnaar RL, Lauc G: Effects of detergents on the redistribution of gangliosides and GPI-anchored proteins in brain tissue sections. *J Histochem Cytochem* 2007, 55:805–812
27. Saalbach A, Wetzig T, Hausteiner UF, Anderegg U: Detection of human soluble Thy-1 in serum by ELISA: fibroblasts and activated endothelial cells are a possible source of soluble Thy-1 in serum. *Cell Tissue Res* 1999, 298:307–315
28. Sanders YY, Kumbula P: Enhanced myofibroblastic differentiation and survival in Thy-1(-) lung fibroblasts. *Am J Respir Cell Mol Biol* 2007, 36:226–235
29. Hudon-David F, Bouzeghrane F, Couture P, Thibault G: Thy-1 expression by cardiac fibroblasts: lack of association with myofibroblast contractile markers. *J Mol Cell Cardiol* 2007, 42:991–1000
30. Rege TA, Hagood JS: Thy-1, a versatile modulator of signaling affecting cellular adhesion, proliferation, survival, and cytokine/growth factor responses. *Biochim Biophys Acta* 2006, 1763:991–999
31. Hagood JS, Prabhakaran P, Kumbula P, Salazar L, MacEwen MW, Barker TH, Ortiz LA, Schoeb T, Siegal GP, Alexander CB, Pardo A, Selman M: Loss of fibroblast Thy-1 expression correlates with lung fibrogenesis. *Am J Pathol* 2005, 167:365–379
32. Ramadori G, Saile B: Mesenchymal cells in the liver—one cell type or two? *Liver* 2002, 22:283–294
33. Beaussier M, Wendum D, Schiffer E, Dumont S, Rey C, Lienhart A, Housset C: Prominent contribution of portal mesenchymal cells to liver fibrosis in ischemic and obstructive cholestatic injuries. *Lab Invest* 2007, 87:292–303
34. Tomasek JJ, Gabbiani G, Hinz B, Chaponnier C, Brown RA: Myofibroblasts and mechano-regulation of connective tissue remodelling. *Nat Rev Mol Cell Biol* 2002, 3:349–363
35. Forbes SJ, Russo FP, Rey V, Burra P, Rugge M, Wright NA, Alison MR: A significant proportion of myofibroblasts are of bone marrow origin in human liver fibrosis. *Gastroenterology* 2004, 126:955–963
36. Kisseleva T, Uchinami H, Feirt N, Quintana-Bustamante O, Segovia JC, Schwabe RF, Brenner DA: Bone marrow-derived fibrocytes participate in pathogenesis of liver fibrosis. *J Hepatol* 2006, 45:429–438
37. Kamo N, Yasuchika K, Fujii H, Hoppo T, Machimoto T, Ishii T, Fujita N, Tsuruo T, Yamashita JK, Kubo H, Ikai I: Two populations of Thy1-positive mesenchymal cells regulate the in vitro maturation of hepatic progenitor cells. *Am J Physiol Gastrointest Liver Physiol* 2007, 292:G526–G534
38. Dudas J, Mansuroglu T, Batusic D, Saile B, Ramadori G: Thy-1 is an in vivo and in vitro marker of liver myofibroblasts. *Cell Tissue Res* 2007, 329:503–514

2-Acetylaminofluorene Dose-Dependent Differentiation of Rat Oval Cells into Hepatocytes: Confocal and Electron Microscopic Studies

Sándor Paku,¹ Peter Nagy,² László Kopper,² and Snorri S. Thorgeirsson³

The 2-acetylaminofluorene (AAF)/partial hepatectomy (PH) model is one of the most extensively studied experimental systems for oval cell proliferation and differentiation. We have previously described the oval cells as forming ductular structures surrounded by basement membrane, representing extensions of the canals of Hering. Herein we analyze the differentiation of oval cells into hepatocytes after varying degrees of liver damage induced by AAF. At a low dose of AAF, most oval cells synchronously differentiate into small hepatocytes by 6 days after the PH, resulting in complete restoration of the liver structure in 10 days. Higher doses of AAF delay the differentiation process and the new hepatocytes form foci, in contrast to what is observed at the low dose. Qualitatively, the differentiation process seems to be identical at the cellular level under both conditions. The transition from the expanding oval cell population into hepatocytes was correlated with the upregulation of hepatocyte nuclear factor 4 and the disappearance of the basement membrane. Also, the differentiation of oval cells into hepatocytes coincided with the loss of alpha-fetoprotein and OV-6 staining, and the replacement of the biliary cell-specific $\alpha 6$ integrin and connexin 43 with the hepatocyte-specific $\alpha 1$ integrin and connexin 32. In addition, bile canaliculi form between the new hepatocytes. In conclusion, these results indicate the rate of oval cell differentiation into hepatocytes is context dependent and suggest that, under favorable conditions, oval cells can complete this process much faster than previously appreciated. (HEPATOLOGY 2004;39:1353–1361.)

The liver has an enormous regenerative capacity best illustrated by the fact that in rodents a two-thirds loss of liver mass can be replaced in a few days by the compensatory hyperplasia of the surviving hepatocytes.^{1,2} In addition, two stem cell-fed back-up regenerative systems also exist in the liver.^{3–6} The activation of these dormant stem cell systems for liver regeneration takes place when residual hepatocytes are functionally compromised, are unable to divide, or both. We and other investigators have provided

evidence that epithelial cells of the canals of Hering are the most probable candidates for the resident adult liver stem cells.^{1,7} In case of stem cell-fed liver regeneration in rat liver, progeny of the stem cells multiply in an amplification compartment composed of the so-called oval cells.⁸ Oval cells form ductular structures surrounded by a continuous basement membrane,¹ forming elongations of the canals of Hering, and attached their distal end to a hepatocyte of the liver plate.

Recent studies suggest bone marrow cells may be able to transdifferentiate into hepatocytes.^{5,6} It is not yet clear if the bone marrow stem cells form hepatocytes via the oval cells. Petersen et al.⁹ described bone marrow-derived oval cells, but other investigators have detected only the end product, the hepatocyte.^{10,11} Regardless of their origin, oval cells express a phenotype that is transitional between the biliary cells and hepatocytes. Although oval cells display several phenotypic characteristics of the mature hepatocytes (e.g., liver-enriched transcriptional factors,¹² albumin production¹³), they differ structurally and functionally from mature hepatocytes.

The final step of the stem cell-fed regenerative process, that is, the differentiation of the oval cells into hepato-

Abbreviations: AAF, 2-Acetylaminofluorene; PH, partial hepatectomy; HNF, hepatocyte nuclear factor; AFP, α -fetoprotein.

From the ¹Joint Research Organization of the Hungarian Academy of Sciences and Semmelweis University, Budapest, Hungary; ²First Department of Pathology and Experimental Cancer Research, Semmelweis University, Budapest, Hungary; and the ³Laboratory of Experimental Carcinogenesis, Center for Cancer Research, National Cancer Institute, National Institutes of Health, Bethesda, MD.

Received December 5, 2003; accepted January 23, 2004

Supported by OTKA (Egészségügyi Tudományos Tanács Egészségügyi Minisztérium, Hungary) T 042 674 and ETT (Országos Tudományos Kutatási Alap, Hungary) 240/2001.

Reprint requests to: Snorri S. Thorgeirsson, MD, PhD, National Cancer Institute, 37 Convent Drive, MSC 4262, Building 37, Room 4146A, Bethesda, MD 20892-4262. E-mail: snorri_thorgeirsson@nih.gov; fax: (301) 496-0734.

Copyright © 2004 by the American Association for the Study of Liver Diseases. Published online in Wiley InterScience (www.interscience.wiley.com).

DOI 10.1002/hep.20178

Table 1. Antibodies Used for the Immunohistochemical Studies

Antibody	Species	Manufacturer	Catalog Number	Dilution
AFP		Nordic Immunological Labs	ShARa/AFP	1:500
Desmin	Mouse monoclonal	Dako	M0724	1:100
Pan Cytokeratin FITC labeled		Dako	F0859	1:20
OV6	Mouse monoclonal	Gift from Dr. Hixson		1:100
Laminin	Rabbit polyclonal	Dako	Z0097	1:300
Connexin 43	Rabbit polyclonal	Zymed	71-0700	1:100
Connexin 32	Mouse monoclonal	Santa Cruz	SC-7258	1:100
HNF-4	Goat polyclonal	Santa Cruz	Sc-6556	1:100
Integrin α 1	Mouse monoclonal	Serotec	MCA 1791	1:100
Integrin α 6	Mouse monoclonal	Serotec	MCA 2034	1:100
CD26	Mouse monoclonal	Serotec	MCA 924	1:20

Abbreviations: AFP, alpha-fetoprotein; FITC, fluorescein isothiocyanate; HNF-4, hepatocyte nuclear factor-4.

cytes, is the focus of the present study, in which we use the well-characterized acetylaminofluorene (AAF)/partial hepatectomy (PH) experimental model to induce oval cells in the rat liver. Earlier, we observed that differentiation of oval cells into hepatocytes depends on the dose of AAF.¹⁴ For example, a high dose of AAF caused a delay in the differentiation of oval cells into hepatocytes.¹⁵ Similar results also were obtained by Alison et al.^{16,17} We revisited the issue of AAF dose dependency on oval cell differentiation. In particular, we asked how the dose of AAF modifies oval cell differentiation. Herein, we demonstrate two patterns of oval cell differentiation. At a low dose of AAF (i.e., when the hepatocyte damage is mild), the oval cells rapidly and synchronously differentiate into small hepatocytes. In contrast, at a higher dose of AAF (i.e., more extensive damage to hepatocytes), differentiation of oval cells into hepatocytes is delayed and proceeds via an intermediate stage in which small basophilic hepatocytes accumulate in focal nodules. However, hepatocyte differentiation is eventually identical at the cellular level at both low and high AAF doses, that is, it is correlated with sudden upregulation of hepatocyte nuclear factor 4 (HNF-4) and the disappearance of laminin (basement-membrane) staining. Subsequently, oval cells lost their phenotypic characteristics (alpha-fetoprotein (AFP), OV-6 staining, α 6 integrin, connexin 43) and gained hepatocytic features (α 1 integrin, connexin 32, bile canalicular formation) as the differentiation process advanced.

Materials and Methods

Animal Experiments. Male F-344 rats (160–180 g) were used for all experiments and were kept under standard conditions. The animal study protocols were conducted according to National Institutes of Health guidelines for animal care.

AAF/PH Experiment. AAF 2 mg/mL suspended in 1% dimethylcellulose (low dose, 2.5 mg/kg daily; high

dose, 5 mg/kg daily) was given to the rats on 6 consecutive days by gavage. Traditional two-thirds PH was performed¹⁸ on the seventh day, which was followed by six additional AAF treatments. Animals were killed at several time points in pilot experiments to determine the times at which hepatocytes differentiated in the two AAF doses. All of the histological analyses described in the present paper were carried out on livers 6 days after PH in the low-dose model and 12 days after the PH in the high-dose model.

Morphological Analysis. Cryostat sections (15–20 μ m) were fixed in methanol and were incubated overnight with a mixture of the primary antibodies (Table 1); appropriate secondary antibodies were used (Jackson ImmunoResearch, West Grove, PA). All samples were analyzed by confocal laser-scanning microscopy using Bio-Rad MRC-1024 system (Bio-Rad, Richmond, CA). Alpha-fetoprotein reaction was visualized by ABC peroxidase method using DAB as chromogen (Elite kit; Vector Laboratories, Burlingame CA). Electron microscopy was performed as described previously.¹

Retrograde Cholangiography and Analysis of the Bile Duct Structure. The rats were anesthetized with Nembutal. A 30-gauge needle was inserted into the common bile duct, and 1 mL of the 1:10 dilution of fluorescein isothiocyanate-labeled lycopersicon esculentum lectin (Vector Laboratories) was injected slowly. After 15 minutes, the liver was removed and frozen. One hundred-micrometer frozen sections were cut and fixed in 4% paraformaldehyde. Stacks of optical sections (up to 40) were taken at 0.5 to 1- μ m intervals. Horizontal views of the images were made and analyzed using the Bio-Rad Laser Sharp software.

Results

Differentiation of Oval Cells After a High Dose of AAF. Small foci composed of small hepatocytelike cells (Fig. 1A) appear in the liver 10 to 12 days after the partial hepatectomy when 5 mg/kg AAF was administered daily

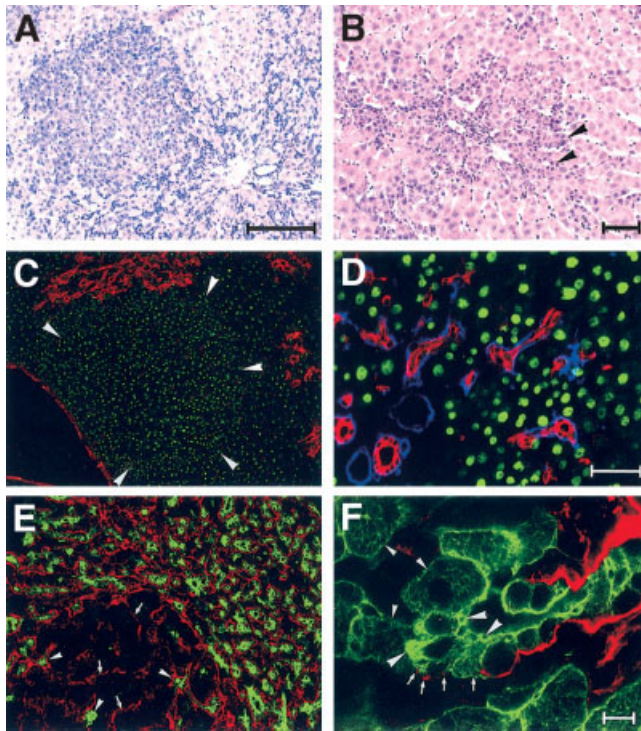


Fig. 1. (A) High-dose model. Basophilic focus composed of small hepatocytes 12 days after partial hepatectomy (PH). Numerous oval cell cords emanate radially from the portal area. (B) Low-dose model. Small basophilic hepatocytes can be observed around the portal tract 6 days after PH. No typical oval cells can be seen. Arrowheads point at small hepatocytes arranged in ductular fashion. (C) High-dose model. HNF-4-positive (green) small hepatocytes within a focus (arrowheads). Note the high density of the nuclei and the almost complete absence of laminin staining within the focus. Oval cell ductules near the focus are laminin positive. (D) Low-dose model. The differentiating small hepatocytes are HNF-4 positive (small green nuclei). OV6-positive (red) and laminin-positive (blue) oval cell ductules close to the portal area are not stained for HNF-4. The nuclei of interlobular bile ducts (lower left corner) are also negative for HNF-4. (E) High-dose model. There is no OV6 (green) staining in the focus except several entrapped oval cell ductules (arrowheads). The numerous oval cells surrounding the focus are strongly stained for OV6 and laminin (red). Scraps of laminin are present in the focus outlining the tubular architecture of the small hepatocytes (arrows). (F) Low-dose model. Differentiating oval cell ductule close to a portal tract. The proximal part of the ductule has continuous laminin (red) staining, whereas distally the basement membrane is fragmented or absent (small arrows). The old hepatocytes show fine reticular cytoplasmic staining for pan cytokeratin (green; arrowheads). Although a strong membranouslike reaction is present in the proximal oval cells, the cytoplasm of the differentiating cells over the fragmented basement membrane already has reticular cytokeratin staining (large arrowheads). Scale bars: (A, C, E), 100 μm ; (B, D), 50 μm ; (F), 10 μm .

to the rats. The cells have all the ultrastructural characteristics of hepatocytes: abundant round nuclei, cytoplasm rich in rough endoplasmic reticulum, mitochondria, occasionally peroxisomes, and glycogen particles are observed. These features are not present in the oval cells. The foci are not composed of randomly arranged individual hepatocytes, but tightly packed cells that form tubular structures (Figs. 1E and 2A). The foci are relatively well

circumscribed and the small basophilic hepatocytelike cells can be distinguished easily from the larger surrounding "old" hepatocytes (Fig. 1A). Oval cells are still numerous in the liver at this stage and are found commonly in contact with the randomly distributed foci.

Differentiation of Oval Cells After a Low Dose of AAF. When 2.5 mg/kg AAF was administered daily, fewer oval cells developed, and the oval cells did not infiltrate the hepatic lobule to the same extent as seen after the high dose was administered. The basic difference between the two doses becomes obvious 5 to 6 days after the PH when oval cells rapidly differentiate into small hepatocytes. The structural configuration of the new hepatocytes was completely different from the foci seen after the high dose of AAF: they were arranged in more-or-less straight ducts (Fig. 1B). However on the cellular level, these differentiated ductular cells were similar to the cells of the

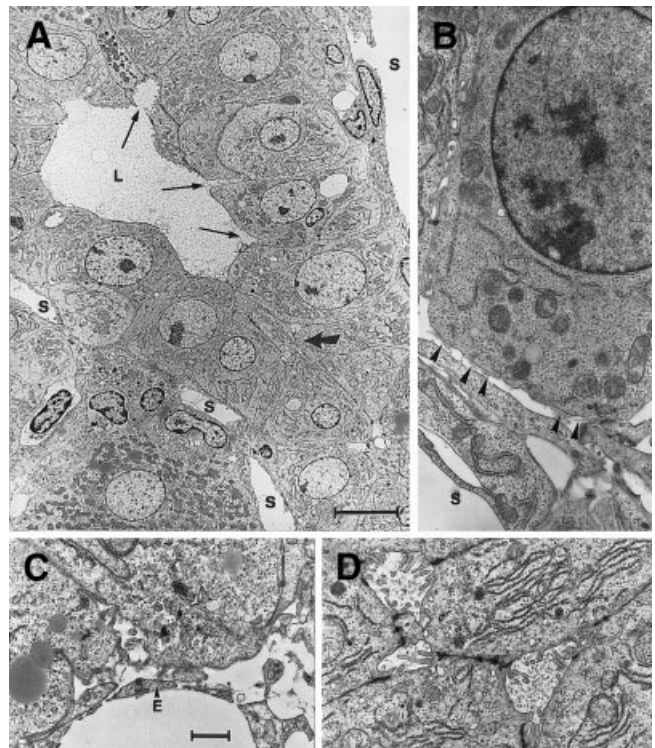


Fig. 2. Ultrastructure of the focus in the high-dose model. (A) Electron micrograph of the periphery of a focus. Small hepatocytes containing numerous low-density mitochondria and rough endoplasmic reticulum form a tubular structure. From the central lumen (L) bile canaliculi originate (arrows). The basal side of the cells face sinusoids (S). An old hepatocyte with dense mitochondria is visible on the bottom. A large arrow points at the area visible at higher magnification on Fig. 2D. (B) A fragmented basement membrane (arrowheads) is visible at the basal surface of a small hepatocyte lacking microvilli. S, sinusoid. (C) The basement membrane is completely absent at the basal surface of the small hepatocytes (E, endothelial cell). (D) Detail of Fig. 2A. Bile canaliculi sealed by desmosomes can be observed between the small hepatocytes. Numerous microvilli project into the lumen of the canaliculi. Scale bars: (A), 10 μm ; (B-D), 2 μm .

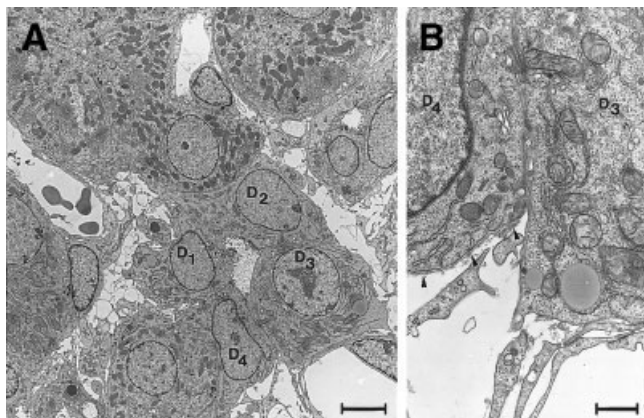


Fig. 3. Ultrastructure of a differentiating ductule in the low-dose model. (A) A short, differentiating ductule near a portal tract in the low-dose model. Two of the ductular cells (D1, D2) are attached to an old hepatocyte, which contains numerous dense mitochondria. One ductular cell (D3) closely resembles to hepatocytes. It has a round nucleus with prominent nucleolus, numerous mitochondria, and organizing rough endoplasmic reticulum. (B) Detail of Fig. 3A. The basement membrane cannot be observed at the basal side of the small hepatocyte (D3), while it is still present (arrowheads) around the nondifferentiated ductular cell (D4). Scale bars: (A), 10 μm ; (B), 2 μm .

foci: small polygonal cells with basophilic cytoplasm and ultrastructural features of hepatocytes (Fig. 3A). Hepatocytic differentiation seemed to occur synchronously in the overwhelming majority of the oval cells. The few unchanged oval cells were located at the proximal end of the ducts, whereas the distal part of the same duct was composed of differentiated small hepatocytes (Fig. 1F). The liver structure was almost normal 10 to 12 days after PH in the low-dose model, whereas it took 23 to 25 days after the high-dose treatment.

Differentiation of Oval Cells Into Hepatocytes

HNF-4 is Upregulated in the Differentiating Cells. HNF-4 is a liver-enriched transcriptional factor that is expressed in the hepatocytes but not in the biliary cells of the normal liver.¹² Oval cells were not decorated by the HNF-4 antibody. However, nuclear staining with the HNF-4 antibody was seen in hepatocytes that formed foci in the high-dose model and in hepatocytes in ductlike structures in the low-dose model (Fig. 1C, D). Newly differentiated hepatocytes were recognized after both low and high doses of AAF by the smaller nuclei and higher cell densities compared with the old hepatocytes. Cells faintly HNF-4 positive also were observed occasionally at the distal ends of the oval cell ductules in the low-dose model (Fig. 4C).

The Basement Membrane Disappears During the Process of Differentiation. Laminin-containing basement membrane surrounds the undifferentiated oval cells, which also have relatively strong cytoplasmic and

membranous cytokeratin staining, unlike the weak reticular staining of the hepatocytes (Fig. 1F).

Differentiating oval cells enlarge and acquire a hepatocytelike reticular pattern of cytoplasmic cytokeratin staining. Simultaneously, the basement membrane disintegrates, starting at the distal end of the oval cell ducts in the low-dose model (Fig. 1F). This observation was confirmed by electron microscopy (Figs. 2B, C and 3B). The paucity or complete lack of laminin staining was characteristic of foci (Fig. 1C,E), but occasional entrapped oval cell ducts were surrounded by basement membrane (Fig. 1E). Also, numerous undifferentiated oval cells located outside foci were still outlined brightly by laminin staining (Fig. 1C, E) in the high-dose model.

Changes in Integrin Expression Correlate With Loss of Basement Membrane. We analyzed the expression of the biliary integrin $\alpha 6$ as well as of integrin $\alpha 1$, which is present on hepatocytes and sinusoidal endothelial cells in the normal liver.¹⁹ The $\alpha 1$ integrin was absent from the oval cell ducts, but it is clearly present on the small hepatocytes located in the foci (Fig. 4A). The density of $\alpha 1$ integrin on small hepatocytes is lower than in the surrounding parenchyma, but the sinusoidal-type arrangement already could be recognized. $\alpha 1$ integrin also was expressed on the small hepatocytes (Fig. 4C) in the low-dose model.

Opposite results were obtained with the $\alpha 6$ integrin. Surfaces of the oval cells facing the basement membrane stained positively, whereas the small hepatocytes in the foci (Fig. 4B) and in the ducts of the low-dose model (Fig. 4D) were negative.

Characteristic Changes in Differentiation Markers

OV-6, AFP Staining, and Desmin-Positive Stellate Cells Disappear During Differentiation. OV-6²⁰ and AFP¹³ are among the most frequently used antibodies to identify oval cell rat liver. OV-6, which is a monoclonal antibody recognizing cytokeratin (CK) 14 and 19,²¹ did not react with the differentiated hepatocytes either in the high-dose (Fig. 1E) or low-dose AAF models (Fig. 1D). AFP staining was lost (data not shown) from the differentiated hepatocytes located in the foci or in differentiated ducts, and desmin-positive stellate cells disappeared simultaneously (Fig. 4E, F).

Changes in Connexin Expression. Hepatocytes express connexin 32 in normal liver, whereas cells of the biliary system express connexin 43.²² Oval cells were positive for connexin 43, but this protein was not present in the newly differentiated small hepatocytes (Fig. 5B). Connexin 32 was entirely lacking in oval cells (Fig. 5A), but it highlighted very clearly the new hepatocytes in both models (Fig. 5A). (The low-dose data are not shown.)

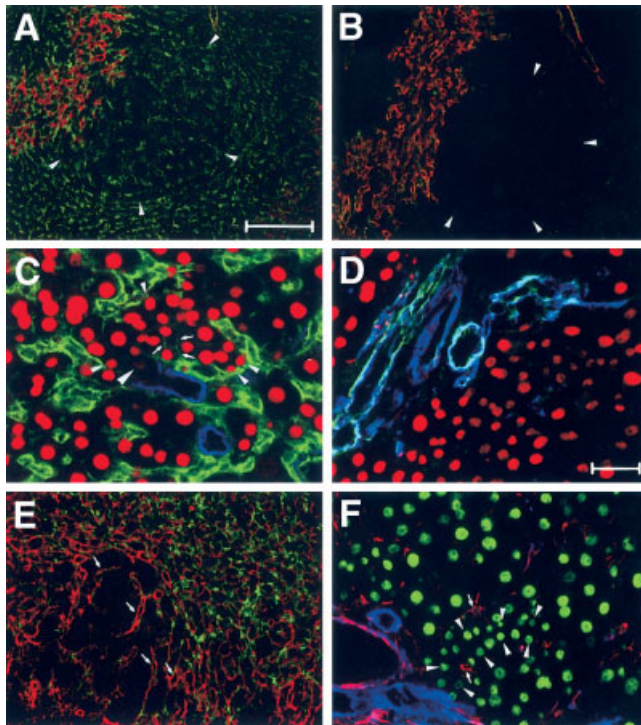


Fig. 4. (A) High-dose model. Focus (arrowheads), 12 days after partial hepatectomy. Sinusoids of the liver parenchyma and the focus staining positively for $\alpha 1$ integrin (green). Note the lower density of sinusoids within the focus. The oval cell ductules bordering the focus are stained red (laminin), demonstrating the lack of colocalization of the two signals. (B) High-dose model. The same focus (arrowheads) as on Fig. 4A in a different sectioning plane stained for $\alpha 6$ integrin. The focus and the liver parenchyma are not reacting with this antibody. Yellowish color of the oval cell ductules bordering the focus shows that $\alpha 6$ integrin (green) overlaps with the positive (red) basement membrane. (C) Low-dose model. HNF-4 positive (small red nuclei) small hepatocytes express $\alpha 1$ integrin (green) mainly at their basal side (arrowheads). Weak $\alpha 1$ integrin positivity also can be observed at the lateral side of these cells in some locations (small arrows). Laminin positivity (blue) cannot be observed around the small hepatocytes. Laminin-positive oval cell ductules are negative for this integrin and HNF-4. However, note a weak HNF-4 nuclear staining in a differentiating cell (large arrowhead). (D) Low-dose model. The periportal area, stained for HNF-4 (red), $\alpha 6$ integrin (green), and laminin (blue). Bile and oval cell ductules are positive for this type of integrin and laminin, whereas the small hepatocytes (small red nuclei) are not stained. (E) High-dose model. There are numerous laminin-positive (red) oval cell ductules, also stained positively for desmin (green). The focus (lower left corner) is negative for desmin except some oval cell ductules enclosed into the focus (arrows). (F) Low-dose model. Only a few desmin-positive (red) stellate cells are visible (arrows) around the HNF-4-positive (green) and laminin-negative (blue) small hepatocytes still forming a ductule (arrowheads). Scale bars: (A, C, E), 100 μm ; (C, D, F), 50 μm .

Bile Canaliculus Formation by the Differentiating Cells. Oval cells, which extend from the canals of Hering, form ducts that are continuous with bile canaliculi in hepatic plates. We studied the structure of the bile drainage system by CD26 staining and by retrograde infusion of a fluorescein isothiocyanate-labeled lectin into the biliary system via the common bile duct.

CD26 or dipeptidylpeptidase IV²³ was expressed at the apical surface or biliary pole on the hepatocytes and on the apical domain of the biliary and oval cells (Fig. 5C). In the low-dose model, the pattern of CD26 staining changed sharply where laminin staining disappeared and the oval cells differentiated. Luminal branching to form starlike

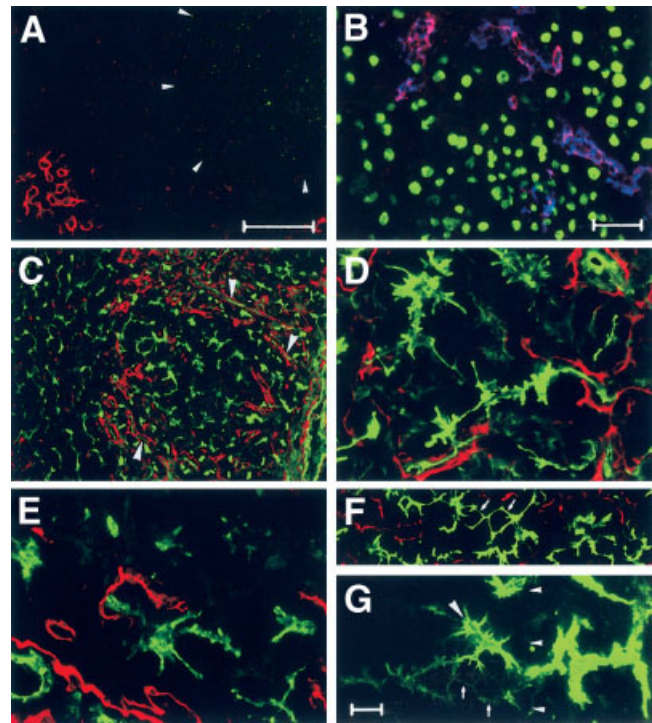


Fig. 5. (A) High-dose model. Connexin 32 (green) is expressed by the small hepatocytes of the focus (arrowheads). The surrounding liver parenchyma express connexin 32 at a very low level, whereas the laminin-positive (red) oval cell ductules are negative. (B) Low-dose model. Oval cell ductules are stained positively for connexin 43 (red) and OV6 (blue). The small hepatocytes marked by HNF-4 (small green nuclei) do not express this connexin and OV-6. (C) High-dose model. Numerous CD26-positive (green) starlike structures are discernible within the focus. CD26 staining reveals the polygonal organization of the bile canaliculi in the normal liver. This antigen shows a linear arrangement (arrowheads) in the oval cell ductules surrounded by basement membrane (laminin, red). (D) High-dose model. Higher magnification of a focus. Development of bile canaliculi (CD26 staining, green) between the small hepatocytes takes place only where regular basement membrane (laminin, red) is not present. (E) Low-dose model. A differentiating oval cell tube near a portal tract. Basement membrane (laminin, red) cannot be observed around the starlike structure (CD26, green) representing bile canaliculi development. (F) High-dose model. Advanced stage of the bile canaliculi development within a focus. Beside the starlike arrangement of the CD26 staining (green), two polygonal structures (arrows) can be seen, showing close similarity to the bile canaliculi network of the normal liver. Some remnants of the basement membrane can also be observed (laminin, red). (G) High-dose model. Peripheral zone of a focus filled partially with fluorescein isothiocyanate labeled lycopersicon esculentum lectin. The border of the focus is marked by arrowheads. The wide lumen of an oval cell ductule is continuous with the narrow bile canaliculi of the focus. Starlike (large arrowhead) and polygonal (small arrows) structures can be recognized within the focus. Scale bars: (A, C), 100 μm ; (B), 50 μm ; (D-G), 10 μm .

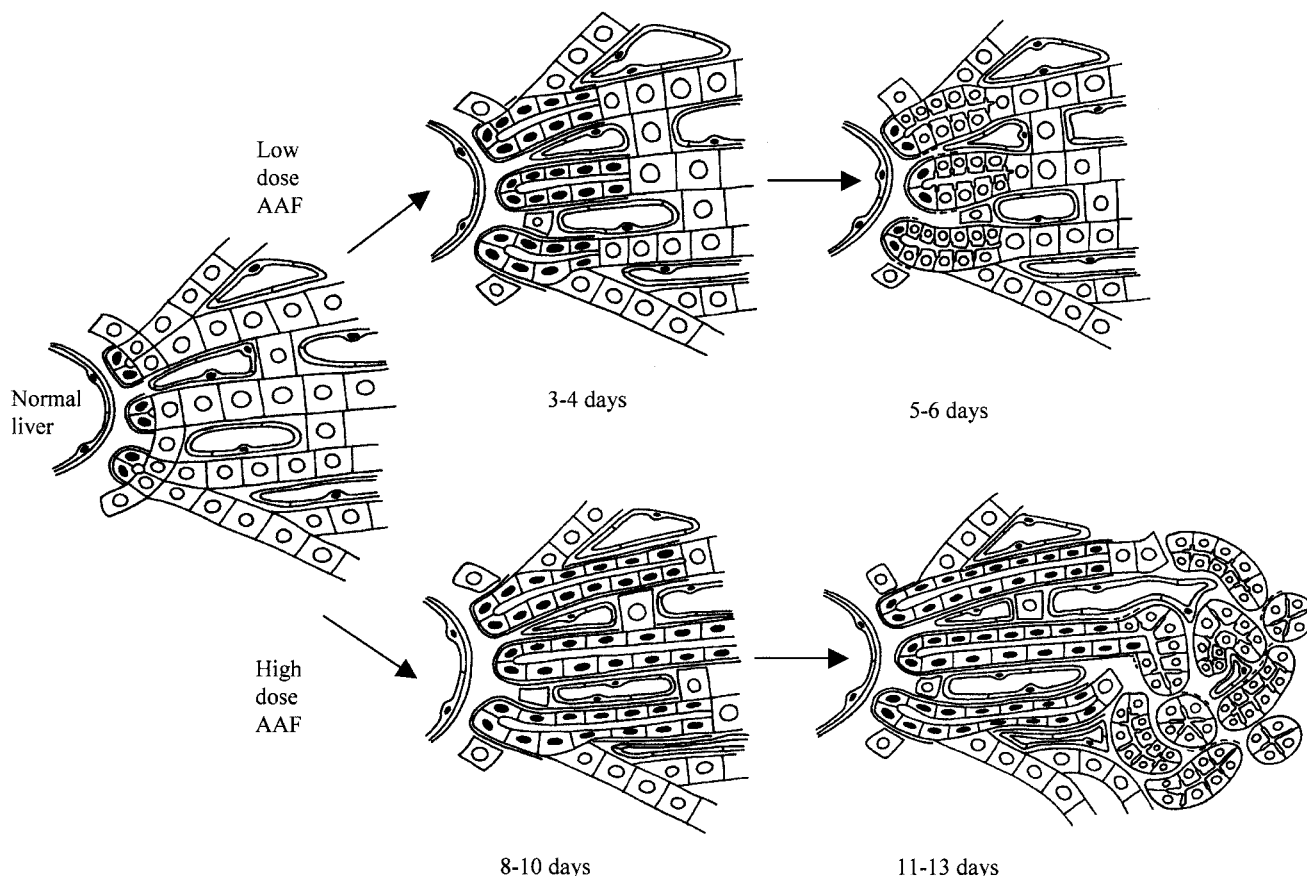


Fig. 6. Schematic representation of the two differentiation models. **Low-dose model:** oval cell ductules penetrate into the liver lobule and differentiate simultaneously into small hepatocytes. **High-dose model:** oval cells penetrate deep into the liver lobule and most of them do not change during the observation period. The differentiating cells arranged in tortuous and branching ductules, which form the foci. The lumen of these ductules is continuous with the larger oval cell ductules. The developing bile canaliculi between the small hepatocytes invaginate from the central lumen of these ductules in both models. (The days mean the time after the partial hepatectomy).

structures was observed in this area, representing the formation of bile canaliculi and the polarization of the new hepatocytes (Fig. 5E). The situation was very similar in the high-dose model, where numerous starlike lumens were detected among differentiating hepatocytes within foci (Fig. 5C, D). Electron microscopy of the foci clearly showed the formation of bile canaliculi from a central lumen between the differentiated small hepatocytes (Fig. 2A, D). Occasionally, polygonal canalicular structures were outlined inside the foci by CD26 staining (Fig. 5F), similar to the pattern of bile canaliculi in the normal liver.

Cholangiography supported the results of CD26 staining. Broad lectin-filled ducts led to foci, where the ducts divided into smaller branches that formed polygonal canalicular structures (Fig. 5G). The newly formed bile canaliculi also could be filled between the small hepatocytes in the low-dose model (data not shown).

Discussion

We report two distinct patterns for the differentiation of oval cells into hepatocytes in the AAF/PH model (Fig. 6). When a low dose of AAF was used, most of the oval cells differentiated synchronously and rapidly into small hepatocytes, even while AAF was being administered. Newly formed hepatocytes maintained a ductular arrangement during the early phase of the differentiation process. In contrast, when a high dose of AAF was used, hepatocyte differentiation was delayed by 7 to 10 days, and even at this later time point, most of the oval cells did not differentiate into hepatocytes. Newly formed hepatocytes formed foci scattered throughout the liver with the high dose of AAF. However, the differentiation process seemed to be identical in the two models at the cellular level. The small basophilic cells were very similar to the adult hepatocytes by light microscopic and electron microscopic examination. New hepatocytes lost several phenotypic characteristics of oval cells, for example, AFP and

OV-6 expression. Upregulation of albumin¹³ and CYP3A1¹⁶ in the newly formed cells indicated their functional maturation.

The disappearance of the basement membrane that surrounds the oval cell ductules is closely associated with initiation of the differentiation process. Oval cells always sit on a well-structured basement membrane¹ that is almost completely missing from the foci. Gradual disintegration of the basement membrane was observed even better in the low-dose model. It is well known that the connection with the basement membrane influences the differentiation state of the cell. The close contact with the basement membrane is absolutely required for the maintenance of differentiated tubules in the kidney.²⁴ In the skin, however, the loss of contact is a stimulus for differentiation for the keratinocytes.²⁵ The hepatocytes have no contact with laminin containing structured basement membrane. Yin et al.²⁶ reported that isolated hepatic stem cells expressed biliary or hepatocytic phenotypes in culture, depending on the presence or absence of basement membrane matrix (Matrigel). Matrigel also was found to play an important role in maintaining the biliary phenotype in tissue culture in other experimental systems.^{27,28} These observations are in good agreement with our *in vivo* results.

Integrins are heterodimeric glycoproteins, consisting of α and β subunits, that enable cells to recognize adhesive substrates in the extracellular matrix. The $\alpha 6$ integrin subunit binds laminins exclusively. The expression of the $\alpha 6$ integrin and laminin seem to influence each other. The induction of $\alpha 6$ -containing integrins at the surface of developing epithelial cells is strongly correlated with the deposition of laminin.^{29,30} The downregulation of the laminin receptor was described in differentiating HBC-3 hepatic stem cells in culture.³¹ The disappearance of the $\alpha 6$ integrin from differentiating oval cells is in good agreement with the disintegration of the basement membrane. In the normal liver, $\alpha 6$ and $\alpha 1$ integrins are expressed on biliary cells and hepatocytes, respectively.¹⁹ Therefore, the $\alpha 6$ - $\alpha 1$ switch is another indicator of the hepatocytic differentiation. The opposite change was described when the hepatoblasts differentiated into biliary cells.³² The $\alpha 1$ integrin is present on the basal surface of endothelial cells and on the basolateral surface of small hepatocytes. This polarized expression may promote the establishment of connections with collagenous components of the perisinusoidal space, an important step in the reconstruction of the normal trabecular liver structure.

The upregulation of HNF-4 expression may play a central role in the induction of hepatocytic differentiation of the oval cells. HNF-4 is not present in oval cells, but it clearly decorates the nuclei of small hepatocytes in both

models, and a faint staining was sometimes observed in the transitional cells in the low-dose model. In an earlier work, we failed to detect HNF-4 mRNA in oval cells, although other liver enriched transcriptional factors were present.¹² However, HNF-4 mRNA was upregulated in foci of small basophilic hepatocytes, suggesting a critical role for this transcription factor in the oval cell differentiation.¹² The lack of expression of a functional HNF-4 gene results in embryonic lethality in mice before development of the liver as a result of defects in visceral endoderm function.³³ However, HNF-4 null mouse embryos can be rescued until E12.0 by extraembryonic endoderm complementation.^{34,35} Livers from these endoderm-complemented embryos were morphologically and histologically indistinguishable from wild-type embryos. When the mRNA level of hepatocyte-specific genes was compared between wild-type and HNF-4 null livers, it was found that the expression of these genes were either downregulated or undetectable in the genetically manipulated mice. Similar results were found in adult hepatocytes that lack HNF-4.³⁶ These data suggest that HNF-4 is not required during ontogenesis for the competency of hepatic precursor cells or for their specification, but it must be present during the final step of hepatocyte differentiation to establish the hepatocytic gene expression pattern. This observation is consistent with our current results that indicate the critical role of HNF-4 in the transition of oval cells into hepatocytes.

HNF-4 also is expressed in the intestinal glands,³⁷ and intestinal metaplasia is another option for the oval cells.³⁸ One of the major differences between the intestinal glands and hepatocytes is that the enterocytes reside on a laminin-containing basement membrane. It is possible that the upregulation of HNF-4 without the disintegration of the basement membrane may be responsible for the "abnormal" differentiation of oval cells into intestinal epithelium.

Connexins form special membrane structures, the gap junctions (connexons), which play crucial role in the intercellular communication. Connexin 32 is expressed on hepatocytes, and connexin 43 is expressed on the biliary epithelial cells in the normal rat liver.³⁹ Zhang and Thorgeirsson⁴⁰ reported that the mRNA for connexin 43 is expressed in the oval cells and connexin 32 in the small hepatocytes of the foci. Here we confirm this observation at the protein level. The switch from connexin 43 to connexin 32 can be observed in both the low-dose and high-dose models of oval cell differentiation. Because connexin 32 and connexin 43 hemichannels do not form heterotopic patent channels,⁴¹ the described switch is required for the newly formed hepatocytes to be integrated into the preexisting liver plates and to communicate with the pre-

existing hepatocytes. It also may be of importance that the stellate cells also express connexin 43.⁴² The expression of identical connexins on the oval cells and stellate cells may be important in the establishment of the close communication between these two cell types. The loss of connexin 43 from the oval cells coincides with the disappearance of stellate cells. It is well documented that the stellate cells provide a battery of growth factors that support the proliferation of oval cells.⁴³ The inductive role of mesenchymal cells during the specification of hepatic lineage also is well known.⁴⁴ Stellate cells may provide support for the growth of oval cells, as does the portal mesenchyme during embryogenesis. This notion is supported by the suggestion that the stellate cells may be derived from the embryonic septum transversum.⁴⁴

We observed the development of biliary canaliculi among the newly formed hepatocytes in both models by infusing the biliary system with fluorescein isothiocyanate-labeled lectin via the common bile duct. The pentagonal and hexagonal bile canalicular patterns in the foci are similar to the arrangement present in the normal liver. This structural similarity indicates the architectural remodeling in the foci toward the normal hepatic structure. The CD26 epitope is present on the canalicular surface of the normal hepatocytes.²³ The similar CD26 staining pattern on the newly formed small hepatocytes marks the functional polarization of these cells.

The morphological and immunophenotypical characteristics clearly show that oval cells differentiate into hepatocytes at both low and high doses of AAF. Although both the rate of differentiation and timing of the process differ with AAF dose, the differentiation process at the cellular level seems to be identical. Furthermore in both models, the differentiating small hepatocytes can regenerate the liver after two-thirds PH, because the old hepatocytes do not show mitotic activity. At this point, we can only speculate about the cause of focus formation, when a high dose of AAF was applied. A plausible explanation may be that the high dose of AAF inhibits the low dose-type differentiation of the oval cells, as suggested by Alison et al.¹⁶ However, the inhibitory effect of the high dose of AAF primarily may affect the later stages of oval cell differentiation into hepatocytes, and this in turn can attenuate the necessary remodeling needed to rebuild the liver structure. It is possible that this or a similar scenario can contribute to the focus formation seen after administration of the high dose of AAF. Whether this process involves genetic or adaptive epigenetic mechanisms, or both, is not clear. However, we have not observed liver tumors in the rats subjected to the high AAF doses used here, suggesting that if a mutation(s) is involved in the process, it may not be carcinogenic. Nevertheless, the fo-

cus formation pattern of oval cell differentiation after high doses of AAF identifies, independent of the precise mechanism(s), an efficient differentiation process that is functional under adverse conditions. Therefore, further characterization of the high-dose model may be very useful to delineate the factors that can be used to enhance the differentiation efficiency of the hepatic stem cells. This issue may have important implications for the clinical application of adult liver stem cells. Also, the fact that oval cells can, under favorable conditions (e.g., in the low-dose AAF model), rapidly differentiate in new hepatocytes that effectively integrate into liver plates raises the intriguing possibility that adult liver stem cells may contribute to liver regeneration and repair more often than previously anticipated. Finally, this study provides no evidence that hematopoietic bone marrow stem cells are involved in the generation of new hepatocytes through oval cells, which seem to be totally derived from epithelial cells of the canals of Hering.

References

1. Paku S, Schnur J, Nagy P, Thorgeirsson SS. Origin and structural evolution of the early proliferating oval cells in rat liver. *Am J Pathol* 2001;158:1313-1323.
2. Michalopoulos GK, DeFrances MC. Liver regeneration. *Science* 1997;276:60-66.
3. Forbes S, Vig P, Poulsom R, Thomas H, Alison M. Hepatic stem cells. *J Pathol* 2002;197:510-518.
4. Fausto N, Campbell JS. The role of hepatocytes and oval cells in liver regeneration and repopulation. *Mech Dev* 2003;120:117-130.
5. Austin TW, Lagasse E. Hepatic regeneration from hematopoietic stem cells. *Mech Dev* 2003;120:131-135.
6. Wagers AJ, Sherwood RI, Christensen JL, Weissman IL. Little evidence for developmental plasticity of adult hematopoietic stem cells. *Science* 2002;297:2256-2259.
7. Grisham JW, Porta EA. Origin and fate of proliferated hepatic ductal cells in the rat: electron microscopic and autoradiographic studies. *Exp Mol Pathol* 1964;86:242-261.
8. Grisham JW, Thorgeirsson SS. Liver stem cells. In: Potten, CS, ed. *Stem Cells*. London: Academic Press, 1997:233-282.
9. Petersen BE, Bowen WC, Patrene KD, Mars WM, Sullivan AK, Murase N, et al. Bone marrow as a potential source of hepatic oval cells. *Science* 1999;284:1168-1170.
10. Theise ND, Badve S, Saxena R, Henegariu O, Sell S, Crawford JM, et al. Derivation of hepatocytes from bone marrow cells in mice after radiation-induced myeloablation. *HEPATOLOGY* 2000;31:235-240.
11. Alison MR, Poulsom R, Jeffery R, Dhillon AP, Quaglia A, Jacob J, et al. Hepatocytes from non hepatic adult stem cells. *Nature* 2000;406:257.
12. Nagy P, Bisgaard HC, Thorgeirsson SS. Expression of hepatic transcription factors during liver development and oval cell differentiation. *J Cell Biol* 1994;126:223-233.
13. Evarts RP, Nagy P, Marsden E, Thorgeirsson SS. In situ hybridization studies on expression of albumin and alpha-fetoprotein during the early stage of neoplastic transformation in rat liver. *Cancer Res* 1987;47:5469-5475.
14. Evarts RP, Nagy P, Nakatsukasa H, Marsden E, Thorgeirsson SS. In vivo differentiation of rat liver oval cells into hepatocytes. *Cancer Res* 1989;49:1541-1547.
15. Evarts RP, Hu Z, Omori N, Omori M, Marsden ER, Thorgeirsson SS. Precursor-product relationship between oval cells and hepatocytes: com-

- parison between tritiated thymidine and bromodeoxyuridine as tracers. *Carcinogenesis* 1996;17:2143–2151.
16. Alison MR, Golding M, Sarraf CE, Edwards RJ, Lalani EN. Liver damage in rat induces hepatocyte stem cells from biliary epithelial cells. *Gastroenterology* 1996;110:1182–1190.
 17. Alison M, Golding M, Lalani EN, Nagy P, Thorgeirsson S, Sarraf C. Wholesale hepatocytic differentiation in the rat from ductular oval cells, the progeny of biliary stem cells. *J Hepatol* 1997;26:343–352.
 18. Higgins GM, Anderson RM. Experimental pathology of the liver: restoration of the liver on the white rat following partial surgical removal. *Exp Pathol* 1931;12:186–202.
 19. Scoazec JY. Expression of cell-matrix adhesion molecules in the liver and their modulation during fibrosis. *J Hepatol* 1995;22(Suppl 2):20–27.
 20. Dunsford HA, Sell S. Production of monoclonal antibodies to preneoplastic liver cell populations induced by chemical carcinogens in rats and to transplantable Morris hepatomas. *Cancer Res* 1989;49:4887–4893.
 21. Bisgaard HC, Parmelee DC, Dunsford HA, Sechi S, Thorgeirsson SS. Keratin 14 protein in cultured nonparenchymal rat hepatic epithelial cells: characterization of keratin 14 and keratin 19 as antigens for the commonly used mouse monoclonal antibody OV-6. *Mol Carcinog* 1993;7:60–66.
 22. Bode HP, Wang L, Cassio D, Leite MF, St-Pierre MV, Hirata K, et al. Expression and regulation of gap junctions in rat cholangiocytes. *HEPATOLOGY* 2002;36:631–640.
 23. Hong W, Doyle D. cDNA cloning for a bile canaliculus domain-specific membrane glycoprotein of rat hepatocytes. *Proc Natl Acad Sci U S A* 1987;84:7962–7966.
 24. Bulger RE. Kidney morphology. In: Earley LE, Gottschalk CW, eds. *Strauss and Welt's Diseases of the Kidney*. 3rd ed. Boston: Little, Brown, 1979:3–39.
 25. Adams JC, Watt FM. Fibronectin inhibits the terminal differentiation of human keratinocytes. *Nature* 1989;340:307–309.
 26. Yin L, Sun M, Ilic Z, Leffert HL, Sell S. Derivation, characterization and phenotypic variation of hepatic progenitor cell lines isolated from adult rats. *HEPATOLOGY* 2002;35:315–324.
 27. Couchie D, Holic N, Chobert MN, Corlu A, Laperche Y. In vitro differentiation of WB-F344 rat liver epithelial cells into biliary lineage. *Differentiation* 2002;69:209–215.
 28. Strick-Marchand H, Weiss MC. Inducible differentiation and morphogenesis of bipotential liver cell lines from wild-type mouse embryos. *HEPATOLOGY* 2002;36:794–804.
 29. Chen WT, Chen JM, Mueller SC. Coupled expression and colocalization of 140K cell adhesion molecules, fibronectin and laminin during morphogenesis and cytodifferentiation of chick lung cells. *J Cell Biol* 1986;103:1073–1090.
 30. Bronner-Fraser M, Artinger M, Muschler J, Horwitz AF. Developmentally regulated expression of $\alpha 6$ integrin in avian embryos. *Development* 1992; 115:197–211.
 31. Plescia C, Rogler C, Rogler L. Genomic expression analysis implicates Wnt signaling pathway and extracellular matrix alterations in hepatic specification and differentiation of murine hepatic stem cells. *Differentiation* 2001; 68:254–269.
 32. Couvelard A, Bringuier AF, Dauge MC, Nejari M, Darai E, Beniffa JL, et al. Expression of integrins during liver organogenesis in humans. *HEPATOLOGY* 1998;27:839–847.
 33. Duncan SA, Nagy A, Chan W. Murine gastrulation requires HNF-4 regulated gene expression in the visceral endoderm: tetraploid rescue of HNF-4(-/-) embryos. *Development* 1997;124:279–287.
 34. Duncan SA. Mechanisms controlling early development of the liver. *Mech Dev* 2003;120:19–33.
 35. Li J, Ning G, Duncan SA. Mammalian hepatocyte differentiation requires the transcription factor HNF-4 α . *Genes Dev* 2000;14:464–474.
 36. Hayhurst GP, Lee YH, Lambert G, Ward JM, Gonzalez FJ. Hepatocyte nuclear factor 4 α (nuclear receptor 2A1) is essential for maintenance of hepatic gene expression and lipid homeostasis. *Mol Cell Biol* 2001;21: 1393–1403.
 37. Costa RH, Grayson DR, Darnell JE. Multiple hepatocyte-enriched nuclear factors function in the regulation of transthyretin and alpha 1-antitrypsin genes. *Mol Cell Biol* 1989;9:1415–1425.
 38. Thorgeirsson SS, Evarts RP, Bisgaard HC, Fujio K, Hu Z. Hepatic stem cell compartment: activation and lineage commitment. *Proc Soc Exp Biol Med* 1993;204:253–260.
 39. Zhang JT, Nicholson BJ. Sequence and tissue distribution of a second protein of hepatic gap junctions, Cx26, as deduced from its cDNA. *J Cell Biol* 1989;109:3391–3401.
 40. Zhang M, Thorgeirsson SS. Modulation of connexins during differentiation of oval cells into hepatocytes. *Exp Cell Res* 1994;213:37–42.
 41. Ruch RJ, Trosko JE. The role of oval cells and gap junctional intercellular communication in hepatocarcinogenesis. *Anticancer Res* 1999;19:4831–4838.
 42. Dermietzel R, Spray DC. Gap junctions in the brain: where, what type, how many and why? *Trends Neurosci* 1993;16:186–192.
 43. Evarts RP, Nakatsukasa H, Marsden ER, Hsia CC, Dunsford HA, Thorgeirsson SS. Cellular and molecular changes in the early stages of chemical hepatocarcinogenesis in the rat. *Cancer Res* 1990;50:3439–3444.
 44. Zaret KS. Regulatory phases of early liver development: paradigms of organogenesis. *Nature Rev Genet* 2002;3:499–512.

Triiodothyronine accelerates differentiation of rat liver progenitor cells into hepatocytes

Viktória László · Katalin Dezső · Kornélia Baghy ·
Veronika Papp · Ilona Kovalszky · Géza Sáfrány ·
Snorri S. Thorgeirsson · Peter Nagy · Sándor Paku

Accepted: 10 July 2008 / Published online: 29 July 2008
© Springer-Verlag 2008

Abstract The 2-acetaminofluorene/partial hepatectomy (AAF/Phx) model is widely used to induce oval/progenitor cell proliferation in the rat liver. We have used this model to study the impact of a primary hepatocyte mitogen, triiodothyronine (T3) on the liver regenerating by the recruitment of oval/progenitor cells. Administration of T3 transiently accelerates the proliferation of the oval cells, which is followed by rapid differentiation into small hepatocytes. The oval cell origin of the small hepatocytes has been proven by tracing retrovirally transduced and BrdU marked oval cells. The differentiating oval cells become positive for hepatocyte nuclear factor-4 and start to express hepatocyte specific connexin 32, $\alpha 1$ integrin, Prox1, cytochrom P450s, and form CD 26 positive bile canaliculi. At the same time oval cell specific OV-6 and alpha-fetoprotein expression is lost. The upregulation of hepatocyte specific mRNAs: albumin, tyrosine aminotransferase and tryptophan 2,3-dioxygenase detected by real-time PCR also proves hepatocytic maturation. The hepatocytic conversion of oval cells occurs on the seventh day after the Phx in this

model while the first small hepatocytes appear 5 days later without T3 treatment. The administration of the primary hepatocyte mitogen T3 accelerates the differentiation of hepatic progenitor cells into hepatocytes *in vivo*, and that may have therapeutic potential.

Keywords Oval cell · Maturation · Regeneration · Retroviral transduction · Primary mitogen

Abbreviations

AAF	2-Acetaminofluorene
BrdU	Bromodeoxyuridine
HNF-4	Hepatocyte nuclear factor 4
Phx	Partial hepatectomy
T3	Triiodothyronine
AFP	Alpha-fetoprotein
TAT	Tyrosine aminotransferase
TO2	Tryptophan 2,3-dioxygenase
Cx	Connexin

Supported by OTKA T 42674 and ETT 32/2006.

V. László · K. Dezső · K. Baghy · V. Papp · I. Kovalszky ·
P. Nagy (✉) · S. Paku
First Department of Pathology and Experimental Cancer Research,
Semmelweis University, Üllői út 26,
1085 Budapest, Hungary
e-mail: nagy@korf1.sote.hu

G. Sáfrány
National Research Institute for Radiobiology and Radiohygiene,
Budapest, Hungary

S. S. Thorgeirsson
Laboratory of Experimental Carcinogenesis,
Center for Cancer Research, National Cancer Institute,
National Institutes of Health, Bethesda, MD, USA

Introduction

The “oval cell” proliferation in the rat liver represents a stem cell derived regenerative process (Alison 2003; Grisham and Thorgeirsson 1997; Batusic et al. 2005). The stem cell compartment is activated when hepatocytes are compromised (e.g., viral infection, chemical toxicity) and not able to respond to proliferative stimuli needed for liver regeneration. The oval cells constitute the transit amplifying or progenitor cell compartment in the liver, and form a branching ductular network which is the extension of the canals of Hering (Paku et al. 2001). It has been reported that bone marrow derived oval cells may contribute to the regenerative process (Petersen et al. 1999) but this transdifferentiation

process is very inefficient if it occurs at all (Wagers et al. 2002; Thorgeirsson and Grisham 2006). However, it is generally agreed that the oval cells are able to differentiate into cholangiocytes and hepatocytes replacing the lost liver parenchyme (Alison 2003; Grisham and Thorgeirsson 1997; Fausto 2004; Paku et al. 2004). The growth regulation of these cells has been characterized. There are several growth factor/receptor systems, which are active during this process and are responsible for the expansion of the oval cell population (Grisham and Thorgeirsson 1997; Fausto 2004). The differentiation of the oval cells can be induced by different compounds in vitro (Kaplanski et al. 2000; Kamiya et al. 2002; Heng et al. 2005), but there are hardly any data about the in vivo modulation of the differentiation.

The primary hepatocyte mitogens are able to induce hepatocyte proliferation even without preceding liver damage (Columbano and Shinozuka 1996). Their biological effect has been studied in several experimental models, but the influence of primary hepatocyte mitogens on oval cells has not been investigated. One of the primary mitogens, triiodothyronine (T3), has been reported (Malik et al. 2003) to enhance the regenerative capacity of the liver following Phx. Another one, WY 14,643 induced the differentiation of oval cells (Kaplanski et al. 2000) in vitro. Here we investigated, if T3 can influence the stem cell driven liver regeneration. Oval/progenitor cell proliferation was generated by the widely used AAF/Phx model (Tetamatsu et al. 1984). We found that a single dose of the primary hepatocyte mitogen T3 (Francavilla et al. 1994) accelerated the proliferation and differentiation of oval cells into hepatocytes. The hepatocytic differentiation of the oval cells was confirmed by morphological, immunophenotypical and mRNA expression characterization.

Materials and methods

Animal experiments

Male F-344 rats (160–180 g) were used for all experiments and were kept under standard conditions. At least four animals were used for each experimental time points (unless otherwise marked). The animal study protocols were conducted according to National Institutes of Health guidelines for animal care.

AAF/Phx experiment

2-Acetylaminofluorene (AAF) (2 mg/ml suspended in 1% dimethylcellulose) in a dose of 5 mg/kg was administered to rats daily for four consecutive days by gavage. Traditional two-thirds partial hepatectomy (Phx) was performed (Higgins and Anderson 1931) on the fifth day, which was followed by four additional AAF treatments (Fig. 1a).

Treatment by triiodothyronine

AAF/Phx experiment was performed as described above. T3 (400 µg/kg i.p.) was injected into the rats on the fifth day following the Phx (Fig. 1b). The rats were sacrificed 48 h after the mitogen treatment. Tissue samples were taken for histology, blood was drawn from the right ventricle of the heart for laboratory examinations. The control animals were treated by the AAF/Phx protocol but at the time of the mitogen treatment were administered only by the solvent.

Additional control groups

Additional preliminary control experiments were performed: AAF/sham operation + T3; Phx + T3; normal rat + T3. Neither of these protocols resulted in oval cells, therefore these data were not shown.

For pulse, labeling 100 mg/kg BrdU (Paku et al. 2001) was given to the rats at 18, 24, 48 and 96 h after the mitogen treatment and they were sacrificed 1 h later.

For pulse chase experiment 200 mg/kg BrdU was injected into the rats 2 h before the T3 treatment. The pulse animals were sacrificed 1 h later (without mitogen treatment). The chase animals were sacrificed 48 h after the mitogen treatment.

Apoptotic cell death has been scored histologically based on the detection of condensed and fragmented nuclei and cells (Wyllie et al. 1980).

Morphological analysis

Frozen sections (10–20 µm) were fixed in methanol (4% paraformaldehyde for beta galactosidase) and were incubated at room temperature (1 h) with a mixture of different primary antibodies (Table 1) and with appropriate secondary antibodies afterwards (Jackson Immunoresearch).

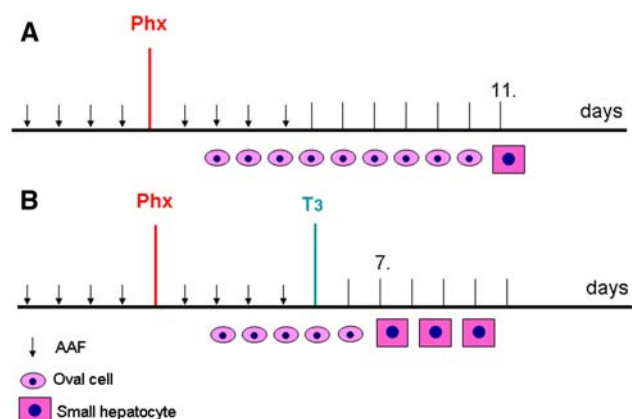


Fig. 1 Schematic representation of the experimental protocols. The first hepatocytes appeared on the eleventh day in the control group (a), whereas they showed up on the seventh day in the T3 treated animals (b)

Table 1 Primary antibodies used for the immunohistochemical studies

Antibody	Species	Manufacturer	Catalog number	Dilution
Laminin	Rabbit polyclonal	Dako	Z0097	1:200
HNF-4	Goat polyclonal	Santa Cruz Biotechnology	SC-6556	1:100
BrdU	Mouse monoclonal	Becton-Dickinson	347580	1:100
Connexin 32	Goat polyclonal	Santa Cruz Biotechnology	SC-7258	1:100
CD 26	Mouse monoclonal	Serotec	MCA924	1:20
OV-6	Mouse monoclonal	R&D Systems	MAB 2020	1:100
Cytochrome P450	Rabbit polyclonal	MBL	BV-3084-3	1:100
AFP	Mouse monoclonal	Nordic Immunological Laboratories	ShARa/AFP	1:50
$\alpha 1$ integrin	Mouse monoclonal	Serotec	MCA 1791	1:100
Thyroid hormone receptor beta-1	Mouse monoclonal	Affinity Bioreagents	MA1-216	1:10
<i>E. coli</i> beta galactosidase	Goat polyclonal	Serotec	4600-1409	1:1000
Prox 1	Rabbit polyclonal	Reliatech	102-PA30	1:20
Dlk-1	Goat polyclonal	R&D	AF1144	1:100

All samples were analyzed by confocal laser scanning microscopy using Bio-Rad MRC-1024 system (Bio-Rad, Richmond CA). For the BrdU staining the sections were pretreated with HCl as described before (Paku et al. 2004).

Determination of labeling index of oval cells and small hepatocytes

Labeling indexes were determined by using 3–4 animals at each time point. About 500–1,000 nuclei were counted per animal.

Oval cells

Oval cells basement membrane was highlighted by incubating frozen sections with anti-laminin primary antibody followed by biotinylated secondary antibody and TRITC conjugated streptavidin (red fluorescence). The same sections were treated with 2 N HCl, followed by BrdU staining (green fluorescence) (Paku et al. 2001). Nuclei were stained by DAPI. Areas around portal tracts were randomly selected using a 100 \times objective. The number of labeled and the total number nuclei surrounded by continuous basement membrane were determined.

Small hepatocytes

Small hepatocytes frozen sections were stained by HNF-4 antibody (green fluorescence) followed by HCl treatment and BrdU staining (red fluorescence). Nuclei of small hepatocytes were identified according to their size and density (small hepatocytes have a considerable smaller nucleus

than the old hepatocytes and are arranged frequently as small groups with high density). BrdU labeled and total number of HNF-4 positive nuclei of small hepatocytes was determined.

Real-time PCR

Frozen sections (10 μ m) were fixed in acetone, dried at room temperature and stained with RNase-free hematoxylin. Laser microdissection of tissue sections was performed by using PALM MicroBeam system. About 500–1,000 cells were collected in lysis buffer and total RNA was isolated by RNeasy Mini Kit (Qiagen, Hilden, Germany). MMLV Reverse Transcriptase (Invitrogen, Carlsbad, CA) was used for cDNA synthesis as recommended by the supplier. PCR was performed by ABI Prism 7000 Sequence Detection System Applied Biosystems, Foster City, CA), using ABI TaqMan assays for albumin (Assay ID: Rn00592480_m1), AFP (Assay ID: Rn0056061_m1), tryptophan 2,3-dioxygenase (Assay ID: Rn00574499_m1), tyrosine aminotransferase (Assay ID: Rn00562011_m1), according to the manufacturer's instructions. Beta-actin was used as endogenous control. Relative gene expressions were calculated by the 2 $[-\Delta\Delta C(T)]$ method (Livak and Schmittgen 2001).

Retroviral transduction

We used the amphotropic retroviral vector (kindly provided by Nicholas Ferry, France) containing the *E. coli* β -galactosidase gene coupled to the nuclear localization signal from a SV 40 large T antigen, produced by the TEL-CeB6 producing cell line (Avril et al. 2004). To increase

the concentration of retroviral particles the supernatant was centrifuged at 20,000g for 4 h, as described by Yang et al. (2002). Retroviral titer was determined by infecting NIH 3T3 cells in 24-well dishes with 500 μ l of serial dilutions of the retrovirus containing supernatant. The cells were stained 48 h later with X-gal and the titer was defined. After concentration, the titer routinely reached 5×10^6 per milliliter. The viruses were injected into the liver of the AAF/Phx treated animals 2 days after the Phx through the common bile duct. The first sets of rats were sacrificed 3 days later without T3 treatment (pulse). The second sets of rats were injected by T3 on the fifth day following the Phx and sacrificed 2 days later (chase).

Results

T3 enhances the oval cell proliferation and accelerates liver regeneration

A single dose of the thyroid hormone was given on the fifth day after the partial hepatectomy for the rats treated according to the AAF/Phx experimental protocol. Following the treatment the relative liver weight (liver/body weight) of the T3 treated rats increased in 48 h compared to the control (solvent treated) rats (Table 2).

The histological structure of the livers changed dramatically in the T3 treated animals. The majority of the oval cells disappeared. Small, sometimes trabecularly arranged polygonal cells emerged in the periportal zone. They had round nuclei and looked like small hepatocytes (Fig. 2a, b).

The rate of DNA synthesis was measured by BrdU pulse labeling (Table 3.). Practically there was no labeling in the hepatocytes in any of the studied timepoints. BrdU incorporation was significantly higher in the oval cells of the rats at 18 h after administration of T3 compared to the solvent treated rats. The BrdU was also taken-up late by the newly formed polygonal cells, although the labeling index was lower than in the oval cells of the control rat livers. Later at 96 h, the proliferation rate of the remaining oval cells returned to the control level. The oval cells carry the thyroid hormone receptor that is they may be influenced by this hormone (Fig. 2c).

Table 2 Effect of T3 treatment on liver weight and functional activity of the liver

	Relative liver weight (%)	Serum bilirubin concentration (μ mol/l)	Plasma prothrombin level (%)
Control	2 \pm 0.25	17.6 \pm 16.9	21.3 \pm 18.5
T3	2.6 \pm 0.41*	5.4 \pm 4.9*	49.2 \pm 25.5*

* $P < 0.05$

The T3 treatment induced hepatocyte hyperplasia is followed by a wave of apoptosis (Francavilla et al. 1994) in the normal liver. Practically no such apoptosis response was observed in the AAF/Phx treated animals after the mitogenic treatment (2.25 ± 1.26 apoptosis per 5,000 cells vs. 19.66 ± 3.21 apoptosis per 5,000 cells in the controls, normal untreated rats 4 days after T3 administration, $P < 0.01$).

The small polygonal cells derive from the oval cells

Although the dynamics of histomorphological changes indicated the oval cell origin of the newly formed small polygonal cells, this relationship was verified by two independent pulse chase experiments.

1. BrdU was given to the rats 2 h before the T3 treatment. The first set of animals was killed 1 h later that is before the T3 administration. BrdU was incorporated, in addition to the non-parenchymal cells, into the nuclei of the oval cells, no staining was present in the “old” hepatocytes (Fig. 2d). The oval cells could be identified by laminin staining, the basement membrane surrounded tubular arrangement (Paku et al. 2004) is highly characteristic for these cells in the AAF/Phx model. Dlk-1, another oval cell marker (Jensen et al. 2004; Tanimizu et al. 2004) also decorates a subset of oval cells, a portion of the BrdU positive cells are also Dlk-1 positive (Fig. 2e). The second set of rats was sacrificed at 48 h following the T3 treatment. BrdU decorated the nuclei of the small, hepatocyte like cells which were also positive for HNF-4 and CYP 450. The BrdU staining was present in small dots indicating the dilution of the pyrimidine analogue since the administration (Fig. 2f, g). The “old” hepatocytes remained negative at the 48 h time-point as well.
2. The proliferating OV-6 positive oval cells were also exclusively marked in another experiment by beta-galactosidase expressing retroviruses 2 days after the Phx that is 3 days before the T3 administration (Fig. 3a). When the labeled oval cells were traced 2 days after the T3 treatment, groups of the small polygonal cells, expressing CYP 450 were found with beta-galactosidase positive nuclei (Fig. 3b) without any labeling in “old” hepatocytes.

The oval cells differentiate rapidly into small basophilic hepatocytes following triiodothyronine treatment

We have performed several studies to demonstrate that the oval cell derived small polygonal cells are functional hepatocytes indeed. The upregulation of HNF-4 (Fig. 2f, 4a, b) in the small cells already supports this notion (Hakoda et al.

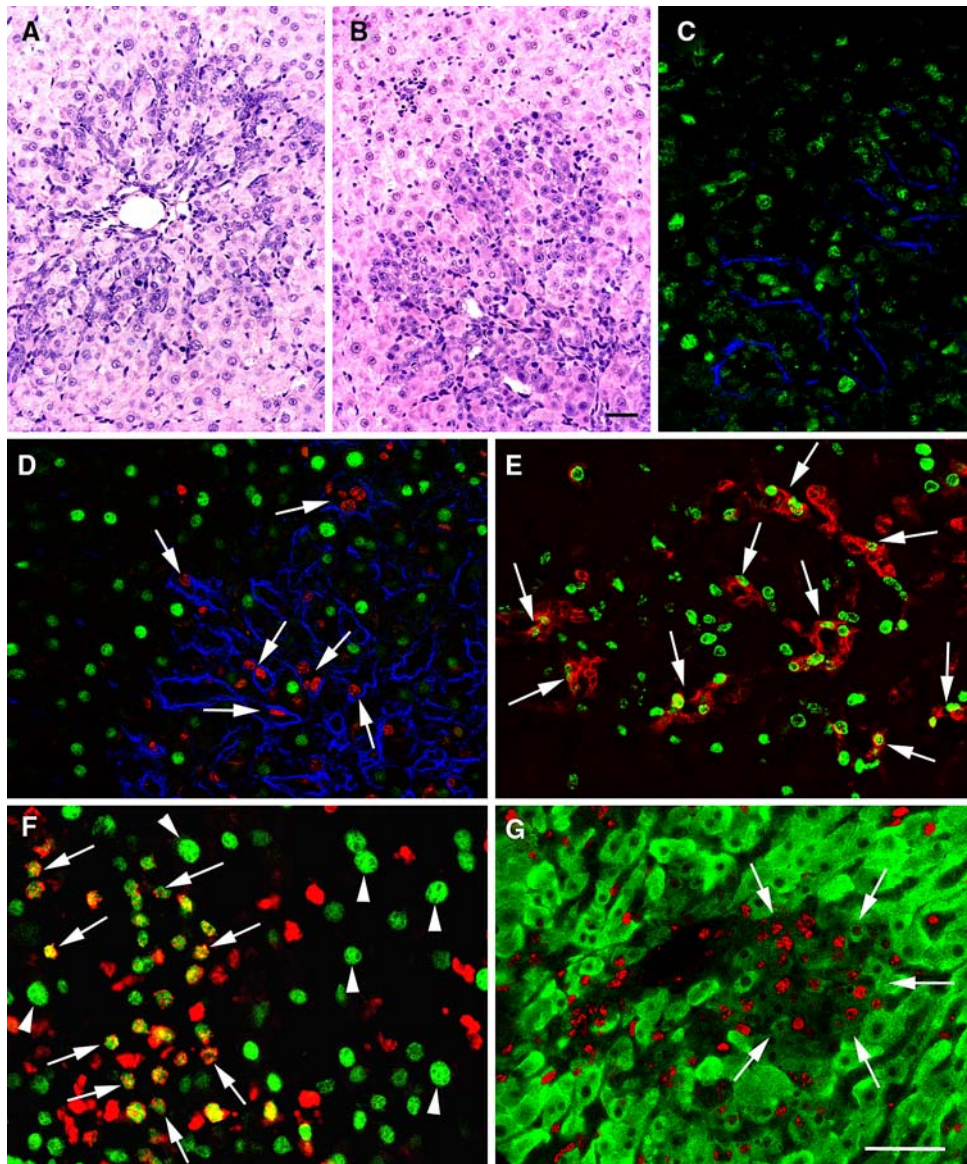


Fig. 2 **a, b** AAF/Phx experiment, H&E staining, seventh day following Phx. Control rat (**a**), T3 treated animal (**b**), T3 was given on the fifth day after Phx. Note the appearance of small basophilic hepatocytes, oval cells can be hardly seen. **c** The reaction with thyroid hormone receptor antibody (*green*) resulted in nuclear staining in the hepatocytes as well as in the laminin (*blue*) surrounded oval cells. (AAF/Phx experiment, 5 days after Phx) **d–g** Pulse-chase experiment, with BrdU of AAF/Phx treated rats. **d** Fifth day after Phx, 1 h after BrdU administration (“before” T3 treatment). BrdU (*red*) is incorporated into the nuclei of laminin (*blue*) surrounded oval cells (*arrows*) and scattered non parenchymal cells. Note the HNF-4 positive (*green*)

nuclei of the hepatocytes do not contain BrdU. **e** The same animal as on “D”. Dlk-1 (*red*) stains a subpopulation of oval cells. Note the partial costaining of BrdU (*green*) and Dlk-1 (*arrows*). **f** Two days after T3 treatment. Colocalization of small BrdU (*red*) dots and HNF-4 (*green*) in nuclei. Note that the HNF4 and BrdU positive nuclei of the “new” hepatocytes (*arrows*) are smaller, than those of the “old” hepatocytes (*arrowheads*). **g** The same liver as on “E”. Note the presence of BrdU in CYP 450 expressing cells. Two days after T3 treatment a group of small hepatocytes (*arrows*) shows weaker reaction intensity for cytochrome P 450 (*green*) than the surrounding old hepatocytes. Scale bar for **a, b**: 25 μ m; **c, d, e, f, g**: 50 μ m

2003; Parviz et al. 2003). The disappearance of the oval cell specific OV-6 (Dunsford and Sell 1989), AFP (Petropoulos et al. 1985) and laminin reaction (Fig. 4c) indicates severe phenotypic changes. CD 26 staining demonstrated the formation of the bile canaliculi among the small polygonal cells (Fig. 4d). At the same time immunohistochemistry indicated the rapid gain of hepatocyte specific Cx32, α 1

integrin (Fig. 4e, f) and cytochrome P450 IIE1 expression (Fig. 2g, 3b and 4a), all these antigens are completely missing from the oval cells. A recently described marker of hepatocytic differentiation, Prox1 (Dudas et al. 2006) was also present in the differentiating oval cells and small hepatocytes following the T3 treatment (Fig. 4b). Interestingly a few OV-6+ cells was already Prox1+ but HNF4-. This is

Table 3 Labeling index of oval cells and small hepatocytes following T3 treatment

		18 h	24 h	48 h	96 h
Control	Oval cells	17 ± 1.7	18.9 ± 2.1	14.9 ± 0.3	11.5 ± 2.9
T3	Oval cells	30.2 ± 0.7*	17.6 ± 3.8	11.5 ± 1.8**	8.2 ± 0.6
	Small hepatocytes	–	–	8.7 ± 2.5	11.3 ± 2.7

* $P < 0.05$ between 18 h control and T3

** $P < 0.05$ between 18 and 48 h T3

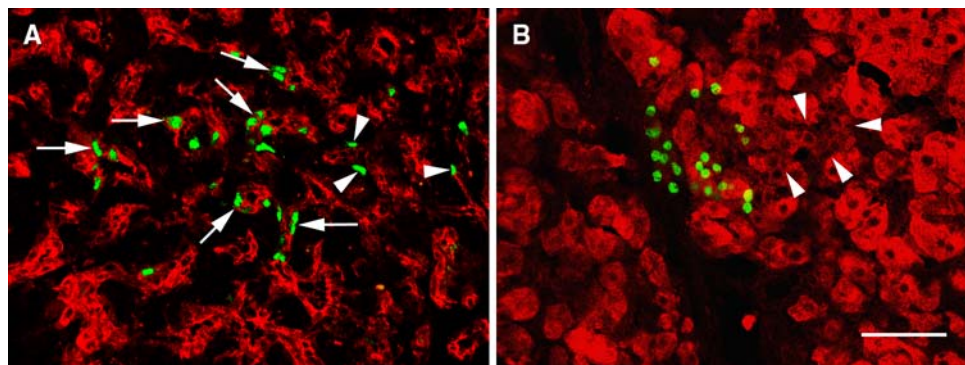


Fig. 3 Pulse-chase experiment, with beta-galactosidase expressing retroviruses of AAF/Phx treated rats. The virus was injected into the liver 2 days after the Phx, 3 days later the rat was treated by T3 (pulse animals were sacrificed “before” T3 treatment) and sacrificed after 2 more days (*chase*). **a** Immunohistochemical detection of beta-galactosidase (*green*) in a “pulse” animal. The viruses transduced OV-6 positive (*red*) oval cells (*arrows*) and a few non-parenchymal cells

(*arrowheads*). **b** Immunohistochemical detection of beta-galactosidase (*green*) in a “chase” animal. There is nuclear staining in groups of small, CYP 450 (*red*) expressing hepatocytes indicating that they are the progenies of the oval cells. Unlabeled small hepatocytes with less intense CYP 450 staining are also present (*arrowheads*). Scale bar: 50 μm

in good agreement with Dudas et al’s original description, this observation may indicate the heterogeneity of the differentiation reaction or that Prox1 is an earlier marker of the hepatocytic commitment of oval cells, than HNF4.

The changes of gene expression were studied by real-time RT-PCR. Oval cells were microdissected from the liver of T3 treated animals 48 h after the T3 treatment as well as from control (solvent treated AAF/Phx) rats. Newly formed small hepatocytes 48 h after the T3 treatment and hepatocytes from normal, healthy untreated rats were also dissected. The gene expression was compared in normal hepatocytes and small polygonal cells appearing at 48 h after the T3 treatment (Fig. 5). The expression of albumin, TAT and TO2 was significantly upregulated in the newly formed hepatocytes compared to the oval cells, while the AFP expression sharply dropped. There were some changes between the T3 treated and untreated oval cells but the change were more dramatic in the small hepatocytes indicating qualitative alterations.

The functional capacity of the newly formed hepatocytes was revealed by blood chemistry tests. The decrease of the serum bilirubin level and increase of prothrombin level 2 days after the T3 treatment indicated better liver functions (Table 2).

Discussion

T3 is a well known mitogen for hepatocytes. A single dose of this hormone induces a massive hyperplastic reaction of the hepatocytes and hepatomegaly in normal rat (Franca-villa et al. 1994). T3 has been reported to enhance the regenerative capacity of the liver following Phx (Malik et al. 2003). Here we tested if T3 treatment can influence oval cell dependent liver regeneration. A single dose of the thyroid hormone was given on the fifth day after the partial hepatectomy for the rats treated according to the AAF/Phx experimental protocol. This treatment resulted in augmented relative liver weight in 48 h. The enhanced liver growth was most probably the consequence of the accelerated oval cell proliferation and differentiation. The differentiation process was verified by the establishment of hepatocytic morphological, immunophenotypical markers and transcription of hepatocyte specific genes (TAT, TO2, CYP 450) in the progenies of the oval cells. The blood chemistry data indicated improving liver function. Although it must be mentioned, that the mitogen was administered 24 h after the last AAF treatment and the small hepatocytes showed up after subsequent 48 h. Therefore, the decreasing mitoinhibitory effect of AAF on the

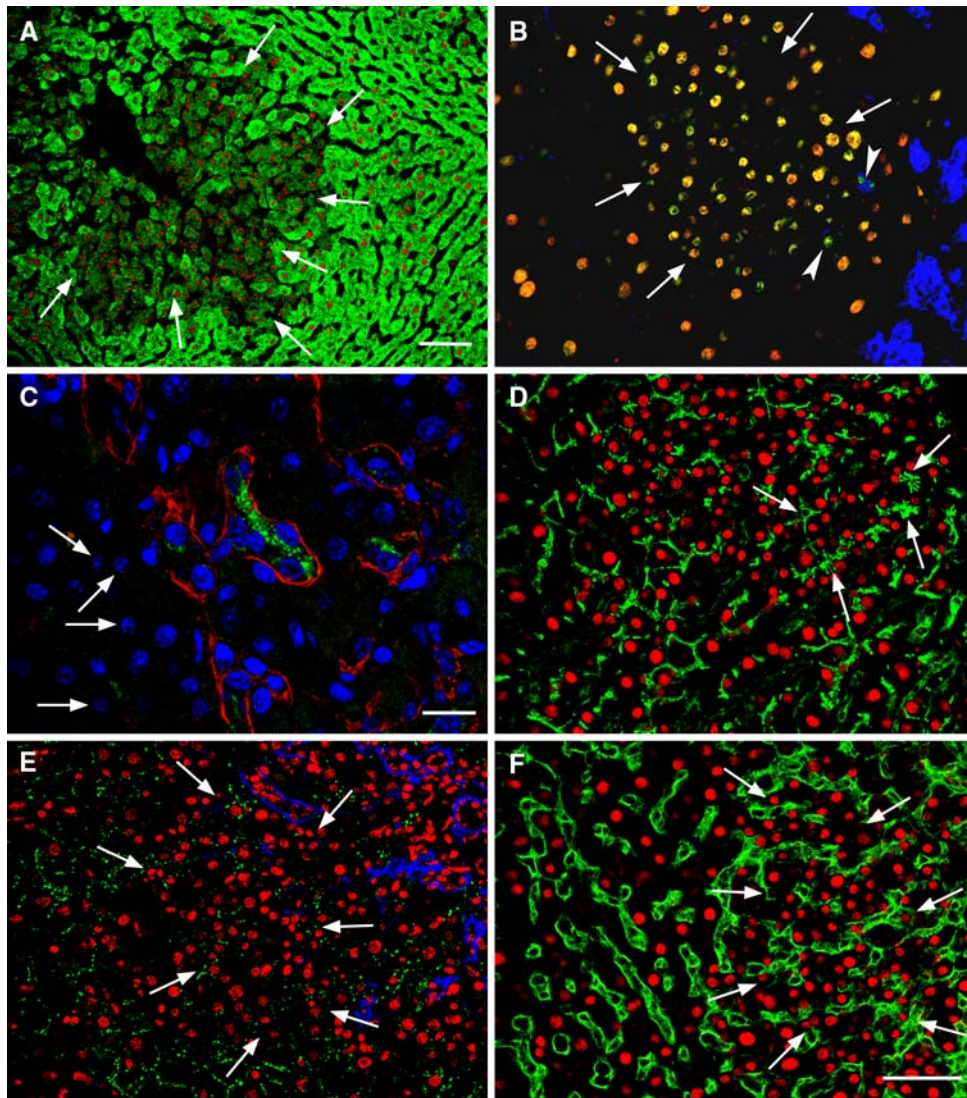


Fig. 4 Immunohistochemical characterization of the differentiated “small” hepatocytes 2 days after T3 treatment. **a** A small island (arrows) of new hepatocytes is characterized by pale Cyp 450 (green) and positive nuclear HNF4 (red) staining. **b** The nuclei in another group of small hepatocytes (arrows) are also positive for HNF4 (red) and Prox-1 (green), the double staining results in mostly yellow nuclei. Note the lack of Prox-1 reaction in the OV6 (blue) positive oval cells (right lower corner). A few Prox1 and OV6 positive but HNF4 negative (arrowhead) differentiating cells are also present near the focus as described by Dudas et al. (2007). **c** AFP (green) positive oval cells are present within the ductules surrounded by laminin positive basement membrane material (red). AFP positivity can not be observed over the differentiating hepatocytes (arrows). Nuclei are stained by TOTO-3 (blue). **d** Star like CD26 positive structures (green, arrows) represent

the developing bile canalicules between the differentiating hepatocytes. All hepatocytes express HNF4 in their nuclei (red). **e** Connexin 32 (green) positive gap junctions are represented by small dot like signals between the young hepatocytes (arrows), which can be recognized from their small nuclei (red, propidium iodide). No signal is present in the left over laminin (blue) surrounded oval cell ductules. Hexagonally arranged Cx 32 staining can be seen on the “old” hepatocytes. **f** $\alpha 1$ integrin positivity (green) is present at the basal side of the small hepatocytes (right side of the picture). Note the ductular arrangement of the nuclei of the small hepatocytes (arrows). Normal liver structure can be observed on the left side of the picture. All hepatocytes express HNF4 in their nuclei (red). Scale bar for **a**: 100 μm ; **b**, **d**, **e**, **f**: 50 μm ; **c**: 25 μm

“old” hepatocytes and the contribution of the mitogenic response of these cells can not be excluded unanimously.

Lead nitrate was also able to accelerate the differentiation of the oval cells (data not shown). WY 14,643 another primary hepatocyte mitogen induced the differentiation of oval cells (Kaplanski et al. 2000) in vitro. That is other primary hepatocyte mitogens might also be able to promote

this form of liver regeneration. The molecular mechanism of the rapid differentiation induced by the mitogens is not known yet, but it appears to be coupled to cell proliferation. The DNA replication increases transiently in the oval cells after T3 treatment. It is well documented in the final phase of liver ontogeny that the terminal differentiation is accompanied with the rapid growth of the liver (Duncan 2003).

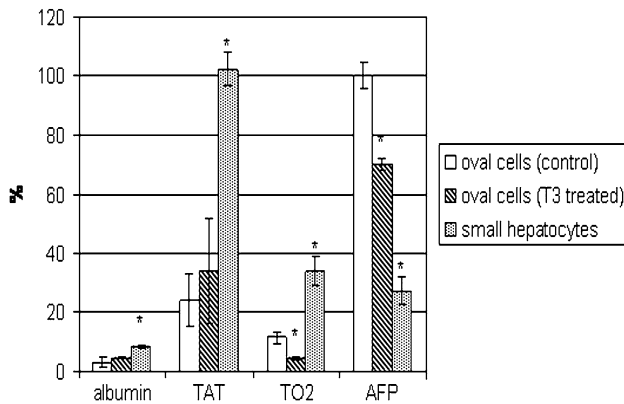


Fig. 5 Real-time RT-PCR analysis of gene expression in microdissected cell populations. The gene expression of control oval cells (AAF/Phx experiment seventh day after Phx), oval cells after T3 treatment (AAF/Phx experiment, T3 was given on the fifth day after Phx, the rats were sacrificed on the seventh day) and small hepatocytes (AAF/Phx experiment, T3 was given on the fifth day after Phx, the rat was sacrificed on the seventh day) were compared with the expression level of hepatocytes from normal liver. The expression level of albumin, TAT and TO2 was compared to normal, untreated hepatocytes (100%). Since AFP mRNA could not be detected in the normal hepatocytes, the expression level of control oval cells was taken as 100% with this probe

The so-called focus formation in several oval cell proliferation models is also an indication of the intense cell proliferation at the onset of differentiation (Paku et al. 2004; Sell et al. 1987; Factor et al. 1994). Finally, HGF, a well-known mitogen for the liver, has been also reported to accelerate oval cell proliferation and to promote their differentiation (Hasuike et al. 2005). The thyroid hormone has been recently described to increase the NF- κ B and STAT3 activity in the liver (Fernández et al. 2007). These transcriptional factors play role in the growth regulation of the oval cells (Sánchez et al. 2004), therefore, alterations of these nuclear factors also might participate in the rapid differentiation.

T3 was able to reduce the formation of hepatocellular carcinomas in a rat chemical hepatocarcinogenesis model (Ledda-Columbano et al. 1999, 2000). The exact mechanism of this inhibition was not clear. Considering our observation one can not exclude the possibility that the thyroid hormone induced the differentiation of the tumor precursor cells.

Gordon et al. (2000) described the existence of the small hepatocyte-like progenitor cells (SHPC) in the liver as a novel liver progenitor cell population. However, the two pulse chase experiments in our case clearly excluded the participation of this cell population in the presently studied experiment. BrdU and the retroviruses marked the dividing cell population in the pulse phase of the lineage tracing experiments. This included, in addition to the oval cells, endothelial and stellate/myofibroblast cells (but no hepato-

cytes). Therefore, theoretically the mesenchymal origin of the small hepatocytes can not be excluded, but this option is highly unlikely. Our previous (Paku et al. 2001, 2004) and recent tracing observations indicate the small hepatocytes are most likely the progenies of the oval cells. The presence of the thyroid hormone receptor in the oval cells supports, that they can be influenced by this hormone.

The sequence of differentiation events following the T3 treatment, is almost identical with the steps we described (Paku et al. 2004) during the spontaneous differentiation of oval cells in the AAF/Phx experiment. However, the first new hepatocytes appear 11–12 days following the Phx in the traditional (noT3) experiment (Fig. 1a), they are already present on the seventh day when T3 was administered to the rats (Fig. 1b). That is, the thyroid hormone accelerated the differentiation process. In our recent study, the increased expression of several hepatocyte specific enzymes (TAT, TO2, CYP450) indicates the real functional differentiation of the hepatocytes. The biological significance of the maturation process is confirmed by the blood chemistry data. The decrease of the serum bilirubin level and increase of prothrombin level 2 days after the T3 treatment indicated better synthetic functions (Table 2). The prolonged prothrombin time is an excellent marker of liver failure and strong independent prognostic sign in patients (Bosch et al. 2003). The serum bilirubin and prothrombin time are two of the three laboratory parameters which are used to calculate the widely accepted MELD score (Model for End-stage Liver Disease), the best predictor of survival among different populations of patients with advanced liver disease (Kamath and Kim 2007). No changes were observed in the serum level of the transaminases and albumin (data not shown); this can be explained by the lack of hepatocyte injury and the long half-life of albumin (~20 days).

The T3 induced liver hyperplasia in normal rat is followed by a rapid wave of apoptosis. This compensatory reaction has not occurred in our model, therefore this accelerated regeneration process secures permanently liver function.

Hepatic progenitor cells are commonly observed in a wide variety of human liver diseases (Roskams et al. 2003, 2004). The efficiency of this alternative regenerative process is unclear. There are reported cases in which these endogenous progenitor cells are able to reconstitute the liver tissue and function (Fujita et al. 2000). However, ductularly arranged progenitor cells are frequently seen in failed livers at autopsy and in livers removed at transplantation indicating that the stem cell compartment is activated but has failed re-establish liver functions in these cases. Therefore, improving the efficiency of the regenerative response of liver progenitor cells might have a substantial clinical impact.

In conclusion, we observed accelerated differentiation of liver progenitor cells *in vivo* after the administration of the primary hepatocyte mitogen, T3. In addition to the morphological alterations, functional signs of maturation were also demonstrated. The “drug” induced accelerated differentiation of hepatic progenitor cells might serve as a possible treatment modality for several liver diseases.

Acknowledgments The authors would like to thank Sándor Spisák for helping in microdissection.

References

- Alison MR (2003) Characterization of the differentiation capacity of rat-derived hepatic stem cells. *Semin Liv Dis* 23:325–335
- Avril A, Pichard V, Bralet MP, Ferry N (2004) Mature hepatocytes are the source of small hepatocyte-like progenitor cells in the retrorsine model of liver injury. *J Hepatol* 41:737–743
- Batusic DS, Cimica V, Chen Y, Tron K, Hollemann T, Pieler T, Ramadori G (2005) Identification of genes specific to “oval cells” in the rat 2-acetylaminofluorene/partial hepatectomy model. *Histochem Cell Biol* 124:245–260
- Bosch J, D’amico G, García-Pagán JC (2003) Portal hypertension. In: Schiff ER (ed) *Schiff’s diseases of the liver*. Lippincott Williams & Wilkins, Philadelphia, pp 429–486
- Columbano A, Shinozuka H (1996) Liver regeneration versus direct hyperplasia. *FASEB J* 10:1118–1128
- Dudas J, Elmaouhoub A, Mansuroglu T, Batusic D, Tron K, Saile B, Papoutsis M, Pieler T, Wilting J, Ramadori G (2006) Prospero-related homeobox 1 (Prox1) is a stable hepatocyte marker during liver development, injury and regeneration, and absent from “oval cells”. *Histochem Cell Biol* 126:549–562
- Duncan SA (2003) Mechanisms controlling early development of the liver. *Mech Dev* 120:19–33
- Dunsford HA, Sell S (1989) Production of monoclonal antibodies to preneoplastic liver cell populations induced by chemical carcinogens in rats and to transplantable Morris hepatomas. *Cancer Res* 49:4887–4893
- Factor VM, Radaeva SA, Thorgeirsson SS (1994) Origin and fate of oval cells in Dipin-induced hepatocarcinogenesis in the mouse. *Am J Pathol* 145:409–422
- Fausto N (2004) Liver regeneration and repair: hepatocytes, progenitor cells, and stem cells. *Hepatology* 39:1477–1487
- Fernández V, Castillo I, Tapia G, Romanque P, Uribe-Echevarria S, Uribe M, Cartier-Ugarte D, Santander G, Vial MT, Videla LA (2007) Thyroid hormone preconditioning: protection against ischaemia-reperfusion liver injury in the rat. *Hepatology* 45:170–177
- Francavilla A, Carr BI, Azzarone A, Polimeno L, Wang Z, Van Diehl DH, Subbotin V, Prelich JG, Starzl TE (1994) Hepatocyte proliferation and gene expression induced by triiodothyronine *in vivo* and *in vitro*. *Hepatology* 20:1237–1241
- Fujita M, Furukawa H, Hattori M, Todo S, Ishida Y, Nagashima K (2000) Sequential observation of liver cell regeneration after massive hepatic necrosis in auxiliary partial orthotopic liver transplantation. *Mod Pathol* 13:152–157
- Gordon GJ, Coleman WB, Hixson DC, Grisham JW (2000) Liver regeneration in rats with retrorsine-induced hepatocellular injury proceeds through a novel cellular response. *Am J Pathol* 156:607–619
- Grisham JW, Thorgeirsson SS (1997) Liver stem cells. In: Potten CS (ed) *Stem cells*. Academic Press, London, pp 233–282
- Hakoda T, Yamamoto K, Terada R, Okano N, Shimada N, Suzuki T, Mizuno M, Shiratori Y (2003) A crucial role of hepatocyte nuclear factor-4 expression in the differentiation of human ductular hepatocytes. *Lab Invest* 83:1395–1402
- Hasuike S, Ido A, Uto H, Moriuchi A, Tahara Y, Numata M, Nagata K, Hori T, Hayashi K, Tsubouchi H (2005) Hepatocyte growth factor accelerate the proliferation of hepatic oval cells and possibly promotes the differentiation in a 2-acetylaminofluorene/partial hepatectomy model in rats. *J Gastroenterol Hepatol* 20:1753–1761
- Heng BC, Yu H, Yin Y, Lim SG, Cao T (2005) Factors influencing stem cell differentiation into the hepatic lineage *in vitro*. *J Gastroenterol Hepatol* 20:975–987
- Higgins GM, Anderson RM (1931) Experimental pathology of the liver: restoration of the liver of the white rat following partial surgical removal. *Exp Pathol* 12:186–202
- Jensen CH, Jauho EI, Santoni-Rugiu E, Holmskov U, Teiser B, Tygstrup N, Bisgaard HC (2004) Transit-amplifying ductular (oval) cells and their hepatocytic progeny are characterized by a novel and distinctive expression of delata like protein/preaapocyte factor 1/fetal antigen 1. *Am J Pathol* 164:1347–1359
- Kamath PS, Kim WR (2007) The model for end-stage liver disease (MELD). *Hepatology* 45:797–805
- Kamiya A, Kojima N, Kinoshita T, Sakai Y, Miyajima A (2002) Maturation of fetal hepatocytes *in vitro* by extracellular matrices and Oncostatin M: induction of tryptophan oxygenase. *Hepatology* 35:1351–1359
- Kaplanski C, Pauley CJ, Griffiths TG, Kawabata TT, Ledwith BJ (2000) Differentiation of rat oval cells after activation of peroxisome proliferator-activated receptor α 3. *Cancer Res* 60:580–587
- Ledda-Columbano GM, Perra A, Piga R, Pibiri M, Loi R, Shinozuka H, Columbano A (1999) Cell proliferation induced by 3, 3’, 5-triiodo-L-thyronine is associated with a reduction in the number of preneoplastic hepatic lesions. *Carcinogenesis* 20:2299–2304
- Ledda-Columbano GM, Perra A, Loi R, Shinozuka H, Columbano A (2000) Cell proliferation induced by triiodothyronine in rat liver is associated with nodule regression and reduction of hepatocellular carcinomas. *Cancer Res* 60:603–609
- Livak KJ, Schmittgen TD (2001) Analysis of relative gene expression data using real-time quantitative PCR and the 2⁻[Delta Delta C(T)] method. *Methods* 25:402–408
- Malik R, Mellor N, Selden C, Hodgson H (2003) Triiodothyronine enhances the regenerative capacity of the liver following partial hepatectomy. *Hepatology* 37:79–86
- Paku S, Schnur J, Nagy P, Thorgeirsson SS (2001) Origin and structural evolution of the early proliferating oval cells in rat liver. *Am J Pathol* 158:1313–1323
- Paku S, Nagy P, Kopper L, Thorgeirsson SS (2004) 2-Acetylaminofluorene dose-dependent differentiation of rat oval cells into hepatocytes: confocal and electron microscopic studies. *Hepatology* 39:1353–1361
- Parviz F, Matullo C, Garrison WD, Savatski L, Adamson JW, Ning G, Kaestner KH, Rossi JM, Zaret KS, Duncan SA (2003) Hepatocyte nuclear factor 4 α controls the development of hepatic epithelium and liver morphogenesis. *Nature Gen* 34:292–296
- Petersen BE, Bowen WC, Patrene KD, Mars WM, Sullivan AK, Murase N, Boggs SS, Greenberger JS, Goff JP (1999) Bone marrow as potential source of hepatic oval cells. *Science* 284:1168–1170
- Petropoulos CJ, Yaswen P, Panzica M, Fausto N (1985) Cell lineages in liver carcinogenesis: possible clues from studies of the distribution of a fetoprotein RNA sequences in cell populations isolated from normal, regenerating, and preneoplastic rat livers. *Cancer Res* 45:5762–5768
- Roskams TA, Libbrecht L, Desmet VJ (2003) Progenitor cells in diseased human liver. *Semin Liv Dis* 23:385–396
- Roskams TA, Theise ND, Balabaud C, Bhagat G, Bhathal PS, Bioulac-Sage P, Brunt EM, Crawford JM, Crosby HA, Desmet V, Finegold MJ, Geller SA, Gouw AS, Hytiroglou P, Knisely AS, Kojiro

- M, Lefkowitz JH, Nakanuma Y, Olynyk JK, Park YN, Portmann B, Saxena R, Scheuer PJ, Strain AJ, Thung SN, Wanless IR, West AB (2004) Nomenclature of the finer branches of the biliary tree: canals, ductules, and ductular reactions in human livers. *Hepatology* 39:1739–1745
- Sánchez A, Factor VM, Schroeder IS, Nagy P, Thorgeirsson SS (2004) Activation of NF- κ B and STAT3 in rat oval cells during 2-acetylaminofluorene/partial hepatectomy induced liver regeneration. *Hepatology* 39:376–385
- Sell S, Hunt JM, Knoll BJ, Dunsford HA (1987) Cellular events during hepatocarcinogenesis in rats and the question of premalignancy. *Adv Cancer Res* 48:37–111
- Tanimizu N, Tsujimura T, Takahide K, Nakamura K, Kodama T, Miyajima A (2004) Expression of Dlk/Pref-1 defines a subpopulation of oval cell compartment of rat liver. *Gene Expression Patterns* 5:209–218
- Tetamatsu M, Ho RH, Tohru K, Ekem JK, Farber E (1984) Studies on the proliferation and fate of oval cells in the liver of rats treated with 2-acetylaminofluorene and partial hepatectomy. *Am J Pathol* 114:418–430
- Thorgeirsson SS, Grisham JW (2006) Hematopoietic cells as hepatocyte stem cells: a critical review of the evidence. *Hepatology* 43:2–8
- Wagers AJ, Sherwood RI, Christensen JL, Weissman IL (2002) Little evidence for developmental plasticity of adult hematopoietic stem cells. *Science* 297:2256–2259
- Wyllie AH, Kerr JF, Currie AR (1980) Cell death: the significance of apoptosis. *Int Rev Cytol* 68:251–306
- Yang J, Friedman MS, Bian H, Crofford LJ, Roessler B, Mc Donagh KT (2002) Highly efficient genetic transduction of primary human synoviocytes with concentrated retroviral supernatant. *Arthritis Res* 4:215–219

Biological Perspectives

Alternative Vascularization Mechanisms in Cancer

Pathology and Therapeutic Implications

Balázs Döme,^{*} Mary J.C. Hendrix,[§] Sándor Paku,[†]
József Tóvári,[†] and József Tímár[‡]

From the Department of Tumor Biology and Thoracic Oncology,^{} National Koranyi Institute of Pulmonology, Budapest, Hungary; Department of Tumor Progression, National Institute of Oncology,[‡] Budapest, Hungary; First Institute of Pathology and Experimental Cancer Research,[†] Semmelweis University, Budapest, Hungary; and Children's Memorial Research Center,[§] Feinberg School of Medicine, Northwestern University, Chicago, Illinois*

Although cancer cells are not generally controlled by normal regulatory mechanisms, tumor growth is highly dependent on the supply of oxygen, nutrients, and host-derived regulators. It is now established that tumor vasculature is not necessarily derived from endothelial cell sprouting; instead, cancer tissue can acquire its vasculature by co-option of pre-existing vessels, intussusceptive microvascular growth, post-natal vasculogenesis, glomeruloid angiogenesis, or vasculogenic mimicry. The best-known molecular pathway driving tumor vascularization is the hypoxia-adaptation mechanism. However, a broad and diverse spectrum of genetic aberrations is associated with the development of the “angiogenic phenotype.” Based on this knowledge, novel forms of antivascular modalities have been developed in the past decade. When applying these targeted therapies, the stage of tumor progression, the type of vascularization of the given cancer tissue, and the molecular machinery behind the vascularization process all need to be considered. A further challenge is finding the most appropriate combinations of antivascular therapies and standard radio- and chemotherapies. This review intends to integrate our recent knowledge in this field into a rational strategy that could be the basis for developing effective clinical modalities using antivascular therapy for cancer. (*Am J Pathol* 2007, 170:1–15; DOI: 10.2353/ajpath.2007.060302)

Until recently, vascularization of malignant tumors was considered the exclusive result of directed capillary ingrowth (endothelial sprouting). However, recent advances have been made in identifying the processes involved in angiogenesis and vascular remodeling. Consequently, the simplistic model of an invading capillary sprout has been deemed insufficient to describe the entire spectrum of morphogenic and molecular events required to form a neovascular network. Before discussing the different ways a tumor is vascularized, we should emphasize that these mechanisms are not mutually exclusive; in fact, in most cases they are interlinked, participating concurrently in physiological as well as in pathological angiogenesis. Although the various types of cancer vascularization share some molecular features and may be controlled in part by similar sets of regulatory factors, a considerable variety of differences also exists. Although the molecular regulation of endothelial sprouting has been extensively studied and reviewed in the literature, the morphogenic and molecular events associated with alternative cancer vascularization mechanisms are less understood. Therefore, this review focuses on the pathogenesis of the different forms of “nonsprouting angiogenesis” and, more specifically, on the possibilities and the potential use of novel antiangiogenic and vascular targeting strategies against alternative tumor vascularization mechanisms.

Supported by grants from the Ministry of Economy GVOP-KMA-0040-2004 (J.Ti.) and KFIIF-00063/2005 (B.D.); Ministry of Health ETT-410/2006 (B.D.), ETT-383/2006 (S.P.); National Science TS49887, D048519, F046501 (J.Tó.); Ministry of Education NKFP1a-0024-05 (J.Ti.); and National Institutes of Health/National Cancer Institute grants CA59702 and CA80318 (M.J.C.H.).

The authors indicate no potential conflicts of interest.

Accepted for publication September 19, 2006.

Address reprint requests to József Tímár, M.D., Ph.D., Department of Tumor Progression, National Institute of Oncology, Rath Gy.7-9, Budapest, H-1122 Hungary. E-mail: jtimar@oncol.hu.

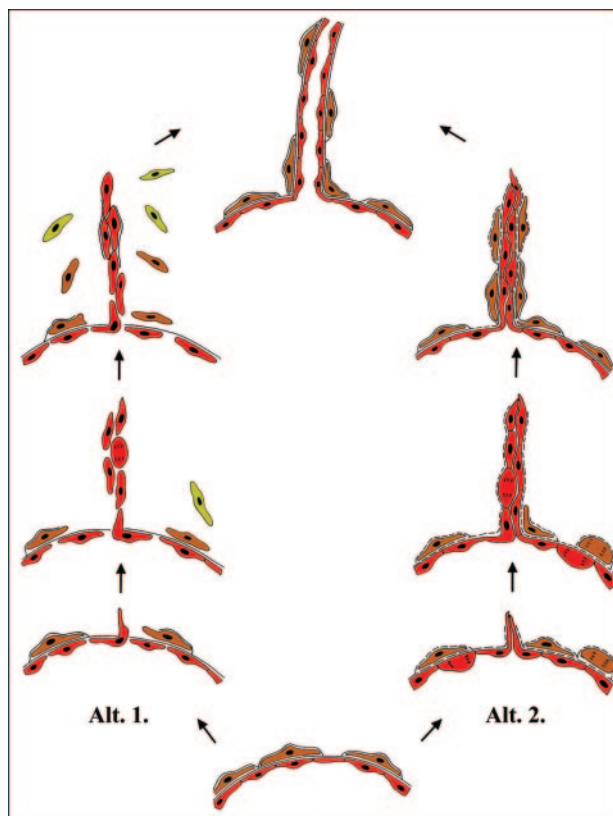


Figure 1. Endothelial sprouting. Schematic representation of the EC sprouting models suggested by Ausprunk and Folkman (Alt. 1¹) and by Paku and Paweletz (Alt. 2²). Red cells represent endothelial cells; brown cells are pericytes. Yellow cells are mural cells of other origin (fibroblasts or bone marrow-derived cells). See *Vascularization Mechanisms in Cancer* for details.

Vascularization Mechanisms in Cancer

Endothelial Sprouting

The best-known mechanism by which tumors promote their own vascularization is inducing new capillary buds from pre-existing host tissue capillaries. The first description of this process dates back to the 1970s, when Ausprunk and Folkman¹ suggested the following sequence for tumor-induced capillary sprouting (Figure 1, Alt. 1). 1) The basement membrane is locally degraded on the side of the dilated peritumoral postcapillary venule situated closest to the angiogenic stimulus, interendothelial contacts are weakened, and endothelial cells (ECs) emigrate into the connective tissue, toward the angiogenic stimuli. 2) There is formation of a solid cord by ECs succeeding one another in a bipolar fashion. 3) Lumen formation occurs by cell-body curving of a single EC or by participation of more ECs in parallel with the synthesis of the new basement membrane and the recruitment of pericytes/mural cells. The main disadvantages of this model are its inability to identify the nature and origin of the stimulus necessary for lumen formation and the assumption that dedifferentiation and redifferentiation take place during the same process, manifest in the loss and regaining of luminal-basal EC polarity. Furthermore, although it has been well established that the stimulus necessary for lumen formation comes from the developing basement

membrane, according to this model, basement membrane deposition occurs after lumen formation. In the early 1990s, a different sprouting model was described² (Figure 1, Alt. 2). This model suggests a three-stage sequence to explain ultrastructural changes during tumor-induced endothelial sprouting. 1) There is structural alteration of the basement membrane characterized by the loss of electron density (gel-sol transition) over the entire circumference of the dilated “mother vessel” (although basement membrane components such as laminin and collagen IV can still be detected by immunohistochemistry). Partial and regulated degradation of the altered basement membrane occur only at places where EC processes (connected by intercellular junctions) are projecting into the connecting tissue. 2) Further migration of ECs, which are arranged in parallel, maintaining their basal-luminal polarity and forming a slit-like lumen, takes place continuously with the lumen of the mother vessel and sealed by intact interendothelial junctions. Basement membrane of low electron density is deposited continuously by the polarized ECs while only the very tip of the growing capillary bud is free of basement membrane material. 3) Proliferating pericytes of the mother vessel migrate along the basement membrane of the capillary bud, resulting in complete pericyte coverage of the new vessel. In parallel, the appearance of electron-dense basement membrane around the maturing capillary buds (sol-gel transition) can be observed. According to the above model, no stimulus is necessary for the induction of lumen formation, because ECs do not lose their polarity during the process.

The molecular background of capillary sprouting has been extensively studied and reviewed in the literature.³ During the process, vessels initially dilate and become leaky in response to vascular permeability factor/vascular endothelial growth factor (VPF/VEGF).⁴ This is mediated by the up-regulation of nitric oxide, the development of fenestrations and vesiculo-vacuolar organelles, and by the redistribution of CD31/PECAM-1 and vascular endothelial (VE)-cadherin. The so-called gel-sol transition of the basement membrane, probably mediated by matrix metalloproteases (MMPs), gelatinases, and the urokinase plasminogen activator system, could be partly responsible for the initiation of EC proliferation and migration. Ang-2 (Angiopoetin-2, a mediator of Tie-2 signaling) is involved in the detachment of pericytes and loosening of the matrix. A vast number of molecules stimulate endothelial proliferation and migration, including transforming growth factor (TGF)- β 1, tumor necrosis factor (TNF)- α , members of the chemokine system and the VEGF, fibroblast growth factor, and platelet-derived growth factor (PDGF) families.³ It could be argued that integrins represent the most important adhesion receptors in migrating ECs.⁵ A wide variety of integrins have been shown to be expressed during sprouting, including $\alpha_1\beta_1$, $\alpha_2\beta_1$, $\alpha_3\beta_1$, $\alpha_5\beta_1$, $\alpha_v\beta_5$, and $\alpha_v\beta_3$. Perhaps the most important among them is $\alpha_v\beta_3$, which mediates the migration of ECs in the fibrin-containing cancer stroma and maintains the sol state of the basement membrane because of its ability to bind to MMP-2. During maturation of nascent vessels, PDGF-BB recruits pericytes and smooth muscle cells,

whereas TGF- β 1 and Ang-1/Tie-2 stabilize the interaction between endothelial and mural cells.³ All in all, sprouting is controlled by a tightly regulated balance of proangiogenic factors and inhibitors: an angiogenic cytokine promotes EC proliferation, migration, or lumen formation, whereas an inhibitor interferes with these steps and modulates the proliferation or migration activity of ECs. However, individual tumor types use various combinations of proangiogenic and inhibitory cytokines.³

Vessel Co-Option

When tumors arise in or metastasize to a pre-existing, usually well-vascularized, tissue, their growth not only depends on expansion, like a balloon, more typical of slow-growing benign tumors, but also on the invasion of host tissue, allowing the cancer cells close contact with the surface of blood vessels. Therefore, malignant cells may initially associate with and grow preferentially along pre-existing microvessels. Until recently, however, no studies have focused on the role played by the host vasculature in the process of tumor vascularization. Although in 1987 Thompson⁶ had already proposed that tumors acquire their vasculature by incorporation of host tissue capillaries, the first study suggesting the existence of vessel co-option was not published until 1999 by Holash et al.⁷ In their model, Holash and colleagues found that co-option is limited to the initial phases of tumorigenesis.⁷ However, additional morphological evidence in human malignancies suggests that co-option of pre-existing blood vessels might persist during the entire period of primary or metastatic tumor growth. In cutaneous melanoma, we found that during tumor growth, there are no signs of directed vessel ingrowth; instead, these tumors appear to grow by co-opting the massive vascular plexus present in the peritumoral connective tissue.⁸ In non-small cell lung cancer, a putatively nonangiogenic growth pattern was observed.⁹ In this "alveolar type" of growth, cancer cells filled the alveoli, entrapping but not destroying the co-opted alveolar capillaries. In liver metastases of human colorectal carcinomas, different growth patterns (replacement, pushing, and desmoplastic) were observed, depending on the degree of differentiation. In replacement growth type, the architecture of the liver was preserved, and the ECs of sinusoids showed low mitotic activity. However, pushing and desmoplastic tumor types destroyed the liver architecture.¹⁰ According to our previous results in experimental hepatic metastases, during growth of sinusoidal-type metastases, invading cancer cells advance between the basement membrane and the endothelial lining of the sinusoids and evoke proliferation of ECs. This process resulted in the development of large tortuous vessels without basement membrane inside the tumor nodules. Conversely, sprouting-type angiogenesis was observed in portal-type metastases. The replacement growth pattern corresponded to sinusoidal-type metastases of undifferentiated tumors, whereas desmoplastic tumors showed similarities to portal-type metastases.¹¹ In the pushing-type growth pattern, we recently described a mechanism for the development of blood

supply and supportive connective tissue¹² (Figure 2). This process includes the proliferation of smooth muscle actin-positive stellate, but not endothelial, cells on the surface of the tumor spheroid accompanied by capillarization of the sinusoids in this region. Because of the pressure of the tumor and the proliferating stellate cells, the hepatocytes disappear from the closest vicinity of the tumor, leading to the fusion of the sinusoids and the appearance of vascular lakes at the surface of the tumor. Together with the collagen-producing cells, these vascular lakes are incorporated into the tumor, resulting in the development of vessel-containing connective tissue columns that traverse the tumor. These columns represent the main structural and functional unit, providing blood supply for the inner part of the growing metastasis. Thus, the presence of the above mechanisms further supports earlier observations that vascularization of metastases in the liver is a heterogeneous process, depending on the degree of tumor differentiation or localization of the metastases within the liver.¹³

Although sprouting capillaries are more vulnerable to apoptosis than their quiescent counterparts,¹⁴ maintenance of incorporated mature microvessels depends on the survival of ECs as well. The continued survival of co-opted ECs is intimately tied to their local microenvironment and, in particular, to the presence of pericytes, survival-promoting cytokines, and extracellular matrix proteins. Thus, the molecular repertoire that ECs may use to survive during vessel co-option is diverse and may vary for a given tumor type or host environment. The major players that control this process are angiopoietins and VEGF.⁷ Based on the model of vessel co-option described by Holash et al.⁷ and in other recent studies,¹⁵ Ang-1 activates Tie-2 and induces subsequent signal transduction pathways favoring EC survival, endothelial quiescence, and tumor-vessel maintenance. Conversely, Ang-2 is thought to act as a nonsignaling Tie-2 ligand that binds to endothelial Tie-2 and thereby negatively interferes with agonistic Ang-1/Tie-2 signals. In co-opted blood vessels, the up-regulation of Ang-2 disrupts the interaction between Tie-2 and Ang-1, which in turn causes the destabilization of capillary walls (ie, the detachment of pericytes from the endothelial tube).¹⁶ Once ECs are separated from pericytes, they become particularly vulnerable. In the presence of VEGF, EC survival and new vessel growth are promoted; however, the lack of stimulatory factors results in the regression of destabilized vessels.¹⁷

VEGF was first described as a survival factor for retinal ECs and has now been shown to promote survival in different EC models. This antiapoptotic and survival function of VEGF seems to depend on an interaction between vascular endothelial growth factor receptor (VEGFR)-2, β -catenin, and VE-cadherin.¹⁸ However, targeting of VEGF has been shown to result in apoptosis only in newly formed tumor vessels and in the developing vasculature of the neonatal mouse but not that of adult mice or of quiescent tumor vascular networks.¹⁷ In summary, although cytokines responsible for EC survival could be the key molecules, their precise role in initiation and maintenance of vessel co-option still requires investigation.

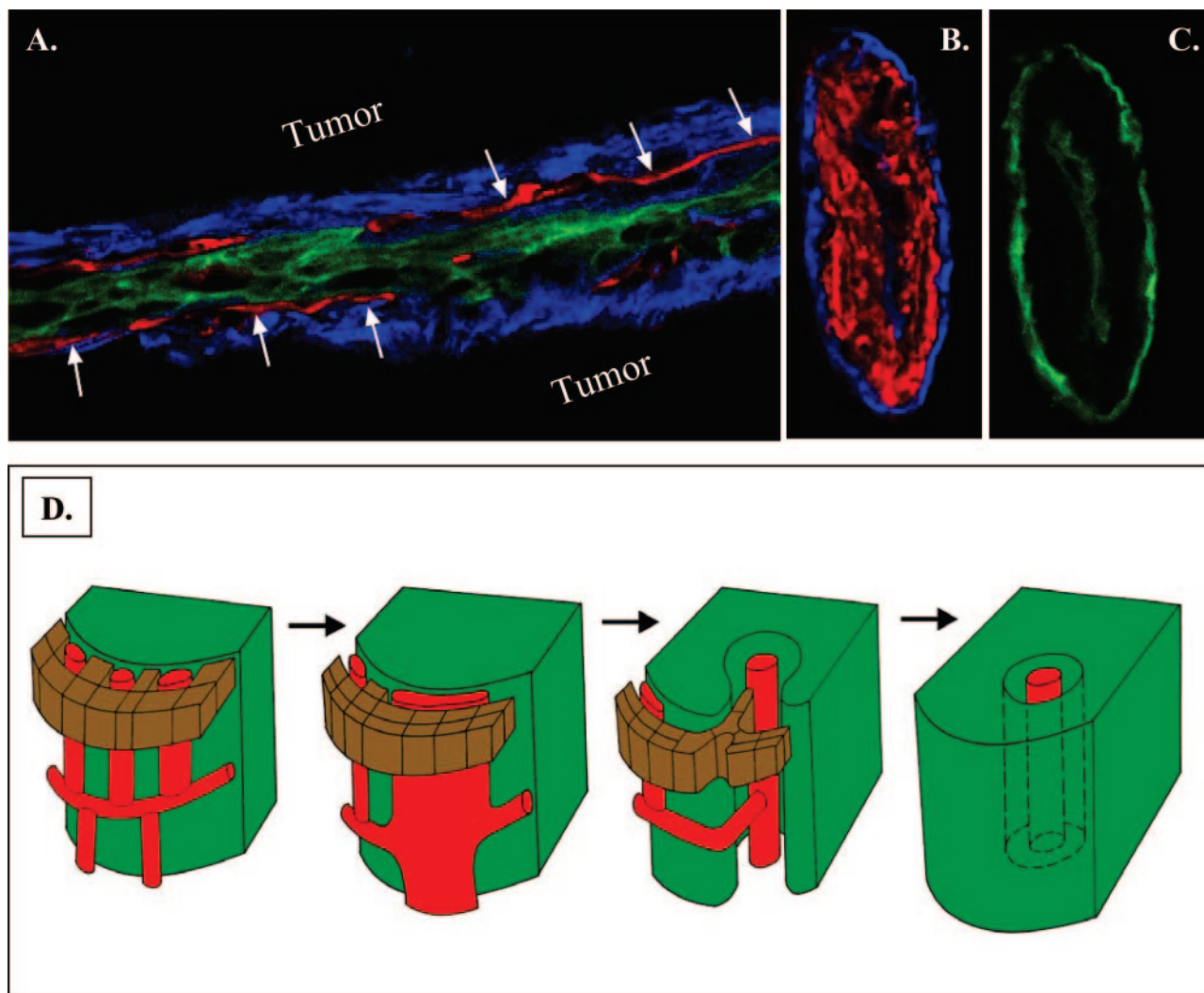


Figure 2. Examples for vessel co-option. **A–D:** Pushing-type angiogenesis in liver metastases of colorectal cancer. **A:** Cross-section of a compressed invagination. SMA-expressing cells (blue fluorescence) facing the tumor tissue, hepatocytes are crowded in the middle of the invagination (pan-cytokeratin, green fluorescence). Continuous CD31 staining (red fluorescence), representing fused sinusoids (**arrows**), is visible in contact with the SMA-positive cells. Note the paucity of sinusoids between the hepatocytes. **B:** Laminin (blue fluorescence) co-localizes with $\alpha 6$ integrin within the columns. The column tightly packed with SMA-positive cells (red fluorescence). **C:** $\alpha 6$ integrin (green fluorescence) is present at the periphery of the column and around the central vessel. **D:** Schematic representation of the development of vasculature in pushing-type liver metastases. For better visibility of the vessels, hepatocytes are depicted only in the upper part of the drawings. At the early stage of the tumor development, the tumor faces normal liver architecture. As the compression of the tumor grows, the hepatocytes “step back,” and fusion of the sinusoids takes place. The fused vessel, together with the newly synthesized connective tissue, is incorporated into the tumor. The pressure of the tumor results in the separation of the vessel from the liver parenchyma. The vessel in the direction of the axis of the column remains connected to the sinusoidal system of the liver. Column formation is finished by the back-to-back fusion of the basement membranes of the tumor bulges. Green, tumor; brown, hepatocytes; red, sinusoids and central vessel.

Intussusceptive Microvascular Growth (IMG)

IMG refers to vessel network formation by insertion of connective tissue columns, called tissue pillars, into the vessel lumen and to subsequent growth of these pillars, resulting in partitioning of the vessel lumen (Figure 3). This type of angiogenesis, which has been observed in a wide variety of normal and malignant tissues, is faster and more economical than sprouting, occurs within hours or even minutes and does not primarily depend on EC proliferation, basement membrane degradation, and invasion of the connective tissue.¹⁹ However, in contrast to sprouting, IMG can work only on existing vessel networks. The most important feature of IMG, therefore, seems to be its ability to increase the complexity and

density of the tumor microvessel network already built by sprouting, independent of EC proliferation. In addition, IMG can provide more surface area for further sprouting. Its molecular regulation, however, is poorly understood since IMG was first described only a few years ago. Nevertheless, the role of some players is gradually becoming clearer. We know that local stimuli, such as intravascular shear stress, might induce a cascade of physiological or pathological reactions in ECs, and new capillary development by tissue pillar formation could be one of them.²⁰ Furthermore, intussusception is certainly synchronized by several cytokines. Major candidates are those capable of mediating information between ECs or from ECs to mural cells, such as PDGF-BB, angiopo-

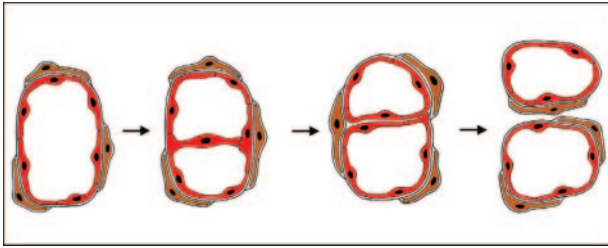


Figure 3. Intussusceptive microvascular growth. Schematic representation of intussusceptive microvessel growth. The first step of the process is the development of the transluminal endothelial bridge. This is followed by the reorganization of the endothelial lining, a process that is largely unknown. The division of the vessel is completed by the development of a connective tissue pillar through the vessel lumen. Red cells are endothelial cells; brown cells are pericytes. Gray, basement membrane.

etins, and their Tie receptors, TGF- β , monocyte chemoattractant protein-1, and ephrins and Eph-B receptors.¹⁹

After the initial stage of immature capillary network formation by sprouting, additional vascular growth and development of complex vascular beds, including their continuous remodeling and adaptation, may occur by intussusception in cancers. The absence of intense EC proliferation in IMG implies that neovascularization by this mechanism would be resistant to angiostatic treatment in itself.

Glomeruloid Angiogenesis

Glomeruloid bodies (GBs) are best known in high-grade glial malignancies, where they are one of the diagnostic histopathological features of glioblastoma multiforme. However, these complex vascular aggregates have also been described in a wide variety of other malignancies.²¹ They are composed of several closely associated microvessels surrounded by a variably thickened basement membrane within which a limited number of pericytes are embedded. In recent studies, the presence of GBs was associated with markers of aggressive tumor behavior and significantly reduced survival in cancer patients.²² In the first animal model,²³ GBs developed in mother vessels from recruitment and proliferation of ECs and pericytes (in the absence of tumor cells), and VEGF was essential for their induction and maintenance. In contrast to this model and based on our previous results in the first experimental tumor model of glomeruloid angiogenesis,²⁴ we believe that GB formation starts immediately after tumor cell extravasation, much earlier than necrosis appears within the metastases. We found that the proliferating and migrating tumor cells are able to pull the capillaries and the adjacent capillary branching points into the tumor cell nests. This process leads to the appearance of simple coiled vascular structures that later develop into GBs with multiple narrowed afferent and efferent capillaries (Figure 4). Despite the absence of sprouting angiogenesis, necrosis was scarce in these lesions, suggesting that the blood supply from the pre-existent vascular bed is sufficient to provide the tumor cells with oxygen and nutrients. This type of GB formation cannot be termed as true angiogenesis; it rather represents a remodeling of the existing vasculature of the host

tissue. Whether GBs represent an accelerated form of angiogenesis or a dysfunctional, possibly abortive, form remains an open question. However, it cannot be excluded that “active” and “passive” types of glomeruloid angiogenesis can operate concurrently in various cancer types.

Postnatal Vasculogenesis: The Role of Endothelial Progenitor Cells

Vasculogenesis (defined as the *in situ* differentiation of vascular ECs from primitive precursor cells) has long been thought to occur only in the early phases of vascular development. Recent studies, however, have demonstrated that circulating bone marrow-derived endothelial progenitor cells (EPCs) home to sites of physiological and pathological neovascularization and differentiate into ECs (Figure 5). EPCs may be mobilized by tumor tissue-derived cytokines from the bone marrow by a mechanism recently described by Asahara et al.²⁵ Best characterized among these cytokines is VEGF. During tumor progression, the level of circulating VEGF has been shown to rise, and this level was found to correlate with the number of EPCs in the circulation. Furthermore, PDGF-CC promoted vascularization in part by stimulating outgrowth of EPCs. In contrast, Ang-1 was shown to reduce EPC mobilization from bone marrow (reviewed in Ref. 26).

After homing, ie, after adhesion and insertion of EPCs into the monolayer of surrounding mature vascular ECs, additional local stimuli may promote the activation of local endothelium to express adhesion molecules to recruit EPCs. This process may be completed by mechanisms not yet elucidated. In addition to the physical contribution of EPCs to newly formed microvessels, the angiogenic cytokine release of EPCs may be a supportive mechanism to improve neovascularization as well.²⁷ It is also important to note that Lyden et al recently identified VEGFR-1⁺ hematopoietic progenitor cells that multiply in the bone marrow, mobilize to the peripheral blood along with VEGFR-2⁺ EPCs, and incorporate into pericapillary connective tissue, thus stabilizing tumor vasculature.²⁸ More interestingly, these cells seem to home in before the tumor cells arrive, promoting metastatic growth by forming niches where cancer cells can locate and proliferate.²⁹

Although EPCs obviously participate in the vascularization process of malignant tumors, it is still unclear whether they are essential for these processes or what the relative contribution of EPCs is compared with that of *in situ* proliferating ECs. Moreover, it has yet to be determined whether EPCs can be targeted to treat certain types of malignancies, or alternatively—as they are endowed with the capacity to home to the tumor vasculature—can be used to deliver toxins or vascular-targeting agents.

Vasculogenic Mimicry

“Vasculogenic mimicry” is defined by the unique ability of aggressive melanoma cells to express an EC phenotype

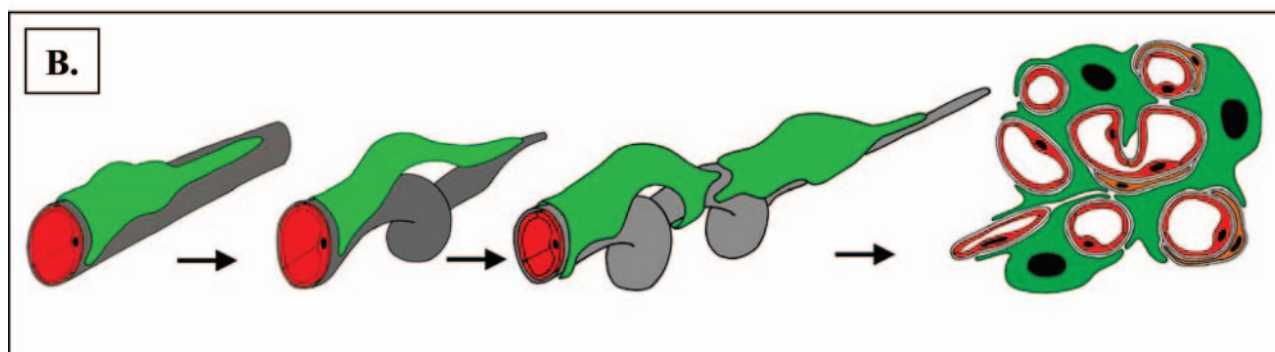
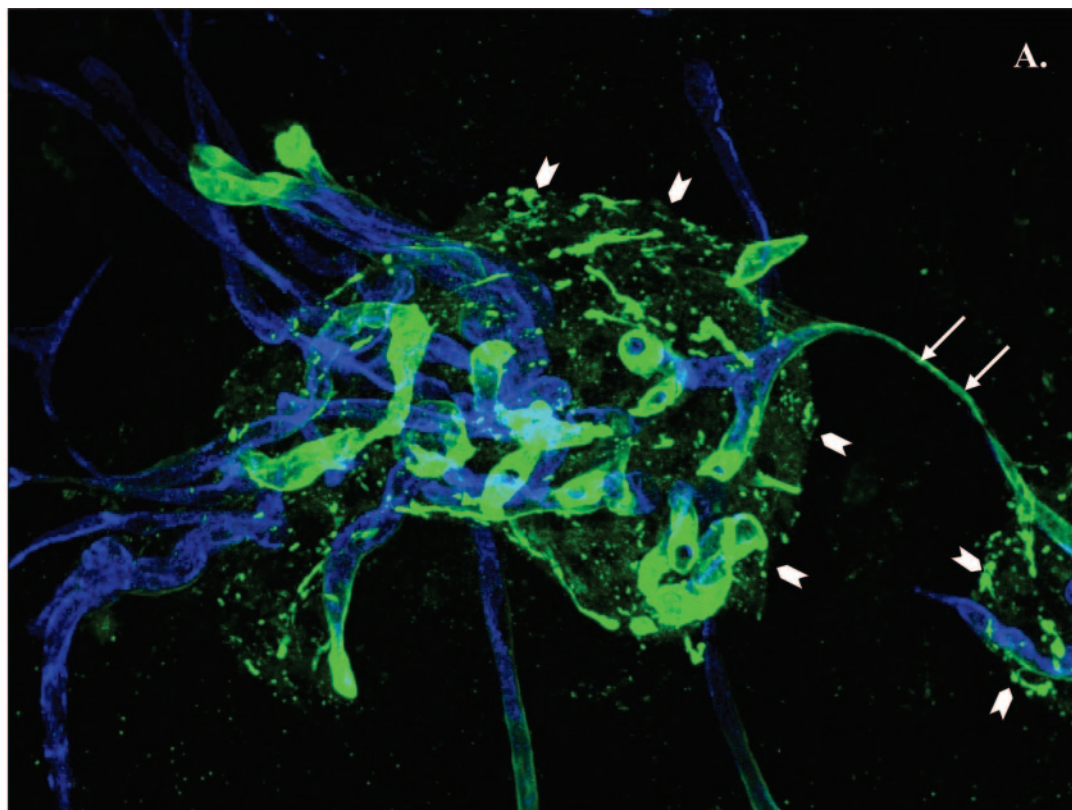


Figure 4. Glomeruloid angiogenesis. **A:** Experimental brain metastases stained for laminin (green fluorescence) and CD31 (blue fluorescence), 28 days following intracarotid inoculation of the A2058 human melanoma cell line. Glomeruloid bodies are connected to each other by a capillary that is very small in diameter (**arrows**). The outlines of the metastases are clearly visible because of the strong laminin positivity of the tumor cells (**arrowheads**). **B:** Schematic representation of glomeruloid body formation. Following extravasation, the tumor cells (green) adhere firmly to the abluminal surface of the capillary basement membrane (gray). In the first step, because of the contractile force of the tumor cell a loop develops on the capillary. Proliferating tumor cells pull the capillary inward, resulting in the development of further loops and reduction of the diameter of the capillary segment lying outside the glomeruloid body. The last drawing shows the cross-section of a fully developed glomeruloid body built by ECs (red), pericytes (brown), and tumor cells (green). Extreme large cytoplasmic projections of the tumor cells adhere to different segments of the capillary.

and to form vessel-like networks in three-dimensional culture, “mimicking” the pattern of embryonic vascular networks and recapitulating the patterned networks seen in patients’ aggressive tumors correlating with a poor prognosis.³⁰ Comparative global gene analyses of aggressive and poorly aggressive human cutaneous and uveal melanoma cell lines unexpectedly revealed the ability of aggressive tumor cells to express genes (and proteins) associated with multiple cellular phenotypes and their respective precursor stem cells, including endothelial, epithelial, pericyte, fibroblast, and several other

cell types.^{31–33} These new and intriguing findings support the premise that aggressive melanoma cells acquire a multipotent, plastic phenotypea concept that challenges our current thinking on how to target tumor cells that can possibly masquerade as other cell types, particularly with embryonic stem cell-like properties. The etiology of the melanoma vasculogenic phenotype remains unclear; however, it seems to involve dysregulation of the lineage-specific phenotype and the concomitant transdifferentiation of aggressive cancer cells into other cell types—such as endothelial-like cells. Vasculogenic

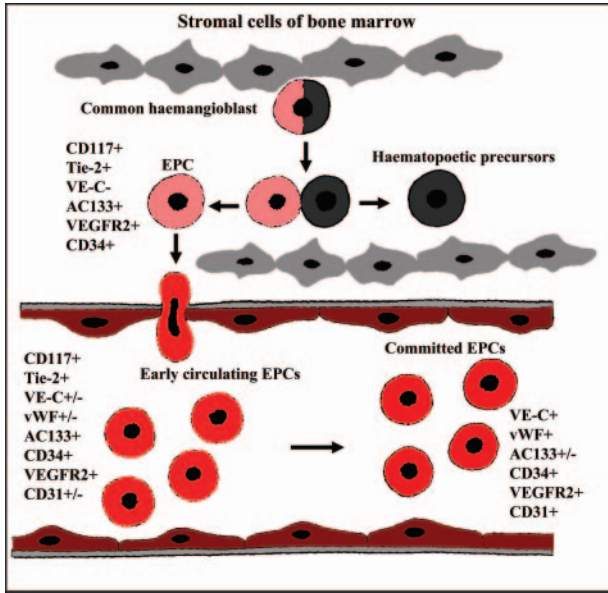


Figure 5. Endothelial progenitor cells. Schematic representation of postnatal vasculogenesis. The term “EPC” encompasses a group of cells existing in a variety of stages ranging from common hemangioblasts to fully differentiated ECs. Although their putative precursors and the exact differentiation lineage of EPCs remain to be determined, to date it is widely accepted that early EPCs (localized in the bone marrow or immediately after migration into the circulation) are AC133⁺/CD34⁺/VEGFR-2⁺ cells, whereas circulating EPCs are positive for CD34 and VEGFR-2, lose AC133, and begin to express cell surface markers typical of mature ECs such as CD31, VE-cadherin, and von Willebrand Factor (vWF).

mimicry has been confirmed in breast, prostate, ovarian, chorio-, and lung carcinomas; synovial-, rhabdomyo-, and Ewing sarcomas; and pheochromocytoma.³⁴ Expression profiling studies revealed that the most significantly up-regulated genes by aggressive melanoma cells include those that are involved in angiogenesis and vasculogenesis, such as the genes encoding VE-cadherin, erythropoietin-producing hepatocellular carcinoma-A2 (EphA2), MMPs, and laminin 5 γ 2 chain (LAMC2). These molecules, with their binding partners, are a few of the factors required for the formation and maintenance of blood vessels and also for vasculogenic mimicry in melanomas. Perhaps equally significant is the down-regulation of the gene *MART-1* (melanoma antigen recognized by T cell 1, also called Melan-A), a classic marker for melanocytes and melanoma, by aggressive melanoma cells. The concept of vasculogenic mimicry was developed further to include the existence of a fluid-conducting, laminin-containing extracellular matrix meshwork, providing a site for nutritional exchange for aggressive tumors, and therefore possibly preventing necrosis (Figure 6).^{34,35} Functional studies revealed the close association of tumor-cell-lined networks with angiogenic mouse vessels at the human-mouse interface and the cooperation between the two systems.^{36,37} The molecular dissection of the physiological mechanisms critical to the function of the fluid-conducting meshwork revealed the biological relevance of the up-regulated expression of tissue factor pathway-associated genes—essential for the anticoagulation properties of the intratumoral, extracellular matrix-rich extravascular fluid-conducting path-

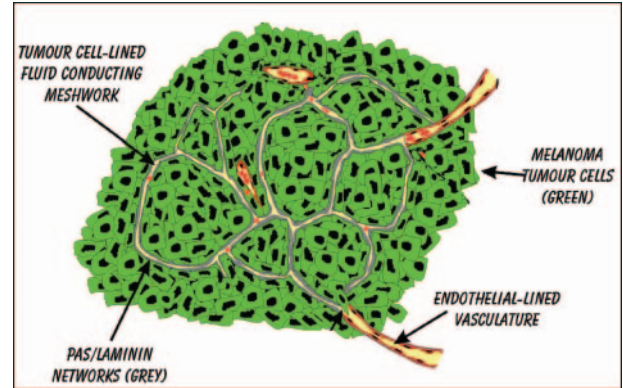


Figure 6. Vasculogenic mimicry. This diagram represents the current interpretation of data generated from several studies involving the use of tracers and perfusion analyses of mice containing aggressive melanoma cells (green) during tumor development. The endothelial-lined vasculature is closely apposed to the tumor cell-formed fluid conducting meshwork, and hypothetically, it is presumed that as the tumor remodels, the vasculature becomes leaky, resulting in the extravascular conduction of plasma. There is also evidence of a physiological connection between the endothelial-lined vasculature and the extravascular melanoma meshwork.

way. Gene profiling, protein detection, and immunohistochemistry validation demonstrated up-regulation of tissue factor (TF), TF pathway inhibitor 1 (TFPI-1), and TFPI-2—critical genes that initiate and regulate the coagulation pathways—in aggressive, as opposed to poorly aggressive, melanoma. It was found that TFPI-2 contributes to vasculogenic mimicry and endothelial transdifferentiation by melanoma cells, whereas TFPI-1 has anticoagulant functions for perfusion of fluid-conduction meshworks formed by TF-expressing melanoma cells. Additional studies have focused on the signal transduction pathways that regulate blood vessel formation and stabilization during vasculogenesis and angiogenesis, addressing critical signaling events that regulate melanoma vasculogenic mimicry and their endothelia-like phenotype.^{38–40} It was demonstrated that VE-cadherin and EphA2 were co-localized in cell-cell junctions and VE-cadherin can regulate the expression of EphA2 at the cell membrane by mediating its ability to become phosphorylated through interactions with its membrane-bound ligand, ephrin-A1. These studies illuminate a novel signaling pathway that could be potentially exploited for therapeutic intervention. Additional investigation uncovered the role of phosphoinositide 3-kinase (PI3K) as a critical regulator of vasculogenic mimicry, specifically affecting membrane type-1 MMP (MT1-MMP) and MMP-2 activity. Both MMPs are essential for the process of vasculogenic network formation by aggressive melanoma tumor cells, and the downstream effect on the cleavage of laminin 5 γ 2 chain into the γ 2' and γ 2x promigratory fragments.^{38,39} Furthermore, these results showed that blocking PI3K resulted in abrogation of vasculogenic mimicry. Most recent studies have identified focal adhesion kinase (FAK)-mediated signal transduction pathways to promote not only the aggressive phenotype but also vasculogenic mimicry of melanoma cells as well.⁴⁰ In addition, expression of a negative regulator of FAK signaling, the FAK-related non-kinase in aggressive melanoma cells, resulted in an inhibition of melanoma vas-

culogenic mimicry concomitant with a decrease in melanoma cell invasion and migration. This biological effect was mediated in part through an extracellular signal-regulated kinase 1/2 signaling pathway that resulted in a down-regulation of urokinase and MMP-2/MT1-MMP activity.⁴⁰ These results suggest that FAK may serve as a new target for therapeutic intervention in treating aggressive melanomas with capabilities for vasculogenic mimicry.

Antivascular Therapy of Cancer

It has been over 30 years since Judah Folkman hypothesized that tumor growth is angiogenesis dependent.⁴¹ Subsequent research has led to the identification of several regulators of angiogenesis, some of which represent therapeutic targets. However, although antivascular agents are often highly active in preclinical studies, recent clinical trials including these agents have been both encouraging and disappointing. Because of the predominant role of capillary sprouting and its main molecular mediator VEGF in tumor vascularization, inhibition of VEGF seems to be necessary but is probably insufficient to halt tumor progression permanently in many cancer types. Due to the existence of multiple vascularization mechanisms and angiogenic signaling pathways, inhibition of just a single pathway will presumably trigger alternative vascularization mechanisms and additional growth factor pathways. Consequently, application of antivascular therapy in cancer patients requires the identification of the individual vascularization profile and the molecular machinery behind the vascularization process and, furthermore, the individualization of antivascular therapy to realize any potential benefits.^{42,43} In the second part of this review, we will briefly summarize the antivascular therapies that are currently being tested in the clinic. Subsequently, we will give an overview of how these classes of agents can be incorporated in the current multimodality of anticancer strategies. Finally, we will discuss potential novel approaches that enforce tumor regression by exploiting the emerging basic knowledge of tumor vascularization.

Antivascular Strategies in Cancer Therapy: Current Status of the Clinical Development

Any classification of antivascular strategies is difficult, with overlap in several features. However, the main categories of these approaches that have been developed are angiosuppressive (anti-angiogenic agents) and vascular-targeting therapies (vascular-disrupting agents).⁴⁴ Although metronomic chemotherapy (MCT) uses conventional cytotoxic drugs, the main targets of this strategy are the tumor ECs. This is the reason that Browder et al⁴⁵ coined the term "anti-angiogenic chemotherapy" to describe this treatment and why MCT is discussed here.

It is beyond the scope of this review to discuss all drugs that affect tumor capillaries. Therefore, we concentrate here on the agents that are at a more advanced stage of clinical development.

Angiosuppressive Therapy (Antiangiogenic Agents)

This approach is motivated by the fact that neoangiogenesis in cancer requires the induction of EC proliferation by specific or nonspecific mitogens. These agents target the production of endothelial mitogens, the mitogens themselves, their endothelial receptors, the associated signaling pathways, the endothelial integrins and the MMPs⁴⁶ (Table 1). Consequently, it is most probable that angiosuppressive therapy can only be applied when cancer vascularization involves EC sprouting and/or postnatal vasculogenesis (Table 2).

Despite the promising preclinical results with these agents, in the early clinical trials positive responses in patients were rarely seen. The clinical breakthrough for angiosuppressive therapy came from a phase III trial demonstrating a significantly prolonged survival when bevacizumab, an anti-VEGF antibody, was used with chemotherapy in metastatic colorectal cancer patients.⁴⁷ Based on these results, bevacizumab became the first antiangiogenic agent to be approved by the United States Food and Drug Administration (FDA) for cancer treatment. In subsequent phase III trials, bevacizumab in combination with standard chemotherapy improved overall survival in lung cancer patients and progression-free survival in breast cancer patients.⁴² In addition, it has been reported to be active in patients with metastatic renal-cell cancer as monotherapy (benefit in progression-free survival but not in overall survival).⁴⁸

Further clinical success was obtained recently with broad-spectrum multitargeted agents that target VEGF receptors and other tyrosine kinases present in endothelial and cancer cells (Table 1). Phase III trials have demonstrated the efficacy of SU11248/sunitinib [targeting VEGFR-1, -2; platelet-derived growth factor receptor (PDGFR), FLT3, and c-Kit] and BAY-43-9006/sorafenib (targeting VEGFR-2, -3; PDGFR, RET, c-Kit, and Raf) in the treatment of patients with renal cancer.⁴² Based on these results, sunitinib and sorafenib are now approved by the FDA as monotherapies for kidney cancer. Promising results have also been found with the combination of ZD6474 [targeting VEGFR2, epidermal growth factor receptor (EGFR), and RET] and chemotherapy in non-small cell lung cancer patients. Interestingly, replacing bevacizumab with similar tyrosine kinase (TK) inhibitors, such as PTK787/ZK 222584/vatalanib (targeting VEGFR-1, -2, -3; PDGFR- β , and c-Kit), in the combined regimen did not result in similar efficacy in chemotherapy-naïve or previously treated colorectal cancer patients.⁴⁹ However, the clinical success of bevacizumab, sunitinib, and sorafenib as novel medicines for the treatment of cancer patients has confirmed the relevance of angiogenesis research and has stimulated the search for novel and more effective antiangiogenic approaches. Ac-

Table 1. Examples of Antivascular Agents in Clinical Development

Agent	Target/mechanism of action	Phase
Angiosuppressive and anti-HIF-1 agents		
Anti-VEGF agents		
Bevacizumab	mAb against VEGF-A	III; FDA-approved in colorectal cancer
VEGF-trap	VEGF-A, PIGF, VEGF-B binding	I
VEGF-AS	VEGF-A, VEGF-C, VEGF-D	I
VEGFR and other TK receptor targeting agents		
IMC-1C11	mAb against VEGFR2	I
ZD6474	VEGFR-2, EGFR, RET	I/II
PTK787/ZK222584 (vatalanib)	VEGFR-1, -2, -3; PDGFR- β , c-Kit	II/III
BAY 43-9006 (sorafenib)	VEGFR-2, -3; PDGFR, RET, c-Kit, Raf	III; FDA-approved in renal cancer
SU11248 (sunitinib)	VEGFR-1, -2; PDGFR, FLT3, c-Kit	III; FDA-approved in renal cancer
AG-013736	VEGFR-1, -2, -3; PDGFR- β , c-Kit	I/II
Angiozyme	VEGFR-1 mRNA-destroying ribozyme	I/II
Integrin signaling		
EMD 121974 (Cilengitide)	Mimicking the RGD ligand recognition peptidic domain common to α_v integrin ligands	I/II
MEDI-522 (Vitaxin)	mAb against $\alpha_v\beta_3$	I/II
Miscellaneous		
Thalidomide	Multiple inhibitory effect on bFGF, VEGF, and TNF- α -induced EC sprouting	I/II
AE-941	Inhibitor of MMP-2, -9, -12, and VEGFR-2	II/III
Marimastat	MMP2/9	III
Bay-12-9566	MMP2/9	III
AG3340	MMP2/9	III
Endostatin	Integrin $\alpha_5\beta_1$	II/III
ABT-627	Endothelin receptor	II/III
Nonselective inhibitors of HIF-1		
Topotecan and other camptothecin analogues, DX-2-1, GL331	Topoisomerase I/II	Preclinical; phase I
2-Methoxyestradiol	Microtubules	I
YC-1	Soluble guanyl cyclase	Preclinical
PX-478	Translation/deubiquitination	Preclinical
17-AAG, geldanamycin, radicicol, KF58333	HSP-90	Preclinical
VDAs		
Ligand-directed VDAs		
L19 single chain Fv	ED-B domain of fibronectin	Preclinical
mAb against endoglin linked to ricin-A	Endoglin	Preclinical
Anti-VCAM-1 AB linked to coagulation inducing protein TF	VCAM-1	Preclinical
Anti-TES-23 linked to neocarzinostatin	CD44-related EC marker	Preclinical
Naked AB against phosphatidylserine	Phosphatidylserine	Preclinical
$\alpha_v\beta_3$ targeting ligand delivering EC apoptosis inducing ATP $^{\mu}$ -Raf	Targeted ATP $^{\mu}$ -Raf gene	Preclinical
Small molecule VDAs		
CA4-prodrug; AVE8062 and Oxi4503 (synthetic analogues of combretastatin)	Actin polymerization, filament stabilization via Rho signaling pathway	I/II
ZD6126	Inhibition of EC microtubule polymerization	I
ABT-751	β -Tubulin	I
DMXAA (analogue of flavone acetic acid)	TNF- α release, induction of nuclear factor- $\kappa\beta$	I/II

mAb, monoclonal antibody; PIGF, placenta growth factor; bFGF, basic fibroblast growth factor; 17-AAG, 17-N-allylamino-17-demethoxygeldanamycin; VCAM-1, vascular cell adhesion molecule-1; CA4, combretastatin-A4.

cordingly, various angiosuppressive strategies are being actively investigated, most of which are registered with the clinical trials database of the National Cancer Institute (<http://www.nci.nih.gov/clinicaltrials>).

Vascular Targeting Therapy (Vascular Disrupting Agents; VDAs)

Vascular targeting therapy (including anti-EC antibodies and ligand based and small molecule VDAs; Table 1) recognizes the fact that clinical diagnosis of cancer

frequently occurs when the tumor tissue has already established its vasculature.^{44,46} This strategy relies on ability of VDAs to distinguish the ECs of tumor capillaries from normal ones based on their different phenotype, increased proliferative potential and permeability, and inherent dependence on the tubulin cytoskeleton. VDAs cause selective and rapid shut-down of the established tumor capillaries, resulting in extensive cancer cell death in the central areas of tumors, although they leave the perfusion in peripheral tumor regions relatively intact.^{44,50} It is evident from

Table 2. Theoretical Strategy of Antivascular Therapy of Cancer According to the Stage of Tumor Progression and to the Mechanisms of Vascularization

Type of vascularization	Individual cancer cells in host tissue	Microscopic tumor pre-angiogenic phase	Microscopic tumor angiogenic phase	Macroscopic tumor
Sprouting	Antiangiogenic agents; metronomic chemotherapy	Antiangiogenic agents; metronomic chemotherapy	Antiangiogenic agents; metronomic chemotherapy	Antiangiogenic agents; "vascular targeting" therapy; metronomic chemotherapy
Intussusceptive microvascular growth	N.A.	N.A.	Vascular targeting therapy; metronomic chemotherapy	Vascular targeting therapy; metronomic chemotherapy
Vessel co-option	N.A.	N.A.	Vascular targeting therapy	Vascular targeting therapy
Glomeruloid angiogenesis	N.A.	N.A.	Vascular targeting therapy	Vascular targeting therapy
Vasculogenic mimicry	N.A.	N.A.	Vascular targeting therapy; metronomic chemotherapy	Vascular targeting therapy; metronomic chemotherapy
Postnatal vasculogenesis (endothelial progenitors)	N.A.	N.A.	Antiangiogenic agents; vascular targeting therapy; metronomic chemotherapy	Antiangiogenic agents; vascular targeting therapy; metronomic chemotherapy

N.A., not applicable.

the mechanism of VDAs that the effects of these drugs do not depend on the type of vascularization occurring in a given cancer. Based on promising preclinical developments, several VDAs have entered clinical development.⁵¹

MCT and Its Antivascular Effects

Among the different antivascular strategies, MCT merits particular mention. MCT refers to the close, even daily, administration of chemotherapeutic drugs in doses below the maximum tolerated dose, over prolonged periods, and with no extended drug-free breaks. Phase II trials of MCT, sometimes applied in combination with antiangiogenic drugs, have yielded promising results in adult patients with advanced cancer.^{52,53} Furthermore, pediatric oncologists successfully use a metronomic-like modality of chemotherapies called "maintenance chemotherapy" to treat various pediatric malignancies such as acute lymphoblastic leukemia, neuroblastoma, or Wilms' tumor; however, the anti-angiogenic background of maintenance chemotherapy is poorly described.⁵⁴

Although cytotoxic effects of MCT in the tumor parenchyma could still contribute to the observed efficacy of metronomic regimens, preclinical studies suggest that the primary targets of MCT are the tumoral ECs. Low-dose chemotherapy affects tumor capillaries directly (growth arrest and apoptosis of activated ECs) but also induces the production of an angiogenesis inhibitor thrombospondin-1 and suppresses the mobilization of EPCs.⁵²

As mentioned above, several phase I and II studies were performed involving low, continuous doses of cytotoxic drugs, with encouraging results.⁵³ However, the clinical benefits of MCT remain to be validated in randomized prospective phase III trials. There is also a need for surrogate markers to help define the optimal dose of this approach. Circulating ECs⁵⁵ and EPCs⁵⁶ have been

used successfully as markers in preclinical and early clinical studies but have not yet been validated clinically. Further challenges are the definition of valid clinical endpoints, the confirmation of long-term safety of MCT, and the identification of suitable antiangiogenic agents and VDAs to be combined with MCT. Finally, it will be important to determine the types of vascularization that might be the most responsive to this therapy. MCT is probably more effective in EC sprouting, postnatal vasculogenesis, IMG, and vasculogenic mimicry (Table 2). However, detailed clinicopathologic analysis is needed to confirm this hypothesis.

Considerations for Combination Treatment Strategies

Because antivascular agents and traditional anticancer strategies have distinctive target cells and mechanisms of action, it should be possible to achieve an increase in therapeutic efficacy with little or no increase in toxicity. In fact, although some antivascular agents have demonstrated activity as monotherapies, most human trials to date indicate that they are most effective when combined with conventional antitumor strategies, especially chemotherapy.^{42,43}

Combination of Angiosuppressive and Chemo- and/or Radiation Therapy

Angiosuppressive therapy reduces cancer growth by suspending the blood supply, resulting in hypoxia. Because hypoxia itself is a major cause of ineffective chemo-irradiation therapy,⁵⁷ one would expect that a further decrease in intratumoral oxygen levels would deteriorate the efficacy of a cytotoxic regime, but experimental and clinical data do not support this scenario. In

several preclinical models, a combination of cytotoxic drugs (taxanes, cisplatin, or 5-fluorouracil) with angiogenesis inhibitors (TNP470, endostatin, SU11248) produced at least additive but in certain cases synergistic antitumoral effects.⁴⁶ Thalidomide, a still ill-defined angiogenesis inhibitor, has also been shown successful preclinically in combination with standard anticancer regimens in solid tumors.⁵⁸ In addition to experimental data, there are now clinical examples of the improved efficacy of chemotherapy in combination with an angiostatic agent. As mentioned above, bevacizumab in combination with chemotherapy improved overall survival in colorectal and lung cancer patients and progression-free survival in breast cancer patients (see review⁴²). In addition, the combination of bevacizumab and chemotherapy was found to be active in pancreatic⁵⁹ and ovarian⁶⁰ cancer patients.

There are several explanations for the improved efficacy. An obvious effect of angiogenesis inhibitors is the decrease in interstitial pressure in cancer tissue improving the delivery of cytotoxic agents. Furthermore, a hypothesis called "normalization of tumor vasculature" was put forth by Jain and colleagues recently to explain the clinical effects of antiangiogenic agents.⁴² According to this theory, tumor vasculature is structurally insufficient to provide maximal blood supply for cancer cells as a result of capillary leakiness and tortuosity. Because the key regulator cytokine family of tumoral vessels is the VEGF/VEGFR system, targeting it could potentially help in the "normalization" of tumor vasculature and in the improvement of the delivery of chemotherapeutic agents.⁴² Accordingly, recent experimental data indicate that anti-VEGF therapy induces rapid alterations in tumor vasculature. Within a few hours, EC proliferation is halted, luminal stability vanishes, and circulation ceases in tumor capillaries. Some ECs undergo apoptosis and disappear. Remaining capillaries lack endothelial fenestrations and have reduced VEGFR-2 and VEGFR-3 expression.⁶¹ Thus, inhibition of VEGF signaling devastates some tumor capillaries and transforms others into a more normal phenotype.⁴²

Further mechanisms for the additional benefits experienced for combined chemo- and angiostatic therapy might be the direct killing of proliferating ECs and/or the inhibition of the mobilization/viability of EPCs by cytotoxic drugs. Results of preclinical studies support this hypothesis. On the other hand, VEGF inhibition might have direct cytotoxic effects on tumor cells that aberrantly express VEGF receptors and depend to some extent on VEGF for their survival. Finally, it has also been suggested recently that antiangiogenic agents prevent rapid cancer cell repopulation during the break periods between courses of chemotherapy (see review⁴³).

Experimental studies indicate that antiangiogenic therapy in combination with irradiation is an encouraging concept for the improvement of the radiation response of tumors.⁶² In addition, recent discoveries show that the EC layer of the tumor vessels is one key target of radiotherapy.⁶³ In fact, the antivascular effect of radiotherapy predicts its anti-cancer effect.⁶⁴ Thus far, although early phase human trials have also yielded promising results,

there are no large phase III trials known in which such combinations were successfully applied. Nevertheless, the discovery of the "normalization window" of angiostatic agents when combined with radiotherapy in preclinical models⁶⁵ suggests that it would be as difficult to design a successful combination strategy with radiation as with chemotherapy.

In this normalization window (the time period during which the vasculature normalizes and hypoxia decreases), the antiangiogenic drugs improve the efficacy of chemoradiotherapy.⁴² Although these studies were performed in experimental tumor systems, one may expect a similar effect on the human tumor vasculature and oxygenation. However, intratumoral hypoxia, responsible for chemo- and radiotherapy resistance and triggering molecular pathways that promote cancer progression, is due not only to the inefficient blood supply by the abnormal tumor vessels but to the systemic anemia of the host as well.⁶⁶ Unfortunately, although the oxygen tension of experimental tumors tends to rise with increasing Hb levels⁶⁷ and treatment with recombinant human erythropoietin (rHuEpo) significantly reduces the risk for red blood cell transfusions in cancer patients, correction of anemia with rHuEpo does not necessarily improve survival of cancer patients.⁶⁶ The issue of Epo/EpoR co-expression in tumor cells and EpoR expression in ECs is critical in this perspective. The expression of EpoR in tumor cells has raised the possibility that exogenous rHuEPO may directly influence cancer cell proliferation, apoptosis, or sensitivity to chemoradiation therapy. In addition, the EpoR expression in ECs has suggested potential effects of Epo on the tumor capillaries, such as the stimulation of angiogenesis.⁶⁸ However, as it has been suggested by experimental studies, the overall direct effect of Epo-EpoR signaling on tumor progression and therapy is not a straightforward one. For instance, rHuEpo administration has recently been shown to be associated with decreased intratumoral VEGF expression, remodeling of tumor capillaries, and increased chemosensitivity to 5-fluorouracil treatment of human tumor xenografts.⁶⁹ In a preclinical myeloma model, rHuEpo induced tumor regression and antitumor immune responses.⁷⁰ In addition, human kidney carcinoma and myelomonocytic leukemia cell lines treated with rHuEpo exhibited an increase in apoptosis in response to chemotherapy.⁷¹ Overall, these findings warrant additional experimental and clinical research of rHuEpo to clarify further the risks of its use as well as optimize its known or potential benefits.

Combination of VDAs and Chemo- and/or Radiation Therapy

VDAs work best in the poorly perfused hypoxic central tumor areas, leaving a viable rim of well-perfused cancer tissue at the periphery, which rapidly regrows.⁵⁰ Consequently, responses of tumors to VDAs given as single agents have been poor; however, combination therapy with chemoradiotherapy, which targets cancer cells at the tumor periphery, has produced promising responses in preclinical models. Nevertheless, the timing and se-

quencing of VDAs and chemo-irradiation therapies are important in such treatments. By far the greatest enhancement was observed when the VDA was administered within a few hours after chemo- and/or irradiation therapy. Based on these experimental results, the VDA compounds 5,6-dimethylxantlenone-4-acetic acid (DMXAA) and combretastatin A4 phosphate (CA4P) are being evaluated in human phase II trials in combination with conventional anticancer therapies.⁵¹

Combination of Angiosuppressive and Vascular Disrupting Agents

Because both angiogenesis and the integrity of the existing vasculature are critical to tumor progression and survival, dual targeting of the tumor vasculature would seem to have considerable promise. Preclinical results demonstrated that this strategy could significantly enhance therapeutic response beyond that achieved with either antivascular agent alone.⁵¹ One example of this strategy is the combination of the inhibitor of VEGFR2-associated TK ZD6474 with the microtubulin-disrupting VDA ZD6126.⁷² Further combinations that are under preclinical testing include the combination of OXi-4503, CA4P, and DMXAA with bevacizumab. Clinical testing of combined antivascular therapy has started with the recent initiation of a phase I human trial combining CA4P with bevacizumab.⁵¹

Theoretical Considerations for Designing Antivascular Therapy of Cancer

From the discussion above it is clear that the combination of either angiosuppressive or the vascular disrupting therapies with conventional chemoradiotherapy of cancer is highly problematic and must be carefully designed in cases where the sequence of the multiple types of agents might be critical. The molecular machinery behind the vascularization process and type of tumor vascularization are further issues that have to be taken into account. Thus, an efficient antivascular cancer therapy could be designed based on the identification of the molecular targets of the angiogenic geno-/phenotype (molecular pathway-based approach) or on the vascularization mechanism (vascular mechanism-based approach). However, it is most probable that the two approaches would have to be combined. We propose below a rationale for the design of antivascular strategies with the aim that such consideration may help to improve the clinical efficacy of these novel therapies.

Molecular Pathway-Based Antivascular Therapy of Cancer

Because of its pivotal role in neovascularization, the VEGF/VEGFR axis has been a major target of basic and clinical research. It is, therefore, not surprising that most of the antivascular strategies currently in clinical development focus on inhibition of VEGF signaling.^{46,73} However, the development of the angiogenic phenotype of

cancer is characterized by several interconnected pathways. One of the major triggers of this phenotype is tissue hypoxia, which is responsible for the activation of gene expression of angiogenic cytokines through up-regulation of the transcription factor hypoxia inducible factor-1 α (HIF1- α). Nevertheless, HIF-1 may already be active in particular cancers due to hyperactive growth factor signaling or genetic alteration of the HIF1 α gene itself or its regulators [ie, von Hippel-Lindau (VHL) and p53].⁷⁴ Because HIF-1 plays such a central role in triggering numerous pathways responsible for cancer progression, disruption of the HIF-1-mediated pathways is expected to cause cancer cell death due to a combination of metabolic dysregulation and reduced microvessel growth. The aim of anti-HIF-1 therapy (used as an antivascular modality) therefore might be to cause the angiogenic phenotype of cancer to revert to a less angiogenic one, thereby preventing the production of the major angiogenic cytokines.⁷⁵ HIF1 α can be inhibited by guanyl cyclase or HSP90 inhibitors and even by the targeting of topoisomerase-1, and several of such agents are in clinical trials (Table 1). However, none of the currently available inhibitors seems to disrupt the HIF-1 pathway as their exclusive target.⁷⁵ If the additional targets of non-selective HIF-1 inhibitors are also involved in cancer progression, these agents could be therapeutically beneficial, but inhibition of the pathways involved in normal cellular homeostasis could result in an unacceptable toxicity profile. Therefore, the design of more specific HIF-1 targeting agents is the focus of current research efforts. However, it is also important to note that HIF-1 targeting alone may not be enough to halt angiogenesis and tumor progression, as HIF-independent pathways may bypass or overcome HIF inhibition. Consequently, a combination of anti-HIF agents with conventional anticancer modalities or other molecular-targeted drugs may be required.

VEGF expression is not only associated with hypoxia or VHL mutations but also is influenced by a broad spectrum of onco- and tumor suppressor genes. A growing body of evidence suggests that inactivation of tumor suppressor genes such as p53 and PTEN and activation of oncogenes such as Ras, c-Src, EGFR, human epidermal growth factor receptor 2 (HER-2), FBJ murine osteosarcoma viral oncogene homolog (FOS), neurotrophic receptor tyrosine kinase B (trkB), V-p3K, and Bcl-2 are connected to the up-regulation of VEGF. Consequently, molecular targeting of these regulators is also a potential strategy for indirectly modulating the VEGF/VEGFR axis.⁷³ For example, based on the results of recent clinical trials, cetuximab (a monoclonal antibody that binds to EGFR with high specificity) induces a significant decrease in circulating VEGF levels in colon cancer patients,⁷⁶ or likewise, imatinib mesylate (a specific inhibitor of Bcr/Abl protein TK activity) reduces VEGF plasma concentration⁷⁷ and bone marrow microvessel densities⁷⁸ in patients with chronic myeloid leukemia. However, preclinical and early phase clinical data demonstrate that the addition of anti-VEGF therapy to anti-EGFR therapies generates further beneficial effects on angiogenesis inhibition and tumor reduction.⁴² This suggests that inhibiting upstream signaling of VEGF does not necessarily provide the same benefit as the direct targeting

of it and, more importantly, that the dual targeting of cancer and endothelial cells might become a successful practice in clinical oncology.

Mechanism-Based Antivasular Therapy of Cancer

A proposal for the application of antivasular therapies according to the alternative vascularization mechanisms in cancer is summarized in Table 2. Probably the most important aspect of mechanism-based antivasular therapy is its strict dependence on the stage of tumor progression. Interestingly, antivasular therapy may have an effect at the very early stages of tumor growth. This idea was put forward by Li et al,⁷⁹ who analyzed the earliest events that take place during the onset of tumor neovascularization and found that individual tumor cells exhibited a chemotaxis-like growth pattern toward the host vasculature. When the tumor cell population reached approximately 60 to 80 cells, clear evidence of perivascular tumor cell migration (ie, vessel co-option), and host vessel dilation was observed. Moreover, in a mouse model of glomeruloid angiogenesis, our group found that even single tumor cells can induce radical changes in the host tissue vasculature²⁴ (Figure 4). These observations are important in two ways. First, they suggest that anti-invasive agents (which are not yet available clinically) may have a therapeutic effect on the interaction between cancer and endothelial cells and, consequently, on the processes of vessel co-option and glomeruloid angiogenesis. Second, the finding that single tumor cells can induce increased capillary permeability/tortuosity highlights the need for application of angiosuppressive/anti-angiogenic therapy at the very early stages of cancer progression. These considerations may be true for the next step of tumorigenesis (pre-angiogenic phase) as well.

After the onset of "angiogenic switch," elevated serum levels of angiogenic growth factors in cancer patients may activate and mobilize EPCs to support local microvessel growth.²⁶ If we accept this assumption, then, in addition to angiogenesis inhibitors and metronomic chemotherapy,⁵² ligand-based, EPC-specific VDAs may also be useful in eliminating circulating EPCs throughout the further stages of tumor progression (Table 2). Furthermore, because IMG can be effective only in tumor capillary networks already built by other vascularization mechanisms (mainly sprouting and vessel co-option), steps should be taken to impede the additional increase in the density of the tumor tissue capillary bed following the angiogenic switch. This could be achieved by the use of VDAs and/or "metronomic chemotherapy," which both target the cytoskeleton of ECs responsible for the remodeling of capillary walls.

Because ischemic milieu is what forces aggressive tumor cells to express endothelial genes and form vascular channels,^{33,80} the initiation of this mechanism is most likely simultaneous with the angiogenic switch. Therefore, when vasculogenic mimicry plays a role in the nutrient supply in cancer, besides the use of ligand-

based VDAs against cancer cells with endothelial phenotype, targeting those pathways responsible for the development of this mechanism such as Eph2A, PI3K, or FAK seems to be an appropriate strategy. On the other hand, metronomic scheduling of chemotherapy⁵² may also effectively target cancer cells with vasculogenic geno/phenotype when both physiological angiogenesis inhibitors and angiosuppressive drugs are unable to modify this vascularization mechanism.⁸⁰

The next stage of malignant progression is when tumor tissue reaches macroscopic size detectable by simple or sophisticated imaging techniques. As we know, for cancer survival "the edge is the future and the center is history,"⁸¹ because active tumor vascularization processes, resulting in vascular networks built by defective new capillaries, occur mainly, though not exclusively, at the tumor periphery. Consequently, at this stage the main target of antivasular therapies is the invading front of the cancer tissue. However, since in addition to causing chemo- and radiotherapy resistance, reduction of vascularity in the center of tumors can lead to the appearance of more aggressive/highly metastatic hypoxia-resistant cancer cells and to the induction of vasculogenic mimicry, when designing antivasular strategies central tumor areas cannot be neglected. We should emphasize, therefore, that in the case of clinically detectable tumors the whole range of antivasular weapons should be used theoretically. Although antiangiogenic agents targeting proliferating ECs could possibly be the key drugs at the tumor boundary, established tumor vasculature might well be attacked by VDAs and/or metronomic chemotherapy in the central tumor areas. Altogether, it seems feasible that antivasular therapy in tumors can only be successful if the entire vascular network and all of the possible vascularization mechanisms are targeted and, furthermore, if the phenotypic analysis of tumor capillaries/vascular channels is adequately performed.

Conclusion

Although tumors, as other tissues, require a vessel network supplying them with blood, tumor vasculature is not necessarily derived by EC proliferation and sprouting of new capillaries. In addition to alternative vascularization mechanisms, the novel antivasular strategies must be harmonized with the stage of tumor progression and with the molecular mechanism responsible for the angiogenic phenotype. A further challenge is to combine antivasular strategies with the existing therapeutic regimes in at least an additive manner. We have provided here proposals for a rational application of antivasular agents with the notion that these therapies have to be individually tailored in a given cancer type. Better understanding of the different vascularization mechanisms of the various cancer types will certainly help to fine-tune these novel anti-cancer strategies.

Acknowledgments

We are grateful to Sirpa Jalkanen (Medicity, University of Turku, Turku, Finland) and to Sándor Eckhardt (National Institute of Oncology, Budapest, Hungary) for critique and suggestions.

References

1. Ausprunk DH, Folkman J: Migration and proliferation of endothelial cells in preformed and newly formed blood vessels during tumor angiogenesis. *Microvasc Res* 1977, 14:53–65
2. Paku S, Paweletz N: First steps of tumor-related angiogenesis. *Lab Invest* 1991, 65:334–346
3. Carmeliet P: Angiogenesis in life, disease and medicine. *Nature* 2005, 438:932–936
4. Dvorak HF, Brown LF, Detmar M, Dvorak AM: Vascular permeability factor/vascular endothelial growth factor, microvascular hyperpermeability, and angiogenesis. *Am J Pathol* 1995, 146:1029–1039
5. Serini G, Valdembrì D, Bussolino F: Integrins and angiogenesis: a sticky business. *Exp Cell Res* 2006, 312:651–658
6. Thompson WD, Shiach KJ, Fraser RA, McIntosh LC, Simpson JG: Tumours acquire their vasculature by vessel incorporation, not vessel ingrowth. *J Pathol* 1987, 151:323–332
7. Holash J, Maisonpierre PC, Compton D, Boland P, Alexander CR, Zagzag D, Yancopoulos GD, Wiegand SJ: Vessel cooption, regression, and growth in tumors mediated by angiopoietins and VEGF. *Science* 1999, 284:1994–1998
8. Döme B, Paku S, Somlai B, Timar J: Vascularization of cutaneous melanoma involves vessel co-option and has clinical significance. *J Pathol* 2002, 197:355–362
9. Pezzella F, Pastorino U, Tagliabue E, Andreola S, Sozzi G, Gasparini G, Menard S, Gatter KC, Harris AL, Fox S, Buysse M, Pilotti S, Pierotti M, Rilke F: Non-small-cell lung carcinoma tumor growth without morphological evidence of neo-angiogenesis. *Am J Pathol* 1997, 151:1417–1423
10. Vermeulen PB, Colpaert C, Salgado R, Royers R, Hellems H, Van Den Heuvel E, Goovaerts G, Dirix LY, Van Marck E: Liver metastases from colorectal adenocarcinomas grow in three patterns with different angiogenesis and desmoplasia. *J Pathol* 2001, 195:336–342
11. Paku S, Lapis K: Morphological aspects of angiogenesis in experimental liver metastases. *Am J Pathol* 1993, 143:926–936
12. Paku S, Kopper L, Nagy P: Development of the vasculature in "pushing-type" liver metastases of an experimental colorectal cancer. *Int J Cancer* 2005, 115:893–902
13. Paku S, Bodoky G, Kupcsulik P, Timar J: Blood supply of metastatic hepatic tumors: suggestions for improved delivery of chemotherapeutic agents. *J Natl Cancer Inst* 1998, 90:936–937
14. Brooks PC, Montgomery AM, Rosenfeld M, Reisfeld RA, Hu T, Klier G, Cheresch DA: Integrin alpha v beta 3 antagonists promote tumor regression by inducing apoptosis of angiogenic blood vessels. *Cell* 1994, 79:1157–1164
15. Scharpfenecker M, Fiedler U, Reiss Y, Augustin HG: The Tie-2 ligand angiopoietin-2 destabilizes quiescent endothelium through an internal autocrine loop mechanism. *J Cell Sci* 2005, 118:771–780
16. Holash J, Wiegand SJ, Yancopoulos GD: New model of tumor angiogenesis: dynamic balance between vessel regression and growth mediated by angiopoietins and VEGF. *Oncogene* 1999, 18:5356–5362
17. Benjamin LE, Golijanin D, Itin A, Podes D, Keshet E: Selective ablation of immature blood vessels in established human tumors follows vascular endothelial growth factor withdrawal. *J Clin Invest* 1999, 103:159–165
18. Ferrara N, Gerber HP, LeCouter J: The biology of VEGF and its receptors. *Nat Med* 2003, 9:669–676
19. Kurz H, Burri PH, Djonov VG: Angiogenesis and vascular remodeling by intussusception: from form to function. *News Physiol Sci* 2003, 18:65–70
20. Osawa M, Masuda M, Kusano K, Fujiwara K: Evidence for a role of platelet endothelial cell adhesion molecule-1 in endothelial cell mech-
- anosignal transduction: is it a mechanoresponsive molecule? *J Cell Biol* 2002, 158:773–785
21. Brat DJ, Van Meir EG: Glomeruloid microvascular proliferation orchestrated by VPF/VEGF: a new world of angiogenesis research. *Am J Pathol* 2001, 158:789–796
22. Straume O, Chappuis PO, Salvesen HB, Halvorsen OJ, Haukaas SA, Goffin JR, Begin LR, Foulkes WD, Akslen LA: Prognostic Importance of Glomeruloid Microvascular Proliferation Indicates an Aggressive Angiogenic Phenotype in Human Cancers. *Cancer Res* 2002, 62:6808–6811
23. Sundberg C, Nagy JA, Brown LF, Feng D, Eckelhoefer IA, Manseau EJ, Dvorak AM, Dvorak HF: Glomeruloid microvascular proliferation follows adenoviral vascular permeability factor/vascular endothelial growth factor-164 gene delivery. *Am J Pathol* 2001, 158:1145–1160
24. Döme B, Timar J, Paku S: A novel concept of glomeruloid body formation in experimental cerebral metastases. *J Neuropathol Exp Neurol* 2003, 62:655–661
25. Asahara T, Kawamoto A: Endothelial progenitor cells for postnatal vasculogenesis. *Am J Physiol* 2004, 287:C572–C579
26. Garmy-Susini B, Varner JA: Circulating endothelial progenitor cells. *Br J Cancer* 2005, 93:855–858
27. Urbich C, Aicher A, Heeschen C, Dernbach E, Hofmann WK, Zeiher AM, Dimmeler S: Soluble factors released by endothelial progenitor cells promote migration of endothelial cells and cardiac resident progenitor cells. *J Mol Cell Cardiol* 2005, 39:733–742
28. Lyden D, Hattori K, Dias S, Costa C, Blaikie P, Butros L, Chadburn A, Heissig B, Marks W, Witte L, Wu Y, Hicklin D, Zhu Z, Hackett NR, Crystal RG, Moore MA, Hajar KA, Manova K, Benezra R, Rafii S: Impaired recruitment of bone-marrow-derived endothelial and hematopoietic precursor cells blocks tumor angiogenesis and growth. *Nat Med* 2001, 7:1194–1201
29. Kaplan RN, Riba RD, Zacharoulis S, Bramley AH, Vincent L, Costa C, MacDonald DD, Jin DK, Shido K, Kerns SA, Zhu Z, Hicklin D, Wu Y, Port JL, Altorki N, Port ER, Ruggero D, Shmelkov SV, Jensen KK, Rafii S, Lyden D: VEGFR1-positive haematopoietic bone marrow progenitors initiate the pre-metastatic niche. *Nature* 2005, 438:820–827
30. Maniotis AJ, Folberg R, Hess AR, Sefter EA, Gardner LMG, Pe'er J, Trent JM, Meltzer PS and Hendrix MJC: Vascular channel formation by human melanoma cells in vivo and in vitro: vasculogenic mimicry. *Am J Pathol* 1999, 155:739–752
31. Sefter EA, Meltzer PS, Kirschmann DA, Pe'er J, Maniotis AJ, Trent JM, Folberg R and Hendrix MJC: Molecular determinants of human uveal melanoma invasion and metastasis. *Clin Exp Metast* 2002, 19:233–246
32. Sefter EA, Meltzer PS, Schatteman GC, Gardner LMG, Hess AR, Kirschmann DA, Sefter REB and Hendrix MJC: Expression of multiple molecular phenotypes by aggressive melanoma tumor cells: role of vasculogenic mimicry. *Crit Rev Oncol Hematol* 2002, 44:17–27
33. Hendrix MJC, Sefter EA, Hess AR and Sefter REB: The molecular plasticity of human melanoma cells. *Oncogene* 2003, 22:3070–3075
34. Hendrix MJC, Sefter EA, Hess AR, Sefter REB: Vasculogenic mimicry and tumour-cell plasticity: lessons from melanoma. *Nature Rev Cancer* 2003, 3:411–421
35. Maniotis AJ, Chen X, Garcia C, DeChristopher PJ, Wu D, Pe'er J, Folberg R: Control of melanoma morphogenesis, endothelial survival, and perfusion by extracellular matrix. *Lab Invest* 2002, 82:1031–1043
36. Hendrix MJC, Sefter EA, Meltzer PS, Hess AR, Gruman LM, Nickoloff BJ, Miele L, Sheriff DD, Schatteman GC, Bourdon MA, Sefter REB: The stem cell plasticity of aggressive melanoma tumor cells. *Germinal Stem Cells*. Edited by ES Sell. Totowa, NJ, Humana Press, Inc., 2004, pp 297–306
37. Ruf W, Sefter EA, Prtrovan R, Weiss RM, Gruman LM, Margaryan NV, Sefter REB, Miyagi Y, Hendrix MJC: Differential role of tissue factor pathway inhibitor-1 and 2 (TFPI-1 and 2) in melanoma vasculogenic mimicry. *Cancer Res* 2003, 63:5381–5389
38. Walker-Daniels J, Hess AR, Hendrix MJ, Kinch MS: Differential regulation of EphA2 in normal and malignant cells. *Am J Pathol* 2003, 162:1037–1042
39. Hess AR, Sefter EA, Sefter REB, Hendrix MJC: Phosphoinositide 3-kinase regulates MT1-MMP and MMP-2 activity during melanoma cell vasculogenic mimicry. *Cancer Res* 2003, 63:4757–4762
40. Hess AR, Postovit LM, Margaryan NV, Sefter EA, Schneider GB, Sefter REB, Nickoloff BJ, Hendrix MJC: Focal adhesion kinase pro-

- notes aggressive melanoma phenotype. *Cancer Res* 2005, 65:9851–9860
41. Folkman J: Tumor angiogenesis: therapeutic implications. *N Engl J Med* 1971, 285:1182–1186
 42. Jain RK, Duda DG, Clark JW, Loeffler JS: Lessons from phase III clinical trials on anti-VEGF therapy for cancer. *Nat Clin Pract Oncol* 2006, 3:24–40
 43. Kerbel RS: Antiangiogenic therapy: a universal chemosensitization strategy for cancer? *Science* 2006, 312:1171–1175
 44. Siemann DW, Bibby MC, Dark GG, Dicker AP, Eskens FA, Horsman MR, Marme D, Lorusso PM: Differentiation and definition of vascular-targeted therapies. *Clin Cancer Res* 2005, 11:416–420
 45. Browder T, Butterfield CE, Kraling BM, Shi B, Marshall B, O'Reilly MS, Folkman J: Antiangiogenic scheduling of chemotherapy improves efficacy against experimental drug-resistant cancer. *Cancer Res* 2000, 60:1878–1886
 46. Gasparini G, Longo R, Fanelli M, Teicher BA: Combination of antiangiogenic therapy with other anticancer therapies: results, challenges, and open questions. *J Clin Oncol* 2005, 23:1295–1311
 47. Hurwitz H, Fehrenbacher L, Novotny W, Cartwright T, Hainsworth J, Heim W, Berlin J, Baron A, Griffing S, Holmgren E, Ferrara N, Fyfe G, Rogers B, Ross R, Kabbinavar F: Bevacizumab plus irinotecan, fluorouracil, and leucovorin for metastatic colorectal cancer. *N Engl J Med* 2004, 350:2335–2342
 48. Yang JC, Haworth L, Sherry RM, Hwu P, Schwartzentruber DJ, Topalian SL, Steinberg SM, Chen HX, Rosenberg SA: A randomized trial of bevacizumab, an anti-vascular endothelial growth factor antibody, for metastatic renal cancer. *N Engl J Med* 2003, 349:427–434
 49. Morabito A, De Maio E, Di Maio M, Normanno N, Perrone F: Tyrosine kinase inhibitors of vascular endothelial growth factor receptors in clinical trials: current status and future directions. *Oncologist* 2006, 11:753–764
 50. Tozer GM, Kanthou C, Baguley BC: Disrupting tumour blood vessels. *Nat Rev Cancer* 2005, 5:423–435
 51. Chaplin DJ, Horsman MR, Siemann DW: Current development status of small-molecule vascular disrupting agents. *Curr Opin Investig Drugs* 2006, 7:522–528
 52. Kerbel RS, Kamen BA: The anti-angiogenic basis of metronomic chemotherapy. *Nat Rev Cancer* 2004, 4:423–436
 53. Baruchel S, Stempak D: Low-dose metronomic chemotherapy: myth or truth? *Onkologie* 2006, 29:305–307
 54. Kamen BA, Glod J, Cole PD: Metronomic therapy from a pharmacologist's view. *J Pediatr Hematol Oncol* 2006, 28:325–327
 55. Mancuso P, Colleoni M, Calleri A, Orlando L, Maisonneuve P, Pruneri G, Agliano A, Goldhirsch A, Shaked Y, Kerbel RS, Bertolini F: Circulating endothelial-cell kinetics and viability predict survival in breast cancer patients receiving metronomic chemotherapy. *Blood* 2006, 108:452–459
 56. Shaked Y, Emmenegger U, Man S, Cervi D, Bertolini F, Ben-David Y, Kerbel RS: Optimal biologic dose of metronomic chemotherapy regimens is associated with maximum antiangiogenic activity. *Blood* 2005, 106:3058–3061
 57. Vaupel P, Kelleher DK, Hockel M: Oxygen status of malignant tumors: pathogenesis of hypoxia and significance for tumor therapy. *Semin Oncol* 2001, 28(Suppl 8):29–35
 58. Sleijfer S, Kruit WH, Stoter G: Thalidomide in solid tumours: the resurrection of an old drug. *Eur J Cancer* 2004, 40:2377–2382
 59. Kindler HL, Friberg G, Singh DA, Locker G, Nattam S, Kozloff M, Taber DA, Karrison T, Dachman A, Stadler WM, Vokes EE: Phase II trial of bevacizumab plus gemcitabine in patients with advanced pancreatic cancer. *J Clin Oncol* 2005, 23:8033–8040
 60. Cohn DE, Valmadre S, Resnick KE, Eaton LA, Copeland LJ, Fowler JM: Bevacizumab and weekly taxane chemotherapy demonstrates activity in refractory ovarian cancer. *Gynecol Oncol* 2006, 102:134–139
 61. Baluk P, Hashizume H, McDonald DM: Cellular abnormalities of blood vessels as targets in cancer. *Curr Opin Genet Dev* 2005, 15:102–111
 62. Nieder C, Wiedenmann N, Andratschke N, Molls M: Current status of angiogenesis inhibitors combined with radiation therapy. *Cancer Treat Rev* 2006, 32:348–364
 63. Garcia-Barros M, Paris F, Cordon-Cardo C, Lyden D, Rafii S, Haimovitz-Friedman A, Fuks Z, Kolesnick R: Tumor response to radiotherapy regulated by endothelial cell apoptosis. *Science* 2003, 300:1155–1159
 64. Lövey J, Lukits J, Remenar E, Koronczay K, Kasler M, Nemeth G, Timar J: Antiangiogenic effects of radiotherapy but not initial microvessel density predict survival in inoperable oropharyngeal squamous cell carcinoma. *Strahlenther Onkol* 2006, 182:149–156
 65. Winkler F, Kozin SV, Tong RT, Chae SS, Booth MF, Garkavtsev I, Xu L, Hicklin DJ, Fukumura D, di Tomaso E, Munn LL, Jain RK: Kinetics of vascular normalization by VEGFR2 blockade governs brain tumor response to radiation: role of oxygenation, angiotensin-1, and matrix metalloproteinases. *Cancer Cell* 2004, 6:553–563
 66. Bohlius J, Weingart O, Trelle S, Engert A: Cancer-related anemia and recombinant human erythropoietin—an updated overview. *Nat Clin Pract Oncol* 2006, 3:152–164
 67. Boogaerts M, Mittelman M, Vaupel P: Beyond anaemia management: evolving role of erythropoietin therapy in neurological disorders, multiple myeloma and tumour hypoxia models. *Oncology* 2005, 69(Suppl 2):22–30
 68. Hardee ME, Arcasoy MO, Blackwell KL, Kirkpatrick JP, Dewhirst MW: Erythropoietin biology in cancer. *Clin Cancer Res* 2006, 12:332–339
 69. Tóvári J, Gilly R, Raso E, Paku S, Bereczky B, Varga N, Vago A, Timar J: Recombinant human erythropoietin alpha targets intratumoral blood vessels, improving chemotherapy in human xenograft models. *Cancer Res* 2005, 65:7186–7193
 70. Mittelman M, Neumann D, Peled A, Kanter P, Haran-Ghera N: Erythropoietin induces tumor regression and antitumor immune responses in murine myeloma models. *Proc Natl Acad Sci USA* 2001, 98:5181–5186
 71. Carvalho G, Lefaucheur C, Cherbonnier C, Metivier D, Chapel A, Pallardy M, Bourgeade MF, Charpentier B, Hirsch F, Kroemer G: Chemosensitization by erythropoietin through inhibition of the NF-kappaB rescue pathway. *Oncogene* 2005, 24:737–745
 72. Shi W, Siemann DW: Targeting the tumor vasculature: enhancing antitumor efficacy through combination treatment with ZD6126 and ZD6474. *In Vivo* 2005, 19:1045–1050
 73. Hicklin DJ, Ellis LM: Role of the vascular endothelial growth factor pathway in tumor growth and angiogenesis. *J Clin Oncol* 2005, 23:1011–1027
 74. Pugh CW, Ratcliffe PJ: Regulation of angiogenesis by hypoxia: role of the HIF system. *Nat Med* 2003, 9:677–684
 75. Welsh SJ, Koh MY, Powis G: The hypoxic inducible stress response as a target for cancer drug discovery. *Semin Oncol* 2006, 33:486–497
 76. Vincenzi B, Santini D, Russo A, Silletta M, Gavasci M, Battistoni F, Di Cuozzo G, Rocci L, Gebbia N, Tonini G: Angiogenesis modifications related with cetuximab plus irinotecan as anticancer treatment in advanced colorectal cancer patients. *Ann Oncol* 2006, 17:835–841
 77. Legros L, Bourcier C, Jacquelin A, Mahon FX, Cassuto JP, Auberger P, Pages G: Imatinib mesylate (STI571) decreases the vascular endothelial growth factor plasma concentration in patients with chronic myeloid leukemia. *Blood* 2004, 104:495–501
 78. Kvasnicka HM, Thiele J, Staib P, Schmitt-Graeff A, Griesshammer M, Klose J, Engels K, Kriener S: Reversal of bone marrow angiogenesis in chronic myeloid leukemia following imatinib mesylate (STI571) therapy. *Blood* 2004, 103:3549–3551
 79. Li CY, Shan S, Huang Q, Braun RD, Lanzen J, Hu K, Lin P, Dewhirst MW: Initial stages of tumor cell-induced angiogenesis: evaluation via skin window chambers in rodent models. *J Natl Cancer Inst* 2000, 92:143–147
 80. van der Schaft DWJ, Sefter EA, Hess AR, Gruman LM, Kirschmann DA, Yokoyama Y, Sefter REB, Griffioen AW, Hendrix MJC: Differential effects of angiogenesis inhibitors on vascular network formation by endothelial and melanoma cells. *J Natl Cancer* 2004, 96:1473–1477
 81. Thompson WD: Tumour versus patient: vascular and tumour survival versus prognosis. *J Pathol* 2001, 193:425–426

SEMINAR**Current Concepts of Tumor-Induced Angiogenesis**

Sándor PAKU

Research Unit of Molecular Pathology, Joint Research Organization of the Hungarian Academy of Sciences and Semmelweis University of Medicine, Budapest, Hungary

Tumor induced angiogenesis is responsible for the nutrition of the growing tumor and can also increase the probability of hematogenous tumor dissemination. Data obtained from morphological analysis of tumor angiogenesis can contribute to the development of new anti-angiogenic therapies. Based on in vitro and in vivo observations several models of angiogenesis were introduced, explaining the mechanism of lumen formation and the timing of basement membrane deposition. (1) Lumen is formed either by cell body curving or by fusion of intracellular vacuoles of nonpolarized endothelial cells. New basement membrane is deposited after lumen formation. (2) Slit-like lumen is immediately formed by migrating polarized endothelial cells. Basement membrane is continuously deposited during endothelial cell migration, only cellular processes of the endothelial cell migrating on the tip of the growing capillary are free of deposited basement membrane material. (3) Development of transluminal bridges in larger vessels – a process called intussusceptive growth –

Key words: tumor, metastasis, angiogenesis, morphology

leads to the division of the vessels. These models, however, describe angiogenesis in tissues rich in connective tissue. Different processes of angiogenesis take place in organs – such as liver, lungs, adrenals, which are the most frequent sites of metastasis – having high vessel density without sufficient space for capillary sprouting. In the case of liver metastases of Lewis lung carcinoma the proliferation of endothelial cells was elicited only by direct contact between tumor and endothelial cells, leading to the development of large convoluted vessels inside the metastases. These vessels were continuous with the sinusoidal system, suggesting that these metastases have dual blood supply. This observation, among others, is in contrast to the generally accepted view that liver tumors have arterial blood supply. The increasing number of data demonstrating the dual or venous blood supply of liver metastases should be taken into consideration in the therapy of liver metastasis. (Pathology Oncology Research Vol 4, No 1, 62–75, 1998)

Introduction

Two, morphologically different processes take part in the development of new vessels. During angiogenesis new vessels arise from preexisting ones, contrary to vasculogenesis, which occurs at early embryonic development, when vessels are organized from primordial endothelial cells.^{1,3}

Tumor induced angiogenesis has two effects on malignancy. On the one hand the developing vasculature feeds

the tumor, on the other hand it increases the probability of tumor dissemination via the vascular system. Although tumors generally lack lymphatic vessels and lymphangiogenesis has not been observed during tumor progression,⁴ recent results have shown that VEGF-C transgenic mice develop a hyperplastic lymphatic capillary system in the skin, raising the possibility of lymphangiogenesis also in the case of tumors.⁵

It is generally accepted that tumors cannot grow beyond the size of 2 mm in diameter without eliciting angiogenic response. In case of tumor cells lodged in distant organs, the temporary lack of the angiogenesis inducing ability, can lead to the development of dormant metastases.^{1,2}

There are ample data showing inverse correlation between tumor vascularity and patient survival.⁶ Opposite

Received: Nov 20, 1997; *accepted:* Jan 5, 1998

Correspondence: Sándor PAKU, Ph.D., First Institute of Pathology and Experimental Cancer Research, Semmelweis University of Medicine, Üllői út 26, 1085 Budapest, Hungary. Tel (36)(1) 266-1638; fax: (36)(1) 117-1074; e-mail paku@korb1.sote.hu

results suggest, however, that simple vessel counting (determination of vessel number in places of highest vessel density, so called hot spots) does not represent the more complex relationship between tumor vascularity and metastasis.⁷ Instead, the detection of disseminated tumor cells at the invasion front, or determination of blood or lymph vessel invasion appear to be parameters that – although more difficult to determine – are more closely related to the metastatic process.^{8,9}

Tumor vasculature has two important further effects on the therapy of tumors. It can itself be a target for therapy (anti-angiogenic therapy), and it is responsible for delivering therapeutic agents to tumor cells.^{10,11} Morphological analysis of *in vivo* angiogenesis as well as determination of the spatial distribution of cell-cell, cell-matrix adhesion molecules, extracellular matrix components, matrix remodelling enzymes and angiogenesis factors during the process can lead to development of new anti-angiogenic strategies.

Tumor angiogenesis is initiated by disturbing the balance between angiogenesis activators and inhibitors, already in the stage of dysplasia or *in situ* carcinoma before the progression to invasive tumor stage.¹² Positive mediators of this process are the angiogenic factors produced directly by tumor cells, or by host cells recruited to the peritumoral space. Numerous polypeptide and small molecular weight angiogenic factors has been identified, recently reviewed by Bouck et al.¹¹ Similarly, extracellular matrix molecules and their degradation products has been shown to induce angiogenesis alone, or in combination with the above factors.¹³

Angiogenesis in vitro

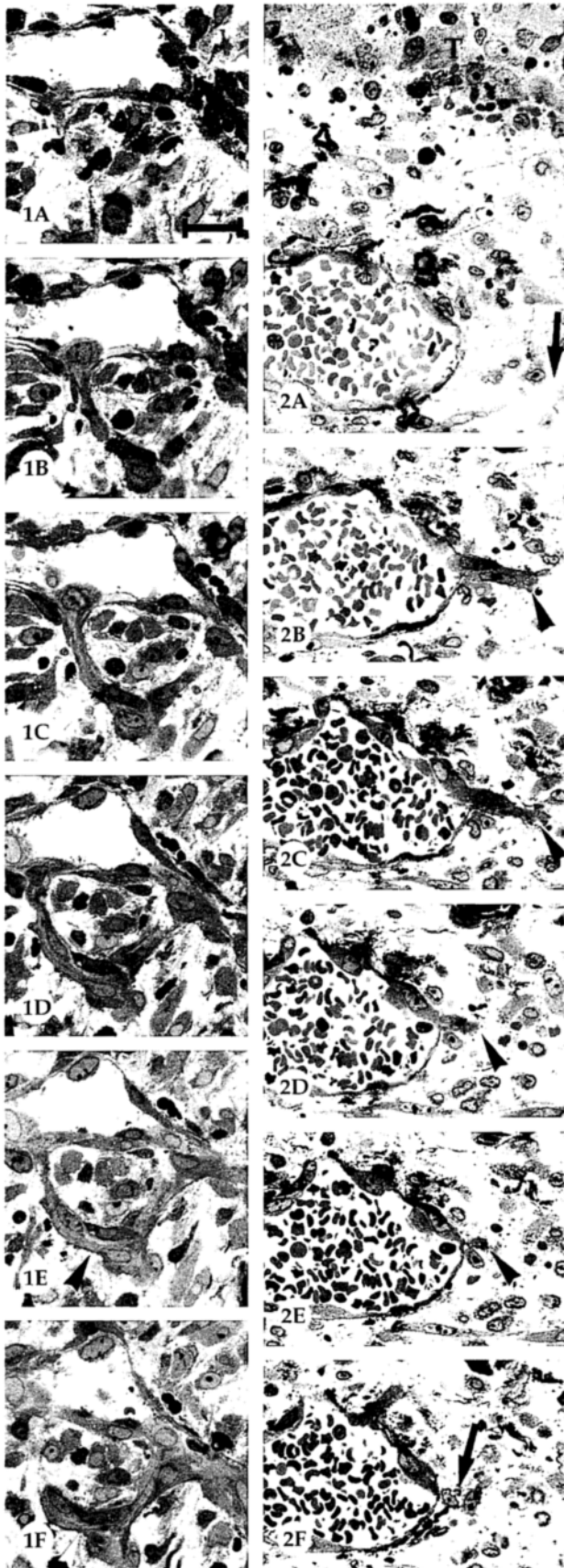
The effect of angiogenesis factors and extracellular matrix components on endothelial cell behaviour has been extensively studied using *in vitro* cultured endothelial cells of different origin. Endothelial cells can undergo a process called *in vitro* angiogenesis cultured on different matrices. Tubular structures consisting of several endothelial cells were found to develop on surfaces coated with gelatin or fibronectin in overconfluent cultures.¹⁴⁻¹⁶ Similar structures were seen to arise rapidly, after seeding endothelial cells on a gel consisting of basement membrane components (Matrigel).^{17,18} Although the cords on the surface of the extracellular matrix were formed by numerous elongated endothelial cells, and in cross section the cells enclosed a primitive lumen sealed by intercellular junctions,¹⁴⁻¹⁸ the lumen often contained extracellular matrix material or cellular debris and the basal-apical polarization of the endothelial cells was not demonstrated.^{14,17} Tube formation proved not to be an exclusive characteristic of endothelial cells, because many other cell types were able to form cords and networks on basement membrane matrix

gel.¹⁹ With decreasing malleability of the gel the cord formation diminished, suggesting that cord formation is more dependent on the mechanical properties of the matrix than on the cell type.¹⁹ This manner of endothelial cell organization is more resemblant to the process of vasculogenesis, since angiogenesis is characterized by migration of endothelial cells into the matrix (a process called sprouting) from a polarized layer of endothelial cells. To examine angiogenesis *in vitro*, it is more relevant to study the *in vitro* model systems using endothelial cells cultured to confluency on the top of collagen I gel or human amniotic membrane or aortic rings explanted into fibrin gel.²⁰⁻²⁴ In the former case the treatment of such cultures with FGF or PMA resulted in invasion of the gel, or the basement membrane by the endothelial cells which process depended on the production of collagenase IV and plasminogen activator.²⁰⁻²² Tube-like structures appeared in the collagen matrix, which showed a lumen delineated by endothelial cells, connected by intercellular junctions.^{20,21} More importantly, polarized deposition of the basement membrane was observed in these structures.²⁰ Similar polarized deposition of fibronectin, laminin, and collagen IV was observed around the developing capillaries in the case of aortic rings explanted into fibrin gel.²⁴

Angiogenesis in vivo

Angiogenesis in primary tumors

Fibrin and collagen I are the components of the provisional extracellular matrix during tumor development and wound healing *in vivo*.²⁵ Fibrin gel was shown to induce angiogenesis when implanted subcutaneously.²⁶ The development of the fibrin containing stroma in and around the tumor is controversial. Numerous ultrastructural studies on the angiogenic vasculature of tumors and healing wounds have suggested that leakiness of the vessels is caused by open interendothelial junctions.²⁷⁻³⁰ It is well known that tumor vessels usually show abnormal structure, such as fragmented or ultrastructurally not detectable basement membrane and the absence of pericytes.^{31,32} The lumen of the tumor vessels is often covered by extremely thin fragile endothelial cells showing fenestrations, or vascular spaces are present delineated by tumor cells. It is not clear, however, whether these alterations are characteristic to the angiogenic process or are caused by the invasive activities of the tumor cells. The possibility that tumor invasive activities play role in the enhanced leakiness of tumor vessels is supported by the observation – made on corrosion casting specimens of colon tumors – that resin leakage was observed only in carcinomas and not in adenomas.³³ Examination of the angiogenic vasculature under normal condition demonstrated that angiogenic vessels are not permeable for molecules larger than



20 kD.³⁴ Other ultrastructural reports have also shown the absence of open interendothelial junctions during tumor angiogenesis, although tumor vasculature showed leakiness for larger 70-150 kD molecules.³⁵ The leakiness of tumor vessels, as suggested by Dvorak's group, is mediated by vesiculo-vacuolar organelles (VVO) present in endothelial cells of the neovasculature induced by VEGF.³⁶ However, recent results revealed that the endothelial cells in the vasculature of VEGF transfected tumor are fenestrated and contain open interendothelial junctions.³⁷

The developing tumor matrix also contains other extracellular matrix proteins, such as fibronectin, vitronectin and thrombospondin. The former two proteins have a positive effect on tumor angiogenesis by inducing chemotaxis of endothelial cells. The role of thrombospondin is more complicated, since its ability to induce angiogenesis indirectly *in vitro* as well as elevated mRNA level and deposition around breast carcinomas^{41,42} seems to contradict its pronounced ability to inhibit angiogenesis *in vitro* and *in vivo*.¹¹

The morphology of *in vivo* angiogenesis has been studied most frequently in subcutaneous tissue, rabbit cornea and chick chorioallantoic membrane, in normal and pathological conditions such as inflammation, wound healing and tumor development.^{3,28-31,43-45}

The main pitfall in studying angiogenesis is the misidentification of vessel structures as tips or distal parts of growing capillaries. To avoid this, serial sectioning must be performed. The situation is less complicated in case of avascular tissues where the growing new vessels are not mingled with preexisting or older vessels, but serial sectioning cannot be avoided when examining, for example, tumor angiogenesis in subcutaneous tissue. As shown in *Figure 1A-F*, sections of a small capillary loop can easily be misidentified as a tip. In contrast, a real tip as shown on *Figure 2A-F* is only discernible in serial sections.

According to ultrastructural studies, the most commonly used description of the angiogenic process (which is considered to be valid also in case of tumor induced angiogenesis) can be summarized as follows (*Figure 1A,B*): *a*. dilatation of postcapillary venules situated around the tumor; *b*. local degradation of the basement membrane on the side of the vessel located more closely to the angiogenic stimulus; *c*. weakened intercellular contacts between

Figure 1. A-F. Serial sections of a short loop of a capillary (arrowheads). This loop does not show an opened lumen and returns to the original vessel. X 280.

Figure 2. A-F. Serial sections of a short newly formed capillary (arrowheads). Arrows in *Figure 2A* and *2F* points to regions, which show that the capillary does not continue into the connective tissue. X 280.

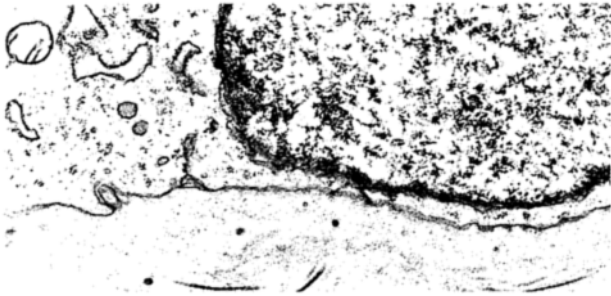


Figure 3. Part of a dilated venule near the tumor. Beneath the endothelial cell there is no basement membrane. X 9000.



Figure 4. Similar vessels as shown on Figure 3. Basement membrane material reacting positively for laminin can be detected beneath the endothelial cell. X 9000

endothelial cells and the start of emigration into the connective tissue, toward the angiogenic stimulus; *d.* the formation of a solid cord by endothelial cells following each other arranged in bipolar fashion, with mitotic endothelial cells observed in the middle of the sprout; *e.* formation of the lumen, occurring either by fusion of intracellular vacuoles, or by cell body curving of a single endothelial cell; *f.* loop formation by fusion of different sprouts; *g.* appearance of pericytes along the sprout and the synthesis of a new basement membrane.

The main disadvantage of this model is its inability to identify the nature and origin of the stimulus necessary for lumen formation. It also assumes that dedifferentiation and redifferentiation take place during the process, manifest in the loss and regaining of luminal-basal polarity. A large number of publications dealing with the effect of Matrigel on the behavior of endothelial cells suggest that stimulus necessary for lumen formation derives from the developing basement membrane.^{17,18} According to this model the importance of the basement membrane in the

process of lumen formation is rather questionable, because basement membrane deposition occurs after lumen formation, which presumes the existence of basal-luminal polarity. If basement membrane synthesis occurs before lumen formation it must proceed around the whole circumference of a nonpolarized cell, excluding that lumen formation occurs later by cell body curving. Lumen formation by fusion of intracellular vacuoles allows basement membrane deposition around the cell, but to increase lumen size in such capillaries the cells must undergo transversal division, implicating a change in cell polarity. Seamless type endothelial cells have very rarely been found *in vivo*, and it has been suggested that they are present only where growing capillaries meet preexisting vessels during loop formation.⁴⁶

A different model was suggested based on data obtained from ultrastructural examination of angiogenesis, using a rat nonmetastatic pancreatic adenocarcinoma cell line growing subcutaneously (*Figure 14C*).⁴⁷ The first step in this type of angiogenesis was the alteration of the base-

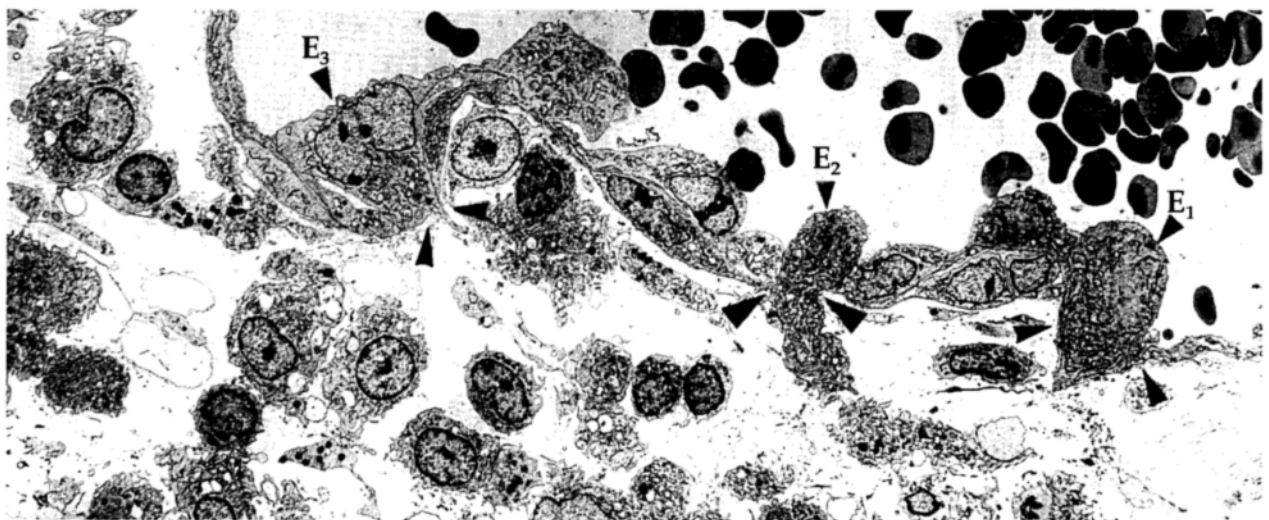


Figure 5A. In the wall of the extended venule three endothelial cells (E1,E2,E3) are seen in different stages of emigration into the connective tissue (arrowheads). X 1400.

ment membrane over the entire circumference of venules, characterized by loss of electron density (Figure 3), but basement membrane components (laminin, collagen IV) could be detected by immunoelectronmicroscopy (Figure 4). Interestingly, fibronectin was also detectable in these basement membranes. This so called gel-sol transition of the basement membrane, probably mediated by matrix metalloproteinases or plasminogen activator, can be partly responsible for the initiation of cell division and migration (Figure 5A,B).⁴⁸ Conversely migrating endothelial cells express elevated level of uPA.⁴⁹ It has been shown that gelatinase A can be activated by membrane type metalloproteinase and also by uPA/plasmin,^{48,50} and bFGF, VEGF and TNF can increase the expression of uPA and its receptor.⁵¹ Partial and regulated proteolysis of the base-

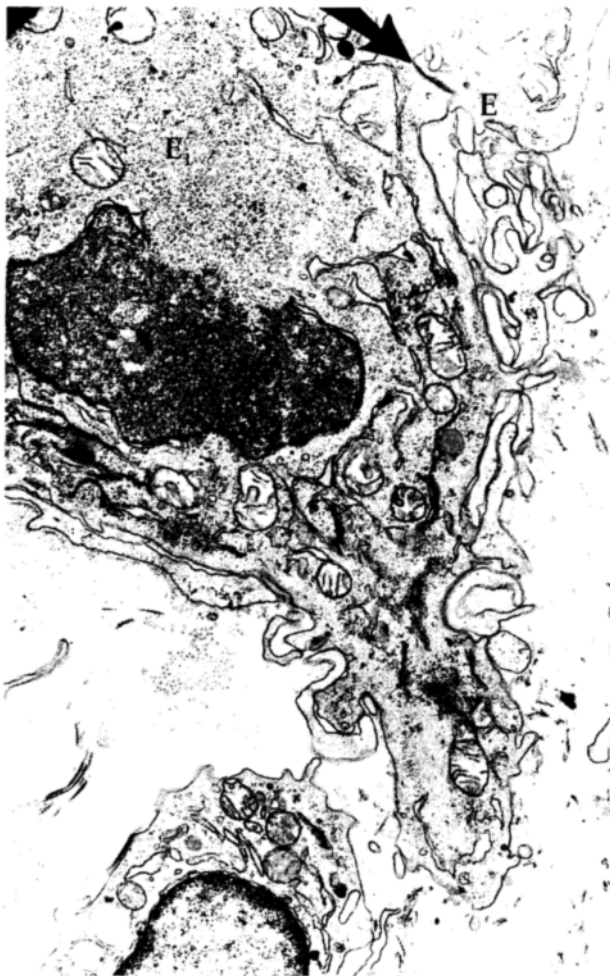


Figure 5B. Detail of the region shown in Figure 5A at another plane of sectioning. The emigrating endothelial cell (E1) is dividing, the nucleus is reconstituted. The endothelial cell is in connection with another endothelial cell (E) via interendothelial junction (arrow). Around the leading process of the endothelial cell and beneath the other endothelial cell (E) no basement membrane can be observed. X 6900.

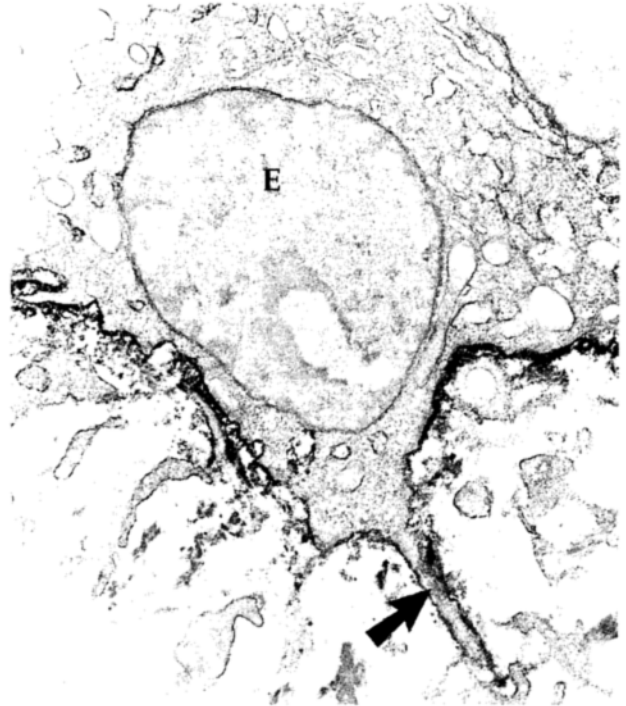


Figure 6. The process (arrow) of the endothelial cell (E) projecting into the connective tissue is free of deposited basement membrane material. Other parts of the subendothelium stains positively for laminin. X 9000.

ment membrane can lead to exposition of different domains of laminin, for example SIKVAV, which has been shown to induce endothelial cell proliferation and angiogenesis, and has also been able to enhance the production

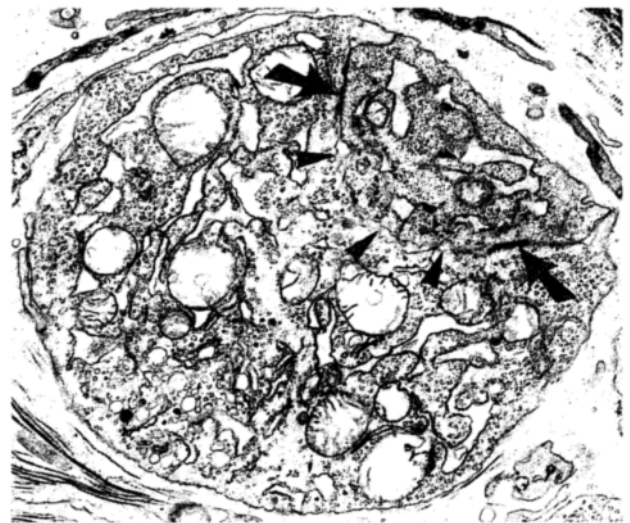


Figure 7. Cross section of a newly formed capillary. The slit-like lumen (arrow heads) is sealed by intercellular junctions (arrows). Basement membrane cannot be identified around the endothelial cells. X 11000.

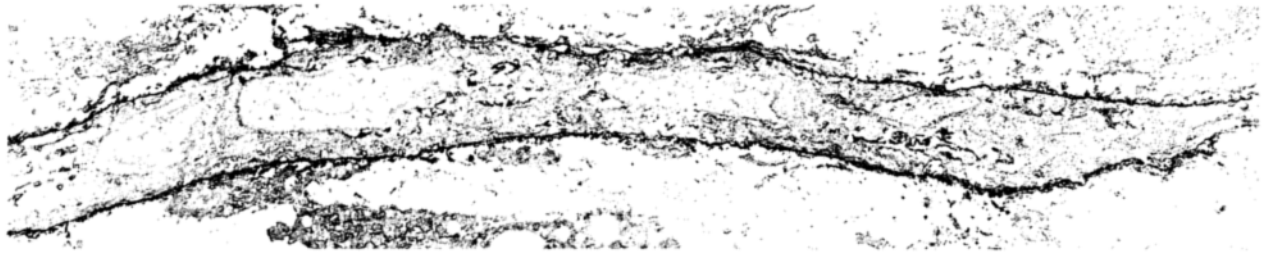


Figure 8. Longitudinal sections of a long newly formed capillary. Dilated lumen and pericytes cannot be observed. Basement membrane material staining positively for laminin is deposited around the capillary. X 2400

of proteases.⁵² bFGF can also be deliberated from the endothelial basement membrane during this process.⁵³ The regulated manner of basement membrane degradation is further supported by the observation that small vessels express high levels of TIMP-1 mRNA.⁵⁴ Loosening of intercellular contacts was not observed, suggesting that loss of contact inhibition is not responsible for initiation of cell division and migration (*Figure 5B*). Immunoelectron-microscopy showed complete degradation of basement membrane only at places where cellular processes were projecting into the connective tissue (*Figure 6*). During further migration, endothelial cells were arranged in parallel maintaining their polarity (basal-luminal), consequently a slit-like lumen was immediately formed between the endothelial cells (*Figs. 7-9*). This lumen was continuous with the lumen of the original vessel and was sealed by intact interendothelial junctions (*Figure 7*). This type of premature capillaries reached several hundred microns

in length (*Figure 8*). Similar structures containing slit-like lumen were observed by others suggesting that this type of angiogenesis also occurs in normal and other pathological conditions.⁴³⁻⁴⁵ The development of a slit-like lumen makes it easier to overcome the resistance of the connective tissue during tip advancing. Immunocytochemical analysis of the distribution of PECAM-1 during angiogenesis showed that this cell adhesion molecule is evenly distributed along the basal and luminal surfaces of endothelial cells in normal vessels, but is relocalized to intercellular junctions and to the apposed surface of the endothelial cells.⁵⁵ These results are in accordance with the observation that intact intercellular junctions are necessary for polarized migration of endothelial cells, at the same time, they also raise the possibility that during capillary growth the slit-like lumen is at least partially sealed (PECAM-1 homotypic interaction), preventing the dilatation of the lumen.

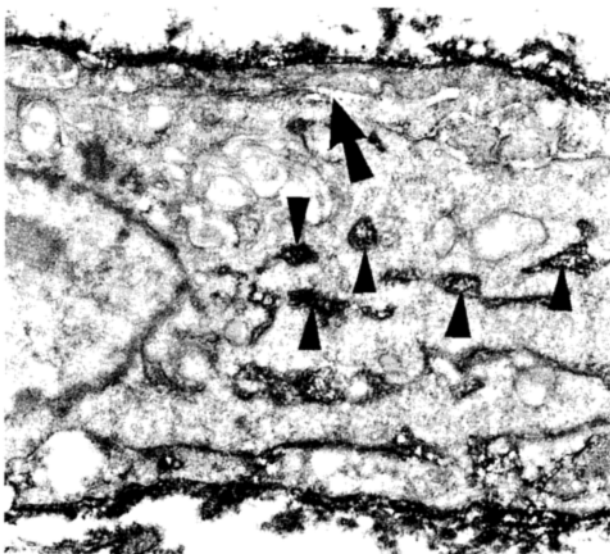


Figure 9. Detail of a capillary with slit-like lumen (arrow). Amorphous laminin positive material can be observed around the capillary. Note the laminin positive material in the endoplasmic reticulum cisternae of the endothelial cell (arrowheads). X 11000.

Basement membrane was found deposited immediately by the polarized endothelial cells and only cellular processes of cells migrating on the very tip of the growing capillary were seen to be free of basement membrane material. According to this model no stimulus is necessary for induction of lumen formation and the retained polarity of endothelial cells allows the continuous deposition of the basement membrane. Interstitial collagens were shown to enhance proliferation of endothelial cells, whereas other results suggested an increased deposition of collagen I by differentiating capillary tubes during *in vitro* angiogenesis.^{56,57} In this model, endothelial cells are separated from interstitial collagens by basement membrane during capillary growth, which phenomenon questions the importance of these molecules in the growth and differentiation of endothelial cells. The role of gelatinases has been extensively studied during angiogenesis, however, in the former model its role was restricted to the initial degradation, contrary to this model where it can contribute to the maintenance of the sol state of the basement membrane. As it has been shown, only processes of endothelial cells located at the tip of growing capillary are in contact with interstitial collagens. This phenomenon suggests an important role for interstitial collagenases during tip advancing.



Figure 10. Immunoelectronmicroscopy of a young capillary composed of three endothelial cell. Amorphous fibronectin-positive material is deposited around the capillary. There is no positive material in the endoplasmic reticulum cisternae of the cells. Material staining positively for fibronectin can be observed in the connective tissue (arrows). X 8100.

Supportive of this is the observation that VEGF can induce interstitial collagenase expression in endothelial cells.⁵⁸ As mentioned above the extracellular matrix surrounding the tumor frequently contains fibrin, fibronectin, vitronectin and thrombospondin. The wide substrate specificity of the plasminogen activator/plasmin system implicates an important role for these enzymes in angiogenesis. It has also been shown that uPA can enhance cellular migration independent of its proteolytic activity⁵⁹ and recently it has been demonstrated that uPAR is a receptor for vitronectin,⁶⁰ which is present in the peritumoral matrix and probable in the immature basement membrane of the growing capillaries. The importance of uPA in tumor angiogenesis has further been supported by the observation that anti-uPA antibody was able to inhibit network development in vitro and more importantly, uPA antagonist or mutant uPA expression was able to inhibit tumor growth.^{61,62}

Vast number of data suggest that integrins play a pivotal role in cell migration, differentiation and apoptosis.^{63,64} Recently it was demonstrated that specific integrins are

expressed in the newly developed growing capillaries. The most important among them is the $\alpha\beta3$ integrin which, as it was suggested, mediates the migration of endothelial cells in the fibrin containing tumor matrix.⁶⁵ This suggestion is in concert with the first model, but does not disagree with the second model either, where it was shown that the synthesized new basement membrane contains fibronectin (Figure 10). Since fibronectin immunoreactivity could not be observed in the endoplasmic reticulum of endothelial cells (Figure 10), in contrast to laminin and collagen IV (Figure 9), it is probable that this molecule is not synthesized by endothelial cells, but rather incorporated into basement membrane from the tumor matrix (Figure 10), providing a ligand for $\alpha\beta3$ integrin. Beside mediating migration of endothelial cells on the developing basement membrane, $\alpha\beta3$ can also play a role in the maintenance of the sol state of the basement membrane as a consequence of its ability to bind the matrix metalloproteinase MMP-2.⁶⁶ Interference with the ligand binding activity of this integrin by antibodies or RGD peptides was able to induce apoptosis of endothelial cells in growing capillaries,⁶⁷ and inhibit wound healing and tumor growth.⁶⁸ Some discrepancy exists, however, between the

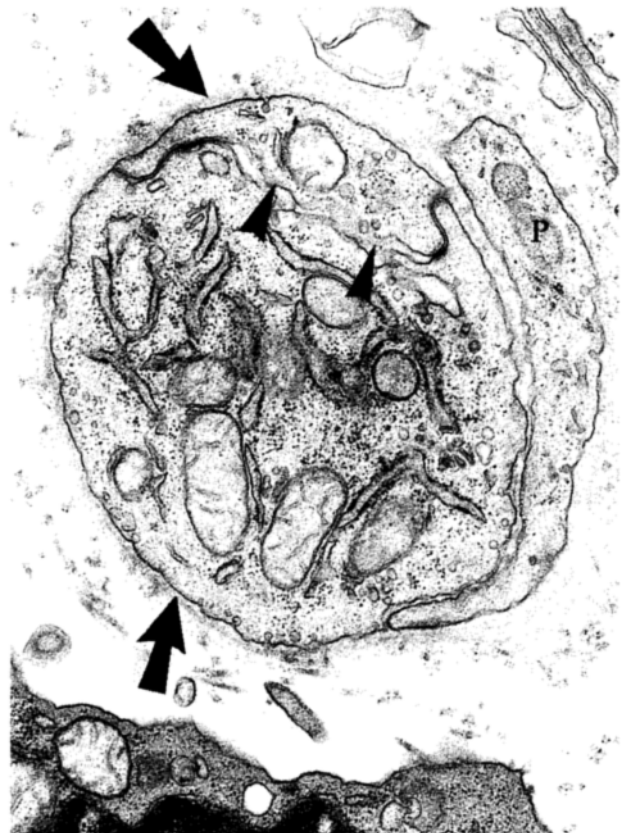


Figure 11. Newly formed capillary still showing slit-like lumen (arrow heads) but well defined basement membrane (arrows) and pericyte (P) can be observed around the capillary. X 11000.

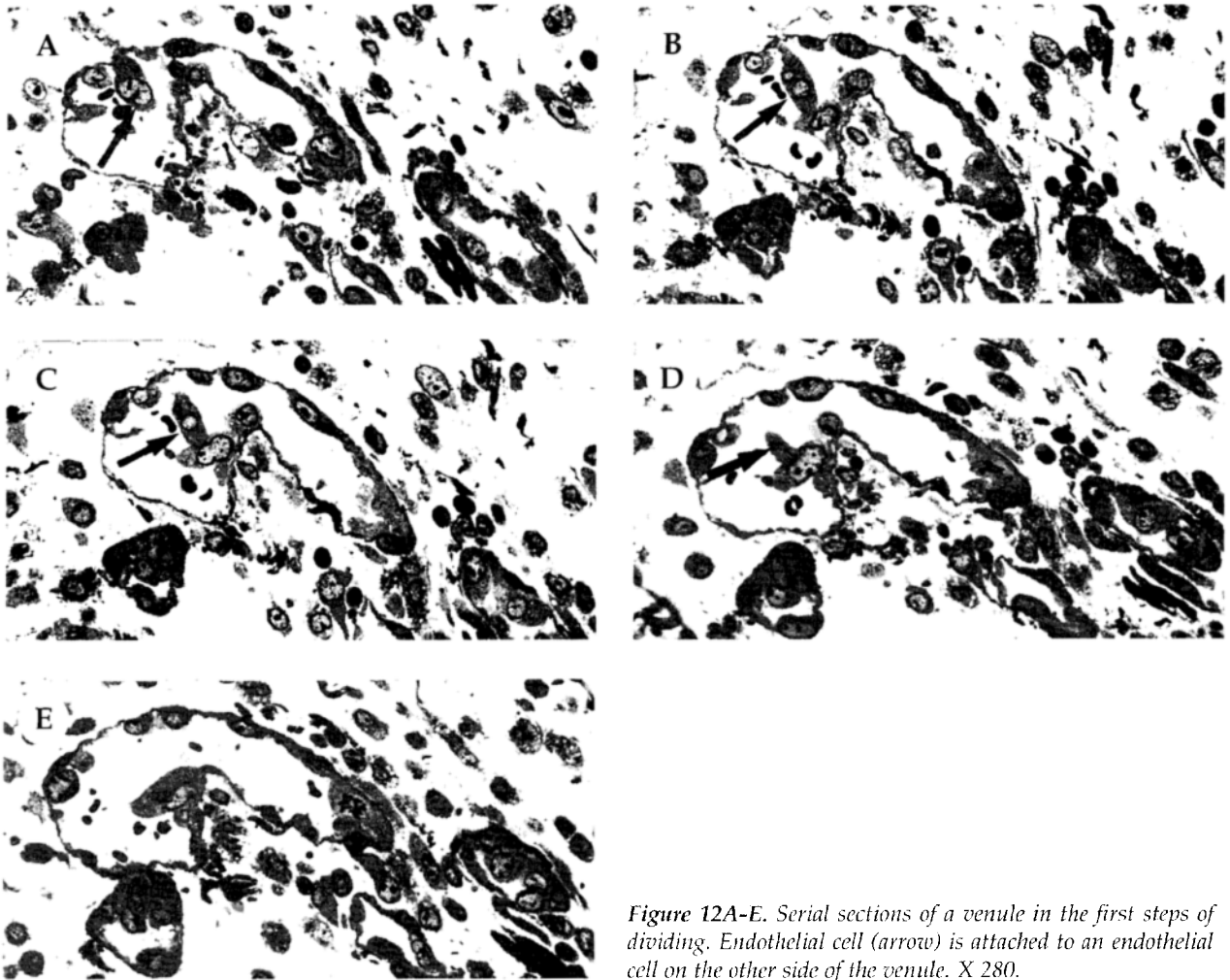


Figure 12A-E. Serial sections of a venule in the first steps of dividing. Endothelial cell (arrow) is attached to an endothelial cell on the other side of the venule. X 280.

second model and the proposed role of $\alpha v \beta 3$ integrin, since it was shown that Matrigel down regulates the expression of this integrin.⁶⁹ The selectivity of therapies based on the exclusive expression of $\alpha v \beta 3$ on newly growing capillaries is somewhat questioned by a recent observation detecting $\alpha v \beta 3$ integrin on parent vessels as well.⁷⁰ Other integrins may also be a target for anti-angiogenic therapies such as the laminin binding $\alpha 6 \beta 4$ integrin, detected on the entire length of the capillary sprout, and also in the parent vessels.⁷¹ In contrast to these results reduced staining for $\alpha 6$ integrin was observed in growing capillaries *in vivo*, which is in agreement with the well known notion that cell migration needs reduced adhesivity.⁵⁵ The positive effect of the reduction of adhesion on angiogenesis is supported by the observation that anti-integrin antibodies, enhanced, instead of reduction, the formation of tubules *in vitro*.⁷² Interesting results pointed out the important role of the tumor derived extracellular matrix in angiogenesis. Tumor cells deficient in fibronectin receptor or $\beta 1$ integrin developed a defective vasculature, characterized by small irregular leaky vessels, which phenome-

non resulted in reduced tumor growth as well.^{73,74} One possible explanation for this could be, the defective anchorage of the basement membrane deposited by the endothelial cells to the surrounding extracellular matrix. This is further supported by earlier observations that inhibition of crosslinks between collagen molecules caused regression of newly growing capillaries.⁷⁵

Regular basement membrane and pericytes appeared at later stage of capillary maturation (Figure 11). Increasing deposition of collagen IV,⁷⁶ the sol-gel transition of the basement membrane and the appearance of pericytes may all contribute to the cessation of endothelial cell proliferation and migration. It has been shown that latent TGF- β is activated by uPA in cocultures of endothelial cells and pericytes,⁷⁷ where the former down regulates the VEGF receptor on endothelial cell.⁷⁸

Numerous data suggest that the growth of capillary sprouts is not oriented towards the tumor, instead the process yields a high density anastomosing network of capillaries at the tumor periphery, a process leading to the observed phenomenon that vessel density is higher

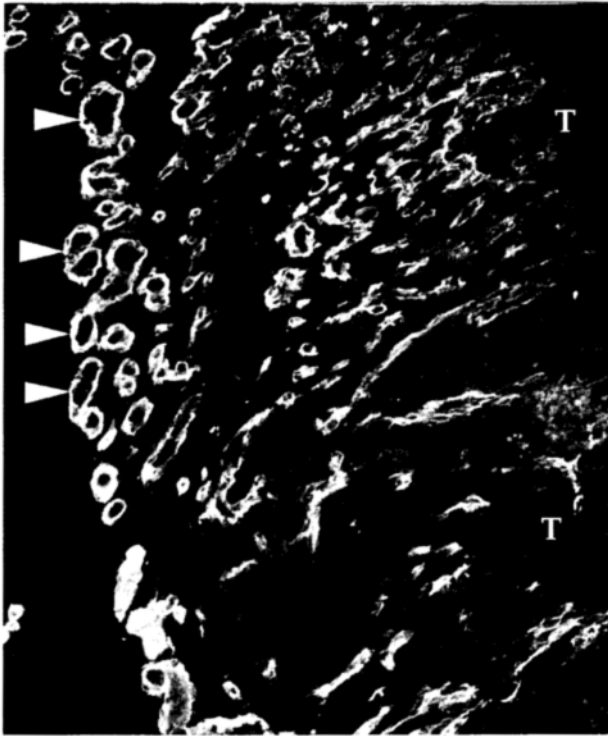


Figure 13. Numerous large caliber vessels (arrow heads) are stained positively for laminin outside the capillary sprouting area. T; Tumor. X 110.

around the tumor than inside of it. A possible explanation is that the continuously growing tumor incorporates the vessels at the tumor periphery, thereby thinning out the network, whereas a new network develops at the advancing tumor border.⁷⁹

A third type of angiogenesis involving larger vessels has been described recently. This process is called intussusceptive growth of vessels, culminating in the division of vessels (*Figure 14D*).^{80,81} The process is not completely known, but it starts with the projection of an endothelial cell into the lumen of the vessel and the attachment to endothelial cells on the other side (*Figure 12A-E*). Finally transluminal connective bridges develop, dividing the vessel into two or more parts. The process -which yields a high number of large caliber vessels situated outside the area of the active capillary growth (*Figure 13*) – probably does not contribute to the nutrition of the tumor significantly, but rather provides more sites for sprouting.

Angiogenesis in metastases

The above described models of angiogenesis are based on observations made in tissues that contain high amounts of connective tissue fibers, and can also be valid in case of tumors such as melanomas, skin-, breast-, colon cancer. The connective tissue has two important

roles in angiogenesis: it allows the build-up of a gradient of the angiogenic factor and provides space for vessel sprouting. The question arises, what kind of angiogenesis takes place in highly vascularised organs such as liver, lungs or adrenals, which in humans are the most frequent sites of metastasis ?

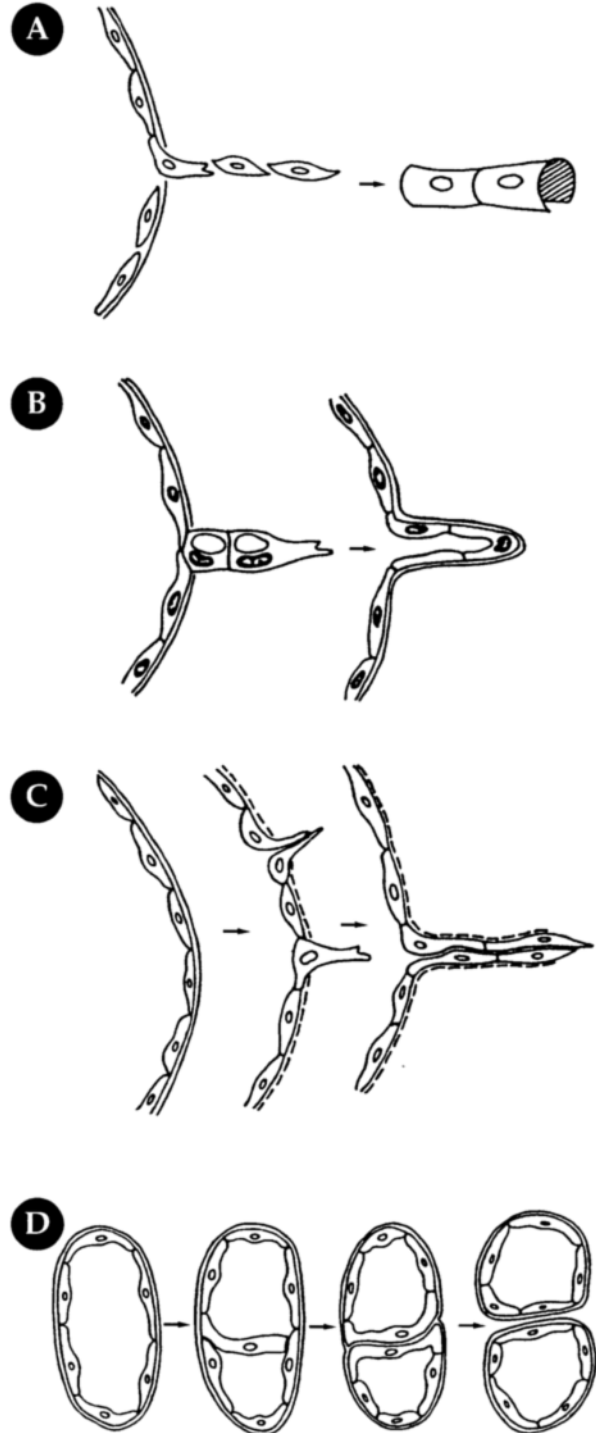


Figure 14A-D. Schematic representation of the different models of angiogenesis.

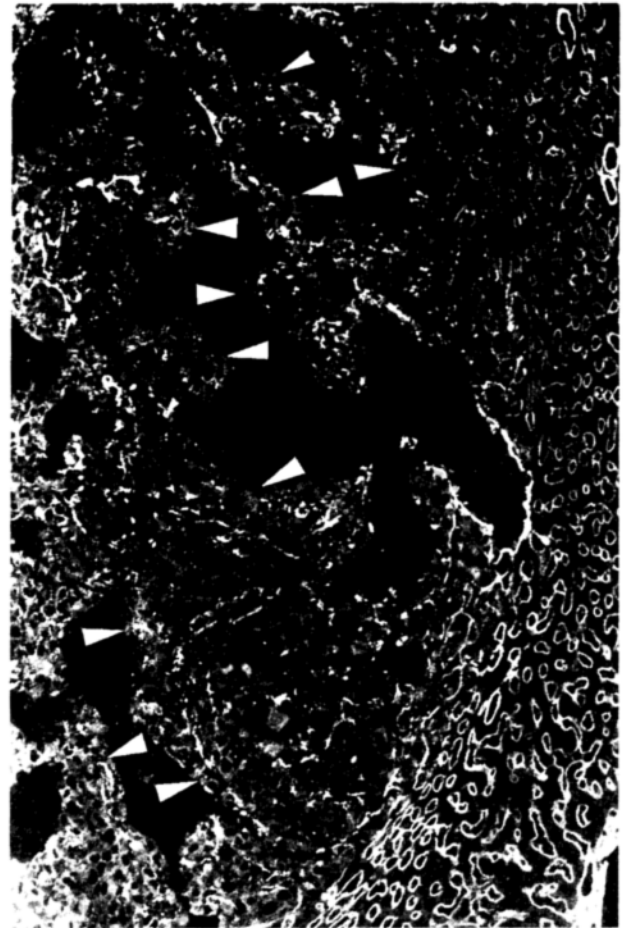


Figure 16. Cryosection of a liver metastasis stained for laminin. The walls of the large convoluted vessels stain negatively for laminin (arrow heads). X 75.

A process of angiogenesis, was described in case of liver metastases of Lewis lung carcinoma, showing remarkable differences to the models described above.⁸² Neither dilatation, or increase in the number of the vessels, nor enhanced proliferation of endothelial cells could be observed around the metastases, suggesting the absence of sprouting activity in this region. This indicates that the angiogenic stimulus could not reach the endothelial cells around the tumor, which can be explained by the high vascularity of the liver being responsible for diluting or flushing out the factor. The sparse connective tissue cannot provide sufficient space for diffusion of the angiogenic factor, and also impedes the migration of endothelial cells, thereby the development of new capillaries. Initiation of endothelial cell proliferation was caused by direct contact

Figure 15A-D. Serial sections of a liver metastasis of the 3LL-HH tumor. Large convoluted (V) and smaller vessels (asterisks) can be seen in the metastasis. Two sinusoids of the liver are continuous with these vessels (arrows). X 90.

between tumor cells and endothelial cells (*Figure 18*). Invading tumor cells migrated along the basement membrane of sinusoids and larger vessels, detaching the endothelial cells from their own basement membrane (*Figures 18, 19*). Interestingly the basement membrane was not degraded and remained on the surface of hepatocytes, even when these cells became enclosed into the tumor (*Figure 20*). The observation that proliferative activity is restricted to endothelial cells situated inside the metastases can be explained by results demonstrating that mRNAs of VEGF receptors (KDR, flt-1) were more strongly expressed in metastases of colorectal tumors than in the surrounding liver tissue.⁸³

The proliferating endothelial cells formed large convoluted vessels deeply penetrating into the metastases (*Figures 15B, 16*). These vessels were even lacking an immunohistochemically detectable basement membrane (*Figures 16, 17*). This observation is rather unusual

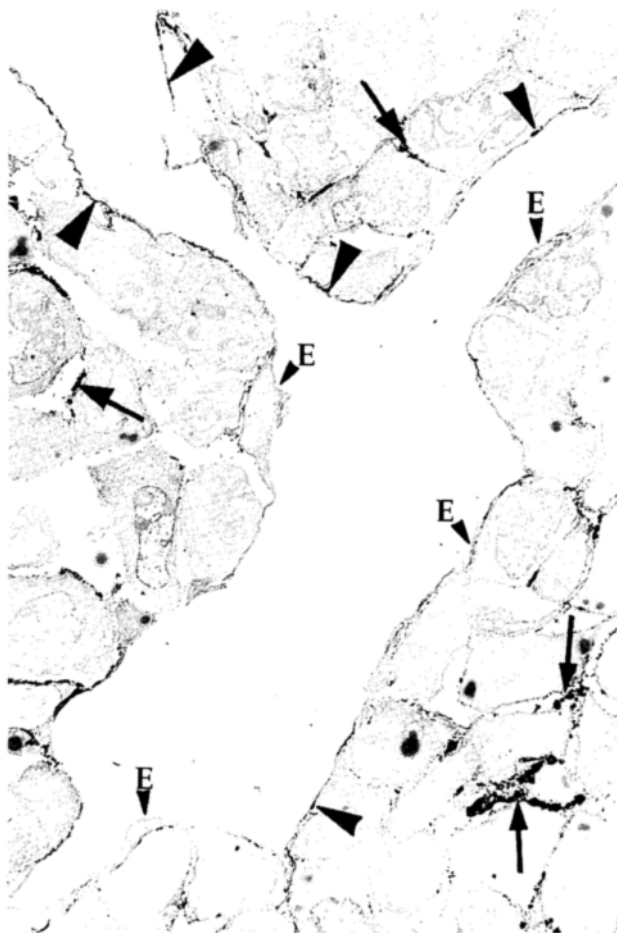


Figure 17. Immunoelectronmicroscopy of a part of a convoluted vessel inside a metastasis. Under the endothelial cells (E) laminin positive material can be observed only in small spots (arrow heads). Similar material is deposited in some areas by the tumor cells (arrows). X 1.000.

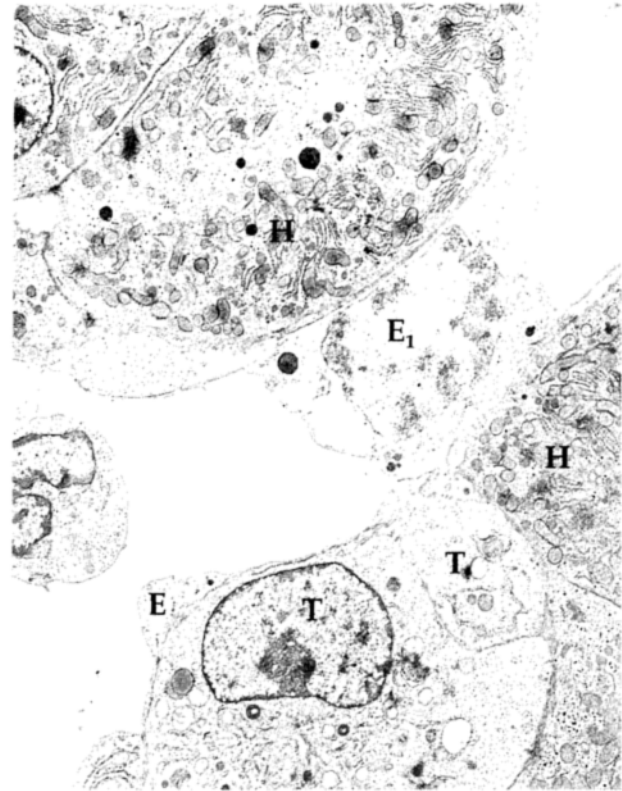


Figure 18. 3LL-HH tumor cells (T) migrating between the endothelial cells (E) and hepatocytes (H) in a sinusoid at the periphery of a metastasis. The endothelial cell (E1) in the vicinity of the tumor cells shows chromatin condensation. X 3.000.

although lack of electron density is commonly observed in case of liver sinusoids, lymphatic capillaries or tumor vessels. Complete loss of basement membrane (loss of anchorage) – as was mentioned earlier – leads to apoptosis and vessel regression. It must be noted, however, that in 3LL tumors – although having a very poorly developed stroma – the tumor cells deposited some laminin containing material, which could serve as substrate for attachment of endothelial cells in these new vessels. This attachment took place only at some spots on the surface of tumor cells, resulting weak anchorage which can be responsible for the high fragility of these vessels (*Figure 17*). In serial sections these vessels were continuous with the sinusoidal system of the liver consequently supplied mainly by the portal vein (*Figure 15A-D*).

Another less frequently observed type of 3LL-HH liver metastases showed a different pattern of vasculature. These metastases contained small vessels with detectable basement membranes, and were located in the vicinity of portal tracts. Their vasculature probably raised by sprouting from the peribiliary plexus, in the periportal connective tissue, suggesting that blood supply was originating mainly from the hepatic artery.

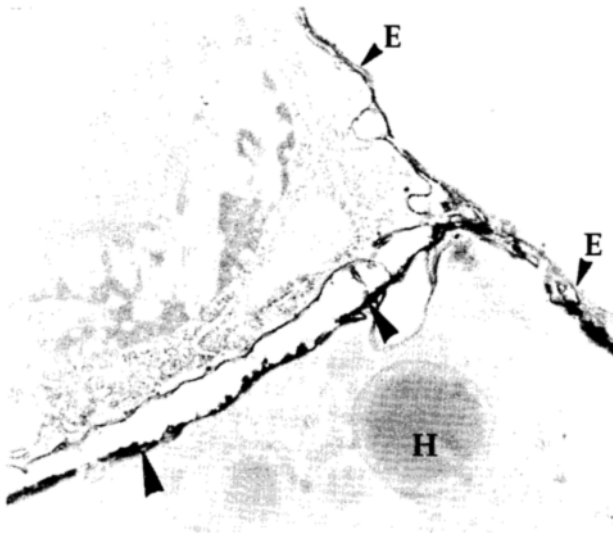


Figure 19. Invading tumor cell (T) in a sinusoid detaches the endothelial cell (E) from the basement membrane (arrow heads). The laminin positive material remains associated with the hepatocyte (H). X 10,000.

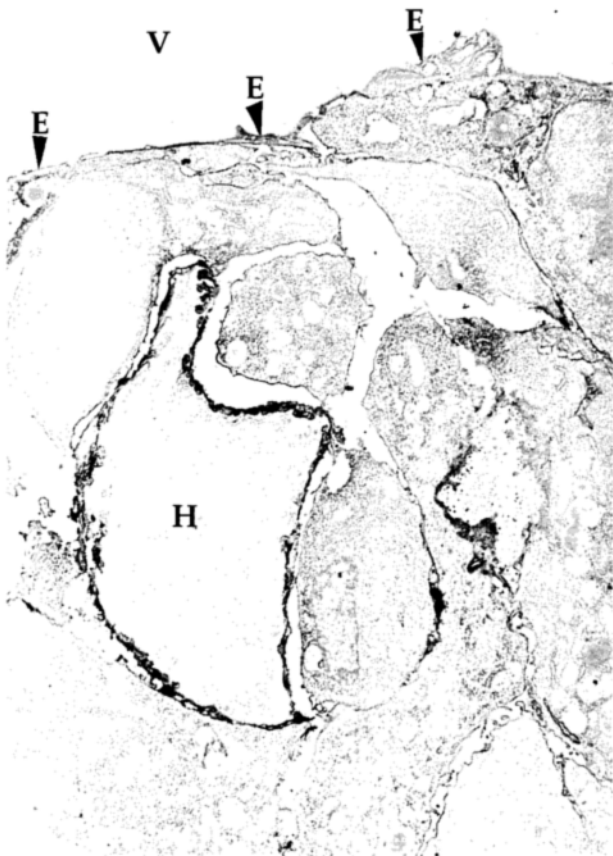


Figure 20. The surface of a hepatocyte (H) enclosed into the metastasis still stains positively for laminin. E; Endothelium, V; Vessel lumen. X 1.300.

Therapeutic considerations

The above results strongly suggest that the type of vasculature and blood supply can be dependent on the localization of metastases in organs having both arterial and venous blood supply. Accordingly, these and other observations support the possibility that the tissue architecture of organs, in which angiogenesis is taking place, has an important impact on the process of angiogenesis and consequently on the structure of the developing neovasculature. On the other hand the properties of tumor cells can also determine the outcome of the angiogenic response. For example the previously described process of angiogenesis in liver metastases can be valid in case of anaplastic tumors having high invasive ability and poorly developed tumor stroma. Well differentiated tumors, however, showing the same tissue architecture in primary tumors as in metastases, probably elicit a different type of angiogenesis. The widely used methods in the therapy of primary and secondary liver tumors (hepatic artery infusion, hepatic artery ligation and chemoembolization) are based on the notion that most tumors in the liver have an arterial blood supply.⁸⁴⁻⁸⁶ In contrast to this, it is generally accepted that during angiogenesis, new vessels originate mainly from postcapillary venules.^{2,3} Several authors suggest, however, that new capillaries can originate from arterioles or large veins, containing elastic laminae and smooth muscle cells, demonstrating the fact that such structures cannot prevent the emigration of endothelial cells.^{87,88} A number of data suggest that a considerable portion of human and experimental liver metastases have portal blood supply,^{89,91} and even vessels, originating from hepatic sinusoids can contribute to the nutrition of the entire metastatic nodule, not only to the supply of the tumor periphery.⁹² According to these facts, more attention should be paid in the future to the portal blood supply of liver metastases in the design of locoregional therapy.

References

1. *Blood ChH, Zetter BR:* Tumor interactions with the vasculature: angiogenesis and tumor metastasis. *Biochem Biophys Acta* 1032:89-118, 1990.
2. *Folkman J:* Tumor angiogenesis. *Adv Cancer Res* 43:175-203, 1985.
3. *Pawletz N, Knierim M:* Tumor-related angiogenesis. *Crit Rev Oncol Hematol* 9:197-242, 1989.
4. *de Waal RMW, van Altena MC, Erhard H et al:* Lack of lymphangiogenesis in primary cutaneous melanoma. *Am J Pathol* 150:1951-1957, 1997.
5. *Jeltsch M, Kaipainen A, Joukov V et al:* Hyperplasia of lymphatic vessels in VEGF-C transfected mice. *Science* 276:1423-1425, 1997.
6. *Wiedner N:* Intratumor microvessel density as a prognostic factor in cancer. *Am J Pathol* 147:9-19, 1995.
7. *Busam KJ, Berwick M, Blessing K et al:* Tumor vascularity is not a prognostic factor for malignant melanoma of the skin. *Am J Pathol* 147:1049-1056, 1995.

8. Gabbert H, Meier S, Gerharz CD *et al*: Tumor cell dissociation at the invasion front: a new prognostic parameter in gastric cancer patients. *Int J Cancer* 50:202-207, 1992.
9. Gabbert H, Meier S, Gerharz CD *et al*: Incidence and prognostic significance of vascular invasion in 529 gastric-cancer patients. *Int J Cancer* 49:203-207, 1991.
10. Jain RK: Vascular and interstitial barriers to delivery of therapeutic agents in tumors. *Cancer Metastasis Reviews* 9:253-266, 1990.
11. Bouck N, Stelmach V, Hsu SC: How tumors become angiogenic. *Adv Cancer Res* 69: 135-174, 1996.
12. Hanahan D, Folkman J: Patterns and emerging mechanisms of the angiogenic switch during tumorigenesis. *Cell* 86:353-364, 1996.
13. Vernon RB, Sage EH: Between molecules and morphology. Extracellular and creation of vascular form. *Am J Pathol* 147:873-883, 1995.
14. Folkman J, Haudenschild C: Angiogenesis in vitro. *Nature* 288:551-556, 1980.
15. Maciag T, Kadish J, Wilkins L *et al*: Organizational behavior of human umbilical vein endothelial cells. *J Cell Biol* 94:511-520, 1982.
16. Ingber DE, Folkman J: Mechanochemical switching between growth and differentiation during fibroblast growth factor-stimulated angiogenesis in vitro: role of extracellular matrix. *J Cell Biol* 109:317-330, 1989.
17. Kubota Y, Kleinman HK, Martin GR, Lawley TJ: Role of laminin and basement membrane in the morphological differentiation of human endothelial cells into capillary like structures. *J Cell Biol* 107: 1589-1598, 1988.
18. Grant DS, Kibbey MC, Kinsella JL *et al*: The role of basement membrane in angiogenesis and tumor growth. *Path Res Pract* 190:854-863, 1994.
19. Vernon RB, Angello JC, Iruela-Arispe ML *et al*: Reorganization of basement membrane matrices by cellular traction promotes the formation of cellular networks in vitro. *Lab Invest* 66:536-547, 1992.
20. Montesano R, Vassalli JD, Baird A *et al*: Basic Fibroblast Growth Factor induces angiogenesis in vitro. *Proc Nat Acad Sci* 83:7297-7301, 1986.
21. Montesano R, Orci L: Tumor promoting phobol esters induce angiogenesis in vitro. *Cell* 42: 469-477, 1985.
22. Mignatti P, Tsuboi R, Robbins E, Rifkin DB: In vitro angiogenesis on the human amniotic membrane: requirement for Fibroblast Growth Factor-induced proteinases. *J Cell Biol* 108: 671-682, 1989.
23. Nicosia RF, Tchao R, Leighton J: Histiotypic angiogenesis in vitro: light microscopic ultrastructural and autoradiographic studies. *In Vitro* 18:538-549, 1982.
24. Nicosia RF, Madri JA: The microvascular extracellular matrix. *Am J Pathol* 128:78-90, 1987.
25. Nagy JA, Brown LF, Senger DR *et al*: Pathogenesis of tumor stroma generation: a critical role for leaky blood vessels and fibrin deposition. *Biochim Biophys Acta* 948:305-326, 1988.
26. Dvorak HF, Harvey VS, Estrella P *et al*: Fibrin containing gels induce angiogenesis. *Lab Invest* 57:673-686, 1987.
27. Warren BA: Tumor angiogenesis. In *Angiogenesis, vascular morphology and blood flow of experimental and human tumors*. (Ed: Peterson HI) CRC Press, 1979, pp. 49-75.
28. Cliff WJ: Observations on healing tissue: a combined light and electron microscopic investigation. *Philos Trans R Soc London Biol Sci* 246:305-325, 1963.
29. Schoefl GI: Studies on inflammation III. Growing capillaries: their structure and permeability. *Virchows Arch (A)* 337:97-141, 1963.
30. Ausprunk DH, Folkman J: Migration and proliferation of endothelial cells in preformed and newly formed blood vessels during tumor angiogenesis. *Microvasc Res* 14:53-65 1977.
31. Warren BA: Origin and fate of blood borne tumor emboli. *Cancer Biol Rev* 2:98-169, 1981.
32. Paku S, Timar J, Lapis K: Ultrastructure of invasion in different tissue types by lewis lung tumor variants. *Virchows Arch (A)* 417:435-442, 1990.
33. Skinner SA, Frydman GM, O'Brien PE: Microvascular structure of benign and malignant tumors of the colon in humans. *Dig Dis Sci*40:373-384, 1995.
34. Rizzo V, DeFouw DO: Capillary sprouts restrict macromolecular extravasation during normal angiogenesis in the chick chorioallantoic membrane. *Microvasc Res* 52:47-57, 1996.
35. Dvorak HF, Nagy JA, Dvorak JT, Dvorak AM: Identification and characterization of the blood vessels of solid tumor that are leaky to circulating macromolecules. *Am J Pathol* 133:95-109, 1988.
36. Kohn S, Nagy JA, Dvorak HF, Dvorak AM: Structural basis of hyperpermeability of tumor blood vessels. *Lab Invest* 67:596-607, 1992.
37. Robert WG, Palade GE: Neovasculature induced by Vascular Endothelial Growth Factor is fenestrated. *Cancer Res* 57:765-772 1997.
38. Bowersox JC, Sorgente N: Chemotaxis of aortic endothelial cells in response to fibronectin. *Cancer res* 42:2547-2551, 1982.
39. Leavesley DI, Shwartz MA, Rosenfeld M, Cheresh DA: Integrin beta1- and beta3- mediated endothelial cell migration is triggered through distinct signaling mechanisms. *J Cell Biol* 121:163-170, 1993.
40. Nicosia RF, Tuszynsky GP: Matrix-bound thrombospondin promotes angiogenesis in vitro. *J Cell Biol* 124: 183-193, 1994.
41. Bertin N, Clezardin Ph, Kubiak R, Frappart L: Thrombospondin-1 and -2 messenger RNA expression in normal, benign, and neoplastic human breast tissues: correlation with prognostic factors, tumor angiogenesis and fibroblastic desmoplasia. *Cancer Res* 57:396-399, 1997.
42. Tuszynsky GP, Nicosia RF: Localization of thrombospondin and its cysteine-serine-valine-threonine-cysteine-glycine receptor in human breast carcinoma. *Lab Invest* 70:228-233, 1994.
43. Cavallo T, Sade R, Folkman J, Cotran R: Ultrastructural autoradiographic studies of the early vasoproliferative response in tumor angiogenesis. *Am J Pathol* 70:345-362, 1973.
44. Wakui S: Two- and three dimensional ultrastructural observation of two cell angiogenesis in human granulation tissue. *Virchows Arch (B)* 56:127-139, 1988.
45. Konerding MA, Van Ackern C, Hinz S *et al*: Ultrastructural studies of tumor angiogenesis in human xenotransplanted tumors. *Int J Radiat Biol* 60:49-53, 1992.
46. Bar Th, Guldner F-H, Wolff JR: Seamless type endothelial cells of blood capillaries. *Cell Tissue Res* 235:99-106, 1984.
47. Paku S, Paweletz N: First steps of tumor-related angiogenesis. *Lab Invest* 65:334-345, 1991.
48. Lewalle JM, Munaut C, Pichot B *et al*: Plasma membrane-dependent activation of gelatinase A in human vascular endothelial cells. *J Cell Physiol* 165:475-483 1995.
49. Pepper MS, Sappino A-P, Stocklin R *et al*: Upregulation of urokinase receptor expression on migrating endothelial cells. *J Cell Biol* 122: 673-684, 1993.
50. Montgomery AMP, DeClerck YA, Langley KE *et al*: Melanoma mediated dissolution of extracellular matrix: contribution of urokinase-dependent and metalloproteinase -dependent proteolytic pathways. *Cancer Res* 53:693-700, 1993.
51. Koolwijk P, van Erck MGM, de VreeWJA *et al*: Cooperative effect of TNF alpha, bFGF, VEGF on formation of tubular

- structures of human microvascular endothelial cells in a fibrin matrix. Role of urokinase activity. *J Cell Biol* 132:1177-1188, 1996.
52. Grant DS, Kinsella JL, Fridman R et al: Interaction of endothelial cells with laminin A chain peptide (SIKVVAV) in vitro and induction of angiogenic behavior in vivo. *J Cell Physiol* 153:614-625, 1992.
 53. O'Brien T, Cranston D, Fuggle S et al: Two mechanisms of basis fibroblast growth factor induced angiogenesis in bladder cancer. *Cancer Res* 57:136-140, 1997.
 54. Lindsay C, Thorgeirsson UP, Tsuda H, Hirohashi S: Expression of tissue inhibitor of metalloproteinase-1 and type IV collagenase/gelatinase messenger mRNAs in human breast cancer. *Human Pathol* 28:359-366, 1997.
 55. Berger R, Albelda SM, Berd D et al: Expression of platelet-endothelial cell adhesion molecule-1 (PECAM-1) during melanoma induced angiogenesis in vivo. *J Cutan Pathol* 20:399-406, 1993.
 56. Madri JA, Pratt BM: Endothelial cell-matrix interactions: in vitro models of angiogenesis. *J Histochem Cytochem* 34:85-91, 1986.
 57. Iruela-Arispe ML, Hasselaar P, Sage H: Differential expression of extracellular proteins is correlated with angiogenesis in vitro. *Lab Invest* 64:174-186, 1991.
 58. Unemori EN, Ferrara N, Bauer EA, Amento EP: Vascular endothelial growth factor induces interstitial collagenase expression in human endothelial cells. *J Cell Physiol* 153:557-562, 1992.
 59. Busso N, Masur SK, Lazega D et al: Induction of migration by pro-urokinase binding to its receptor: possible mechanism for signal transduction in human epithelial cells. *J Cell Biol* 126:259-270, 1994.
 60. Wei Y, Waltz DA, Rao N et al: Identification of the urokinase receptor as an adhesion receptor for vitronectin. *J Biol Chem* 269:32380-32388, 1994.
 61. Min HY, Doyle LV, Vitt CR et al: Urokinase receptor antagonists inhibit angiogenesis and primary tumor growth in syngenic mice. *Cancer Res* 56:2428-2433, 1996.
 62. Evans CP, Elfman F, Parangi S et al: Inhibition of prostate cancer neovascularization and growth by urokinase-plasminogen activator receptor blockade. *Cancer Res* 57:3594-3599, 1997.
 63. Huttenlocher A, Sandborg R, Horwitz AF: Adhesion in cell migration. *Curr Opin Cell Biol* 7:697-706, 1995.
 64. Ruoslahti E, Reed JC: Anchorage dependence, integrins, and apoptosis. *Cell* 77:477-478, 1994.
 65. Brooks PC, Clark RAF, Cheresh DA: Requirement of vascular integrin v3 for angiogenesis. *Science* 264: 569-571, 1994.
 66. Brooks PC, Stromblad S, Sanders LC et al: Localization of matrix metalloproteinase MMP-2 to the surface of invasive cells by interaction with integrin v3. *Cell* 85:683-693, 1996.
 67. Brooks PC, Montgomery AMP, Rosenfeld M et al: Integrin v3 antagonists promote tumor regression by inducing apoptosis of angiogenic blood vessels. *Cell* 79:1157-1164, 1994.
 68. Christofidou-Solomidou M, Bridges M, Murphy GF et al: Expression and function of endothelial cell v integrin receptors in wound-induced human angiogenesis in human skin/SCID mice chimeras. *Am J Pathol* 151:975-983, 1997.
 69. Boudreau N, Andrews C, Srebrow A et al: Induction of angiogenic phenotype by Hox D3. *J Cell Biol* 139:257-264, 1997.
 70. Max R, Gerristen RRCM, Nooijnen PTGA et al: Immunohistochemical analysis of integrin v3 expression on tumor-associated vessels of human carcinomas. *Int J Cancer* 71:320-324, 1997.
 71. Enestein J, Kramer R: Confocal microscopic analysis of integrin expression on the microvasculature and its sprouts in the neonatal foreskin. *J Invest Dermatol* 103:381-386, 1994.
 72. Gamble JR, Matthias LJ, Meyer G et al: Regulation of in vitro capillary tube formation by anti-integrin antibodies. *J Cell Biol* 121:931-943, 1993.
 73. Schreiner CL, Fisher M, Bauer J, Juliano RL: Defective vasculature in fibronectin-receptor-deficient CHO cell tumors in nude mice. *Int J Cancer* 55:436-441, 1993.
 74. Bloch W, Forsberg E, Lentini S et al: $\alpha 1$ integrin is essential for teratoma growth and angiogenesis. *Lab Invest* 77:265-278, 1997.
 75. Ingber D, Folkman J: Inhibition of angiogenesis through modulation of collagen metabolism. *Lab Invest* 59: 44-51, 1988.
 76. Form DM, Pratt BM, Madri JA: Endothelial cell proliferation during angiogenesis. *Lab Invest* 55:521-530, 1986.
 77. Oldridge A, Saunders KB, Smith SR, D'Amore PA: An activated form of transforming growth factor is produced by cocultures of endothelial cells and pericytes. *Proc Nat Acad Sci* 86:4544-4548, 1989.
 78. Mandriota SJ, Menoud P-A, Pepper MS: Transforming growth factor 1 down regulates vascular endothelial growth factor receptor 2/flk-1 expression in vascular endothelial cells. *J Biol Chem* 271:11500-11505, 1996.
 79. Thompson WD, Shiach KJ, Fraser RA et al: Tumours acquire their vasculature by vessel incorporation, not by vessel ingrowth. *Lab Invest* 61: 323-332, 1987.
 80. Nagy JA, Morgan ES, Herzberg KT et al: Pathogenesis of ascites tumor growth: angiogenesis, vascular remodeling, and stroma formation in the peritoneal lining. *Cancer Res* 55:376-385, 1995.
 81. Patan S, Munn LL, Jain RK: Intussusceptive microvascular growth in human colon adenocarcinoma xenograft: a novel mechanism of tumor angiogenesis. *Microvasc Res* 51:260-272, 1996.
 82. Paku S, Lapis K: Morphological aspects of angiogenesis in experimental liver metastases. *Am J Pathol* 143:926-936, 1993.
 83. Warren RS, Yuan H, Matli MR et al: Regulation by vascular endothelial growth factor of colon cancer tumorigenesis in a mouse model of experimental liver metastasis. *J Clin Invest* 95: 1789-1797, 1995.
 84. Bredis C, Young G: The blood supply of neoplasms in the liver. *Am J Pathol* 30:969-985, 1954.
 85. Archer SG, Gray BN: Vascularization of small liver metastases. *Br J Surg* 76: 545-548, 1989.
 86. Lin G, Lunderquist A, Hagerstrand I, Boijesen E: Postmortem examination of the blood supply and vascular pattern of small liver metastases. *Surgery* 96: 517-526, 1984.
 87. Hori K, Suzuki M, Tanda S, Saito S: In vivo analysis of tumor vascularization in the rat. *Jpn J Cancer Res* 81:279-288, 1990.
 88. Diaz-Flores L, Gutierrez R, Valladares F et al: Intense vascular sprouting from rat femoral vein induced by postaglandins E1 and E2. *Anat Rec* 238:68-76, 1994.
 89. Haugeberg G, Strohmeyer T, Lierse W, Bocker W: Histological investigation of gelatine-injected liver specimens with special regard to the vascularization of micrometastases. *J Cancer Res Clin Oncol* 114:415-419, 1988.
 90. Riemenschneider T, Ruf C, Kratzsch HC et al: Arterial, portal or combined arterio-portal regional chemotherapy in experimental liver tumours. *J Cancer Res Clin Oncol* 118:597-600, 1992.
 91. Taniguchi H, Daidoh T, Shioaki Y, Takahashi T: Blood supply and drug delivery to primary and secondary human liver cancers studied with in vivo bromodeoxyuridine labeling. *Cancer* 71: 50-55, 1993.
 92. Terayama N, Terada T, Nakanuma Y: A morphometric and immunohistochemical study on angiogenesis of human metastatic carcinomas of the liver. *Hepatology* 24:816-819, 1996.

Original Paper

Vascularization of cutaneous melanoma involves vessel co-option and has clinical significance

Balázs Döme^{1,4}, Sándor Paku^{1,2}, Beáta Somlai³ and József Tímár^{1,4*}

¹ 1st Institute of Pathology and Experimental Cancer Research, Semmelweis University, Budapest, Hungary

² Department of Molecular Pathology, Joint Research Organization of the Hungarian Academy of Sciences and Semmelweis University, Budapest, Hungary

³ Department of Dermato-Venerology, Semmelweis University, Budapest, Hungary

⁴ Department of Tumour Progression, National Institute of Oncology, Budapest, Hungary

*Correspondence to:

Dr J. Tímár, Department of Tumour Progression, National Institute of Oncology, Budapest, Ráth Gy. u. 7-9, H-1122 Hungary.
E-mail: jtimar@oncol.hu

Abstract

This study was undertaken to determine the role and the fate of the peritumoural vascular plexus during the vascularization of human malignant melanoma (hMM) and in an appropriate murine melanoma model system. The prognostic significance of the vascularity of different tumour areas was also evaluated. Despite morphometry revealing several-fold higher microvessel densities (MVDs) in the peritumoural tissue than at the centre of the tumour, the development of visceral metastases of hMM was exclusively correlated with the MVD of the tumour centre. Furthermore, the 5-year survival of the patient group with low tumour centre MVD ($<30/\text{mm}^2$, $n=29$) was 100%, compared to 1/16 patients alive with high tumour centre MVD ($>30/\text{mm}^2$, $n=16$). Morphometric analysis and three-dimensional reconstruction of vessel networks of both human and murine melanomas showed clearly that the peritumoural vascular plexus present at the melanoma base is continuously being incorporated into the growing tumour mass. Once vessels become incorporated, sprouting ceases and the proliferating endothelial cells (EC) take part only in vessel dilatation. Moreover, the immunohistochemical and ultrastructural characterization of microvessels demonstrated that the pericyte coverage of endothelial tubes was complete in all of the investigated areas, in both human and murine melanomas. Copyright © 2002 John Wiley & Sons, Ltd.

Keywords: vessel incorporation; melanoma; intratumoural vessels; prognosis

Received: 31 October 2001

Accepted: 12 February 2002

Introduction

In the past decade, systematic studies have provided ample evidence that tumour progression correlates with tumour-induced angiogenesis [1], but this issue has remained controversial in the case of human malignant melanoma (hMM) of the skin [2–13]. Most of these studies used the principle of selecting the vascular ‘hot spots’ as a basic approach [1,14], but it should be kept in mind that the site of tumour cell intravasation does not necessarily correspond to the area of the highest MVD, especially when the ‘hot spot’ is located outside the tumour mass. Neo-angiogenesis has been considered as synonymous with directed vessel ingrowth in almost all of these studies, although alternative mechanisms seem to exist, both experimentally and in human tumours [15,16]. It has been reported recently that non-small cell lung carcinoma grows without inducing neo-angiogenesis [17], and the growing glioma and mouse adenocarcinoma can co-opt (i.e. incorporate) host vessels [18,19]. However, the mechanisms of vessel ingrowth and incorporation probably operate in different proportions in various tumour types.

It has long been speculated [20–22] that tumour vasculature is characterized by a distinct maturation

defect, namely the absence of pericytes, that is thought to be at least partially responsible for the irregular, tortuous and leaky blood vessels found within tumours. If we accept the concept of vessel co-option, the level of coverage by pericytes in different microvascular beds must be relevant; the nascent, unstable and vulnerable intratumoural vessels, which have not had enough time to differentiate, might therefore dictate the clinical course to a greater extent than the more mature incorporated vessels.

Despite the high vascularity at the tumour base (hot spots) observed several times in hMM [5,9,23,24], this phenomenon has remained experimentally unexplained, probably because of the difficulty of modelling the primary hMM. In experimental models, the rapid growth kinetics of melanoma make the observation of progression and angiogenesis difficult in the very early stages, corresponding to human tumours in radial growth phase. If the process of vascularization of these rapidly growing mouse tumours is very different from hMM, then these models may be less useful for therapeutic studies, particularly when anti-angiogenic drugs are investigated.

To clarify the role of the peritumoural vascular plexus in the process of vascularization of hMM, we decided to follow up the development and fate of this

dc_301_11

peritumoural vessel network in a suitable mouse tumour model system. For this purpose we performed morphometry and 3D reconstruction of the vasculature in hMM samples and studied the growth, mechanism of vascularization and EC proliferation in B16 mouse melanoma after intradermal inoculation. To analyse microvessel maturation, we also investigated the distribution of pericytes in human and mouse melanomas.

Materials and methods

Clinical data

This study used 45 primary hMM cases with a minimum follow-up period of 5 years, four non-tumourous skin biopsy samples and three naevi. The two sexes were represented equally. Tumours had no detectable metastases at the time of diagnosis and were categorized according to thickness (thin <1.5 mm, $n=13$; medium thick 1.5–4.0 mm, $n=17$; and thick >4.0 mm, $n=15$; Table 1A) and to the actual type of progression (non-metastatic, $n=15$; lymph node-metastatic, $n=14$; and organ-metastatic, $n=16$; Table 1B).

Animal model

Inbred C57Bl/6 mice were anaesthetized and 10^4 B16 cells in 1 μ l Hanks' solution were inoculated intradermally, next to the epidermal–dermal junction, under a

dissecting microscope by using a precision syringe (0.15 mm diameter, Hamilton). To prove the proper localization of the injection sites, tumour cells were labelled with membrane permeant reactive fluorescent tracer (CellTracker Green, Molecular Probes Inc., 5 μ m) and were injected intradermally into six mice, which were sacrificed by anaesthesia immediately or 24 h after injection.

Morphometry of human and mouse tumours

Three different tumoural and peritumoural regions were assessed separately for each section. These were: (I) the tumour centre; (II) the tumour periphery—a 100 μ m wide band of tumour immediately adjacent to the invasive edge; and (III) the peritumoural host tissue—a 200 μ m wide band of host connective tissue immediately adjacent to the tumour periphery. MVD and microvessel perimeter were determined by double labelling of blood vessels for CD31 (anti-human CD31; Dako, 1:40 or anti-mouse CD31, 1:100, Pharmingen; DAB) and laminin (anti-laminin, Dako, 1:50; Fast-Blue). Two sections per hMM and three sections from each mouse (5–10 fields of 20 \times , 40 \times objective/section/region) were analysed using CUE-2 software as described previously [25]. In parallel, MVD was also determined by applying the vascular hot spot technique, as recommended [14]. The diameter of the tumours was determined with a 2 \times objective.

Table 1. Comparison of vascular parameters of the human malignant melanoma of the skin according to the thickness (A) and to the clinical course (B)

A

Tumour thickness	Tumour centre		Tumour periphery		Peritumoural host tissue	
	MVD (n/mm ²)	Perimeter (μ m)	MVD (n/mm ²)	Perimeter (μ m)	MVD (n/mm ²)	Perimeter (μ m)
<1.5 mm $n=13$	22.4 \pm 6.3	73 \pm 25.1	78.3 \pm 28.2	71 \pm 19.9	141 \pm 66.7	72.4 \pm 10.1
1.5–4 mm $n=17$	32.5 \pm 10	80.8 \pm 27.3	98.9 \pm 27.7	75.7 \pm 16.4	137 \pm 55.3	75.3 \pm 17
>4 mm $n=15$	31.3 \pm 7.9	104 \pm 31.7 ^{a,b}	96.8 \pm 22.8	94.8 \pm 21.2	149 \pm 41.8	84.3 \pm 8.7

B

Metastasis	Tumour centre		Tumour periphery		Peritumoural host tissue	
	MVD (n/mm ²)	Perimeter (μ m)	MVD (n/mm ²)	Perimeter (μ m)	MVD (n/mm ²)	Perimeter (μ m)
None $n=15$	21 \pm 5.1	77.3 \pm 24.2	77.2 \pm 27.1	70.6 \pm 21.1	140 \pm 65.2	70.8 \pm 13.8
Lymph node $n=14$	25.9 \pm 5.4	82.4 \pm 30.3	98.7 \pm 28.3	76.9 \pm 17.2	120.2 \pm 54.3	77.2 \pm 12.7
Organ $n=16$	39.8 \pm 6.7 ^c	98.1 \pm 29.7	98.1 \pm 23.3	94 \pm 19.2	132.8 \pm 44.3	84.0 \pm 12.3

Data are expressed as mean \pm SD. Statistical analysis was performed by ANOVA single factor method.

^a $p < 0.05$ (vs. peritumoural host tissue);

^b $p < 0.05$ (vs. thin tumour group);

^c $p < 0.05$ (vs. non-metastatic group).

dc_301_11

Assessment of EC labelling index with bromodeoxyuridine (BrdU)

Two hours before the mice were sacrificed, 200 mg/kg BrdU in saline was injected intraperitoneally. Sections were fixed in methanol and reacted sequentially with anti-mouse CD31, rhodamine-conjugated anti-rat IgG (1:50, Jackson ImmunoResearch Inc.), 2N HCl (10 min, 20°C), anti-BrdU antibody (1:100, Becton-Dickinson), biotinylated anti-mouse IgG (1:100, Vector), streptavidin-FITC (1:100, Amersham), and with TOTO-3 (MolecularProbes Inc., 5 µm). Slices were viewed by confocal microscopy (Bio-Rad MRC1024). The labelling index of ECs was determined by counting the labelled as well as all the EC nuclei (100/studied area) along the vessel walls.

Transmission electron microscopy

Animals were perfused via the left ventricle with phosphate-buffered saline for 10 min and with 2.5% glutaraldehyde in 0.05 M Na-cacodylate (pH 7.2) for 15 min at room temperature. Tumour pieces were processed as described previously [25] and analysed on a Philips CM10 electron microscope.

3D visualization of tumour vasculature

Sections (100 µm) were cut and transferred to 24-well plates containing methanol. Blood vessels were identified by immunostaining with anti-CD31 antibodies as described above. To avoid compression, small pieces of cover slip of 150 µm thickness were inserted on both sides of the mounted slice. For 3D reconstruction, up to 80 serial optical sections at 0.5–2 µm intervals were used. Digitized image stacks were further processed using Bio-Rad-LaserSharp software.

Characterization of vessel phenotype by immunohistochemical double and triple labelling

On 5 µm cryosections, different combinations of primary antibodies (anti-CD31 antibodies; anti-laminin; anti-SMA, 1:100, Dako) were used simultaneously. After washing, slices were incubated simultaneously with the appropriate secondary antibodies (Cy5-conjugated anti-mouse IgG; FITC-conjugated anti-rat IgG; rhodamine-conjugated anti-rabbit IgG; all from Jackson ImmunoResearch Inc., 1:50) with or without nuclear staining with TOTO-3.

Statistical analysis

Experimental data were evaluated using either ANOVA single factor analysis, Mantel-Cox generalized salvage analysis or two-tailed *t*-test. A *p*-value less than 0.05 was required for significance.

Results

Microvessel density of hMM

In all the applied categories (Table 1), MVD was highest in the peritumoural host tissue and the tumour periphery was significantly more vascular than the tumour centre. Comparison of the MVD of tumour periphery and peritumoural host tissue of hMM, characterized by various categories of thickness and clinical progression, did not reveal any significant differences. The MVDs of the tumour centre showed only a slight but non-significant elevation with increasing tumour thickness (Table 1A) and there was no correlation between tumour centre MVD and growth phase (data not shown).

The comparison of tumour centre MVDs according to the type of clinical progression of the disease indicated a significant 90% increase in the organ-metastatic compared to the non-metastatic tumours (Table 1B, $p < 0.05$). Tumour centre MVD was not statistically significantly different in tumours characterized by lymphatic progression, nor did peritumoural MVDs differ in these clinical categories.

Out of the 45 patients, 15 were lost within 60 months and the tumour centre MVD of these patients was significantly higher than in who survived (40.12 ± 5.07 vs. 23.78 ± 5.04 , $p < 0.025$). Next, tumour centre MVD ranges were established (<10 , <20 , <30 , <40 and $<50/\text{mm}^2$) and compared to disease outcome (5-year survival). We found that 100% of patients whose tumours were categorized by a central MVD less than $30/\text{mm}^2$ were alive at 60 months, compared to one out of 16 patients alive with tumours having a central MVD higher than $30/\text{mm}^2$ ($p < 0.025$, Figure 1). Collectively, we have concluded that both the visceral progression as well as the 5-year survival of human skin melanoma patients were associated exclusively with the MVD of the tumour centre.

MVDs in the peritumoural areas by the 'hot spot

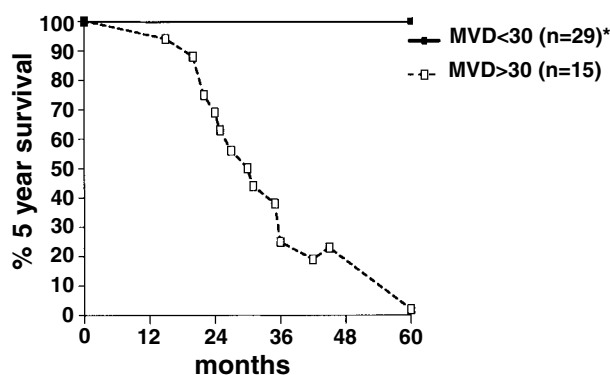


Figure 1. Survival analysis of primary malignant melanoma patients. 100% of the patients whose tumours were categorized by tumour centre MVD less than $30/\text{mm}^2$ were alive after a 5-year follow-up period, compared to one survivor out of 16 patients whose tumours had a central MVD higher than $30/\text{mm}^2$. Statistical analysis was performed using the Mantel-Cox generalized salvage analysis. * $p < 0.025$

dc_301_11

technique' were 164 ± 48 , 144 ± 50 and 171 ± 92 in non-metastatic, lymph node-metastatic and organ-metastatic cases, respectively. MVD in non-tumourous skin was similar to the MVD of benign melanocytic tumours (68 ± 37.1 and 55 ± 7.5 , respectively).

Vessel perimeters of hMM

Vessel perimeters were highest in the tumour centre and there was no difference in this respect between the various categories (Table 1). The vessel perimeter in the tumour centre was highest in the group of thick (>4 mm) tumours ($p < 0.05$ vs. peritumoural host tissue), and was moderate in the group of medium thick (1.5–4 mm), organ-metastatic, lymph node-metastatic and non-metastatic tumours. There was no increase in the group of thin (<1.5 mm) tumours.

Peritumoural host tissue and tumour periphery microvessel perimeters were more similar to each other than to tumour centre microvessel perimeters in all the applied thickness and progression categories. The tendency to an increased microvessel perimeter at the tumour centre was correlated with clinical progression and growing thickness, but only the latter proved to be statistically significant ($p < 0.05$).

Murine skin melanoma model

To analyse angiogenesis from an early stage, we followed vessel network development during tumour growth, from the intradermal inoculation of 10^4 B16 cells until the tumours reached 4–5 mm in diameter (Figure 2A), which corresponds to a thick hMM. Cells were deposited into the papillary dermis, next to the

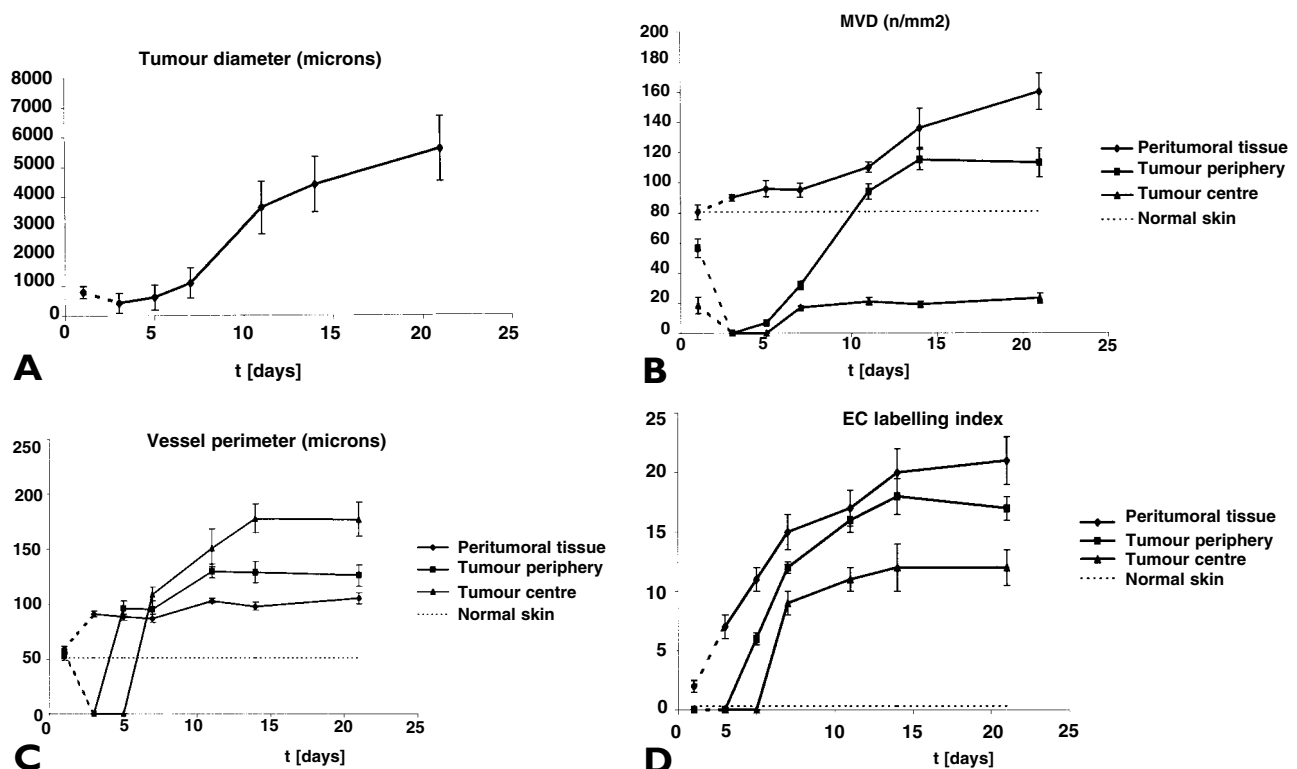


Figure 2. Tumour diameters (A) and alterations of vascular parameters (B, C, D) of B16 murine melanoma. Groups of three mice were sacrificed by anaesthesia at 1, 3, 5, 7, 11, 14 and 21 days. Data are means \pm SEM. The decrease of MVD and vessel perimeter between days 1 and 3 can be explained by the regression of the existing host vessels of the dermis, following the injection of the tumour cell suspension. The mean MVD, vessel perimeter and EC labelling index in normal mouse skin were 80.7 ± 7 , 51.5 ± 2.5 and 0.33 ± 0.15 , respectively (mean \pm SD, $n = 3$).

(B) Microvessel density (n/mm^2)

$p < 0.05$ peritumoural tissue vs. tumour periphery on days 3, 5, 7, 14, 21
peritumoural tissue vs. tumour centre on days 3–21
tumour periphery vs. tumour centre on days 7–21

(C) Microvessel perimeter (μm)

$p < 0.05$ peritumoural tissue vs. tumour periphery on days 3, 11, 14, 21
peritumoural tissue vs. tumour centre on days 3, 5, 11, 14, 21
tumour periphery vs. tumour centre on days 5, 14, 21

(D) EC labelling index

$p < 0.05$ peritumoural tissue vs. tumour periphery on days 3, 5, 7, 21
peritumoural tissue vs. tumour centre on days 3–21
tumour periphery vs. tumour centre on days 5–21

dc_301_11

epidermal–dermal junction. The tumour tissue showed a solid, nodular growth pattern, without forming a meshwork of septa, and it was not circumscribed with a fibrous capsule, which is a common feature of subcutaneously inoculated or xenotransplanted tumours. Three weeks after intradermal tumour implantation, regional lymph node and lung metastases were found.

MVD of B16 melanoma (Figure 2B)

In all the investigated areas, the increasing MVDs reached a plateau at different time points after tumour inoculation. In the centre of the tumour, a plateau was reached around $20/\text{mm}^2$ on day 7, followed by the tumour periphery, with a plateau value around $100/\text{mm}^2$ on day 14. Peritumoural host tissue MVD increased up to a level around $150/\text{mm}^2$, which was reached in the middle of the third week. It is also important to note that peritumoural host tissue MVD was highest, tumour centre MVD was lowest and tumour periphery MVD was intermediate, at all time points.

Microvessel perimeters of B16 melanoma (Figure 2C)

Vessel perimeters increased with time to a different extent in the different areas of the tumour: vessel dilatation was slight in the peritumoural areas (from $59\ \mu\text{m}$ to $105\ \mu\text{m}$), considerable in the tumour periphery (from $55\ \mu\text{m}$ to $126\ \mu\text{m}$), and the highest in the tumour centre (from $53\ \mu\text{m}$ to $177\ \mu\text{m}$). Similarly to MVD, vessel dilatation also showed a tendency to reach a plateau at different time points (day 11 in the case of peritumoural host tissue and tumour periphery, and day 14 in the case of tumour centre). Additionally, the increase of perimeter followed the direction from peritumoural host tissue towards tumour centre, independently of tumour age and size.

EC proliferation of B16 melanoma (Figure 2D)

The EC labelling index showed the highest increase in the peritumoural host tissue (from 2% to 21%), the lowest increase in the tumour centre (from 0 to 12%) and a moderate increase at the tumour periphery (from 0 to 17%). Furthermore, the EC labelling index was always the highest peritumourally and was always lower in the tumour centre than in the periphery. EC proliferation reached a plateau at day 14 in the three studied areas.

Phenotype of human and murine melanoma microvessels

CD31 antibodies marked the vasculature intensively. Pericytes, which are α smooth muscle actin-positive, completely covered the microvessel walls in the different intra- and peritumoural areas (Figure 3) and were embedded within the basement membrane (BM) surrounding the endothelial tube (Figure 6). At the tumour boundary, the BM of microvessels was single layered, while in the tumour centre it was multilaminated. The

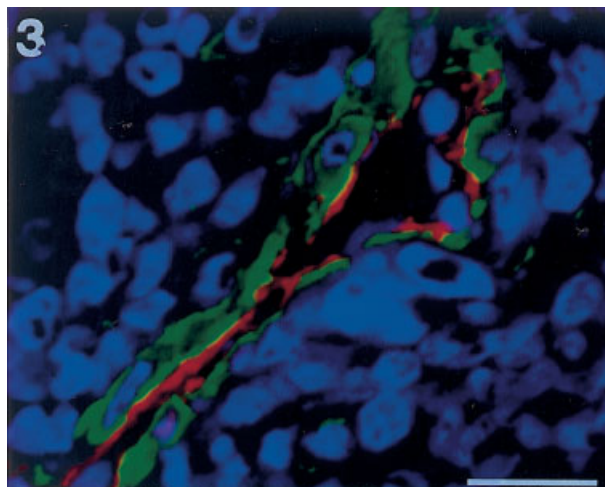


Figure 3. Pericyte recruitment of melanoma vessels. Capillary of an 11-day-old B16 tumour stained for CD31 (red fluorescence) and SMA (green fluorescence) shows the complete pericyte coverage of the endothelial tube. Nuclear staining was applied with TOTO-3 (blue fluorescence). Scale bar $25\ \mu\text{m}$

space between these concentric layers was filled with melanoma cells (Figure 4). The number of layers increased towards the centre of the tumour, and also with time. The presence of multilaminated BM around the microvessels is the result of the invasive activity of tumour cells (Figure 6), but this phenomenon did not have an influence on the presence and distribution of pericytes around the endothelial tube.

3D visualization of human and murine melanoma vasculature (Figure 5)

3D reconstruction of confocal data made clear the presence of the peritumoural vascular envelopes with high MVDs. At the tumour boundary, the vessels were arranged parallel to the surface of the tumour, with

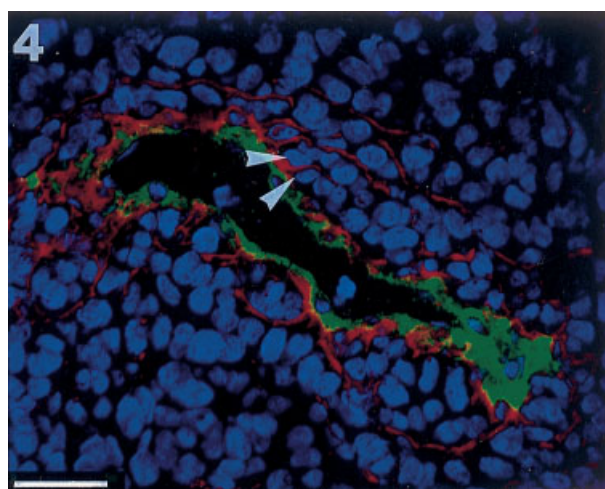


Figure 4. Concentric BM layers (laminin, red fluorescence) around the endothelial tube (CD31, green fluorescence) of a capillary in the centre of a 4 mm thick human melanoma nodule. The invading tumour cells are apparently detaching the ECs from their basal lamina (arrowheads). Nuclear staining was applied with TOTO-3 (blue fluorescence). Scale bar $50\ \mu\text{m}$

dc_301_11

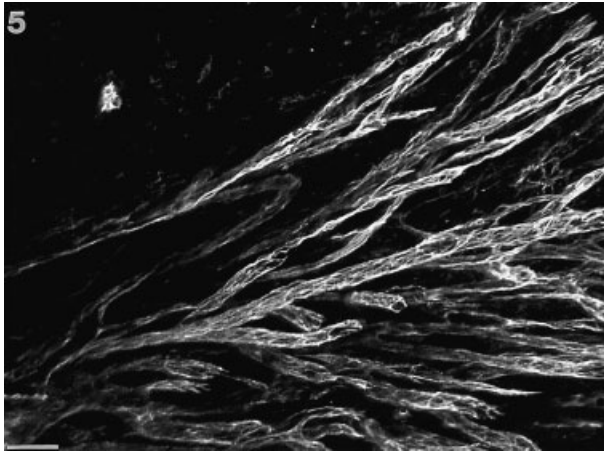


Figure 5. The horizontal view of a stack of confocal images shows the 3D architecture of the prominent vascular plexus (stained by CD31-Mab) present at the tumour boundary in a 3.75 mm thick human melanoma (80 optical sections at 1 μ m intervals). Vessels are running parallel to the surface of the tumour spheroid. Note the delicate staining of interendothelial junctions. The tumour is present at the upper left. Scale bar 100 μ m

numerous lateral connections and blind ends. Direct offshoots occurred with dichotomous and multiple branching. There appeared to be no vessels present which intruded centripetally into the tumour nodule. The intratumoural capillaries were less densely arranged than the peritumoural ones; they took an arched course and exhibited dilatation towards the centre of the tumour.

Discussion

In this study we present the novel finding that during angiogenesis in the human and murine melanoma, there is no morphological evidence of directed vessel ingrowth; instead, these tumours appear to grow by incorporating the massive, tumour-induced vascular plexus present in the peritumoural connective tissue.

In studies comparing melanoma vascularity with prognosis, increased vascularity at the tumour base is a

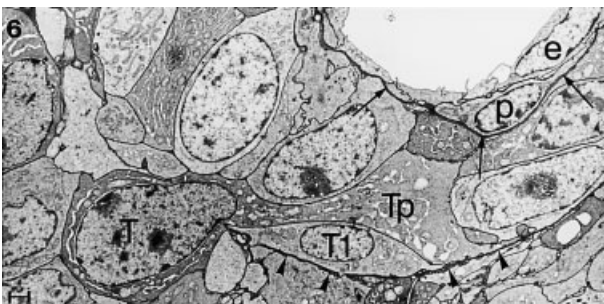


Figure 6. Electron micrograph of a tumour cell (T) migrating into the space between the well-defined concentric BM layer (arrowheads) and the BM of the microvessel (arrows). Another tumour cell (T1) is lying on the surface of the BM. e, endothelial cell; p, pericyte; Tp, tumour cell process. Scale bar 1 μ m \times 4600

common observation [5,9,23,24]. Similarly, in our hMM cases MVDs were several-fold higher in the peritumoural tissue and in the tumour periphery than in the centre of the tumour, and this difference increased with tumour thickness. Until now, however, no studies have focused on the role played by this prominent peritumoural vascular plexus in the process of melanoma vascularization. The observation of a similar microvessel distribution in mouse mammary adenocarcinoma has led Thompson to make the following statement: ‘the growing tumour infiltrates out and expands between the surrounding newly formed vessels and thus the density of vessels is progressively diluted’ [19]. In order to test the hypothesis that hMM incorporates its peritumoural vascular plexus, we used intradermally inoculated B16 tumours as a relevant mouse melanoma model system. The following observations, taken together, imply to us that the growing melanoma engulfs its peritumoural vasculature.

Firstly, morphometry of murine melanoma vasculature indicated that tumour periphery MVD increased dramatically, approaching peritumoural host tissue MVD, while tumour centre MVD increased to a relatively lower level. Since the increase of tumour periphery MVD was almost twice as high as the increase of peritumoural host tissue MVD in the period of the first 11 days, it can be concluded that the majority of the vessels in the tumour periphery were derived from the pre-existing dermal and the newly developed peritumoural capillaries. Secondly, 3D reconstruction of vessel networks using serial optical sections revealed that the peritumoural vascular plexus is composed of vessels running parallel to the tumour surface, without signs of radial orientated growth. This fact alone is sufficient to support the idea that the vessel network at the melanoma base is continuously becoming incorporated into and thinned out by the growing tumour. Furthermore, it becomes clear that the vascular architecture of human melanoma is comparable to that of the intradermally inoculated murine melanoma.

The parallel increase of the tumour diameter and the MVD of the peritumoural tissue and the tumour periphery (between day 7 and day 11) clearly shows the decisive role in tumour growth of the newly formed and pre-existing vessels.

Various studies in different systems have been done by others on the cytokinetics of ECs [26–28]. It is important to note that in contrast to the observation of Denekamp, who found endothelial mitoses only at the tumour edge [28], our measurement did not give such an extreme result: we found an increased proliferation rate of ECs in the vessels of the peritumoural dermis, compared to the lower proliferative activity of the ECs in the tumour centre. This observation corresponds to the mathematical framework described by Ramanujan [29]. According to this model, central regions of the tumours experience anti-angiogenic effects. Towards the periphery of the tumour, the behaviour reverses

dc_301_11

and angiogenic factors predominate, with a peak of angiogenesis at the tumour boundary.

The observation that vessel perimeters increased and MVD decreased towards the tumour centre lets us conclude that within the tumour the newly formed ECs participate in vessel dilatation, instead of providing a source of new vessel production.

At the tumour periphery and in the peritumoural dermis, the BM adjacent to the ECs was single layered, while in the tumour centre it becomes multilaminated. The space between these concentric BM layers was filled with melanoma cells. This phenomenon suggests that the BM of the intratumoural vessels are constantly invaded by tumour cells, during which process the ECs and pericytes become detached from their own BM and are forced to produce a new layer. Since the ECs are proliferating, the disruption of the BM allows vessel expansion, followed by new BM deposition. The old subendothelial BM layers are pushed outwards (away from the vessel) by the invading tumour cells. The absence of sprouting activity of the intratumoural vessels can be explained in two ways. The increasing number of BM layers may impede the branching of endothelial tubes (the increase of MVD); alternatively, the lack of support by an appropriate extracellular matrix within the tumour may prevent the sprouting of new capillaries [30].

Although in all thickness and clinical progression categories the peritumoural dermis was more vascularized than the investigated tumour areas, morphometry demonstrated significant increase in tumour centre MVD in the case of visceral metastatic tumours, suggesting that intratumoural vessels might be the site of intravasation. This is consistent with a previous study in which vascular invasion was observed within the melanoma nodules, but not peritumourally [31]. This idea was further corroborated by the fact that all 29 patients whose tumour was characterized by central MVD of less than 30/mm² were alive after 5 years, while all but one died in whom the central tumour MVD was higher than 30/mm². The fact that the MVDs of the tumour centre did not relate to thickness or growth phase, taken along with the above observations, suggests that the tumour centre MVD may be an independent prognostic factor in hMM.

Previous studies suggest that the recruitment of pericytes can be used as a hallmark of blood vessel maturation in malignancies [20–22]. We assumed that in addition to the increase of tumour centre vessel perimeter, the vulnerable and immature intratumoural vessels being in intimate contact with tumour cells might also influence the prognosis of hMM in an unfavourable way. We therefore examined the distribution of pericytes in vessel walls of different intra- and peritumoural areas. On the basis of both immunohistochemical and electron microscopic analysis, we found that the pericyte coverage of vessel walls was complete in the three different areas, both in human and murine melanomas. This suggests that the pericyte coat most probably does not act as a passive shield

against the intravasation of tumour cells. Accordingly, an active role for pericytes in the process of intravasation cannot be excluded.

The fact that the BM of the intratumoural vessels was constantly invaded by tumour cells, implying a higher intravasation rate of tumour cells in this area, suggests that the intratumoural vessels of hMM are more important in the metastatic process than the peritumoural vascular plexus, which corresponds to the 'hot spots'. This assumption, however, would need further experimental and clinical support.

Acknowledgement

This work was supported by the Ministry of Welfare (T445/2000) and Semmelweis University.

References

- Weidner N. Intratumour microvessel density as a prognostic factor in cancer. *Am J Pathol* 1995; **147**: 9–19.
- Fallowfield ME, Cook MG. The vascularity of primary cutaneous melanoma. *J Pathol* 1991; **164**: 241–244.
- Smolle J, Soyer HP, Hofmann-Wellenhof R, Smolle-Juettner FM, Kerl H. Vascular architecture of melanocytic skin tumours: a quantitative immunohistochemical study using automated image analysis. *Pathol Res Pract* 1989; **185**: 740–745.
- Srivastava A, Laidler P, Hughes LE, Woodcock J, Shedden EJ. Neovascularization in human cutaneous melanoma: a quantitative morphological and Doppler ultrasound study. *Eur J Cancer Clin Oncol* 1986; **22**: 1205–1209.
- Srivastava A, Laidler P, Davies RP, Horgan K, Hughes LE. The prognostic significance of tumour vascularity in intermediate-thickness (0.76–4.0 mm thick) skin melanoma: a quantitative histologic study. *Am J Pathol* 1988; **133**: 419–423.
- Graham CH, Rivers J, Kerbel RS, Stankiewicz KS, White WL. Extent of vascularization as a prognostic indicator in thin (<0.76 mm) malignant melanomas. *Am J Pathol* 1994; **145**: 510–514.
- Straume O, Salvesen HB, Akslen LA. Angiogenesis is prognostically important in vertical growth phase melanomas. *Int J Oncol* 1999; **15**: 595–599.
- Busam KJ, Berwick M, Blessing K, *et al.* Tumour vascularity is not a prognostic factor for malignant melanoma of the skin. *Am J Pathol* 1995; **147**: 1049–1056.
- Carnochan P, Briggs JC, Westbury G, Davies AJ. The vascularity of cutaneous melanoma: a quantitative histological study of lesions 0.85–1.25 mm in thickness. *Br J Cancer* 1991; **64**: 102–107.
- Guffey JM, Chaney JV, Stevens GL, *et al.* Immunohistochemical assessment of tumour vascularity in recurrent Clark II melanomas using antibody to type IV collagen. *J Cutan Pathol* 1995; **22**: 122–127.
- Lin EY, Piepkorn M, Garcia R, Byrd D, Tsou R, Isik FF. Angiogenesis and vascular growth factor receptor expression in malignant melanoma. *Plast Reconstr Surg* 1999; **104**: 1666–1674.
- Marcovall J, Moreno A, Graells J, *et al.* Vascular density and survival in cutaneous melanoma. *Br J Dermatol* 1996; **134**: 809–810.
- Ilmonen S, Kariniemi AL, Vlaykova T, Muhonen T, Pyrhonen S, Asko-Seljavaara S. Prognostic value of tumour vascularity in primary melanoma. *Melanoma Res* 1999; **9**: 273–278.
- Vermeulen PB, Gasparini G, Fox SB, *et al.* Quantification of angiogenesis in solid human tumours: an international consensus on the methodology and criteria of evaluation. *Eur J Cancer* 1996; **32A**: 2474–2484.
- Paku S, Paweletz N. First steps of tumour-related angiogenesis. *Lab Invest* 1991; **65**: 334–346.

dc_301_11

16. Paku S. Current concepts of tumour-induced angiogenesis. *Pathol Oncol Res* 1998; **4**: 62–75.
17. Pezzella F, Pastorino U, Tagliabue E, et al. Non-small-cell lung carcinoma tumour growth without morphological evidence of neo-angiogenesis. *Am J Pathol* 1997; **151**: 1417–1423.
18. Holash J, Maisonpierre PC, Compton D, et al. Vessel cooption, regression, and growth in tumours mediated by angiopoietins and VEGF. *Science* 1999; **284**: 1994–1998.
19. Thompson WD, Shiach KJ, Fraser RA, McIntosh LC, Simpson JG. Tumours acquire their vasculature by vessel incorporation, not vessel ingrowth. *J Pathol* 1987; **151**: 323–332.
20. Benjamin LE, Golijanin D, Itin A, Podes D, Keshet E. Selective ablation of immature blood vessels in established human tumours follows vascular endothelial growth factor withdrawal. *J Clin Invest* 1999; **103**: 159–165.
21. Dvorak HF. Tumours: wounds that do not heal. Similarities between tumour stroma generation and wound healing. *N Engl J Med* 1986; **315**: 1650–1659.
22. Eberhard A, Kahlert S, Goede V, Hemmerlein B, Plate KH, Augustin HG. Heterogeneity of angiogenesis and blood vessel maturation in human tumours: implications for antiangiogenic tumour therapies. *Cancer Res* 2000; **60**: 1388–1393.
23. Fallowfield ME. Vascular volume in B16 allografts and human melanoma xenografts estimated by means of Hoechst 33342. *J Pathol* 1989; **157**: 249–252.
24. Algire GH. Microscopic studies of the early growth of a transplantable melanoma of the mouse, using the transparent-chamber technique. *J Natl Cancer Inst* 1943; **4**: 13–20.
25. Paku S, Lapis K. Morphological aspects of angiogenesis in experimental liver metastases. *Am J Pathol* 1993; **143**: 926–936.
26. Tannock IF. Population kinetics of carcinoma cells, capillary endothelial cells, and fibroblasts in a transplanted mouse mammary tumor. *Cancer Res* 1970; **30**: 2470–2476.
27. Gunduz N. Cytokinetics of tumour and endothelial cells and vascularization of lung metastases in C3H/He mice. *Cell Tissue Kinet* 1981; **14**: 343–363.
28. Denekamp J, Hobson B. Endothelial-cell proliferation in experimental tumours. *Br J Cancer* 1982; **46**: 711–720.
29. Ramanujan S, Koenig GC, Padera TP, Stoll BR, Jain RK. Local imbalance of proangiogenic and antiangiogenic factors: a potential mechanism of focal necrosis and dormancy in tumours. *Cancer Res* 2000; **60**: 1442–1448.
30. Ingber DE, Folkman J. Mechanochemical switching between growth and differentiation during fibroblast growth factor-stimulated angiogenesis *in vitro*: role of extracellular matrix. *J Cell Biol* 1989; **109**: 317–330.
31. Fallowfield ME, Cook MG. Vascular invasion in malignant melanomas: an independent prognostic variable? *Am J Surg Pathol* 1989; **13**: 217–220.

A New Mechanism for Pillar Formation during Tumor-Induced Intussusceptive Angiogenesis

Inverse Sprouting

Sándor Paku,* Katalin Dezső,* Edina Bugyik,*
József Tóvári,[†] József Tímár,[‡] Péter Nagy,*
Viktoria Laszlo,[§] Walter Klepetko,[§] and
Balázs Döme^{§¶}

From the 1st Institute of Pathology and Experimental Cancer Research* and the 2nd Department of Pathology,[‡] Semmelweis University, Budapest, Hungary; the Department of Experimental Pharmacology,[†] National Institute of Oncology, Budapest, Hungary; the Department of Thoracic Surgery,[§] Translational Thoracic Oncology Laboratory, Medical University of Vienna, Vienna, Austria; and the Department of Tumor Biology,[¶] National Koranyi Institute of Pulmonology, Budapest, Hungary

One of the hallmarks of intussusceptive angiogenesis is the development of intraluminal connective tissue pillars. The exact mechanism of pillar formation has not yet been elucidated. By using electron and confocal microscopy, we observed intraluminal nascent pillars that contain a collagen bundle covered by endothelial cells (ECs) in the vasculature of experimental tumors. We proposed a new mechanism for the development of these pillars. First, intraluminal endothelial bridges are formed. Second, localized dissolution of the basement membrane occurs and a bridging EC attaches to a collagen bundle in the underlying connective tissue. A pulling force is then exerted by the actin cytoskeleton of the ECs via specific attachment points, which contain vinculin, to the collagen bundle, resulting in suction and subsequent transport of the collagen bundle into and through the vessel lumen. Third, the pillar matures through the immigration of connective tissue cells and the deposition of new collagenous connective tissue. The proposed simple mechanism generates a connection between the processes of endothelial bridging and intussusceptive angiogenesis and identifies the source of the force behind pillar formation. Moreover, it ensures the rapid formation of pillars from pre-existing building blocks and the maintenance of EC polarity. To describe it, we

coined the term inverse sprouting. (*Am J Pathol* 2011, 179:1573–1585; DOI: 10.1016/j.ajpath.2011.05.033)

Angiogenesis is the formation of new blood vessels from pre-existing ones. Several different forms exist,¹ but so far endothelial sprouting^{2,3} and intussusceptive angiogenesis^{4–8} have been investigated the most intensively.

Endothelial sprouting is characterized by the parallel migration of capillary bud endothelial cells (ECs). During this process, proliferating ECs maintain their basal-luminal polarity and form a slit-like lumen that is continuous with the lumen of the so-called mother vessel. Basement membrane material is deposited continuously by the sprout ECs, whereas only the tip of the growing bud is in contact with the collagenous connective tissue matrix. As the final step, proliferating pericytes of the mother vessel migrate along the basement membrane of the sprout, resulting in the maturation of the new vessel.²

In contrast to endothelial sprouting, the other major angiogenic mechanism, intussusceptive microvascular growth, or intussusceptive angiogenesis, which has been described in a wide variety of normal and pathological conditions, is faster and does not depend primarily on EC proliferation. The most characteristic feature of intussusceptive angiogenesis is the insertion of connective tissue columns, called tissue pillars, into the lumen and the subsequent growth of these pillars, resulting in partitioning of the vessel lumen and the consequent increase in the density of the given capillary network. According to

Supported by the Hungarian Scientific Research Fund (OTKA-NK73119 to S.P., J.Tó., J.Ti., and B.D.), European Economic Community/Norwegian Financial Mechanism-HU0125 (S.P., J.Tó., J.Ti., and B.D.), ReglonCo-L00052 (Cross-border Co-operation Program Hungary–Austria 2007–2013 to J.Tó. and B.D.).

Accepted for publication May 31, 2011.

Supplemental material for this article can be found at <http://ajp.amjpathol.org> or at doi: 10.1016/j.ajpath.2011.05.033.

Address reprint requests to Sándor Paku, Ph.D., 1st Institute of Pathology and Experimental Cancer Research, Semmelweis University, 1085 Üllői út 26, Budapest, Hungary. E-mail: paku@korb1.sote.hu.

the current view, the development of tissue pillars is preceded by the formation of vessel wall folds or the protrusions of the opposite points of the vessel wall into the lumen.^{4–8} However, the origin of the force generating these invaginations has not yet been clarified. Although it is believed that perivascular cells or pericytes may play a role in this initial step by exerting a pushing force on the vessel wall, this concept is questionable because the structure of the cellular cytoskeleton allows only pulling forces at high strength, whereas pushing forces are several hundredfold lower in magnitude.^{9,10}

Another phenomenon thought to be different from intussusceptive angiogenesis, but also leading to vascular division, was described as well. This process is characterized by the development of intraluminal bridges formed by ECs, followed by the development of connective tissue by an unknown mechanism within these bridges.^{11–13}

Based on our observation of the vascularization of s.c. growing tumors in mice, we present herein the detailed mechanism of intraluminal pillar formation, which offers a rationale for the puzzles previously discussed and incorporates the previous two concepts.

Materials and Methods

Animals and Tumor Lines

The C38 mouse colorectal carcinoma line was maintained by serial s.c. transplantations in C57Bl/6 mice, as previously described.^{14,15} Tumor tissue was cut into cubes measuring 5 × 5 × 5 mm. Animals were anesthetized with ketamine, 80 mg/kg, and xylazine, 12 mg/kg (Sigma Chemical Co, St Louis, MO); one piece of tumor tissue was transplanted into the back of each mouse. Animals were sacrificed 3 weeks after tumor inoculation. For analysis of immunofluorescence labeling with monoclonal antibodies, the tumors were transplanted into mice with severe combined immunodeficiency to reduce non-specific staining.

HT25 human colon carcinoma cells were cultured in RPMI 1640 medium supplemented with 10% fetal bovine serum (Sigma Chemical Co). The s.c. tumors were produced by injecting 2 × 10⁶ tumor cells into the back of anesthetized male mice with severe combined immunodeficiency, as previously described.¹⁶ Animals were sacrificed 4 weeks after tumor inoculation.

Electron Microscopy and 3D Reconstruction of Semithin Sections

Preparation of tumor samples for electron microscopy was performed as previously described.¹⁴ In brief, the anesthetized animals (three mice for each tumor line) were perfused via the left ventricle with PBS for 10 minutes and with 4% paraformaldehyde and 1% glutaraldehyde in PBS (pH 7.2) for 15 minutes at room temperature. The s.c. tumors were removed, cut into 1 × 2-mm pieces, and immersed in the same fixative for an additional 2 hours. The pieces were post-fixed in 1% OsO₄, 0.5% K-ferrocya-

nide in PBS for 2 hours, dehydrated in a graded series of acetone, and embedded in Spurr's mixture.

A total of 8 to 10 serial semithin sections were cut, stained by 0.5% toluidine blue (pH 8.5), and analyzed for the presence of pillars. The structures identified on the last semithin section were followed backward to ensure that they represented pillars and were not simply vessel bifurcations or other structures. Areas of interest were trimmed out by comparing the structures on the cut surface of the tissue blocks with the semithin sections and then serially sectioned by an RMC MT-7 ultramicrotome (Research and Manufacturing Co, Tucson, AZ). The sections were placed on thin bar grids, stained with 2% uranyl acetate and lead citrate, and analyzed using a Philips CM10 electron microscope (Eindhoven, The Netherlands). Pillars cut lengthwise were also examined during analysis of serial ultrathin sections. In this case, the entire thickness of the pillar was available for analysis at the ultrastructural level.

Serial semithin sections were captured by an Olympus DP50 camera (Olympus, Tokyo, Japan). Digitized images were transferred to the BioVis3D software program (BioVis3D, Montevideo, Uruguay). Three-dimensional (3D) reconstructions were performed using color contouring to highlight the recreated structures.

Immunofluorescence Analysis

Frozen sections (15- μ m thick) were fixed in methanol and were incubated at room temperature (for 1 hour) with a mixture of the following primary antibodies: monoclonal anti-mouse CD31 (dilution, 1:100; catalogue no. 01951D; Pharmingen, San Diego, CA), polyclonal anti-collagen I (dilution, 1:100; catalogue no. AB765P; Chemicon, Billerica, MA), monoclonal anti-vinculin (dilution, 1:100; catalogue no. V4505; Sigma Chemical Co), monoclonal anti-integrin α -1 (dilution, 1:20; catalogue no. 555001; BD Pharmingen, San Jose, CA), polyclonal anti-integrin α -1 (dilution, 1:50; catalogue no. sc-10728; Santa-Cruz Biotechnology, Santa-Cruz, CA), monoclonal anti-integrin α -2 (dilution, 1:100; catalogue no. 108901; Biologend, San Diego), polyclonal anti-integrin α -2 (dilution, 1:200; catalogue no. AB1936; Millipore, Billerica, MA), polyclonal anti-integrin α -11 (dilution, 1:100; catalogue no. sc-98740; Santa-Cruz Biotechnology), and monoclonal anti-mouse CD29 (dilution, 1:100; catalogue no. 550531; Pharmingen). After washing, appropriate secondary antibodies conjugated with fluorescein isothiocyanate, tetra rhodamine isothiocyanate, or Cy5 were used (all from Jackson ImmunoResearch Inc., Suffolk, UK). The vinculin and integrin α -2 signals were amplified by using an appropriate biotinylated secondary antibody (dilution, 1:200; Vector Laboratories, Burlingame, CA), followed by streptavidin fluorescein isothiocyanate (Jackson ImmunoResearch Inc.). To analyze the localization of actin filaments within the pillars, the sections were reacted with phalloidin-tetra rhodamine isothiocyanate (dilution, 1:500; catalogue no. P1951; Sigma Chemical Co).

Sections were scanned by eye for the presence of pillars using a \times 100 objective. Only pillars running parallel and lying completely within the sectioning plane

were analyzed by a Bio-Rad MRC 1024 confocal microscope (Bio-Rad, Richmond, CA). For 3D reconstructions, 30 to 40 optical sections were generated.

Determination of the Size of Collagen Bundles

The size of the collagen bundles was determined at the ultrastructural level in the peritumoral connective tissue and within the pillars. Measurements were made on digitalized electron micrographs (original magnification, $\times 1500$ to $\times 7000$) taken from s.c. tumors of both cancer cell lines using Olympus Quick Photo Micro software (Olympus). In the peritumoral connective tissue, collagen bundles tightly packed with collagen fibers were chosen randomly (>250). In cross sections, the smallest diameter of the bundle was measured. After their identification in semithin sections, >50 pillars were analyzed at the ultrastructural level. Only pillars exclusively containing collagen fibers, but no pillars with connective tissue cells, were chosen. The total thickness of the pillars (including ECs) was also measured.

In Vivo Treatments

To study the effects of angiogenesis-modulating agents on tumor vascularization and pillar formation, groups of six mice bearing C38 tumors received recombinant human erythropoietin α (rHuEPO, epoetinum α ; Janssen-Cilag, Shaffhausen, Switzerland),¹⁶ PTK787/ZK22854 (vatalanib; Novartis/Schering AG, Berlin, Germany)¹⁷ (obtained from Selleck Chemicals LLC, Houston, TX), or the vehicle as a control. In mice treated with vatalanib, tumors were allowed to grow for 12 days before treatment. Then, mice were treated orally with 100 mg/kg vatalanib (PTK787/ZK222584, dissolved in water containing 5% dimethyl sulfoxide and 1% Tween-80) for 4 days, as in a previous study.¹⁸ Mice treated with rHuEPO were given 150 IU/kg in physiological salt solution three times per week i.p. from day 1 after tumor inoculation, as previously described.¹⁶ The mice in all groups were sacrificed on day 17, and tumors were removed, weighed, and frozen.

CD31-labeled frozen sections were scanned by eye using a $\times 100$ objective to determine the number of pillars within the entire section. The total area of the sections was determined using Olympus Quick Photo Micro software. To determine the area fraction of CD31-positive blood vessels in tumor sections, two to three confocal images were taken from each tumor section using a $\times 4$ objective (area, 11.3 mm²). The micrographs were analyzed using ImageJ software (NIH, Bethesda, MD). Results are expressed as the number of pillars per squared millimeter of tumor tissue or microvessel area.

Analysis of Skin Wounds

Animals were anesthetized and shaved. A 1-cm-long full-thickness incision was made in the dorsal skin of C57 black mice. The wounds were partially closed by a single nylon suture. The mice were euthanized on days 3, 5, 7, and 10 after wounding. Two mice were sacrificed at each time point. The wounds and the surrounding intact skin, measuring 2 \times 2 mm, were removed and cut further into

1 \times 2-mm pieces, with the long axis running perpendicular to the wound. These pieces were fixed and embedded for electron microscopy, as previously described. Eighty-six tissue blocks were semithin sectioned and analyzed (total area, approximately 250 mm²) for the presence of pillars using a $\times 63$ objective.

Statistical Analysis

Statistical analysis was performed using the Student's *t*-test.

Results

Development of Intraluminal Connective Tissue Pillars

Intussusceptive angiogenesis was observed in s.c. tumors of both cancer cell lines. This type of angiogenesis was the main means of new vessel formation. Endothelial sprouting with characteristic slit-like lumen-containing capillaries² was scarcely detected. Intussusception was mainly detected in angiogenic hot spots peritumorally, but it also occurred within the tumor mass. The first step of intussusception is thought to be the development of protrusions or infoldings of the vessel wall within the lumen.⁶ We analyzed 89 infolds sharply intruding into the vessel lumens in >172 serially sectioned areas (semithin sections) altogether. None of these structures projected into the lumen by themselves. By tracing them over several serial sections, we found that each capillary infold was connected to a different part of the vessel lumen (on the opposite or the same side). These infolds proved to be pillars, part of blind-ending lumens or simple vessel ramifications (Figure 1; see also Supplemental Figure S1 at <http://ajp.amjpathol.org>). In areas of intensive intussusception, proliferating ECs (Figure 1, H and L; see also Supplemental Figure S1H at <http://ajp.amjpathol.org>) and intraluminal endothelial bridges were frequently observed (Figure 1, H–M and K–O; and Figure 2, A–E). These bridges either were simple EC processes projecting into the vessel lumen and attaching to the endothelial tube in a different position (Figure 2F) or were formed by the participation of cellular processes of different ECs (Figure 2G). However, the most characteristic phenomenon of this type of tumor-induced intussusceptive angiogenesis was the development of transluminal pillars containing tightly packed collagen fibers covered by ECs (Figure 2H). The pillars either spanned the vessel lumen or originated and terminated on the same side of the vessel (Figures 1 and 3). The diameters of these collagen bundles did not differ significantly from those within the peritumoral connective tissue (Table 1). The overall diameter (including the EC layer) of the pillars corresponded well with those observed earlier in other studies (2.5 μ m).⁴ The fibers were oriented parallel to the axis of the pillars (Figure 3, B–D) and were covered by several ECs. However, the basement membrane under these cells was generally absent (Figures 2H and 3G). Moreover, neither pericytes nor other cells were present in

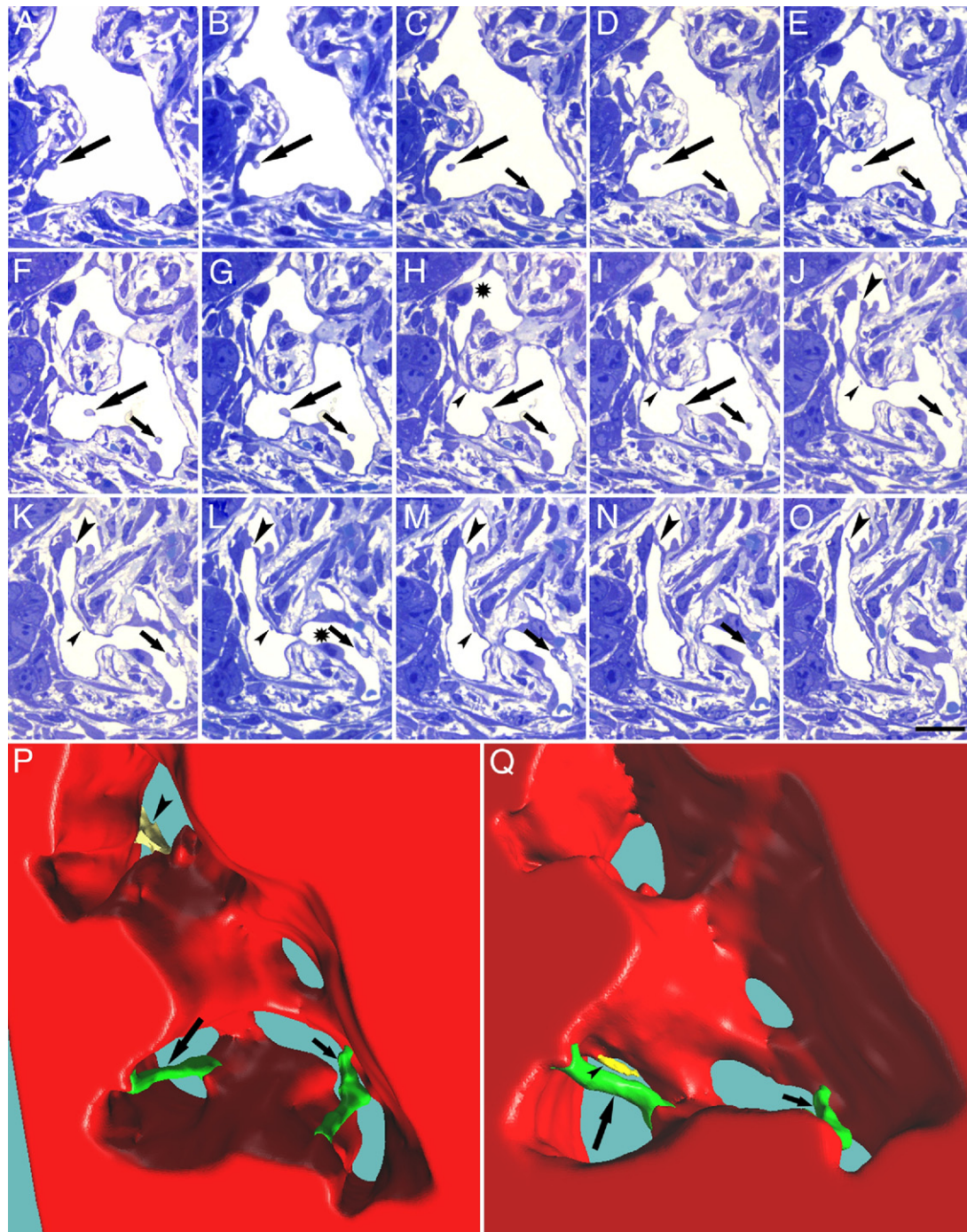


Figure 1. Light microscopic appearance and 3D reconstruction of endothelial bridges and pillars. **A–O:** 0.5- μm thick serial semithin sections were cut over a distance of 10 μm in an area of intensive intussusceptive angiogenesis. Serial sections $>10 \mu\text{m}$. Two pillars are visible. One starts in **A** (section 2, **large arrow**), runs through the lumen, and joins the vessel wall in **H** (section 13). There is a sharp protrusion of the vessel wall in **I** (**large arrow**, section 15). The other pillar (**small arrow**) starts in **C** (section 6), reaches the other side of the lumen in **L** (section 19), makes a turn, and joins the same side of the vessel in **N** (section 21). Two endothelial bridges are also visible. One (**large arrowhead**) is positioned between the opposite sides of the vessel lumen (**J–O**); the other smaller one (**small arrowhead**) starts and ends on the same side of the vessel (**H–M**). There is a proliferating EC (**asterisk**) in **H** and **L**. Scale bar = 20 μm . **P** and **Q:** 3D reconstruction of 25 semithin sections represented in **A–O**. The vessel wall and the surrounding tissue are indicated in red, pillars separated from the vessel wall and containing collagen bundles are indicated in green, and endothelial bridges are indicated in yellow. **P** and **Q** are different views from above to show the localization of both endothelial bridges.

these small nascent pillars. Along the pillars, cut parallel to their axis, high electron density areas could be observed in the membrane of the ECs, suggesting specific adhesion between the ECs and the collagen bundle. In accordance with this observation, immuno-

fluorescence analysis revealed vinculin-containing adhesion spots along the pillars (Figure 4, A–D). However, although immunolabeling with antibodies against integrin α -1, α -2, or α -11 demonstrated high α -2 and α -11 expression levels in the pericapillary connective tissue,

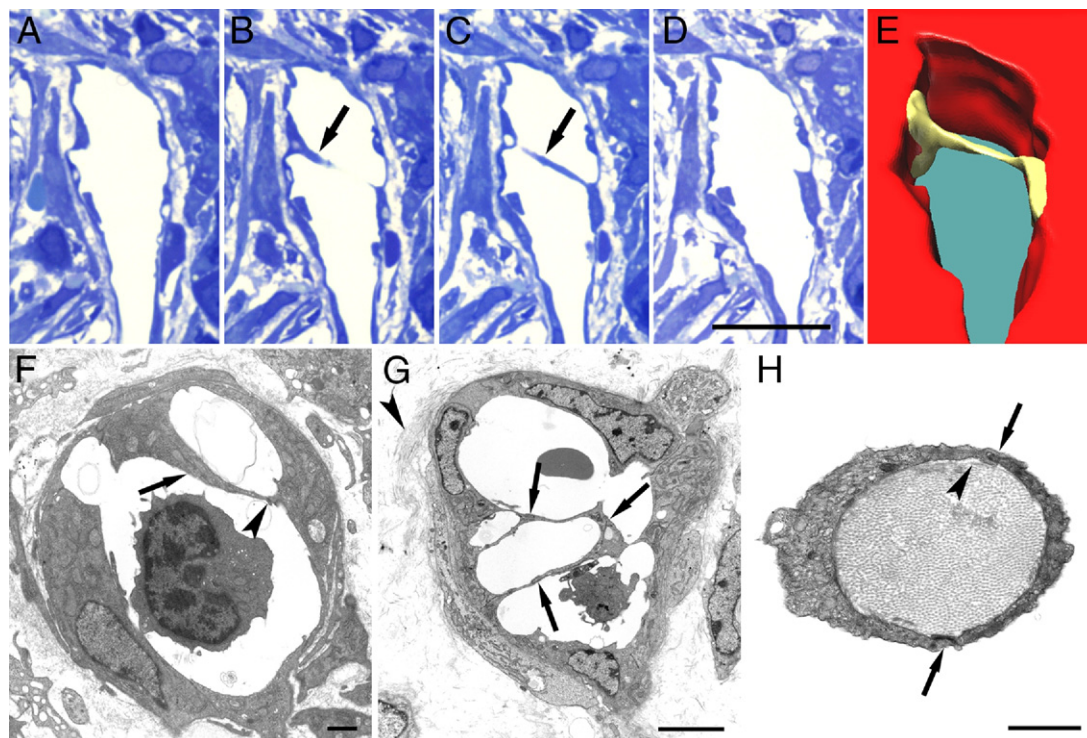


Figure 2. 3D and ultrastructure of endothelial bridges and transcapillary pillars. **A–D:** Serial semithin sections of an endothelial bridge. The bridge (**arrows**) is present only in two consecutive sections. The light blue staining (collagen core) within the bridge is absent. Scale bar = 20 μm . **E:** 3D reconstruction of 13 semithin sections. The endothelial bridge and the nuclear area of the ECs are highlighted in yellow, and the vessel wall and the surrounding tissue are shown in red. **F:** An endothelial bridge formed by a single cellular process (**arrow**). The process is attached to the EC itself (**arrowhead**). Scale bar = 1 μm . **G:** Endothelial bridges formed by cellular processes of several ECs. **Arrows** point at intercellular junctions. The collagen bundle is located close to the vessel (**arrowhead**). Scale bar = 5 μm . **H:** Cross section of a transluminal pillar. The pillar is formed by a collagen bundle tightly packed with fibers and by two covering ECs. **Arrows** point at interendothelial junctions. Some basement membrane material is visible below the ECs at the upper part of the pillar (**arrowhead**). Scale bar = 1 μm .

these collagen-binding integrin subunits were either occasionally present as small dots at a low density at the abluminal surface of pillar-forming ECs (as in the case of α -2 labeling; see Supplemental Figure S2, A and B, at <http://ajp.amjpathol.org>) or totally absent (as in the case of α -1 or α -11 labeling; see Supplemental Figure S2, E and F, at <http://ajp.amjpathol.org>). Nevertheless, in more developed pillars, we could detect large integrin α -2-containing adhesion spots (see Supplemental Figure S2, C and D, at <http://ajp.amjpathol.org>). Staining for integrin β -1 showed no specific localization of this subunit that was distributed evenly under the ECs of the vessel and pillars (data not shown).

The part of the cell body of the ECs that formed the pillars frequently contained a high density of microfilaments, excluding all other cellular organelles (Figure 3, G and H). These microfilaments were generally not in a parallel arrangement; rather, they formed a mesh. The presence of polymerized actin within the ECs of the pillars was also confirmed by phalloidin staining (Figure 4, E and F). The microfilaments were attached to the membrane through specific structures that appeared as dots (approximately 50 nm, Figure 5A) when the plane of the section ran parallel to the membrane and as tiny rods (<200 nm, Figure 5B) when the plane of the section was perpendicular to it. The adhesion spots were arranged in a regular manner along individual collagen fibers (Figures 3G and 5A) and were connected to each other by

microfilaments (Figure 5B). In these attachment regions, the collagen fibers were in close contact with the plasma membrane of the EC (Figure 5C). Confocal and electron microscopic analysis of serial sections of the pillars and extensive light revealed that, in a small portion of the pillars, the collagen bundles did not span the whole length of the pillar. In these cases, as in the intraluminal endothelial bridges previously described, the rest of the pillar was composed only of ECs (Figures 6 and 7, A and B; see also Supplemental Figure S3 at <http://ajp.amjpathol.org>). Collagen bundles situated in the nascent pillars extended into the connective tissue (Figure 7, C and D). Maturing pillars, into which cellular processes extended, or larger pillars containing pericytes and other connective tissue cells were also present in the vessel lumens (Figure 7, E and F).

Effects of Angiogenesis-Modulating Agents on Tumor Capillary Parameters and Pillar Formation

In the next set of experiments, we also studied whether rHuEPO (which recently induced intussusceptive angiogenesis in the chick embryo chorioallantoic membrane assay)¹⁹ or the anti-angiogenic drug vatalanib (an oral small-molecule multitargeted tyrosine kinase inhibitor that blocks all known vascular endothelial

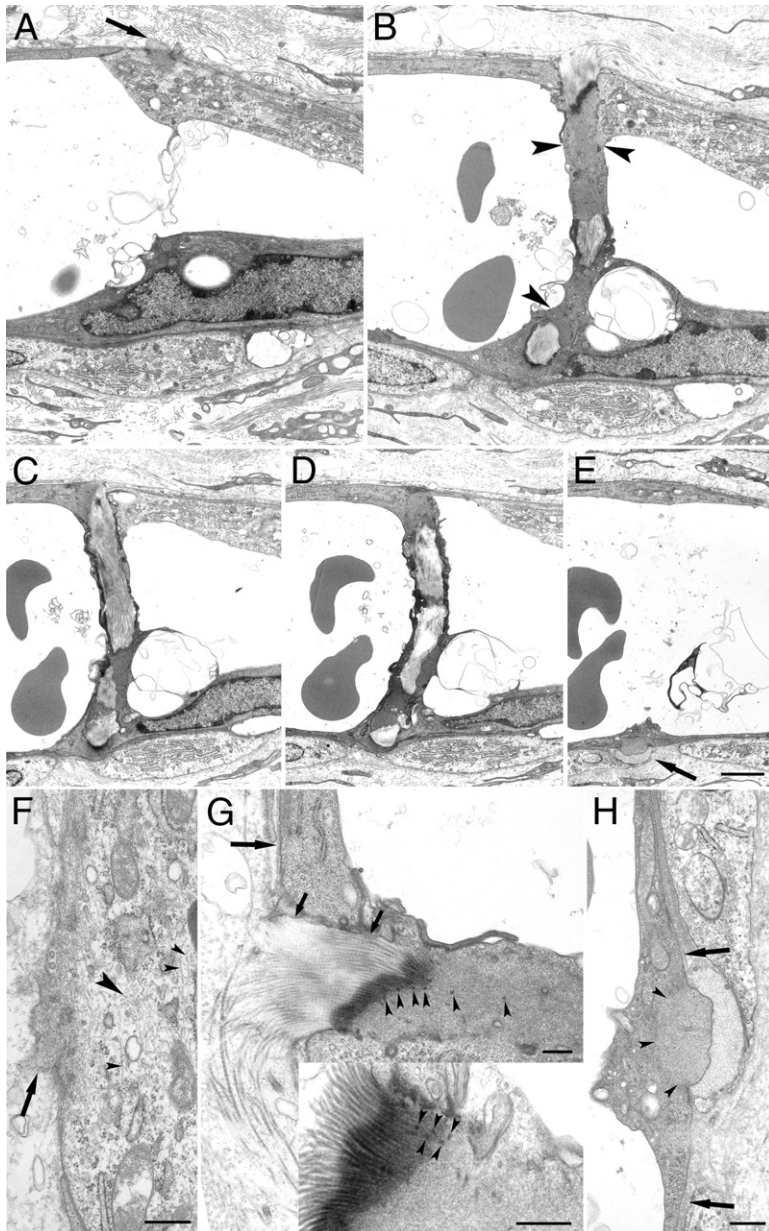


Figure 3. Ultrastructure of the pillar. **A–E:** Serial ultrathin sections (approximately 100 nm) of a nascent pillar (**A**, section 3; **B**, section 14; **C**, section 20; **D**, section 22; **E**, section 36). The pillar was present in 22 sections. The collagen bundle is densely packed with fibers and oriented parallel to the axis of the pillar (**B–D**). **A–E:** The collagen bundle does not extend into the connective tissue (**up**). **E:** In contrast, the collagen bundle is still visible (**arrow**) and runs with a sharp change in direction along the circumference of the vessel (**down**). This suggests that the putative direction of the collagen bundle transport is from right to left. Apparently, the bundle just reached the left side of the vessel. In **A**, an **arrow** points at a small process of the EC, indicating the location of the pillar. The body parts of the ECs in contact with the collagen bundle show homogeneous staining because of the high microfilament content (**arrowheads** in **B**). Scale bar = 2 μm . **F–H:** High-power micrographs showing details of the pillar region (**F**, section 1; **G**, section 14; **G inset**, section 10; **H**, section 36). **F** represents the first section that suggests the presence of a pillar. The small cellular process (**arrow**) is densely packed within a meshwork of microfilaments. Microfilaments are also present under the plasma membrane in the left part of the cell. The **large arrowhead** points at an area containing intermediate filaments, whereas small **arrowheads** point at microtubules. Scale bar = 0.5 μm (**F**). **G:** Details of **B**. The cell body above the collagen bundle contains many microfilaments but no other organelles. The high electron density of the plasma membrane is cut at a low angle. Adhesion spots are also visible (**small arrowheads**). A basement membrane is lacking in the area where the EC faces the collagen bundle (**small arrows**). However, it is present in other areas of the vessel wall (**large arrow**). **Inset:** An adhesion area where the plasma membrane is cut at a low angle. The adhesion spots are situated exactly and regularly above the collagen fibers (**small arrowheads**). Scale bar = 0.5 μm (**G** and **inset**). **H:** The collagen bundle (cut perpendicularly) of the pillar extends outside into the connective tissue and runs around the circumference of the vessel. Although adhesion spots are not visible, a basement membrane is not present at the area where the EC faces the collagen bundle. Many microfilaments are present in this body part (**arrowheads**) of the EC. An intact basement membrane is present under the other parts of the EC (**arrows**). Scale bar = 1 μm .

growth factor receptors, with additional activity against platelet-derived growth factor receptor and c-kit)¹⁷ could affect pillar formation in our C38 colon carcinoma model system.

In C38 tumors treated with rHuEPO, pillar densities of tumor sections were significantly increased compared

with untreated controls (Table 2). In accordance with our previous findings,¹⁶ a tendency toward an increased tumor microvessel surface in mice treated with rHuEPO was also observed. However, when pillar density was calculated for the area of tumor microvessels, the difference in pillar densities between tumors in the rHuEPO-

Table 1. Collagen Bundle Diameters in the Peritumoral Connective Tissue and in Transcapillary Pillars

Value	Diameter (μm)		
	Collagen bundles within the peritumoral connective tissue ($n = 260$)	Collagen bundles within the pillars ($n = 55$)	Pillars (including endothelium) ($n = 55$)
Mean \pm SD	1.61 \pm 0.9	1.72 \pm 1.0*	2.5 \pm 1.1
Range	0.3–5.9	0.4–5.0	0.8–5.8

*The diameters of the collagen bundles of the connective tissue and the pillars did not differ significantly ($P = 0.4$).

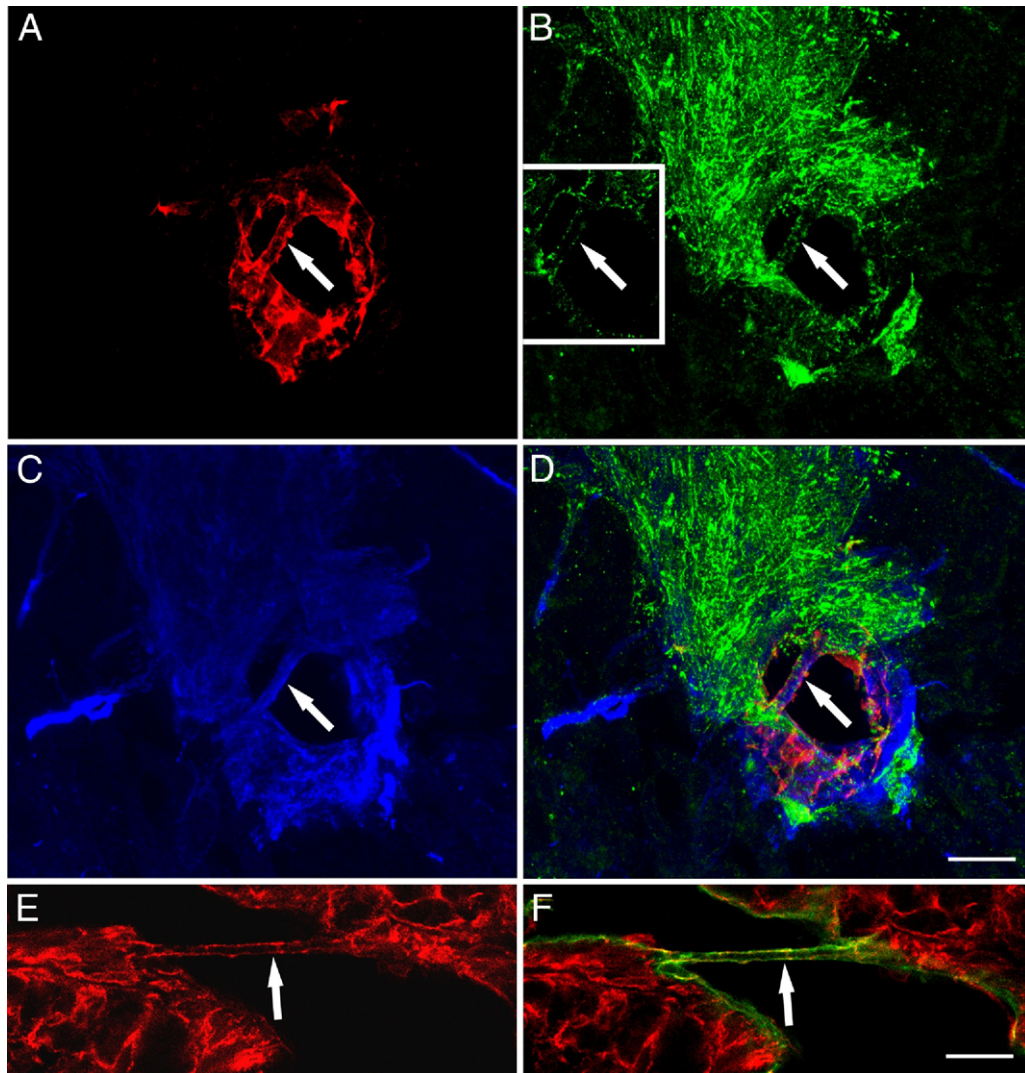


Figure 4. Immunofluorescent labeling of pillars. **A–D:** Vessel with pillar (**arrow**) stained for CD31 (**A**, red), vinculin (**B**, green), and collagen I (**C**, blue). The pictures show horizontal views of 35 optical sections. CD31 and vinculin are present mainly on the two sides of the pillar, whereas collagen is positioned in the middle. **D** shows the merged picture. **Inset:** One optical section showing that vinculin is present in small spots along the periphery of the pillar (green). There is a high density of adhesions in the connective tissue. Black areas (except for the vessel lumen) correspond to tumor tissue. Scale bar = 20 μm (**A–D**). **E** and **F:** Vessel with pillar (**arrow**) stained for CD31 (green) and phalloidin (red). Phalloidin staining, representing filamentous actin, colocalizes with CD31 staining at the sides of the pillar. Myfibroblasts outside of the vessel are also stained by phalloidin-tetra rhodamine isothiocyanate. Scale bar = 20 μm (**E** and **F**).

treated and control groups remained statistically nonsignificant (Table 2).

In mice treated with vatalanib, significantly decreased tumor burdens and a tendency toward reduced microvessel areas were observed. Moreover, tumor samples in the vatalanib group had significantly more pillars/tumor microvessel areas than those in the control group (Table 2).

Vascularization of Skin Wounds

To elucidate the process of pillar formation in conditions other than tumor-induced angiogenesis, we also analyzed full-thickness cutaneous incision wounds (3, 5, 7, and 10 days after wounding) for the presence of pillars. However, endothelial sprouting was the characteristic mechanism of angiogenesis in the healing wounds

(mostly 5 and 7 days after wounding); we failed to detect any signs of pillar formation (data not shown).

Discussion

Although the formation of transluminal pillars^{4–8} is considered the most characteristic feature of intussusceptive microvascular growth, the exact mechanism of this process has yet to be completely clarified. By investigating the vascularization of experimental tumors growing in mice, we present herein the putative sequence of steps of transluminal pillar development during intussusceptive angiogenesis (Figure 8). First, transluminal endothelial bridges are formed. Second, collagen bundles adjacent to the vessel are seized by the abluminal side of a bridge-forming EC. The force exerted by the actin cytoskeleton of the EC through specific vinculin-containing attachment

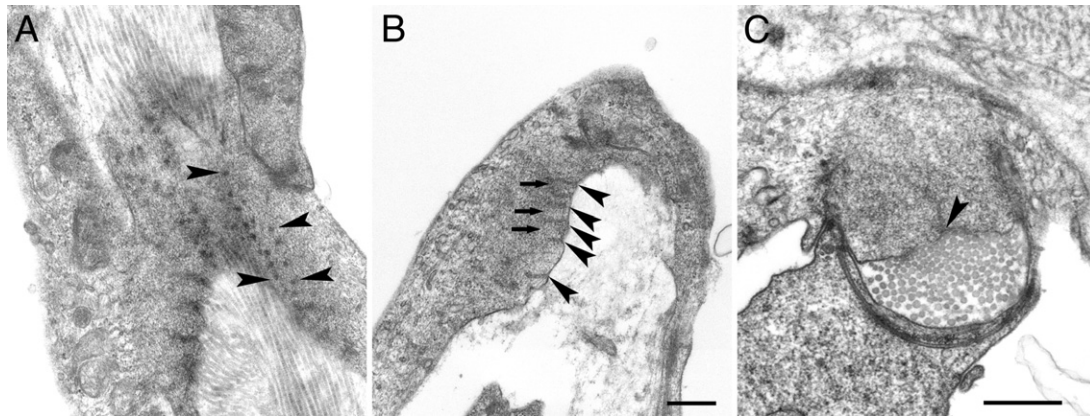


Figure 5. The ultrastructure of the adhesion region. **A** and **B**: Serial sections of an adhesion region. **A**: Adhesions (appearing as dots, **arrowheads**) are arranged into rows and spaced regularly (the sectioning plane is parallel to the plasma membrane of the EC). There is a high density of microfilaments in this region. **B**: When the sectioning plane is perpendicular to the plasma membrane of the EC, the same adhesions appear as rods (**arrowheads**). Microfilaments connect the rods to each other (**arrows**). Scale bar = 0.5 μm (**A** and **B**). **C**: Cross section of a pillar at an adhesion region. The collagen fibers are in close contact with the plasma membrane of the EC. Only one rod is visible (**arrowhead**), which faces a collagen fiber. The plasma membrane is thickened. Scale bar = 0.5 μm .

points on the collagen bundle pulls the pillar into and through the vessel lumen. Finally, maturation of these nascent pillars occurs via the migration of pericytes and myofibroblasts into the collagen core of the pillar and the deposition of additional collagenous connective tissue by these cells.

The sequence of events during intussusceptive angiogenesis was analyzed in detail in the chicken chorioallantoic membrane and in developing lung tissue, and it was concluded that the appearance of collagen bundles is the last step of pillar formation.^{4,5} In these models, protrusion of the vascular wall into the lumen, interendothelial adherence, and perforation of the endothelial bilayer by reorganization of the interendothelial junctions were the first events. These events were promptly followed by the appearance of perivascular cells within the pillar. Interestingly, although transluminal pillars were formed under different conditions in our study (ie, during tumor vascularization because there were no signs of pillar formation in healing cutaneous wounds), the initial size of pillars (approximately 2.5 μm) was remarkably similar to that observed in nontumorous conditions (<2.5 μm).^{4,5}

Intussusceptive angiogenesis, which results in high local vascular density, is initiated by rapid nascent pillar formation, followed by slow pillar enlargement (a noninvasive process for which extensive connective tissue synthesis is required). Therefore, one reason for the lack of intussusceptive angiogenesis in skin wounds could be that neither pillar development nor the intussusceptive angiogenesis itself is an invasive process; thus, both are not suitable to vascularize initially avascular spaces (such as a fibrin clot). Also, during intussusception in nontumorous tissues, the area covered by the vasculature can be increased solely by the collagenous matrix deposited by the connective tissue cells immigrating into the pillars. In tumor tissues, the invading tumor mass incorporates and occupies the newly formed vasculature (including the developing pillars). Tumor cells are able to both incorporate into the pillars and contribute to their growth; therefore, they help to dilute the newly formed capillary network. In contrast, during wound healing, the

fibrin clot (an existing avascular extracellular matrix) is invaded/occupied by sprouting vessels. This can occur rapidly (within days) and is necessary to supply the incoming collagen-synthesizing cells with nutrients. Another reason for the difference in the presence of intussusceptive angiogenesis between skin wounds and tumors could be that a sustained angiogenic stimuli elicited by tumors (often referred to as never-healing wounds)¹² is necessary to induce/maintain intussusceptive angiogenesis.

In the mechanism proposed herein, the formation of transluminal endothelial bridges is immediately followed by the appearance of a collagen bundle within the pillar. This collagen bundle may serve as a highway for later immigration of other cells (eg, pericytes and myofibroblasts) into the pillar. The deposition of an additional extracellular matrix by these cells can result in the enlargement of the pillar.

The driving force behind the formation of the protrusion in the vessel lumen during intussusceptive microvascular growth remains elusive. Although it is believed to be exerted by perivascular cells, such as pericytes or myofibroblasts,^{4–6} a cell's pushing force (which can be exerted only through filopodia or lamellipodia) is only in the 10 to 100 pN range.⁹ In contrast, contractile forces generated by cells lie in the several hundred nanonormal range.¹⁰ According to our model, no extraluminal force is necessary for the formation of the pillar. Slender EC processes floating in the lumen can contact other parts of the endothelial tube (probably to the same side initially). Additional growth of cytoplasmic processes of ECs can result in the repositioning of this initial contact to reach farther parts of the lumen. This may be followed by the formation of endothelial bridges consisting of several ECs. The contractile force exerted by the microfilaments present at a high density within the ECs forming the bridge may be strong enough to pull a collagen bundle into and through the lumen. The highly edematous and loosely organized peritumoral connective tissue might allow this process. However, the presence of adhesions at a high density on the myofibroblasts of the pericapillary

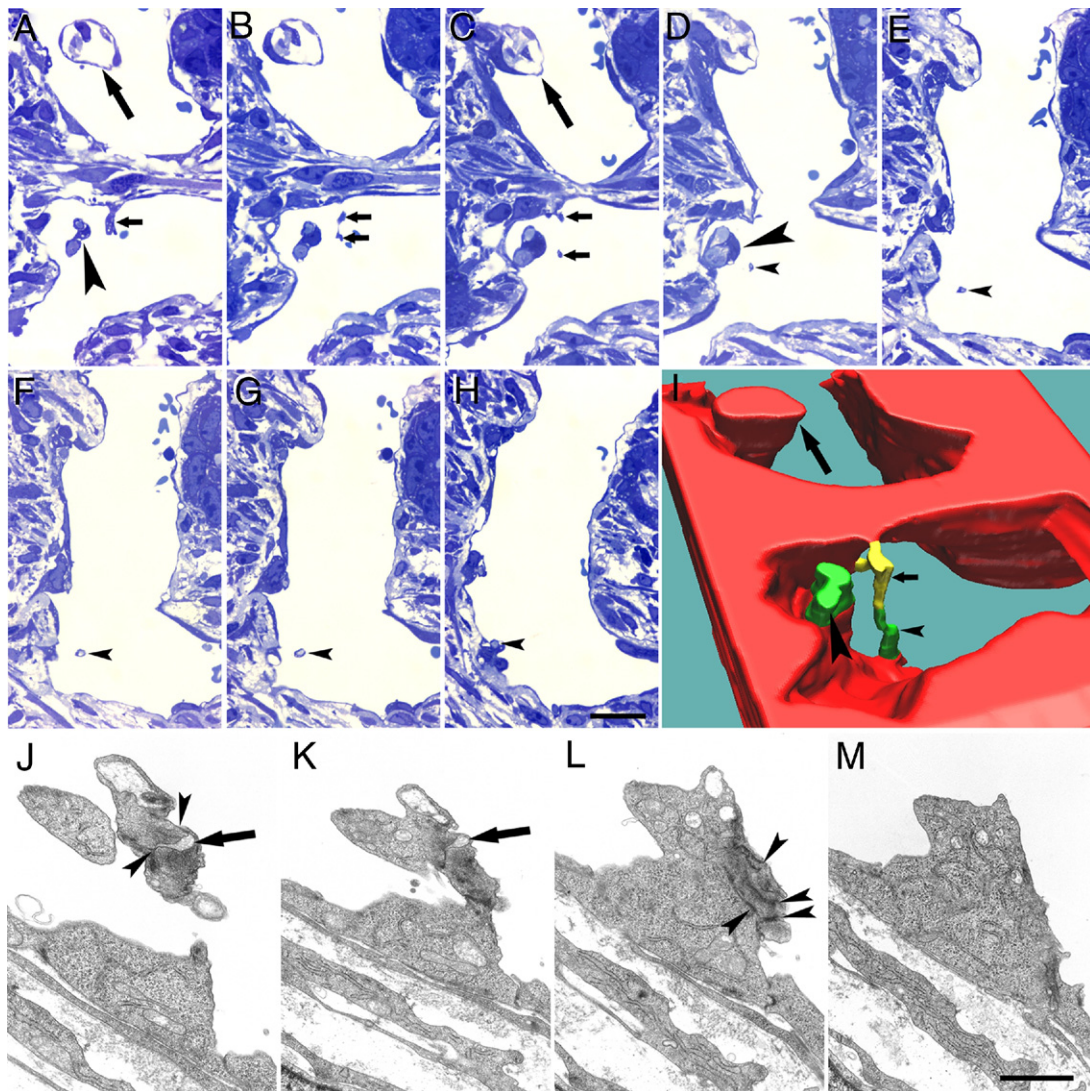


Figure 6. Pillar development. **A–H:** Developing pillar partially filled with a collagen bundle. Small **arrows** mark the part of the pillar consisting only of ECs. The bridge is attached to the vessel wall at two positions (**A** and **C**). The collagen core of the pillar (light blue staining) is discernible first on **D** (**small arrowhead**). The pillar increases in thickness during its further run before it joins the vessel wall (**small arrowheads**). **Large arrows** mark a twin pillar that joins the vessel wall on **C** and blends into it on the following sections. Scale bar = 20 μm (**A–I**). **I:** 3D reconstruction of 30 semithin sections represented in **A–H**. The vessel wall and the surrounding tissue are shown in red, pillars separated from the vessel wall and containing a collagen bundle are shown in green, and the endothelial bridges are shown in yellow. The structure marked by the small **arrow** and **arrowhead** in yellow and green, respectively, indicates that the collagen bundle does not fill the whole length of the pillar. **J–M:** Serial ultrathin sections of a pillar partially filled with a collagen bundle. The sections represent the transitional area where the pillar continues in a short endothelial bridge. The tiny collagen bundle (**arrows** in **J** and **K**) contains only approximately 20 individual collagen fibers. The pillar is sealed by endothelial junctions (**arrowheads** on **J**). The body part of the ECs in the vicinity of the collagen bundles (**J**) contains microfilaments at a high density. The collagen bundle is absent in **L** and **M**. Numerous interendothelial junctions are visible in **L** (**arrowheads**), suggesting that more ECs of the bridge have joined each other in this region. These junctions are absent in **M**, suggesting that the bridge terminates in a single EC. This implies that the other ECs of the bridge have not yet reached this side of the vessel. Scale bar = 1 μm (**J–M**).

connective tissue suggests that the collagen matrix is under tension, through either indirect (ie, fibronectin fibrils) or direct attachment of these cells to the collagen bundles. These attachments may counteract the movement of the collagen bundles. Although we do not have direct evidence for the movement of the collagen bundles, the observed similarity between the diameter of the collagen bundles within the pillar and within the connective tissue, and, moreover, the discovery of collagen bundles extending only halfway into the lumen (while their other end extended into the connective tissue) have led us to conclude that pre-existing collagen bundles are

transferred by these ECs through the lumen. The observation that collagen bundles are transferred in a hand-over-hand cycle in the case of fibroblasts *in vitro* supports this hypothesis. This process was dependent on integrin α -2/ β -1-mediated adhesion and on the contractile activity of the actomyosin cytoskeleton.²⁰ However, in our case, the adhesion receptor responsible for the binding of collagen I in the pillar remains unknown. We could not detect integrin α -1 or α -11 expression levels, and integrin α -2 was present only occasionally at a low density, which did not correlate with the number of adhesion spots containing vinculin within the pillar. This calls into question

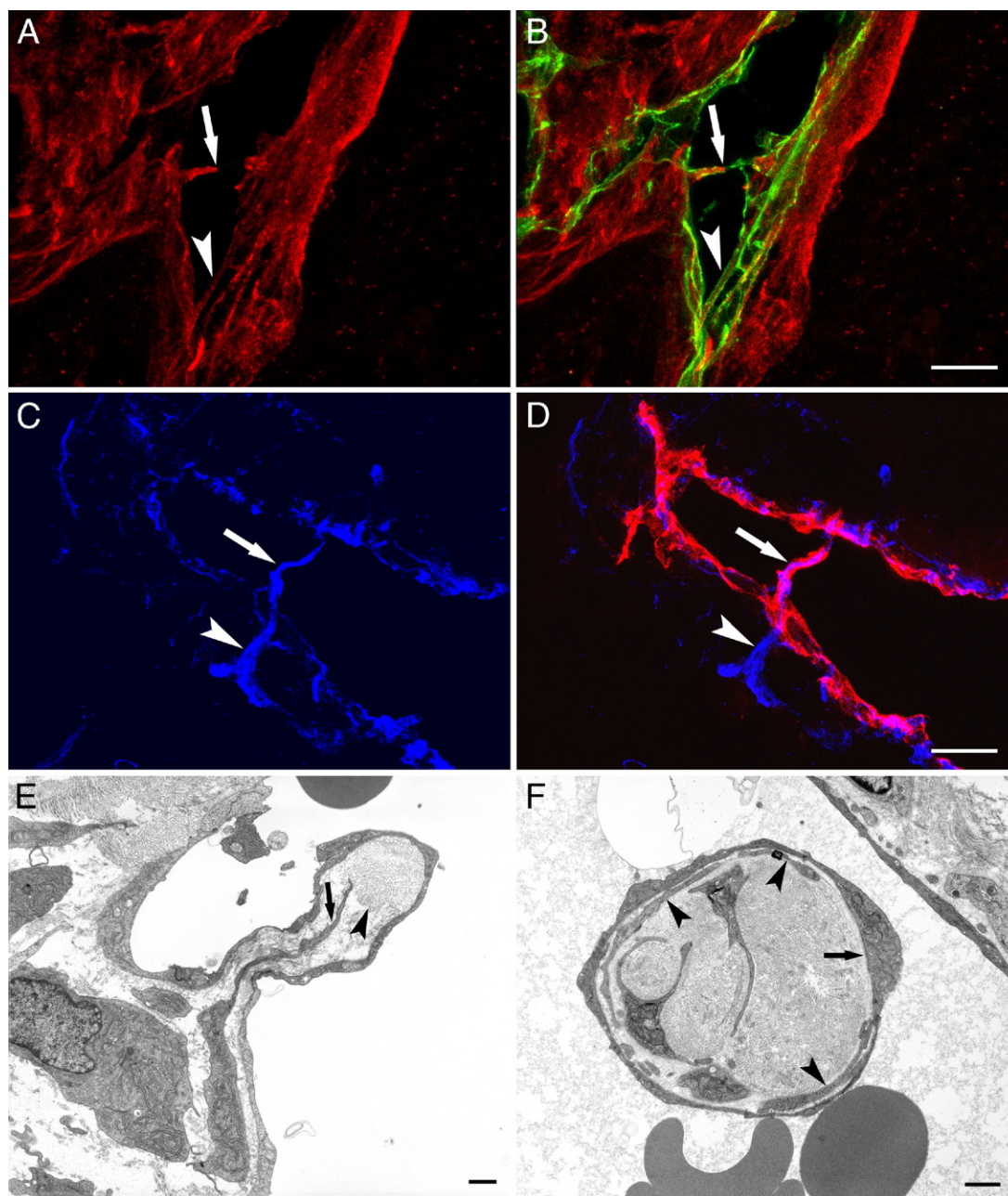


Figure 7. Pillar development and maturation. **A and B:** Horizontal view of 33 optical sections. Double labeling for CD31 (green) and collagen I (red). **A:** Collagen labeling. **B:** Merged red and green channels. The collagen bundle extends only halfway into the vessel lumen within the developing pillar (**arrow**). Another pillar (**arrowhead**) is completely filled with collagen. Scale bar = 20 μm (**B**). **C and D:** Horizontal view of 32 optical sections. Double labeling for CD31 (red) and collagen (blue). **C:** Collagen labeling. **D:** Merged red and blue channels. The collagen bundle originating from the pericapillary connective tissue spans the entire length of the pillar (**arrow**). Scale bar = 20 μm (**D**). **E:** Base of a maturing pillar. A connective tissue cell extends a process (**arrow**) toward the original collagen core of the pillar (**arrowhead**). Scale bar = 1 μm . **F:** Mature pillar containing numerous cells and collagen bundles. The basement membrane is visible on the right side of the pillar under the endothelium (**arrow**). Flat cells under the ECs (**arrowheads**) are presumably pericytes, although they are not covered by a basement membrane. Scale bar = 1 μm .

the role of these integrin subunits in the transport of the collagen bundle. Nevertheless, the presence of adhesion spots containing large α -2 subunits may be the consequence of the maturation process during which myofibroblasts migrate into the pillar. In these cells, integrin α -2 was observed at a high density in the connective tissue surrounding the vessels. Despite the lack of collagen I-binding α subunits within the pillar, integrin β -1 was evenly distributed along the vessel and the pillars, suggesting

that this integrin is paired with laminin-binding α subunits at the basal surface of the ECs.

Electron-dense adhesion sites containing vinculin were observed along the pillars, indicating that the ECs are attached firmly to the collagen bundle. The adhesion spots were unique in structure because they were placed regularly along individual collagen fibers, extended >100 nm from the membrane into the cytoplasm, and were connected to microfilaments. Recently, a strikingly similar

Table 2. Effect of Angiogenesis-Modulating Agents on Tumor Growth and Pillar Densities

Variable	Treatments		
	Control	rHuEPO	Vatalanib
C38 colon carcinoma s.c. tumor weight (g)	2.73 ± 0.72	2.77 ± 1.12	1.46 ± 0.82*
Relative vessel area (%vessel/tumor area)	1.47 ± 0.32	1.75 ± 0.28	1.21 ± 0.14
No. of pillars/vessel area (no./mm ²)	21 ± 3	25 ± 5	32 ± 6*
No. of pillars/tumor area (no./mm ²)	0.31 ± 0.04	0.43 ± 0.06*	0.38 ± 0.08

Results are expressed as mean ± SD.

* $P < 0.05$.

structure was discovered during the analysis of the ultra-structural architecture of focal adhesions in *in vitro* cultured cells. Patla et al²¹ found that the membrane-cytoskeleton interaction within focal adhesions is mediated through vinculin-containing particles located at the cell membrane and attached to actin fibers. Their observation strongly supports our idea that the transluminal transport of the collagen bundle is mediated by the force exerted by the actin cytoskeleton via the adhesion spots (ie, particles).

The finding that collagen fibers touch the plasma membrane of the ECs suggests that ECs adhere directly to the collagen bundle rather than attach to other extracellular matrix elements, such as the basement membrane or fibronectin fibrils. This latter extracellular matrix component is involved in the formation of fibronexus junctions,

which are thought to be responsible for force transmission by myofibroblasts and ECs.^{22,23}

In a recent study,²⁴ the tyrosine kinase inhibitor vatalanib (PTK787/ZK22854) delayed the intussusceptive-dependent maturation of the vascular network in the developing chicken chorioallantoic membrane. In contrast, other researchers¹⁹ reported that rHuEPO can induce intussusceptive angiogenesis in the same angiogenesis assay. Therefore, we also decided to study whether these angiogenesis-modulating molecules have an effect on pillar formation in our C38 tumor model. We found that rHuEPO treatment resulted in a significant increase in intratumoral pillar numbers. However, possibly because of the concomitant increase in intratumoral capillary surface (a phenomenon that corresponds with our previous observations on rHuEPO's effects on tumor capillaries),¹⁶

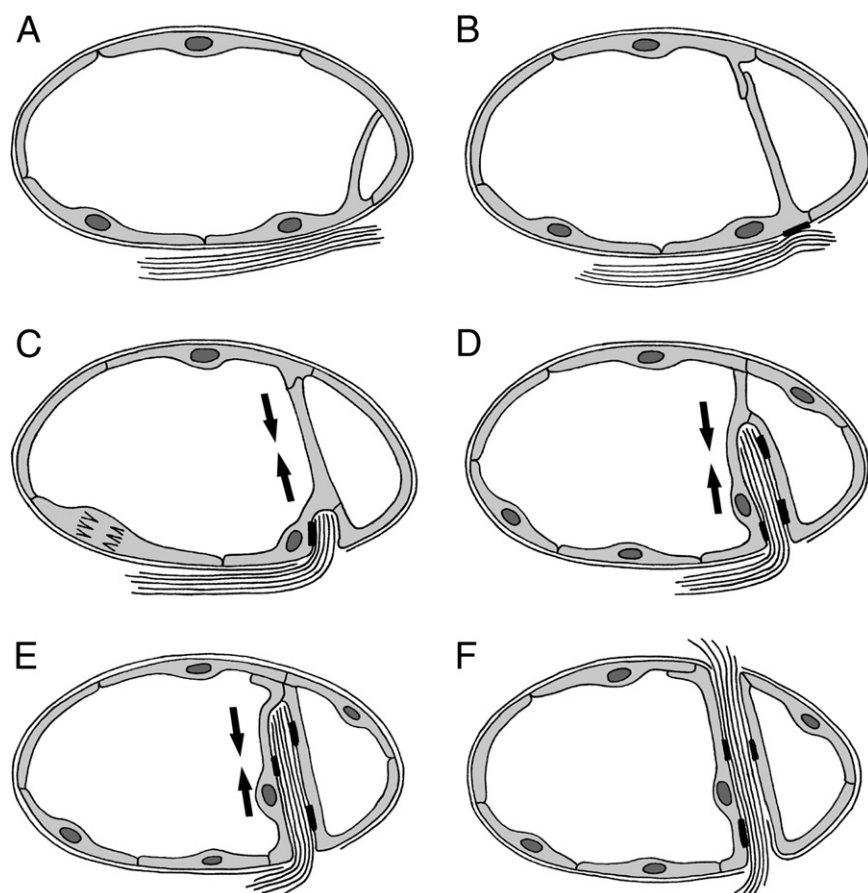


Figure 8. Schematic representation of the putative process of pillar formation. **A:** Simple endothelial bridges are formed. **B:** Bridges can reposition themselves, and more ECs may be involved in bridge formation. On the abluminal side of the ECs that form the bridge, the basement membrane is locally disrupted. An EC from the bridge adheres to a nearby collagen bundle. **C and D:** The collagen bundle, seized firmly through specific adhesion sites, is transferred through the lumen by the bridge-forming ECs as they exert a pulling force on it. **Arrows** indicate the direction of this force. **E:** The collagen bundle reaches the other side of the lumen. The interendothelial junctions are reorganized, ensuring that the luminal and basal polarity of the ECs is maintained during the process. **F:** The collagen bundle is transferred into the connective tissue on the other side of the vessel. A nascent pillar, consisting only of a collagen bundle and the covering ECs, is established. Pillar maturation and enlargement occur through the immigration of fibroblasts/myofibroblasts and pericytes into the pillar and through the subsequent extracellular matrix deposition performed by these cells.

this difference remained nonsignificant when pillar densities were calculated for intratumoral microvessel areas. Thus, these results do not unequivocally indicate that rHuEPO induces pillar formation; they may only suggest that more capillary surface was provided for pillar formation. However, in our experiments with vatalanib, we found a significant increase in pillar densities defined for the microvessel areas in C38 tumors, suggesting an activity for this drug similar to that reported in another earlier study by the previously mentioned researchers.¹⁸ In this study, their group observed a switch from endothelial sprouting to intussusceptive angiogenesis after treatment of mammary carcinoma allografts with vatalanib. Altogether, both our results and theirs support the general notion that inhibition of just a single tumor vascularization mechanism can trigger alternative ones. This can help tumors to develop resistance to anti-angiogenic treatments.^{1,25}

The main limitation of this study is the lack of direct *in vivo* evidence for collagen bundle movement. However, each of the available real-time imaging techniques has serious shortcomings/confounding factors that could hamper its use in studying *in vivo* pillar formation in tumorous conditions. Red blood cell flow makes it impossible to detect an unstained transluminal collagen bundle using common phase-contrast microscopy (S. Paku, unpublished data). The obscuring effect of the blood stream would also exist when using confocal reflection imaging.²⁶ The only way to overcome this problem would be to detect harmonic signals generated during multiphoton excitation. However, although this method highlights unstained fibrillar collagen,^{27,28} the penetration depth of the second harmonic signal is limited by the light-scattering effect of turbid media (to approximately 200 μm),²⁹ such as the peritumoral s.c. tissue. An additional key problem with *in vivo* pillar imaging is that the equipment should be focused on an object that does not exist at the beginning of the observation period (ie, the probability that a collagen bundle will move in front of a high-power objective is extremely low). Nevertheless, the confocal and ultrastructural evidence we have presented strongly suggests that the observed collagen bundles are transferred through the lumen by the bridge-forming ECs. The evidence includes the following: i) the adhesion sites along the pillars, ii) the dense actin filament network within the pillars, iii) the similarity between pillar and connective tissue collagen bundle diameters, and iv) collagen bundles extending only halfway into the lumen with their other end extended into the connective tissue.

In summary, this study reports the detailed mechanism of connective tissue pillar formation during tumor-induced intussusceptive angiogenesis. This new mechanism of pillar formation can also be termed inverse sprouting. During the normal sprouting process, ECs maintain their polarity, migrate surrounded by connective tissue, and form a slit-like lumen.² During pillar formation, ECs are surrounded by the vessel lumen and the connective tissue is situated inside the sprout. As in normal sprouting, ECs involved in inverse sprouting also maintain their polarity. Meanwhile, the complete EC coverage of the collagen bundle ensures that the collagen core of

the pillar is not in contact with blood elements during the process. These results provide a better understanding of this type of angiogenesis and may also represent a new piece to the puzzle of cancer therapy via angiogenesis inhibition.

References

1. Dome B, Hendrix MJ, Paku S, Tovari J, Timar J: Alternative vascularization mechanisms in cancer: pathology and therapeutic implications. *Am J Pathol* 2007, 170:1–15
2. Paku S, Paweletz N: First steps of tumor-related angiogenesis. *Lab Invest* 1991, 65:334–346
3. van Hinsbergh VW, Koolwijk P: Endothelial sprouting and angiogenesis: matrix metalloproteinases in the lead. *Cardiovasc Res* 2008, 78:203–212
4. Makanya AN, Hlushchuk R, Djonov VG: Intussusceptive angiogenesis and its role in vascular morphogenesis, patterning, and remodeling. *Angiogenesis* 2009, 12:113–123
5. Djonov V, Baum O, Burri PH: Vascular remodeling by intussusceptive angiogenesis. *Cell Tissue Res* 2003, 314:107–117
6. Burri PH, Hlushchuk R, Djonov V: Intussusceptive angiogenesis: its emergence, its characteristics, and its significance. *Dev Dyn* 2004, 231:474–488
7. Patan S, Tanda S, Roberge S, Jones RC, Jain RK, Munn LL: Vascular morphogenesis and remodeling in a human tumor xenograft: blood vessel formation and growth after ovariectomy and tumor implantation. *Circ Res* 2001, 89:732–739
8. Patan S, Munn LL, Jain RK: Intussusceptive microvascular growth in a human colon adenocarcinoma xenograft: a novel mechanism of tumor angiogenesis. *Microvasc Res* 1996, 51:260–272
9. Cojoc D, Difato F, Ferrari E, Shahapure RB, Laishram J, Righi M, Di Fabrizio EM, Torre V: Properties of the force exerted by filopodia and lamellipodia and the involvement of cytoskeletal components. *PLoS One* 2007, 2:e1072
10. Burton K, Park JH, Taylor DL: Keratocytes generate traction forces in two phases. *Mol Biol Cell* 1999, 10:3745–3769
11. Nagy JA, Chang SH, Dvorak AM, Dvorak HF: Why are tumour blood vessels abnormal and why is it important to know? *Br J Cancer* 2009, 100:865–869
12. Dvorak HF: Rous-Whipple Award Lecture: how tumors make bad blood vessels and stroma. *Am J Pathol* 2003, 162:1747–1757
13. Zhou A, Egginton S, Hudlická O, Brown MD: Internal division of capillaries in rat skeletal muscle in response to chronic vasodilator treatment with alpha1-antagonist prazosin. *Cell Tissue Res* 1998, 293:293–303
14. Paku S, Kopper L, Nagy P: Development of the vasculature in "pushing-type" liver metastases of an experimental colorectal cancer. *Int J Cancer* 2005, 115:893–902
15. Dezso K, Bugyik E, Papp V, László V, Dóme B, Tóvári J, Timár J, Nagy P, Paku S: Development of arterial blood supply in experimental liver metastases. *Am J Pathol* 2009, 175:835–843
16. Tóvári J, Gilly R, Rásó E, Paku S, Bereczky B, Varga N, Vágó A, Timár J: Recombinant human erythropoietin alpha targets intratumoral blood vessels, improving chemotherapy in human xenograft models. *Cancer Res* 2005, 65:7186–7193
17. Wood JM, Bold G, Buchdunger E, Cozens R, Ferrari S, Frei J, Hofmann F, Mestan J, Mett H, O'Reilly T, Persohn E, Rösel J, Schnell C, Stover D, Theuer A, Towbin H, Wenger F, Woods-Cook K, Menrad A, Siemeister G, Schirner M, Thierauch KH, Schneider MR, Drevs J, Martiny-Baron G, Totzke F: PTK787/ZK 222584, a novel and potent inhibitor of vascular endothelial growth factor receptor tyrosine kinases, impairs vascular endothelial growth factor-induced responses and tumor growth after oral administration. *Cancer Res* 2000, 60:2178–2189
18. Hlushchuk R, Riesterer O, Baum O, Wood J, Gruber G, Pruschy M, Djonov V: Tumor recovery by angiogenic switch from sprouting to intussusceptive angiogenesis after treatment with PTK787/ZK222584 or ionizing radiation. *Am J Pathol* 2008, 173:1173–1185
19. Crivellato E, Nico B, Vacca A, Djonov V, Presta M, Ribatti D: Recombinant human erythropoietin induces intussusceptive microvascular growth *in vivo*. *Leukemia* 2004, 18:331–336

20. Meshel AS, Wei Q, Adelstein RS, Sheetz MP: Basic mechanism of three-dimensional collagen fibre transport by fibroblasts. *Nat Cell Biol* 2005, 7:157–164
21. Patla I, Volberg T, Elad N, Hirschfeld-Warneken V, Grashoff C, Fässler R, Spatz JP, Geiger B, Medalia O: Dissecting the molecular architecture of integrin adhesion sites by cryo-electron tomography. *Nat Cell Biol* 2010, 12:909–915
22. Eyden B: The myofibroblast: phenotypic characterization as a prerequisite to understanding its functions in translational medicine. *J Cell Mol Med* 2008, 12:22–37
23. Eyden B: Fibronexus junctions associated with in vivo human endothelium. *Ultrastruct Pathol* 2009, 33:28–32
24. Baum O, Suter F, Gerber B, Tschanz SA, Buergy R, Blank F, Hlushchuk R, Djonov V: VEGF-A promotes intussusceptive angiogenesis in the developing chicken chorioallantoic membrane. *Microcirculation* 2010, 17:447–457
25. Hillen F, Griffioen AW: Tumour vascularization: sprouting angiogenesis and beyond. *Cancer Metastasis Rev* 2007, 26:489–502
26. Friedl P, Maaser K, Klein CE, Niggemann B, Krohne G, Zänker KS: Migration of highly aggressive MV3 melanoma cells in 3-dimensional collagen lattices results in local matrix reorganization and shedding of alpha2 and beta1 integrins and CD44. *Cancer Res* 1997, 57:2061–2070
27. Provenzano PP, Eliceiri KW, Keely PJ: Multiphoton microscopy and fluorescence lifetime imaging microscopy (FLIM) to monitor metastasis and the tumor microenvironment. *Clin Exp Metastasis* 2009, 26:357–370
28. Brown E, McKee T, diTomaso E, Pluen A, Seed B, Boucher Y, Jain RK: Dynamic imaging of collagen and its modulation in tumors in vivo using second-harmonic generation. *Nat Med* 2003, 9:796–800
29. Balu M, Baldacchini T, Carter J, Krasieva TB, Zadayan R, Tromberg BJ: Effect of excitation wavelength on penetration depth in nonlinear optical microscopy of turbid media. *J Biomed Opt* 2009, 14:010508

A Novel Concept of Glomeruloid Body Formation in Experimental Cerebral Metastases

BALÁZS DÖME, MD, JÓZSEF TÍMÁR, MD, PhD, AND SÁNDOR PAKU, PhD

Abstract. Glomeruloid bodies (GBs), tumor-associated vascular structures with a superficial resemblance to renal glomeruli, are important histopathological features of glioblastoma multiforme, but have also been described in other types of tumors and in cerebral metastases. The purpose of this study was to elucidate the pathogenesis of these lesions in an appropriate murine model of experimental brain metastases. To do so, we injected cells from 5 different tumor lines into the internal carotid artery of mice and investigated the development, composition, and fate of GBs growing within tumor nodules. Immunohistochemical analyses and 3-dimensional reconstruction of the cerebral vasculature showed clearly that the proliferating and migrating tumor cells pull the capillaries (and the adjacent capillary branching points) into the tumor cell nest. Initially, this process led to the appearance of simple coiled vascular structures, which later developed into chaotic and tortuous vascular aggregates with multiple narrowed afferent and efferent microvessels. Despite the absence of sprouting angiogenesis, the very low level of endothelial cell proliferation index and the ruptures of the stretched and narrowed capillary segments observed frequently between the metastatic tumor nodules, necrosis was scarce in these lesions, implying that the blood supply from the multiple afferent microvessels and from the preexistent vascular bed sufficed to provide the tumor cells with oxygen and nutrients.

Key Words: Experimental brain metastasis; Endothelium; Glomeruloid body; Microvessel.

INTRODUCTION

The appearance of cerebral metastases is often associated with the terminal stage of cancer. Despite developments of both diagnostic modalities and new therapeutic strategies, the median survival of patients with brain metastases is less than 6 months, which has not substantially changed during the past 2 decades (1).

In contrast to the widely accepted view that most tumors and metastases begin to grow as avascular spheroids, there is also evidence that a subset of tumors instead initially grows by the use of preexistent vessels, a process referred to as co-option (2–4). Indeed, the perivascular migration of tumor cells is a common observation, especially in the central nervous system (5–10). It has also been hypothesized recently that in the highly vascularized brain, metastases of tumor cells grow without the increase of intratumoral microvessel density and the induction of sprouting angiogenesis (11), even if these cells are engineered to express recombinant VEGF-A₁₆₅ (12). The formation of complex multilumen vascular channels has been considered to be the result of nonsprouting (i.e. intussusceptive) angiogenesis in these studies, although the presence of glomeruloid bodies (GBs) in primary and

metastatic cerebral cancers is well known (13–16). However, there is only 1 detailed description of this type of “angiogenesis” in an animal model in which the authors found that the injection of an adenoviral vector engineered to express VEGF induced the development of GBs in normal ear skin of athymic mice (17).

The purpose of the present study was to determine the steps of GB formation in experimental brain metastases by human and mouse cancer cells. We report the novel finding here that the co-opted brain capillaries have a passive role in GB pathogenesis with a relatively low level of endothelial cell (EC) proliferation and without morphological evidence of sprouting activity. The tumor cells adhering and proliferating on the surface of basement membranes (BM) of cerebral microvessels pull the capillaries into the tumor nodules, looping and coiling them up, leading to the appearance of florid microvascular structures with a superficial resemblance to renal glomeruli.

MATERIALS AND METHODS

Animals, Tumor Cell Lines, and Injections

Inbred C57Bl/6 and SCID mice were anesthetized and $2.5\text{--}5 \times 10^5$ tumor cells in 0.2 ml Hanks' solution were injected into the right internal carotid artery as described previously (18). The highly metastatic 3LL-HH tumor line was maintained in C57Bl/6 mice by serial intrasplenic transplantation of tumor cells obtained from liver metastasis as described previously (18). The B16 mouse melanoma and the A2058 and WM983 human melanoma cells were cultured in RPMI-1640 supplemented with 10% fetal bovine serum and 100 Units/ml penicillin, 0.1 mg/ml streptomycin (all from Sigma Chemical Co., St. Louis, MO). The 293 human renal cell carcinoma cells were cultured in Eagle's MEM supplemented with 10% horse serum and 100 Units/ml penicillin, 0.1 mg/ml streptomycin (Sigma). Before injections, cells were harvested by trypsinization and washed in

From First Institute of Pathology and Experimental Cancer Research (BD, JT, SP), Semmelweis University; Department of Molecular Pathology (SP), Joint Research Organization of the Hungarian Academy of Sciences and Semmelweis University; Department of Tumor Progression (BD, JT), National Institute of Oncology, Budapest, Hungary.

Correspondence to: Sándor Paku, PhD, First Institute of Pathology and Experimental Cancer Research, Semmelweis University, 1085 Üllői Ut 26, Budapest, Hungary. E-mail: paku@korbl.sote.hu

This work was supported by grants from the Hungarian National Science Foundation (OTKA T-26439) and the Ministry of Education (NKFP 1/48/2001) and the Semmelweis University.

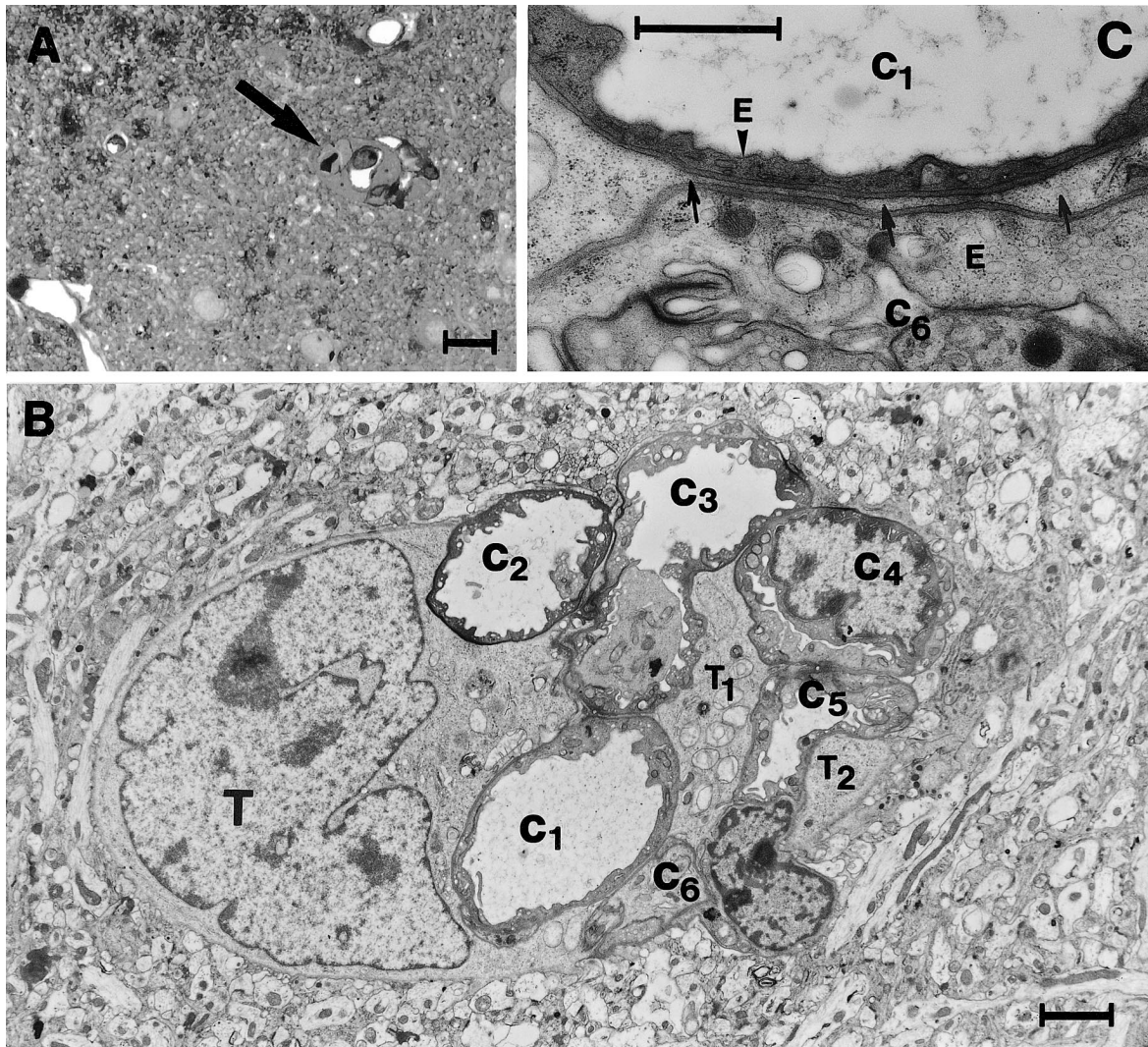


Fig. 1. **A:** Lewis lung tumor cell (arrow) located in the cortex of mouse brain 3 days after tumor cell inoculation. Scale bar: 10 μ m. **B:** Electron micrograph of the tumor cell shown in (A). Six capillary lumens (C1–C6) are visible in the vicinity of the extravascular tumor cell. One process of the tumor cell (T1) is in contact with 5 of the 6 capillaries. Another process of the tumor cell (T2) adheres to the outer side of capillary 5 (C5). Scale bar: 2 μ m. **C:** Higher magnification of the area between capillary 1 and 6. A thin cytoplasmic bridge (arrows) can be observed between the capillaries, connecting the process to the main body of the cell. E; endothelium, Scale bar: 1 μ m.

Hanks' balanced salt solution (HBSS). Groups of 5 mice were killed by anesthesia at various time points (3, 5, 7, 11, 14 days after tumor cell injection in the cases of 3LL-HH and B16; 14, 21, 30 days in the cases of 293, A2058, and WM983). Experiments were carried out in accordance with the animal protection laws of the Ethic Committee of Semmelweis University.

Transmission Electron Microscopy

Animals were perfused via the left ventricle with phosphate buffered saline for 10 min and with 2.5% glutaraldehyde in 0.05 M Na-cacodylate (pH 7.2) for 15 min at room temperature. Brains were removed, cut into 1 \times 2-mm pieces and immersed in 2.5 glutaraldehyde for 2 hours. The pieces were processed as described previously (19) and analyzed on a Philips CM10 electron microscope.

3D Visualization of the Vasculature of Brain Metastases

Sections 100 μ m in thickness were incubated at room temperature for 6 to 12 hours in a mixture of anti-laminin (rabbit polyclonal 1:50; DAKO Corp., Carpinteria, CA) antibody for BM identification plus anti-mouse CD31 (rat monoclonal, 1:100; Pharmingen, San Diego, CA) antibody for EC identification or anti- α SMA (mouse monoclonal, 1:100; DAKO Corp.) or anti-desmin (mouse monoclonal 1:200; DAKO Corp.) antibody for pericyte identification. After several rinses with PBS, specimens were incubated simultaneously for 6 hours at room temperature with the appropriate secondary antibodies (Cy5-conjugated anti-mouse IgG; FITC-conjugated anti-rat IgG; rhodamine-conjugated anti-rat IgG; rhodamine-conjugated anti-rabbit IgG; FITC-conjugated anti-rabbit IgG, all from Jackson

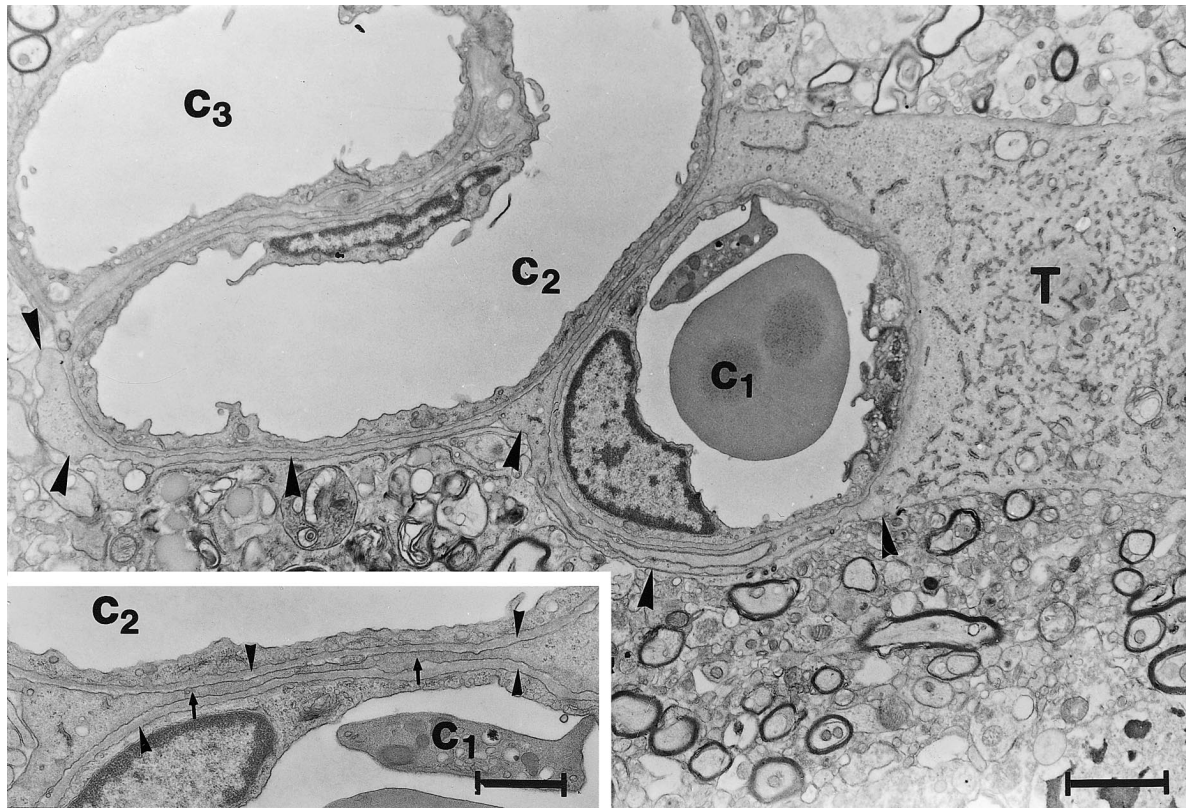


Fig. 2. Extremely long and thin process (arrowheads) of a Lewis lung tumor cell (T) adhering and advancing along the capillary basement membrane. One of the 3 capillaries (C1) is completely engulfed by the tumor cell. Scale bar: 2 μ m. Inset shows the region between capillary 1 and 2. The thin process of the tumor cell (arrows) adheres to both of the capillary basement membranes (arrowheads). Scale bar: 1 μ m

Immunoresearch, West Grove, PA; 1:50) with or without nuclear staining with TOTO-3 (Molecular Probes, Eugene, OR; 5 μ M) or propidium iodide (0.5 μ g/ml, 5 min). For the lectin staining of brain vasculature, FITC-labeled *Lycopersicon esculentum* lectin (100 μ g in 0.1 ml of 0.9% NaCl; Vector Laboratories, Burlingame, CA) was injected into the lateral tail vein 15 min before the animals were killed with Nembutal overdose. Sections (100 μ m) were cut and transferred to 6-well plates containing methanol (-20° C). To avoid compression, small pieces of cover slip of 150- μ m thickness were inserted on both sides of the mounted slice. For 3D reconstruction, up to 80 serial optical sections at 0.5- to 1.5- μ m intervals were used. Digitized image stacks were further processed using Bio-Rad LaserSharp software (Bio-Rad, Hercules, CA).

Assessment of Endothelial Cell Labeling Index with Bromodeoxyuridine (BrdU)

Two hours before the mice were killed, 200 mg/kg BrdU in saline was injected intraperitoneally. Sections were fixed in methanol (-20° C) and reacted sequentially with rat anti-mouse CD31, rhodamine-conjugated anti-rat IgG (1:50, Jackson Immunoresearch), 2N HCl (10 min, 20° C), anti-BrdU antibody (1:100, Becton-Dickinson, Franklin Lakes, NJ), biotinylated anti-mouse IgG (1:100, Vector), streptavidin-FITC (1:100, Vector), and with TOTO-3. Slices were viewed by confocal microscopy. The labeling index of ECs was determined by counting the labeled as

well as all the EC nuclei (100/studied area) along the vessel walls.

RESULTS

To elucidate the steps of GB formation from the very early stages, we followed serially the growth of metastases from individual extravasated cells to tumors reaching 1 to 1.5 mm in diameter and investigated EC proliferation and the distribution of pericytes. All mice injected with cells into the internal carotid artery developed cerebral tumors, predominantly in the parenchyma and in the choroid plexus, with smaller deposits in the meninges. The growth rate of tumor lesions varied among the different cell lines. The process was most rapid in case of murine tumors (3LL-HH and B16) and was much slower in case of human cell lines (293, A2058, and WM983). Injection of a higher number of cells led to a higher number of metastases; however, the morphology of the individual lesions was not affected. Four of the 5 tumor cell lines produced GBs subsequent to intracarotid artery implantation. Although the growth pattern of the different tumor lesions was similar (perivascular migration), we were unable to detect GBs in B16 melanomas.

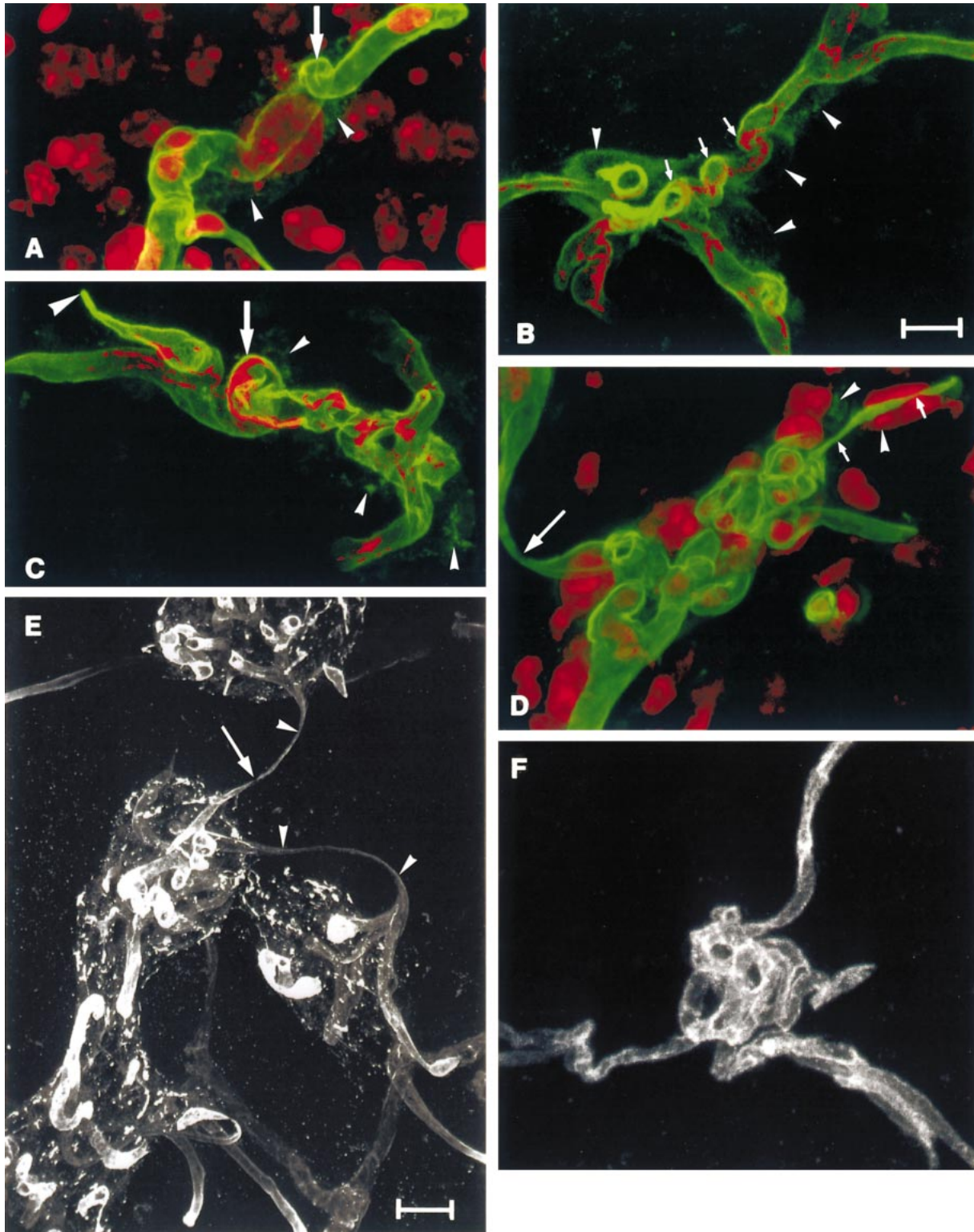


Fig. 3. **A:** Single loop of a cerebral capillary (arrow) induced by a large Lewis lung tumor cell adhering to the capillary basal membrane (laminin, green). Note the laminin positivity of the cytoplasm of the tumor cell (arrowheads). **B:** Immunofluorescent staining of microvessels for the endothelial cell marker CD31 (red) and the basal membrane component laminin (green). Laminin-positive Lewis lung tumor cells are attached to the capillaries (arrowheads). One of the capillaries contains a triple helical structure (arrows). **C:** Irregular capillary covered by several tumor cells (small arrowheads). One pronounced loop (arrow) is observable. The red signal, corresponding to desmin-positive pericytes follows the green signal representing the capillary basement membrane. A ruptured blind ended capillary is also present (large arrowhead). **D:** Small glomeruloid body consisting

The first changes in capillary structure were evident as early as day 3 in the case of 3LL-HH and day 14 in the case of human tumors. Electron microscopic analysis showed numerous capillary lumens in the vicinity of the extravasated tumor cells, some of them were apparently situated within the body of the tumor cells (Fig. 1). Tumor cells produced often extremely long cellular processes, which advanced along the basement membranes and encircled the capillaries (Fig. 2). Confocal microscopic analysis has revealed that the first step in the development of the multiluminal structures observed in sections was the appearance of single microvascular helices induced by the tumor cell firmly adhering to the basement membrane and tugging the capillary (Fig. 3A). As the extravasated tumor cells started to proliferate along the BM of the capillaries, the number of the loops increased (Fig. 3B). The development of helical structures involved the whole capillary tube, including pericytes (Fig. 3C).

After 3 to 7 days in the case of 3LL-HH and 14 to 21 days in the cases of 293, A2058, and WM983, the tumor cells began to increase in number, preferentially migrating along preexisting brain vessels while also adhering to each other, and ultimately organized into metastatic tumor cell nests. As a result, they further looped and twisted the capillaries, which led to the development of small GBs in the micrometastases (Fig. 3D). Electron microscopic examination has not shown damaged endothelial cells or pericytes within these lesions.

EC labeling index within the foci elevated to a relatively low level (1%–2%) and remained there. Later (7–10 days for 3LL-HH; 21–30 days for 293, A2058, and WM983), the continuously proliferating and migrating tumor cells pulled the capillaries into the metastatic tumor nodules, leading to a tangled and chaotic intratumoral vascular network with multiple microvessel loops and spirals. This phenomenon led to the dramatic augmentation of microvessel density within the metastatic lesions, with a slightly higher EC labeling index than in the normal brain and without morphological evidence of branching activity. Concomitant with these events, between the tumor cell nests the diameters of the stretched capillary segments radically decreased and, sometimes, the increasing microvessel strain led to the rupture of the

capillary walls (Fig. 3E). There appeared to be preexisting capillary branching points present, which were incorporated into the tumor cell nest. In the GBs supplied by multiple afferent microvessels, perfusion was often reduced but not shut down entirely, whereas sometimes the devolution of GBs supplied by a single afferent microvessel could be observed. Despite the microvessel ruptures and the absence of “neovascularization,” necrosis was scarce in the tumor cell nests, probably because of the incorporated preexistent vascular bed and the multiple afferent microvessels supplying the tumor cells (Fig. 3F).

It is also important to note that we did not detect differences between the vasculature within the lesions and that in the surrounding normal brain tissue with regard to pericyte coverage and distribution (assessed by desmin and α SMA immunoreactivity).

DISCUSSION

In the current study we investigated the development, composition, and fate of GBs in the central nervous system of mice. For this purpose, we injected cells from 5 different tumor lines (3LL-HH, B16, 293, A2058, and WM983) into the internal carotid artery of C57Bl/6 and SCID mice and studied the growth, mechanism of vascularization, and the EC proliferation of cerebral metastases. Although B16 melanomas showed the uniform pattern of growth (migration along preexistent vessels), they failed to produce glomeruloid lesions. 3D reconstruction of the vasculature by staining the capillaries with antibodies against different microvessel wall components (anti-CD31, anti-laminin, anti-desmin, and anti- α SMA) and with *Lycopersicon esculentum* lectin demonstrated that in contrast to the prevailing view, during GB formation there is no morphological evidence of sprouting or intussusceptive angiogenesis; instead, migrating and proliferating tumor cells of the metastases pull the brain capillaries into the tumor spheroid. The pulling force is generated by the contractile cytoskeleton of the tumor cells spreading on the surface of the capillary BM and also adhering to each other. This force induces the stretching (coupled to the reduction of the capillary diameters) of the capillary segments between the tumor

←

of numerous capillary loops inside of a micrometastasis of the Lewis lung tumor cell line. The diameter of a capillary segment (large arrow) lying outside the glomeruloid body is significantly reduced. Tumor cells (arrowheads) are attached to the other very small diameter capillary (small arrow). **E:** Brain metastases stained for laminin, 28 days following inoculation of the A2058 human tumor cell line. Glomeruloid bodies inside of the metastases are connected to each other by very small diameter capillaries. A small discontinuity can be observed in one of these capillaries (arrow). The outline of the metastases are clearly visible because of the strong laminin positivity of the tumor cells. **F:** Glomeruloid body inside of a metastasis of the WM983 human tumor cell line, 28 days following tumor cell inoculation. The capillaries of the glomeruloid body are well perfused by FITC-labeled *Lycopersicon esculentum* lectin. The pictures are horizontal views of stacks of confocal images (60–80 optical sections at 1- μ m intervals). Nuclear staining was performed using propidium iodide (red) in (A) and (D). Scale bars: A–D = 20 μ m; E, F = 50 μ m.

nodules and the parallel appearance of microvessel loops (i.e. vascular coiling) within the tumor cell nests. The growing tumor, expanding between the host vessels, incorporates the surrounding capillary branching points, resulting in a chaotic and tortuous intratumoral vessel network with multiple afferent and efferent microvessels supplying the GB.

Various studies have analyzed the exact nature of the cells comprising these elaborate vascular structures and elucidated the microvascular morphology in GBs grown in different types of human tumors and malformations. These vascular aggregates with a superficial resemblance to renal glomeruli are one of the diagnostic histological features of glioblastoma multiforme (14, 20) and have also been described in gastrointestinal carcinomas (21), thymomas (22), cutaneous vascular tumors (23), ovarian teratomas (24), and in brain metastases of lung cancer (13). They are composed of several closely associated capillaries surrounded by variably thickened BM within which a limited number of pericytes is embedded (14). Until now, however, the pathogenesis of GBs in experimental tumor systems has remained unexplained. In a previous study based on immunohistochemical and light microscopic methods, the formation of multilumen vascular structures and transvascular bridges in experimental cerebral metastases is thought to be a form of nonsprouting (i.e. intussusceptive) angiogenesis (11). Accordingly, in our experimental system we observed similar structures by light and electron microscopy, which make possible only a 2D morphological assessment of the gross vascular network, but cannot adequately describe the 3D microvascular architecture. We applied therefore 3D reconstruction of confocal data, which revealed a different mechanism of GB formation.

The only study dealing with this type of “angiogenesis” (in which the authors describe the steps of GB development, stabilization, and regression induced by locally expressed VEGF) was performed in the ear skin of nude mice in the absence of neoplastic cells (17). In this animal model, GBs develop in mother vessels from recruitment and proliferation of ECs and VEGF is essential for their induction and maintenance. The commentary on this article by Sundberg et al suggests a 5-stage sequence to explain vascular changes during brain tumor progression (25): 1) vessel co-option; 2) angiopoietin-2 mediated apoptosis of ECs; 3) tumor necrosis; 4) VEGF expression of hypoxic tumor cells surrounding central necrosis; and 5) GB formation. In contrast to this hypothesis, we have observed that GB formation starts immediately after tumor cell extravasation, much earlier than necroses appear within the metastases. Furthermore, our results suggest that co-opted microvessels most probably act as a passive string during GB development, and that this type of GB formation is not related to neoangiogenesis. However, it cannot be excluded that “active” and “passive” type of

GB formation can operate concurrently in various tumor types.

The central nervous system is unique in the structure and function of its mesenchyme. In normal adult brain the “stroma” consists of a dense network of oligodendrocytes, astrocytes, and numerous intertwining neuronal processes (26). The parenchyma of the adult brain is generally a counter-adhesive and nonpermissive environment for migration of tumor cells (27). A well-defined extracellular matrix, which can provide a surface for the migrating tumor cells, exists only around the cerebral capillaries and in the glial limitans externa. The presence of the classical BM proteins, laminin, collagen type IV, and fibronectin, is limited to these structures (27, 28). The absence of a supportive connective tissue in the brain parenchyma is important in 2 ways. The tumor cells are forced to proliferate along the preexisting microvessels, a process referred to as perivascular migration or vessel co-option (3). Alternatively, the lack of anchorage of the cerebral microvessel network allows the force exerted by the tumor cells firmly adhering to the capillary basement membrane to cause capillary stretching (tug of war between the adjacent tumor nests) and the appearance of microvessel loops within the tumor nodules. Although sprouting activity was completely absent and only a slight increase of the EC labeling index (1%–2%) was found within the metastatic foci, 3D reconstruction of the vasculature demonstrated that GBs are tufted collections of vascular channels (including the pericytes and the BM surrounding the endothelial tube), suggesting that the local increase of microvessel density does not necessarily mean active angiogenesis and EC proliferation. Despite the fact that the microvessel segments were thinned down or sometimes ruptured between the GBs, tumor necrosis was scarce, although we were able to follow the fate of GBs until the metastases reached 1.5 mm in diameter.

In summary, our results suggest that the development of vascular aggregates in micrometastases provides surface and blood supply for the proliferating tumor cells, but this process cannot be termed as true angiogenesis; rather, it represents a remodeling of the existing vasculature of the brain.

REFERENCES

1. Reijneveld JC, Voest EE, Taphoorn MJ. Angiogenesis in malignant primary and metastatic brain tumors. *J Neurol* 2000;247:597–608
2. Zagzag D, Amirnovin R, Greco MA, et al. Vascular apoptosis and involution in gliomas precede neovascularization: A novel concept for glioma growth and angiogenesis. *Lab Invest* 2000;80:837–49
3. Holash J, Maisonpierre PC, Compton D, et al. Vessel cooption, regression, and growth in tumors mediated by angiopoietins and VEGF. *Science* 1999;284:1994–98
4. Döme B, Paku S, Somlai B, Timar J. Vascularisation of cutaneous melanoma involves vessel co-option and has clinical significance. *J Pathol* 2002;197:355–62

5. Ballinger WE Jr, Schimpff RD. An experimental model for cerebral metastasis: Preliminary light and ultrastructural studies. *J Neuro-pathol Exp Neurol* 1979;38:19–34
 6. Kawaguchi T, Tobai S, Nakamura K. Extravascular migration of tumor cells in the brain: An electron microscopic study. *Invasion Metastasis* 1982;2:44–50
 7. Nicolson GL, Kawaguchi T, Kawaguchi M, Van Pelt C. Brain surface invasion and metastasis of murine malignant melanoma variants. *J Neurooncol* 1987;4:209–18
 8. Kawaguchi T, Kawaguchi M, Dulski KM, Nicolson GL. Cellular behavior of metastatic B16 melanoma in experimental blood-borne implantation and cerebral invasion. *Invasion Metastasis* 1985;5:16–30
 9. Kawaguchi T, Kawaguchi M, Miner KM, Lembo TM, Nicolson GL. Brain meninges tumor formation by in vivo-selected metastatic B16 melanoma variants in mice. *Clin Exp Metastasis* 1983;1:247–59
 10. McGrady BJ, McCormick DF, Toner PG. Ultrastructural aspects of tumour invasion in the central nervous system. *J Pathol* 1993;169: 89–97
 11. Fidler IJ, Yano S, Zhang RD, Fujimaki T, Bucana CD. The seed and soil hypothesis: Vascularisation and brain metastases. *Lancet Oncol* 2002;3:53–57
 12. Kusters B, Leenders WP, Wesseling P, et al. Vascular endothelial growth factor-A(165) induces progression of melanoma brain metastases without induction of sprouting angiogenesis. *Cancer Res* 2002;62:341–45
 13. Ito T, Kitamura H, Nakamura N, Kameda Y, Kanisawa M. A comparative study of vascular proliferation in brain metastasis of lung carcinomas. *Virchows Arch A Pathol Anat Histopathol* 1993;423: 13–17
 14. Rojiani AM, Dorovini-Zis K. Glomeruloid vascular structures in glioblastoma multiforme: An immunohistochemical and ultrastructural study. *J Neurosurg* 1996;85:1078–84
 15. Wesseling P, Schlingemann RO, Rietveld FJR, Link M, Burger PC, Ruiter DJ. Early and extensive contribution of pericytes/vascular smooth muscle cells to microvascular proliferation in glioblastoma multiforme: An immuno-light and immuno-electron microscopic study. *J Neuropathol Exp Neurol* 1995;54:304–10
 16. Plate KH, Breier G, Weich HA, Mennel HD, Risau W. Vascular endothelial growth factor and glioma angiogenesis: Coordinate induction of VEGF receptors, distribution of VEGF protein and possible in vivo regulatory mechanisms. *Int J Cancer* 1994;59:520–29
 17. Sundberg C, Nagy JA, Brown LF, et al. Glomeruloid microvascular proliferation follows adenoviral vascular permeability factor/vascular endothelial growth factor-164 gene delivery. *Am J Pathol* 2001;158:1145–60
 18. Paku S, Dome B, Toth R, Timar J. Organ specificity of the extravasation process: An ultrastructural study. *Clin Exp Metastasis* 2001; 18:481–92
 19. Paku S, Lapis K. Morphological aspects of angiogenesis in experimental liver metastasis. *Am J Pathol* 1993;143:926–36
 20. McLendon R, Enterline D, Tien R, Thorstad W, Bruner J. Tumors of central neuroepithelial origin. In: Bigner D, McLendon R, Bruner J, eds. Russell and Rubinstein's pathology of tumors of the nervous system. New York: Oxford University Press, 1998:307–571
 21. Ohtani H. Glomeruloid structures as vascular reaction in human gastrointestinal carcinoma. *Jpn J Cancer Res* 1992;83:1334–40
 22. Blaker H, Dragoje S, Laissue JA, Otto HF. Pericardial involvement by thymomas. Entirely intrapericardial thymoma and a pericardial metastasis of thymoma with glomeruloid vascular proliferations. *Pathol Oncol Res* 1999;5:160–63
 23. Scheers C, Kolivras A, Corbisier A, et al. POEMS syndrome revealed by multiple glomeruloid angiomas. *Dermatology* 2002;204: 311–14
 24. Baker PM, Rosai J, Young RH. Ovarian teratomas with florid benign vascular proliferation: A distinctive finding associated with the neural component of teratomas that may be confused with a vascular neoplasm. *Int J Gynecol Pathol* 2002;21:16–21
 25. Brat DJ, Van Meir EG. Glomeruloid microvascular proliferation orchestrated by VPF/VEGF: A new world of angiogenesis research. *Am J Pathol* 2001;158:789–96
 26. Nakanishi H, Hosoda S, Takahashi Y, Goto S, Tamura J. Alteration of tumour cell arrangement related to connective tissue stroma in metastatic brain tumours. Histological and immunohistochemical studies of 68 autopsy cases. *Virchows Arch A Pathol Anat Histopathol* 1989;414:485–95
 27. Giese A, Westphal M. Glioma invasion in the central nervous system. *Neurosurgery* 1996;39:235–50
 28. Chintala SK, Sawaya R, Gokaslan ZL, Fuller G, Rao JS. Immunohistochemical localization of extracellular matrix proteins in human glioma, both in vivo and in vitro. *Cancer Lett* 1996;101: 107–14
- Received November 6, 2002
 Revision received February 4, 2003
 Accepted February 11, 2003

ORIGINAL ARTICLE

Lack of Angiogenesis in Experimental Brain Metastases

Edina Bugyik, MS, Katalin Dezső, MD, Lilla Reiniger, MD, PhD, Viktória László, PhD, József Tóvári, PhD, József Tímár, MD, PhD, DSc, Péter Nagy, MD, PhD, Walter Klepetko, MD, Balázs Döme, MD, PhD, and Sándor Paku, PhD

Abstract

Angiogenesis is believed to be essential for the growth of metastatic tumors in the brain. We analyzed the vascularization of tumors formed by 4 epithelial cell lines (C38, ZR75, HT25, and H1650) and a fibrosarcoma (HT1080) cell line injected into the brains of mice. No peritumoral angiogenesis was observed. Tumors apparently acquired their vasculature by incorporation of native vessels. Vessel density was lower, but vessel diameter and vascular cell proliferation were higher within all tumors versus those in the peritumoral tissue. There was an inverse correlation between the number of incorporated vessels and vascular cell proliferation. Epithelial tumors with pushing growth patterns had lower vessel density and elevated vascular cell proliferation compared with invasive tumors. The incorporated vessels retained their normal structure, with the exception of astrocyte foot processes that were replaced by tumor cells. Attachment to the vascular basement membrane led to the differentiation of the ZR75 breast cancer cells. In the HT1080 metastases, there was intussusceptive angiogenesis, that is, the fibrosarcoma cells that were attached to the vessel caused lumen splitting and filled the developing pillars. Branching angiogenesis was not observed either in the tumors or in control cerebral wounds. These data suggest that sprouting angiogenesis is not needed for the incipient growth of cerebral metastases and that tumor growth in this model is a result of incorporation of host vessels.

Key Words: Angiogenesis, Astrocyte, Brain, Carcinoma, Endothelial cell, Fibrosarcoma, Metastasis.

INTRODUCTION

It is generally accepted that angiogenesis is necessary for sustained growth of both primary and secondary brain

tumors (1–4). The term *angiogenesis* refers to an increase in vessel density along with the increase in endothelial cell (EC) proliferation and is frequently used as a synonym for vessel sprouting. In addition to incorporating host vessels, tumors can also acquire their vasculature by inducing intussusceptive microvascular growth or glomeruloid angiogenesis (5). These vascularization mechanisms can act in concert to promote tumor growth.

During sprouting, ECs degrade the underlying basement membrane and migrate into the connective tissue while they maintain their basal-luminal polarity and immediately form a slit-like lumen, which is continuous with the lumen of the mother vessel. The polarized ECs continuously synthesize their own basement membrane, and only the leading process of the tip cell keeps contact with the interstitial collagen or with the provisional fibronectin/fibrin-rich extracellular matrix. The connective tissue is essential for basement membrane deposition because it is not deposited on the surface of other cells under normal conditions (6).

Intussusceptive angiogenesis refers to blood vessel formation by insertion of connective tissue columns, called tissue pillars, into the vessel lumen; the subsequent growth of these pillars results in partitioning of the lumen (5). According to the current view, the first steps of intussusceptive angiogenesis are the protrusion of the vascular wall into the lumen and the development of inter-EC adherence. These are promptly followed by the perforation of the EC bilayer by reorganization of inter-EC junctions. Finally, perivascular cells appear, and a collagenous matrix is deposited within the pillar (7). However, our most recent findings suggest an alternative model, that is, the suction and the subsequent transport of a preexisting pericapillary collagen bundle through the vessel lumen by ECs as a first step, followed by the immigration of connective tissue cells and the deposition of new collagenous connective tissue (8). Nevertheless, both models require extracellular matrix material, especially collagen fibers or cells that are able to produce that material because the pillar, the most important structure of this type of angiogenesis, contains collagen fiber(s) (7). Thus, both sprouting and intussusception require a collagenous matrix containing fibronectin, fibrin, and collagen I. Because the brain parenchyma lacks these molecules (with the exception of artery walls), the significance of these types of angiogenesis during vascularization of brain metastasis is questionable.

In contrast, in a model of glomeruloid body formation described earlier by our group in experimental brain metastases,

From the 1st Institute of Pathology and Experimental Cancer Research (SP, KD, EB, LR, PN) and the 2nd Department of Pathology (JTi), Semmelweis University; Department of Tumor Biology (BD), National Koranyi Institute of Pulmonology; Department of Experimental Pharmacology (JTo), National Institute of Oncology, Budapest, Hungary; and Translational Thoracic Oncology Laboratory (VL, WK, BD), Department of Thoracic Surgery, Medical University of Vienna, Vienna, Austria.

Send correspondence and reprint requests to: Sándor Paku, PhD, 1st Institute of Pathology and Experimental Cancer Research, Semmelweis University, 1085 Üllői út 26, Budapest, Hungary; E-mail: paku@korb1.sote.hu

Drs Döme and Paku contributed equally as senior investigators of this work. This study was supported by a Hungarian Scientific Research Fund (OTKA-NK73119 to SP, BD, JTi, and JTo), the EGT/Norwegian Financial Mechanism (HU0125 to BD, JTi, JTo, and SP), and by RegIonCo (L00052; Cross-border Co-operation Program Hungary-Austria 2007–2013 to BD and JTo).

the presence of collagenous matrix was not necessary because loops of the glomeruloid bodies were generated by the pulling force of tumor cells firmly attached to the basement membrane of the capillaries. This process includes a simple reorganization of the original vascular structure of the brain parenchyma with minimal proliferative activity of the ECs (9). A different process of glomeruloid body formation occurs in response to vascular endothelial growth factor (VEGF), with proliferation of primitive ECs and pericytes in the wall of mother vessels. Although collagen was detected around the glomeruloid bodies in the brain (10), the question of whether the presence of this matrix element is required in the process is yet to be answered.

Increasing data suggest that vessel incorporation plays an important role in the vascularization of both primary and metastatic brain tumors, at least in the initial phase of their progression (11, 12). Küsters et al (11) showed that sprouting angiogenesis is not necessary for vascularization of melanoma brain metastases in an experimental mouse model even in the presence of high level of VEGF; instead, the tumors they observed grew by vessel incorporation.

Previously, by injecting cancer cells into the carotid artery of mice, we described a process of glomeruloid body formation in brain metastases of anaplastic tumors (9). However, using that method, a very large number of micrometastases developed; the large overall tumor burden thereby killed the animals before the metastases could evolve into "macrometastases" (1–2 mm in diameter).

To ensure the development of "macrometastases" in the present study, we injected cells of a human anaplastic fibrosarcoma cell line and murine and human epithelial tumor cells of colonic, breast, and lung origin directly into the brain parenchyma. These cell lines formed differentiated tumors and did not show the frequently observed pronounced perivascular spread. They therefore proved to be more suitable to study the consequences of the presumed angiogenic switch. Our results suggest that an angiogenic switch does not occur during the growth of these tumors in the brain parenchyma and that they are supplied by the incorporated host vessels.

MATERIALS AND METHODS

Animals and Tumor Cell Lines

The C38 murine colorectal carcinoma line was maintained by serial subcutaneous transplantations in C57BL/6 mice. To produce brain metastases, subcutaneous tumors were removed and cut into pieces (~2 mm³) with a surgical blade and were digested in RPMI-1640 medium (catalog no. R8758; Sigma-Aldrich, St Louis, MO), supplemented with 0.7 mg/ml collagenase (37°C for 45 minutes; Sigma-Aldrich). Cells were filtered through 4-fold sterile gauze and centrifuged (800 × rpm, 10 minutes, 4°C). The pellet was resuspended in 10 ml of medium without any supplement; cells were counted, and after centrifugation, the supernatant was removed. C57BL/6 mice received 10⁴ cells in a volume of 2 μl.

Zr-75-1 human breast carcinoma (ZR75), HT25 human colorectal carcinoma, H1650 lung adenocarcinoma, and HT1080 human fibrosarcoma cells were cultured in RPMI-1640 medium supplemented with 10% fetal bovine serum (Sigma). Cells

in exponential growth phase were harvested by trypsinization for 5 minutes at 37°C (trypsin-EDTA; Sigma) and resuspended in RPMI-1640 medium. After counting and centrifugation (800 × rpm, 10 minutes, 4°C), pellets were resuspended in serum-free RPMI-1640 medium. After centrifugation, the supernatant was removed, and the pellet was resuspended (40–60 × 10⁶ cells in a volume of 100–150 μl). Male SCID mice received 8 to 12 × 10⁵ cells in a volume of 2 μl.

For tumor inoculation, mice were anesthetized with intraperitoneal injection of ketamine-xylazine (80:12 mg/kg; Sigma). A midline incision was made in the scalp and the right parietal bone was drilled with a 21-gauge needle (Braun, Melsungen, Germany) 2 mm posterior to the coronal suture and 1 mm lateral to the sagittal suture. Cells were slowly injected using a 10-μl Hamilton syringe. After inoculation, the syringe was left in place for 15 to 30 seconds to prevent the outflow of cells because of pressure changes in the brain. The overlying skin was then closed. Mice were killed 7 to 10 days after inoculation of the C38 and HT1080 tumor cell lines and 21 to 28 days after inoculation of the ZR75, H1650, and HT25 tumor cell lines.

To investigate the general impact of the direct injection process on brain parenchyma, we examined mouse brains after needle wounding as a control. The wounding was performed under the same conditions as those applied during tumor inoculation with the exception of tumor cell injections. Mice were killed after 2, 3, 4, 5, 7, 9, 14, and 21 days.

Immunofluorescence

Primary antibodies and reagents used for immunofluorescence are listed in Table 1. Appropriate secondary antibodies (Jackson ImmunoResearch, West Grove, PA) were used. All samples were analyzed by confocal laser scanning microscopy using the Bio-Rad MRC-1024 system (Bio-Rad, Richmond, CA).

Assessment of Vascular Cell Proliferation by Bromodeoxyuridine Incorporation

At 1 hour before mice were killed, 200 mg/kg bromodeoxyuridine (BrdU; Sigma) in saline was injected intraperitoneally. Brains were removed and frozen. Ten-micrometer-thick cryostat sections were stained with toluidine blue and examined by light microscope. The sample was selected for immunofluorescence analysis when the tumor was localized in the brain parenchyma without affecting the corpus callosum. Methanol fixed (10 minutes at –20°C) frozen sections were incubated with 2N HCl (10 minutes at 20°C) and incubated with primary antibodies against BrdU and laminin (1 hour at 20°C; Table 1). After incubating with appropriate secondary antibodies, sections were counterstained with diaminophenylindole. Sections were analyzed by a Nikon TE300 fluorescent microscope (Tokyo, Japan) using a 100× objective with a field diameter of 200 μm. Blood vessels within the tumor and within 200 μm distance from the periphery of the lesion (tumor or needle wound) were identified by laminin staining. All nonlabeled and labeled nuclei lying within the basement membrane (i.e. ECs and pericytes) were counted (100–500 cells/animal, 3–6 animals/tumor line).

TABLE 1. Primary Antibodies and Fluorescent Dyes Used for Immunofluorescence

Antibody	Species	Manufacturer	Catalog No.	Dilution
BrdU	Mouse monoclonal	Becton Dickinson (San Jose, CA)	347580	1:50
CD31	Rat monoclonal	BD Pharmingen (San Diego, CA)	550275	1:50
CD49c	Mouse monoclonal	Novocastra (Newcastle, UK)	NCL-CD49c	1:100
Claudin 3	Rabbit polyclonal	Invitrogen (Carlsbad, CA)	34-1700	1:50
Collagen I	Rabbit polyclonal	Chemicon (Temecula, CA)	AB765P	1:100
Smooth muscle actin	Mouse monoclonal	DAKO (Carpinteria, CA)	M0851	1:200
Desmin	Rabbit polyclonal	Lab Vision (Fremont, CA)	RB-9014-P	1:200
Epithelial membrane antigen	Mouse monoclonal	Novocastra	NCL-EMA	1:50
Glial fibrillary acidic protein	Mouse monoclonal	BD Pharmingen	556330	1:100
Laminin	Rabbit polyclonal	DAKO	Z0097	1:200
Laminin 5	Rabbit polyclonal	Abcam (Cambridge, UK)	14509	1:50
Pan-cytokeratin-FITC	Mouse monoclonal	Sigma (St Louis, MO)	F0397	1:50
Diamino-phenylindole		Sigma	32670	1:100
Propidium iodide		Invitrogen	P3566	1:500
TOTO-3		Invitrogen	T3604	1:500

The labeling index (LI) was calculated by dividing the number of labeled nuclei by the total number of nuclei counted. In C38-derived tumors, the LI was also determined for the vessels touching the periphery of the tumor.

Morphometry

Tumor size was determined using micrographs captured with the 4× objective. The brains were serially sectioned and the largest extension (area) of the tumor was measured. A theoretical diameter of the lesion was calculated from these data. Vessel density (n/mm²), vessel size (diameter), and density of branching points were determined on micrographs of CD31- and laminin-immunostained sections captured with a 10× objective. All vessels (not only capillaries) in the intratumoral and peritumoral region (up to 200 μm from the tumor margin) were analyzed. Vessel size was determined by measuring the smallest extension of the objects outlined by laminin staining.

All parameters were determined using Quick Photo Micro 2.2 software (Olympus, Tokyo, Japan). During evaluation of branching points, the peritumoral area was used as reference to avoid biased results owing to the differences in branching intensity in the different cutting planes. Results are expressed as fold increase compared with the surrounding parenchyma. The above parameters, including BrdU labeling, were determined in the cell-transferred and needle wounding control brains. Data were evaluated using Student *t*-test.

Western Blot Analysis

For the C38 tumor, cells were obtained from primary cultures and prepared as described above but without collagenase digestion. For all analyzed cell lines, cultured cells were harvested by trypsinization and resuspended in RPMI-1640 supplemented with 10% fetal bovine serum. After counting, cells were washed in RPMI-1640 and sterile PBS. Cells (1×10^7) were resuspended and homogenized in 1 ml of lysis buffer containing 10 mmol/L Tris, pH 7.5, 1 mmol/L EDTA, 150 mmol/L NaCl, 1% Triton X-100, 0.5 mmol/L sodium orthovanadate, and protease inhibitor cocktail (Sigma).

After 30 minutes of incubation (4°C), lysates were centrifuged (15 minutes, 13,000 × rpm, 4°C). Supernatants were stored at −80°C. To determine total protein concentration, the Bio-Rad Protein Assay based on the Bradford dye-binding procedure (Bio-Rad) and BSA standard series were used. Protein samples were denatured in sodium dodecyl sulfate sample buffer (95°C for 10 minutes).

About 12.5% polyacrylamide gel was prepared for PAGE as follows: 80 μg of protein sample was loaded per lane, 1 ladder per gel (2 μl; Precision Plus Dual Color Protein Standard; Bio-Rad). After running and transfer, the membrane was blocked with 5% dried milk in PBS (overnight at 4°C). The membrane was incubated with anti-VEGF antibody (1:1000) (Abcam, Cambridge, UK), biotinylated secondary antibody, and finally with an ABC kit (Vector Laboratories, Burlingame, CA). The membranes were developed by ECL (catalog no. 34077; Thermo Scientific, Hampton, NH) or DAB (Vector).

Quantitative Real-Time Reverse Transcription–Polymerase Chain Reaction Analysis of Cell Lines and Microdissected Tissues

Vascular endothelial growth factor A, platelet-derived growth factor β (PDGF-β), and angiopoietin 1 (Ang-1) expressions were analyzed in cell cultures. Total RNA was extracted from cells using TRIzol (Invitrogen). The expressions of angiogenic factors and their receptors were analyzed using 12-μm-thick frozen brain sections. The sections were fixed in methanol (−20°C for 10 minutes) and were stained with RNase-free hematoxylin. Intratumoral and peritumoral (within 200 μm distance from the periphery of the lesion) regions were microdissected (180–250 μm²/animal, 2 animals/tumor cell line) using the PALM MicroBeam system (Carl Zeiss MicroImaging, Jena, Germany). Total RNA was isolated using RNAqueous-Micro Kit (Applied Biosystems, Weiterstadt, Germany).

High-capacity complementary DNA (cDNA) reverse transcription kit (Applied Biosystems) was used for cDNA synthesis as recommended by the supplier. Pooled cDNA

TABLE 2. TaqMan Assays Used for Quantitative RT-PCR Analysis

Cell Lines: C38	HT25, H1650, ZR75, HT1080
VEGF-A (Mm01281449)	VEGF-A (Hs00173626)
PDGFβ (Mm01298578)	PDGFβ (Hs00234042)
ANG-1 (Mm01129232)	ANG-1 (Hs00162807)
VEGFR-2 (Mm00440099)	VEGFR-2 (Mm00440099)
PDGFRβ (Mm01262489)	PDGFRβ (Mm01262489)
TIE-2 (Mm00443242)	TIE-2 (Mm00443242)

ANG-1, angiopoietin-1; PDGF, platelet-derived growth factor; PDGFR, platelet-derived growth factor receptor; TIE-2, receptor tyrosine kinase for ANG-1; VEGF, vascular endothelial growth factor; VEGFR, vascular endothelial growth factor receptor.

samples of 2 animals were used for polymerase chain reaction (PCR) analysis. Quantitative RT-PCR was performed by the ABI Prism 7300 Sequence Detection System, using ABI TaqMan gene expression assays (Table 2). β-actin (part no. 4352935E, Assay ID: Mm00607939) was used as an endogenous control. All samples were run in triplicate in a 20-μl reaction volume. Results were obtained as threshold cycle (CT) values. Expression levels were calculated using the ΔCT method. The values were calculated as a ratio to β-actin expression. The expression levels of the human angiogenic factors were determined using human-specific β-actin primers in the intratumoral samples. Because the RNA of the intratumoral growth factor receptors was of murine origin in the case of the human tumors, low intratumoral murine β-actin levels could lead to distortion of the data resulting in extremely high relative receptor RNA levels as compared with peritumoral brain tissue. Therefore, the intratumoral values were related to the peritumoral murine β-actin levels. The data were also corrected by the vessel content (vessel number × vessel size ≈ vessel surface) of the given tissue. For a good comparison, the same procedure was applied for the C38 murine colon carcinoma tumor line.

RESULTS

We studied the process of vascularization in 5 tumor cell lines (C38 murine colon carcinoma, HT25 colon, H1650 lung and ZR75 mammary carcinomas and HT1080 fibrosarcoma) injected directly into the brain parenchyma of mice. The largest area occupied by the tumor was determined for each case (Table 3). From these data, a theoretical diameter of the lesion was calculated. The average of diameters in each tumor type reached the postulated size of tumors (1–2 mm diameter) at which angiogenic switch should occur.

Of the 5 tumors, the 2 colon carcinomas (Figs. 1A and 2A, B) and the anaplastic fibrosarcoma (Fig. 2E) showed pushing-like growth patterns (13, 14). The H1650 lung and ZR75 mammary carcinoma cell lines showed more invasive characteristics; the lung adenocarcinoma cells remained cohesive (Figs. 1B and 2C), but the brain parenchyma adjacent to the mammary carcinoma contained scattered round single tumor cells (Figs. 1C and 2D).

We determined the vessel density inside and within a 200-μm distance from the periphery of the tumors (Table 3).

TABLE 3. Morphometric Analysis of Peritumoral and Intratumoral Vessels in Brain Tissue

	Tumor Lines										
	Normal Cortex		C38		HT25		H1650		ZR75		HT1080
No. animals used	4		6		4		4		4		5
Tumor size, mm ²			6 ± 3.4		2 ± 1.4		2.7 ± 1.1		2.3 ± 0.4		3.1 ± 2.1
Tumor diameter, mm (calculated)			2.6 ± 0.7		1.5 ± 0.6		1.8 ± 0.4		1.7 ± 0.2		1.9 ± 0.7
Vessel density, n/mm ²	348 ± 18	Peri	306 ± 30*	Intra	322 ± 87*	Peri	349 ± 44*	Intra	314 ± 52*	Peri	310 ± 55*
Vessel size, μm	9.9 ± 03	Peri	9.4 ± 0.7*	Intra	9.1 ± 0.7*	Peri	9.4 ± 0.1*	Intra	10.3 ± 1.7*	Peri	10.0 ± 0.7*
Labeling index, %		Peri	2.2 ± 0.5	Intra	2.2 ± 1.3	Peri	0.3 ± 0.2	Intra	1.8 ± 0.5	Peri	1.0 ± 0.5
Branching points		Peri	0.4 ± 0.27	Intra	0.34 ± 0.17	Peri	1.28 ± 0.73	Intra	0.9 ± 0.5	Peri	4.1 ± 1.78‡

Values are mean ± SD.

*No significant difference from normal cortex.

†Significant difference between peritumoral and intratumoral values.

‡Significant difference in branching points between the HT1080 and the other tumors.

In touch indicates vessels in contact with the surface of the tumor; intra, intratumoral vessels; peri, vessels within 200 μm distance from the surface of the metastatic nodule.

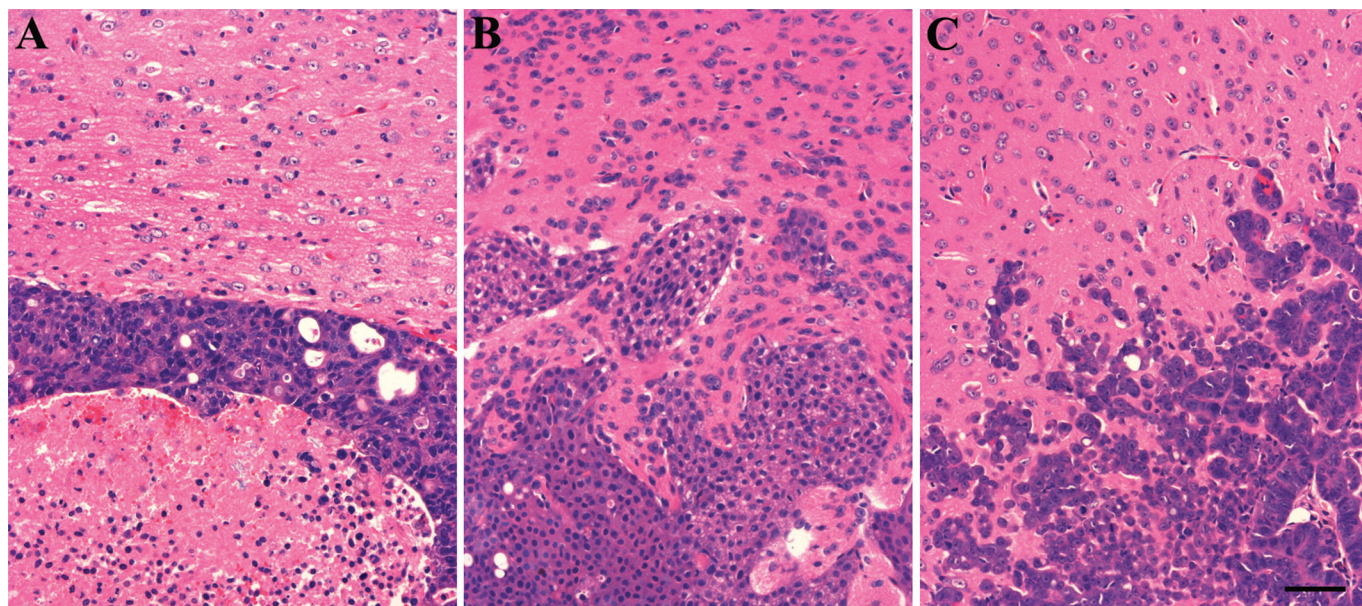


FIGURE 1. Hematoxylin and eosin–stained sections of representative tumors showing invasive growth patterns. **(A)** The pushing-type HT25 colon carcinoma has a smooth surface. **(B)** Cohesive cell islands of the H1650 lung carcinoma extend into the brain parenchyma. **(C)** Scattered single cells and small tumor nests infiltrate at the border of the ZR75 breast carcinoma. Scale bar = 50 μm (**A–C**).

All tumors had decreased vessel density compared with surrounding brain parenchyma. In addition, there was no significant change in the vessel density around the tumors compared with control animals and no sprouting vessels were observed. Moreover, although vessel dilatation is characteristic of mother vessel formation preceding sprouting angiogenesis (6), this phenomenon was not observable in the peritumoral brain parenchyma (Table 3 and Fig. 2). An exception was the C38 murine colon carcinoma where the vessels in touch with the surface of the tumor were considerably dilated compared with control vessels (Table 3 and Figs. 2A, F). The diameters of intratumoral vessels were significantly increased in all tumors compared with the vessels in the surrounding parenchyma, but this can be considered biologically significant only in the 2 colon carcinomas. Supporting this theory, the LIs of the vascular cells (ECs cells and pericytes) were considerably increased only within the pushing growth type tumors. In the 2 more invasive tumors (ZR75 and H1650), the LI of the vascular cells within the tumor remained at a moderate low level. Characteristically, the proliferation rate of the peritumoral vascular cells was negligibly low in the case of all tumor types (Table 3).

In the HT 1080 tumor (which also showed a pushing-type growth pattern), a high vascular cell proliferation rate was not accompanied by marked dilatation of the vessels. This can be explained by our observation that, in this tumor, a process reminiscent of intussusceptive angiogenesis takes place (Fig. 3A). Transluminal pillars (hallmarks of this type of angiogenesis [7]) inserting into the vessels contained no collagen bundles; instead, they were filled with tumor cells (Fig. 3B). In accordance with the intussusceptive angiogenesis-like process taking place in the HT1080 tumor, the number

of vessel ramifications (branching points) was significantly higher than in the other tumors (Table 3).

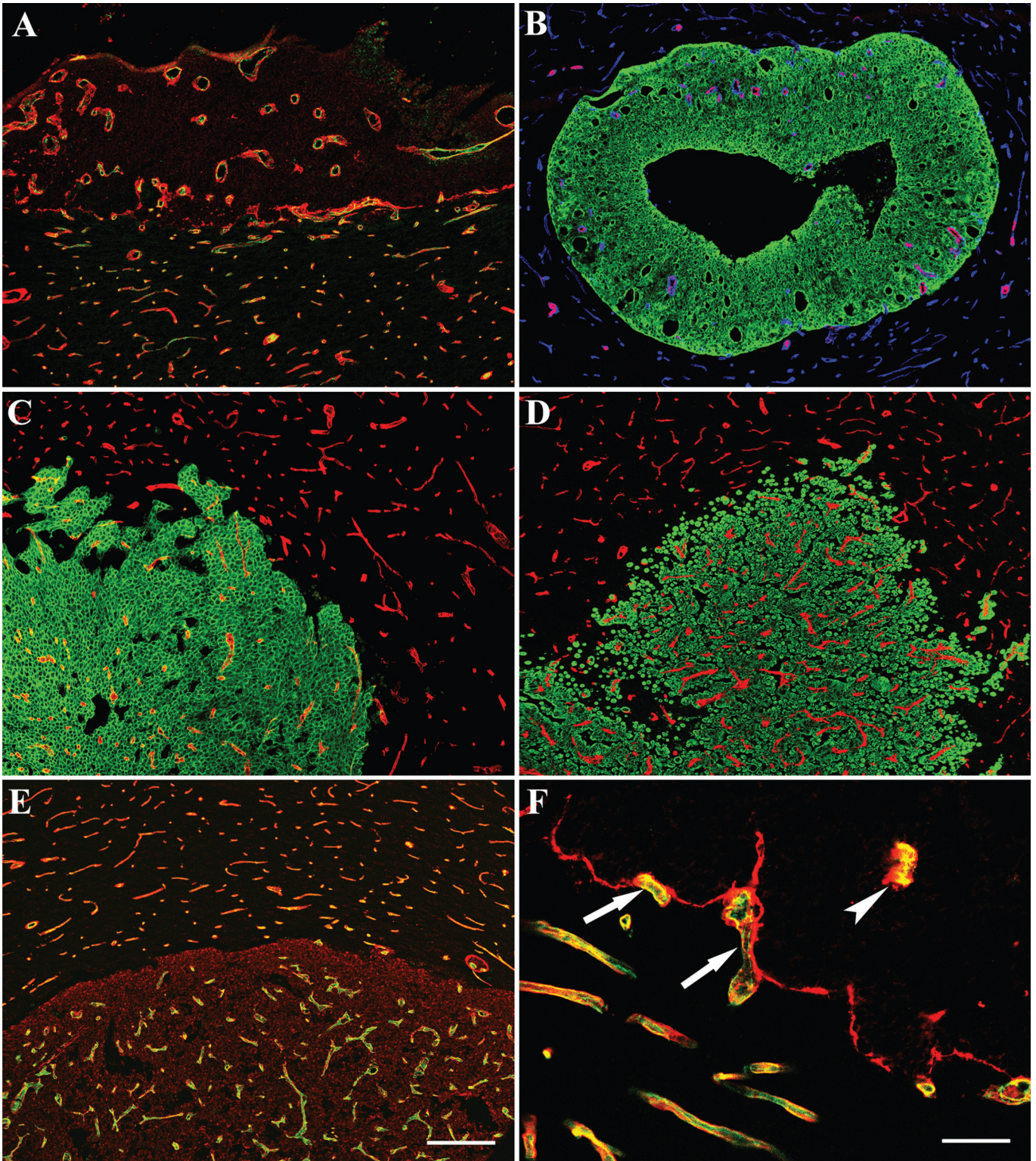
In connection with the proliferation activity (LI) of the intratumoral and peritumoral vascular elements, we analyzed VEGF, PDGF- β , and Ang-1 expressions by quantitative real-time RT-PCR in the 5 tumor cell lines and in microdissected intratumoral areas of their brain metastases (Fig. 4). Messenger RNA (mRNA) expression levels of these angiogenic factors in the cell lines and in the tumor samples correlated well (Figs. 4A, B). Interestingly, the C38 murine colon carcinoma and the HT1080 fibrosarcoma lines (i.e. those with the two highest intratumoral vascular cell LI) showed the lowest intratumoral angiogenic factor levels. Microdissected intratumoral HT25 samples showed the highest VEGF and Ang-1 mRNA expression levels (Fig. 4B). With respect to PDGF- β , examination of microdissected intratumoral areas revealed that brain metastases of the ZR75 cell line exhibited the highest mRNA expression of this angiogenic factor (Fig. 4B).

The expressions of VEGFR-2 (VEGF receptor 2), PDGFR- β (PDGF receptor β), and Tie-2 (an angiopoietin receptor involved in blood vessel remodeling and stabilization) were also determined in microdissected intratumoral and peritumoral areas of brain metastases. Messenger RNA expression of these receptors was always higher in the tumor areas than in the peritumoral brain tissue (Fig. 5). To investigate the potential role of the key angiogenic molecule VEGF in the growth of experimental cerebral metastases further, we carried out Western blot analysis of the 5 cell lines. Although quantitative RT-PCR analysis showed large differences in VEGF expression levels among the cell lines (Fig. 4A), only small variations were observed in protein expression levels (Fig. 4C). Neither the intratumoral angiogenic factor mRNA

levels (VEGF, PDGF- β , and Ang-1) nor the intratumoral mRNA expression of their receptors (VEGFR-2, PDGFR- β , and Tie-2) correlated with the proliferation rate (i.e. LI) of the intratumoral vascular cells. Furthermore, there was no sig-

nificant correlation between VEGF protein levels and the LI of intratumoral blood vessels.

In the pushing-type tumor growth pattern, the brain parenchyma was displaced and the vessels incorporated into the



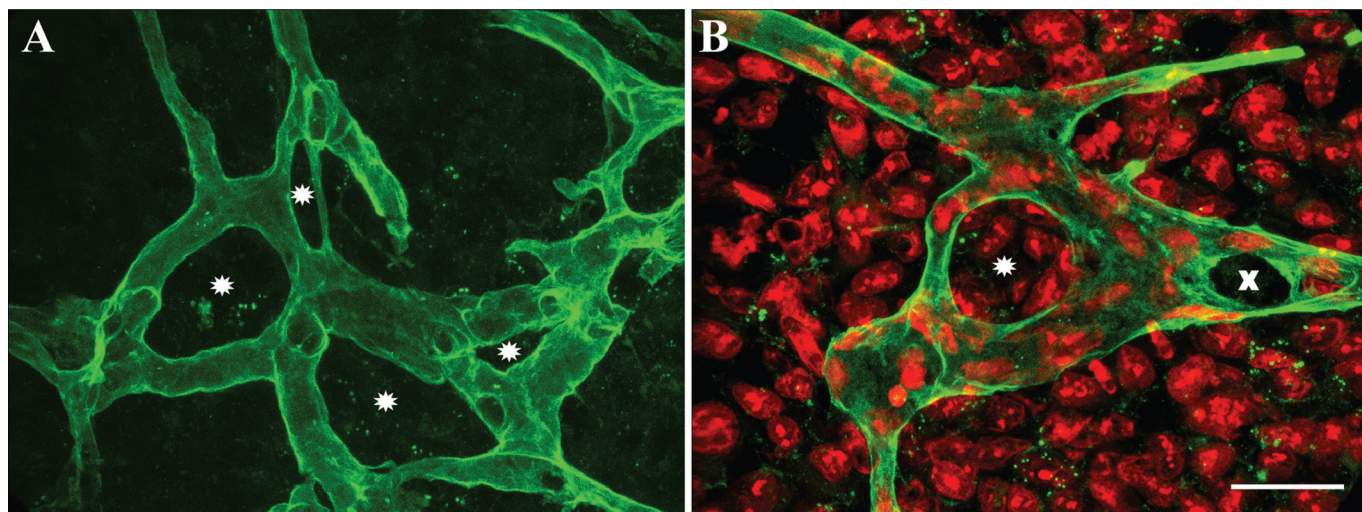


FIGURE 3. (A) Structure of intratumoral vessels of the HT1080 fibrosarcoma. The section is stained for laminin. Horizontal view of 32 optical sections. Numerous loops (intraluminal pillars) (asterisks) were formed during the intussusceptive angiogenesis-like process. (B) Vessel loop within the HT1080 tumor. The section is stained for laminin and by propidium iodide to highlight the cell nuclei. Numerous tumor nuclei are visible in the intraluminal pillar. The black hole labeled “X” is not a pillar; it represents the lumen of a vessel originating from this area. Scale bar = 25 μm (A, B).

tumors (Figs. 2A, B, F). Astrocytes were detached from the vessels in all tumor types but, with the exception of the ZR75 mammary carcinoma (Figs. 6A–D), only small numbers of these cells were incorporated into the tumors. In contrast, desmin-positive pericytes covered by basement membrane remained attached to the vessels and became incorporated (Figs. 6B, D). The intratumoral vessels showed remarkable changes. For example, their pericytes started to express smooth muscle actin (SMA) (Figs. 6E, F), but collagen I-containing extracellular matrix material around the intratumoral vessel was not deposited in any of the tumors (data not shown). In the C38 colon carcinoma tumors, even vessels just touching the periphery of the tumor were covered with SMA-positive pericytes. Human tumor cells were attached to the basement membrane of the vessels and deposited their own basement membrane on the

surface of the vascular basement membrane (Fig. 7A). This newly synthesized basement membrane contained laminin 5; the tumor cells attached it using the α_3 -integrin (Figs. 7B, C). The consequence of this attachment process was most intriguing in the mammary carcinoma cell line. Scattered, round tumor cells in the parenchyma eventually became invasive, detached the astrocytes from the basal surface of the capillaries, and came into contact with the basement membrane. This close proximity apparently induced these tumor cells to differentiate, that is, they became polarized with claudin 3 and EMA expression at their apical and α_3 -integrin at their basal surface (Figs. 7D–H).

As a control, we also analyzed the effects on vessel density, size, vascular cell proliferation, and extracellular matrix deposition from day 1 to day 21 after needle wounding

FIGURE 2. Overview of brain metastases of tumors of different origin. Similar micrographs were used to determine the morphometric parameters of the peritumoral and intratumoral vessels. Note the normal appearance and distribution of the peritumoral vessels. (A) C38 colon carcinoma 7 days after inoculation. The section is stained for CD31 (green) and laminin (red). The tumor (upper part of the micrograph) contains dilated vessels. (B) HT25 colon carcinoma 28 days after tumor inoculation. The section is stained for pan-cytokeratin (green), smooth muscle actin (SMA; red), and laminin (blue). Anti-human pan-cytokeratin highlights the smooth surface of the tumor, which is characteristic feature of the pushing type of tumor growth. The intratumoral vessels are moderately dilated and are frequently stained positively for SMA. (C) H1650 lung carcinoma 28 days after tumor inoculation. The section is stained for α_3 -integrin (green) and laminin (red). The anti-human integrin staining highlights the tumor. The border of the tumor shows invading tumor cell groups that remain cohesive and are in contact with the main body of the tumor. The vessel density is lower within the tumor than in the surrounding parenchyma but the vessels are not noticeably dilated. (D) ZR75 mammary carcinoma 21 days after tumor inoculation. The section is stained for pan-cytokeratin (green) and laminin (red). Anti-human pan-cytokeratin staining highlights the tumor. Note the compact structure of the tumor in the center and the scattered single tumor cells in the parenchyma at the periphery of the tumor. Vessels inside the tumor are not markedly dilated. (E) HT1080 fibrosarcoma 8 days after tumor inoculation. The section is stained for CD31 (green) and laminin (red). Laminin synthesized by the tumor cells highlights the tumor. As in the case of HT25 colon carcinoma, the smooth tumor-parenchyma interface indicates a pushing-like growth pattern. Note the numerous branching of the vessels within the tumor. (F) High-power micrograph of the periphery of the C38 colon carcinoma stained for CD31 (green) and laminin (red). Laminin is localized at the tumor (upper right part of the picture)–parenchyma interface. The tumor “flows” around the vessels (arrows), thereby incorporating them into the tumor. Arrowhead indicates an incorporated vessel. Scale bars = 200 μm (A–E); 50 μm (F).

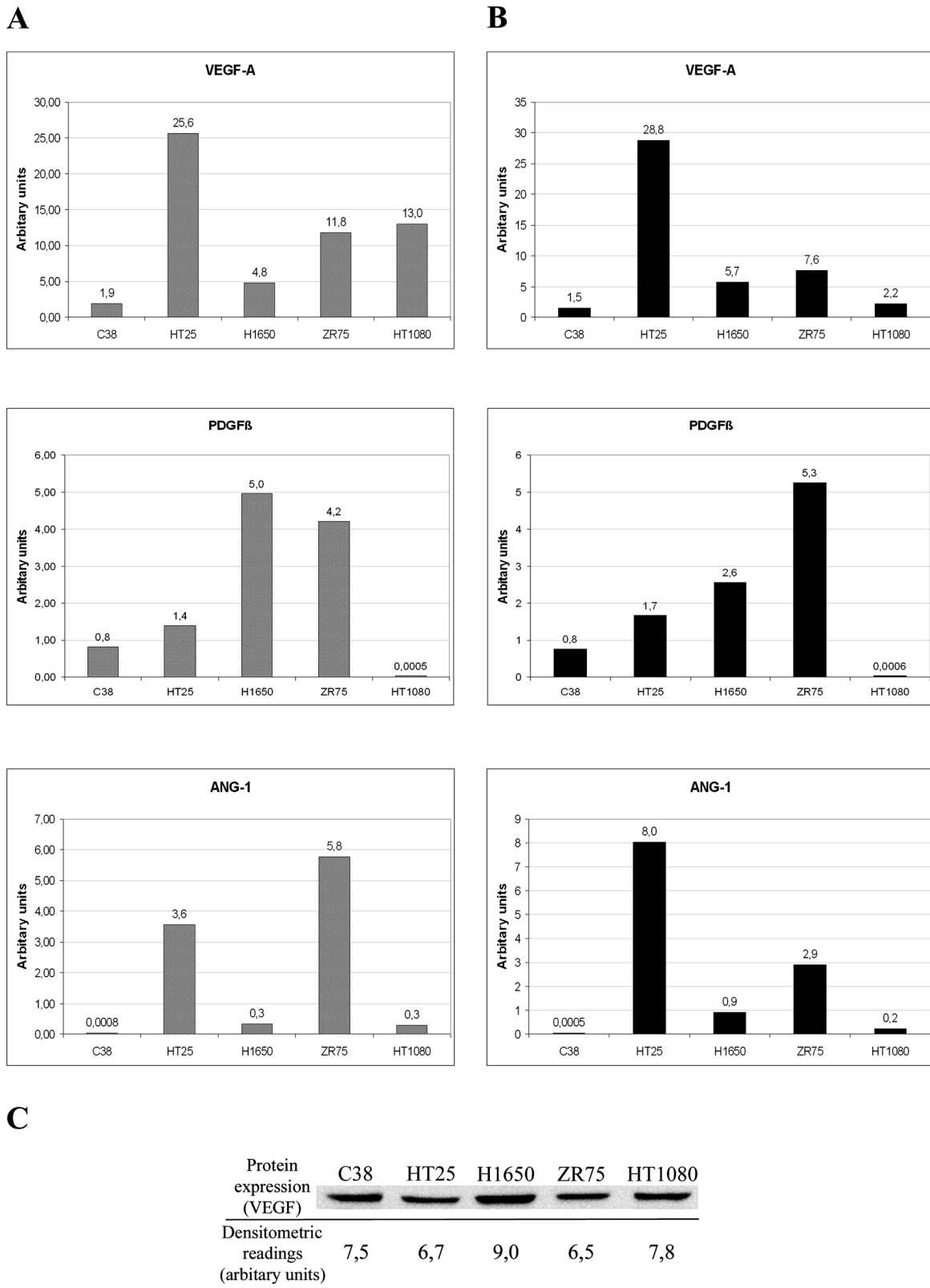


FIGURE 4. (A) Analysis of vascular endothelial growth factor (VEGF), platelet-derived growth factor-β (PDGF-β), and angiopoietin-1 (Ang-1) expression in cultured tumor cell lines by quantitative RT-PCR. **(B)** Analysis of VEGF, PDGF-β, and Ang-1 expressions in micro-dissected intratumoral samples by quantitative RT-PCR. **(C)** Analysis of VEGF expression in cultured tumor cell lines by Western blot.

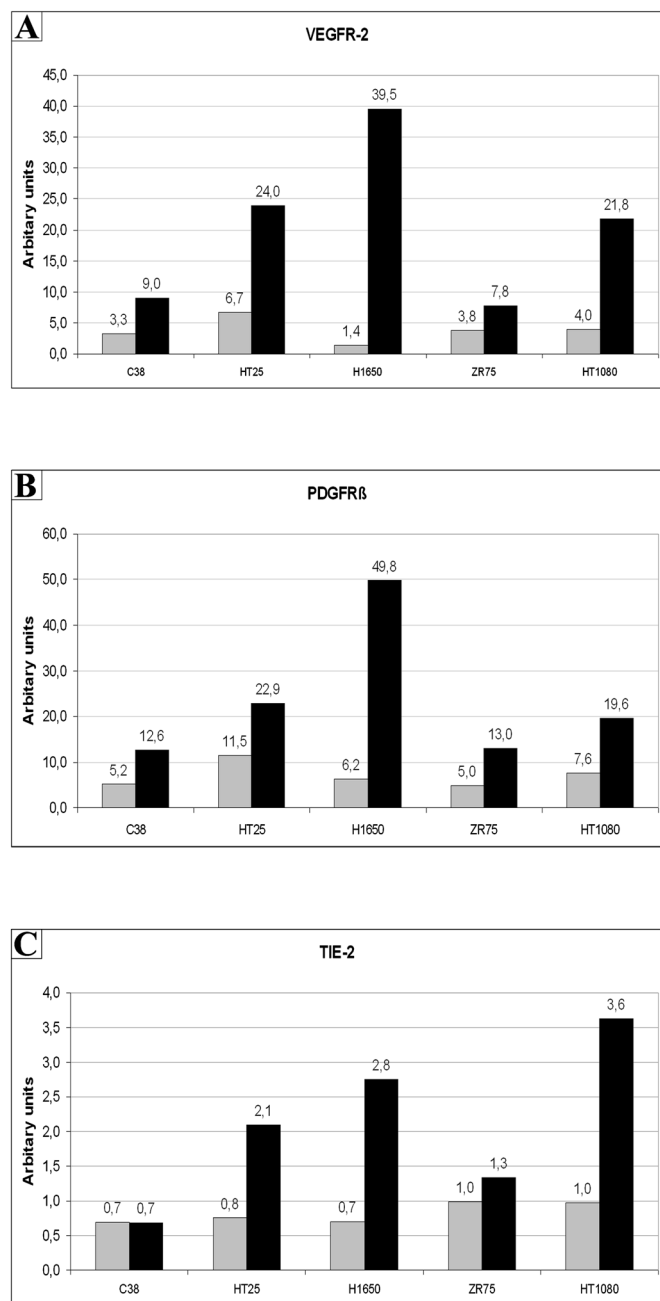


FIGURE 5. Comparison of vascular endothelial growth factor receptor-2 (VEGFR-2) (A), platelet-derived growth factor-β (PDGF-β) (B), and Tie-2 (C) expression in microdissected peritumoral brain (a 200-μm-wide band of brain tissue immediately adjacent to the surface of the metastatic nodule; gray columns) to those of microdissected intratumoral samples (black columns).

(Figs. 8A, B). We did not detect an increase in vessel density inside or around the wound at any time point. In contrast, vessel numbers were significantly lower up to day 9, and the vessel diameters did not change. Proliferating vascular cells were detected between days 2 and 5, with a peak at day 3, but the LI remained negligibly low (Fig. 8B). No deposition of

collagenous extracellular matrix material within or around the wound could be detected up to day 21 after wounding.

DISCUSSION

It is widely believed that under pathologic conditions angiogenesis (sprouting) occurs in the brain. Increased vessel density compared with the normal brain was observed in brain tumors or metastases and after medial cerebral artery occlusion or needle wounding (1, 15–20). In contrast, others have reported decreased vascular density within metastases (21, 22) and that tumors in the brain can grow by vessel co-option without inducing sprouting angiogenesis (11, 12). These authors found that antiangiogenic therapy for experimental brain metastases can trigger alternative vascularization mechanisms (e.g. vessel co-option) and thus might promote increased metastatic potential (11, 12). Similarly, proinvasive effects of antiangiogenic drugs have been observed in a number of preclinical glioblastoma studies (23–25). Thus, primary and metastatic brain tumors targeted with angiogenesis inhibitors may evade their incapability to stimulate new vessel growth by becoming more invasive and/or switching to vessel co-option. Although magnetic resonance imaging (26, 27) and autopsy tissue (28) findings in glioblastoma patients have also suggested increased invasion as a mode of escape from antiangiogenic therapy, there are only limited clinical data to support the existence of such an adaptive mechanism in secondary brain tumors. However, antiangiogenic drugs have not been systematically investigated in cerebral metastases, mainly owing to concerns about the potential bleeding adverse effects. Nevertheless, human trials have been launched to study the clinical effects of these drugs in metastatic brain tumors (29).

On the basis of the results of the present study, we conclude that in the experimental system used no sprouting and intussusceptive angiogenesis takes place in the brain parenchyma during tumor growth; this was also observed after needle wounding. The tumors acquired their vasculature merely by incorporation of preexisting host vessels. Sprouting and intussusceptive angiogenesis are always accompanied by an increase in vessel density compared with the normal tissue (5, 6), but we did not observe this in the peritumoral brain parenchyma in which there was only a very low level of vascular cell proliferation that corresponded with a lack of capillary sprouting. The drop in vessel density within the tumor compared with the peritumoral tissue supports earlier observations that tumors grow into the peritumoral vessel network and thereby dilute it (30, 31). We previously made a similar observation in cases of human and experimental primary melanomas in which robust sprouting angiogenesis was observed in the peritumoral connective tissue but which ceased completely as the vessels became incorporated into the tumor tissue that lacked connective tissue (31).

The lack of sprouting and intussusceptive angiogenesis is most probably due to the absence of connective tissue matrix in the brain parenchyma and within the tumors themselves. Collagen III was detected in a series of autopsy cases in brain metastases of differentiated human tumors (32), whereas in the present experimental paradigm, there was a lack of connective tissue. This discrepancy may be due to the

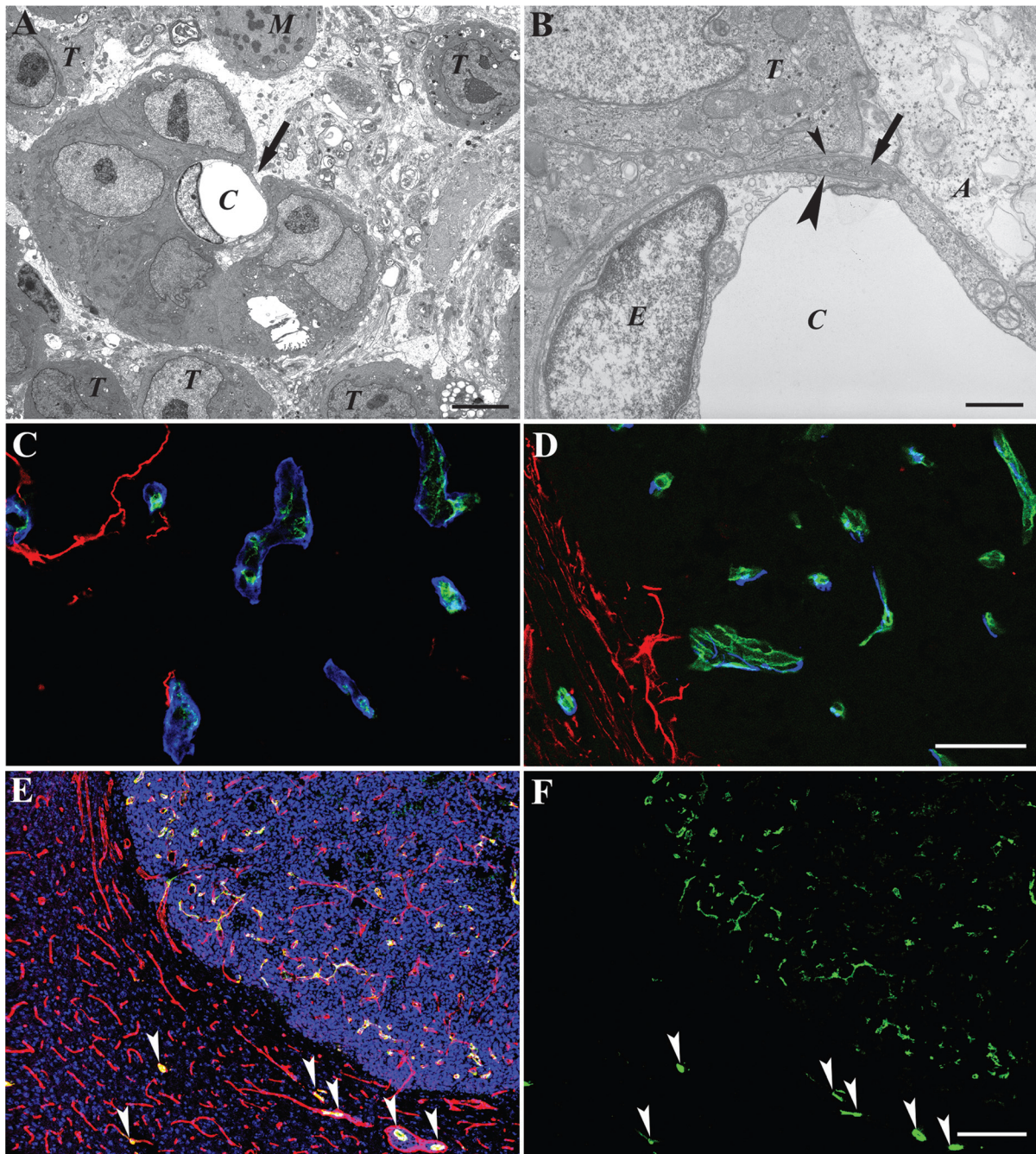


FIGURE 6. (A) ZR75 tumor cells are attached to a brain capillary (C) but the capillary is not yet completely covered by tumor cells. The tumor cells are also tightly adhered to each other. Astrocyte foot processes still cover a small area (arrow). In contrast, in the brain parenchyma, single tumor cells (T) are dispersed. One of these tumor cells is in mitosis (M). (B) Higher magnification of the capillary shown in A in a different sectioning plane. The tumor cell (T) is adhered directly to the basement membrane of the capillary (C), similarly to the remaining astrocytes (A). The pericyte (arrow) keeps its original position between its own (small arrowhead) and the capillary (large arrowhead) basement membrane. E indicates endothelial cell; T, tumor cell. (C) Intratumoral area of the H1650 lung carcinoma. The section is stained for CD31 (green), glial fibrillary acidic protein (GFAP, red), and laminin (blue). The incorporated vessels are completely covered by basement membrane; GFAP-positive cells are rarely incorporated by the tumor. (D) Section of a HT1080 brain metastasis stained for CD31 (green), GFAP (red), and desmin (blue). The incorporated vessels are positive for the pericyte marker desmin. GFAP-positive cells are present only at the surface of the metastasis. (E, F) Section of a HT1080 brain metastasis stained for smooth muscle actin (SMA) (green), laminin (red), and TOTO3 (blue). E corresponds to the merged picture of the red, green, and blue channels. F shows the SMA staining. TOTO3 staining highlights tumor nuclei. In the brain parenchyma, only arterioles are positive for SMA (arrowheads). In contrast, most of the intratumoral vessels are positive for SMA; there is particularly strong staining at the periphery of the metastasis. Scale bars = 5 μ m (A); 1 μ m (B).

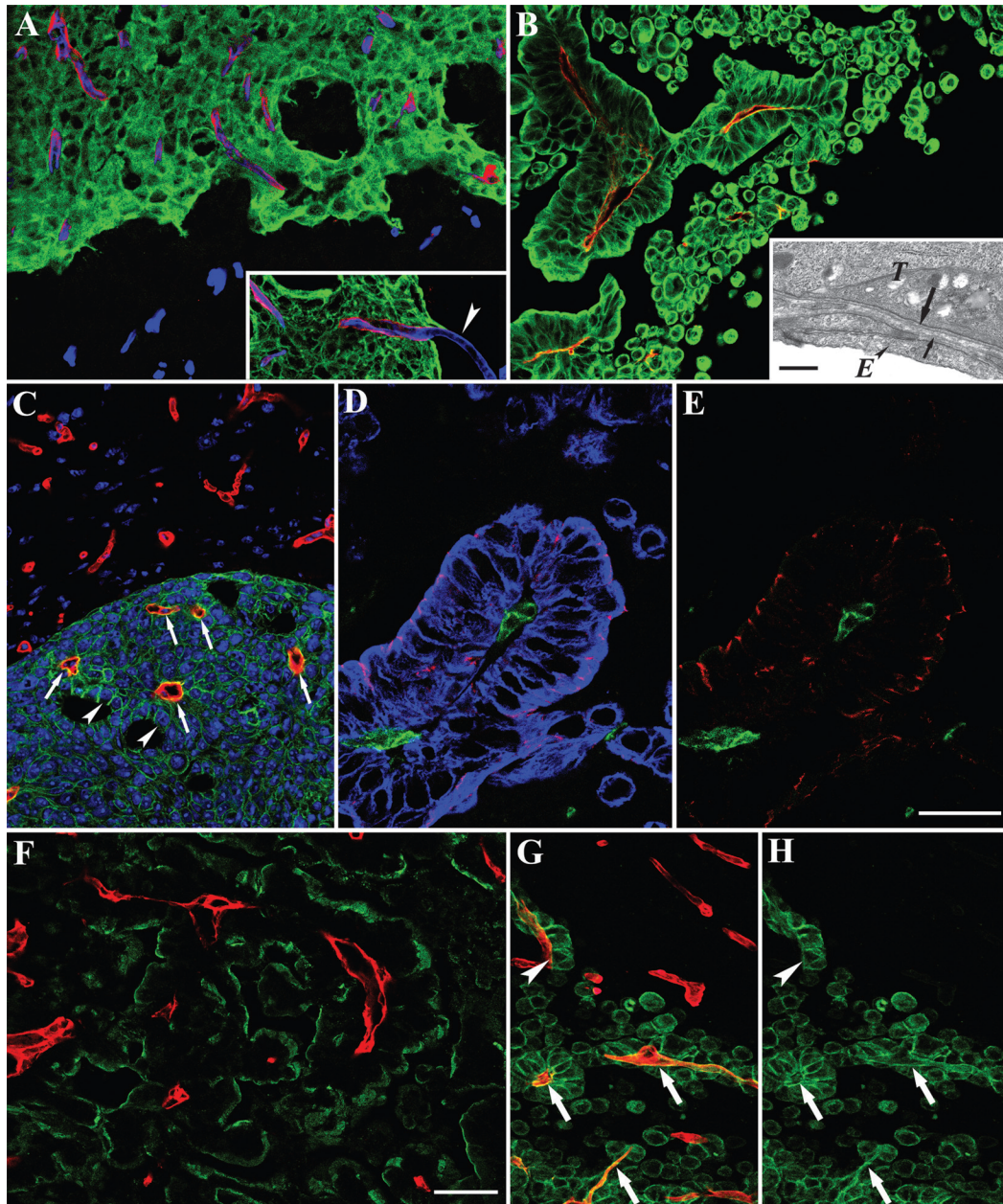


FIGURE 7. (A) Sections of H1650 and HT25 (inset) tumors stained for monoclonal anti-human laminin (red) and polyclonal anti-laminin (blue); the latter reacts with both human and mouse laminin. The tumors are highlighted by anti-human pan-cytokeratin (green). Note that human laminin is deposited on the surface of the vascular basement membrane. Inset shows a vessel that is incorporated partially into the tumor (arrowhead). Human laminin is deposited exactly as far as the tumor extends along the capillary. (B) ZR75 tumor stained for laminin 5 (red). The tumor is highlighted by anti-human pan-cytokeratin (green). Laminin 5 is deposited inside the tumor on the basal side (which corresponds to the surface of the incorporated vessels) of the polarized tumor cell nests. Inset shows that a separate basement membrane (large arrow) of the tumor (T) is deposited in the close vicinity of the vascular basement membrane (small arrow). E indicates endothelial cell. (C) HT25 tumor stained for α_3 -integrin (green) and laminin (red). Nuclei are stained by TOTO3 (blue). Yellow color indicates colocalization of the integrin and laminin at the outer surface of the vessels (arrows). The integrin is also present at the lateral but not at the apical surface (arrowheads) of the tumor cells. (D, E) ZR75 mammary carcinoma stained for CD31 (green), claudin3 (red), and pan-cytokeratin (blue). D shows the triple labeled tissue; E shows the green and the red signal. Claudin is expressed on the apical surface of the tumor cells, which show a differentiated pattern organized around the vessel. (F) ZR75 tumor stained for epithelial membrane antigen (EMA, green) and laminin (red). EMA is expressed on the apical surface of the tumor cells, which is organized in a differentiated fashion around the basement membrane of the vessels. (G, H) ZR75 tumor stained for α_3 -integrin (green) and laminin (red). G shows the double labeling; H shows the localization of the integrin. Note that the green signal outlines the outer surface of the vessels (arrows). Arrowhead points at a vessel that is only partially populated by tumor cells. Scale bars = 50 μ m (A–C, F–H); 25 μ m (D, E); 1 μ m (B, inset).

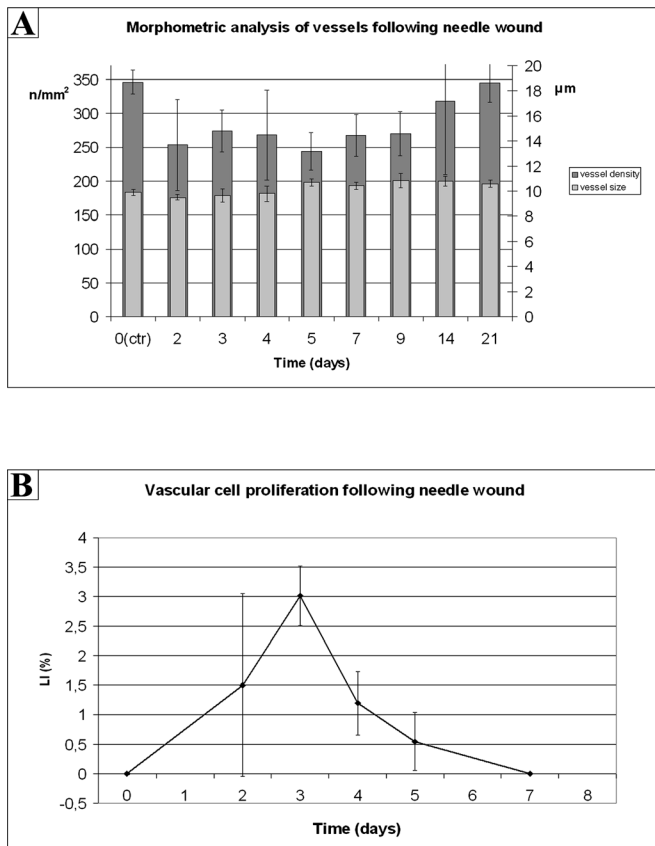


FIGURE 8. (A, B) Morphometric parameters of vessels **(A)** and proliferation rate of vascular cells **(B)** after needle wounding. There was a significant difference ($p < 0.05$) between vessel density of control brain parenchyma (ctr) and vessel density around the wounds at days 2, 3, 4, 5, 7, and 9. LI indicates labeling index.

longer existence of metastases in the human brain that might allow the tumor to contact sites where collagen-producing cells are located (e.g. the leptomeninges). Another explanation could be the differentiation of pericytes into collagen-producing cells by detachment and migration away from the vessels (33). In the present study, there was no suggestion that this transdifferentiation occurred; pericytes were consistently localized near the vessels and were covered by intact basement membrane to which the tumor cells attached. In contrast, in pushing-type metastases of the C38 tumor in the liver, collagen I-containing connective tissue was always situated between the vessel and the tumor; extracellular matrix-producing and SMA-expressing cells appeared very early at the surface of the growing tumor nodule and became incorporated into the tumor together with the vessels formed by the fusion of sinusoids (13). Such cells were not observed in the brain metastases or around needle wounds in the present study.

There was a correlation between the growth pattern and the vascular structure of the tumors. The 2 epithelial tumors with pushing growth characteristics (C38 and HT25) incorporated fewer vessels that were more dilated compared with those within the 2 more invasive tumors. Together with the finding that the proliferation of vascular cells was increased

within these tumors, this suggests that the newly formed ECs provide a source for capillary dilatation instead of participating in new vessel formation.

Vascular cell proliferation rates did not correlate with VEGF, PDGF- β , or Ang-1 mRNA expression of the tumor cell lines, either in vitro or in the microdissected tumor samples. Similarly, there was no obvious association between in vitro VEGF protein expression of the cell lines and proliferation rates of vascular cells within the metastases. However, we found an increase in the mRNA levels of their receptors as we moved from peritumoral brain tissue toward intratumoral areas, regardless of tumor type in laser-capture microdissection samples. This might be connected either to an increase in intratumoral vascular cell proliferation or to the capillary-stabilizing effects of PDGF- β or Ang-1 (34). Nevertheless, the intratumoral vascular cells themselves could produce both PDGF- β and Ang-1 (35).

The data suggest that the low level of vessel incorporation in the 2 epithelial tumors with pushing growth characteristics was compensated for by an increased surface area of the intratumoral vessels and, vice versa, the high rate of vessel incorporation made the increase of individual vessel surface unnecessary in the H1650 and ZR75 tumors. On the other hand, the HT1080 tumor showed enhanced proliferation of vascular cells without an increase in vessel diameters. This might be explained by the observed intussusceptive angiogenesis-like process within this tumor. A similar process was observed during in vivo microscopy in human gliomas (36, 37). Collagen-containing pillars within the vessel lumen are the hallmarks of intussusceptive angiogenesis and the “normal” mode of this angiogenesis type requires the presence of collagen bundles or cells that are able to synthesize collagen (7). Although the mechanism of the formation of these pillars is debated, the mechanism observed here is different because this process is dependent on the activities of the tumor cells. Within the growing tumor, forces that can press the opposite sides of the vessels inward may be generated, leading to the contact of the luminal surfaces of ECs to each other. This can be followed by the reorganization of the inter-EC junctions and, subsequently, the formation of a pore in the vessel wall, as described by Burri et al (7). The pore increases in size as it is immediately filled by invading tumor cells. This process is another example (along with the formation of glomeruloid bodies owing to the pulling force exerted by tumor cells attached to the basal membrane of the brain capillaries [9]) of how tumor cells can reorganize the vessel structure of the brain. In this respect, this process cannot be termed *true* angiogenesis because it is dependent on the invasive capacity of the tumor cells.

In the brain parenchyma, the lack of connective tissue (and of cells which are able to produce it) leaves the tumor cells with only one extracellular matrix element to attach to, that is, the vascular basement membrane. This attachment results in a mechanical insult of the vessel (which can lead to the development of glomeruloid bodies [9]). In response to this impulse, pericytes of the incorporated vessels start to express the contractile cytoskeletal element SMA. According to the observed SMA expression patterns, this mechanical effect seems to be the highest at the tumor periphery, including the

vessel incorporation zone. The basement membrane also promotes the survival, growth of tumor, and differentiation of tumor cells in the brain (38, 39). Indeed, we observed that breast cancer cells “floating” in the brain parenchyma showed undifferentiated morphology, but on attachment to the vascular basement membrane, they formed differentiated papillary structures with claudin 3 and EMA expression at the apical surface and laminin 5 and α_3 -integrin expression at the basal surface.

In summary, the distinct structure and composition of the brain parenchyma (a lack of connective tissue collagen-producing cells) apparently prevents sprouting and intussusception so that brain metastases acquire their vasculature exclusively by vessel incorporation in the mouse brain. This phenomenon may also be valid for small metastases in the human brain. Although a small therapeutic window would remain open in the case of tumors with high intratumoral vascular cell proliferation activity, confirmatory human results would prompt the need to rethink the use of antiangiogenic agents under these conditions.

REFERENCES

- Folkman J. What is evidence that tumors are angiogenesis dependent? *J Natl Cancer Inst* 1990;82:4–6
- Jain RK, di Tomaso E, Duda DG, et al. Angiogenesis in brain tumors. *Nat Rev Neurosci* 2007;8:611–22
- Fidler IJ, Yano S, Zhang R, et al. The seed and soil hypothesis: Vascularization and brain metastases. *Lancet Oncol* 2002;3:53–57
- Holash J, Maisonpierre PC, Compton D, et al. Vessel cooption, regression, and growth in tumors mediated by angiopoietins and VEGF. *Science* 1999;284:1994–98
- Dome B, Hendrix MJ, Paku S, et al. Alternative vascularization mechanisms in cancer: Pathology and therapeutic implications. *Am J Pathol* 2007;170:1–15
- Paku S, Paweletz N. First steps of tumor-related angiogenesis. *Lab Invest* 1991;65:334–46
- Burri PH, Hlushchuk R, Djonov V. Intussusceptive angiogenesis: Its emergence, its characteristics, and its significance. *Dev Dyn* 2004;231:474–88
- Paku S, Dezso K, Bugyk E, et al. A new mechanism for pillar formation during tumor-induced intussusceptive angiogenesis: Inverse sprouting. *Am J Pathol* 2011;179:1573–85
- Dome B, Timar J, Paku S. A novel concept of glomeruloid body formation in experimental cerebral metastases. *J Neuropathol Exp Neurol* 2003;62:655–61
- Stiver SI, Tan X, Brown LF, et al. VEGF-A angiogenesis induces a stable neovasculature in adult murine brain. *J Neuropathol Exp Neurol* 2004;63:841–55
- Küstters B, Leenders WP, Wesseling P, et al. Vascular endothelial growth factor-A(165) induces progression of melanoma brain metastases without induction of sprouting angiogenesis. *Cancer Res* 2002;62:341–45
- Leenders WP, Küstters B, Verrijp K, et al. Antiangiogenic therapy of cerebral melanoma metastases results in sustained tumor progression via vessel co-option. *Clin Cancer Res* 2004;10:6222–30
- Paku S, Kopper L, Nagy P. Development of the vasculature in “pushing-type” liver metastases of an experimental colorectal cancer. *Int J Cancer* 2005;115:893–902
- Vermeulen PB, Colpaert C, Salgado R, et al. Liver metastases from colorectal adenocarcinomas grow in three patterns with different angiogenesis and desmoplasia. *J Pathol* 2001;195:336–42
- Machein MR, Knedla A, Knoth R, et al. Angiopoietin-1 promotes tumor angiogenesis in a rat glioma model. *Am J Pathol* 2004;165:1557–70
- Kim LS, Huang S, Lu W, et al. Vascular endothelial growth factor expression promotes the growth of breast cancer brain metastases in nude mice. *Clin Exp Metastasis* 2004;21:107–18
- Krupinski J, Kaluza J, Kumar P, et al. Role of angiogenesis in patients with cerebral ischemic stroke. *Stroke* 1994;25:1794–98
- Sun Y, Jin K, Xie L, et al. VEGF-induced neuroprotection, neurogenesis, and angiogenesis after focal cerebral ischemia. *J Clin Invest* 2003;111:1843–51
- Yu SW, Friedman B, Cheng Q, et al. Stroke-evoked angiogenesis results in a transient population of microvessels. *J Cereb Blood Flow Metab* 2007;27:755–63
- Salhia B, Angelov L, Roncari L, et al. Expression of vascular endothelial growth factor by reactive astrocytes and associated neoangiogenesis. *Brain Res* 2000;883:87–97
- Schlageter KE, Molnar P, Lapin GD, et al. Microvessel organization and structure in experimental brain tumors: Microvessel populations with distinctive structural and functional properties. *Microvasc Res* 1999;58:312–28
- Sakariassen PØ, Prestegarden L, Wang J, et al. Angiogenesis-independent tumor growth mediated by stem-like cancer cells. *Proc Natl Acad Sci U S A* 2006;103:16466–71
- Rubenstein JL, Kim J, Ozawa T, et al. Anti-VEGF antibody treatment of glioblastoma prolongs survival but results in increased vascular cooption. *Neoplasia* 2000;2:306–14
- Kunkel P, Ulbricht U, Bohlen P, et al. Inhibition of glioma angiogenesis and growth in vivo by systemic treatment with a monoclonal antibody against vascular endothelial growth factor receptor-2. *Cancer Res* 2001;61:6624–28
- Du R, Lu KV, Petritsch C, et al. HIF1alpha induces the recruitment of bone marrow-derived vascular modulatory cells to regulate tumor angiogenesis and invasion. *Cancer Cell* 2008;13:206–20
- de Groot JF, Fuller G, Kumar AJ, et al. Tumor invasion after treatment of glioblastoma with bevacizumab: Radiographic and pathologic correlation in humans and mice. *Neuro Oncol* 2010;12:233–42
- Gerstner ER, Chen PJ, Wen PY, et al. Infiltrative patterns of glioblastoma spread detected via diffusion MRI after treatment with cediranib. *Neuro Oncol* 2010;12:466–72
- di Tomaso E, Snuderl M, Kamoun WS, et al. Glioblastoma recurrence after cediranib therapy in patients: Lack of “rebound” revascularization as mode of escape. *Cancer Res* 2011;71:19–28
- Eichler AF, Chung E, Kodack DP, et al. The biology of brain metastases—translation to new therapies. *Nat Rev Clin Oncol* 2011;8:344–56
- Thompson WD, Shiach KJ, Fraser RA, et al. Tumours acquire their vasculature by vessel incorporation, not vessel ingrowth. *J Pathol* 1987;151:323–32
- Dome B, Paku S, Somlai B, et al. Vascularization of cutaneous melanoma involves vessel co-option and has clinical significance. *J Pathol* 2002;197:355–62
- Nakanishi H, Hosoda S, Takahashi Y, et al. Alteration of tumour cell arrangement related to connective tissue stroma in metastatic brain tumours. Histological and immunohistochemical studies of 68 autopsy cases. *Virchows Arch A Pathol Anat Histopathol* 1989;414:485–95
- Sundberg C, Ivarsson M, Gerdin B, et al. Pericytes as collagen-producing cells in excessive dermal scarring. *Lab Invest* 1996;74:452–66
- Armulik A, Abramsson A, Betsholtz C. Endothelial/pericyte interactions. *Circ Res* 2005;97:512–23
- Wakui S, Yokoo K, Muto T, et al. Localization of Ang-1, -2, Tie-2, and VEGF expression at endothelial-pericyte interdigitation in rat angiogenesis. *Lab Invest* 2006;86:1172–84
- Winkler F, Kienast Y, Fuhrmann M, et al. Imaging glioma cell invasion in vivo reveals mechanisms of dissemination and peritumoral angiogenesis. *Glia* 2009;57:1306–15
- Nico B, Crivellato E, Guidolin D, et al. Intussusceptive microvascular growth in human glioma. *Clin Exp Med* 2010;10:93–98
- Carbonell WS, Anson O, Sibson N, et al. The vascular basement membrane as “soil” in brain metastasis. *PLoS One* 2009;4:e5857
- Nelson CM, Bissell MJ. Of extracellular matrix, scaffolds, and signaling: Tissue architecture regulates development, homeostasis, and cancer. *Annu Rev Cell Dev Biol* 2006;22:287–309

Development of the vasculature in “pushing-type” liver metastases of an experimental colorectal cancer

Sándor Paku^{1*}, László Kopper² and Péter Nagy²

¹Department of Molecular Pathology, Joint Research Organization of the Hungarian Academy of Sciences and Semmelweis University, Budapest, Hungary

²First Department of Pathology and Experimental Cancer Research, Semmelweis University, Budapest, Hungary

A mechanism for stroma formation (development of vasculature and supportive connective tissue) is suggested in an experimental “pushing-type” colorectal carcinoma liver metastasis model. The key element is the appearance of smooth muscle actin (SMA)-positive cells and the sinusoidal lakes at the border of the metastases. These lakes are the consequence of the disappearance (‘stepping back’ of hepatocytes from the border zone, resulting in the fusion of partially capillarized sinusoids. The growing tumor incorporates SMA-expressing cells and sinusoidal lakes. SMA-positive cells produce collagenous matrix, whereas the lakes become the central vessels within the connective tissue columns. Formation of these columns within the tumor is a consequence of the compression atrophy of the base of the incorporated liver tissue, leading to partial separation of the innermost part of the invagination containing functional vessel(s) from the surrounding liver.

© 2005 Wiley-Liss, Inc.

Key words: vasculature; pushing-type liver metastases; colorectal cancer

Several different mechanisms of angiogenesis exist in primary tumors and metastases, *e.g.*, capillary sprouting,¹ intussusceptive angiogenesis,^{2,3} vessel incorporation⁴ and glomeruloid body formation.^{5,6} Tumor-induced angiogenesis depends on both tumor type and site of tumor growth.⁷ Sprouting-type angiogenesis occurs in tissues containing large amounts of collagenous matrix (*e.g.*, skin).⁴ In contrast, in organs containing a vast number of microvessels and a low amount of connective tissue (*e.g.*, lungs and liver, the main targets for metastasis), formation of new capillaries is less important. In this “soil”, tumors can grow without neoangiogenesis by simply incorporating the preexisting vasculature.⁸ The incorporation of new and preexisting host vessels is also a basic option for tumor vascularization in primary malignant melanomas.⁴

Three different growth patterns (replacement, pushing and desmoplastic) for liver metastasis of colorectal and breast cancers have been described.^{9,10} During replacement growth, the architecture of the liver is preserved and the endothelial cells of sinusoids show low proliferative activity. However, pushing and desmoplastic types of growth disturb the liver architecture. In the pushing growth pattern, severely compressed liver parenchyma is present at the surface metastases, whereas a fibrous capsule develops at the tumor–liver parenchyma interface in the desmoplastic growth pattern.

Earlier, we described 2 angiogenesis patterns, depending on the localization of the metastases of the anaplastic 3LL-HH tumor within the liver.⁷ During growth of sinusoidal-type metastases, invading tumor cells advanced between the basement membrane and the endothelial lining of the sinusoids, evoking proliferation of endothelial cells. This process resulted in the development of large tortuous vessels without basement membrane inside the tumor nodules. Conversely, sprouting-type angiogenesis was observed in portal-type metastases. The replacement growth pattern corresponds to sinusoidal-type metastases of undifferentiated tumors, while the desmoplastic one shows similarities to portal-type metastases.

However, no mechanism of angiogenesis is known for pushing-type liver metastases.

In the present report, we describe a mechanism for the development of vasculature and supportive connective tissue in pushing-type liver metastases of an experimental colorectal cancer. The process includes the proliferation of smooth muscle actin (SMA)-positive hepatic stellate cells on the surface of the tumor spheroid accompanied by fusion of the sinusoids, forming vascular lakes in this region. Together with the proliferating and collagen-producing stellate cells, these vascular lakes are incorporated into the tumor mass. The entrapped sinusoidal lakes are partially separated from the liver tissue by the invading tumor mass, resulting in the development of vessel-containing connective tissue columns, which traverse the tumor.

Material and methods

Animals and tumor line

The C38 colorectal carcinoma line was maintained by serial s.c. transplantations in C57Bl/6 mice. (Inbred C57Bl/6 mice from our institute were used throughout the studies.) Tumor tissue was cut into small pieces in serum-free RPMI-1640 medium and digested by collagenase I (Sigma, St. Louis, MO; 7 mg collagenase/10 ml medium) at 37°C for 30 min; the suspension was filtered through 4-fold gauze. After centrifugation and washing, the viability of the tumor cells was determined by the trypan blue exclusion test. Liver metastases were produced by injecting 2×10^5 tumor cells into the spleen of mice anesthetized by sodium pentobarbital (Nembutal, 70 mg/kg). Animals were killed 9, 13 or 20 days following tumor cell inoculation.

Electron microscopy

Anesthetized animals (2 at each time point) were perfused *via* the left ventricle with PBS for 10 min and with 4% paraformaldehyde and 1% glutaraldehyde in PBS (pH 7.2) for 15 min at room temperature. Livers were removed, cut into 1×2 mm pieces and immersed in the same fixative for an additional 2 hr. Pieces were postfixed in 1% OsO₄ and 0.5% K-ferrocyanide in 0.05 M Na-cacodylate for 2 hr, dehydrated in a graded series of acetone, contrasted en bloc with 2% uranylacetate and embedded in Spurr’s mixture. More than 40 different metastases were analyzed on semithin sections stained by 0.5% toluidine blue (pH 8.5), of which 15 were processed for electron microscopic analysis. Areas of interest were trimmed out by comparing the structures on the cut surface of the tissue blocks with the semithin sections. Ultrathin sections were cut by an RMC MT-7 ultramicrotome, stained with lead citrate and analyzed using a Philips (Hamburg, Germany) CM10 electron microscope.

Grant sponsor: Hungarian Medical Research Council; Grant number: 128/2003.

*Correspondence to: First Institute of Pathology and Experimental Cancer Research, Semmelweis University, 1085 Üllői út 26, Budapest, Hungary. Fax: +36-1-317-1074. E-mail: paku@korb1.sote.hu

Received 14 April 2004; Accepted after revision 5 November 2004

DOI 10.1002/ijc.20886

Published online 23 February 2005 in Wiley InterScience (www.interscience.wiley.com).

TABLE I – MORPHOMETRIC ANALYSIS OF VASCULARIZATION OF C38 COLON CARCINOMA METASTASES

	Days after tumor inoculation		
	9	13	20
Number of metastases analyzed	181	112	81
% avascular metastases	80.1	2.7	0
Total area of metastases analyzed (mm ²)	27.1	116.1	554.1
Mean ± SD of radius of cross sections of metastases (μm)	206 ± 71	544 ± 186	1,313 ± 687
Range (μm)	90–478	187–1,230	444–3,395
Total length of invaginations (μm)	13,933	142,662	595,868
Mean ± SD of length of invaginations/unit area of metastases (μm/mm ²)	452 ± 284	1,170 ± 210*	1,161 ± 417

We used 6, 8 and 8 mice at 9, 13 and 20 days after tumor inoculation, respectively. * $p < 0.05$ (vs. 9th day).

Immunofluorescence analysis

For immunofluorescence studies, 3, 5 and 4 mice were used at 9, 13 and 20 days after tumor inoculation, respectively.

Livers were removed and frozen in isopentane chilled with liquid nitrogen. Cryostat sections (15–20 μm) were fixed in methanol (–20°C) and incubated at room temperature (1 hr) with a mixture of the following primary antibodies: polyclonal antibodies, antilaminin (dilution 1:100, catalogue Z0097; Dako, Carpinteria, CA), antifibronectin receptor (dilution 1:100; GIBCO, Grand Island, NY), antifibronectin (dilution 1:100, catalogue F3648; Sigma-Aldrich, St. Louis, MO); MAbs, antimouse CD31 (dilution 1:100, catalogue 01951D), anti- α_6 integrin (dilution 1:100, catalogue 33771A; both from Pharmingen, San Diego, CA), anti- α SMA (dilution 1:100, catalogue M0851), antidesmin (dilution 1:100, catalogue M0724) and FITC-conjugated anticytokeratin (dilution 1:100, catalogue F0859; all from Dako).

After washing, appropriate secondary antibodies conjugated with FITC, TRITC or CY5 were used (all from Jackson ImmunoResearch, West Grove, PA).

Bromodeoxyuridine (BrdU) labeling of proliferating cells was performed as follows. One hour before mice were killed, 200 mg/kg BrdU in saline were injected i.p. Cryostat sections fixed in methanol were reacted with 2 N HCl (15 min, 20°C), anti-BrdU antibody (dilution 1:100, catalogue 347580; Becton Dickinson, Mountain View, CA) and fluorescent secondary antibody. Apoptotic cells were detected using the TACS *in situ* fluorescent apoptosis detection kit (R&D Systems, Abingdon, UK).

FITC-labeled *Lycopersicon esculentum* lectin (100 μg in 0.1 ml of 0.9% NaCl, catalogue FL1171; Vector, Burlingame, CA) was injected into the lateral tail vein 15 min before killing, for supravital staining of the vasculature of the liver and metastases.

Specimens were analyzed by confocal laser-scanning microscopy using the MRC-1024 system (Bio-Rad, Richmond, CA).

Morphometry

For quantitative analysis 6, 8 and 8 mice were used at 9, 13 and 20 days after tumor inoculation, respectively. To ensure that separate metastases were studied, mice were injected with different numbers of tumor cells (9 days, 2×10^5 ; 13 days, 5×10^4 ; 20 days, 2×10^4). Cross sectional areas of metastases were determined on toluidine blue-stained cryosections using Olympus-Vanox Cue2 image analysis software ($\times 2$ objective lens; Olympus, Tokyo, Japan). Cross sections which contained no central necrotic areas, representing tips of metastases, were excluded from the study. Vascularization of the metastases was analyzed on parallel cryosections stained for CD31 and laminin ($\times 4$ objective lens). Metastases were considered vascularized when within them invaginations > 100 μm containing CD31 staining, lined by laminin staining and surrounded by viable tumor cells were observed.

Invagination lengths or, in the case of columns, the length of the columns' large axis were determined using Bio-Rad LaserSharp software. Data were analyzed using Student's *t*-test.

Results

Day 9 after inoculation of tumor cells

Most of the metastases were avascular (Table I), showing central necrosis. However, all metastases > 600 μm in diameter were vascularized. Nonvascularized metastases were circular in cross section and composed of polarized tumor cells residing on an incomplete basement membrane according to electron microscopy. Immunohistochemistry, however, showed almost continuous laminin staining around tumor spheroids (Fig. 1a). CD31 and α_6 integrin were expressed on the hepatic sinusoids in the vicinity of the metastases (Fig. 1a,b). Laminin immunostaining was strong around these sinusoids. SMA-expressing stellate cells accumulated at the surface of metastases and around the sinusoids facing the tumor (Fig. 1c).

Day 13 after inoculation of tumor cells

Four days later, CD31 was expressed throughout the liver on the endothelial cells. On the contrary, α_6 integrin expression

FIGURE 1 – (a) Border zone of a tumor spheroid (T) 9 days after tumor inoculation. The tumor is covered by almost continuous laminin staining (red). Sinusoids of the liver (L) close to the tumor express CD31 (green). Sinusoids close to the basement membrane of the tumor are yellow. (b,c) Border zone of a tumor spheroid (T). Triple labeling for α_6 integrin, laminin and SMA. For clarity, the localization of α_6 integrin is shown in (b). (b) α_6 integrin is present at the periphery of the tumor and on sinusoids facing the tumor (arrowheads). (c) SMA-positive cells (red) are accumulated mainly between the sinusoid and the tumor. The sinusoid (positive for α_6 integrin) shows strong laminin staining (blue, arrowheads). (d) Localization of fluorescent *Lycopersicon esculentum* lectin at the periphery of a metastasis. Note the reduced staining of sinusoids in the vicinity of the tumor (arrowheads). Tumor cells at the periphery of the metastasis are extensively labeled by BrdU (red nuclei). N, Necrotic area. (e) Electron micrograph of a sinusoid in the vicinity of the tumor 13 days following tumor inoculation. Connective tissue separates the large sinusoid from the tumor (upper left corner). On the other side of the sinusoid, hepatocytes are visible (lower right corner). Bundles of collagen covered by endothelial cells are localized within the sinusoid (arrows). (f) Detail of (e). The endothelial cell (E) has no fenestration and structured basement membrane. Collagen bundles are visible beneath the endothelial cell (arrows). Pericytes are not present around the vessel. Connective tissue cells with dilated endoplasmic reticulum (arrowheads) are located far from the vessel. (g) Detail of (e). Collagen bundle covered by endothelial cells. Arrow points at an intercellular junction between endothelial cells. Scale bars: (a,d) = 20 μm, (b,c) = 50 μm, (e) = 5 μm, (f) = 1 μm, (g) = 0.5 μm.

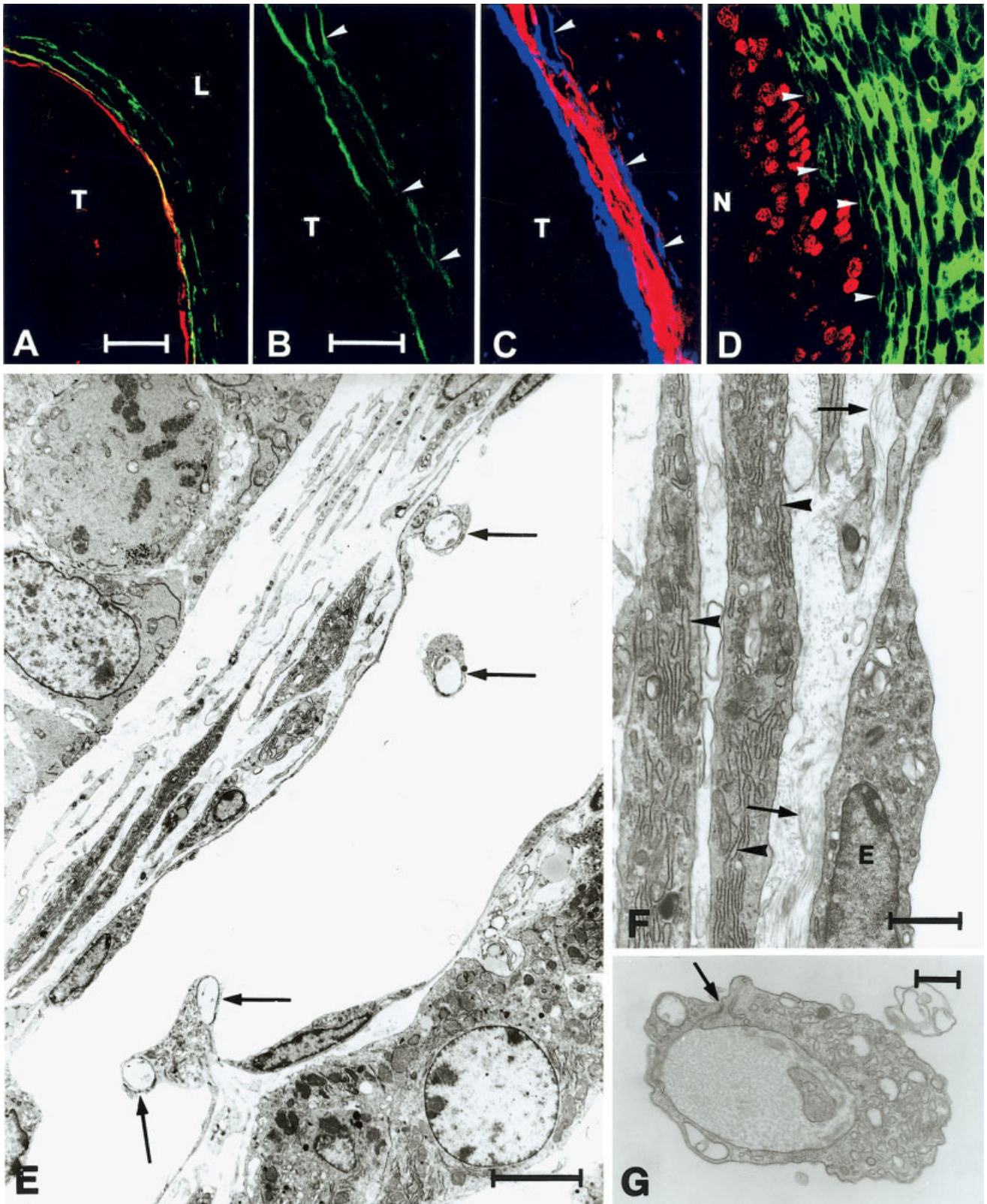


FIGURE 1

remained localized to the sinusoids facing the tumor. These sinusoids were strongly compressed but still perfused at low level, as shown by *L. esculentum* lectin staining and BrdU incorporation of

tumor cells at the periphery of the metastasis (Fig. 1d). Incomplete capillarization of sinusoids was noticeable ultrastructurally (Fig. 1e,f). The number of fenestrations was reduced, and struc-

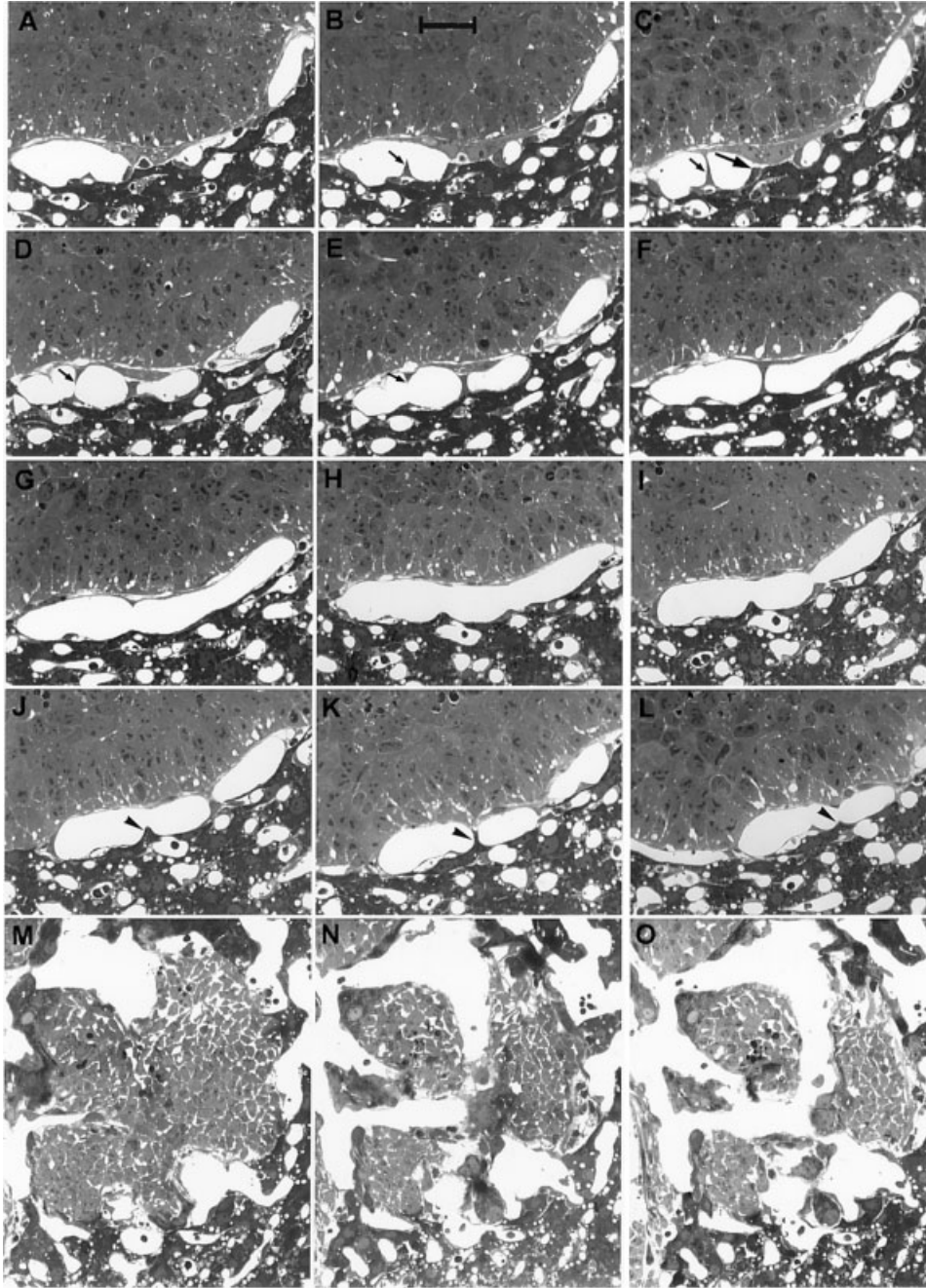


FIGURE 2 – Serial semithin sections of C38 colorectal carcinoma metastases 13 days following tumor inoculation. Sections were cut at 2 μm distances. (a–l) First steps of sinusoidal lake formation. (b–e) and (j–l) Small cytoplasmic processes of endothelial cells (small arrows) and a hepatocyte (arrowheads) connect the 2 sides of the lake. (c) Hepatocytes extend only halfway between the sinusoids, where they face connective tissue cells (large arrow). (m–o) Serial tangential sections of the tip of another metastasis are visible. (m) Dilated sinusoids are in contact with the metastasis. These sinusoids are in continuity with each other, as shown in (o), forming a large vascular lake on the surface of the metastasis. Scale bar = 25 μm .

tured basement membrane could not be observed. Proliferating SMA-positive cells (with dilated endoplasmic reticulum) accumulated at the tumor side of the sinusoids, while hepatocytes disappeared from this region (Fig. 1e). On the contrary, neither necrotic nor apoptotic hepatocytes could be observed. Other vessels facing the tumor were completely surrounded by SMA-positive cells. These cells, however, did not show the characteristic localization of pericytes; they were neither apposed to endothelial cells nor surrounded by basement membrane. A large amount of collagen was deposited around them (Fig. 1f). The fusion of capillarized sinusoids led to the appearance of large sinusoidal lakes on the tumor surface (Figs. 1e,2). The fusion was evidenced by the presence of collagen bundles within sinusoids, which were part of the supportive structure of the liver tissue and remained after the disappearance of hepatocytes (Fig. 1e,g). Endothelial cell processes

frequently formed bridges within the sinusoids, representing the last step of fusion (Fig. 2).

By this time, numerous deep invaginations could be observed within the metastases (Table I, Fig. 3a), which were produced when the new tumor masses bulged from the tumor spheroid into the liver parenchyma. Bulges were often free of basement membrane and SMA-positive cell coverage (Fig. 3a). Incorporated liver tissue plates had a unique appearance when the sectioning plane was perpendicular to the surface. SMA-positive cells were found at the tip and the 2 sides; hepatocytes accumulated in the middle of invaginations (Fig. 3a–c). Almost continuous CD31 staining (representing incorporated sinusoidal lakes) was observed between hepatocytes and SMA-positive cells or embedded into the latter cells (Fig. 3b,c). The sinusoidal structure was still normal at the base of invaginations (Fig. 3b).

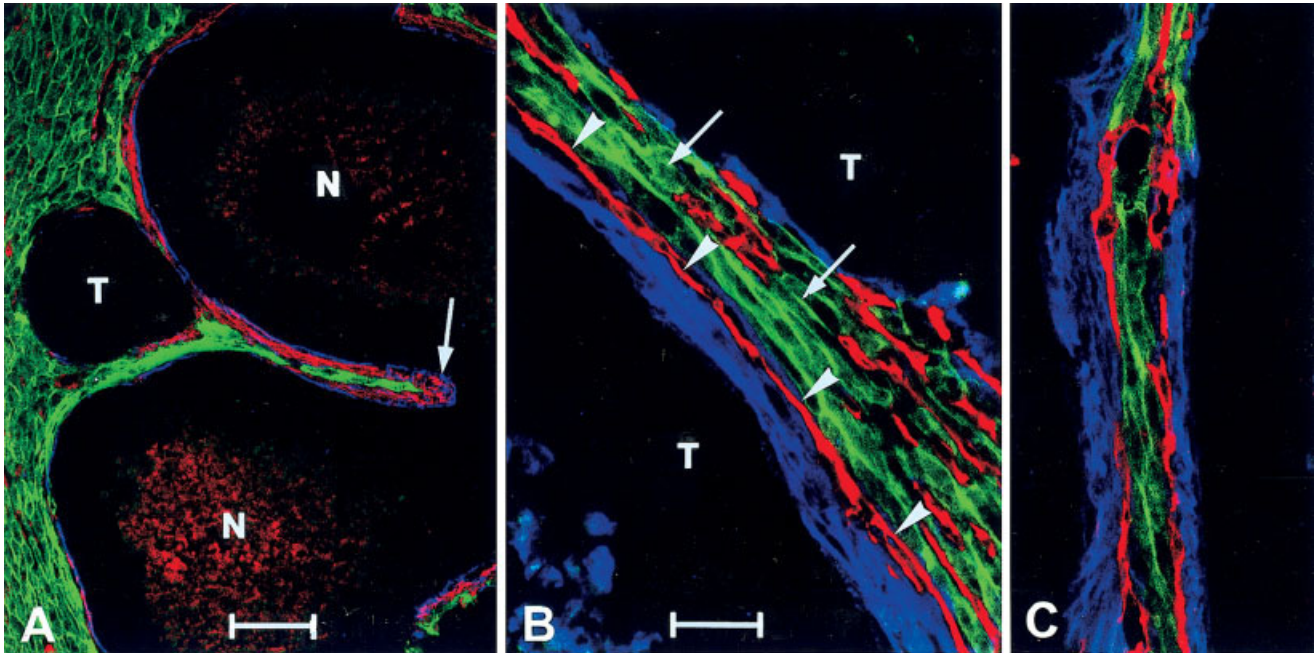


FIGURE 3 – (a) Large invagination in a metastasis 13 days following tumor cell inoculation. In the deepest part of the invagination (arrow), hepatocytes stained by anticytokeratin antibody (green) are surrounded by SMA-positive cells (red) and laminin staining (blue). Note the absence of SMA and laminin staining around the small tumor bulge (T). N, Necrotic area. (b) Basal part of an invagination. Continuous CD31 staining (red), representing a sinusoidal lake (arrowheads), is visible in contact with SMA-positive cells (blue) at the surface of the lower tumor spheroid (T). Note the regular sinusoidal structure of the liver in the lower right area. Areas of packed hepatocytes (green) without sinusoids are also present (arrows). (c) Deeper part of a strongly compressed invagination. Both sides of the invagination are delineated by SMA-positive cells (blue) and almost continuous CD31 staining (red). Sinusoids are not present between the hepatocytes (green). Scale bars: (a) = 100 μm , (b,c) = 50 μm .

Day 20 after inoculation of tumor cells

By day 20, beside the deep invaginations another characteristic structure could frequently be observed within the tumor tissue. These structures had a circular shape in cross section composed of an outer basement membrane and usually one central CD31-positive vessel (Fig. 4a–c). Occasionally, small columns without vessels were also present (Fig. 4a,b). The central vessel consisted of a single layer of endothelial cells (Fig. 4e), expressing α_6 integrin and surrounded by laminin-positive material (Fig. 4a,b). These vessels showed partial capillarization similar to the peritumoral sinusoidal lakes (low number of fenestrations, lack of regular basement membrane and pericytes; Fig. 4e,f). The space between the vessel and the outer basement membrane was filled by SMA-positive cells (Fig. 4c), type I collagen (Fig. 4e,f) and fibronectin (not shown). SMA-positive cells strongly expressed fibronectin receptor, whereas this integrin was expressed only at a low level on the central vessels (Fig. 4d). Occasionally, hepatocytes were identified between SMA-positive cells, suggesting a sinusoidal origin of the central vessel (Fig. 5a). Proliferation of SMA-positive and endothelial cells also continued at this stage (Fig. 5b). Capillary sprouts with slit-like lumen were present within the large columns (Fig. 5c,d). Serial sectioning revealed the above structures to be branching connective tissue columns traversing the metastasis, with the central vessels being continuous with the sinusoids of the liver parenchyma (Fig. 6). Proliferating tumor cells were present around these hardly perfused columns. A considerable proportion of these columns, however, were not perfused at all, leading to large necrotic areas in the metastases (Fig. 5e,f). The length of the invaginations/unit area on day 20 remained unchanged compared to day 13 (Table I).

Discussion

Here, a model is suggested for the vascularization of “pushing-type” liver metastases. The key element is the appearance of SMA-positive cells and sinusoidal lakes at the border of the meta-

stases. Stellate cells support the vessels after being incorporated into the tumor mass by producing collagenous matrix, whereas the sinusoidal lakes form vessels located centrally within the connective tissue columns. These columns represent the main structural and functional unit, providing blood supply for the inner part of the growing tumor. The putative process is depicted in Figure 7.

From a mechanical point of view, there are 2 factors that can contribute to the development of the sinusoidal lakes: the appearance of SMA-positive cells and the pressure of the tumor. These 2 factors may be responsible for the disappearance (“step back”) of hepatocytes from the border zone of the tumor and the liver tissue. Similar to Dingemans *et al.*,¹¹ we were unable to observe apoptotic or necrotic hepatocytes in this zone despite the severe distortion of these cells. Therefore, we propose that hepatocytes move

FIGURE 4 – (a,b) Numerous columns are localized within a metastasis 20 days following tumor inoculation. Triple labeling for α_6 integrin, laminin and SMA. For clarity, the localization of α_6 integrin is shown in (a). (a) α_6 integrin is present at the periphery of the column and around the central vessel. (b) Laminin (blue) colocalizes with α_6 integrin within the columns. Note the presence of small-diameter columns lacking central vessel (arrows), composed of SMA-positive cells (red) surrounded by laminin. (c) Cross section of a column tightly packed with SMA-positive cells (red). The column contains CD31-positive vessels (green) and is surrounded by basement membrane of the tumor (blue). This picture corresponds to panel 14 in Figure 6. (d) Distribution of the fibronectin receptor within a column. The basal surface of the tumor cells (arrowheads) and the connective cells of the column are strongly stained. In contrast, the central vessel (V) shows weak staining. (e) Longitudinal section of a column within the tumor. Tumor cells are visible on the upper and lower parts of the figure. Connective tissue cells are oriented parallel to the axis of the column. Very thin endothelial cells delineate the central vessel. Pericytes are not present. (f) High-power micrograph of an endothelial cell of a central vessel showing fenestrations (arrows). The endothelial cell is partially covered by structured basement membrane (arrowheads). Scale bars: (a,b) = 50 μm , (c) = 10 μm , (d) = 25 μm , (e) = 10 μm , (f) 1 μm .

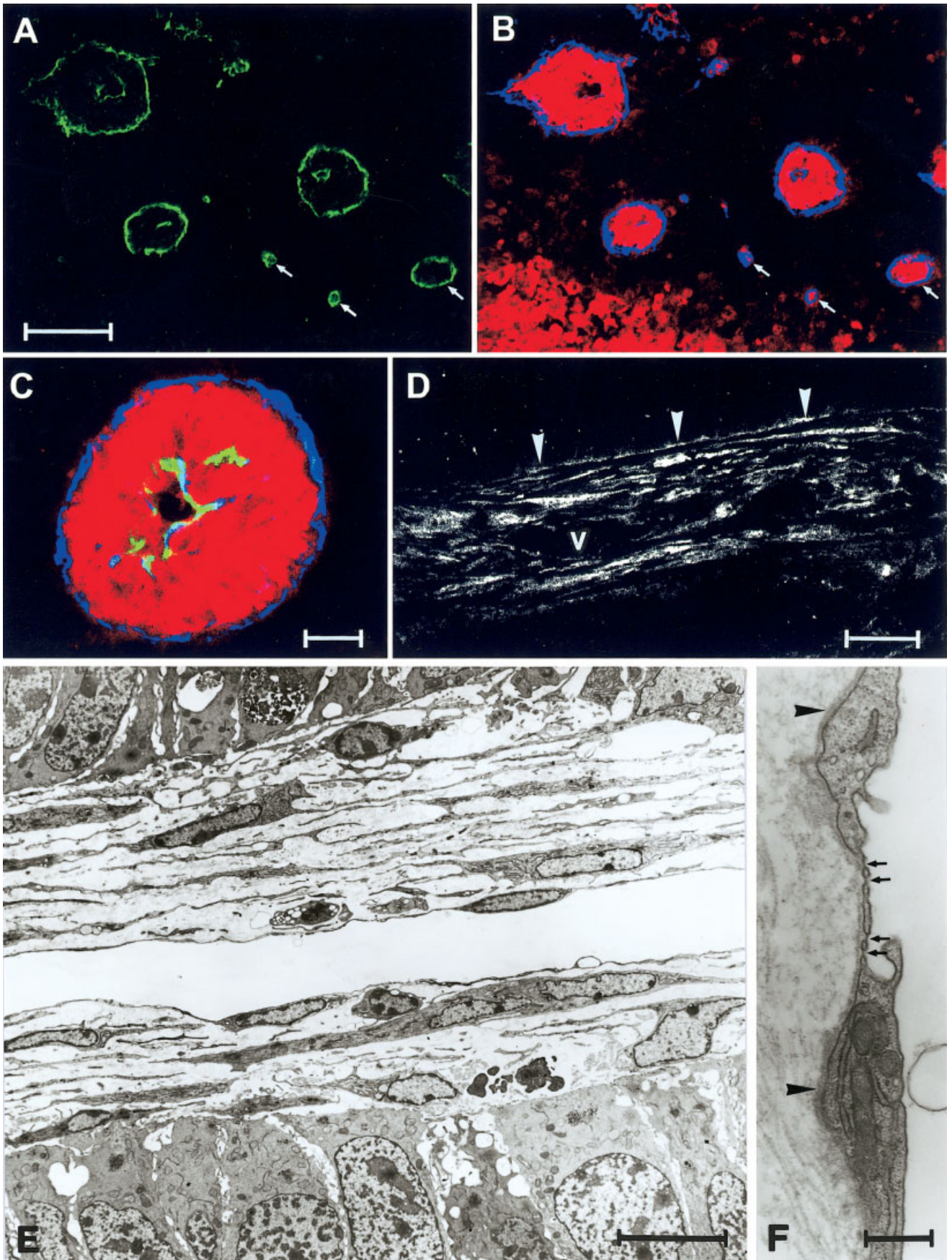


FIGURE 4

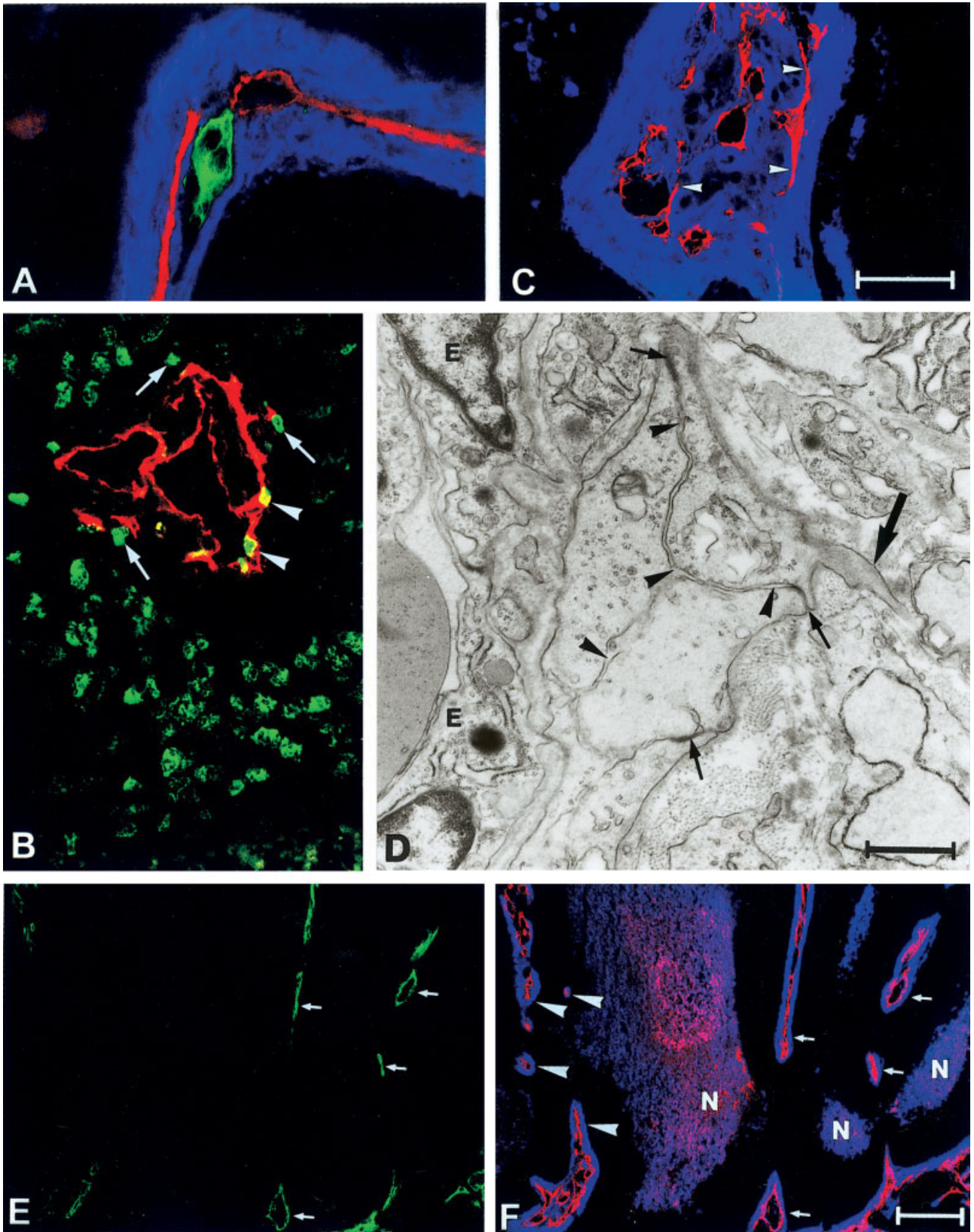


FIGURE 5

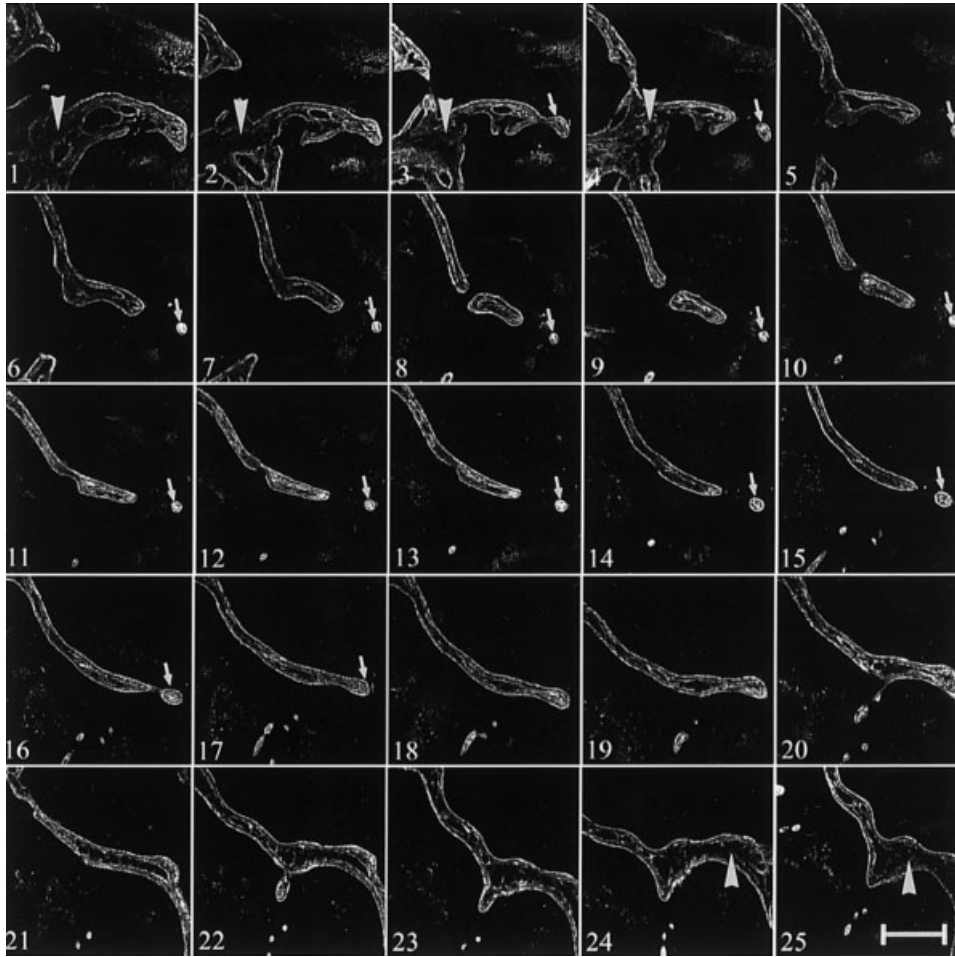


FIGURE 6 – Serial section of a 20-day-old liver metastasis stained for laminin. Sections were cut at 20 μm distances. In panels 1–4, 24 and 25, normal liver tissue is also present (arrowheads), whereas the other pictures show incorporated tissue. Note the column (arrows), which is separated from the liver tissue in panel 4 and shows continuity with the invagination again in panel 17. Scale bar = 300 μm .

out of this zone, leaving space for the formation of sinusoidal lakes. In an excellent study, Kuruppu *et al.*¹² demonstrated the presence of sinusoidal lakes at the periphery of experimental colorectal carcinoma liver metastases by SEM analysis of corrosion casts; the significance of these structures in the vascularization of the metastases was, however, not addressed. Fusion of the sinusoids can be considered as a reverse intussusceptive angiogenesis.²

FIGURE 5 – (a) Longitudinal section of a well-developed column containing a central vessel (red) and distorted hepatocytes (green) surrounded by SMA-positive cells (blue). (b) Twenty-day-old tumor stained for CD31 (red) and BrdU (green). Numerous proliferating endothelial (arrowheads) and connective tissue cells (arrows) are present within the column. Proliferating tumor cells are visible around the column. (c) Large column containing SMA-positive cells (blue), CD31-positive (red), dilated vessels and capillary sprouts (arrowheads). (d) Cross section of capillary sprout located in the vicinity of a central mother vessel. The sprout has a slit-like lumen (arrowheads), which is sealed by intercellular junctions (arrows). Note the process of the endothelial cell (large arrow), which extends into the connective tissue, suggesting active growth of the sprout. E, Endothelial cells of the mother vessel. (e,f) Section of a 20-day-old liver metastasis of a mouse injected with FITC-conjugated *Lycopersicon esculentum* lectin (green) and stained for CD31 (red) and SMA (blue). For clarity, the localization of the lectin is shown in (e). Arrows point at well-perfused vessels within the columns; however, a considerable portion of the columns are not or are only partially perfused (arrowheads in f and lack of green color at these areas in e). Black areas in (f) represent viable tumor tissue, whereas pink areas represent necrotic tumor tissue (N). Scale bars: (a–c) = 50 μm , (d) = 1 μm , (e,f) = 100 μm .

α_6 integrin is present exclusively in large portal vessels and capillaries around the bile ducts in normal liver. In hepatocellular carcinomas and cirrhosis, this integrin is expressed in sinusoids as a part of the capillarization process.^{13,14} In our case, however, expression of this integrin was confined to the sinusoids facing the tumor. These sinusoids were always surrounded by stellate cells. Yet, the capillarization process was not complete since the SMA-positive cells were not positioned as real pericytes (they had no basement membrane). The fragile structure of these vessels was maintained during vascularization of the metastases. The presence of α_6 integrin in tumor vessels may negatively influence the efficiency of antiangiogenic treatments, based on the observation that α_v and α_5 integrins are upregulated during angiogenesis in endothelial cells.^{15,16} The main cellular elements of the connective tissue columns, the SMA-expressing cells, express a high level of fibronectin receptor. They could, therefore provide an alternative target for therapy with this receptor's antagonist.

It has been shown that the growth pattern of liver metastases is dependent on the degree of differentiation.¹⁰ The replacement growth pattern was characteristic for tumors showing less glandular differentiation, whereas differentiated tumors grew by compressing the liver parenchyma (pushing growth pattern) or eliciting a fibrotic response (desmoplastic growth pattern) at the border of the metastases. The presence of a fibrous capsule containing myofibroblasts and collagen I around primary and secondary liver tumors is common. According to various studies, 20–60% of colorectal carcinoma liver metastases are encapsulated, which is considered to be a mechanical barrier against tumor invasion and is associated with better prognosis.^{9,10,17,18} Different factors can be responsible

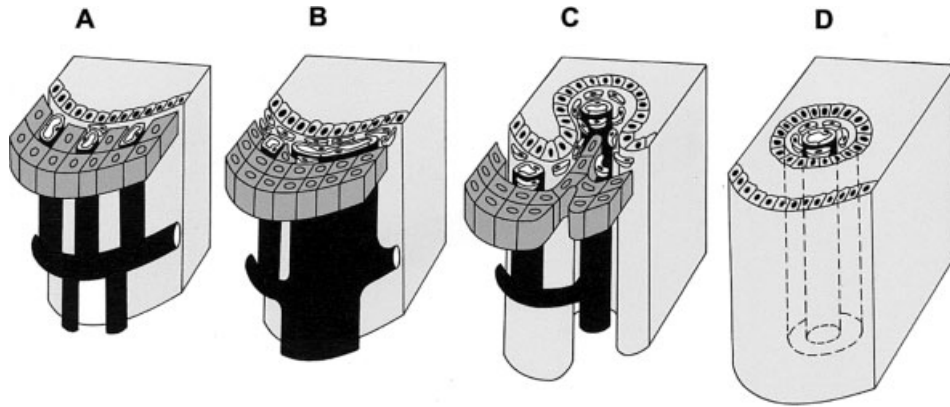


FIGURE 7 – Schematic representation of column formation. For better visibility of vessels, hepatocytes are depicted only on the upper part of the drawings. (a) At the early stage of tumor development, the tumor faces normal liver architecture. (b) SMA-positive cells accumulating at the tumor–liver parenchyma interface. Owing to the compression of the tumor, hepatocytes “step back” and fusion of the sinusoids takes place. (c) The fused vessel, together with SMA-positive cells, is incorporated into the tumor. (d) The pressure of the tumor bulges causes separation of the central vessel from the liver parenchyma. The vessel in the direction of the axis of the column remains connected to the sinusoidal system of the liver. Column formation is finished by back-to-back fusion of the basement membranes of the tumor bulges. Column is surrounded by viable tumor cells. Light gray, tumor; dark gray, hepatocytes; black, sinusoids and central vessel; white, SMA-positive cells and cut surface of endothelial cells.

for the capsule formation, such as transforming growth factor- β , hypoxia and simple mechanical pressure.^{19,20} There is evidence that the main cellular components of these capsules are activated SMA-expressing hepatic stellate cells.¹⁹ The mechanical pressure exerted by differentiated carcinomas (pushing growth pattern) can be a major factor for the activation and accumulation of hepatic stellate cells around metastases.²⁰ An important role of these contractile cells can be to decrease the size of the “wound” in the liver caused by the growing tumor. Hepatic stellate cells were not accumulated on the surface of the metastases in sinusoidal metastases (replacement growth pattern) of the B16 melanoma; instead, they were scattered in the tumor nodules. They are thought to create a proangiogenic microenvironment and to be responsible for the recruitment and survival of endothelial cells. Similarly, Vermeulen *et al.*⁹ reported the absence of a fibrotic response in colorectal metastases with the replacement growth pattern. These data and our earlier observations made on the sinusoidal type of 3LL-HH tumor metastases⁷ suggest that undifferentiated highly invasive tumors do not induce a fibrotic capsule.

The growth of a tumor as an avascular sphere in the liver is limited because the development of central necrosis weakens the mechanical stability of the metastases, though the sinusoids at the periphery would support further growth. In C38 colon carcinoma, further expansion of the metastases takes place by the bulging of new tumor masses from the original spheroid into the liver. This process immediately leads to the development of invaginations, which consequently results in early vascularization of the metastases (all metastases $>600\ \mu\text{m}$ in diameter are vascularized). During the growth of the bulge(s), the pressure will increase at the base of the incorporated liver tissue. However, the innermost part of the invagination (base of the bulge) is a distinctive place since the pressure of the tumor is lower here. A similar situation is when a sheet of paper is folded and the ends are pressed together. As mentioned above, the sinusoids at the surface of the tumor are strongly compressed. (The architecture of these sinusoids could be revealed only by applying a slightly higher perfusion rate during fixation.) Following incorporation, these fused sinusoids can land at the innermost part of the invagination, where these vessels can open up owing to the lower pressure and start to deliver blood into the tumor. The appearance of connective tissue columns within the liver metastases appears to be a unique feature of the C38 tumor. These structures are produced by the increasing pressure of the tumor at the base of the invagination, resulting in separation of the innermost part of the invaginated tissue from the rest of the liver. This separation is completed by the disappearance of the back-to-

back basement membranes of the tumorous glands, which is a frequent observation in colorectal cancers.²¹ In the axial direction, however, the column will remain in continuity with the liver parenchyma (Fig. 7). This finding strongly suggests that these metastases are supplied with blood originating from the hepatic sinusoids. As proliferating endothelial and SMA-positive cells are regular observations within the columns, these structures probably grow in length and width during tumor development. The tumor continues to bulge not only into the liver parenchyma but also into the columns within the tumor, pinching off further pieces from the column. The vessels of these new columns are in all probability produced by sprouting-type angiogenesis, observed within these structures. However, the pinching process can also lead to the appearance of small columns without vessels. Proliferation of endothelial and SMA-positive cells as well as the pinching process should result in an increase in length of the invaginations/unit area of the metastases. Nonetheless, this parameter remained unchanged. There are 2 mechanisms to explain this contradiction. On the one hand, the growing tumor lowers the density of the invaginations or columns (by dilution). On the other hand, the pressure of the tumor, as observed frequently, obstructs the perfusion of the columns, leading to necrosis not only of the tumor cells but also of the columns.

It is conceivable that in well-differentiated tumors the back-to-back fusion of the tumor glands does not take place, leaving the invaginations intact, which leads to the absence of column formation. Nevertheless, also in these tumors, the vessels in the innermost part of the invaginations are most probably responsible for the nutrition of the tumor.

Desmoplastic metastases, far from portal tracts, can also be considered as pushing-type metastases. The extent of connective tissue accumulation can depend on the growth rate of the metastases. On the surface of slow-growing metastases, more connective tissue can accumulate due to the low incorporation rate. If the sinusoids are embedded in connective tissue for a longer time at the surface of the metastases, sprouting-type angiogenesis can take place. Together with these newly developed vessels, the connective tissue is incorporated, similarly to primary tumors. It has been shown that metastases with the pushing growth pattern have a higher endothelial cell proliferation rate than desmoplastic ones, which is in accordance with the supposed slow growth of these metastases.⁹

The process for the development of vasculature in liver metastases of the C38 tumor presented here may represent a general mechanism for the vascularization of pushing-type liver metastases.

ses of differentiated tumors of various origins (colon, breast, lung carcinomas).

Our present study further supports earlier observations that vascularization of metastases in the liver is a heterogeneous process,

depending on the degree of tumor differentiation or localization of the metastases within the liver.^{7,9,10} This notion should be taken into consideration when new antiangiogenic therapies against liver metastases are designed.

References

1. Paku S, Paweletz N. First steps of tumor-related angiogenesis. *Lab Invest* 1991;65:334–46.
2. Djonov V, Baum O, Burri PH. Vascular remodeling by intussusceptive angiogenesis. *Cell Tissue Res* 2003;314:107–17.
3. Nagy JA, Morgan ES, Herzberg HT, Manseau EJ, Dvorak AM, Dvorak HF. Pathogenesis of ascites tumor-growth angiogenesis, vascular remodeling and stroma formation in the peritoneal lining. *Cancer Res* 1995;55:376–85.
4. Döme B, Paku S, Somlai B, Timár J. Vascularization of cutaneous melanoma involves vessel co-option and has clinical significance. *J Pathol* 2002;197:355–62.
5. Sundberg C, Nagy JA, Brown LF, Feng D, Eckelhoefer IA, Manseau EJ, Dvorak AM, Dvorak HF. Glomeruloid microvascular proliferation follows adenoviral vascular permeability factor/vascular endothelial growth factor-164 gene delivery. *Am J Pathol* 2001;158:1145–60.
6. Döme B, Timar J, Paku S. A novel concept of glomeruloid body formation in experimental cerebral metastases. *J Neuropathol Exp Neurol* 2003;62:655–61.
7. Paku S, Lapis K. Morphological aspects of angiogenesis in experimental liver metastases. *Am J Pathol* 1993;143:926.
8. Pezzella F, Pastorino U, Tagliabue E, Andreola S, Sozzi G, Gasparini G, Menard S, Gatter KC, Harris AL, Fox S, Buyse M, Pilotti S, et al. Non-small-cell lung carcinoma tumor growth without morphological evidence of neo-angiogenesis. *Am J Pathol* 1997;151:1417–23.
9. Vermeulen PB, Colpaert C, Salgado R, Royers R, Hellemans H, Van den Heuvel E, Goovaerts G, Dirix LY, Van Marck E. Liver metastases from colorectal adenocarcinomas grow in three patterns with different angiogenesis and desmoplasia. *J Pathol* 2001;195:336–42.
10. Stessels F, Van den Eynden G, Van der Auwera I, Salgado R, Van den Heuvel E, Harris AL, Jackson DG, Colpaert CG, van Marck EA, Dirix LY, Vermeulen PB. Breast adenocarcinoma liver metastases, in contrast to colorectal cancer liver metastases, display a non-angiogenic growth pattern that preserves the stroma and lacks hypoxia. *Br J Cancer* 2004;90:1429–36.
11. Dingemans KP, van den Bergh Weerman MA, Keep RF, Das PK. Developmental stages in experimental liver metastases: relation to invasiveness. *Int J Cancer* 1994;57:433–9.
12. Kuruppu D, Christophi C, Maeda H, O'Brien PE. Changes in the microvascular architecture of colorectal liver metastases following the administration of SMANCS/Lipiodol. *J Surg Res* 2002;103:47–54.
13. Torimura T, Ueno T, Kin M, Inuzuka S, Sugawara H, Tamaki S, Tsuji R, Sujaku K, Sata M, Tanikawa K. Coordinated expression of integrin alpha6beta1 and laminin in hepatocellular carcinoma. *Human Pathol* 1997;28:1131–8.
14. Couvelard A, Scoazec JY, Feldman G. Expression of cell–cell and cell–matrix adhesion proteins by sinusoidal endothelial cell in normal and cirrhotic liver. *Am J Pathol* 1993;143:738–52.
15. Reinmuth N, Liu WB, Ahmad SA, Fan F, Stoeltzing O, Parikh AA, Bucana CD, Gallick GE, Nickols MA, Westlin WF, Ellis LM. $\alpha_5\beta_3$ integrin antagonist S247 decreases colon cancer metastasis and angiogenesis and improves survival in mice. *Cancer Res* 2003;63:2079–87.
16. Stoeltzing O, Liu WB, Reinmuth N, Fan F, Parry GC, Parikh AA, McCarty MF, Bucana CD, Mazar AP, Ellis LM. Inhibition of integrin $\alpha_5\beta_1$ function with a small peptide (ATN-161) plus continuous 5-FU infusion reduces colorectal liver metastases and improves survival in mice. *Int J Cancer* 2003;104:496–503.
17. Lunevicius R, Nakanishi H, Ito S, Kozaki K, Kato T, Tatematsu M, Yasui K. Clinicopathological significance of fibrotic capsule formation around liver metastasis from colorectal cancer. *J Cancer Res Clin Oncol* 2001;127:193–9.
18. Okano K, Yamamoto J, Kosuge T, Yamamoto S, Sakamoto M, Nakanishi Y, Hirohashi S. Fibrous pseudocapsule of metastatic liver tumors from colorectal carcinoma—clinicopathologic study of 152 first resection cases. *Cancer* 2000;89:267–75.
19. Olaso E, Salado C, Egilegor E, Gutierrez V, Santisteban A, Sancho-Bru P, Friedman SL, Vidal-Vanaclocha F. Proangiogenic role of tumor-activated hepatic stellate cells in experimental melanoma metastasis. *Hepatology* 2003;37:674–85.
20. Gabbiani G. The myofibroblast in wound healing and fibrocontractive diseases. *J Pathol* 2003;200:500–3.
21. Hewitt RE, Powe DG, Holland CM, Gray T, Turner DR. Apparent fusion of basement membranes in colorectal carcinoma. *Int J Cancer* 1992;50:20–5.

assert but, rather, we referred to the substantial evidence supporting that theory [reviewed in (3,4)]. Secondly, while the specific epidemiologic study (5) that Jacobson et al. cited did identify some positive associations between some use of artificial sweeteners (AS) and bladder cancer in several subgroups, the authors concluded "... that past AS use has had a minimal effect, if any, on bladder cancer rates. We also conclude that the positive associations in this study do not by themselves establish a causal link between AS use and bladder cancer." Moreover, it should be noted that the authors did not distinguish between saccharin and cyclamates in the study (5) when recording their data on exposure of subjects to artificial sweeteners. Thus, the study that Jacobson et al. cite as being consistent with animal studies demonstrating the carcinogenicity of saccharin in fact supports our statement in the editorial that there is no conclusive epidemiologic data on the effect of saccharin on human bladder cancer incidence.

In addition to these points of disagreement with the comments of Jacobson et al., I would also bring to their attention that the point of the editorial was to criticize current dependence on the use of seemingly inappropriate animal models and/or invalid experimental designs in animal studies to identify potential hazards in humans, not to pass judgment on the role of saccharin as a human carcinogen. In view of the flaws in the experimental design of the study reported by Takayama et al. (2), we were simply using the case of saccharin to reinforce the validity of our argument. To date, animal models have not provided substantially useful information on the mechanisms of action of saccharin in humans, and they have not been successful in proving definitively whether saccharin is indeed a cancer risk for humans.

It appears that Jacobson et al. have missed our point about the need for better risk assessment models that rely more on human data. Rather, they seem to have misinterpreted the editorial as a declaration that saccharin is not a carcinogen in humans. Furthermore, given the points of the editorial, it is unclear how Dr. Squire's past affiliation with the International Life Sciences Institute

or his independent consulting activities with the Calorie Control Council bear any relevance upon its content. If the intent of Jacobson et al. is to protect the health of the public, their efforts would be better spent on encouraging the Food and Drug Administration and the National Toxicology Program to expand their attempts to develop and implement more reliable testing strategies.

JOANNE ZURLO

References

- (1) Zurlo J, Squire RA. Is saccharin safe? Animal testing revisited [editorial]. *J Natl Cancer Inst* 1998;90:2-3.
- (2) Takayama S, Sieber SM, Adamson RH, Thorgeirsson UP, Dalgard DW, Arnold LL, et al. Long-term feeding of sodium saccharin to nonhuman primates: implications for urinary tract cancer. *J Natl Cancer Inst* 1998;90:19-25.
- (3) Whysner J, Williams GM. Saccharin mechanistic data and risk assessment: urine composition, enhanced cell proliferation, and tumor promotion. *Pharmacol Ther* 1996;71:225-52.
- (4) Ellwein LB, Cohen SM. The health risks of saccharin revisited. *Crit Rev Toxicol* 1990;20:311-26.
- (5) Hoover RN, Strasser PH. Artificial sweeteners and human bladder cancer. Preliminary results. *Lancet* 1980;1:837-40.

Notes

Affiliations of author: J. Zurlo, Center for Alternatives to Animal Testing and Department of Environmental Health Sciences, The Johns Hopkins School of Hygiene and Public Health, Baltimore, MD.

Correspondence to: Joanne Zurlo, Ph.D., The Johns Hopkins Center for Alternatives to Animal Testing, 111 Market Place, Suite 840, Baltimore, MD 21202-6709. E-mail: jzurlo@caat.spharbor.jhu.edu

Blood Supply of Metastatic Hepatic Tumors: Suggestions for Improved Delivery of Chemotherapeutic Agents

On the basis of the results of various multicenter trials, we have learned that the regional chemotherapy of liver metastases of colon cancer is much superior to the systemic chemotherapy (1) and is currently accepted as an alternative strategy to control tumor progression. However, only a limited improvement is observed so far in hepatic arterial infusion technique to make this route of che-

motherapy even more effective (2). In the protocols currently in use, the chemotherapeutic agent(s) (mostly 5-fluorouracil [5-FU] and its derivatives) are administered continuously into the hepatic artery (1). This mode of delivery is based upon early reports suggesting that liver tumors primarily receive blood supply via hepatic artery (3). This theory is now held as a dogma and perhaps, as we believe, is limiting the efforts to improve the efficiency of the regional chemotherapy for the treatment of liver metastases.

Extensive experimental evidence is now available which enables us to re-evaluate the idea of arterial blood supply to hepatic metastases. Several groups in the past two decades, e.g., in Sweden (4), Germany (5), Hungary (6) and Japan (7), have provided experimental evidence to suggest that primary as well as metastatic tumors in the liver receive blood supply from both the hepatic artery and the portal vein. The mixed blood is delivered by deeply invading vessels originating from hepatic sinusoids (6,7). In fact, in certain tumor types, the portal vein is the predominant supplier of the blood to the tumor nodule (6). Experimental studies have also indicated that, after the occlusion of the hepatic artery, the therapy of recurring tumor metastases can be developed from unaffected peripheral area(s) including the neighboring sinusoids, which predominantly receive their blood supply (at least 75%) from the portal vein. Such results can be expected because it is now well understood that new vessels can originate from venules during angiogenesis.

We believe that the time has come for scientists and clinicians to reconsider the old dogma and redesign the methodology of regional chemotherapy of liver metastases. The new approach must be based on a strategy that allows delivery of the therapeutic agent(s) via both the hepatic artery and portal vein. The improved design can permit the accumulation of the drug in the tumor irrespective of the actual route of the blood supply available to the individual tumor nodule. The devices and methodology for arterial delivery are already available in the form of totally implantable pumps, hepatic arterial catheters, or implantable percutaneous subclavian arterial cath-

eters (1). Any one of these devices can be combined with the transjugular intrahepatic portal vein catheter technique. This hypothesis seems to us worthy of testing in clinical trials.

SÁNDOR PAKU
GYÖRGY BODOKY
PÉTER KUPCSULIK
JÖZSEF TÍMÁR

References

- (1) Daly JM, Kemeny NE. Chapter 50.2 Treatment of metastatic cancer. In: Cancer, principles and practice of oncology, 5th edition, volume 2 eds. DeVita VT, Hellman S, Rosenberg SA, Philadelphia: Lippincott-Raven Publ. Co, 1997:2551-70.
- (2) Harmantas A, Rotstein LE, Langer B. Regional versus systemic chemotherapy in the treatment of colorectal carcinoma metastatic to the liver. Is there a survival difference? Meta-analysis of the published literature. *Cancer* 1996;78:1639-45.
- (3) Breedis C, Young C. The blood supply of neoplasms in the liver. *Am J Pathol* 1954;30:969-75.
- (4) Lin G, Landerquist A, Hagerstrand I, Boijesen E. Postmortem examination of the blood supply and vascular pattern of small liver metastases in man. *Surgery* 1984;96:517-26.
- (5) Haugeberg G, Strohmeyer T, Lierse W, Bocker W. The vascularization of liver metastases. Histological investigation of gelatine-injected liver specimens with special regard to the vascularization of micrometastases. *J Cancer Res Clin Oncol* 1988;114:415-9.
- (6) Paku S, Lapis K. Morphological aspects of angiogenesis in experimental liver metastases. *Am J Pathol* 1993;143:926-36.
- (7) Terayama N, Terada T, Nakanuma Y. A morphometric and immunohistochemical study on angiogenesis of human metastatic carcinomas of the liver. *Hepatology* 1996;24:816-9.

Notes

Affiliations of authors: S. Paku, Research Unit of Molecular Pathology, Joint Research Organisation of the Hungarian Academy of Sciences and Semmelweis University of Medicine, Budapest; G. Bodoki, Department of Chemotherapy, National Institute of Oncology, Budapest; P. Kupcsulik (1st Department of Surgery), J. Timár (1st Institute of Pathology and Experimental Cancer Research), Semmelweis University of Medicine, Budapest, Hungary.

Correspondence to: József Timár MD., Ph.D., D.Sc.; 1st Institute of Pathology and Experimental Cancer Research, Semmelweis University of Medicine, Budapest, VIII. Ullői út 26., H-1085 Hungary. E-mail: jtimar@korb1.sote.hu

Re: Alcohol Dehydrogenase 3 Genotype and Risk of Oral Cavity and Pharyngeal Cancers

Recently, Harty et al. (1) reported in the *Journal* that alcohol dehydrogenase type 3 (ADH₃), a polymorphic enzyme that metabolizes ethanol to acetaldehyde, modified the risk of development of oropharyngeal cancers in a cohort of Puerto Ricans who had high levels of alcohol consumption.

We investigated whether these findings could be reproduced in another population, from part of a hospital-based, case-control study performed in France among Caucasians (2). In our study, only case subjects (n = 165) with histologically confirmed squamous carcinoma of the oral cavity and pharynx were included. Control subjects (n = 234) were individuals without a history of cancer and were frequency matched for sex, age, and hospital.

The main conditions diagnosed among control subjects were rheumatologic (n = 74; 32%), infectious and parasitic (n = 24; 10%), respiratory (n = 21; 9%), cardiovascular (n = 19; 8%), and digestive (n = 14; 7%) diseases as well as traumatic injuries (n = 12; 5%). Severe liver diseases were exclusion criteria for both case subjects and control subjects.

ADH₃ genotypes were determined with the use of a polymerase chain re-

action DNA amplification assay (3) for 68 patients with oral cavity cancer, 51 patients with pharyngeal cancer, and 167 control subjects. Genotype determinations were performed by investigators who were blinded to the source of the specimens.

Lifetime use of tobacco (cigarettes, cigars, or pipe) and alcohol consumption were recorded during a personal interview conducted by seven trained interviewers. Alcohol beverages were converted into grams of pure ethanol, and the average daily consumption was calculated by dividing the cumulative lifetime consumption by the overall duration of drinking. Odds ratios (ORs) were calculated by unconditional logistic regression, including sex, age, and smoking as confounding factors. The interaction between ADH₃ genotype (ADH₃¹⁻¹ versus ADH₃¹⁻² or ADH₃²⁻²) and levels of daily alcohol consumption was studied to test the equality of the effect of ADH₃ genotypes across the drinking levels (4). To this end, the average daily consumption of alcohol was divided according to the approximated quartile distribution observed among the control subjects.

The risk of oropharyngeal cancer associated with the ADH₃¹⁻¹ genotype, compared with the ADH₃¹⁻² and the ADH₃²⁻² genotypes combined, was slightly, although not significantly, increased (OR = 1.4; 95% confidence interval = 0.8-2.3) (Table 1). The risk of cancer rose significantly with increased daily consumption of alcohol (χ^2 two-

Table 1. Number of case and control subjects* and odds ratios† (95% confidence intervals) of oropharyngeal cancer according to ADH₃ genotypes and alcohol consumption‡

ADH ₃ genotype	Average consumption of ethanol§				Total§,
	≤40 g/day	41-80 g/day	81-120 g/day	>120 g/day	
ADH ₃ ¹⁻² and ADH ₃ ²⁻²	1 (referent) 6/26	2.3 (0.8-7.0) 18/35	3.4 (1.0-10.9) 13/19	5.8 (1.9-17.6) 29/22	1 (referent) 66/102
ADH ₃ ¹⁻¹	1.7 (0.5-5.5) 10/23	3.4 (1.1-10.9) 14/19	5.3 (1.3-21.6) 8/7	6.3 (1.8-21.4) 17/11	1.4 (0.8-2.3) 49/60
Total¶	1 (referent) 16/49	2.2 (1.0-4.6) 32/54	3.2 (1.3-7.5) 21/26	4.8 (2.2-10.7) 46/33	

*Data on smoking (cigarettes, cigars, pipe) and/or alcohol exposure were missing for four case subjects and five control subjects.

†Odds ratios are adjusted for sex, age, and exposure to smoking (cigarettes, cigars, or pipe).

‡Interaction test between ADH₃ genotypes and levels of alcohol consumption: χ^2 two-sided test for homogeneity = 0.4 for 3 degrees of freedom, *P* = 0.94.

§Values in columns for each group = top line: odds ratio (95% confidence interval); bottom line: number of case subjects/number of control subjects.

||Also adjusted for daily consumption of ethanol.

¶Also adjusted for ADH₃ genotype.

Tumorigenesis and Neoplastic Progression

Development of Arterial Blood Supply in Experimental Liver Metastases

Katalin Dezső,* Edina Bugyik,* Veronika Papp,*
Viktória László,* Balázs Döme,^{†‡} József Tóvári,[†]
József Tímár,[§] Péter Nagy,* and Sándor Paku*

From the First Institute of Pathology and Experimental Cancer Research,* and the 2nd Department of Pathology,[§] Semmelweis University, Budapest, Hungary; the Department of Tumor Biology,[†] National Koranyi Institute of Pulmonology, Budapest, Hungary; and the Department of Cardio-Thoracic Surgery,[‡] Medical University of Vienna, Vienna, Austria

In this study, we present a mechanism for the development of arterial blood supply in experimental liver metastases. To analyze the arterIALIZATION process of experimental liver metastases, we elucidated a few key questions regarding the blood supply of hepatic lobules in mice. The microvasculature of the mouse liver is characterized by numerous arteriportal anastomoses and arterial terminations at the base of the lobules. These terminations supply one hepatic microcirculatory subunit per lobule, which we call an arterial hepatic microcirculatory subunit (aHMS). The process of arterIALIZATION can be divided into the following steps: 1) distortion of the aHMS by metastasis; 2) initial fusion of the sinusoids of the aHMS at the tumor parenchyma interface; 3) fusion of the sinusoids located at the base of the aHMSs, which leads to the disruption of the vascular sphincter (burst pipe); 4) incorporation of the dilated artery and the fused sinusoids into the tumor; and 5) further development of the tumor vasculature (arterial tree) by proliferation, remodeling, and continuous incorporation of fused sinusoids at the tumor–parenchyma interface. This process leads to the inevitable arterIALIZATION of liver metastases above the 2000- to 2500- μm size, regardless of the origin and growth pattern of the tumor. (*Am J Pathol* 2009, 175:835–843; DOI: 10.2353/ajpath.2009.090095)

It is widely accepted that hepatic metastases and tumors are predominantly supplied by arterial blood, a notion that serves as the basis for hepatic arterial chemotherapy and chemoembolization.^{1–7} The most cited article on this

field dates back to the 1950s.¹ Since then numerous papers have been published using human and experimental materials and different methods such as corrosion casting, confocal and electron microscopy, angiography, radiolabeled microspheres, and *in vivo* microscopy, have been used to study the blood supply of liver metastases.^{2–16} A large proportion of these articles have confirmed the original observation of Breedis and Young,¹ but no mechanism for the development of the arterial blood supply in metastases has ever been presented.^{2–7} On the other hand, numerous papers, including ours, have emphasized the contribution of the portal vein, either directly or through the sinusoids in the blood supply of hepatic metastases.^{8–14} This apparent contradiction might result from the observed continuity of the sinusoidal with the tumor vasculature and the presumption that blood flows in an “outside-in” direction from the sinusoids toward the tumor vasculature. Most of the studies dealing with the blood supply of metastases have neglected the importance of arteriportal anastomoses and other interspecies differences in the hepatic microcirculation, which could lead to seriously biased results. According to the observations of Yamamoto et al¹⁵ there are extensive arteriportal anastomoses throughout the vascular tree in rats, whereas a separate arterial and portal tree, without direct arteriportal communication, can be observed in hamster and human liver. Opinions about the presence of arteriportal anastomoses in mice are controversial^{10,16}; therefore, we have addressed this question first.

The classic lobule can be divided into several conical hepatic microcirculatory subunits (HMSs) supplied by a single inlet portal venule. Hepatic arterioles terminate either on the inlet venules or directly on sinusoids. The

Supported by the National Science Found of Hungary (grant NK73119) and by the Hungarian Medical Research Council (grant 383/2006). Balázs Döme is a recipient of the Bolyai Janos Scholarship of the Hungarian Academy of Sciences. Jozsef Tovari is a recipient of the Eotvos Hungarian State Fellowship.

Accepted for publication April 21, 2009.

Supplemental material for this article can be found on <http://ajp.amjpathol.org>.

Address reprint requests to Sándor Paku, Ph.D., First Institute of Pathology and Experimental Cancer Research, Semmelweis University, 1085 Üllői út 26, Budapest, Hungary. E-mail: paku@korb1.sote.hu.

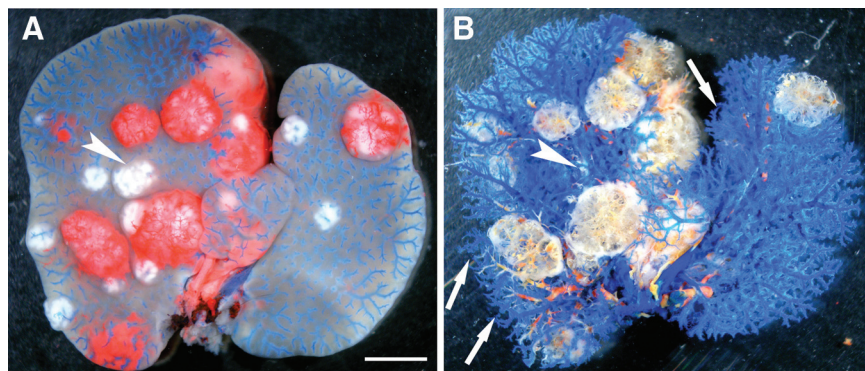


Figure 1. A: Liver lobes after the casting procedure containing arterial (red) and mixed blood (white) metastases of the C38 tumor line. The blue resin fills only the terminal portal venules. **B:** The same lobes after corrosion. **Arrows** point to the hollow spaces of metastases not having arterial blood supply. **Arrowhead** points to a metastasis of which only the base was filled by the red resin; therefore its arterial connection was undetectable on the uncorroded specimen (**arrowhead** on **A**). Scale bar = 3 mm.

number of these terminations within a lobule is species-dependent. The blood flow through the inlet venules and terminal arterioles is regulated by sphincters.¹⁷ The most detailed studies on microcirculation of the liver and vessel architecture of liver metastases were performed by corrosion casting. However, in these studies the livers were completely filled with uncolored resin, which made analyzing the three-dimensional organization of the deep interlobular vessels difficult.^{10,14,15}

In the present study, we used a two color corrosion casting technique to analyze the blood supply in liver metastases of experimental tumors in mice. A special filling method was used to prevent the mixing of the "portal and arterial resin" upstream of the hepatic sinusoids. This technique enabled us to analyze separately the contribution of the two vascular systems to the blood supply of liver metastases and to establish the steps of the arterialization process.

Materials and Methods

Animals and Tumor Lines

The C38 colorectal carcinoma line was maintained by serial subcutaneous transplantations in C57Bl/6 mice, as described earlier.¹³ Liver metastases were produced by injecting 2×10^4 tumor cells into the spleen of C57Bl/6 mice. Vascular casting was performed 15 to 18 days following tumor cell injection.

The highly metastatic Lewis lung carcinoma (3LL-HH) tumor line was maintained by serial intrasplenic transplantations of tumor cells obtained from liver metastases. Single cell suspensions were prepared from 14-day-old 3LL-HH liver metastases, as described earlier.¹² 10^3 tumor cells were injected into the spleen of C57Bl/6 mice. Vascular casting was performed 12 days following tumor cell injection.

A2058 human melanoma cells were cultured in RPMI-1640 supplemented with 10% fetal bovine serum (Sigma Chemical Co., St. Louis, MO). To produce liver metastases, 2×10^4 cells were injected into the spleen of anesthetized male SCID mice. Vascular casting was performed 28 to 33 days following tumor cell injection.

Vascular Corrosion Casting

A two-color corrosion casting procedure was used to analyze the arterialization of liver metastases. Mice were anesthetized and a ligature was placed onto the vena cava just above the renal veins to prevent retrograde filling of the liver. The portal vein was cannulated (22G, Braun Melsungen AG, Melsungen, Germany) and secured with a tie; the chest was opened and the vascular system was flushed through the left ventricle with PBS containing heparin. When the effluent was clear, the thoracic aorta was cannulated (22G, Braun Melsungen AG, Melsungen, Germany). To remove air from this cannula a ligature was placed onto the aorta above the bifurcation into the iliac arteries. The aortic cannula was filled retrograde with PBS through a 30G needle connected to a syringe inserted into the abdominal aorta below the ligature. After filling, the ligature was tightened. The ligature on the vena cava was also tightened. Blue casting medium (Mercox 2-CL, Ladd Research, Williston, VT) was injected through the portal vein. The injection was monitored under a dissecting microscope and stopped when the resin reached the sinusoids (~ 0.2 ml resin) (Figure 1A and B). The blue resin was allowed to become thick and 1 ml of red casting medium was injected through the thoracic aorta. The filling of the portal system with resin was necessary to prevent the flow of the red resin through arteriportal anastomoses (described in Results) into the portal system and subsequently into the sinusoids and metastases resulting in false observations. However, all routes were left open where the arterial system was in direct connection with the sinusoids and metastases.

Altogether 53 animals were used for corrosion casting: 10 control, and 16, 15, and 12 mice bearing C38, 3LL-HH, and A2058 metastases, respectively.

Determination of the Percentage of Arterial Metastases and the Size of the Metastases

After the injection of the blue and red resins into the portal and arterial system, the livers were removed and cut in lobes; then every lobe was photographed from each side (Olympus SZ61 dissecting microscope, Olympus 7070 or DP 50 camera, Olympus Japan). Once the resin was

cured completely the lobes were placed overnight in 35% KOH at 60°C. The casts were washed in running tap water and placed in distilled water. Again, every lobe was photographed under water from each side. Metastases on the surface of uncorroded specimens were counted and their diameters were measured (Quick Photo Micro, Olympus, Japan). Most of the arterial metastases were completely filled with red resin, but some were only partially filled. In this case, the resin was not always visible on the surface of the uncorroded specimens. Therefore, the determination of the origin of the blood supply was performed by comparing the uncorroded and corroded specimens (Figure 1, A and B). On the corroded specimens, metastases filled with any amount of the red resin through an artery directly connected to the metastasis were designated as "arterial." Metastases not having an arterial blood supply appeared on the corroded specimens as holes. In some cases the red color turned white either because the color particles were filtered out or the color was lost during the corrosion procedure. To determine the size of the metastases and the origin of the blood supply, 484, 907, and 485 metastases were analyzed from the C38, 3LL-HH, and A2058 tumor lines respectively.

Determination of the Diameter of the Arteries and the Accompanying Portal Veins

Livers from four control animals were used to determine normal porto-arterial diameter ratio in 167 randomly chosen branch pairs originating from seven different orders of the vascular tree of the mouse liver. Altogether 729 arterial metastases were isolated (252, 305, 172; C38, 3LL-HH, A2058), under the dissecting microscope using fine forceps. Each metastasis was photographed under water, and if metastases were supplied by one arterial branch, the diameter of the portal vein and the supplying artery was determined at the entry into the metastases. The diameter of the portal and arterial branches were measured ~1000 μm upstream from the metastasis wherever possible. The size of the completely filled metastases was easily determined by measuring the extension of the structure filled with the red resin. With incompletely filled metastases, the extension of the hollow space left by the metastases in the portal tree was measured.

Determination of the Rate of Cell Proliferation in the Arteries Supplying the Metastases

This procedure was performed only with the C38 tumor, because this tumor line produced a large proportion of metastases with centrally localized (described below), easily discernible arteries. 5-Bromo-2'-deoxyuridine (BrdU) labeling and tissue processing, with the exception of vascular casting were performed as described above. Large metastases (>2 mm, eight pieces) located at the periphery of the liver were chosen and cut perpendicular to the flat surface of the lobe. The upper half of the metastasis was cut away. Subsequently, serial sections were cut until the artery was discernible on

toluidine blue stained cryosections. Further 6 to 10 serial sections were cut and double labeling was performed for BrdU (Becton Dickinson, San Jose, CA) and NG2 proteoglycan (Chemicon, Billerica, MA). Nuclei were counterstained by 4,6-diamidino-2-phenylindole (Sigma Chemical Co., St. Louis, MO). BrdU labeled and the total number of arterial wall cells (endothelial and smooth muscle cells, >2000) was determined, using a $\times 40$ or $\times 60$ objective (Nikon TE 300 fluorescent microscope).

Determination of the Proliferation Rate of Tumor Cells in the Arterial and Mixed Blood Metastases

BrdU labeling of proliferating tumor cells was performed as follows. One hour before the above described vascular casting was performed, 200 mg/kg BrdU (Sigma Chemical Co., St. Louis, MO) was injected intraperitoneally. Following the casting procedure livers were removed and frozen. Cryostat sections (10 μm) were fixed in methanol (-20°C) treated with 2 N HCl (15 minutes, 20°C), anti-BrdU antibody (dilution 1:50, Cat. No: 347580, Becton-Dickinson, San Jose, CA), and fluorescent secondary antibody (Jackson ImmunoResearch Inc., West Grove, PA). Nuclei were counterstained by TOTO3 (Molecular Probes, Carlsbad, CA) or 4,6-diamidino-2-phenylindole. The number of BrdU-labeled and total number of tumor cells were determined using micrographs captured by the Bio-Rad MRC-1024 (Bio-Rad, Richmond, CA) confocal microscope (four animals for each tumor, three to five metastases from each animal). Counting was performed using the morphometry system described above. Blood supply of the metastases was identified according to the autofluorescence of the dye in the resin. Arterial metastases had a strong red fluorescence (Ex568/Em580 \pm 32). In contrast, the mixed blood metastases were dark, or when filled with blue resin, had weak green fluorescence (Ex488/Em522 \pm 32).

Scanning Electron Microscopy

Isolated vascular trees and metastases (over 240 specimens) were glued wet on metal stubs. After drying, the samples were coated with gold by a HBA 1 high-vacuum metal evaporator (Carl Zeiss, Jena, Germany). Observations were made using a Hitachi S-2360 N scanning electron microscope (Hitachi, Tokyo, Japan) at 15–25 KV accelerating voltage.

Results

Microvascular Architecture of the Normal Mouse Liver

Arterioportal anastomoses were observed throughout the hepatic vasculature. The arterial blood entered the portal veins either directly or through the peribiliary plexus (Figure 2, A and B). Arteries run in the vicinity of the peribiliary plexus. From the peribiliary plexus blood was also shed directly into sinusoids whose inlets were regularly spaced

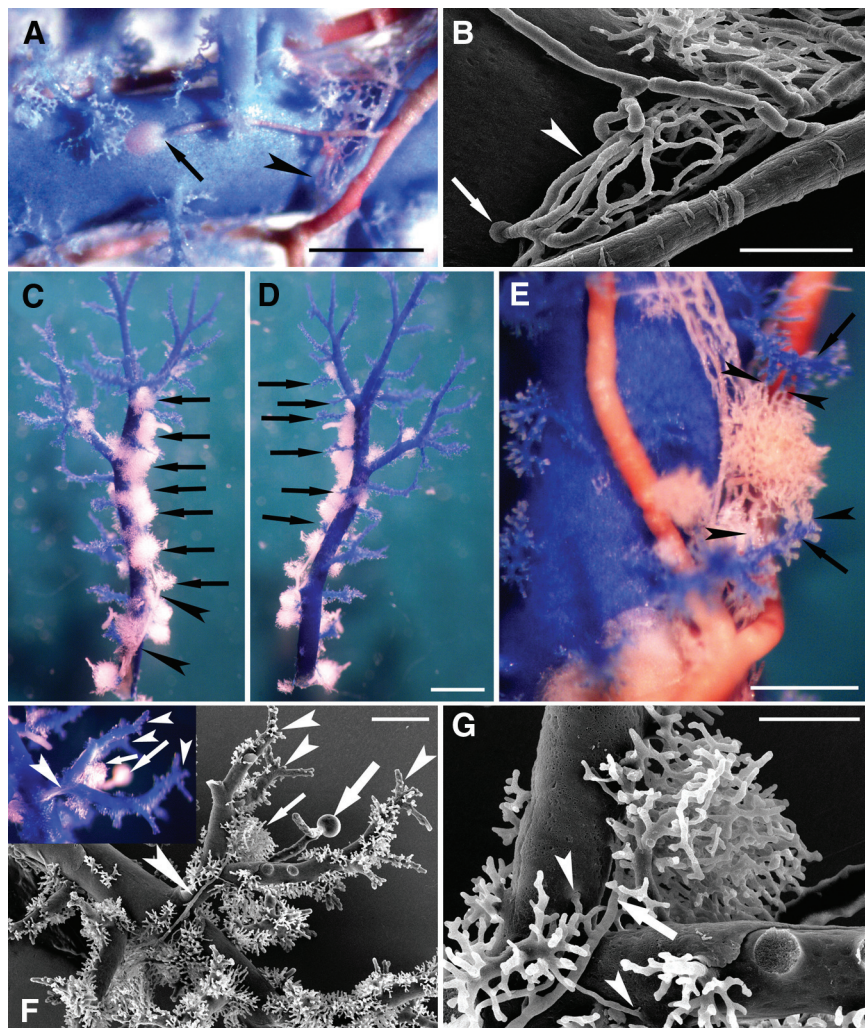


Figure 2. Normal mouse liver. **A:** Direct arterioportal anastomosis (**arrow**) on a large trunk of the portal tree. A small amount of the red resin is spread on the previously hardened blue resin. Scale bar = 1 mm. **B:** Detail of **A** (**arrowhead** in **A**) viewed under the scanning electron microscope. Anastomosis between the peribiliary plexus and the portal vessel. Numerous capillaries of the peribiliary plexus (**arrowhead**) joined into one vessel that enters the large trunk of the portal vein (**arrow**). Scale bar = 300 μm . **C** and **D:** Detail of a vascular tree of the liver viewed from opposite directions. The portal vein is filled with blue resin. Scale bar for **C,D** = 500 μm . **C:** Shows the side where the artery (**arrowhead**) is running. Note the numerous aHMSs (**arrows**) spaced regularly between terminal portal venules (marked by **arrows** on **D**) along the portal vein. Each space between the terminal portal venules corresponds to one lobule. **D:** No aHMSs are visible on the other side of the portal vein. **E:** Light micrograph of a single aHMS located above the peribiliary plexus and between terminal portal venules (**arrows**) at the base of the lobule. The space between the terminal portal venules determines the extension of the lobule. The red resin, which fills the sinusoids of the aHMS is in connection (**arrowheads**) with blue resin of the terminal portal venules, showing that the aHMS is part of the lobule. Scale bar = 200 μm . **F,G:** An arterial HMS at the periphery of the vascular tree of the liver, SEM images. **F:** The arteriole (**large arrowhead**) runs up on the portal venule and terminates in an aHMS at the base of the lobule (**small arrowhead**). The lobule is defined by the tree terminal portal venules (**small arrowheads**). Note that the red resin (**inset**) is present in the central venule (**large arrow**). The **inset** shows light micrograph of the same area. Scale bar = 200 μm . **G:** High power micrograph of the aHMS shown on Figure 2F. The main branch of the arteriole terminates in the aHMS (**arrow**). Smaller branches form direct anastomoses (**arrowheads**) with the portal venule. Scale bar = 90 μm .

between terminal portal venules at the base of the lobules (Figure 2, C–E). Short arterio-sinusoidal twigs were also observed in this region. Since the blood was shed from the peribiliary plexus into the closest lobules, asymmetry could be observed in the distribution of the arterial blood around larger portal tracts (Figure 2, C and D). Other lobules, especially those situated on the opposite side (according to the artery) of the portal tract, were supplied by arterioles (marginal branches) running around the large portal tract ending either at the base of the terminal portal venules forming arterioportal anastomoses or running up on the portal venules. These latter arterioles terminated on sinusoids at the base of lobules (Figure 2, F and G). Similar terminations were observed at the peripheral areas of the vascular tree. Usually one or two terminations were detectable per lobule. Since the sinusoids were intentionally not filled through the portal system, only that part of the lobule was visible, which was also fed directly by the arterial system. The resin entering the lobules through the arterioles formed conical structures that corresponded to the HMSs.¹⁷ To distinguish these HMSs from the others supplied exclusively by portal inlet venules, we called this subunit arterial microcirculatory subunit (aHMS). However it should be kept in

mind that this subunit also drained mixed blood. No aHMSs were observed at the surface of the liver.

The Arterialization Process of Metastases

The Rate of Arterialization

Three different tumor lines that frequently metastasize into the liver, and exhibit different growth patterns, were used for the experiments. The highly invasive 3LL-HH tumor line is characterized by replacement type growth, whereas the C38 colon carcinoma shows pushing type of growth and the A2058 human melanoma line has an intermediate growth pattern.^{12,13,18} The earliest arterialization of the metastases was observed in the case of the highly invasive Lewis lung tumor line (Figure 3). Forty percent of the metastases had well developed arterial blood supply below the diameter of 800 μm . The other two lines, especially the differentiated colon carcinoma, acquired their arterial blood supply at a considerably slower rate. Only half of the metastases of the colon carcinoma were arterialized at the size of ~ 1500 μm . However, the arterialization process accelerated later and almost all C38 metastases had arterial blood supply at the diameter of

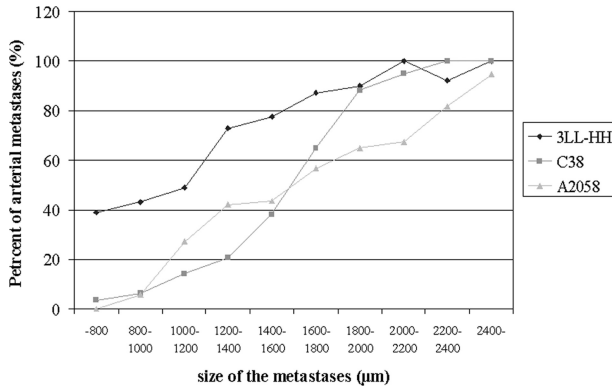


Figure 3. Percentage of arterial metastases in relation to metastasis size.

2000 μm , similar to the fast growing Lewis lung carcinoma. For the slow growing human melanoma, this value was about 2500 μm .

Sequential Events of the Arterialization

Small avascular metastases and metastases supplied with mixed blood through the sinusoids generally ap-

peared on the corrosion specimens as holes, since the liver vasculature through the portal system was filled only to the sinusoids (Figure 1, A and B). However, micrometastases which early invaded the area of terminal portal venules were readily filled through the portal system and stained blue (Figure 4A and B). The majority of these metastases were not in contact with aHMSs. The process of arterialization was deduced mostly by the examination of the well-organized C38 metastases allowing a clear view of the intra- and peritumoral vessels. The first step of the arterialization process was the distortion of the aHMSs by the metastases (Figure 4C), ie, the spherical metastasis impressed into the aHMS while the sinusoidal structure of the aHMS remained intact. This was followed by initial fusion of the sinusoids of the aHMS owing to the compression of the tumor (Figure 4, D and E). The process of sinusoidal fusion was described earlier in detail by our group for the C38 tumor line.¹³ The present corrosion casting studies confirmed these data, and demonstrated sinusoidal fusion at the periphery of the two other studied tumor types, as well. However, the extent of the fusion differed among the tumor lines. It was most pronounced around the differentiated colon tumor fol-

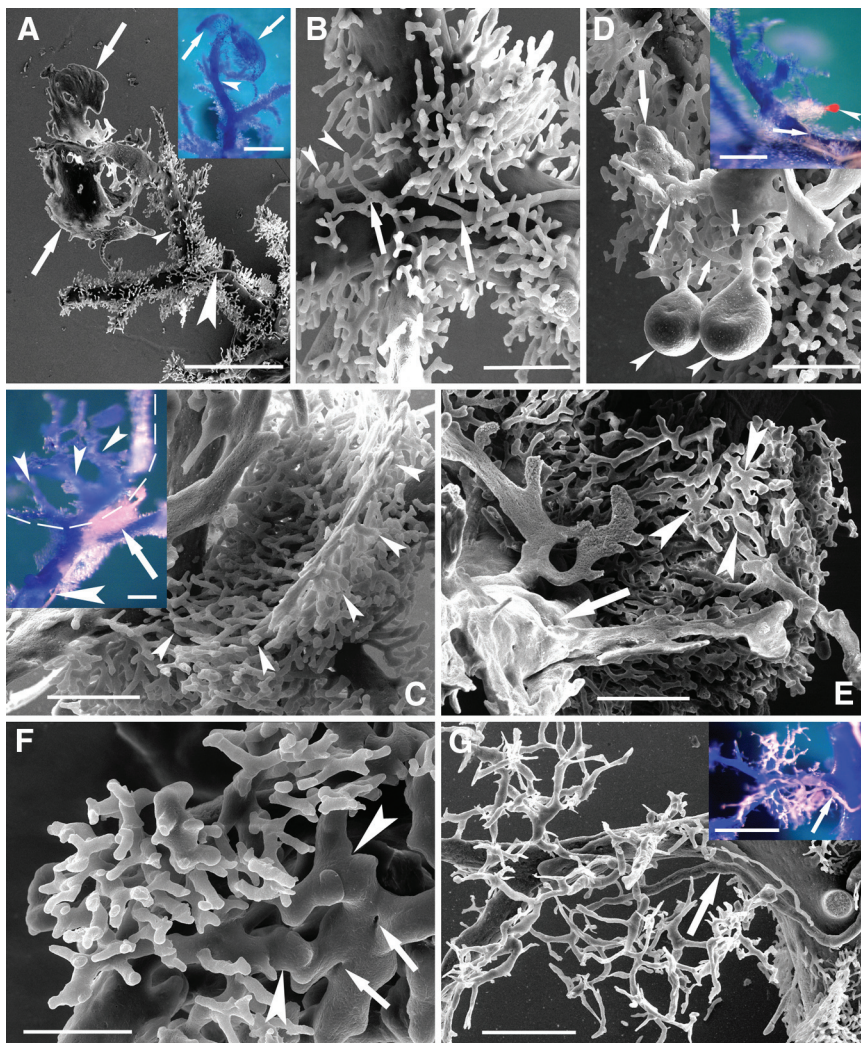


Figure 4. **A:** A C38 micrometastasis on the surface of the liver grows close to a terminal portal venule (small arrowheads). The vascular lake (arrows) at the surface of the metastasis is filled with blue resin (inset) injected through the portal vein. An arteriole (large arrowhead) is visible close to the ramification of the portal venule, which later represents the base of the lobule. The metastasis has not yet reached this region. Scale bar = 500 μm ; 500 μm (inset). **B:** Detail of **A**. The arteriole branched off (arrows) is close to the fork of the terminal portal venule. The resin hardly entered the aHMS (arrowheads). Scale bar = 90 μm . **C:** Impression of a C38 metastasis in an aHMS (small arrowheads). The sinusoids of the aHMS are nearly normal in structure. Inset shows the same aHMSs filled with red resin (arrow) at the base of the metastasis and the supplying arteriole (large arrowhead). Broken line marks the border of the metastasis. Small arrowheads point at the terminal portal venules entrapped within the metastasis. Scale bars: 100 μm ; 200 μm (inset). **D:** Compressed aHMS at the base (inset) of a C38 metastasis. Initial fusion of the sinusoids of the HMS is discernible (arrows). Other sinusoids of the aHMS are normal in structure (small arrows). On the inset the arrow points to an arteriole supplying the HMS. Drops of the resin (red dot) on the light micrograph marked by arrowhead) are present in the central venule (arrowheads). Scale bars: 90 μm ; 300 μm (inset). **E:** The "nest" of a metastasis viewed from the top (from the surface of the liver). The sinusoids of the aHMS at the base of the metastasis are partially fused (arrowheads). Arrow points at a portal vessel within the metastasis projecting toward the surface of the liver. Scale bar = 100 μm . **F:** Fusion of sinusoids in the metastasis of the 3LL-HH tumor. Large vascular lakes are not formed at the surface; instead tortuous vessels appear within the metastasis (large arrowheads). Note the impressions left by small tissue pillars (arrows) within the tumor vessels representing the last step of the fusion (reverse intussusceptive angiogenesis). The low density tortuous tumor vessels are continuous with the high density sinusoids of the surrounding liver tissue. Scale bar = 60 μm . **G:** Small A2058 metastasis. The centrally located non-dilated artery (arrow) ramifies into delicate intratumoral vessels. Scale bars: 200 μm ; 500 μm (inset).

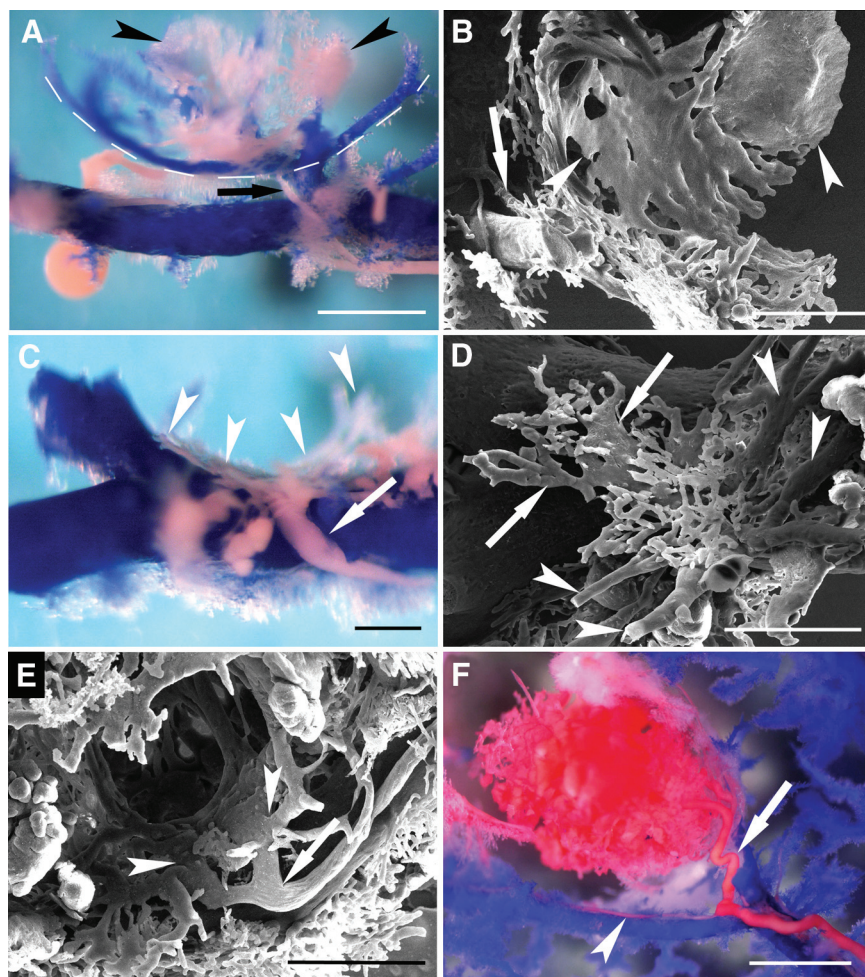


Figure 5. A,B: Formation of a vascular lake from an aHMS at surface of the metastasis of the C38 tumor line. **A:** The **arrow** points to the non-dilated arteriole feeding the severely distorted and fused aHMS (**arrowheads**). A broken line is drawn along two terminal portal venules that are pushed aside by the growing tumor mass and thereby outlines the border of the metastasis. Scale bar = 500 μm . **B:** The area marked by **arrowheads** on **A** is viewed from above by the scanning electron microscope. Extensive fusion of the sinusoids leads to vascular lake formation (**arrowheads**). The **arrow** points to the supplying arteriole. Scale bar = 200 μm . **C:** Part of an arterIALIZED C38 micrometastasis. The supplying arteriole is severely dilated (**arrow**) and ramifying into vessels, which delineate the surface (**arrowheads**) of the metastasis. The arteriole has not yet been incorporated into the metastasis. Scale bar = 100 μm . **D:** Scanning electron micrograph of the same structure shown on (**C**) viewed from above. Fused sinusoids (**arrows**) and vessels (**arrowheads**) are organized into basket-like form. Scale bar = 200 μm . **E:** ArterIALIZED C38 micrometastasis. Dilated arteriole (**arrow**) feeds the metastasis. The area where most of the branches arise (**arrowheads**) is just incorporated into the tumor but the vessels run on or close to the surface of the metastasis. The center of the metastasis is avascular. Scale bar = 200 μm . **F:** 3LL-HH metastasis supplied by a strongly dilated artery (**arrow**). There is an extreme size difference between the artery running toward the tumor and the artery accompanying the neighboring portal vein (**arrowhead**). Note that the two portal veins are about the same size. Scale bar = 1 mm.

lowed by the highly invasive 3LL-HH tumor line (Figure 4F). The sinusoidal fusion was least advanced in the neighborhood of the metastases of the human melanoma cell line, which corresponded to the delicate vessel structure of its metastases (Figure 4G, and supplemental Figure S1, A and B, at <http://ajp.amjpathol.org>). Vascularization of the metastases was initiated by the incorporation of these fused sinusoids. Extensive sinusoidal fusion in the case of the C38 colon carcinoma led to the development of vascular lakes on the surface of the metastases that were directly connected to the arterial system (Figure 5, A and B). When the fusion reached the base of the aHMS, the arterialization of the metastasis was just complete (Figure 5, C and D). The fused sinusoids, together with the supplying artery, were incorporated into the tu-

mor (Figure 5E). As the aHMSs were located at the base of the lobules, the artery entered the majority of the metastases from the hilar region.

Architecture of the Supplying Arteries

A large proportion of the metastases were supplied by one arterial branch (Table 1). However, there was a tendency, especially in the case of the A2058 tumor line, for larger tumors to acquire more supplying arterial branches (supplementary Table S1, supplementary Figure S1C at <http://ajp.amjpathol.org>). The arteries supplying the metastases became strongly dilated while the neighboring arterial branches originating from this supplying artery were generally collapsed (Figure 5F). A high proportion of the

Table 1. Percent of Metastases Supplied by the Different Number of Arterial Branches

	Percent of metastases supplied directly by one arterial branch	Percent of metastases supplied directly by two arterial branches	Percent of metastases supplied directly by three or more arterial branches	Percent of metastases supplied through the peribiliary plexus	Total number of metastases analyzed
3LL-HH	68 (n.d.)	16,5	1	14,5	294
C38	82 (50)	9	—	9	252
A2058	63 (9)	22	6	9	172

(), percent of metastases with centrally positioned arterial branch. n.d., not determined.

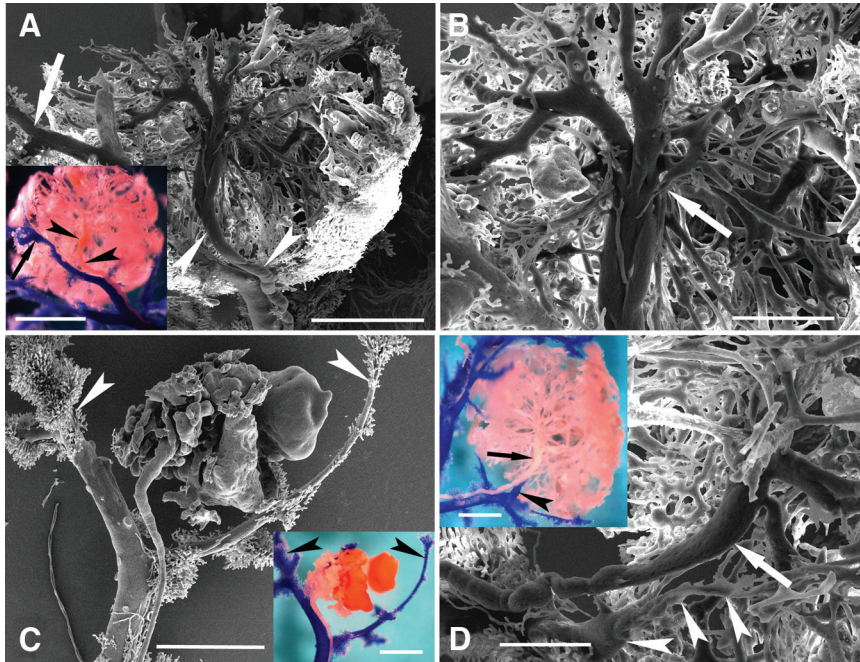


Figure 6. **A:** C38 metastasis with a well-developed central arterial tree (**black arrowheads** on the **inset**). The portal vein was pushed aside (**arrows**). No ramifications can be observed on the SEM micrograph along the trunk of the arterial tree (**white arrowheads**). Scale bars: 600 μm ; 1 mm (**inset**). **B:** Detail of **A**. Vascular branches originate from one small area of the arterial tree (**arrow**) located in the center of the metastasis. Scale bar = 300 μm . **C:** 3LL-HH metastasis. The centrally located artery dilates gradually toward the center of the metastasis where it ends in tortuous vascular lakes. The metastasis is not completely filled by the resin; its borders are defined by the portal branches (**arrowheads**). Scale bars: 600 μm ; 500 μm (**inset**). **D:** C38 metastasis with a strongly dilated funnel-like artery (**arrow**). Both the artery and the portal vein (**arrowhead**) are located centrally. The portal vein is extremely compressed obstructing the resin flow. Note that there are no ramifications along the trunk of the artery. The branching point of the artery is located in the center of the metastasis. Scale bars: 200 μm ; 500 μm (**inset**).

arterial “trees” was centrally positioned within the metastases of the C38 colon carcinoma, but this phenomenon was also observed in the metastases of the other tumor lines (Table 1, Figure 6, A–C, and supplemental Figure S1D at <http://ajp.amjpathol.org>).

The structure of the supplying artery inside the tumor, especially in the case of the C38 colon carcinoma, was unique. The diameter increased toward the center of the metastasis. No ramification could be observed along the trunk; all branches originated from a small area of this artery, which was approximately located in the center of the metastasis (Figure 6, A–D). The ratio of the diameters of the portal vein running parallel to the metastasis supplying artery dropped significantly compared with that in the control liver (supplemental Table S2, at <http://ajp.amjpathol.org>). This ratio decreased with increasing tumor size (Figure 7A). The diameter of the supplying artery increased linearly with increasing tumor size (Figure 7B). The extent of dilatation dropped rapidly upstream, but persisted to some extent up to 1 mm from the metastasis (supplemental Table S2 at <http://ajp.amjpathol.org>). The BrdU labeling index of the arterial wall cells at the base of the metastasis was $6.9 \pm 2.3\%$, suggesting that cell proliferation contributed significantly to the dilatation of the arteries. Ten to fifteen percent of the metastases were supplied with arterial blood through the peribiliary plexus (Table 1). The artery accompanying the peribiliary plexus was not directly involved in the supply of these metastases. The portal vessels in the majority of the metastases were displaced, although a portion remained central but severely compressed (Figure 6D). Rarely (<5%), the metastases were supplied by arterial blood through arteriportal anastomoses inside the tumor.

Consequences of the Arterial Blood Supply

We questioned whether the metastases acquired an arterial blood supply because they had grown bigger or whether the arterial blood supply provided a growth advantage to the metastases. There was no difference in the rate of tumor cell proliferation between metastases supplied arterially or portally (mixed blood) in two of the mouse cell lines (C38 and 3LL-HH). However, the proliferation rate was slightly but significantly increased in the arterially supplied metastases of the A2058 human melanoma cell line (Table 2, supplemental Figure S1, E and F, at <http://ajp.amjpathol.org>).

Discussion

Using three different tumor lines, we have shown that metastases more than 2000 to 2500 μm in diameter in the mouse liver inevitably become arterialized. Although the importance of arteries in nourishing metastases has long been recognized, mechanisms for the evolution of arterial blood supply have never been presented.^{1–7} Here we describe a mechanism for the arterialization of metastases in the mouse liver. This process can be divided into the following steps (Figure 8): 1) distortion of the aHMS by the metastasis; 2) initial fusion of the sinusoids of the aHMS at the tumor parenchyma interface; 3) fusion of the sinusoids located at the base of the HMS, leading to the disruption of the sphincter (burst pipe); 4) incorporation of the dilated artery and the fused sinusoids; and 5) further development of the tumor vasculature (arterial tree) by proliferation, remodeling, and continuous incorporation of fused sinusoids at the surface of the tumor.

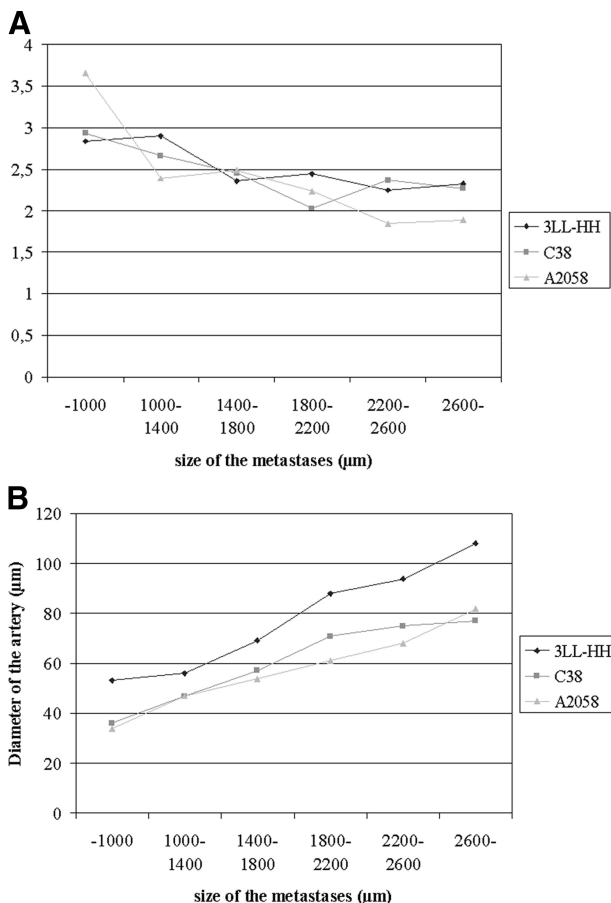


Figure 7. A: Portal vein-artery ratio in relation to metastasis size. **B:** Diameter of the supplying artery at the entry to the metastasis in relation to metastasis size.

The key element in the arterialization of the metastases is the so-called aHMS observed in the mouse liver. The situation is more complicated in the human liver, where no direct arteriportal anastomoses are present, but arteries run in the interlobular vascular septa terminating on sinusoids along the whole circumference of the lobules.^{15,17} Thereby, all HMSs are connected to arterioles, (in that sense all HMSs in the human liver are aHMSs) increasing the probability that an arteriole will be hit by a metastasis. This strongly suggests that metastases in the human liver become arterialized even earlier than in the mouse liver. Thus, arterialization takes place at the level of liver lobules. The size of a surface lobule in the mouse liver is approximately $500 \times 500 \times 600 \mu\text{m}$ (unpublished observation). However, the actual size of the arterialized metastases is considerably larger, which can be explained by the expansive growth of the tumors resulting in

Table 2. Labeling indexes of metastases supplied preferentially by arterial or portal blood

	Arterial metastases	Portal (mixed blood) metastases
3LL-HH	50,1 ± 3,7	50,7 ± 5,4 n.s.
C38	55,2 ± 1,1	55,0 ± 4,2 n.s.
A2058	38,3 ± 2,5	34,1 ± 1,9*

Mean ± SD; n.s., not significant; *, $P < 0.05$.

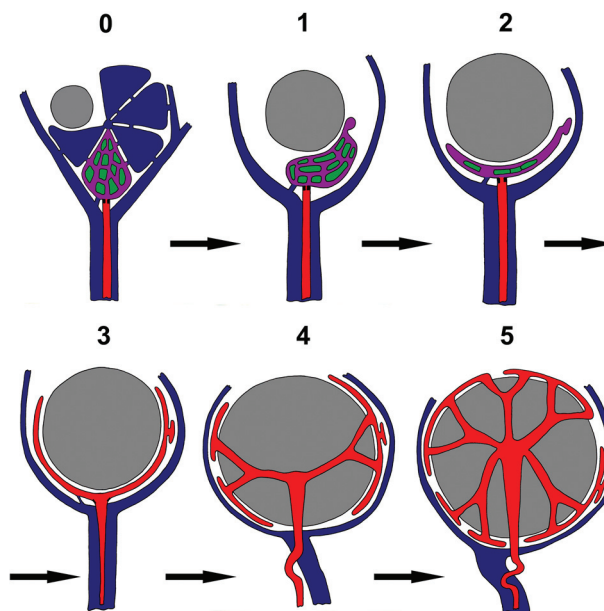


Figure 8. Schematic representation of the arterialization process in liver metastases. **Step 0:** Micrometastasis growing within the liver lobule. The arterial HMS has normal architecture. **Step 1:** Distortion of the aHMS by the metastasis. **Step 2:** Initial fusion of the sinusoids of the aHMSs at the tumor parenchyma interface. **Step 3:** Fusion of the sinusoids located at the base of the HMSs, leading to the disruption of the sphincter (burst pipe). **Step 4:** Incorporation of the dilated artery and the fused sinusoids. **Step 5:** Further development of the tumor vasculature (arterial tree) by proliferation, remodeling, and continuous incorporation of fused sinusoids at the surface of the tumor. Blue - mixed portal and arterial blood, Purple - mixed blood in the arterial HMSs, Red - arterial blood, Green - hepatocytes, Gray - tumor tissue, Black boxes - arterial sphincters.

certain displacement of bases of the surrounding aHMSs. This displacement is probably the lowest in the highly invasive rapidly growing tumor (3LL-HH), which becomes arterialized at a size closest to that of a lobulus.

Arteries enter the metastases from the hilar direction, which can explain the failure to detect direct connection between arteries and metastases in an *in vivo* microscopic study.¹⁶ The authors of the above study suggested that arterial blood entered the metastases through portal branches. Our observation contradicts this hypothesis, as in the vast majority of metastases, a separate arterial “tree” is responsible for nourishment of the metastases. The unique structure (no ramification along the trunk) of the central arterial tree suggests that no sprouting type angiogenesis takes place from this vessel and the moderate proliferation rate of cells constructing the arterial wall contributes only to the dilatation of the artery. The area of extensive ramification probably represents the original inlet of the artery into the sinusoids, modified by fusion, cell division, and incorporation.

The preferred growth of the tumors around the arteries may be related to the pressure difference between the arterial and portal systems. The low pressure portal and central veins are pushed aside by the metastasis, while the tumor grows around the firm standing, dilated, high-pressure artery. The high percentage of metastases supplied by only one artery can be explained if we view a metastasis as a burst pipe (reduced resistance owing to the dilated artery and the fused sinusoids) in the arterial system, which results

in subsequent drop in the pressure and collapse of the neighboring arteries. These arteries are then pushed away by the growing tumor preventing the development of further supplying artery branches. The observation that the A2058 human melanoma has a larger percentage of metastases supplied by more arteries may be related to the small caliber intratumoral vessels, which may cause higher resistance to blood flow through the tumor, leaving the neighboring arteries uncollapsed. From these arteries new supplying branches can develop. Larger metastases could acquire further arterial blood supply from more distant, large arterial branches where the effect of the pressure drop caused by the metastasis is not so pronounced.

The finding that metastases with an arterial blood supply had no or only slight growth advantage over metastases supplied by mixed blood suggests that metastases become arterialized as a result of their increased size. This supports the notion, that the process of arterialization is purely mechanical in nature, governed by the pressure relationships in the liver vasculature.

The significant differences in the microvascular architecture between the mouse and human livers can have other consequences besides the possible earlier arterialization of the metastases in the human liver. Since arterioles in the human liver terminate on the whole surface of the lobules, a growing metastasis can hit more arterioles simultaneously, resulting in a higher portion of metastases supplied by more arteries. This phenomenon can also reduce the number of human liver metastases having their arterial entry from the hilar direction. It is also important to note, however, that arterial connections on the surface of the metastasis might not all be functional (they will not feed the metastasis from an outside-in direction) if a dilated artery within the metastasis forces these arteries into collapse.

The observation that metastases, during their growth, develop an arterial blood supply contradicts the suggested role of sinusoids in nourishing liver metastases. The sinusoidal system is continuous with the vasculature of the tumor, but according to the frequently observed central localization of the arteries, and considering that central veins are always located outside the metastases, blood should flow in an inside-out direction. In fact, *in vivo* microscopic studies have demonstrated that fluorescent dye or microspheres could not enter the metastases when injected into the portal system, whereas following arterial delivery the fluorescence appeared first within the metastasis, and the blood drained into the surrounding sinusoids.^{6,16} Sinusoids surrounding the metastasis play no role in supplying the inner part of the metastases. They serve only as building blocks during the development of the tumor vasculature by sinusoid fusion and incorporation. However, portal vessels and sinusoids could have a role in the nourishment of the periphery of the metastases, especially when the arterial flow is blocked.

The rationale for using hepatic arterial infusion is that it can maximize the exposure of metastatic colorectal cancer cells in the liver to high target concentrations of chemotherapeutic agents by their localized infusion.¹⁹ Although our experimental results provide further theoretical background for this therapeutic approach and hepatic arterial infusion has demonstrated superior response rates compared with

systemic chemotherapeutic treatments,¹⁹ its impact on the overall survival of colorectal cancer patients with hepatic metastasis is still unclear.^{20–22} Nevertheless, our results may also serve as a theoretical basis for further research into the effects of other anticancer drugs (such as novel targeted agents) administered intra-arterially.

References

1. Breedis C, Young G: The blood supply of neoplasms in the liver. *Am J Pathol* 1954, 30:969–977
2. Archer SG, Gray BN: Vascularization of small liver metastases. *Br J Surg* 1989, 76:545–548
3. Lin G, Lunderquist A, Hägerstrand I, Boijesen E: Postmortem examination of the blood supply and vascular pattern of small liver metastases in man. *Surgery* 1984, 96:517–526
4. Ackerman NB: The blood supply of experimental liver metastases. IV Changes in vascularity with increasing tumor growth. *Surgery* 1974, 75:589–596
5. Ridge JA, Bading JR, Gelbard AS, Benua RS, Daly JM: Perfusion of colorectal hepatic metastases. Relative distribution of flow from the hepatic artery and portal vein. *Cancer* 1987, 59:1547–1553
6. Liu Y, Matsui O: Changes of intratumoral microvessels and blood perfusion during establishment of hepatic metastases in mice. *Radiology* 2007, 243:386–395
7. Healey JE: Vascular patterns in human metastatic liver tumors. *Surg Gynecol Obstet* 1965, 120:1187–1193
8. Ackerman NB: Experimental studies on the role of the portal circulation in hepatic tumor vascularity. *Cancer* 1986, 58:1653–1657
9. Haugeberg G, Strohmeyer T, Lieser W, Böcker W: The vascularization of liver metastases. Histological investigation of gelatine-injected liver specimens with special regard to the vascularization of micrometastases. *J Cancer Res Clin Oncol* 1988, 114:415–419
10. Kuruppu D, Christophi C, O'Brien PE: Microvascular architecture of hepatic metastases in a mouse model. *HPB Surg* 1997, 10:149–157
11. Terayama N, Terada T, Nakanuma Y: A morphometric and immunohistochemical study on angiogenesis of human metastatic carcinomas of the liver. *Hepatology* 1996, 24:816–819
12. Paku S, Lapis K: Morphological aspects of angiogenesis in experimental liver metastases. *Am J Pathol* 1993, 143:926–936
13. Paku S, Kopper L, Nagy P: Development of the vasculature in "pushing-type" liver metastases of an experimental colorectal cancer. *Int J Cancer* 2005, 115:893–902
14. Nikfarjam N, Muralidharan V, Malcontenti-Wilson C, Christophi C: Scanning electron microscopy study of the blood supply of human colorectal liver metastases. *EJSO* 2003, 29:856–861
15. Yamamoto K, Sherman I, Phillips MJ, Fisher MM: Three-dimensional observations of the hepatic arterial terminations in rat, hamster and human liver by scanning electron microscopy of microvascular casts. *Hepatology* 1985, 5:452–456
16. Kan Z, Ivancev K, Lunderquist A, McKuskey P, Wright KC, Wallace S, McKuskey RS: In vivo microscopy of hepatic tumors in animal models: a dynamic investigation of blood supply to hepatic metastases. *Radiology* 1993, 187:621–626
17. McCuskey RS: Morphological mechanisms for regulating blood flow through hepatic sinusoids. *Liver* 2000, 20:3–7
18. Vermeulen PB, Colpaert C, Salgado R, Royers R, Hellems H, Van Den Heuvel E, Goovaerts G, Dirix LY, Van Marck E: Liver metastases from colorectal adenocarcinomas grow in three patterns with different angiogenesis and desmoplasia. *J Pathol* 2001, 195:336–342
19. Power DG, Healey-Bird BR, Kemeny NE: Regional chemotherapy for liver limited metastatic colorectal cancer. *Clin Colorectal Cancer* 2008, 7:247–259
20. Nelson R, Freels S: Hepatic artery adjuvant chemotherapy for patients having resection or ablation of colorectal cancer metastatic to the liver. *Cochrane Database Syst Rev* 2006, 4:CD003770
21. Alberts SR, Wagman LD: Chemotherapy for colorectal cancer liver metastases. *Oncologist* 2008, 13:1063–1073
22. Mocellin S, Pilati P, Lise M, Nitti D: Meta-analysis of hepatic arterial infusion for unresectable liver metastases from colorectal cancer: the end of an era? *J Clin Oncol* 2007, 25:5649–5654



ACADEMIC
PRESS

dc 3.01.11
Available online at www.sciencedirect.com

SCIENCE @ DIRECT®

Experimental Cell Research 290 (2003) 246–253

Experimental
Cell Research

www.elsevier.com/locate/yexcr

Adhesion dynamics and cytoskeletal structure of gliding human fibrosarcoma cells: a hypothetical model of cell migration[☆]

Sándor Paku,^{a,*} József Tóvári,^b Zsolt Lörincz,^c Ferenc Timár,^a Balázs Döme,^{a,d}
László Kopper,^{a,e} Avraham Raz,^f and József Tímár^b

^a Department of Molecular Pathology, Joint Research Organization of the Hungarian Academy of Sciences and Semmelweis University, Budapest, Hungary

^b Department of Tumor Progression, National Institute of Oncology, Budapest, Hungary

^c Institute of Enzymology, Biological Research Center, Hungarian Academy of Sciences, Budapest, Hungary

^d National Koranyi Institute of TB and Pulmonology, Budapest, Hungary

^e First Institute of Pathology and Experimental Cancer Research, Semmelweis University, Budapest, Hungary

^f Metastasis Research Program, Karmanos Cancer Institute, Detroit, MI, USA

Received 7 April 2003, revised version received 10 June 2003

Abstract

During motility of fibroblast type cells on planar surfaces, adhesions are formed at the anterior of the protruding lamella, which remain stationary relative to the substrate and undergo a maturation process as the cell passes over them. Through these adhesions force is exerted, the orientation of which is parallel to the direction of the movement. Here we show that, during gliding-type motility of human tumor cells, characterized by a semicircular shape, adhesions were found at the outer rim of the cells, along the semicircle. Time-lapse microscopy of GFP-vinculin-expressing cells showed that these adhesions were constantly renewed at the cell edge and followed a curved trajectory according to the graded radial extension model. Eventually, the adhesions reached the long axis of the cell where they were retracted into the cell body. Actin cables formed arcs, with the concave face at the anterior of the lamella found to be oriented in the direction of movement. Since adhesions moved backward with respect to the cell, actin cables connected to these adhesions must continuously grow, reaching maximal size at the long axis of the cell. Contraction of the arcs is responsible for the forward movement of the cell body. © 2003 Elsevier Inc. All rights reserved.

Keywords: Human fibrosarcoma; Cell migration; Adhesion dynamics; GFP-vinculin; GRE model

Introduction

There are considerable differences in the motility behavior of different cell types. Fish epidermal keratocytes move rapidly (10–30 $\mu\text{m}/\text{min}$), practically gliding over the substrate, showing a semicircular shape, which is maintained during cell body translocation [1–4]. A kinematic description of locomotion of keratocytes was presented earlier and

termed the graded radial extension model (GRE model) [1]. This model predicts that every point along the edge of the semicircular lamella moves perpendicularly to the cell edge with a decreasing displacement toward the long axis of the cell. As a result the points of the cell edge move along a curved path with respect to the substrate.

In contrast to keratocytes, the movement of other cell types such as fibroblasts and murine tumor cells is slow (0.5–1 $\mu\text{m}/\text{min}$) and more erratic, but, as a general rule, the extension of the leading lamella is followed by cell body translocation and tail retraction [5–7].

The most striking difference between the two cell types is the direction of the exerted force during motility corresponding to the organization of the cables of the actin cytoskeleton. Actin cables show perpendicular orientation

[☆] Supplementary data associated with this article can be found at doi:10.1016/S0014-4827(03)00334-3.

* Corresponding author. First Institute of Pathology and Experimental Cancer Research, Semmelweis University, H-1085 Üllői út 26, Budapest, Hungary. Fax: +36-1-317-1074.

E-mail address: paku@korb1.sote.hu (S. Paku).

in keratocytes, while they are parallel to the direction of movement in fibroblasts [2,3,6]. It is not clearly understood how the generated forces in both cases are able to produce cell body forward movement, despite the differences in the organization of the actin cytoskeleton. In the case of keratocytes it was suggested that strong propulsive forces, present only in the wings of the cell, are canceled by adhesive traction forces and only pinching forces are detectable [8]. Others have shown that weak centripetal forces in the lamellipodium cause the cell body to be pulled forward and pinching forces are responsible only for detachment of the adhesions [9,10].

It is generally accepted that adhesions formed at the anterior of the cell remain stationary relative to the substrate and undergo a maturation process as the cell passes over them [11–13]. However, the fate of the numerous adhesions produced at the anterior of the wide leading lamella is not clear, considering the triangular form of migrating fibroblast-type cells. It has been suggested that focal adhesions under the cell body play a role only in maintaining the spread shape of the migrating cell [14]. Recently it was reported that the majority of these adhesions rapidly disperse in the lamella and only adhesions localized at the lateral edge will reach the rear of the cell [5]. As polarized bundles of actin filaments are connected to the adhesions, the polarization of the actin filaments and adhesions must change as the cell passes over the adhesions, which would involve the complete remodeling of the adhesions and the actin cytoskeleton. To exert force for forward movement of the cell body and the tail, in the case of fan-shaped migrating cells, the bipolar actin cables originating from the tail of the cell must be coupled to the adhesions at the front of the leading lamella [14]. Considering that the existence of adhesions depends on tension [15], after the release of the adhesion(s) in the tail, adhesions at the front must also be disassembled, which would negatively influence the stability of the leading lamella.

Here we present a hypothetical model of cell migration, which is based on the observation that, during movement of human fibrosarcoma cells, adhesions follow a curved path with respect to the substrate, according to the GRE model [1]. As adhesions move clockwise and counterclockwise on the two sides of the apex of the cell, the connecting actin arcs (oriented perpendicularly to the direction of the movement), which produce the force for forward movement, grow in length as they move backward with respect to the cell. Reaching the long axis of the cell the adhesions at both end of the cable are released, resulting in the disassembly of the entire actin cable.

Materials and methods

Time-lapse microscopy

HT1080 human fibrosarcoma cells (10^5 per well, six-well tissue culture plate, Greiner, Germany) were seeded in

the presence of serum (10% FCS in RPMI 1640, Sigma, St. Louis, MO) on coverslips coated with 50–100 $\mu\text{g/ml}$ Matrigel (Collaborative Research, Bedford, MA). The tumor cells were allowed to spread for 30–60 min, thereafter the cells showed rapid movement for 1–2 h. After spreading, a part of the surface of the coverslips was cleaned by a rubber policeman and an identification mark was placed on the clean area close to the cell front by means of a diamond pencil. The cells were videotaped for 1 h on an inverted microscope (Axiovert 35, Zeiss, Germany) equipped with a heated plate. At the end of the recording the cells were immediately fixed in 4% paraformaldehyde, and, for the later identification of moving cells, a videoprint was made over the recorded area. The coverslip was processed for immunofluorescence and the cells actually moving at the end of the recording were analyzed. The percentage of moving cells in a given time point was up to 5%. In this set of experiments, moving cells were analyzed for the distribution of phosphotyrosine and vinculin.

The distribution of talin, focal adhesion kinase, $\alpha 6$ -integrin, myosin, and actin was determined in moving type cells showing the characteristic semicircular shape.

To determine the average speed of HT1080 cells, coverslips were placed under a confocal microscope (MRC 1024, Bio-Rad, Hercules, CA) equipped with a heated plate (MP10DM, Kitazato, Japan); phase-contrast pictures then were taken every 30–60 s using a 20 \times objective. The net displacement of a nucleolus of each cell was determined ($n = 31$).

The same confocal microscopy system was used to determine the dynamics of adhesions in GFP-vinculin transfected cells. Pictures were taken every 30 s using a 100 \times objective. Overlay of adhesions (merged picture of all pictures taken during the observation period) was made using the Bio-Rad Lasersharp Processing software.

Transfection

HT1080 cells (10^6) were transfected with GFP-vinculin fusion gene containing plasmid, kindly provided by Dr. Benjamin Geiger (The Weizmann Institute of Science, Rehovot, Israel), using FuGENE 6 transfection reagent (Roche Diagnostic, Mannheim, Germany) according to the manufacturer's guidelines. The proportion of transfected cells was 20% maximum and the cultures were used for migration tests for 3 days. The transfection influenced negatively the locomoting activity; both the proportion (<1%) and the speed of the moving cells were found to be decreased.

Immunofluorescence

Cells were fixed in 4% paraformaldehyde for 10 min and permeabilized with 0.5% Triton X-100 for 5 min. The following antibodies were used: polyclonal and monoclonal (PY20) antibody to phosphotyrosine, monoclonal anti-FAK (Transduction Labs), anti-myosin (light chain, clone MY21,

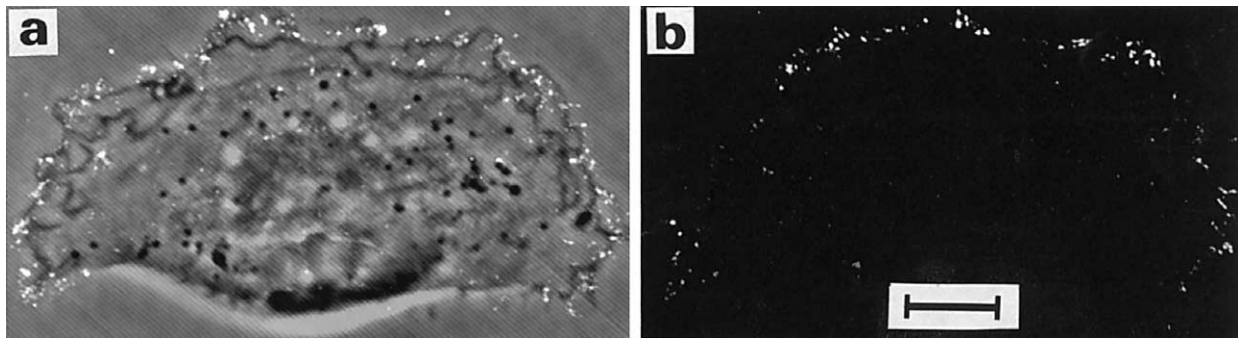


Fig. 1. Distribution of adhesion plaque components. (a) Merged picture of phase-contrast image and phosphotyrosine immunofluorescence signals. The cell shows semicircular shapes and immunofluorescence signals are localized predominantly to the outer rim of the cell. (b) Moving-type cell stained for vinculin. The signals are distributed in a semicircular manner along the cell edge. Similar distribution of talin, focal adhesion kinase, and $\alpha 6$ -integrin was observed (not shown). Bar represents $10 \mu\text{m}$ (a and b).

Sigma), anti- α -actinin (clone BM75.2, Sigma), anti-vinculin (clone VIN-11-5, Sigma), anti-talin (clone TA 205, Novocastra), and anti- $\alpha 6$ -integrin (clone GoH3, Pharmingen). Rhodamine-phalloidin was obtained from Molecular Probes.

Cells were incubated with the above antibodies for 60 min, with biotinylated secondary antibody for 30 min, and then with streptavidin-DTAF (Jackson Immunoresearch) for 30 min.

Results

During the rapid (gliding) movement on Matrigel, the semicircular shape of HT1080 fibrosarcoma cells was maintained and the direction of movement was perpendicular to the long axis of the cell (Fig. 1a, Videos 1 and 2). The average speed of the movement was found to be $1.6 \pm 0.3 \mu\text{m}/\text{min}$ ($n = 31$).

Immunofluorescence analysis of the distribution of phosphotyrosine-containing proteins (Fig. 1a) and adhesion plaque components vinculin (Fig. 1b), talin, FAK, and $\alpha 6$ integrin (not shown) indicated that these components were localized at the outer rim of the cells along the semicircle. Adhesions were not observed under the cell body and a few were found occasionally under the lamella. There were no differences found in the size of the adhesions and distribution of the adhesion components among the different regions of the semicircle, all of the above mentioned components were present in all adhesion sites. Furthermore, no significant differences were found among the adhesions at the level of tyrosine phosphorylation (Fig. 1a). The adhesions were spot-like ($0.5 \mu\text{m}$), or several microns long, oriented toward the rim of the cell.

Time-lapse microscopy of GFP-vinculin-expressing HT1080 cells showed that adhesions at the cell edge were not formed continuously; new adhesions appeared as discrete spots, with increasing intensity, ahead of the existing adhesions. Displacement of the adhesions was the largest

close to the apex ($2\text{--}5 \mu\text{m}$), decreasing toward the long axis of the cell. Adhesions were found to be stationary with respect to the substrate. The time of the adhesion renewal at the cell edge was in the range of minutes (Fig. 2a–c, Video 3). In contrast, retraction of the adhesions into the cell body in the flanks of the cell took place continuously; the adhesions were apparently sliding on the substrate (Fig. 2d–g, Video 4). The retraction of the adhesions was sequential (Fig. 2d–g), but occasionally fusion of the adhesions could also be observed (Fig. 2a–c, Video 3), which produced larger and brighter adhesions at the rear of the cell. These adhesions were eventually also retracted and dispersed in the cell. Because of the discontinuous formation of the adhesions, the path of individual adhesions could not be followed, but overlay of the recorded images revealed that adhesions followed a curved path (Fig. 2h and i). The adhesions were placed forward and sideways with respect to the substrate, but moved backward with respect to the cell along the cell edge. The path of the adhesions became more and more curved, as they got closer to the long axis of the cell, where they were retracted into the cell body. There were slight differences in the distribution of adhesions between motile nontransfected and transfected cells. In videotaped nontransfected cells the adhesions were mostly spot-like, localized in one row to the cell edge, whereas in transfected cells adhesions were frequently found in two rows (Fig. 2h). This could be due to the high concentration of vinculin in transfected cells that may slow down the turnover of the adhesions.

Analysis of cytoskeletal elements in moving-type cells showed that actin cables were present in the form of arcs at the anterior of the lamella (Fig. 3a). The concave face of the arcs was oriented toward the direction of the movement; however, orientation on the dorsal side of the cell reversed in front of the nucleus. α -Actinin was present in the lamellipodia and showed periodical arrangement in the lamella cell body transition zone (Fig. 3b). Myosin aggregates were observed close to the lamellipodium and their density grew toward the nucleus (Fig. 3c). At higher magnification it was

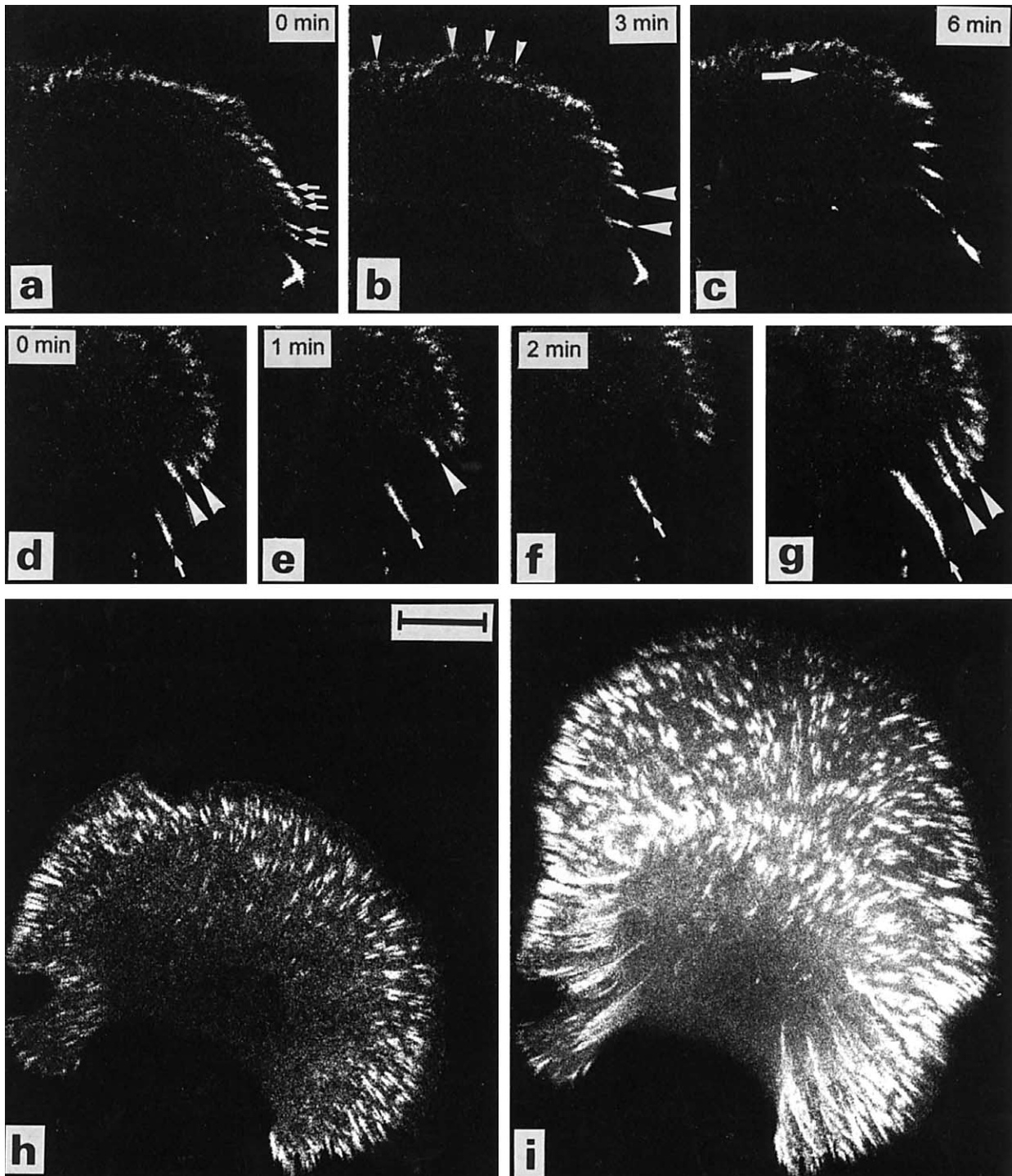


Fig. 2. Dynamics of GFP-vinculin-containing adhesions. (a–c) Time-course of adhesion renewal during gliding motility in GFP-vinculin-transfected cells. The series shows the right wing of the cell, turning slightly to the left. Arrowheads in b point to the developing new adhesion row. Arrow in c points toward the position of the adhesions already removed. The adhesions marked by three and two small arrows in a are fused into the adhesions marked by the upper and the lower large arrowheads in b. (d–f) Time-course of the sequential retraction of two adhesions in the right wing of a moving cell. Arrowheads point to the adhesions retracted. (g) Overlay of the images recorded over 3 min, including the images shown in d–f. Arrowheads point to the retracted adhesions. Arrow points at an adhesion that the cell was not able to retract during the observation period. All three adhesions are sliding on the surface of the substrate. (h and i) Adhesion dynamics during gliding motility of HT1080 cells. (h) Distribution of adhesions at the start of time-lapse microscopy. (i) Overlay of images recorded over 20-min movement of the cell. The adhesions follow a more and more curved path clockwise and counterclockwise on the two sides of the apex of the cell. Reaching the long axis of the cell, the adhesions are retracted into the cell body. Bar represents 10 μm a–i.

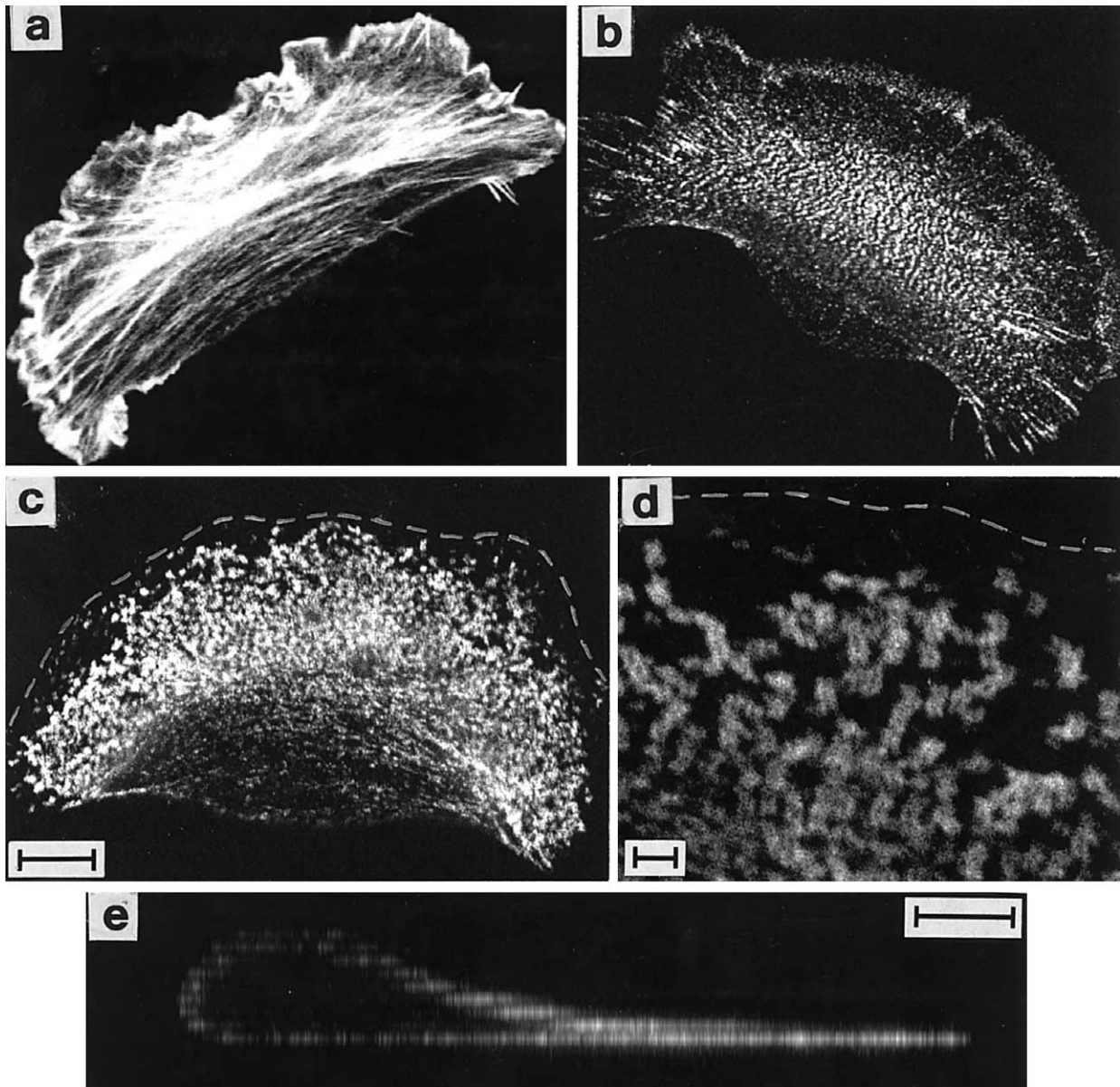


Fig. 3. Distribution of cytoskeletal elements. (a) Distribution of actin cables in locomoting-type cell. Note the concave face of the arcs present in the lamella oriented toward the semicircle. (b) Confocal image of α -actinin signals in a moving-type cell. The signals are distributed periodically from the middle part of the lamella toward the nucleus. (c) Myosin aggregates can be observed close to the cell edge (dashed line), and their density is seen to increase toward the nucleus. The focal plane was adjusted to the ventral surface of the cell. Note the decreased staining in the nuclear region. Periodical arrangement of myosin aggregates is discernible in the left wing of the cell. Bar represents $10\ \mu\text{m}$ (a–c). (d) Myosin molecules organized into doublets, forming ribbons close to the cell edge (dashed line). Bar represents $0.5\ \mu\text{m}$. (e) Side view of a $20\text{-}\mu\text{m}$ -wide part of the middle of the cell shown on c. The staining for myosin decreases on both the ventral and the dorsal surfaces from the base of the lamella toward the nuclear region. Bar represents $5\ \mu\text{m}$.

discernible that myosin molecules were organized into doublets, which were further assembled into ribbons (Fig. 3d). The orientation of these ribbons was perpendicular to the actin filaments and showed periodicity. The side view of moving-type cells stained for myosin indicated that the concentration of myosin was highest in the lamella and in the lamella–cell body transition zone where the membrane starts to rise, decreasing on both the ventral and dorsal side of the cell toward the nuclear region (Fig. 3e).

Discussion

Based on the observed distribution and dynamics of the adhesions and on the structure of the actin cytoskeleton, we propose a hypothetical mechanism of cell migration. This model differs substantially from the widely accepted locomotion model of fibroblast type cells [7].

The observation that adhesions in HT1080 cells were localized and constantly renewed at the leading edge of the

cell means that aging, as well as maturation of the adhesions, does not take place along the leading edge of the cell. This is further supported by the observation that all of the adhesions contained components such as vinculin and FAK, the presence of which in adhesions is considered as a sign of maturation [13,14]. The rapid turnover of the adhesions during migration at the cell edge results in the absence of adhesions under the lamella and the cell body. This observation is in contrast to earlier ones, made on chick embryo fibroblasts and keratocytes, in which talin- and vinculin-containing adhesion sites were found in these regions [6,11]. However, similar to our observations, recent results have shown that, during lamella extension, stationary adhesions were present only in the anterior part of the lamella [5,12]. However, the turnover of these adhesions was somewhat slower than in the case of human fibrosarcoma cells.

As has been shown earlier in the case of keratocytes, to maintain the semicircular shape during gliding motility, the points of the semicircle move perpendicularly to the cell edge, but the displacement decreases from the apex to the long axis of the cell. This means that each point of the cell edge will follow a curved path with respect to the substrate (GRE model) [1]. The observed trajectory of the GFP-vinculin-containing adhesions in HT1080 cells corresponds well with this model. This observation and the fact that neutrophil fragments also locomote according to the above model [17] suggest that graded radial extension of the leading lamella may represent a universal mechanism in cellular movement.

Since actin filaments are attached to the adhesions along the semicircle and the adhesions follow the curved path in the opposite direction on the two sides of the apex of the cell, the length of the actin cables have to increase, reaching maximal size at the long axis of the cell (Fig. 4). It is well established that assembly of the branched network of actin filaments beneath the plasma membrane is responsible for the extension of the lamellipodia. The branching takes place from the side of the preexisting filaments [18]. However, branched actin filaments cannot assemble into a sliding actomyosin system, which is necessary to exert force to propel the cell body forward. Therefore, as it has been suggested, the majority of the newly synthesized actin filaments have to separate from the sides of their mother filaments as the cell advances [18]. We hypothesize that these separated filaments are not depolymerized; instead they will be incorporated into the sliding actomyosin system organized by the myosin molecules. This notion is supported by our observations that myosin aggregates appeared close to the lamellipodium and organized into doublets, which were further assembled into ribbons. The orientation of these ribbons was perpendicular to the actin filaments and showed periodicity, as observed by others, in the case of mammalian fibroblasts [19]. This kind of organization of myosin molecules suggests that a sliding actomyosin system is working immediately behind the lamellipodium. This is in contrast to keratocytes, in which the lamellipodia, which

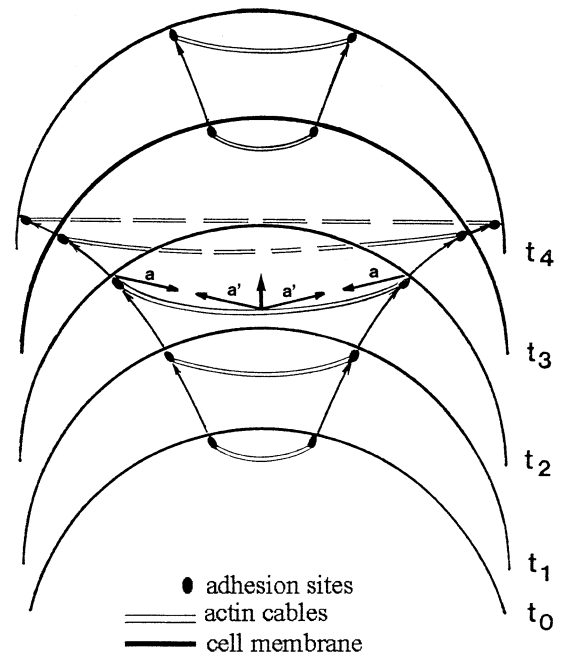


Fig. 4. Schematic representation of the fate of adhesions and actin cables in moving cells. Curved arrows show the path of adhesions in time (t_0-t_4). The actin cables connecting the adhesions grow in length as the cell advances. At t_3 new adhesions and actin cables are added at the apex of the cell. Straight arrows (t_2) represent the forces exerted by an actin cable (a) and the substrate (a'). To generate the resultant force, the forces exerted by the substrate (a') were shifted from the adhesion points to the middle of the actin cable. The resultant force oriented in the direction of the migration is responsible for cell body forward movement.

is devoid of myosin molecules, is wide, thereby the contractile zone is localized in front of the nucleus [2,4]. The periodical arrangement of myosin and α -actinin observed by us suggests that actin cables containing filaments with alternating polarity are responsible for force generation in moving HT1080 cells.

In a portion of moving HT1080 cells, adhesions were elongated and oriented more or less perpendicularly to the cell edge. The orientation of the adhesions is determined by the direction of the force exerted by actomyosin cables coupled to the adhesions [15]. As HT1080 cells moved forward, a new row of adhesions was formed in front of the old one. (To ensure continuous force generation, actin cables must always be connected to the substrate, which means that disassembly of the old adhesions should not take place before assembly of new ones.) Recent results have shed light on a possible mechanism of actin cable elongation. It was shown that the Arp2/3 complex transiently associates with vinculin in adhesions at the leading edge, implicating that branching of actin filaments can also take place within these structures [20]. In the case of keratocytes, the force exerted by the actomyosin system grows toward the long axis of the cell [8,9]. Considering the resemblance in distribution and orientation of the main actin cables between keratocytes and human fibrosarcoma cells, we suppose a similar distribution of forces in the moving HT1080

cells. The increasing force decreases the concavity of the actin cables and causes the new adhesions to have a different orientation compared to the old ones. During this process the orientation of the adhesions becomes more and more parallel to the long axis of the cell. As the adhesions during migration of HT1080 cells remain more or less perpendicularly oriented to the edge, the change in the orientation corresponds to the predictions of the GRE model, which includes the lateral flow of the adhesions.

In keratocytes, propulsive (rearward directed) forces were detected either in the wings of the cell [8] or centripetally oriented in the lamellipodia [9,10]. In the human fibrosarcoma cells, vinculin-containing adhesion sites were observed along the semicircular leading edge through which adhesions, as recent results suggested, force can be exerted [21]. The distribution of the vinculin-containing adhesions and the structure of the actomyosin arcs in HT1080 cells suggest a centripetal orientation of the propulsive forces.

Adhesions and actin cables have to be produced at the apex of the cell, making a continuous force generation possible, resulting in the gliding motility of the human fibrosarcoma cells. The continuous retraction or fusion of adhesions in the flanks and their production at the apex of the cell ensure a steady number of adhesions along the leading edge of the cell.

As adhesions were present only occasionally under the lamella, the actin cables span the entire width of the cell; the interconnected actin cytoskeleton acts as a rubber sheet nailed down at the adhesions. As this system alone determines the shape of the migrating cell, no adhesions are needed under the lamella and the cell body.

The actin cables in the lamella formed arcs due to the dragging force of the cell body, but at the same time the contractile force of the arcs propel the cell body forward (Fig. 4). Similar actomyosin arcs—present exclusively in front of the cell body—have been observed in fish keratocytes and are considered to be responsible for mediating cell body translocation [2,4]. If the actomyosin system is interconnected, the dragging force of the cell body is transmitted to the front of the cell, causing the organizing actin cables behind the leading lamella to take up the concave shape. (The actin arcs observed by confocal microscopy can be rather considered as local increase in the density of the actin filaments of the interconnected actin network.) It must be noted that, to ensure the gliding-type motility, theoretically all of the actin cables have to exert force of the same magnitude in the direction of the movement. Consequently, the component, which is directed perpendicularly to the direction of the movement, grows, as the cables become less concave during backward movement with respect to the cell. For the most efficient forward movement of the cell it is a prerequisite that no adhesions are present under the lamella and the cell body, as these would hamper the free contraction of the arcs, thereby slowing down the movement.

Actomyosin cables were observed on both the ventral and the dorsal sides of the HT1080 cells. It is important to

note that the actomyosin cables on the dorsal side were also connected to the adhesions located at the cell edge, thereby also able to exert force on the substrate, contributing to the forward movement of the cell. A proportion of the actomyosin cables on the ventral side moved under the nucleus, while the cables on the dorsal side became stuck at the lamella–cell body boundary, where the membrane starts to rise. The latter forms the large actin cable, apparently exerting force in the opposite direction of the movement, probably responsible for the retraction of adhesions at the long axis of the cell. However, the force exerted by this cable could be rather low, as the adhesion at its ends glide on the surface of the substrate.

The continuous growth of the actin cables in moving human tumor cells, suggested by us, questions the existence of treadmilling of actin filaments in the sense that, in the lamella, there is no simultaneous polymerization and depolymerization of the filaments; there is only filament growth, until the actin cables reach maximal size.

The release of the adhesions took place simultaneously in the flanks of the cell, probably leading to the disassembly of the entire actin cable. The process can be repeated continuously during movement as the adhesions and actin cables reach the long axis of the cell. The disassembly of the actin cables at the rear of the cell has no direct influence on the tension of the force exerting cables in the front of the lamella.

Moving fibrosarcoma cells with tails have also been observed, showing the classical form of locomoting fibroblast-type cells [6]. In the leading lamella of these cells, however, the distribution and dynamics of the adhesions were identical to the semicircular-shaped cells, except that at the end of the tail one adhesion site was detectable. Actin cables originating from this adhesion spanned the entire cell and were oriented parallel to the direction of movement. However, other cables forming arcs in the leading lamella have been oriented perpendicularly to the direction of movement. These observations strongly suggest that the lamella alone is responsible for the forward movement of the human fibrosarcoma cells. According to the model proposed here, the adhesion in the tail or any other adhesions under the cell body, which the cell were not able to disassemble at the start of the movement, only retard migration.

Acknowledgments

We thank B. Geiger for providing the GFP-vinculin plasmid. This work was supported by grants from the Hungarian National Science Foundation (OTKA T-26439) and the Ministry of Education (NKFP 1/48/2001). J. Tóvári is a recipient of the Bolyai Research Fellowship Grant of the Hungarian Academy of Sciences.

References

- [1] J. Lee, A. Ishihara, J.A. Theriot, K. Jacobson, Principles of locomotion for simple-shaped cells, *Nature* 362 (1993) 167–171.
- [2] K.I. Anderson, Y-L. Wang, J.V. Small, Coordination of protrusion and translocation of the keratocyte involves rolling of the cell body, *J. Cell Biol.* 134 (1996) 1209–1218.
- [3] J. Lee, M. Leonard, T. Oliver, A. Ishihara, K. Jacobson, Traction forces generated by locomoting keratocytes, *J. Cell Biol.* 127 (1994) 1957–1964.
- [4] T.M. Svitkina, A.B. Verkhovskiy, K.M. McQuade, G.G. Borisy, Analysis of the actin–myosin II system in fish epidermal keratocytes: mechanism of cell body translocation, *J. Cell Biol.* 139 (1997) 397–415.
- [5] C. Ballestrem, B. Hinz, B.A. Imhof, B. Wehrle-Haller, Marching at the front and dragging behind: differential α β 3-integrin turnover regulates focal adhesion behavior, *J. Cell Biol.* 155 (2001) 1319–1332.
- [6] L.P. Cramer, M. Siebert, T.J. Mitchison, Identification of novel graded polarity actin filament bundles in locomoting heart fibroblasts: implications for the generation of motile force, *J. Cell Biol.* 136 (1997) 1287–1305.
- [7] A.R. Horwitz, J.T. Parsons, Cell migration—moving on, *Science* 286 (1999) 1102–1103.
- [8] T. Oliver, M. Dembo, K. Jacobson, Separation of propulsive and adhesive traction stresses in locomoting keratocytes, *J. Cell Biol.* 145 (1999) 589–604.
- [9] K. Burton, J.H. Park, L.D. Taylor, Keratocytes generate traction forces in two phases, *Mol. Biol. Cell* 10 (1999) 3475–3769.
- [10] C.G. Galbraith, M.P. Sheetz, Keratocytes pull with similar forces on their dorsal and ventral surfaces, *J. Cell Biol.* 147 (1999) 1313–1323.
- [11] K.I. Anderson, R. Cross, Contact dynamics during keratocyte motility, *Curr. Biol.* 10 (2000) 253–260.
- [12] C.M. Laukaitis, D.J. Webb, K. Donais, A.R. Horwitz, Differential dynamics of α 5 integrin, paxillin, and α -actinin during formation and disassembly of adhesions in migrating cells, *J. Cell Biol.* 153 (2001) 1427–1440.
- [13] J. Lee, K. Jacobson, The composition and dynamics of cell–substratum adhesions in locomoting fish keratocytes, *J. Cell. Sci.* 110 (1997) 2833–2844.
- [14] K.A. Beningo, M. Dembo, I. Kaverina, J.V. Small, Y-L. Wang, Nascent focal adhesions are responsible for generation of strong propulsive forces in migrating fibroblasts, *J. Cell Biol.* 153 (2001) 881–887.
- [15] D. Rivelino, E. Zamir, N.Q. Balaban, U.S. Schwartz, T. Ishizaki, S. Narumiya, Z. Kam, B. Geiger, A.D. Bershadsky, Focal contacts as mechanosensors: externally applied local mechanical force induces growth of focal contacts by an mDia-dependent and ROCK-independent mechanism, *J. Cell Biol.* 15 (2001) 1175–1185.
- [16] J.A. DePasquale, C.S. Izzard, Accumulation of talin in nodes at the edge the lamellipodium and separate incorporation into adhesion plaques at focal contacts in fibroblasts, *J. Cell Biol.* 113 (1991) 1351–1359.
- [17] T. Mizuno, O. Kagami, T. Sakai, K. Kawasaki, Locomotion of neutrophil fragments occurs by graded radial extension, *Cell Motil. Cytoskeleton* 35 (1996) 289–297.
- [18] T. Pollard, G.G. Borisy, Cellular motility driven by assembly and disassembly of actin filaments, *Cell* 112 (2003) 453–465.
- [19] A.B. Verkhovskiy, T.M. Svitkina, G.G. Borisy, Myosin II filament assemblies in the active lamella of fibroblasts: their morphogenesis and role in the formation of actin filament bundles, *J. Cell Biol.* 131 (1995) 989–1002.
- [20] K.A. DeMali, C.A. Barlow, Burridge, Recruitment of the Arp2/3 complex to vinculin: coupling membrane protrusion to matrix adhesion, *J. Cell Biol.* 159 (2002) 881–891.
- [21] C.G. Galbraith, K. Yamada, M.P. Sheetz, The relationship between force and focal complex development, *J. Cell Biol.* 159 (2003) 695–705.



Organ-specificity of the extravasation process: An ultrastructural study

Sándor Paku¹, Balázs Döme^{1,2}, Réka Tóth¹ & József Timár²

¹Department of Molecular Pathology, Joint Research Organization of the Hungarian Academy of Sciences and Semmelweis University, Budapest, Hungary; ²Department of Tumor progression, National Institute of Oncology, Budapest, Hungary

Received 14 September 2000; accepted in revised form 23 April 2001

Key words: basement membrane, endothelium, extravasation, Lewis lung carcinoma, ultrastructure

Abstract

The process of extravasation of the high metastatic Lewis lung carcinoma line was examined in different organs. Four of the five organs (liver, lungs, brain and adrenals) represent the most frequent metastatic sites in humans. In the case of each organ 150–350 tumor cells were analysed. The interaction of tumor cells with endothelial cells and the basement membrane showed significant differences between the organs. In the liver and lungs, endothelial cells were found to migrate onto the surface of the tumor cells, resulting in the removal of tumor cells from the circulation. The process was initiated by development of cytoplasmic projections on the luminal surface of the endothelial cells. In the liver only half of the tumor cells showed basement membrane degradation even after 24 h, although 6 h after injection 40% of the tumor cells were sequestered from the circulation. In the adrenals and brain, tumor cells were not covered by endothelial cells instead, limited retraction of endothelial cells was followed by penetration of the basement membrane. In the kidney both types of tumor cell-endothelial cell interactions were observed, but the process of extravasation was not completed, stopping as the tumor cells reached the basement membrane or the mesangial matrix. The time course of tumor cell extravasation also showed significant differences between the organs. The process was most rapid in case of the liver and adrenals. By 6 h 40–50% of the tumor cells were in the process of extravasation or were in an extracapillary position. These organs are preferential metastatic sites of this tumor line. The time of extravasation was much longer in the other organs (lungs 16 h, brain 48 h), for which this tumor line shows no preference. Conclusions: (1) Type and duration of tumor cell extravasation differ between the organs. (2) The time needed to reach extraluminal position, but not the type of extravasation correlates with the organ preference. (3) Endothelial cells of the lungs and liver can play a much more active role in the process of extravasation than previously suggested. (4) Tumor cells can complete the metastatic process without reaching a complete extracapillary position; contact with the basement membrane or extracellular matrix seems to be sufficient.

Introduction

Extravasation of tumor cells is an important step in completing successful metastasis formation. The cause of metastatic inefficiency is debated, but destruction of tumor cells in the circulation by mechanical forces or the immune system can lead to significant reduction of the number of extravasating tumor cells [1]. Therefore the time spent in the hostile environment of the microcirculation can have a decisive role on the efficiency of the metastatic process and organ preference.

According to *in vivo* ultrastructural studies, extravasation in capillaries can take place in several ways: (1) by tumor cells penetrating the endothelium and basement membrane similarly to leukocytes [2–6]; (2) by retraction of endothelial cells followed by fragmentation of the basement membrane by cellular processes, leading to the destruction of the capillary [7–10]; (3) by endothelial cells covering the tumor cells before the penetration of the basement membrane [11];

(4) by intracapillary proliferation of tumor cells leading to the mechanical destruction of the capillary [12].

These observations are based on studies which analyse the ultrastructure of extravasation of tumor cells of different origin in the lung and liver. In the lung, the time needed for penetration of the endothelium to get into contact with the subendothelial basement membrane and to reach an extracapillary position varied significantly among the tumor lines studied [4, 6–12].

Regarding two other frequent metastatic sites, only two studies were found dealing with the process of extravasation in the brain [4, 6] and one report showing the interaction of hepatoma cells with the capillary endothelium of the adrenal gland [13].

Based on earlier *in vitro* studies, it is generally accepted that the interaction of the tumor cells with the endothelium results in the retraction of endothelial cells, leading to the attachment of the tumor cells to the subendothelium. Subsequently, the adhered tumor cells migrate under the endothelium and spread on the subendothelial basement membrane, followed by reformation of the endothelium mono-

Correspondence to: Sándor Paku, PhD, First Institute of Pathology and Experimental Cancer Research, Semmelweis University, 1085 Üllői Ut 26, Budapest, Hungary. Tel: +36-1-226-1638/4444; Fax: +36-1-317-1074; E-mail: paku@korb1.sote.hu

layer integrity [15]. However, this process represents only elements of the observed diverse interactions between tumor cells of different origin and the capillary wall *in vivo*, which suggest, that during extravasation the properties of the tumor cells determine the response of the endothelium.

The well known variability in ultrastructure and cell surface molecules of the endothelium of different organs [14], is also thought to be responsible for organ preference, however can also play an important role in the process of extravasation.

In this paper we test the hypothesis that a given tumor cell line reaching the capillary bed of different organs, is able to elicit distinct responses of the endothelium. We also investigated the correlation between the time needed to reach extraluminal position in the different organs and organ preference, using the 3LL-HH Lewis lung carcinoma tumor line with a well known metastatic pattern.

Materials and methods

Animals, tumor line and injections

Inbred C57Bl/6 mice from our Institute were used throughout the studies. The high metastatic 3LL-HH tumor line was maintained by serial intrasplenic transplantations of tumor cells obtained from liver metastases. Single cell suspensions were prepared from 14-day-old 3LL-HH liver metastases. Tumor tissue was minced by crossed scalpels and filtered through 4-fold gauze. After centrifugation and washing in medium 199, the viability of tumor cells was determined by a trypan-blue exclusion test (40–50%).

An analysis of extravasation was performed in five organs (liver, lungs, adrenals, brain and kidney).

For the analysis of extravasation in the liver, tumor cells were injected into the splenic vein. Mice were anesthetized and the spleen exposed. The splenic vein was cleaned and tumor cells ($5 \times 10^5/0.2$ ml) were injected by inserting a 30-gauge needle into the vein. After injection, blood was allowed to flow for a minute to ensure that all tumor cells reached the microvasculature of the liver. After removing the needle a small piece of gelspon was pressed onto the vein to prevent excessive bleeding.

In the case of the lungs 5×10^5 tumor cells (0.2 ml) were injected into the lateral tail vein.

In the case of the adrenals and kidney, tumor cells ($10^6/0.2$ ml) were injected into the left ventricle of the heart, as previously described [16].

To analyse the extravasation in the brain, the tumor cells were injected into the left ventricle or into the carotid artery. Injection of tumor cells into the left ventricle yielded a lower cell number in the brain than injection into the carotid artery. When cells were injected into the left ventricle the number of tumor cells in the brain 2–3 days after injection, it was not enough to perform the ultrastructural analysis of extravasation, therefore the tumor cells were injected into the carotid artery. For this the mice were anesthetized and carotid artery prepared for injection under a dissecting microscope. A ligature was placed proximally and the artery was elevated by

curved tweezers. A 30-gauge needle was inserted into the artery just above the elevation and a slow injection of 5×10^5 cells in 0.2 ml was started ensuring free blood flow throughout the process as well as for another 30 s. The ligature was then tightened and the skin closed.

Electron microscopy

Animals were sacrificed at various time points after tumor cell injection. Two mice were used at each time point: (lungs 3, 6, 11, 16, 24 h, liver 1, 3, 6, 16, 24 h; adrenals 1, 3, 6, 16, 24 h; kidney 3, 6, 16, 24 h; brain 3, 24, 48, 72 h). Anesthetized animals were perfused via the left ventricle with phosphate buffered saline for 10 min and with 2.5% glutaraldehyde in 0.05 M Na-cacodylate (pH 7.2) for 15 min at room temperature. Organs were removed, cut into 1×2 mm pieces and immersed in 2.5% glutaraldehyde for 2 h. The pieces were postfixed in 1% OsO_4 , 0.5% K-ferrocyanide in 0.05 M Na-cacodylate for 2 h, dehydrated in graded series of acetone, contrasted *en bloc* with 2% uranylacetate and embedded in Spurr's mixture. Tumor cells were detected on semithin sections stained by 0.5% toluidine blue (pH 8.5). Areas of interest were trimmed out and ultrathin sections were cut, stained with lead citrate and analysed on Philips CM10 electron microscope. From each area 30–40 ultrathin sections were cut and lifted onto formvar coated 75 mesh grids.

Quantitative analysis of tumor cell extravasation

The time necessary for tumor cells to reach an extraluminal position was determined by analysing the interaction of the tumor cells with the capillary wall of the organs at different time points after tumor cell inoculation.

The process of extravasation was divided into the following steps: (1) arrested tumor cells facing intact capillary endothelium; (2) beneath the tumor cells, retraction of the endothelial cells is observable, tumor cells are in contact with the basement membrane; (3a) tumor cells penetrate the endothelium and the basement membrane with cellular processes; (3b₁) tumor cells are partially covered by endothelial cells; (3b₂) tumor cells, which are completely covered by endothelial cells, are in contact with the basal side of the endothelium and/or basement membrane is penetrated by cellular processes; (4) tumor cells are completely extravascular in contact with connective tissue or parenchymal cells. It must be noted that steps 3a and 3b are parallel events.

A minimum of 20 cells were analysed at each time point. To include into a category, each cell on at least 10 ultrathin sections was analysed to ensure that the most advanced stage is recorded. Altogether over 1,000 cells were analysed.

Confocal microscopy

Tumor cells isolated as described above, were labeled by membrane permeant reactive fluorescent tracer, CellTracker Green (Molecular Probes Inc.) at a concentration of $5 \mu\text{M}$ for 20 min. (The treatment had no influence on the metastatic

potential of the tumor cells). After washing in PBS, the number of tumor cells was adjusted to $2 \times 10^6/\text{ml}$, and 0.2 ml cell suspension was injected into the splenic vein of four mice, which were sacrificed 6 and 24 h after injection. Livers were removed, frozen in isopentane chilled with liquid nitrogen and 5 μm cryosections were cut. The sections were fixed in 4% freshly depolymerized paraformaldehyde for 15 min, washed in PBS and reacted with polyclonal antibody against laminin in 1:50 dilution (DAKO) for 60 min. The primary antibody was detected by rhodamine conjugated goat anti-rabbit antibody (Jackson ImmunoResearch Lab. Inc.) The sections were analysed on BIO-RAD MRC1024 confocal microscopy system.

The integrity of the basement membrane was analysed around the circumference of 100 cells for each time point. Since small discontinuities can be detected in the basement membrane of normal sinusoids, degradation was recorded only if one-third of the circumference of the cell was free of any basement membrane label.

Results

Liver (Table 1A)

Tumor cells were arrested mainly in sinusoids close to the periportal area. One hour after injection small cytoplasmic processes were observed protruding through the pores of sinusoidal endothelial cells. (Figure 1). These small projections persisted up to 3–6 h without any significant changes in size. Retraction of endothelial cells was observed by this time, but the endothelial cells were separated at the interendothelial junctions (Figure 2). This event was preceded or paralleled by the development of cytoplasmic projections on the luminal surface of endothelial cells, which were attached to the cell surface of the tumor cells (Figure 3). The attachment points showed increased electron density (Figure 4). The size of the endothelial cell cytoplasmic processes increased and by 6 h 33% of the tumor cells were either partially or completely covered by thin endothelial processes (Figure 5). During this process the shape of the tumor cells showed no significant changes and tumor cell processes projecting under the endothelial cell or spreading on the subendothelial matrix were not observable. Ten percent of the tumor cells were found in extrasinusoidal position, but around the surface of these cells – probably because of the inappropriate sectioning plane – no endothelial cells were detected; these cells were surrounded by hepatocytes. By 16 h only one, and by 24 h no cells were found in intrasinusoidal position, the tumor cells were completely covered by endothelial cells or surrounded by hepatocytes. The extraluminal tumor cells often invaginated into the hepatocytes, which event was accompanied by the disappearance of the cell surface microvilli of hepatocytes (Figure 6).

Since the basement membrane is not detectable in the liver by electron microscopy, we injected fluorescently labeled tumor cells and detected the basement membrane of liver sinusoids around these cells by confocal microscopy,

to determine the degree of basement membrane degradation during the extravasation process.

Surprisingly, after 6 h of injection 90% of the tumor cells were still surrounded by intact basement membrane (Figure 7), although by this time 40% of the cells were in extraluminal position. Even after 24 h only 50% of the cells showed partial or complete degradation of the basement membrane (Figure 8).

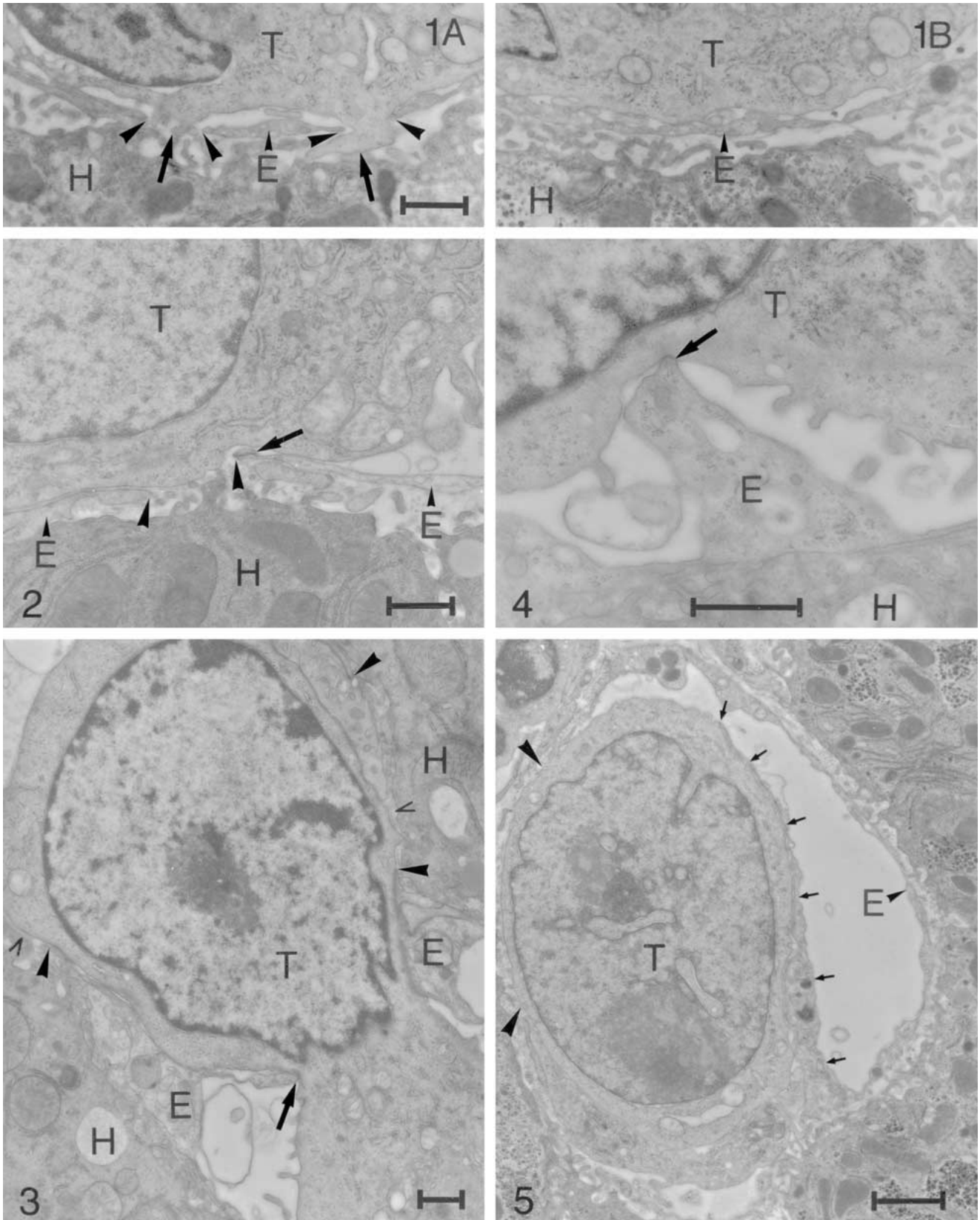
Lung (Table 1B)

The majority of tumor cells were trapped in capillaries and faced intact endothelium for up to 6 h. Even by 11 h following injection, the proportion of tumor cells, around which retracted endothelial cells were present, did not increase significantly, instead projections originating from the luminal surface of the intact endothelial lining, started to cover the tumor cells (Figures 9 and 10). In contrast to the liver, however, no specific adhesion points were observed between the tumor cell surface and the endothelial projections. The size of these cytoplasmic projections was limited, since no cells were found completely covered by the endothelium, while facing the intact endothelial layer of the capillary wall. Having a certain projection size, the endothelial cells were separated at their intercellular junction under or near the tumor cell. Subsequently the tumor cells were found to lie on the surface of the basement membrane and were in contact with the basal surface of the endothelial cells (Figure 11). Fibrin and platelets were frequently associated with the free surface of the tumor cells, but these components were never found between the tumor cells and the capillary wall (Figure 10). Although a considerable number of tumor cells were already completely covered by endothelial cells (17%), the basement membrane was penetrated by only 4% of the cells. Extravascular tumor cells were not found by this time (11 h).

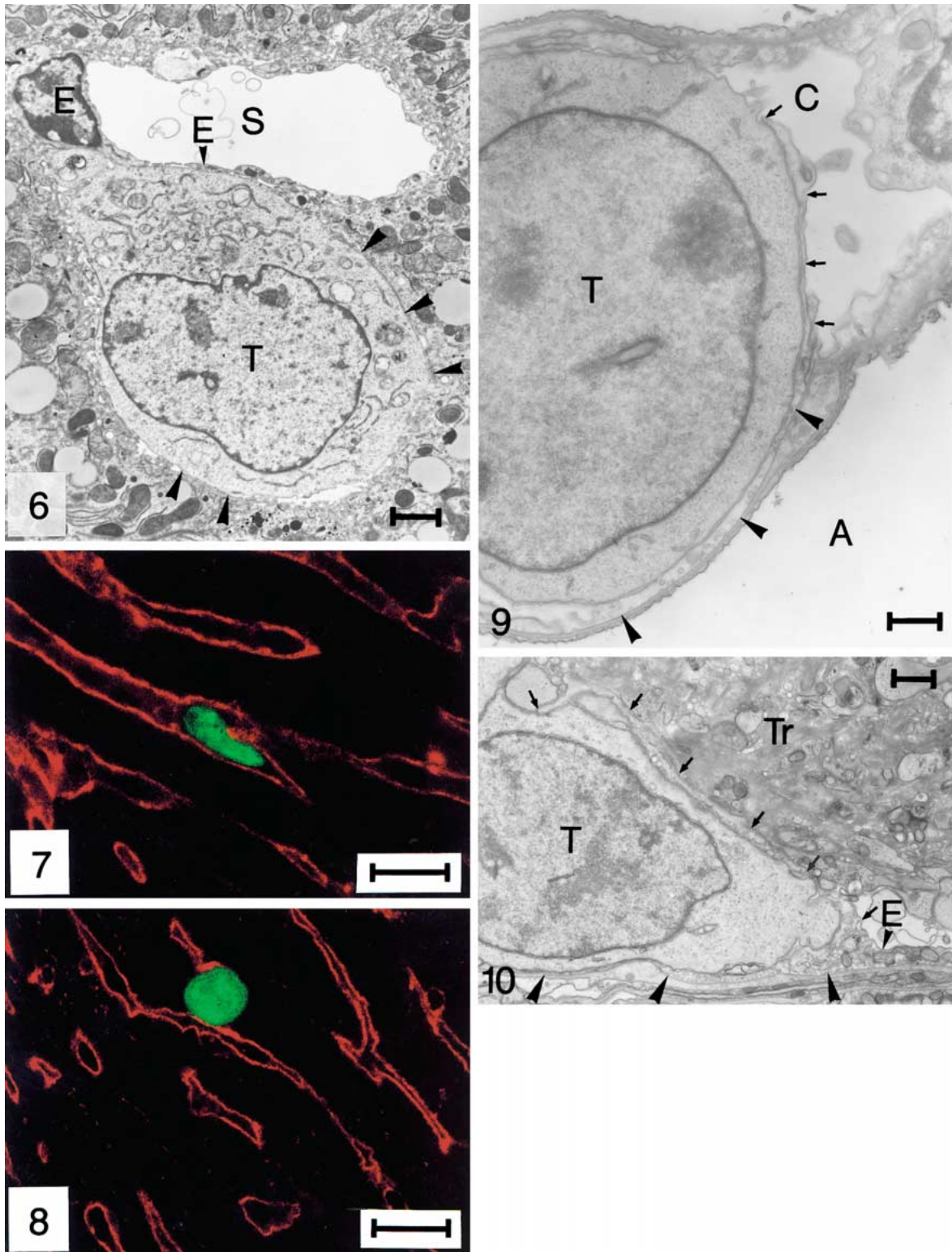
After 16 h the majority of the tumor cells were covered by endothelial cells, which cover consisted of several, single-layered endothelial cells (Figure 12). Half of the endothelialized tumor cells penetrated the basement membrane and a considerable proportion of tumor cells were located extravascularly. Similarly to the liver, during the sequestration of tumor cells from the circulation by the endothelial cells, no significant changes were found in the tumor cell shape. The penetration of the basement membrane, however, took place through small holes (2–4 μm) requiring significant deformation of the tumor cell (Figure 13). No simultaneous penetration of endothelium and the basement membrane was observed. Basement membrane breakthrough always took place in the direction of the connective tissue. Cells moving through the double layered basement membrane separating the alveolar space from the capillary lumen were not observable. 24 h after injection the majority of the tumor cells were situated in the connective tissue.

Adrenals (Table 1C)

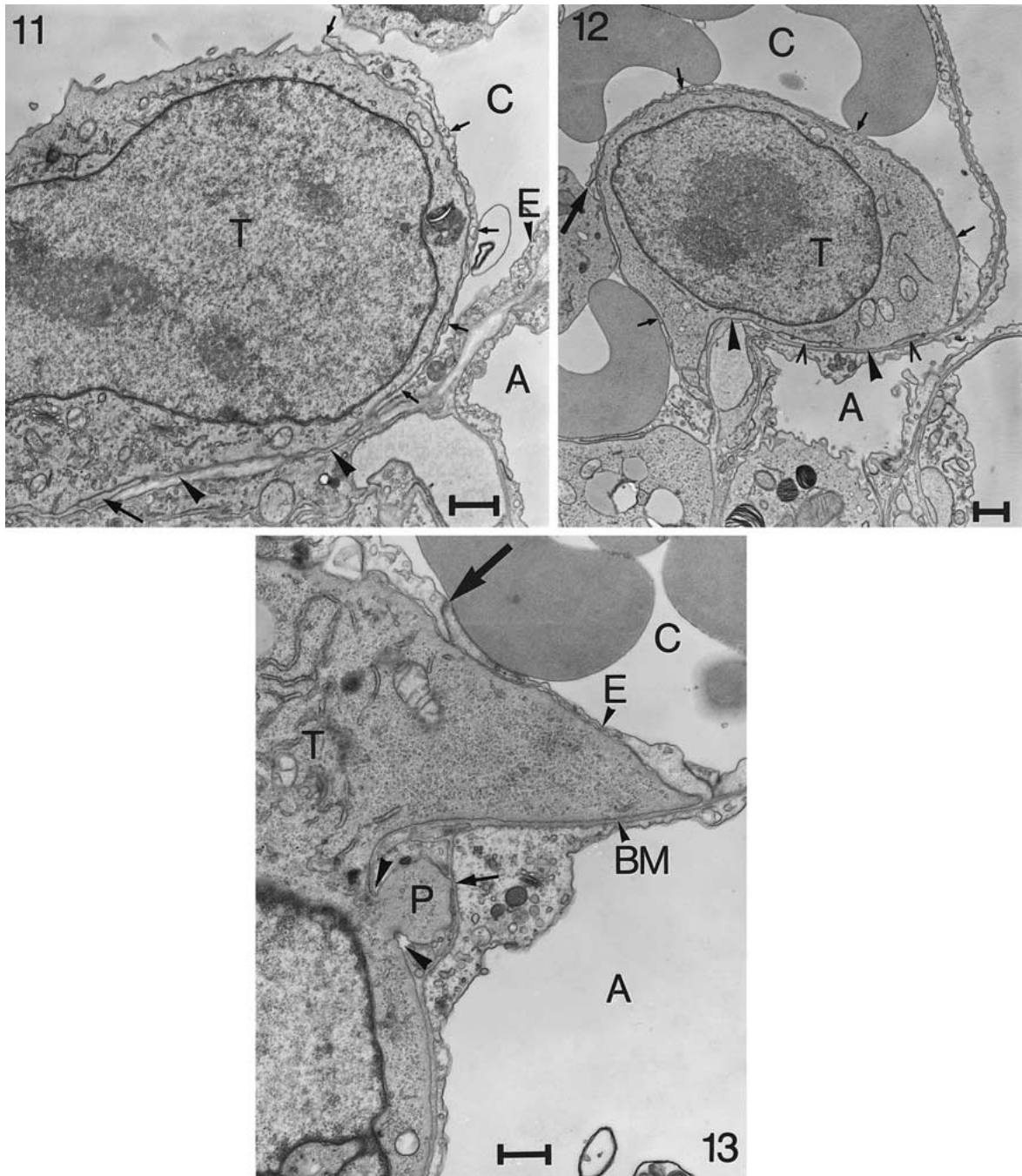
Following intraarterial injection the tumor cells were arrested in adrenal capillaries of the subcapsular region (Fig-



Figures 1-5. (1) Detail of a tumor cell arrested in a sinusoid 6 h after tumor cell inoculation; $\times 12,000$; bar = $1 \mu\text{m}$. A. Small cytoplasmic processes (arrows) of the tumor cell (T) penetrate through the fenestrations (arrowheads) of the endothelium (E). H - hepatocyte. B. The same area at a different section. No interendothelial junctions are visible in this area. (2) Tumor cell in a sinusoid 6 h after inoculation. Retraction of the endothelial cells (E) is observable. Through the opening (arrowheads) the tumor cell (T) is in contact with the subendothelial matrix. The arrow points at an intercellular junction at border of the opening. H - hepatocyte; $\times 12,000$; bar = $1 \mu\text{m}$. (3) Cytoplasmic process originating from the luminal surface of the endothelial cell (E) is attached to the tumor cell (T) (arrow). Gaps are visible in the endothelial lining (arrowheads), through which the tumor cell is attached to the subendothelial matrix (open arrowheads). H - hepatocyte; $\times 8,300$; bar = $1 \mu\text{m}$. (4) Cytoplasmic process of a sinusoidal endothelial cell (E) is attached to the surface of an intraluminal tumor cell (T) Note the increased electron density of the attachment point (arrow). H - hepatocyte; $\times 20,000$; bar = $1 \mu\text{m}$. (5) Tumor cell (T) covered partially by an endothelial cell (E) (arrows) 6 h after inoculation. The tumor cell is in contact at a large area with the subendothelial matrix (arrowheads); $\times 6,400$; bar = $2 \mu\text{m}$.



Figures 6–10. (6) Extraluminal tumor cell 24 h following inoculation. The endothelial (E) lining is intact on surface of the tumor cell. The tumor cell invaginated into the hepatocyte. Arrowheads point in areas where microvilli of the hepatocyte are completely absent. S – sinusoidal lumen; $\times 4,400$; bar = $2 \mu\text{m}$. (7) Intrasinusoidal tumor cell (green) 6 h following inoculation. The basement membrane (red) is intact around the tumor cell. Bar = $20 \mu\text{m}$. (8) Extravasated tumor cell (green) in the liver 24 h following inoculation. The tumor cells is in contact with two sinusoids but large part of the tumor cell surface is free from basement membrane label (red fluorescence) Bar = $20 \mu\text{m}$. (9) Tumor cell (T) arrested in a lung capillary 11 h following inoculation. Cytoplasmic projection (arrows) originating from the luminal surface of the endothelial cell covers a part of the surface of the tumor cell. The endothelial lining is intact under the tumor cell (arrowheads). C – capillary lumen; $\times 10,400$. Bar = $1 \mu\text{m}$. (10) Large process (arrows) of the endothelial cell (E) covers the half of the surface of the tumor cell (T). Retraction of the endothelial cells under the tumor cell is not observable (arrowheads). Tr – thrombus material; $\times 8,200$; bar = $1 \mu\text{m}$.



Figures 11–13. (11) Tumor cell (T) partially covered by an endothelial cell (small arrows) 11 h after inoculation. The basal surface of the endothelial cell is in contact with the tumor cell, which lies on the basement membrane. Small piece of the endothelial cell is still present under the tumor cell (large arrow). E – endothelium; C – capillary lumen; A – alveolar space; $\times 8,200$; bar = $1 \mu\text{m}$. (12) Tumor cell (T) completely covered by endothelial cells (small arrows) 16 h following inoculation. Large arrow point at an intercellular junction. The tumor cell is in contact with the intact basement membrane (arrow heads). Parts of the endothelium are still present under the tumor cell (open arrowheads). C – capillary lumen; A – alveolar space; $\times 6,200$; bar = $1 \mu\text{m}$. (13) Tumor cell (T) process (P) completely covered by endothelial cells (E) penetrates the endothelial basement membrane (arrowheads) 16 h following inoculation. The process is in contact with the basement membrane of the alveolar epithelium (arrow). The large arrow points at an intercellular junction between the covering endothelial cells. BM – basement membrane; C – capillary lumen; A – alveolar space; $\times 8,200$; bar = $1 \mu\text{m}$.

ure 14). No tumor cells were found in the medulla. As early as 3 h after injection tumor cells developed projections through the endothelium and the basement membrane (Figure 15). The size of the opening in the capillary wall was similar to that observed in the lungs ($2\text{--}4 \mu\text{m}$), through which the tumor cells moved into the connective tissue space (Figure 16). The endothelial cells were separated similarly to the liver and lungs, at or near intercellular junctions.

(Figure 17). During the extravasation process extensive retraction of endothelial cells was not observed, the size of the gap in the endothelial lining was always similar to the one seen in the basement membrane. By 6 h 21% of the cells were already in extracapillary position and another 17% were in the process of extravasation. By 16 h a considerable proportion of the cells were localised intravascularly, but

Table 1. Relative distribution of tumor cells among the steps of extravasation in different organs.

A	Time after inoculation				
	1 h	3 h	6 h	16 h	24 h
Liver	Percentage of tumor cells in the different steps of extravasation				
(1) TC contact with EC	93	65	16		
(2) EC retraction	7	35	38	3	
(3a) TC process penetrating EC and BM			5		
(3b ₁) TC partially covered by EC (TC in contact with the subendothelium)			24 (12)	3	
(3b ₂) TC completely covered by EC			8	32	57
(4) TC extravascular No EC visible around TC			11	62	43
	Number of cells examined				
Total number of cells examined 239	28	31	102	31	47

Table 1. Continued.

B	Time after inoculation				
	3 h	6 h	11 h	16 h	24 h
Lung	Percentage of tumor cells in the different steps of extravasation				
(1) TC contact with EC	97	91	69	15	
(2) EC retraction	3	6	3	4	
(3a) TC process penetrating EC and BM					
(3b ₁) TC partially covered by EC (TC in contact with BM)		3	12 (6)	1	
(3b ₂) TC completely covered by EC (BM pierced)			17 (4)	65 (31)	26 (17)
(4) TC extravascular				14	74
	Number of cells examined				
Total number of cells examined 359	29	32	203	72	23

interestingly no cells were found penetrating the capillary wall.

Brain (Table 1D)

Following intraarterial injection the majority of tumor cells were surrounded by intact endothelium for up to 24 h. Extravascular cells were first found 48 h following injection of tumor cells (13%). Endothelial cells were separated at intercellular junctions, but extensive retraction of endothelial

Table 1. Continued.

C	Time after inoculation				
	1 h	3 h	6 h	16 h	24 h
Adrenals	Percentage of tumor cells in the different steps of extravasation				
(1) TC contact with EC	97	83	58	19	4
(2) EC retraction	3	4	2	4	
(3a) TC process penetrating EC and BM		13	17		
(3b ₁) TC partially covered by EC			2		
(3b ₂) TC completely covered by EC					
(4) TC extravascular			21	77	96
	Number of cells examined				
Total number of cells examined 156	31	24	48	26	27

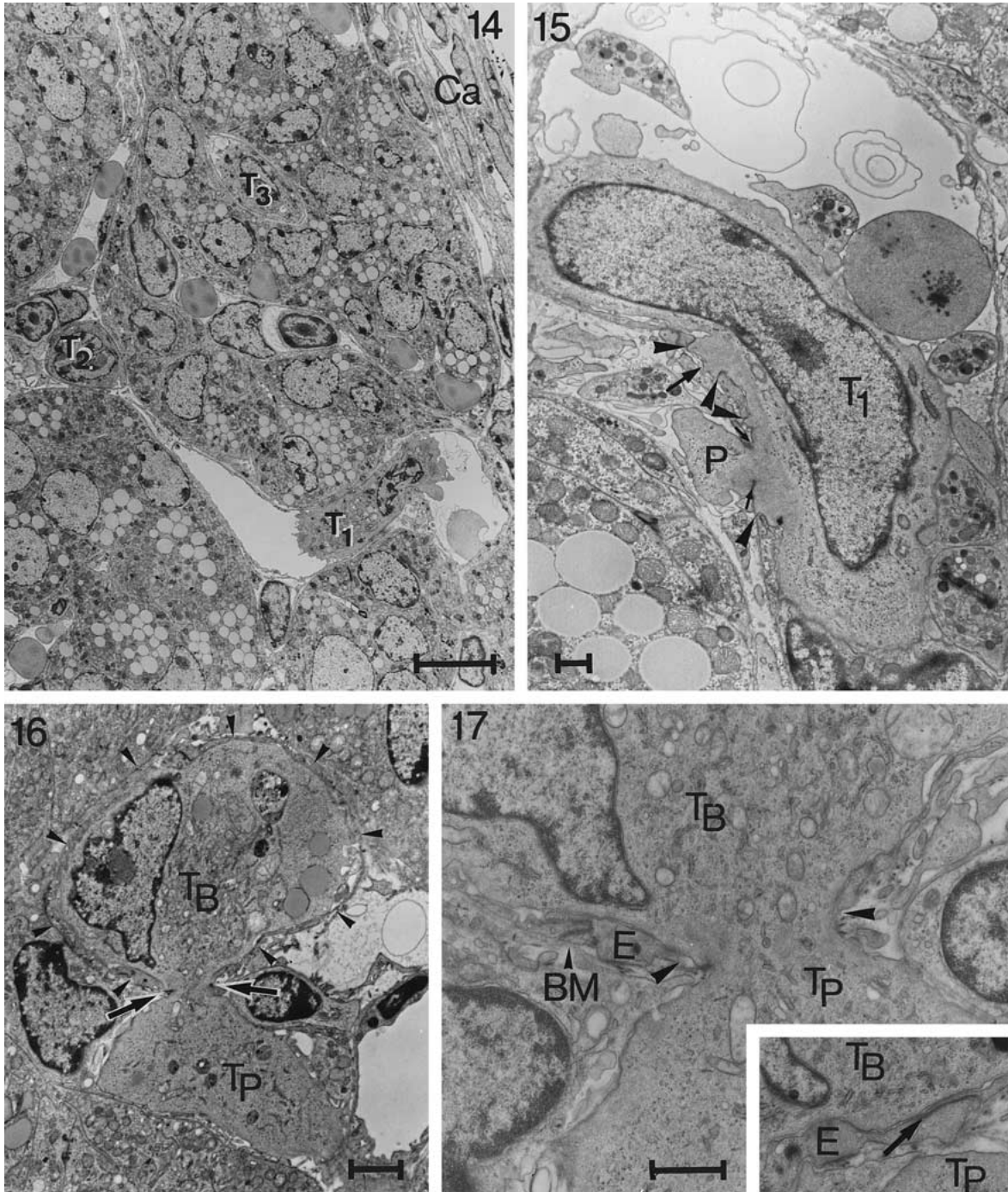
Table 1. Continued.

D	Time after inoculation			
	3 h	24 h	48 h	72 h
Brain	Percentage of tumor cells in the different steps of extravasation			
(1) TC contact with EC	100	95	77	24
(2) EC retraction		5	7	
(3a) TC process penetrating EC and BM			3	
(3b ₁) TC partially covered by EC				
(3b ₂) TC completely covered by EC				
(4) TC extravascular			13	76
	Number of cells examined			
Total number of cells examined 148	20	21	73	34

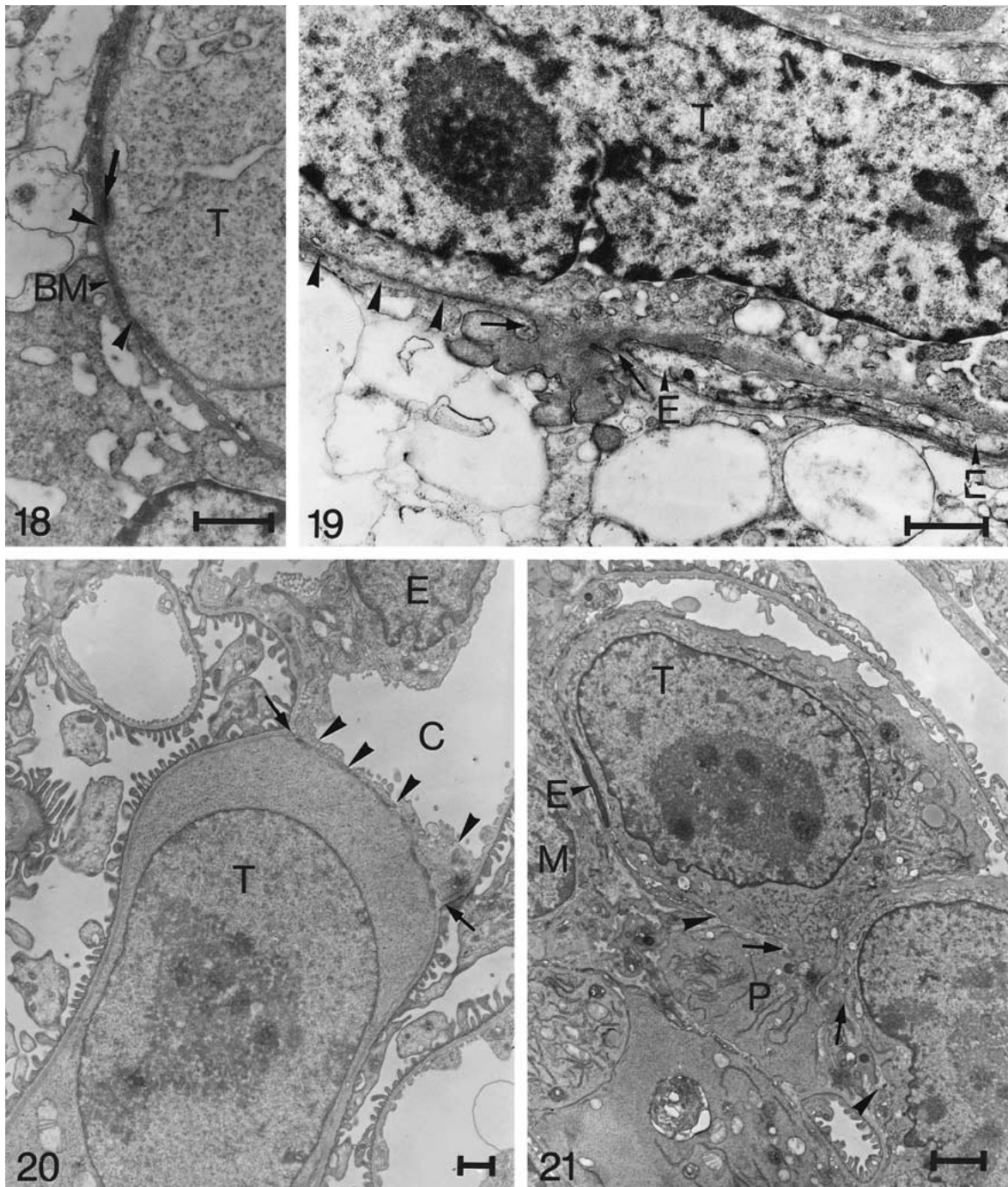
cells was not observed. (Figure 18). Tumor cells arrested in capillaries were never covered by endothelial cells. The penetration of the basement membrane, which was a very rare event, took place through a small gap as observed in case of the lungs and adrenals. (Figure 19). 72 h after injection, tumor cells were still found in the microvasculature of the brain, although 76% of the cells were already in an extracapillary position. No cells were found in the process of extravasation at this time.

Kidney (Table 1E)

Tumor cells were found only in glomerular capillaries. Endothelial cell retraction was observed as early as 3 h after injection. The proportion of tumor cells in contact with



Figures 14–17. (14) Three tumor cells (T1, T2, T3) arrested in the subcapsular region of the adrenal gland, 3 h following intra-arterial inoculation. Ca – adrenal capsule; $\times 1,400$; bar = $10\ \mu\text{m}$. (15) Higher magnification of T1 in a different sectioning plane. The larger process of the tumor cell penetrated the endothelium (arrowheads) and the basement membrane (small arrows). The gap in the endothelium is somewhat larger than the opening in the basement membrane. The smaller process of the tumor cell penetrated the endothelium and punctured basement membrane (large arrow), $\times 6,000$; bar = $1\ \mu\text{m}$. (16) Tumor cell in an advanced stage of extravasation 6 h following inoculation. The tumor cell protrudes through a small gap in the capillary wall (arrows). The body of the tumor cell (TB) locates in the capillary (arrowheads) whereas the large (TP) process extends into the connective tissue, $\times 4,400$; bar = $2\ \mu\text{m}$. (17) Detail of Figure 16. The small gap through which the tumor cell protrudes is bordered by endothelial cells. *Inset:* The area of the gap in the capillary wall in a different sectioning plane. An interendothelial junction (arrow) is visible at this area. E – endothelium; BM – basement membrane; TB – tumor cell body; TP – tumor cell process; $\times 13,000$; bar = $1\ \mu\text{m}$.



Figures 18–21. Detail of a tumor cell (T) arrested in a capillary of the brain, two days following inoculation. A small gap is visible (arrowheads) between the endothelial cells, through which the tumor cell is attached to the basement membrane. Arrow points at the intercellular junction; $\times 14,000$; bar = $1 \mu\text{m}$. (19) Tumor cell (T) arrested in a capillary of the brain two days following inoculation. A small process of the tumor cell protrudes into the perivascular space. The gap (arrows) is bordered by endothelium on the right side (E) whereas on the left side of the gap the endothelium is absent, the tumor cell is attached to the basement membrane (arrowheads); $\times 14,000$; bar = $1 \mu\text{m}$. (20) Tumor cell arrested in a glomerular capillary 16 h after inoculation. The tumor cell is completely covered by the endothelium (arrowheads). Arrows point at the sites where the endothelium is detached from the basement membrane. C – capillary lumen; E – endothelial cell; $\times 6,300$; bar = $1 \mu\text{m}$. (21) Tumor cell (T) in the process of extravasation 16 h following inoculation. The endothelial cells of the glomerular capillary are retracted under the tumor cell (arrowheads). The tumor cell protrudes through a small gap in the basement membrane (arrows) into the mesangium. P – process of the tumor cell; M – mesangial cell; $\times 4,700$; bar = $2 \mu\text{m}$.

Table 1. Continued.

E	Time after inoculation			
	3 h	6 h	16 h	24 h
Kidney	Percentage of tumor cells in the different steps of extravasation			
(1) TC contact with EC	87	46	10	8
(2) EC retraction	13	46	52	43
(3a) TC process penetrating EC and BM		8	12	23
(3b ₁) TC partially covered by EC			14	14
(3b ₂) TC completely covered by EC			10	13
(4) TC extravascular				
	Number of cells examined			
Total number of cells examined 162	23	26	49	64

Steps of the extravasation process: (1) tumor cells facing intact endothelium, (2) retraction of the endothelial cells is observable, tumor cells are in contact with the basement membrane, (3a) tumor cells penetrate the endothelium and the basement membrane with cellular processes, (3b₁) tumor cells are partially covered by endothelial cells, (Number in parentheses represents the percentage of tumor cells in contact with the basement membrane or with the subendothelium), (3b₂) tumor cells which are completely covered by endothelial cells, and are in contact with the basal side of the endothelium. (in Table 1B number in parentheses represents the percentage of tumor cells penetrating the basement membrane by cellular processes). Steps 3a and 3b are parallel events. (4) tumor cells completely extravascular in contact with connective tissue or parenchymal cells.

A minimum of 20 cells were analysed at each time point. To include into a category, each cell on at least 10 ultrathin sections was analysed to ensure, that the most advanced stage is recorded.

the basement membrane increased significantly by 6 h, but only a small number of tumor cells penetrated the basement membrane. Extracapillary tumor cells were not found at this time. After 16 h tumor cells appeared, which were partially or fully covered by endothelial cells (Figure 20), but the proportion of these cells had not changed for up to 24 h. The number of tumor cells penetrating the basement membrane by cellular processes increased for up to 24 h, but surprisingly tumor cells in extravascular position were still not found. The cellular processes penetrating the basement membrane were always oriented toward the mesangium. (Figure 21). Tumor cells penetrating the double layered basement membrane, which separates the capillary lumen from the urinary space were not detected.

Discussion

In this study we analysed the ultrastructure of extravasation of the high metastatic 3LL-HH tumor line in different organs. Four of the five organs chosen (liver, lungs, adrenals,

brain) are the most frequent target organs in humans. Significant differences were found in respect to the time needed for and to the type of extravasation between the organs. Tumor cells reached extraluminal position most rapidly in the liver and adrenals. By 6 h about 20% of the tumor cells were in extravascular position in case of the adrenals, or sequestered from the circulation by endothelial cell cover in case of the liver. Another 20% of the tumor cells were in an advanced stage of extravasation. Earlier we demonstrated, that this 3LL-HH carcinoma line showed liver specificity and preference for adrenals, following intraarterial inoculation [16]. No or negative preference was demonstrated in the case of the lung, kidney and brain, respectively. In accordance with the negative brain preference of this tumor line, the time needed for extravasation proved to be the longest in the brain (>2 days) among the organs examined. This result is in agreement with the observations obtained from the two other studies dealing with the extravasation of hepatoma and Walker carcinosarcoma cells in the brain [4, 6]. Both studies suggested that extravasation took place 3 days following injection. The delay in the onset of extravasation in the brain capillaries is probably caused by the resistance of the specific intercellular junctions present between endothelial cells.

In the lung it took approximately 11 h for the tumor cells to reach extraluminal position, and 16 h were needed for full extravasation. According to other studies, the time necessary to complete the process of extravasation varied significantly among tumor lines (9–48 h), but the majority of lines needed at least 24 h to break through the capillary basement membrane [7–11].

In the lung, adrenal gland and brain a proportion of tumor cells remained in intracapillary position, while the majority of tumor cells were already extravasated with no further cells found in the process of extravasation. This observation suggests that the intracapillary cells do not enter the process of extravasation and will probably be cleared later from the microcirculation.

Two main types of extravasation were observed. In the liver and lung, tumor cells became covered by endothelial cells before penetrating the basement membrane, whereas in the adrenal gland and brain penetration of the basement membrane was preceded only by minor retraction of the endothelial cells. In the lung, data suggest that the tumor cells apparently pause under the endothelial cover before basement membrane invasion and emigration into the connective tissue.

Endothelialization of tumor cells was observed in the case of liver and lung whereas retraction of the endothelium and penetration basement membrane took place in adrenals and brain. Since organ preference was observed only in the case of liver and adrenals, in which organs the tumor cells reached most rapidly extraluminal position, it can be concluded that not the type but the speed of extravasation correlates with organ preference.

It must be emphasized that in the liver, penetration of the basement membrane is not necessary (sequestration of the tumor cells by endothelial cells from the circulation seems to

be sufficient) for successful metastasis formation, because – as shown in our study – by 6 h 10%, while by 24 h only 50% of tumor cells showed degradation of the sinusoidal basement membrane. In organs with well defined basement membranes (lungs, adrenals, brain) the tumor cells moved through small gaps in this structure, similarly to leukocytes. Such a type of movement was not observed in the liver, instead the tumor cells practically sank into the hepatocytes without major changes in shape, during which process the microvilli of the hepatocytes disappeared. Since in the liver the basement membrane is localised between the microvilli of the hepatocytes, the above process can contribute to the disappearance of the basement membrane material. This observation is in contrast with other earlier results, showing large globular cellular processes of lymphosarcoma and mammary carcinoma cells to protrude into the hepatocytes [5, 17].

The phenomenon, that in the liver the basement membrane was present around a significant proportion of tumor cells, is in accordance with our earlier finding, according to which angiogenesis in liver metastases of this tumor line is initiated by the migration of tumor cells on the surface of sinusoidal basement membrane. During this process the endothelial cells become separated from their basement membrane, which is thought to initiate the proliferation of the endothelial cells and of the development of tortuous intratumoral vessels, lacking basement membrane [18]. These observations question the necessity of basement degradation following endothelialization of these tumor cells in the liver.

In the kidney, both types of extravasation could be observed. Since tumor cells localised entirely in the mesangial matrix were not found, the process of extravasation probably stopped, either when tumor cells became sequestered by endothelial cells in glomerular capillary loops having no contact with the mesangium, or when the tumor cells penetrated the endothelium and their processes became projected into the mesangial matrix. Some of the endothelialized tumor cells were found facing entirely the double layered basement membrane, which they were obviously not able to penetrate. A similar observation was made in the lungs, however, in this case the tumor cells were able to penetrate the epithelial basement membrane provided they were already extravasated and localised in the connective tissue. [19]. In other organs such as lungs, adrenals and brain, the tumor cells have to cross only a thin layer (100–200 nm) of basement membrane to reach a compartment with different matrix composition. The tumor cell processes projecting into the mesangial matrix cannot sense other matrix components than that of the basement membrane (mesangial matrix contains basement membrane components such as laminin and collagen IV) [19], which can be a stop signal for migration. The fate of the tumor cells arrested halfway in the process of extravasation is not known, but they probably continue to proliferate, since intravascular mitotic figures were frequently found in all organs.

In the liver and adrenals, most of the tumor cells were arrested in zone 1 and in the subcapsular region, respectively, which observation suggests that tumor cells were trapped

mechanically by size restriction. In all of the organs, the arrested cells suffered extreme deformations, which as it was suggested also by others, excludes rolling of the tumor cells on the surface of endothelial cells [1, 20]. These observations are in contrast to recent results, obtained by intact organ microscopy, showing the arrest of tumor cells in pre-capillary arterioles exceeding the size of the tumor cells [28].

Earlier *in vitro* studies have shown that penetration of endothelial monolayer starts with retraction of endothelial cells followed by migration of the tumor cells under the endothelial cells and spreading on the subendothelial matrix [15]. Retraction of endothelial cells proved to be reversible, leading to the restoration of monolayer integrity above the tumor cells. Sublethal concentrations of H₂O₂, 12-S-HETE and tumor derived retraction factor were shown to mediate reversible retraction of endothelial cells [21–23]. Endothelial cell injury, which can also be caused by H₂O₂ produced by tumor cells may also lead to the exposure of subendothelial extracellular matrix facilitating firm attachment of tumor cells to the capillary wall [24]. Damaged endothelial cells in contact with the arrested tumor cells were never observed in our study, not even in case of the brain, where the long stay of compressed tumor cells in the capillaries caused extreme flattening of the endothelial cells.

In the adrenals, the tumor cells caused only a very limited retraction of endothelial cells. The tumor cells moved through the endothelium and basement membrane simultaneously, similarly to leukocytes, except for neutrophils. In the brain, the retraction of endothelial cells was not closely coupled to the penetration of the basement membrane, but was most probably a rapid event, because an extremely low proportion of tumor cells were found in the process of extravasation compared to the other organs.

Retraction of endothelial cells took place mainly beneath the tumor cells, suggesting that a putative retraction factor cannot be present in a soluble form, but rather it should be expressed on the surface of the tumor cells.

In the liver and adrenals, shortly after initial arrest, small processes were found projecting through the fenestrations of the endothelial cells, but these projections do not seem to play a role in the process of extravasation, since they did not grow with time and endothelial cells were later separated at intercellular junctions. They may, however, have a role in the firm attachment of the tumor cells to the capillary wall. The behaviour of endothelial cells in the liver and lung showed a similarity to that of *in vitro* observations, but flattening of the tumor cells was never observed before penetration of the basement membrane. More importantly, a new feature was noted in the process of tumor cell sequestration from the circulation. In the lung, the retraction of endothelial cells was preceded by the appearance of cytoplasmic projections originating from the apical surface of the endothelial cells. The size of these projections was limited, never covering the entire tumor cell. After dissolution of interendothelial junctions the endothelial cells probably roll their membrane on the surface of the tumor cell, during which process a switch takes place in the membrane polarity from apical to basal,

since the completely covered tumor cells were in contact exclusively with the basal side of the endothelial cells. This observation suggests a more active role of the endothelial cells in the process of extravasation in the liver and lung, as previously suggested. Similarly, endothelium covers neutrophils during extravasation, but the process is different from that observed by us, since – as it was recently shown – the openings in the endothelium are within the body of the endothelial cells (transcellular) [25]. In the liver the dissolution of the interendothelial junctions occurred probably earlier or simultaneously with development of these apical projections. In this case, however, specific attachment points with increased electron density were detected between the tumor and endothelial cell membranes. These structures can play a role in the rapid sequestration of tumor cells from the circulation and thereby in the observed liver preference. The nature of these attachment points, observed only in the liver is not known, but they may contain adhesion molecules, which were shown to redistribute during tumor cell attachment to endothelial monolayer *in vitro* [26].

IL-1 dependent and independent metastasis were detected in organ clusters, during arterial dissemination of B16 melanoma cells [27]. The liver lung and adrenals fall into the group of IL-1 dependent metastasis. Our ultrastructural study showed different types of extravasation of tumor cells in the lungs and adrenals, whereas in the brain, falling into the IL-1 independent group, extravasation proceeded in a similar way as in the adrenals. These observations suggest that IL-1 inducible adhesion molecules cannot mediate the observed difference in the interaction of tumor cells with endothelial cells of the organs studied.

Acknowledgement

This work was supported by the National Science Found of Hungary (T 26439).

References

- Weiss L, Orr WF, Honn KV. Interactions between cancer cells and the microvasculature: a rate regulator for metastasis. *Clin Exp Metastasis* 1989; 7: 127–67.
- Azzarelli B, Easterling K, Norton JA. Leukemic cell- endothelial cell interactions in leukemic cell dissemination. *Lab Invest* 1989; 45: 45–64.
- DeBruyn PPH, Cho Y, Michelson S. Endothelial attachment and plasmalemmal apposition in the transcellular movement of intravascular leukemic cells entering the myeloid parenchyma. *Am J Anat* 1989; 186: 115–26.
- Kawaguchi T, Nakamura K. Analysis of the lodgement and extravasation of tumor cells in experimental models of hematogenous metastasis. *Cancer Met Rev* 1986; 5: 77–94.
- Roos E, Dingemans KP, van de Pavert IV et al. Invasion of lymphosarcoma cells into the perfused mouse liver. *J Natl Cancer Inst* 1977; 58: 399–407.
- Chew EC, Josepson RL, Wallace AC. Morphologic aspects of the arrest of circulating cancer cells. In Weiss L (ed) *Fundamental Aspects of Metastasis*. Amsterdam: North-Holland, 1976; 122–50.
- Crissman JD, Hatfield JS, Menter DG et al. Morphological study of the interaction of intravascular tumor cells with endothelial cells and subendothelial matrix. *Cancer Res* 1988; 48: 4065–72.
- Kinjo M. Lodgement and extravasation of tumour cells in blood-borne metastasis: an electron microscope study. *Br J Cancer* 1978; 38: 293–301.
- Knierim M, Paku S, Paweletz N et al. Ultrastructural studies on the lung colonization by nonmetastatic rat tumor cells. *Anticancer Res* 1986; 6: 669–82.
- Paku S, Paweletz N, Spiess E et al. Ultrastructural analysis of experimentally induced invasion in the lung by tumor cells metastasizing lymphatically. *Anticancer Res* 1986; 6: 957–66.
- Lapis K, Paku S, Liotta LA. Endothelialization of embolised tumor cells during metastasis formation. *Clin Exp Metastasis* 1988; 6: 73–89.
- Machado EA, Gerard DA, Mitchell JR et al. Arrest and extravasation of neoplastic cells. *Virchows Arch A* 1982; 396: 73–89.
- Nakamura K, Kawaguchi T, Asahina S et al. Electronmicroscopic studies on extravasation of tumor cells and early foci of hematogenous metastases. *Gann Monogr Cancer Res* 1977; 20: 57–71.
- Ruoslahti E, Rajotte D. An address system in the vasculature of normal tissues and tumors. *Annu Rev Immunol* 2000; 18: 813–27.
- Nicolson GL. Metastatic tumor cell attachment and invasion assay utilizing vascular endothelial cell monolayers. *J Histochem Cytochem* 1980; 30: 214–20.
- Paku S, Rot A, Ladanyi A et al. Demonstration of the organ preference of liver selected high metastatic Lewis lung tumor line. *Clin Exp Metastasis* 1989; 7: 599–607.
- Dingemans KP. Invasion of liver tissue by blood-borne mammary carcinoma cells. *J Natl Cancer Inst* 1974; 53: 1813–24.
- Paku S, Lapis K. Morphological aspects of angiogenesis in experimental liver metastases. *Am J Pathol* 1993; 143: 926–36.
- Courtoy PJ, Timpl R, Farquhar MG. Comparative distribution of laminin, type IV collagen and fibronectin in the rat glomerulus. *J Histochem Cytochem* 1982; 30: 874–86.
- Thorlacius H, Prieto J, Raud J et al. Tumor cell arrest in the microcirculation: lack of evidence for a leukocyte-like rolling adhesive interaction with vascular endothelium *in vivo*. *Clin Immunol Immunopathol* 1997; 83: 68–76.
- Bradley JR, Thiru S, Pober JS. Hydrogen peroxide-induced endothelial retraction is accompanied by a loss of the normal spatial organization of endothelial cell adhesion molecules. *Am J Pathol* 1995; 147: 627–41.
- Honn KV, Tang DG, Grossi I et al. Tumor cell derived 12(S)-hydroxy-eicosatetraenoic acid induces microvascular endothelial cell retraction. *Cancer Res* 1994; 54: 565–74.
- Kusama T, Nakamori S, Ohigashi H et al. Enhancement of *in vitro* tumor cell transcellular migration by tumor-cell-secreted endothelial-cell-retraction factor. *Int J Cancer* 1995; 63: 112–8.
- Orr WF, Wang HH, Lafrenie RM et al. Interactions between cancer cells and the endothelium in metastasis. *J Pathol* 2000; 190: 310–9.
- Feng D, Nagy JA, Pyne K et al. Neutrophils emigrate from venules by a transendothelial cell pathway in response to FMLP. *J Exp Med* 1998; 187: 903–15.
- Lewalle JM, Bajou K, Desreux J et al. Alteration of interendothelial adherens junctions following tumor cell-endothelial cell interaction *in vitro*. *Exp Cell Res* 1997; 237: 347–56.
- Anasagasti M, Olaso E, Calvo F et al. Interleukin 1-dependent and independent mouse melanoma metastases. *J Natl Cancer Inst* 1997; 89: 645–65.
- Al-Mehdi AB, Tozawa K, Fisher AB et al. Intravascular origin of metastasis from the proliferation of endothelium-attached tumor cells: a new model for metastasis. *Nat Med* 2000; 6: 100–2.

ROLE OF SINUSOIDAL HEPARAN SULFATE PROTEOGLYCAN IN LIVER METASTASIS FORMATION

József TÓVÁRI, Sándor PAKU, Erzsébet RÁSÓ, Gábor POGÁNY, Ilona KOVALSZKY, Andrea LADÁNYI, Károly LAPIS and József TÍMÁR*
1st Institute of Pathology and Experimental Cancer Research, Semmelweis University of Medicine, Budapest, Hungary

Previous studies have indicated that the predominant sites of tumor cell extravasation in the liver are the sinusoidal vessels, where tumor cells contact the sinusoidal endothelium and the subendothelial extracellular matrix containing the basic components of the basement membrane. We studied the role of sinusoidal extracellular matrix in metastasis formation by 3LL-HH murine tumor cells selected for their preferential liver colonization. 3LL-HH tumor cells did not efficiently adhere to cryosections of the liver, but they recognized the sinusoids and vessel walls. Pre-treatment of the mice with polyclonal anti-basement membrane antibodies [anti-laminin, anti-fibronectin and anti-heparan sulfate proteoglycan (HSPG)] significantly modulated the organ distribution of tumor cell colonies following intracardial injection: all 3 antibodies inhibited kidney colonization; anti-laminin and anti-fibronectin antibodies inhibited lung colonization; and only anti-HSPG antibody inhibited liver colonization. In several organs such as the heart, stomach, pancreas and bladder, anti-basement membrane antibody treatment did not alter the process of colonization. Immunofluorescence studies showed that anti-HSPG antibody recognized the basement membranes of sinusoids and blood vessels. Our data suggest a specific involvement of sinusoidal HSPG in the liver colonization of 3LL-HH cells. *Int. J. Cancer* 71:825–831, 1997.

© 1997 Wiley-Liss, Inc.

The metastatic cascade consists of various aspects of tumor cell-matrix interactions including adhesion, digestion and migrations mediated by cell membrane receptors (Liotta, 1986). Although the sequential steps of the metastatic cascade are well characterized, the mechanism of the organ-specific tumor dissemination is poorly understood. Tumor dissemination consists of both random and non-random mechanisms, and organ-specific metastasis is characteristic of several tumor types such as lung, breast or prostate cancers.

Liver metastasis is one of the most frequent complications of tumor dissemination in humans. Therefore, an understanding of the underlying mechanisms might have clinical significance. Studies on liver-specific experimental metastasis models have suggested that tumor cells specifically recognize the liver sinusoidal endothelium and positively respond to a local factor (Hamada *et al.*, 1993; Long *et al.*, 1994). Analysis of the liver-specific tumor phenotype revealed that heparan sulfate proteoglycans (HSPGs) are overexpressed in carcinoma and melanoma cells metastatic to the liver (Tímár *et al.*, 1987, 1992) although the mechanism by which these PGs influence organ-specific metastasis remains unknown.

Morphological analysis of liver dissemination indicated that the predominant sites of tumor cell extravasation are the liver sinusoids (Dingemans *et al.*, 1978; Paku and Lapis, 1993), where tumor cells interact with the sinusoidal endothelium, with the subendothelial basement membrane (Griffiths *et al.*, 1991) and with hepatocytes before initiating local proliferation. Tumor cell-endothelial cell interaction is a complex process in which early steps are mediated by cell-adhesion molecules, subsequently followed by endothelial cell retraction and establishment of tumor cell-subendothelial basement membrane contacts (Honn and Tang, 1992). This implies that to understand the liver-specific metastasis process better, we need more data on the molecular mechanism of tumor cell-sinusoidal basement membrane interactions. We have used here 3LL-HH lung carcinoma cells, characterized by their preferential liver metastatic properties, as an *in vivo* model throughout our studies. Our *in vivo* and *in vitro* data suggest that a component of

the sinusoidal basement membrane, the HSPG, plays a critical role in the formation of liver metastasis.

MATERIAL AND METHODS

Purification of proteoglycans

Liver tissues were homogenized in 3.4 M NaCl, 50 mM Tris HCl (Merck, Darmstadt, Germany), 10 mM EDTA (Serva, Heidelberg, Germany), 5 mM N-ethylmaleimid (Merck), 0.5 mM phenylmethanesulphonyl fluorid (Serva), 0.001% soy bean trypsin inhibitor (Sigma, St. Louis, MO), 5% Gordox (Reanal, Budapest), pH 7.4, and then extracted with 4 M guanidine HCl (Merck), 1% Triton X-100 (Serva), 50 mM sodium acetate (Merck), 10 mM EDTA and protease inhibitors as above, pH 5.0, at 4°C for 48 hr. Cell debris were removed by centrifugation (600g for 30 min). TCA precipitation of supernatant was carried out as described by Lyon and Gallagher (1991) to remove the nucleic acids and most liver proteins. The supernatant containing PGs was dialyzed against 7 M urea (Serva), 0.05 M Tris HCl, pH 7.0 (containing protease inhibitors as above). Dialyzed extract was applied on 1 ml DEAE 52 (Whatman, Clifton, NJ) column equilibrated with 7 M urea, 0.05 M Tris-HCl, pH 7.0. The column was washed with 10 ml of the same buffer containing 0.1 and 0.2 M NaCl, and PGs were eluted by NaCl gradient increasing from 0.2 to 0.8 M.

The protein content of each fraction was determined by a modified Lowry method (Hartree *et al.*, 1972).

Adhesion assays

Five micrometer cryosections were prepared from mouse organs and placed on glass slides. Tumor cells (10^4 /ml) in medium 199 were incubated on cryosections at 37°C in CO₂ atmosphere for 1 hr. The non-adherent cells were removed by repeated washings in medium (2×), and the adherent cells were fixed with 4% paraformaldehyde for 15 min and stained with methylene blue; the cell number/unit area was then counted under light microscope using a 20× lens.

In other tests, 96-well plates were coated overnight at 37°C with isolated PG fractions in PBS (1 µg protein/well or PBS alone) and further incubated for another hour with anti-HSPG antibody (1 µg/well; Tímár and Kovalszky, 1995; Gallai *et al.*, 1996) or PBS. The control wells contained only PBS and PBS + antibody; 10^4 3LL-HH cells in medium 199 were added to each well and incubated for 1 hr at 37°C. After removal of the non-adherent cells, the adherent ones were fixed and counted by phase contrast microscopy.

Motility assay

Chemotaxis was assayed by using 48-well Boyden chamber (Neuro Probe, Pleasanton, CA) and 8 µm pore size uncoated Nucleopore filters (NeuroProbe). The PG fractions or the organ-

Contract grant sponsor: National Science Foundation; Contract grant number: OTKA 13128.

*Correspondence to: 1st Institute of Pathology and Experimental Cancer Research, Semmelweis University of Medicine, Budapest, Ullői út 26., H-1085 Hungary. Fax: (36)-1-117-1074.

Received 24 September 1996; accepted 31 January 1997

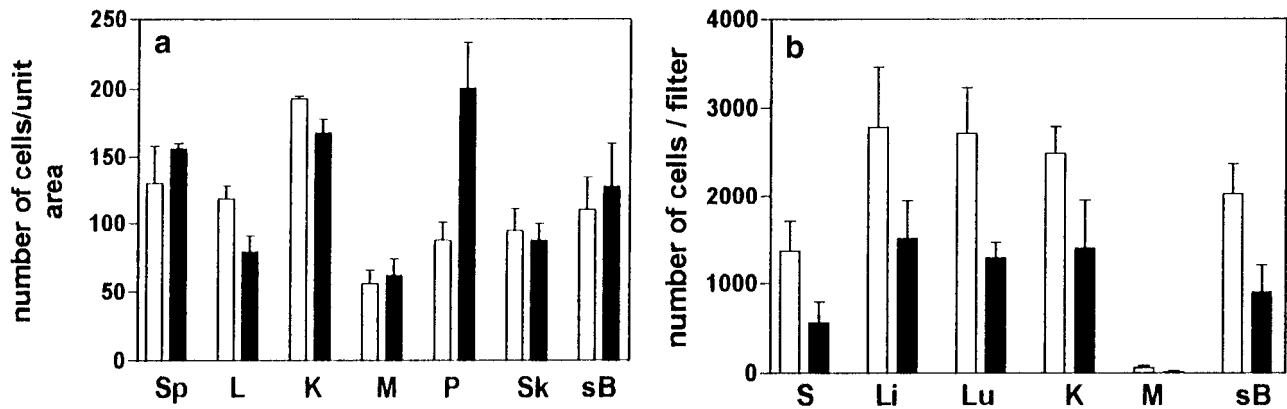


FIGURE 1 – Interaction of Lewis lung tumor clones with mouse liver tissue. (a) Adhesion of 3LL (open bars) and 3LL-HH (black bars) tumor cells to cryosections of mouse organs *in vitro*. Tumor cells were incubated with organ sections for 1 hr at 37°C, the non-adherent cells were removed by repeated washings with fresh medium and the adherent cells were fixed with PFA, stained with methylene blue and counted under the light microscope using a 20× lens. Data are expressed as number of cells/unit area \pm SD; $n = 3$. (b) Chemotactic migration of 3LL (open bars) and 3LL-HH (black bars) cells toward mouse organ homogenates *in vitro*. Organs were homogenized, filtered as described in Material and Methods and used at standard protein concentration (1 μ g/ml) in the lower well of a Boyden chamber. Tumor cells were placed into the upper chamber for 4 hr. The filter was fixed, and cells were stained and counted by light microscopy. Data are expressed as mean number of cells migrated (\pm SD; $n = 4$). Sp, spleen; L, liver; K, kidney; M, muscle; P, pancreas; Sk, skin; sB, small bowel.

derived proteins (500g supernatant of normal homogenized mouse organs) were added in PBS to the lower wells (1 μ g protein/well), while upper wells were filled with 3LL-HH cells (50,000/well) in medium 199 supplemented with 10% FCS (Serva). The chamber was incubated for 4 hr at 37°C in a 5% CO₂ atmosphere. At the end of the assay, filters were removed, fixed in methanol and stained. Cells that had migrated through the pores to the lower side of the filter were counted by light microscopy.

Proliferation assay

Tumor cells were plated on 24-well plates (Costar, Cambridge, MA) at a concentration of 5×10^4 cells/well in 1 ml RPMI supplemented with 5% FCS (Serva). GAGs (50–100 μ g/ml) were added to the wells for 48 hr, and viable cell numbers were counted at the end of the assay after EDTA detachment the using Trypan blue dye exclusion assay and a hemocytometer. Hyaluronic acid (m.w. >700 kDa; Sigma), chondroitin 4/6-sulfate (m.w. 55 kDa; Sigma), heparin (m.w. 12 kDa; Choay, Paris, France) and heparan sulfate (m.w. 35 kDa; Bioetica, Lyon, France) were used as GAGs.

Antibodies to basement membrane components

Polyclonal rabbit anti-serum was raised against purified laminin and fibronectin and was kindly provided by A. Vaheri (Helsinki, Finland). These antibodies recognized their corresponding proteins by Western blot at a dilution of 1:5,000. The rabbit polyclonal anti-HSPG antibody was raised against HSPG fraction, isolated from EHS sarcoma and shown to react predominantly with a high m.w. HSPG having a core protein of 400 kDa corresponding to perlecan (Tímár and Kovalszky, 1995).

Antibody-dependent cell-mediated cytotoxicity

3LL-HH cells were labeled *in vitro* with 2 μ Ci/ml Br[³H]dUrd (Amersham, Aylesbury, UK) in RPMI 1640 medium containing 10% FCS for 24 hr at 37°C, washed 3 times with medium to remove the unbound isotope and incubated with anti-HSPG antibody for 30 min at a 1:100 dilution (control cells were incubated with non-immune rabbit antibody). Syngenic spleen cells were added to the wells at an effector-target ratio of 100:1 for 24 hr in a total volume of 200 μ l/well in 96-well tissue culture plates (Nunc, Roskilde, Denmark), and the released isotope in the medium was determined by liquid scintillation counting (Beckmann), measuring 150 μ l samples from each well. The total releasable label was determined after treating the target cells with 1% SDS. Spontaneous release was measured in the absence of

effector cells. Three to 6 replicates were used for each determination.

Anti-HSPG antibody ELISA

Animals were treated with 0.1 ml undiluted polyclonal rabbit antibody to HSPG; 30, 60, 90 and 120 min after administration of the antibody, the serum was isolated from the animals. Purified extracellular matrix from EHS sarcoma (2 μ g/well; Gallai *et al.*, 1996) was dried onto ELISA plates (Greiner, Nützig, Germany) and blocked with 1% BSA (Sigma); the wells were then incubated with the serum of antibody-treated animals at a dilution of 1:10 for 1 hr, followed by horseradish peroxidase-conjugated anti-rabbit IgG (Vectastain, Vector, Burlingame, CA) for another hour and then TMB substrate (Sigma) (5 washings with buffer between each step). The immunoreaction was measured with an ELISA reader (Labsystems, Shrewsbury, MA).

Animals and tumor lines

Inbred C57Bl/6 mice from our Institute were used throughout our studies. The high liver metastatic 3LL-HH tumor line was maintained by serial intrasplenic transplantations of tumor cells obtained from the liver metastases. Single-cell suspensions were prepared from 14-day-old 3LL-HH liver metastases. Tumor tissue was minced with crossed scalpels and filtered through 4-fold gauze. After centrifugation (550g) and washing in medium 199, the viability of the tumor cells was determined by the Trypan blue exclusion test (>50%).

In vivo treatments

Animals were injected i.v. with 0.1 ml undiluted polyclonal rabbit antibody to laminin, fibronectin and HSPG. Two hours after administration of the antibodies, 2×10^4 tumor cells in 0.1 ml PBS were injected into the left heart ventricle of the mice as described by Paku *et al.* (1989). Animals were sacrificed by a Nembutal overdose 11 days after tumor cell inoculation. The numbers of tumor colonies in internal organs were determined, and the relative percentages of the tumor colonies in organs were calculated.

Immunofluorescence

The distribution of antibodies within the organs 2 hr after injection was determined by immunofluorescence. From each antibody-treated group one animal was sacrificed by Nembutal overdose; the kidneys, adrenal glands and liver were then removed and frozen in isopentane cooled by liquid nitrogen. Five microme-

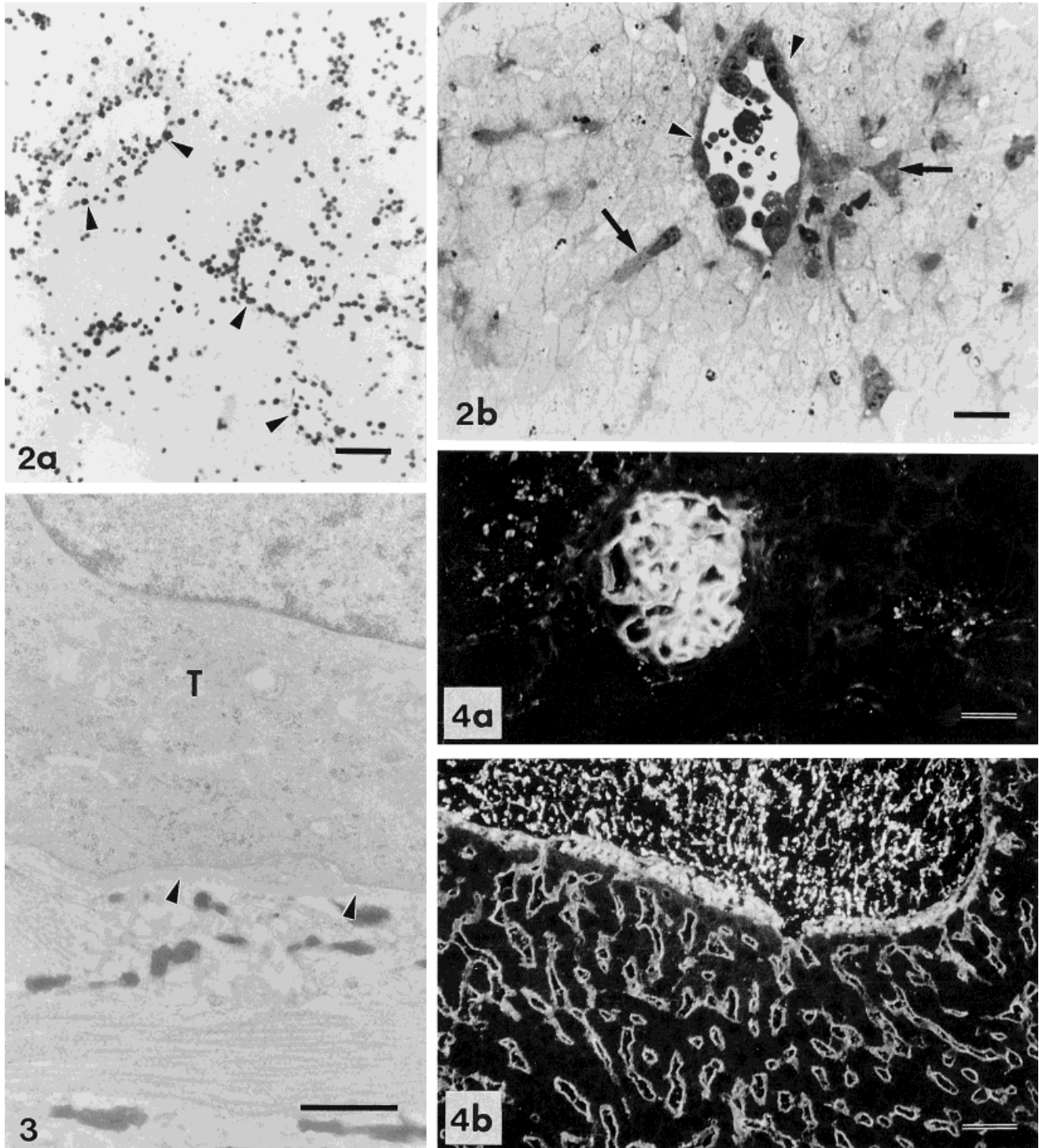


FIGURE 2 – Distribution of adherent 3LL-HH cells over a cryosection of the mouse liver. (a) Light microscopy indicates that tumor cells accumulated over the sinusoids and the portal vessels (arrowheads). Scale bar = 100 μ m. (b) Adherent 3LL-HH cells spread along the liver sinusoids (arrows) and the portal vein (arrowheads). Scale bar = 50 μ m.

FIGURE 3 – Ultrastructure of 3LL-HH cell-liver interactions. Tumor cells were incubated with cryosections of the mouse liver as in Figure 1, and were then fixed and processed for electron microscopy. After 1 hr of incubation, interaction of the tumor cell with the subendothelial basement membrane of a major portal vessel could be observed (arrowheads). T, tumor cell. Scale bar = 1 μ m.

FIGURE 4 – Localization of anti-HSPG antibody by immunofluorescence in mouse organs 4 days after i.v. injection of the antibody. Rabbit polyclonal antibody against basement membrane HSPG was injected i.v. into mice (0.1 ml/animal). The animals were sacrificed by Nembutal overdose on day 4 post-injection, organs were removed and cryosections were made. The anti-HSPG antibody in organs was detected in organ cryosections by a TRITC-conjugated anti-rabbit IgG and photographed using a fluorescent microscope. (a) Mouse kidney. Note the presence of anti-HSPG antibody along the glomerulus basement membrane. Scale bar = 50 μ m. (b) Mouse liver. Note the presence of anti-HSPG antibody along the liver sinusoids and the basement membrane of the portal vessels. Scale bar = 50 μ m.

ter frozen sections were reacted with rhodamine-conjugated goat anti-rabbit antibody (Jackson ImmunoResearch, West Grove, PA). The sections were analyzed on an Olympus (Tokyo, Japan) Vanox epifluorescent microscope.

Electron microscopy

Cryosections (10 μm) were incubated with tumor cells as described above. After incubation, sections were fixed in 2.5% glutaraldehyde for 10 min, rinsed in PBS and post-fixed in 1% OsO_4 . Dehydrated sections were embedded by placing gelatin capsules filled with resin (Spurr, Serva, Heidelberg, Germany) on the mounted sections. After polymerization (70°C, 16 hr) capsules with sections were removed by immersing the slides in liquid nitrogen. Semi-thin sections were stained with 0.5% toluidine blue to select the desired areas for ultrathin sectioning. Ultrathin sections were examined by a Philips (Eindhoven, the Netherlands) CM10 electron microscope.

RESULTS

3LL-HH tumor cells are characterized by preferential metastatic potential to the liver (Paku *et al.*, 1989); we attempted to determine the key factor(s) that might regulate this phenotype. Interestingly, adhesion of unselected and selected Lewis lung tumors (3LL and 3LL-HH) to cryosections of mouse organs did not indicate selective recognition of the liver tissue (Fig. 1a). Similarly, proteins isolated from the liver did not exhibit selective chemotactic activity for 3LL-HH cells when compared with other organs such as lung or kidney (Fig. 1b), suggesting that the recognition of this organ by the 3LL-HH tumor cells is not mediated by a liver cell-specific factor(s). On the other hand, the distribution of 3LL-HH tumor cells over the liver sections was non-random; it showed significant preference for portal vessels and the sinusoids (Fig. 2a), and even tumor cell spreading was observed over these areas (Fig. 2b). Ultrastructural analysis indicated that 3LL-HH tumor cells adhered to the basement membranes of blood vessels and the sinusoids (Fig. 3).

We have used polyclonal antibodies produced against major basement membrane proteins (laminin, fibronectin and perlecan-HSPG) to study the role of basement membrane in the liver-specific dissemination of 3LL-HH tumor cells *in vivo*. These antibodies have been administered into animals *i.v.* before the inoculation of tumor cells to mask the basement membrane protein epitopes theoretically involved in tumor cell-extracellular matrix interactions. The injected antibodies accumulated in the basement membranes of various organs such as kidneys (Fig. 4a) and liver (Fig. 4b), as demonstrated by immunofluorescence. In the liver, the anti-basement membrane antibodies could be detected by immunofluorescence in the sinusoids and portal vessels (Fig. 4b). No serious side effects were detected in animals treated with anti-basement membrane antibodies during the 11 day period. ELISA analysis of the serum of anti-HSPG antibody-injected animals indicated 80% of the antibody in the circulation at 2 hr and 50% on the 2nd day, indicating slow clearance (data not shown).

Among the various anti-basement membrane antibody pretreatments, only anti-HSPG antibody was successful in inhibiting the overall organ colonization of 3LL-HH cells (Table I), although the anti-laminin as well as anti-fibronectin antibodies also exhibited a slight inhibitory potential. In analyzing the number of colonies in various organs, anti-HSPG antibody proved to be effective in the case of the liver (Fig. 5a), all 3 anti-basement membrane antibodies were inhibitory in the case of the kidneys (Fig. 5c) and the anti-laminin antibody was the most effective for the lung colonization (Fig. 5b). The antibody pretreatments did not modulate the colonization of 3LL-HH cells to the heart, stomach, pancreas, muscle and bladder (Table I), suggesting an organ-specific mechanism. Since 3LL-HH cells express all 3 basement membrane components at their surface (Lapis *et al.*, 1986; Tímár *et al.*, 1987) and the injected polyclonal antibodies were detectable in the circulation at the time of tumor cell injection, it is possible that the

TABLE I—ANTI-BASEMENT MEMBRANE ANTIBODY PRETREATMENT OF THE HOST¹

	Control	Treatment		
		α -HSPG	α -LM	α -FN
Effect on dissemination of 3LL-HH cells <i>in vivo</i>				
No. of metastases/ animal	362 \pm 103	191 \pm 67 ²	258 \pm 89	279 \pm 103
Lack of effects on the colonization of various organs by 3LL-HH cells				
Heart	22.8 \pm 6.0	26.0 \pm 5.0	18.2 \pm 8.0	17.0 \pm 6.0
Stomach	13.8 \pm 6.1	12.5 \pm 7.0	10.3 \pm 3.0	11.0 \pm 4.0
Pancreas	21.3 \pm 10.3	18.7 \pm 10	25.0 \pm 10.0	29.0 \pm 10.0
Bladder	3.5 \pm 1.8	4.9 \pm 5.0	4.1 \pm 2.0	5.0 \pm 2.0

¹Mice were pretreated with 0.1 ml of rabbit polyclonal antibody/animal (tail vein injection) 2 hr before intracardial inoculation of 2×10^4 tumor cells. Animals were sacrificed by a Nembutal overdose on day 11 post inoculation. Organs were examined and counted for tumor colonies using a stereo-microscope. Data are expressed as mean number of metastases (\pm SD; n = 10). HSPG, heparan sulfate proteoglycan; LM, laminin; FN, fibronectin. ² $p < 0.05$.

altered organ distribution of 3LL-HH cells is due to antibody-dependent cell-mediated cytotoxicity. 3LL-HH cells were shown to be resistant to the cytotoxic effects of autologous splenocytes in the presence of polyclonal anti-HSPG antibody (at the same concentration that was found in the serum of the antibody-treated mice: 1:100 dilution) (data not shown) excluding an immunological mechanism involved in the modulatory effects of anti-basement membrane antibodies on organ colonization of 3LL-HH cells.

The above data suggest that the liver-specific colonization pattern of 3LL-HH cells depends on the sinusoidal HSPG molecules. We thus next analyzed the interaction of 3LL-HH tumor cells with mouse liver-derived HSPG species. Murine liver PGs have been isolated and step-eluted from the DEAE cellulose column with increasing NaCl concentrations. Further analysis of the PG fractions using HPLC revealed a high molecular mass HSPG (>500 kDa) eluted by 0.4 M NaCl (Tímár and Kovalszky, 1995). Immunoblot analysis indicated that this PG corresponded to perlecan and reacted with the antibody raised against EHS-derived large HSPG (Tímár and Kovalszky, 1995).

To reveal the function of HSPG in the liver colonization of 3LL-HH cells, we analyzed 3 aspects of tumor cell-HSPG interactions: adhesion, migration and proliferation. The 3LL-HH tumor cells adhered *in vitro* to isolated PG fractions of mouse liver, with significant preference for the fraction eluted by 0.4 M NaCl (Fig. 6a). The anti-HSPG antibody (1 $\mu\text{g}/\text{well}$) significantly inhibited the adhesion of tumor cells to this fraction, suggesting the presence of the high m.w. HSPG (perlecan) (Fig. 6a). The liver-derived proteoglycans were not chemotactic for 3LL-HH tumor cells in migration assay when compared with the highly chemotactic liver homogenate itself (Fig. 6b). Finally, 3LL-HH tumor cells were treated with basement membrane-derived heparan sulfate, heparin, chondroitin sulfate and hyaluronic acid *in vitro* for 48 hr, and the effects on cell proliferation were determined. The results indicated a preferential, dose-dependent stimulation by exogenous heparan sulfate and inhibition by hyaluronic acid on the *in vitro* proliferation of 3LL-HH cells (Fig. 7).

DISCUSSION

To understand the mechanism of liver metastasis, we have used a tumor line, the 3LL-HH lung carcinoma, selected for its liver metastatic potential by sequential intrasplenic injections (Pál *et al.*, 1983). This procedure resulted in a significantly increased liver colonization potential as well as resistance to non-specific immune effector cells (Paku *et al.*, 1989; Ladányi *et al.*, 1993).

The mechanism of organ-specific metastatic potential of malignant tumor cells is not fully understood. It has been demonstrated

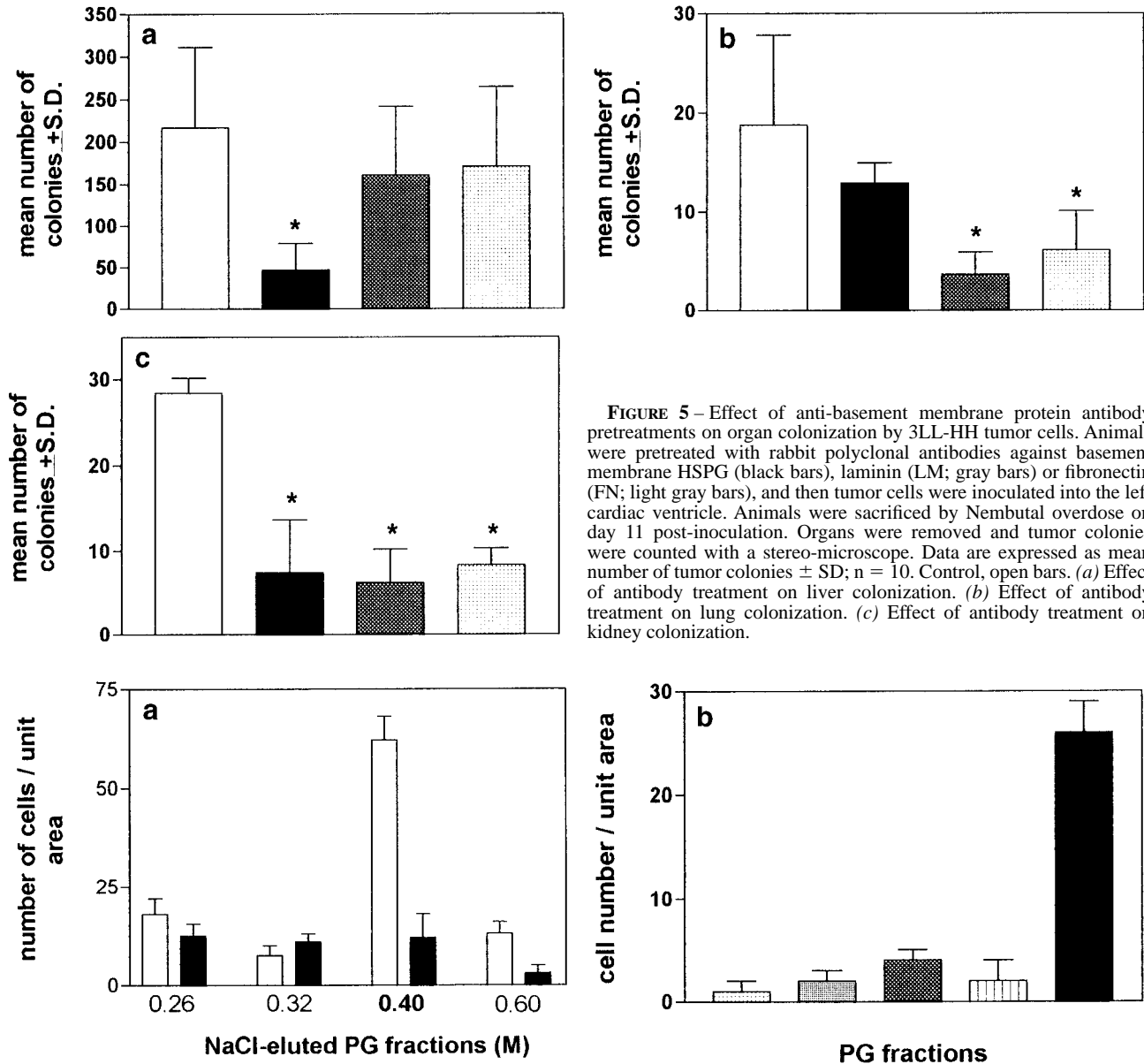


FIGURE 5—Effect of anti-basement membrane protein antibody pretreatments on organ colonization by 3LL-HH tumor cells. Animals were pretreated with rabbit polyclonal antibodies against basement membrane HSPG (black bars), laminin (LM; gray bars) or fibronectin (FN; light gray bars), and then tumor cells were inoculated into the left cardiac ventricle. Animals were sacrificed by Nembutal overdose on day 11 post-inoculation. Organs were removed and tumor colonies were counted with a stereo-microscope. Data are expressed as mean number of tumor colonies \pm SD; n = 10. Control, open bars. (a) Effect of antibody treatment on liver colonization. (b) Effect of antibody treatment on lung colonization. (c) Effect of antibody treatment on kidney colonization.

FIGURE 6—Effects of mouse liver proteoglycans (PG) on the 3LL-HH tumor cells *in vitro*. Proteoglycans were isolated from mouse liver and fractionated on a DEAE 52 column by NaCl gradient into 4 fractions (eluted by 0.26 M, 0.32 M, 0.4 M and 0.6 M NaCl). (a) Adhesion of tumor cells to liver proteoglycans *in vitro*. Tumor cells were incubated on PG-covered microvessels for 1 hr, preincubated with the anti-HSPG antibody (1 hr), washed with serum-free medium (2 \times) and counted under a phase contrast microscope. Data are expressed as number of adherent cells/unit area (using a 20 \times lens) \pm SD; n = 3. Control PG, proteoglycan substrate alone (open bars); PG + α -HSPG Ab, proteoglycan substrate covered by anti-HSPG antibody (black bars). (b) Chemotactic effect of liver proteoglycans on 3LL-HH cells *in vitro*. Boyden chamber assay. Tumor cells were placed on 8 μ m pore size filters for 4 hr, the isolated proteoglycans were used as chemoattractant and liver homogenate was used as positive control. Data are expressed as number of cells migrated/unit area \pm SD; n = 4. Dotted bar, PG/0.26 M; light gray bar, PG/0.32 M; dark gray bar, PG/0.40 M; striped bar, PG/0.60 M; black bar, liver-homogenate.

that the microvessel endothelium of the individual organs expresses an organ-specific membrane phenotype, providing a basis for organ-specific recognition of vessels by the disseminated intravascular tumor cells (Nicolson, 1988). Furthermore, it has been shown that the basement membrane proteins, as common ECM components of organs, are also expressed in an organ-specific manner, providing another tool for selective recognition. A third aspect of the organ specificity of the metastatization is the local cytokine milieu, which provides a unique and organ-specific paracrine mechanism for the local regulation of metastasis-associated events, such as tumor cell-extracellular matrix interaction and proliferation (Nicolson, 1993).

Our present and previous data indicate that 3LL-HH cells do not specifically recognize the liver tissue sections or the liver cells themselves (Lapis *et al.*, 1986), and the liver homogenate does not provide a specific motogenic signal. However, blocking of the basement membrane HSPG epitopes *in vivo* by the pretreatment of mice with a polyclonal antibody inhibits the liver and kidney colonization by 3LL-HH cells. In the case of the liver, it is the only basement membrane component that is important, according to our *in vivo* data. Interestingly, in other organs such as lung or kidney, laminin or fibronectin proved to be equally or more important than HSPG. The role of a selective antibody-mediated effector cell-dependent cytotoxicity against 3LL-HH cells *in vivo* is highly

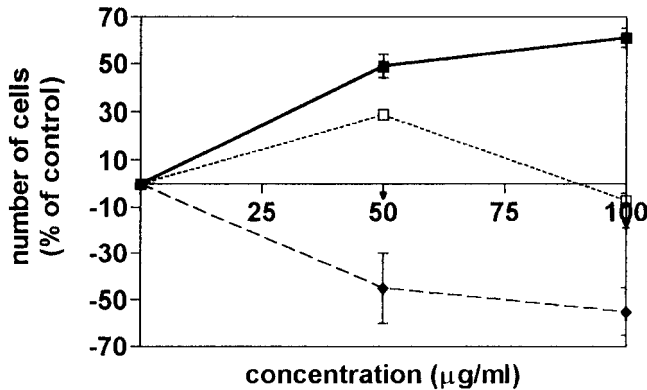


FIGURE 7 – Effect of glycosaminoglycans (GAG) on the proliferation of 3LL-HH cells *in vitro*. Tumor cells were treated with various GAGs for 48 hr in RPMI/5% FCS and the number of viable cells was determined as the end point. Cell number in untreated wells was considered as control and data are expressed as percent of change compared with control \pm SD; n = 3. HS, heparan sulfate (■); HP, heparin (□); CS, chondroitin sulfate (▼); HA, hyaluronic acid (◆).

unlikely, since the 3LL-HH cells are resistant to non-immune effectors *in vitro* and *in vivo* (Ladányi *et al.*, 1993) and spleen cells were not cytotoxic for 3LL-HH cells *in vitro* in the presence of the anti-HSPG antibody.

Our present results call attention to the importance of basement membrane heparan sulfate PGs in the regulation of liver metastasis formation. Immunofluorescence studies and biochemistry provided evidence that perlecan, the major HSPG component of basement membranes, localizes to sinusoids of the liver lobules besides the elementary bile ducts and major vessels (Gallai *et al.*, 1996). Perlecan is produced by endothelial and Ito cells (Rescan *et al.*, 1993; Gallai *et al.*, 1996) whereas hepatocytes express syndecan, a small transmembrane HSPG (Kovalszky *et al.*, 1994). Since 3LL-HH tumor cells extravasate to the liver parenchyma predominantly from liver sinusoids (Paku and Lapis, 1993), interaction with the subendothelial basement membrane must be considered as the first interaction of tumor cells with the local extracellular matrix. 3LL-HH cells were shown to recognize the HSPG fraction of mouse liver in an adhesion assay, and this could be abrogated by an anti-HSPG antibody, suggesting specificity of the interaction. What could be the significance of such an interaction? Basement

membranes are not only boundaries between various tissue compartments but also provide a source for local regulatory molecules involved in tissue differentiation or remodeling (Vlodavsky *et al.*, 1993). Tumor cells are able to proliferate on or migrate along basement membrane of the target organ during metastasis formation (Paku *et al.*, 1990). Since a great majority of cytokines are characterized by their heparan sulfate binding potential (Ruoslahti and Yamaguchi, 1991), it is well accepted that basement membrane HSPG(s) is responsible for such a storage function. In the case of the liver tissue, local growth factors are hepatocyte growth factor (HGF), transforming growth factor- α (TGF- α) and basic fibroblast growth factor (bFGF) (Michalopoulos, 1990). HGF is produced by Ito cells (Ramadori *et al.*, 1992) localized in the perisinusoidal area, whereas TGF- α is produced by proliferating hepatic cells (Michalopoulos, 1990). Other cytokines such as TGF- β are mostly produced by mesenchymal cells (macrophages, fibroblasts and Ito cells) accumulating in the portal area (Michalopoulos, 1990). It is tempting to speculate that the peri-sinusoidal basement membrane may store heparin-binding cytokines, which may affect tumor cell extravasation into the liver parenchyma. Analysis of the putative function of liver-derived HSPG in the metastatic cascade indicated that this HSPG (perlecan) is a preferred adhesive substrate for 3LL-HH tumor cells, but it is not chemotactic for them. We also provided evidence that only heparan sulfate, but not other GAGs, is mitogenic for 3LL-HH cells, suggesting another possible role for liver-derived HS(PG) in tumor metastasis.

Previous studies suggested that liver-metastatic tumor cells, irrespective of their tissue of origin (carcinoma or melanoma), overexpress heparan sulfate and HSPGs. However, no clear connection of this phenotypic marker to the liver metastatic potential has been elucidated (Tímár *et al.*, 1987, 1992). We suggest that local heparan sulfate-binding cytokines of the liver (HGF, TGF β , bFGF) may localize in the peri-sinusoidal area temporarily associated with HSPG/perlecan. These molecules could be mitogenic and/or motogenic for tumor cells expressing appropriate receptors and HSPG at the cell surface. Interference with the local recognition of perlecan-bound cytokines by anti-HSPG antibody may disrupt the sequence of key events in the metastatic cascade of the liver by decreasing the efficiency of extravasation, migration and local proliferation of tumor cells.

ACKNOWLEDGEMENTS

This work was supported by a grant from the National Science Foundation (OTKA 13128) to J.T.

REFERENCES

- DINGEMANS, K.P., ROOS, E., VAN DE BERG-WEERMAN, M.A. and VAN DE PAVERT, I.V., Invasion of liver tissue by tumor cells and leukocytes: comparative ultrastructure. *J. nat. Cancer Inst.*, **60**, 583–598 (1978).
- GALLAI, M., KOVALSZKY, I., KNITTEL, T., NEUBAUER, K., ARMBRUST, T. and RAMADORI, G., Expression of extracellular matrix proteoglycans perlecan and decorin in carbon-tetrachloride-injured rat liver and isolated liver cells. *Amer. J. Pathol.*, **148**, 1463–1471 (1996).
- GRIFFITHS, M.R., KEIR, S. and BURT, A.D., Basement membrane proteins in the space of Disse: a reappraisal. *J. clin. Pathol.*, **44**, 646–648 (1991).
- HAMADA, J., CAVANAUGH, P.G., MIKI, K. and NICOLSON, G.L., A paracrine migration stimulating factor metastatic tumor cells secreted by mouse hepatic sinusoidal endothelial cells: identification as complement component C3b. *Cancer Res.*, **53**, 4418–4423 (1993).
- HARTREE, E.F., Determination of protein: a modification of the Lowry method that gives a linear photometric response. *Anal. Biochem.*, **48**, 422–427 (1972).
- HONN, K.V. and TANG, D.G., Adhesion molecules and tumor cell interaction with endothelium and subendothelial matrix. *Cancer Metastasis Rev.*, **11**, 353–375 (1992).
- KOVALSZKY, I., GALLAI, M., ARMBRUST, T. and RAMADORI, G., Syndecan-1 gene expression in isolated rat liver cells (hepatocytes, Kupffer cells, endothelial and Ito cells). *Biochem. biophys. Res. Comm.*, **204**, 944–949 (1994).
- LADÁNYI, A., TÍMÁR, J. and LAPIS, K., Effect of lentinan on macrophage cytotoxicity against metastatic tumor cells. *Cancer Immunol. Immunother.*, **36**, 123–127 (1993).
- LAPIS, K., TÍMÁR, J., TÍMÁR, F., PÁL, K. and KOPPER, L., Differences in cell surface characteristics of poorly and highly metastatic Lewis lung tumor variants. In: K. Lapis, L.A. Liotta and A.S. Rabson (eds.), *Biochemistry and molecular genetics of cancer metastasis*, pp. 225–235, Nijhoff, Boston (1986).
- LIOTTA, L., Tumor invasion and metastasis—role of the extracellular matrix. *Cancer Res.*, **46**, 1–7 (1986).
- LONG, L.I., NIP, J. and BRODT, P., Paracrine growth stimulation by hepatocyte-derived insulin-like growth factor-1: a regulatory mechanism for carcinoma cells metastatic to the liver. *Cancer Res.*, **54**, 1732–1737 (1994).
- LYON, M. and GALLAGHER, J.T., Purification and partial characterization of the major cell-associated heparan sulfate proteoglycan of rat liver. *Biochem. J.*, **273**, 415–422 (1991).
- MICHALOPOULOS, G.K., Liver regeneration: molecular mechanisms of growth control. *FASEB J.*, **4**, 176–187 (1990).
- NICOLSON, G.L., Organ specificity of tumor metastasis: role of preferential

- adhesion, invasion and growth of malignant cells at specific secondary sites. *Cancer Metastasis Rev.*, **7**, 143–188 (1988).
- NICOLSON, G.L., Paracrine and autocrine growth mechanism in tumor metastasis to specific sites with particular emphasis on brain and lung metastasis. *Cancer Metastasis Rev.*, **12**, 325–343 (1993).
- PAKU, S. and LAPIS, K., Morphological aspects of angiogenesis in experimental liver metastasis. *Amer. J. Pathol.*, **143**, 926–936 (1993).
- PAKU, S., ROT, A., LADÁNYI, A. and LAPIS, K., Demonstration of the organ preference of liver selected high metastatic Lewis lung tumor cell line. *Clin. exp. Metastasis*, **7**, 599–607 (1989).
- PAKU, S., TÍMÁR, J. and LAPIS, K., Ultrastructure of invasion in different tissue types by Lewis lung tumor variants. *Virchows Arch. A.*, **417**, 435–442 (1990).
- PÁL, K., KOPPER, L. and LAPIS, K., Increased metastatic capacity of Lewis lung tumor cells by in vivo selection procedure. *Invasion Metastasis*, **3**, 174–185 (1983).
- RAMADORI, G., NEUBAUER, K., ODENTHAL, M., NAKAMURA, T., KNITTEL, T., SCHWOGEL, S. and MAYER ZUM BUSCHENFELDE, K.-H., The gene of hepatocyte growth factor is expressed in fat-storing cells of rat liver and is downregulated during cell growth and by transforming growth factor β . *Biochem. biophys. Res. Comm.*, **183**, 739–742 (1992).
- RESCAN, P.-Y., LOREAL, O., HASSELL, J.R., YAMADA, Y., GUILLOUZO, A. and CLEMENT, B., Distribution and origin of the basement membrane component perlecan in rat liver and primary hepatocyte culture. *Amer. J. Pathol.*, **142**, 199–208 (1993).
- RUOSLAHTI, E. and YAMAGUCHI, Y., Proteoglycans as modulators of growth factor activities. *Cell*, **64**, 867–869 (1991).
- TÍMÁR, J. and KOVALSZKY, I., Differential expression of proteoglycans on the surface of malignant cells and in the tumor stroma. In: R. Adany (ed.), *Tumor matrix biology*, pp. 23–55, CRC Press, Boca Raton, FL (1995).
- TÍMÁR, J., LADÁNYI, A., LAPIS, K. and MOCZAR, M., Differential expression of proteoglycans on the surface of human melanoma cells characterized by altered experimental metastatic potential. *Amer. J. Pathol.*, **141**, 467–474 (1992).
- TÍMÁR, J., MOCZAR, E., TÍMÁR, F., PÁL, K., KOPPER, L., JENEY, A. and LAPIS, K., Comparative study on Lewis lung tumor lines with low and high metastatic capacity. II. Cytochemical and biochemical differences of glycosaminoglycans. *Clin. exp. Metastasis*, **7**, 659–669 (1987).
- VLODAVSKY, I., BAR-SHAVIT, R., KORNER, G. and FUKS, Z., Extracellular matrix-bound growth factors, enzymes and plasma proteins. In: D.H. Rohrbach and R. Timpl (eds.), *Molecular and cellular aspects of basement membranes*, pp. 327–343, Academic Press, New York (1993).